

Advances in Civil Engineering

# Advancements in the Analysis and Design of Protective Structures against Extreme Loadings 2020

Lead Guest Editor: Li Chen

Guest Editors: Xihong Zhang,, Yanchao Shi, Tuan Ngo, Chiara Bedon, and Piotr Sielicki





---

**Advancements in the Analysis and Design of  
Protective Structures against Extreme Loadings  
2020**



Advances in Civil Engineering

---

**Advancements in the Analysis and  
Design of Protective Structures against  
Extreme Loadings 2020**

Lead Guest Editor: Li Chen

Guest Editors: Xihong Zhang,, Yanchao Shi, Tuan  
Ngo, Chiara Bedon, and Piotr Sielicki



---

Copyright © 2020 Hindawi Limited. All rights reserved.

This is a special issue published in "Advances in Civil Engineering." All articles are open access articles distributed under the Creative Commons Attribution License, which permits unrestricted use, distribution, and reproduction in any medium, provided the original work is properly cited.








# Chief Editor

Cumaraswamy Vipulanandan, USA













## Associate Editors

Chiara Bedon , Italy  
Constantin Chalioris , Greece  
Ghassan Chehab , Lebanon  
Ottavia Corbi, Italy  
Mohamed ElGawady , USA  
Husnain Haider , Saudi Arabia  
Jian Ji , China  
Jiang Jin , China  
Shazim A. Memon , Kazakhstan  
Hossein Moayedi , Vietnam  
Sanjay Nimbalkar, Australia  
Giuseppe Oliveto , Italy  
Alessandro Palmeri , United Kingdom  
Arnaud Perrot , France  
Hugo Rodrigues , Portugal  
Victor Yepes , Spain  
Xianbo Zhao , Australia

## Academic Editors

José A.F.O. Correia, Portugal  
Glenda Abate, Italy  
Khalid Abdel-Rahman , Germany  
Ali Mardani Aghabaglou, Turkey  
José Aguiar , Portugal  
Afaq Ahmad , Pakistan  
Muhammad Riaz Ahmad , Hong Kong  
Hashim M.N. Al-Madani , Bahrain  
Luigi Aldieri , Italy  
Angelo Aloisio , Italy  
Maria Cruz Alonso, Spain  
Filipe Amarante dos Santos , Portugal  
Serji N. Amirkhanean, USA  
Eleftherios K. Anastasiou , Greece  
Panagiotis Ch. Anastasopoulos , USA  
Mohamed Moafak Arbili , Iraq  
Farhad Aslani , Australia  
Siva Avudaiappan , Chile  
Ozgur BASKAN , Turkey  
Adewumi Babafemi, Nigeria  
Morteza Bagherpour, Turkey  
Qingsheng Bai , Germany  
Nicola Baldo , Italy  
Daniele Baraldi , Italy

Eva Barreira , Portugal  
Emilio Bastidas-Arteaga , France  
Rita Bento, Portugal  
Rafael Bergillos , Spain  
Han-bing Bian , China  
Xia Bian , China  
Huseyin Bilgin , Albania  
Giovanni Biondi , Italy  
Hugo C. Biscaia , Portugal  
Rahul Biswas , India  
Edén Bojórquez , Mexico  
Giosuè Boscato , Italy  
Melina Bosco , Italy  
Jorge Branco , Portugal  
Bruno Briseghella , China  
Brian M. Broderick, Ireland  
Emanuele Brunesi , Italy  
Quoc-Bao Bui , Vietnam  
Tan-Trung Bui , France  
Nicola Buratti, Italy  
Gaochuang Cai, France  
Gladis Camarini , Brazil  
Alberto Campisano , Italy  
Qi Cao, China  
Qixin Cao, China  
Iacopo Carnacina , Italy  
Alessio Cascardi, Italy  
Paolo Castaldo , Italy  
Nicola Cavalagli , Italy  
Liborio Cavaleri , Italy  
Anush Chandrappa , United Kingdom  
Wen-Shao Chang , United Kingdom  
Muhammad Tariq Amin Chaudhary, Kuwait  
Po-Han Chen , Taiwan  
Qian Chen , China  
Wei Tong Chen , Taiwan  
Qixiu Cheng, Hong Kong  
Zhanbo Cheng, United Kingdom  
Nicholas Chileshe, Australia  
Prinya Chindaprasirt , Thailand  
Corrado Chisari , United Kingdom  
Se Jin Choi , Republic of Korea  
Heap-Yih Chong , Australia  
S.H. Chu , USA  
Ting-Xiang Chu , China

Zhaofei Chu , China  
Wonseok Chung , Republic of Korea  
Donato Ciampa , Italy  
Gian Paolo Cimellaro, Italy  
Francesco Colangelo, Italy  
Romulus Costache , Romania  
Liviu-Adrian Cotfas , Romania  
Antonio Maria D'Altri, Italy  
Bruno Dal Lago , Italy  
Amos Darko , Hong Kong  
Arka Jyoti Das , India  
Dario De Domenico , Italy  
Gianmarco De Felice , Italy  
Stefano De Miranda , Italy  
Maria T. De Risi , Italy  
Tayfun Dede, Turkey  
Sadik O. Degertekin , Turkey  
Camelia Delcea , Romania  
Cristoforo Demartino, China  
Giuseppe Di Filippo , Italy  
Luigi Di Sarno, Italy  
Fabio Di Trapani , Italy  
Aboelkasim Diab , Egypt  
Thi My Dung Do, Vietnam  
Giulio Dondi , Italy  
Jiangfeng Dong , China  
Chao Dou , China  
Mario D'Aniello , Italy  
Jingtao Du , China  
Ahmed Elghazouli, United Kingdom  
Francesco Fabbrocino , Italy  
Flora Faleschini , Italy  
Dingqiang Fan, Hong Kong  
Xueping Fan, China  
Qian Fang , China  
Salar Farahmand-Tabar , Iran  
Ilenia Farina, Italy  
Roberto Fedele, Italy  
Guang-Liang Feng , China  
Luigi Fenu , Italy  
Tiago Ferreira , Portugal  
Marco Filippo Ferrotto, Italy  
Antonio Formisano , Italy  
Guoyang Fu, Australia  
Stefano Galassi , Italy


Junfeng Gao , China  
Meng Gao , China  
Giovanni Garcea , Italy  
Enrique García-Macías, Spain  
Emilio García-Taengua , United Kingdom  
DongDong Ge , USA  
Khaled Ghaedi, Malaysia  
Khaled Ghaedi , Malaysia  
Gian Felice Giaccu, Italy  
Agathoklis Giaralis , United Kingdom  
Ravindran Gobinath, India  
Rodrigo Gonçalves, Portugal  
Peilin Gong , China  
Belén González-Fonteboa , Spain  
Salvatore Grasso , Italy  
Fan Gu, USA  
Erhan Güneyisi , Turkey  
Esra Mete Güneyisi, Turkey  
Pingye Guo , China  
Ankit Gupta , India  
Federico Gusella , Italy  
Kemal Hacıefendioğlu, Turkey  
Jianyong Han , China  
Song Han , China  
Asad Hanif , Macau  
Hadi Hasanzadehshooiili , Canada  
Mostafa Fahmi Hassanein, Egypt  
Amir Ahmad Hedayat , Iran  
Khandaker Hossain , Canada  
Zahid Hossain , USA  
Chao Hou, China  
Biao Hu, China  
Jiang Hu , China  
Xiaodong Hu, China  
Lei Huang , China  
Cun Hui , China  
Bon-Gang Hwang, Singapore  
Jijo James , India  
Abbas Fadhil Jasim , Iraq  
Ahad Javanmardi , China  
Krishnan Prabhakan Jaya, India  
Dong-Sheng Jeng , Australia  
Han-Yong Jeon, Republic of Korea  
Pengjiao Jia, China  
Shaohua Jiang , China



MOUSTAFA KASSEM , Malaysia  
Mosbeh Kaloop , Egypt  
Shankar Karuppanan , Ethiopia  
John Kechagias , Greece  
Mohammad Khajehzadeh , Iran  
Afzal Husain Khan , Saudi Arabia  
Mehran Khan , Hong Kong  
Manoj Khandelwal, Australia  
Jin Kook Kim , Republic of Korea  
Woosuk Kim , Republic of Korea  
Vaclav Koci , Czech Republic  
Loke Kok Foong, Vietnam  
Hailing Kong , China  
Leonidas Alexandros Kouris , Greece  
Kyriakos Kourousis , Ireland  
Moacir Kripka , Brazil  
Anupam Kumar, The Netherlands  
Emma La Malfa Ribolla, Czech Republic  
Ali Lakirouhani , Iran  
Angus C. C. Lam, China  
Thanh Quang Khai Lam , Vietnam  
Luciano Lamberti, Italy  
Andreas Lampropoulos , United Kingdom  
Raffaele Landolfo, Italy  
Massimo Latour , Italy  
Bang Yeon Lee , Republic of Korea  
Eul-Bum Lee , Republic of Korea  
Zhen Lei , Canada  
Leonardo Leonetti , Italy  
Chun-Qing Li , Australia  
Dongsheng Li , China  
Gen Li, China  
Jiale Li , China  
Minghui Li, China  
Qingchao Li , China  
Shuang Yang Li , China  
Sunwei Li , Hong Kong  
Yajun Li , China  
Shun Liang , China  
Francesco Liguori , Italy  
Jae-Han Lim , Republic of Korea  
Jia-Rui Lin , China  
Kun Lin , China  
Shibin Lin, China

Tzu-Kang Lin , Taiwan  
Yu-Cheng Lin , Taiwan  
Hexu Liu, USA  
Jian Lin Liu , China  
Xiaoli Liu , China  
Xuemei Liu , Australia  
Zaobao Liu , China  
Zhuang-Zhuang Liu, China  
Diego Lopez-Garcia , Chile  
Cristiano Loss , Canada  
Lyan-Ywan Lu , Taiwan  
Jin Luo , USA  
Yanbin Luo , China  
Jianjun Ma , China  
Junwei Ma , China  
Tian-Shou Ma, China  
Zhongguo John Ma , USA  
Maria Macchiaroli, Italy  
Domenico Magisano, Italy  
Reza Mahinroosta, Australia  
Yann Malecot , France  
Prabhat Kumar Mandal , India  
John Mander, USA  
Iman Mansouri, Iran  
André Dias Martins, Portugal  
Domagoj Matesan , Croatia  
Jose Matos, Portugal  
Vasant Matsagar , India  
Claudio Mazzotti , Italy  
Ahmed Mebarki , France  
Gang Mei , China  
Kasim Mermerdas, Turkey  
Giovanni Minafò , Italy  
Masoomah Mirrashid , Iran  
Abbas Mohajerani , Australia  
Fadzli Mohamed Nazri , Malaysia  
Fabrizio Mollaioli , Italy  
Rosario Montuori , Italy  
H. Naderpour , Iran  
Hassan Nasir , Pakistan  
Hossein Nassiraei , Iran  
Satheeskumar Navaratnam , Australia  
Ignacio J. Navarro , Spain  
Ashish Kumar Nayak , India  
Behzad Nematollahi , Australia

Chayut Ngamkhanong , Thailand  
Trung Ngo, Australia  
Tengfei Nian, China  
Mehdi Nikoo , Canada  
Youjun Ning , China  
Olugbenga Timo Oladinrin , United Kingdom  
Oladimeji Benedict Olalusi, South Africa  
Timothy O. Olawumi , Hong Kong  
Alejandro Orfila , Spain  
Maurizio Orlando , Italy  
Siti Aminah Osman, Malaysia  
Walid Oueslati , Tunisia  
SUVASH PAUL , Bangladesh  
John-Paris Pantouvakis , Greece  
Fabrizio Paolacci , Italy  
Giuseppina Pappalardo , Italy  
Fulvio Parisi , Italy  
Dimitrios G. Pavlou , Norway  
Daniele Pellegrini , Italy  
Gatheeshgar Perampalam , United Kingdom  
Daniele Perrone , Italy  
Giuseppe Piccardo , Italy  
Vagelis Plevris , Qatar  
Andrea Pranno , Italy  
Adolfo Preciado , Mexico  
Chongchong Qi , China  
Yu Qian, USA  
Ying Qin , China  
Giuseppe Quaranta , Italy  
Krishanu ROY , New Zealand  
Vlastimir Radonjanin, Serbia  
Carlo Rainieri , Italy  
Rahul V. Ralegaonkar, India  
Raizal Saifulnaz Muhammad Rashid, Malaysia  
Alessandro Rasulo , Italy  
Chonghong Ren , China  
Qing-Xin Ren, China  
Dimitris Rizos , USA  
Geoffrey W. Rodgers , New Zealand  
Pier Paolo Rossi, Italy  
Nicola Ruggieri , Italy  
JUNLONG SHANG, Singapore

Nikhil Saboo, India  
Anna Saetta, Italy  
Juan Sagaseta , United Kingdom  
Timo Saksala, Finland  
Mostafa Salari, Canada  
Ginevra Salerno , Italy  
Evangelos J. Sapountzakis , Greece  
Vassilis Sarhosis , United Kingdom  
Navaratnarajah Sathiparan , Sri Lanka  
Fabrizio Scozzese , Italy  
Halil Sezen , USA  
Payam Shafigh , Malaysia  
M. Shahria Alam, Canada  
Yi Shan, China  
Hussein Sharaf, Iraq  
Mostafa Sharifzadeh, Australia  
Sanjay Kumar Shukla, Australia  
Amir Si Larbi , France  
Okan Sirin , Qatar  
Piotr Smarzewski , Poland  
Francesca Sollecito , Italy  
Rui Song , China  
Tian-Yi Song, Australia  
Flavio Stochino , Italy  
Mayank Sukhija , USA  
Piti Sukontasukkul , Thailand  
Jianping Sun, Singapore  
Xiao Sun , China  
T. Tafsirojjaman , Australia  
Fujiao Tang , China  
Patrick W.C. Tang , Australia  
Zhi Cheng Tang , China  
Weerachart Tangchirapat , Thailand  
Xiixin Tao, China  
Piergiorgio Tataranni , Italy  
Elisabete Teixeira , Portugal  
Jorge Iván Tobón , Colombia  
Jing-Zhong Tong, China  
Francesco Trentadue , Italy  
Antonello Troncone, Italy  
Majbah Uddin , USA  
Tariq Umar , United Kingdom  
Muahmmad Usman, United Kingdom  
Muhammad Usman , Pakistan  
Mucteba Uysal , Turkey





Ilaria Venanzi , Italy  
Castorina S. Vieira , Portugal  
Valeria Vignali , Italy  
Claudia Vitone , Italy  
Liwei WEN , China  
Chunfeng Wan , China  
Hua-Ping Wan, China  
Roman Wan-Wendner , Austria  
Chaohui Wang , China  
Hao Wang , USA  
Shiming Wang , China  
Wayne Yu Wang , United Kingdom  
Wen-Da Wang, China  
Xing Wang , China  
Xiuling Wang , China  
Zhenjun Wang , China  
Xin-Jiang Wei , China  
Tao Wen , China  
Weiping Wen , China  
Lei Weng , China  
Chao Wu , United Kingdom  
Jiangyu Wu, China  
Wangjie Wu , China  
Wenbing Wu , China  
Zhixing Xiao, China  
Gang Xu, China  
Jian Xu , China  
Panpan , China  
Rongchao Xu , China  
HE YONGLIANG, China  
Michael Yam, Hong Kong  
Hailu Yang , China  
Xu-Xu Yang , China  
Hui Yao , China  
Xinyu Ye , China  
Zhoujing Ye, China  
Gürol Yildirim , Turkey  
Dawei Yin , China  
Doo-Yeol Yoo , Republic of Korea  
Zhanping You , USA  
Afshar A. Yousefi , Iran  
Xinbao Yu , USA  
Dongdong Yuan , China  
Geun Y. Yun , Republic of Korea


Hyun-Do Yun , Republic of Korea  
Cemal YİĞİT , Turkey  
Paolo Zampieri, Italy  
Giulio Zani , Italy  
Mariano Angelo Zanini , Italy  
Zhixiong Zeng , Hong Kong  
Mustafa Zeybek, Turkey  
Henglong Zhang , China  
Jiupeng Zhang, China  
Tingting Zhang , China  
Zengping Zhang, China  
Zetian Zhang , China  
Zhigang Zhang , China  
Zhipeng Zhao , Japan  
Jun Zhao , China  
Annan Zhou , Australia  
Jia-wen Zhou , China  
Hai-Tao Zhu , China  
Peng Zhu , China  
QuanJie Zhu , China  
Wenjun Zhu , China  
Marco Zucca, Italy  
Haoran Zuo, Australia  
Junqing Zuo , China  
Robert Černý , Czech Republic  
Süleyman İpek , Turkey

# Contents

## **Analysis of Hazard Area of Dispersion Caused by Leakage from Underground Gas-Storage Caverns in Salt Rock**

Ya Yang, Shigang Yang , Zhan Li , Qin Fang, Jianhua Wu, Jiongwei Cai, and Wensheng Sun  
Research Article (11 pages), Article ID 8876646, Volume 2020 (2020)

## **Partitioned Strong Coupling of Discrete Elements with Large Deformation Structural Finite Elements to Model Impact on Highly Flexible Tension Structures**

Klaus Bernd Sautter , Tobias Teschemacher, Miguel Ángel Celigueta, Philipp Bucher, Kai-Uwe Bletzinger, and Roland Wüchner  
Research Article (28 pages), Article ID 5135194, Volume 2020 (2020)

## **Investigation on Influences of Two Discrete Methods on Galloping Characteristics of Iced Quad Bundle Conductors**

Xiaohui Liu , Guangyun Min , Chuan Wu , and Mengqi Cai   
Research Article (17 pages), Article ID 8818728, Volume 2020 (2020)


## **Experimental Investigation of Unloading-Induced Red Sandstone Failure: Insight into Spalling Mechanism and Strength-Weakening Effect**

Yong Luo , Fengqiang Gong , and Dongqiao Liu  
Research Article (16 pages), Article ID 8835355, Volume 2020 (2020)



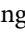
## **Numerical Evaluation of Reinforced Concrete Columns Retrofitted with FRP for Blast Mitigation**

Jing Dong , Junhai Zhao , and Dongfang Zhang   
Research Article (14 pages), Article ID 8884133, Volume 2020 (2020)

## **A Method for Determining Feasibility of Mining Residual Coal above Out-Fashioned Goaf under Variable Load: A Case Study**

Yuxia Guo, Honghui Yuan, Xiaogang Deng, Yujiang Zhang , Yunlou Du, Hui Liu, Guorui Feng, Jiali Xu, Renle Zhao, and Dao Viet Doan  
Research Article. (12 pages), Article ID 8837657, Volume 2020 (2020)



## **Assessment of Cascading Accidents of Frostbite, Fire, and Explosion Caused by Liquefied Natural Gas Leakage**

Chengjun Yue , Li Chen , Hengbo Xiang , Linfeng Xu, Shigang Yang, Zhan Li, Chenxi Xia, and Qin Fang  
Research Article (14 pages), Article ID 8867202, Volume 2020 (2020)


## **Experimental Investigation on Strength and Deformation Characteristics of Red Sandstone at Strain Rates of $10^{-2}$ – $55$ s $^{-1}$**

Jie Shi, Zongmu Luo , Huachao Liu , Dan Wang, Haipeng Shen, and Zeng Li  
Research Article (9 pages), Article ID 8882976, Volume 2020 (2020)

## **Experimental and Mathematical Modeling of Monotonic Behavior of Calcareous Sand**


Haotian Zhang, Zongmu Luo , Yanyu Qiu, Huachao Liu , Juan Gu, and Jian Tang  
Research Article (14 pages), Article ID 8861605, Volume 2020 (2020)

**Computation Method for the Settlement of a Vertically Loaded Pile in Sloping Ground**

Chong Jiang , Wen-yan Wu, Jia-li He, and Lu-jie Chen




Research Article (10 pages), Article ID 2109535, Volume 2020 (2020)

**Physical Modelling of Roll and Pitch Motions of Travelling or Stationary Ship in Large-Scale Landslide-Generated Waves**

Pei-yin Yuan , Ping-yi Wang, and Yu Zhao


Research Article (11 pages), Article ID 8857604, Volume 2020 (2020)

**Experimental and Theoretical Analysis for Isolation Performance of New Combined Isolation Devices under Blast Loading**

Yang Liu, Zhen Liao , Yulong Xue , Zhizhong Li , Luzhong Shao, and Degao Tang

Research Article (13 pages), Article ID 8425785, Volume 2020 (2020)

**Replacing Detonation by Compressed Balloon Approaches in Finite Element Models**

Pierre Legrand, S. Kerampran, and M. Arrigoni 

Research Article (16 pages), Article ID 1497632, Volume 2020 (2020)

## Research Article

# Analysis of Hazard Area of Dispersion Caused by Leakage from Underground Gas-Storage Caverns in Salt Rock

Ya Yang, Shigang Yang , Zhan Li , Qin Fang, Jianhua Wu, Jiongwei Cai, and Wensheng Sun

National Defense College of Engineering, Army Engineering University of PLA, Nanjing 210007, China

Correspondence should be addressed to Shigang Yang; [youngshg@126.com](mailto:youngshg@126.com) and Zhan Li; [lz.9008@163.com](mailto:lz.9008@163.com)

Received 23 April 2020; Revised 19 October 2020; Accepted 30 October 2020; Published 18 December 2020

Academic Editor: Jian Ji

Copyright © 2020 Ya Yang et al. This is an open access article distributed under the Creative Commons Attribution License, which permits unrestricted use, distribution, and reproduction in any medium, provided the original work is properly cited.

To provide information concerning quantitative risk analysis of gas-storage caverns, it is vital to estimate the hazard area of dispersion caused by accidental leakage. The Gaussian plume model is selected to calculate the hazard area caused by continuous leakage; the method of analysis is validated using wind-tunnel experiments of acetylene. Fluent is used to simulate the hazard area of dispersion caused by instantaneous leakage; the method of numerical simulation is verified by Burro/Coyote trials. Furthermore, a sample underground gas-storage cavern in salt rock is examined with respect to the toxic threshold limit value and the upper and lower flammability limits. In doing so, the factors that influence the hazard range of dispersion from salt cavern are discussed. The results indicate that the hazard area decreases with an increase in wind speed and a decrease in atmospheric stability when the leakage is continuous. However, the hazard area decreases with a decrease in wind speed when leakage is instantaneous.

## 1. Introduction

Deep underground salt caverns have been rapidly excavated and extensively utilized in developed European and American countries as “highly secure strategy energy reserve systems” ever since Canada first proposed the idea that rock caves can be used to store liquid and gas in the 1940s [1, 2]. According to statistics, more than 600 seats of natural gas underground storage caverns can be found over the world, with 9.8% of reservoirs built-in salt rock formations. Indeed, underground storage is one of the safest ways of storing large quantities of hydrocarbons. However, gas can leak into the air through the injection-well casing due to the impact of the rheological and mechanical properties of salt rock and due to periodic pressure fluctuations, corrosion, and accidents in construction and general reservoir use [3–5].

The main component of natural gas stored in salt-rock caverns is methane, which is a pure asphyxiating gas, which is harmless under normal circumstances. However, the oxygen content in the air decreases when the concentration of methane is too high; moreover, when the methane content in the premixed gas cloud is 25% to 30%, human beings can be

affected by dizziness, headache, fatigue, increased breathing and heartbeat, ataxia, and suffocation. According to the occupational exposure concentration limits in Switzerland, the allowable toxic threshold limit value (TLV) of methane is  $6,700 \text{ mg/m}^3$  [6]. Repair personnel entering this concentration area need to wear protective equipment. If the concentration of a regional gas cloud is between the lower flammability limit (LFL) and the upper flammability limit (UFL), fire and/or explosions are highly possible, which can cause significant harm to humans and buildings. The flammability limit (volume fraction) of the natural gas is usually 5.3% to 15.1%, corresponding to a concentration of  $35,800\text{--}107,500 \text{ mg/m}^3$  [7]. The area falling within the explosive concentration is called the explosive hazardous area; indeed, people located in this area should evacuate quickly. Therefore, the diffusion process of gas in the atmosphere requires examination after the injection-well casing of a salt-rock cavern fails, and the potential risk zones of gas leakage need to be determined. This will provide a scientific basis for the long-term use and safety control of underground storage caverns.

Many scholars have studied the risk of accidents from underground gas-storage caverns in salt rock. For example,

the nonlinear creep behavior of salt rock was described with a LUBBY2 constitutive model and ADINA software, and the criteria-grading salt-rock reservoir stability was given through numerical analysis by Heusermann et al. [8]. The design parameters that influence surface uplift have been examined by Kim et al. [9]. Contrucci et al. established a high-resolution microseismic monitoring system by examining the cavern collapse and ground-subsidence phenomenon of the Cerville-Buissoncourt salt-rock reservoir in France [10]. The gas-permeation law of salt-rock gas-storage caverns containing sandwiches was studied by Chen et al. [11], and the ground-subsidence patterns of salt-rock gas-storage caverns after destruction was studied by Wang et al. [12]. The stability of salt-rock reservoirs was analyzed by Ma et al. [13], and the jet-fire accident of salt-rock gas-storage caverns was evaluated by Yang et al. [14]. However, research concerning the security protection from leakage is currently lacking and hazard assessments on gas diffusion after leakage are yet to be reported. In this paper, the gas-diffusion model is analyzed and gas-diffusion hazards using relevant theoretical and numerical models, which are validated by experiments. Finally, a sample natural gas storage cavern in salt rock is analyzed with the proposed method and the dangerous areas associated with dispersion caused by leakage are determined according to industry occupational protection standards [15, 16].

## 2. Analysis Model of Hazard Area Associated with Gas Dispersion

The gas-diffusion mechanism has been a heavily debated topic ever since the 1980s. In particular, the flammable gas-diffusion mechanism has been studied using different

methods by many scholars [17, 18]. In doing so, self-preparation programs and commercial software have been developed to simulate gas dispersion.

Experimental research is vital in studying (and developing) fluid mechanics. However, experimental methods require a lot of time and labor. Moreover, precision experimental results require fine modern testing equipment and techniques, and it is difficult to examine complex-flow problems [19]. Therefore, in this paper, the hazard area associated with dispersion caused by leakage from underground gas-storage caverns in salt rock is analyzed using theoretical analysis and numerical simulations.

### 2.1. Theoretical Analysis of Diffusion from Continuous Release.

A number of gas-diffusion models are commonly used: Cox and Carpenter dense gas-diffusion model, the Britter and McQuaid model, the 3D finite-element model, the Gaussian model, the Sutton model, and the American Petroleum Institute gas-diffusion model. Among these models, the Gaussian model can be used with large amounts of data and sophisticated algorithms. In addition, it is relatively easy to use and its results are usually consistent with experimental results. Accordingly, it has been widely used [17, 20, 21].

For ground continuous-point source diffusion, the Gaussian plume model is commonly used to describe gas diffusion [7, 17, 22, 23].

- (1) For  $u > 1$  m/s, the concentration at the point  $(x, y, z)$  where the origin is the leak source and the wind direction is the  $x$ -axis can be calculated as follows:

$$C(x, y, z) = \frac{Q}{2\pi u \sigma_y \sigma_z} \exp\left(-\frac{y^2}{2\sigma_y^2}\right) \left\{ \exp\left[-\frac{(z-H)^2}{2\sigma_z^2}\right] + \exp\left[-\frac{(z+H)^2}{2\sigma_z^2}\right] \right\}, \quad (1)$$

where  $C(x, y, z)$  is the average concentration of the leakage gas at a certain point downwind  $(x, y, z)$  ( $\text{kg}/\text{m}^3$ );  $Q$  is the leakage source strength ( $\text{kg}/\text{s}$ );  $u$  is the average wind speed ( $\text{m}/\text{s}$ );  $H$  is the effective height of the leakage source, ( $\text{m}$ );  $\sigma_x$ ,  $\sigma_y$ , and  $\sigma_z$  are the diffusion coefficient in the direction of  $x$ ,  $y$ , and  $z$ -axis, respectively, ( $\text{m}$ );  $x$  is the downwind

distance, ( $\text{m}$ );  $y$  is the crosswind distance, ( $\text{m}$ );  $z$  is the height above the ground, ( $\text{m}$ ).

- (2) For  $u < 1$  m/s, taking the continuous leakage as the overlay of instantaneous leakage  $Q\Delta t$  in the time of  $\Delta t$ . Thus, the concentration at the point  $(x, y, z)$  where the origin is the leak source and the wind direction is the  $x$ -axis can be calculated as follows:

$$C(x, y, z, t) = \frac{Q_m}{(2\pi)^{3/2} \sigma_x \sigma_y \sigma_z} \exp\left(-\frac{y^2}{2\sigma_y^2}\right) \exp\left[-\frac{(x-ut)^2}{2\sigma_x^2}\right] \left\{ \exp\left[-\frac{(z-H)^2}{2\sigma_z^2}\right] + \exp\left[-\frac{(z+H)^2}{2\sigma_z^2}\right] \right\}, \quad (2)$$

where  $C(x, y, z, t)$  is time average concentration, ( $\text{kg}/\text{m}^3$ );  $t$  is release time( $\text{s}$ );  $Q_m$  is total mass of material release ( $\text{kg}$ ).

2.2. Numerical-Analysis Method of the Diffusion from Instantaneous Release. Since the 1970s, the numerical method based on computational fluid dynamics (CFD) has been



rapidly developing alongside the development of high-power computers and the development of computational methods, such as the finite-difference method, the finite-element method, and the finite-volume method [24]. In addition, on the basis of the theoretical and experimental study, research institutions have developed a number of software systems based on CFD that can simulate gas diffusion, such as DEGADIS developed by the US Coast Guard and the Gas Institute Ltd., the HGSYSTEM developed by American Shell Institute Ltd with the support of 20 chemical and petrochemical companies, the EXSIM developed by the University of Aalborg in Denmark, FLACS developed by Christian Michelsen Institute in Norwegian, PHOENICS developed by the British CHAM Company, CFX developed by UK AEA Technology, STAR-CD developed jointly by Imperial College Institute and CD-adapco Group, and Fluent developed by the FLUENT in the US [19, 25, 26].

### 3. Model Validation

*3.1. Experimental Validation of Theoretical Analysis.* A simple wind tunnel was designed and manufactured by Xu in 1998 [27], as shown in Figure 1. Using this wind tunnel, a number of tests of the horizontal injection diffusion were carried out at different discharge conditions; the actual concentration distribution of acetylene was obtained after gas diffusion and the general laws of gas diffusion were obtained by examining the wind speed and discharge rate. The test data are listed in Table 1.

The mass-volume concentration of acetylene in the wind-tunnel test was calculated using the Gaussian plume model (Equation (1), with the preferably atmospheric stability class D), which was then converted into volume-concentration using equation (3) and compared with experimental data. The results are shown in Figure 2.

$$V = \frac{22.4 \cdot C}{M_w} \times 100, \quad (3)$$

where  $V$  is volume concentration (%);  $C$  is quality-volume concentration ( $\text{kg}/\text{m}^3$ );  $M_w$  is molar mass ( $\text{kg}/\text{kmol}$ ).

From Figure 2, it is evident that the theoretical volume concentration is essentially consistent with the results from the small wind-tunnel tests; with the increase of the gas-release rate, the turbulence of the airflow in the position closer to the discharge pipe mouth is intensified, resulting in uneven mixing of acetylene and air, making the experimental result smaller. But any deviations between calculated and observed values are less than 20%. Accordingly, using the Gaussian plume model is feasible and reasonable.

*3.2. Experimental Validation of Numerical Analysis.* The commercial software of Fluent was selected to simulate the gas-diffusion law. Burro/Coyote series trials were used as verification examples, which were completed by the Lawrence Livermore National Lab in China Lake of California in 1980. The trials concerned continuous leakage from liquefied natural gas (LNG) in the water surface, with a total of 18 diffusions and five combustion tests carried out. Two

relatively integrated datasets were selected to validate the numerical simulations; the associated test conditions are shown in Table 2 [28, 29].

Numerical modeling (and unstructured grids) was carried out using Gambit software. The overall grid size is 5°m; the mesh at the leak source was strengthened. Fluent software was used to simulate gas diffusion; the standard  $k-\epsilon$  turbulence model, incompressible ideal-gas model, and the pressure-based implicit solver were selected. The steady-state solver was utilized to construct a basic wind environment and to simulate gas leakage; the nonsteady-state solver was employed to simulate the diffusion process after the gas leakage stopped. Computational domain size and mesh division are shown in Figures 3 and 4; the calculation results are shown from Figures 5–8.

From Figures 5–8, the maximum distance of LNG horizontal and vertical diffusions calculated by Fluent software consistent with the measured values by test. Although the test results are asymmetric, this is because the wind direction and speed could not be kept constant during the tests; however, with numerical simulations, the wind field could be kept constant, resulting in a bias between the test results and simulation results. Therefore, it is feasible to use fluent software to calculate the instantaneous diffusion concentration distribution of gas.

### 4. Sample Computation and Parametric Study

An injection station of the underground gas-storage cavern in salt rock is examined in this section. The accident scene was set for injection-casing leakage due to corrosion (or other reasons) and the impact of the leakage on the surrounding area was studied, as shown in Figure 9. Leakage source was located at the center of the ground, with the coordinates (67, 62, 0); the diameter of the injection casing was 216 mm, gas injection direction was vertical to the ground, and the leak-source strength of natural gas (or methane) was 173 kg/s, all of which were set according to the existing literature [30]. When chain self-preservation of the instrument is not normal, it needs to manually switch the valve, including the time taken in wearing air respirators, journey, and switching valves. The time of controlling leakage needs 5 min [20, 31]. Accordingly, the time of continuous leakage is five minutes, after which the point of free diffusion following the wind field occurs. Wind speed is, respectively, 2, 5, and 10 m/s from west to east. The law of the concentration distribution of methane leakage and diffusion (and its impact on the surrounding residents) for different wind speeds was analyzed using theoretical analysis and numerical simulations.

*4.1. Theoretical-Calculation Results and Discussion.* For gas-transportation pipelines, the leak-diffusion model can describe the ground continuous-point source diffusion when pipeline rupture or perforation occurs. Hazardous areas of natural gas continuous leakage and the diffusion from gas-storage caverns in salt rock calculated by the Gaussian plume model are shown in Figures 10 and 11, respectively.

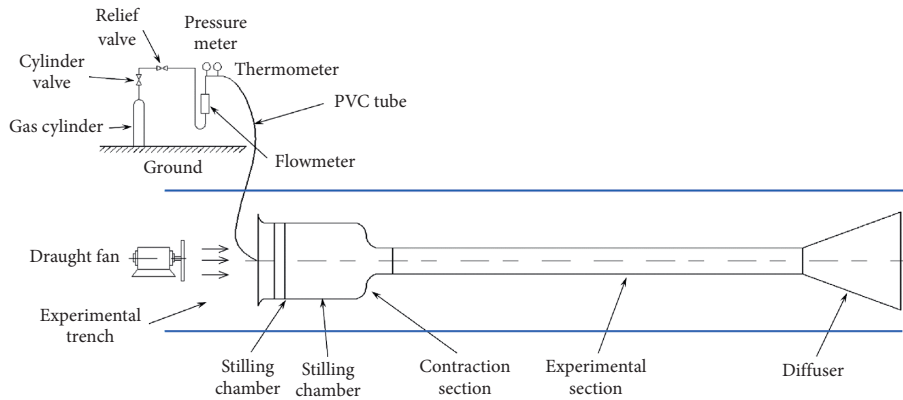


FIGURE 1: Schematic diagram of the experimental system [27].

TABLE 1: Wind-tunnel test data of acetylene diffusion [27].

Height (m)	Concentration (V/%)				Test conditions
	Downwind distance (m)				
	1	2	3	4	
Test 1	0.81	0.0	0.0	0.0	Discharge rate 6 m <sup>3</sup> /h The average wind speed 2.0 m/s Gas temperature -10°C Discharge time 3 min Ambient temperature -10°C
	0.69	0.054	0.201	0.0165	
	0.57	1.004	0.729	0.463	
	0.45	5.77	1.666	0.732	
	0.33	1.262	0.776	0.469	
	0.21	0.358	0.221	0.0253	
	0.09	0.0	0.053	0.0	
Test 2	0.81	0.0	0.053	0.028	Discharge rate 8 m <sup>3</sup> /h The average wind speed 2.0 m/s Gas temperature -10°C Discharge time 3 min Ambient temperature -10°C
	0.69	0.0	0.13	0.302	
	0.57	1.298	0.775	0.532	
	0.45	6.245	1.865	0.758	
	0.33	1.31	0.823	0.483	
	0.21	0.0	0.22	0.103	
	0.09	0.0	0.0	0.082	

Note. The value in the location of the underline is the maximum concentration.

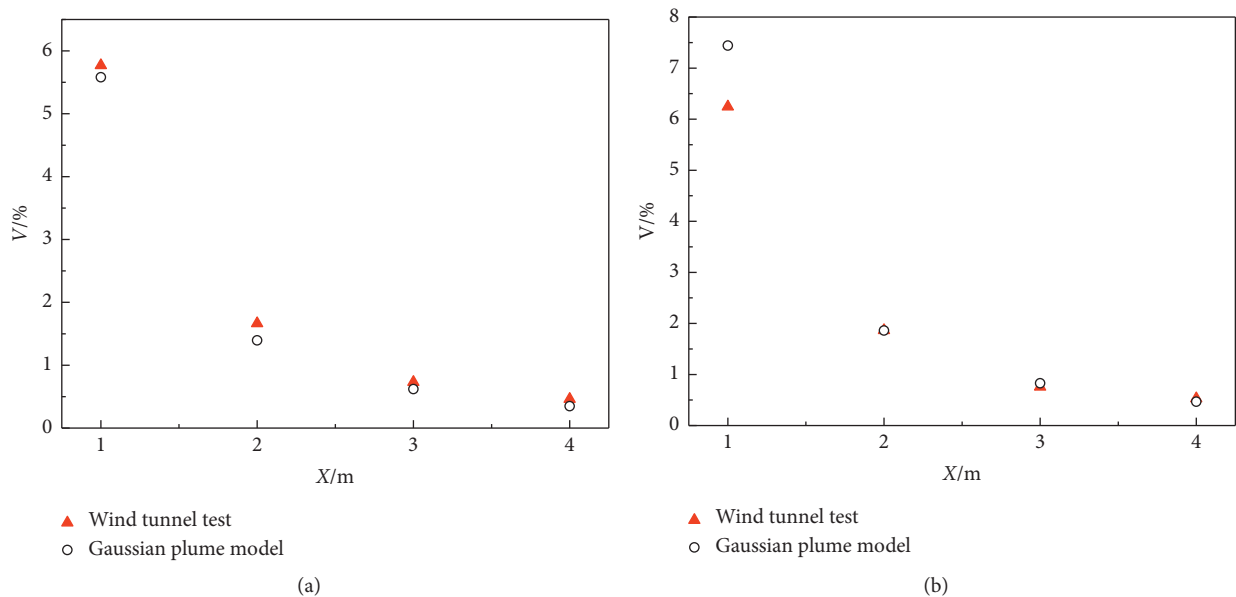


FIGURE 2: Volume-concentration distribution of different downwind distances from a height of 0.45 m (a) Test 1. (b) Test 2.

TABLE 2: Weather and release conditions in Burro/Coyote series trials [28, 29].

Trial number	Liquid pool diameter (m)	Release rate (m <sup>3</sup> /min)	Gas temperature (°C)	Release time (s)	Wind speed (m/s)	Relative humidity (%)	Atmospheric stability class	Ambient temperature (°C)
B9	58	18.4	-164	79	5.7	13.1	D	35.4
C3	58	13.5	-164	65	6.0	11.3	A	38.3

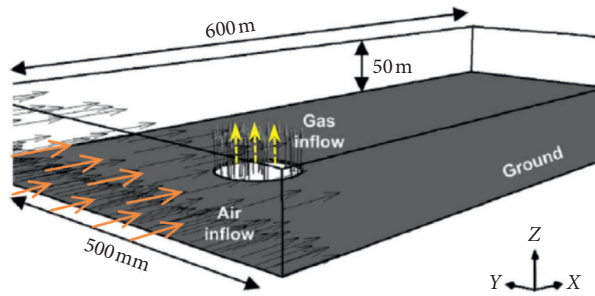


FIGURE 3: Computational domain size and boundary conditions [28, 29].

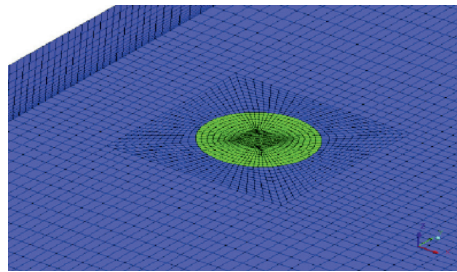


FIGURE 4: Partial mesh.

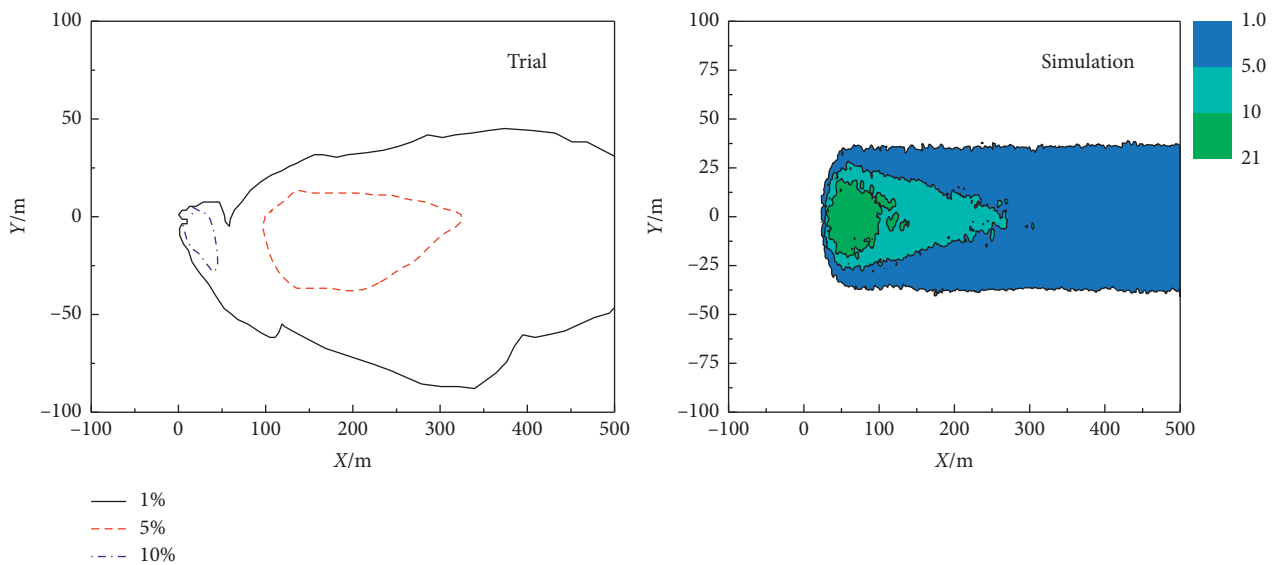


FIGURE 5: Comparison of Burro 9 trial and Fluent simulation for LNG horizontal volume-concentration distribution ( $Z = 1$  m and  $t = 80$  s).

According to Figure 10, fast wind speeds are conducive to gas diffusion; moreover, the hazard area is small when continuous leakage occurs for fast wind speeds. Gas diffusion is

the slowest under calm wind conditions and harm is relatively serious. For example, if the injection-well casing is completely broken, and if the wind speed is 2 m/s, the maximum diffusion

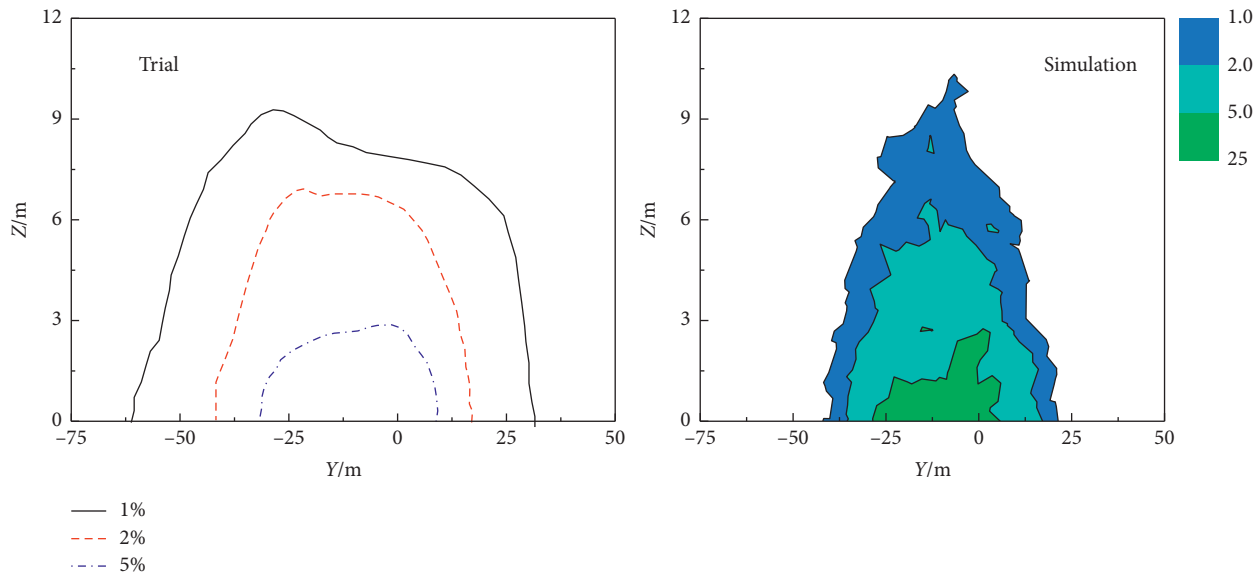


FIGURE 6: Comparison of Burro 9 trial and Fluent simulation for LNG vertical volume-concentration distribution ( $X = 140$  m and  $t = 80$  s).

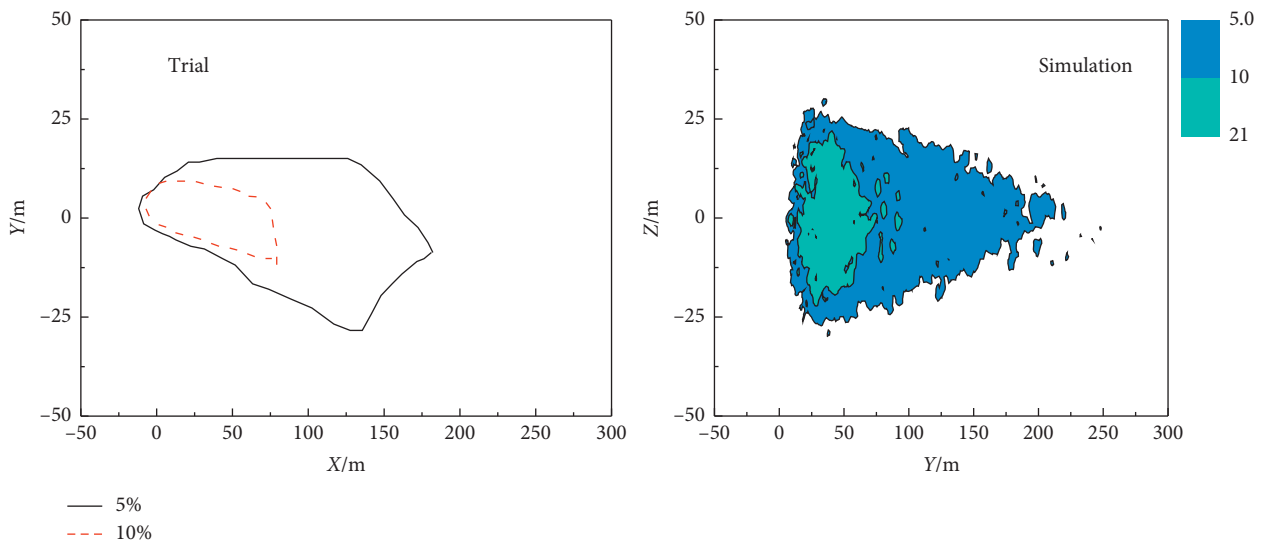


FIGURE 7: Comparison of Coyote 3 trial and Fluent simulation for LNG horizontal volume-concentration distribution ( $Z = 1$  m and  $t = 100$  s).

distance for the downwind direction corresponding to the concentrations of TLV, LFL, and UFL is 315, 135, and 80 m, respectively; if the wind speed is 10 m/s, the distances are 140, 60, and 35 m, respectively. In addition, the maximum diffusion distance at the crosswind direction is small when the wind speed is fast. For instance, if the wind speed is 2 m/s, the maximum diffusion distance at the crosswind direction corresponding to the concentrations of TLV, LFL, and UFL is 60, 25, and 12 m, respectively; if the wind speed is 10 m/s, the distances are 25, 10, and 5 m, respectively.

According to Figure 11, an unstable atmosphere is conducive to gas diffusion and the hazard area is small when continuous gas leakage occurs. For instance, if the

atmospheric stability class is B, the maximum diffusion distance for the downwind direction corresponding to the concentrations of TLV, LFL, and UFL is 240, 105, and 60 m, respectively; if the atmospheric stability class is D, the distances are 460, 190, and 110 m, respectively. Indeed, the atmospheric stability class has almost no effect on the maximum diffusion distance in the crosswind direction.

**4.2. Numerical-Simulation Results and Discussion.** The emergency shut-off valve is usually set in the injection-well casings of underground gas-storage caverns. The valve at both ends is automatically sealed off when pipeline rupture

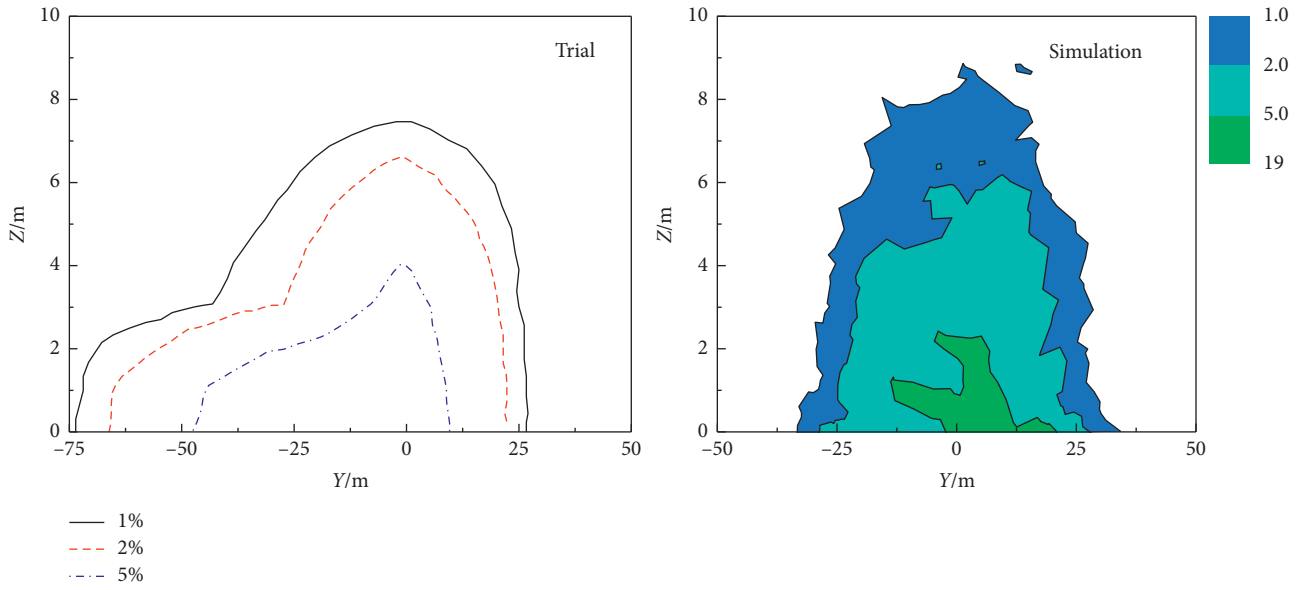


FIGURE 8: Comparison of Coyote 3 trial and Fluent simulation for LNG vertical volume-concentration distribution ( $X = 140$  m and  $t = 100$  s).

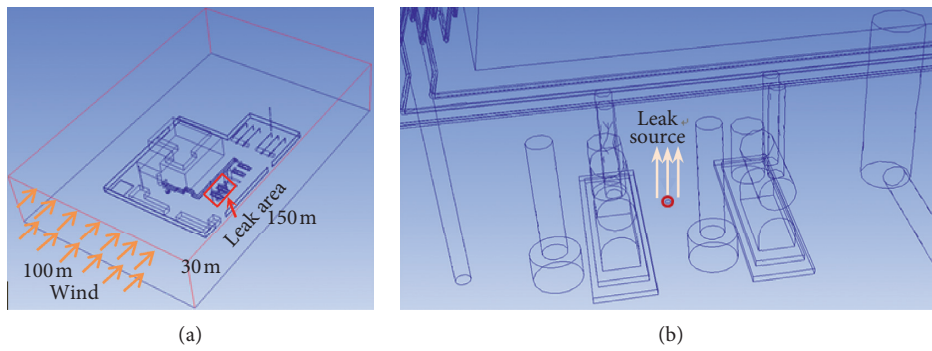


FIGURE 9: Schematic diagram of leakage scene. (a) The geometry of the injection station. (b) Location of the leak source.

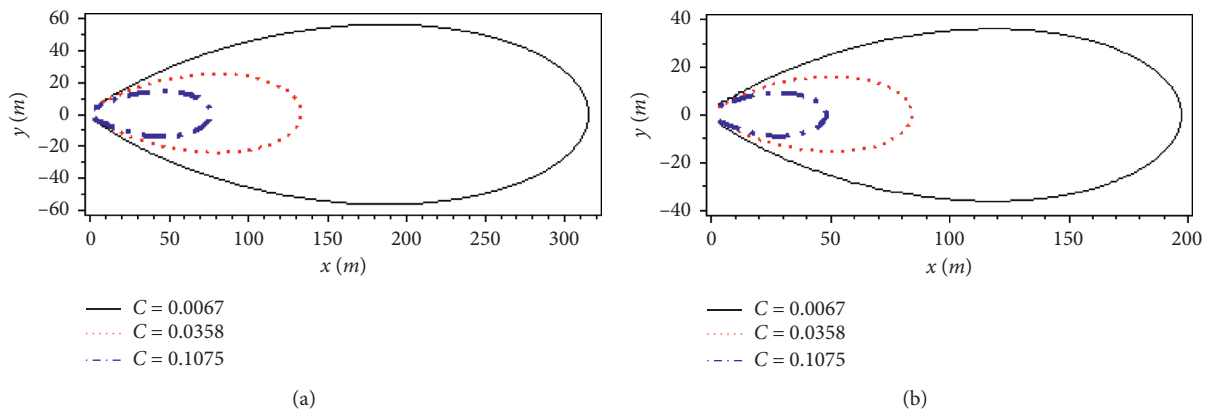


FIGURE 10: Continued.



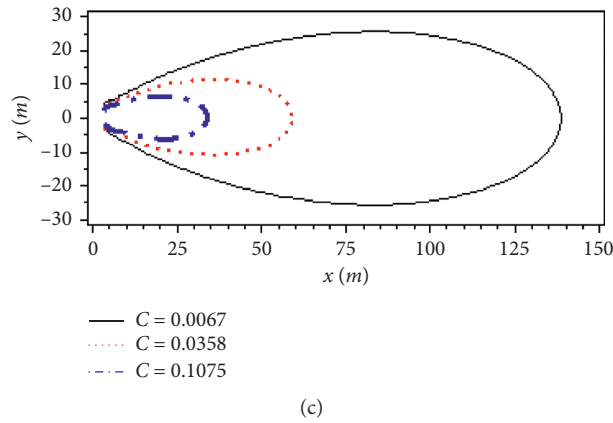


FIGURE 10: Concentration contours of continuous gas diffusion with different wind speeds ( $Q = 173$  kg/s and atmospheric stability class is C). (a)  $u = 2$  m/s. (b)  $u = 5$  m/s. (c)  $u = 10$  m/s.

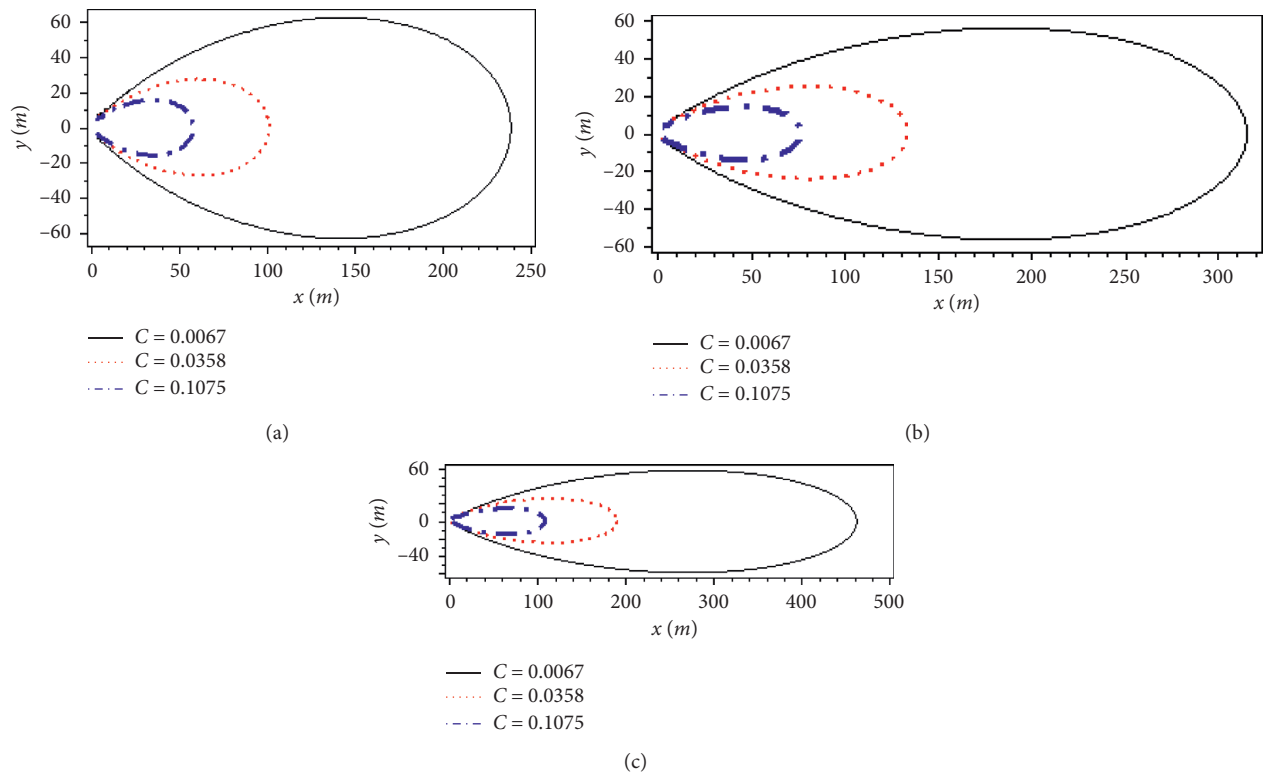


FIGURE 11: Concentration contours of continuous gas diffusion with different atmospheric classes ( $Q = 173$  kg/s and  $u = 2$  m/s). (a) Atmospheric stability class is B. (b) Atmospheric stability class is C. (c) Atmospheric stability class is D.

occurs, after which point any leakage is monitored, with the gas diffusing freely to the surrounding spaces.

Herein, we assumed that the injection station was 80 m long and 60 m wide; moreover, the computational domain was  $150 \times 100 \times 30$  m and, to reduce the influence of boundary conditions on the simulations, the positive direction of the  $x$ -axis was east, the positive direction of the  $y$ -axis was north, and the  $z$ -axis was the vertical direction. Based on the real device layout of the injection station, the model was constructed using Gambit software; unstructured

grids and size functions were used for meshing; grids were smaller for leak source and obstructions; after polyhedral mesh conversion, the final grid had a total of 3,324,044. The injection-station model is shown in Figure 12.

In Fluent, the turbulence model was selected as the standard turbulence  $k-\epsilon$  model, the gas-release simulation was set as the subsonic velocity leak, the incompressible ideal-gas model was selected, and the pressure-based implicit solver was applied. Simulations consisted of three phases: basic wind-field building at different wind

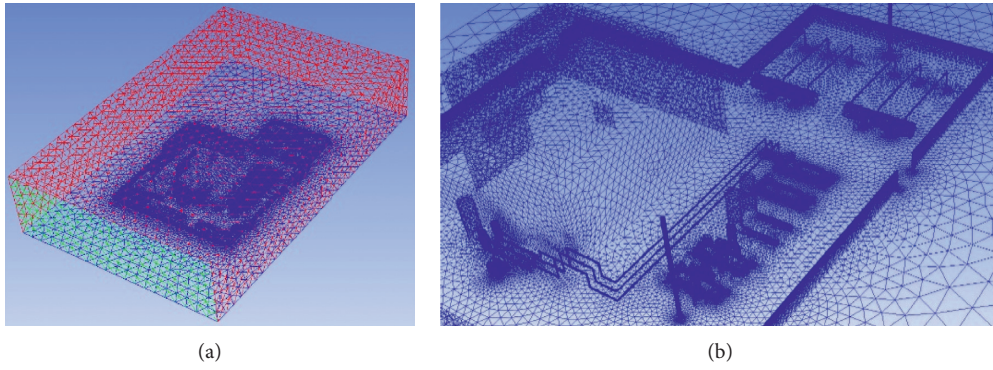


FIGURE 12: Numerical model of the injection station. (a) Surface grid of the calculate zone. (b) Enlarged partial grid.

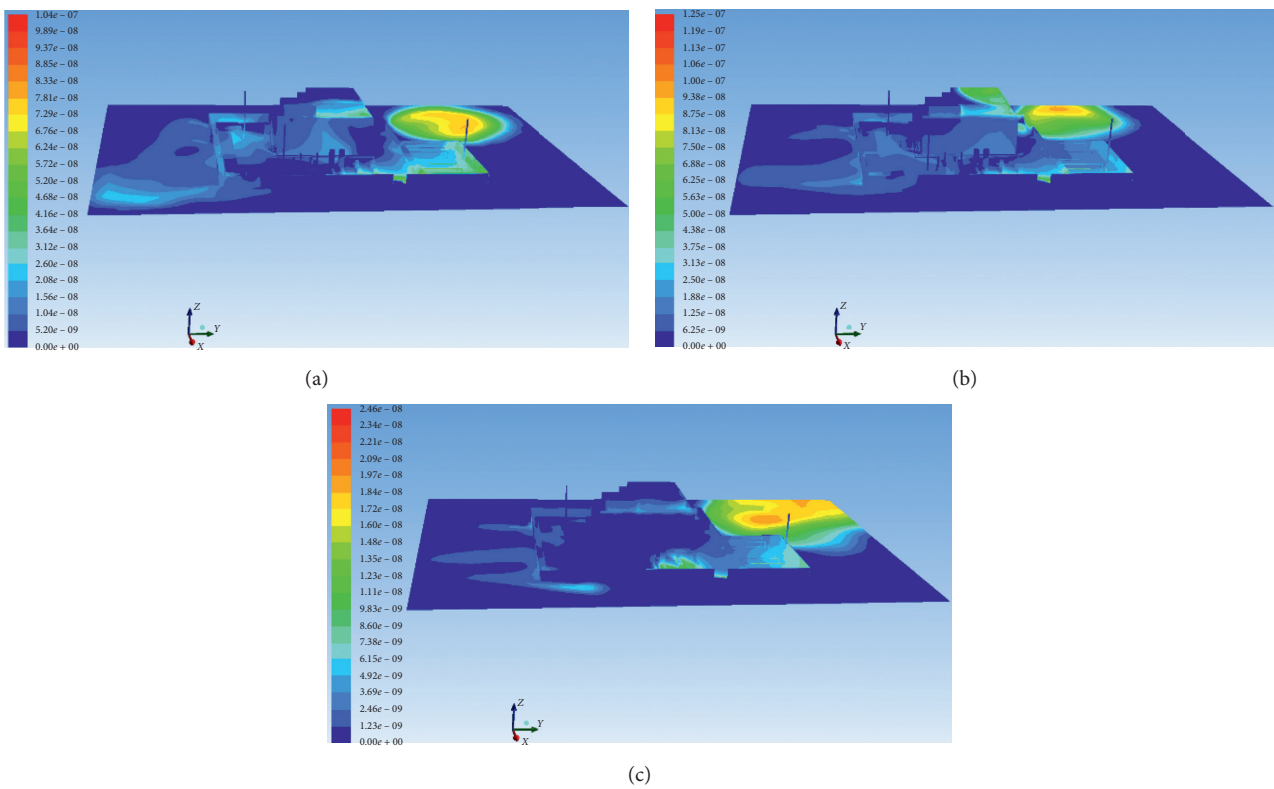


FIGURE 13: Simulation results of concentration-field ( $t = 180$  s). (a)  $u = 2$  m/s. (b)  $u = 5$  m/s. (c)  $u = 10$  m/s.

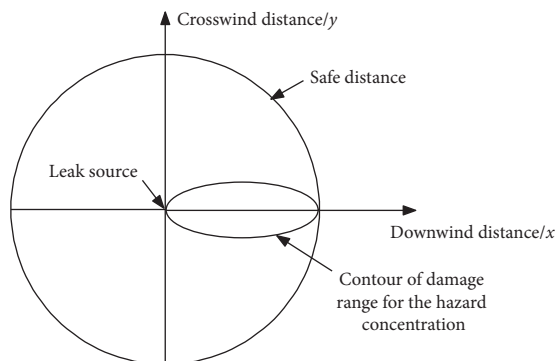


FIGURE 14: Schematic to determine the safety distance with the damage range of the hazard diffusion concentration.

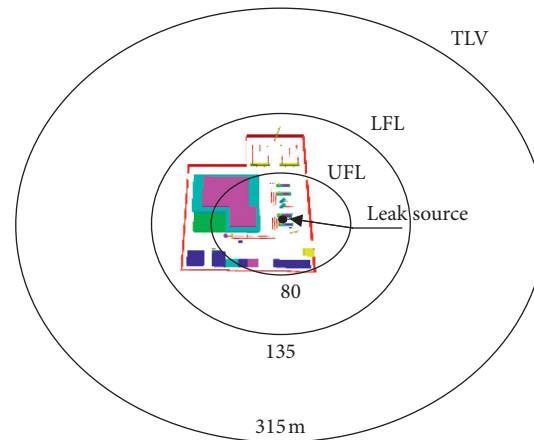


FIGURE 15: Hazardous zone of natural gas diffusion from a gas-storage cavern in salt rock.

directions; initial five minutes of continuous leakage on the basis of a basic wind field; three minutes of free diffusion in the atmosphere after leakage stopped. Simulation results are shown in Figure 13.

According to Figure 13, when the wind speed is increased, the gas cloud drifts further than it would otherwise; moreover, the area of personnel symptoms and the explosive concentration region are both greater when instantaneous leakage occurs.

The calculation concentration contour is elliptic under windy conditions, as can be seen in Figures 10 and 11. When determining the safety distance, all wind directions should be taken into account to identify the damage radius, the value of which is the safe distance for the downwind direction. Therefore, the elliptic-scope hazard range can be extended to take on a circular shape, the radius of which is the downwind direction distance, as shown in Figure 14.

According to the concentration-field distribution of the theoretical calculation in Section 4.1 and the Fluent simulations, the hazardous areas of gas diffusion from the sample gas-storage cavern in salt rock can be advised, as shown in Figure 15.

## 5. Conclusions

In this paper, an integrated analysis method was proposed to assess the hazard area of dispersion caused by accidental leakage from underground gas-storage caverns in salt rock. The Gaussian plume model was used to calculate the hazard area of dispersion caused by continuous leakage and Fluent was selected to simulate the hazard area of dispersion caused by instantaneous leakage. The proposed method was validated by comparing the calculation and numerical-simulation results with the experimental data. Furthermore, a sample underground gas-storage cavern in the salt rock was investigated; the TLV, UFL, and LFL distances resulting from natural gas dispersion were obtained using theoretical analysis and numerical simulation. Moreover, the factors that influence the hazard range of dispersion were discussed. The results indicated that the

hazard area decreases with an increase in wind speed and a decrease in atmospheric stability when the leakage is continuous. However, the hazard area decreases with a decrease in wind speed when the leakage is instantaneous.

## Data Availability

The data used to support the findings of this study are included within the article.

## Conflicts of Interest

The authors declare that they have no conflicts of interest.

## Acknowledgments

The authors gratefully acknowledge the financial support from the Natural Science Foundation of Jiangsu Province of China (Grant nos. BK20180081 and BK20190571) and the National Basic Research Program of China (973 Program) (Grant no. 2015CB058000).


## References

- [1] P. Bérest and B. Brouard, "Safety of salt caverns used for underground storage blow out; mechanical instability; seepage; cavern abandonment," *Oil & Gas Science and Technology*, vol. 58, no. 3, pp. 361–384, 2003.
- [2] L. F. Li, X. W. Zhao, J. H. Luo, H. Zhang, H. J. Yang, and X. Li, "Failure analysis of underground salt cavern gas storage and countermeasures," *Oil & Gas Storage and Transportation*, vol. 29, no. 6, pp. 407–410, 2010.
- [3] P. L. Wickenhauser, B. T. Wagg, and F. A. Barbuto, "Quantitative risk assessment-underground natural gas storage facilities," in *Proceedings of IPC 2006: International Pipeline Conference*, vol. 29, Calgary, Canada, September 2006.
- [4] L. H. Xie, H. L. Li, X. W. Zhao, and H. Zhang, "Statistics and risk analysis of underground gas storage accidents in salt caverns," *China Safety Science Journal*, vol. 19, no. 9, pp. 125–131, 2009.
- [5] C. H. Yang, W. G. Liang, D. H. Wei, and H. J. Yang, "Investigation on possibility of energy storage in salt rock in

- China,” *Chinese Journal of Rock Mechanics and Engineering*, vol. 24, no. 24, pp. 4409–4417, 2005.
- [6] J. Y. Zheng, X. K. Ma, and X. P. Yin, *The Safety of Long Pipeline (Risk Identification, Evaluation and Control)*, Chemical Industry Press, Beijing, China, 2004.
- [7] Z. Q. Wang, *The Study of Leakage Model and Consequence Area of High-Pressure Gas Pipeline*, China University of Geosciences, Beijing, China, 2009.
- [8] S. Heusermann, O. Rolfs, and U. Schmidt, “Nonlinear finite-element analysis of solution mined storage caverns in rock salt using the LUBBY2 constitutive model,” *Computers & Structures*, vol. 81, no. 8–11, pp. 629–638, 2003.
- [9] H.-M. Kim, D. Park, D.-W. Ryu, and W.-K. Song, “Parametric sensitivity analysis of ground uplift above pressurized underground rock caverns,” *Engineering Geology*, vol. 136, pp. 60–65, 2012.
- [10] I. Contrucci, E. Klein, N.-T. Cao, X. Daupley, and P. Bigarré, “Multi-parameter monitoring of a solution mining cavern collapse: first insight of precursors,” *Comptes Rendus Geoscience*, vol. 343, no. 1, pp. 1–10, 2011.
- [11] W. Z. Chen, X. J. Tan, G. J. Wu, and J. P. Yang, “Research on gas seepage law in laminated salt rock gas storage,” *Chinese Journal of Rock Mechanics and Engineering*, vol. 28, no. 7, pp. 1297–1304, 2009.
- [12] T. T. Wang, X. Z. Yan, X. J. Yang, and H. L. Yang, “Dynamic subsidence prediction of ground surface above salt cavern gas storage considering the creep of rock salt,” *Scientia Sinica Technologica*, vol. 41, no. 5, pp. 687–692, 2011.
- [13] L. J. Ma, X. Y. Liu, H. F. Xu, S. G. Yang, and Z. J. Wang, “Stability analysis of salt rock gas storage cavern under uncontrolled blowout,” *Rock and Soil Mechanics*, vol. 32, no. 9, pp. 2791–2797, 2011.
- [14] S. G. Yang, Q. Fang, and Y. D. Zhang, “Consequence quantitative analysis of jet fire caused by gas leakage from underground gas storage caverns in salt rock,” *Chinese Journal of Rock Mechanics and Engineering*, vol. 31, no. 9, pp. 1846–1853, 2012.
- [15] Ministry of Housing and Urban-Rural Development and General Administration of Quality Supervision and Quarantine, *GB50493-2009 Design Code for Detection and Alarm of Combustible and Toxic Gases in Petrochemical Industry*, China Planning Press, Beijing, China, 2009.
- [16] Petroleum and Natural Gas Industry Standard of China, *SY6503-2008 Safety Technical Specification for Combustible Gas Detection and Alarm System in Petroleum and Natural Gas Engineering*, Petroleum Industry Press, Beijing, China, 2008.
- [17] CCPS, *Guidelines for Use of Vapor Cloud Dispersion Models*, Center for Chemical Process Safety of the American Institute of Chemical Engineers, New York, NY, USA, 2nd edition, 1996.
- [18] D. M. Yu, *Quantitative Risk Analysis of Flammable, Explosive and Poisonous Dander in Storage and Transport Process*, China Railway Press, Beijing, China, 2000.
- [19] T. Y. Long, Y. X. Su, W. Y. Xiang, and C. He, *Computational Fluid Dynamics*, Chongqing University Press, Chongqing, China, 2007.
- [20] D. A. Crowl and J. F. Louvar, *Chemical Process Safety: Fundamentals with Applications*, Prentice-Hall, Upper Saddle River, NJ, USA, 2nd edition, 2002.
- [21] CCPS, *Guidelines for Consequence Analysis of Chemical Releases*, Center for Chemical Process Safety of the American Institute of Chemical Engineers, New York, NY, USA, 1999.
- [22] J. M. He, G. D. Ma, and S. X. Wang, *Air Pollution Control Engineering*, Higher Education Press, Beijing, China, 2010.
- [23] N. Nevers, *Air Pollution Control Engineering*, McGraw-Hill Companies, Inc., 2nd edition, 2000.
- [24] L. J. Wei, *Numerical Simulation of Heavy Gas Dispersion*, Beijing University of Chemical Technology, Beijing, China, 2000.
- [25] X. H. Pan, *Theoretical and Experimental Study on Dynamics Process for Accident of Release*, Nanjing University of Technology, Nanjing, China, 2004.
- [26] Z. Z. Han, J. Wang, and X. P. Lang, *FLUENT: Example and Application of Fluid Engineering Simulation*, Beijing Institute of Technology Press, Beijing, China, 2004.
- [27] G. Q. Xu, *The Study of Leakage and Dispersion of Flammable and Toxic Gas*, Dalian University of Technology, Dalian, China, 1998.
- [28] L. H. Anay, P. K. Ronald, and L. E. Donald, “On the application of computational fluid dynamics codes for liquefied natural gas dispersion,” *Journal of Hazardous Materials*, vol. 140, pp. 504–517, 2007.
- [29] S. Spyros and R. Fotis, “Simulation of Coyote series trials-part I: CFD estimation of non-isothermal LNG releases and comparison with box-model predictions,” *Chemical Engineering Science*, vol. 61, pp. 1434–1443, 2006.
- [30] S. G. Yang, Q. Fang, Y. D. Zhang, and L. J. Ma, “Analytical method for gas leakage mass from underground gas storage caverns in salt rock,” *Chinese Journal of Rock Mechanics and Engineering*, vol. 31, no. S2, pp. 3710–3715, 2012.
- [31] B. Zhang, G. M. Chen, J. H. Gong, and Y. Wang, “Optimization of gas detection and alarm instrument networks at gas gathering station based on CFD,” *Journal of China University of Petroleum (Edition of Natural Science)*, vol. 34, no. 5, pp. 141–146, 2010.

## Research Article

# Partitioned Strong Coupling of Discrete Elements with Large Deformation Structural Finite Elements to Model Impact on Highly Flexible Tension Structures

Klaus Bernd Sautter <sup>1</sup>, Tobias Teschemacher,<sup>1</sup> Miguel Ángel Celigueta,<sup>2,3</sup>  
Philipp Bucher,<sup>1</sup> Kai-Uwe Bletzinger,<sup>1</sup> and Roland Wüchner<sup>1,2</sup>

<sup>1</sup>Chair of Structural Analysis, Technical University of Munich, Arcisstr. 21, Munich 80333, Germany

<sup>2</sup>International Centre for Numerical Methods in Engineering (CIMNE), Barcelona 08034, Spain

<sup>3</sup>Universitat Politècnica de Catalunya (UPC), Barcelona 08034, Spain

Correspondence should be addressed to Klaus Bernd Sautter; klaus.sautter@tum.de

Received 10 January 2020; Revised 11 August 2020; Accepted 24 September 2020; Published 21 November 2020

Academic Editor: Xihong Zhang

Copyright © 2020 Klaus Bernd Sautter et al. This is an open access article distributed under the Creative Commons Attribution License, which permits unrestricted use, distribution, and reproduction in any medium, provided the original work is properly cited.

This article presents a staggered approach to couple the interaction of very flexible tension structures with large deformations, described with the finite element method (FEM), and objects undergoing large, complex, and arbitrary motions discretized with particle methods, in this case the discrete element method (DEM). The quantitative solution quality and convergence rate of this partitioned approach is highly time step dependent. Thus, the strong coupling approach is presented here, where the convergence is achieved in an iterative manner within each time step. This approach helps increase the time step size significantly, decreases the overall computational costs, and improves the numerical stability. Moreover, the proposed algorithm enables the application of two independent, standalone codes for simulating DEM and structural FEM as blackbox solvers. Systematic evaluations of the newly proposed iterative coupling scheme with respect to accuracy, robustness, and efficiency as well as cross comparisons between strong and weak FEM-DEM coupling approaches are performed. Additionally, the approach is validated against the rest position of an impacting object, and further examples with objects impacting highly flexible protection structures are presented. Here, the protection nets are described with nonlinear structural finite elements and the impacting objects as DEM elements. To allow the interested reader to independently reproduce the results, detailed code and algorithm descriptions are included in the appendix.

## 1. Introduction

The simulation of lightweight structures impacted by heavy objects can be a challenging problem if numerical methods are used, as both sides have highly different masses. Some of the applications can be as follows: rockfall in protection net structures [1–3], racecourse protection structures to secure both spectators and drivers at the same time, suicide protection nets on bridges or towers, and many more.

The examples in this work are mainly directed towards natural hazards, such as rockfall events which often cause destruction, especially in mountainous or populated areas.

As it is hard to prevent those events, protection structures are built along settlements and roads. In particular, lightweight flexible structures come into operation, as they are able to undergo large deformations and thus are capable of absorbing large amounts of energy with a smooth and comparably slow load transmission, reducing peak loads and maximum stresses. In principle, flexible structures are built to exploit the possibility to reduce stress peaks by their ability to tolerate large deformations. The interaction between the impacting object and very flexible structures calls for an advanced computational approach, as real scale tests are expensive, complex, and not suitable for a quick assessment of such structures.



The abovementioned problems can be divided into two separate problems: the highly deforming fixed protection structures and the freely moving impact objects. Based upon both solutions, an interaction and equilibrium between both need to be found. The net structures can typically show high deflections. However, the topology usually does not change and thus the net can be described with finite element formulations having a meshed discretization. Furthermore, multiple kinematic formulations can be applied within the analyses. Approaches range, e.g., from shell or membrane structures [2, 3] up to cable or beam models [4] or special formulations, such as ring elements [1]. In the following, the decision was made to use cable net models, discretized with cable element formulations (follow Section 2.2), as those provide accurate results for the given problems with comparatively small computational costs. Additionally, this approach allows contact at the correct position and thus allows small objects to pass through the structure.

Furthermore, the impact objects can also be discretized with different methodologies. The current state-of-the-art rockfall impact simulations is to use rigid bodies to simulate impacting rocks on highly flexible structures [1] where damage and deformation of the impacting objects are neglected. The approaches include finite element methods (FEMs [1]), discrete element methods- (DEM-) described structures, or more flexible structures with material point methods (MPMs [5]), and others. Using the FEM makes it possible to accurately describe the continuum of impacting objects. However, the approach can be very costly, as the contact detection can become very complex. DEM provides much optimized contact detection and thus an efficient multiphysics simulation. The drawback is that the continuous expression is complex and dependent upon difficult parameter calibration. Furthermore, the use of MPM might show similar properties as the FEM with fewer contact difficulties. This method can be quite complex in terms of the setup and smears the contact due to its numerical properties. In the following, DEM is chosen to discretize the impact objects used herein, as an efficient algorithm is needed, and no further attention is focused on its continuum description.

Coupling the DEM and the FEM is a common way to simulate various multiphysics problems [6, 7]. In particular, in problems where the interaction between granular materials or rigid objects with large motions and continuous systems is of interest, this combination of discretization methods is frequently used. Various applications, such as the thermomechanical behaviour [8] of contact between frictional bodies [9, 10], assessment of strains in the simulation of shot peening [11, 12], races and balls in ball bearings [13–15], general tribological systems [16, 17] such as the simulation of rail tracks [18], and more advanced investigations, including fracture due to blast loads [19], are studied using DEM-FEM coupling. The DEM is also used to simulate production processes such as rotating machinery [10] and particulate flows [20].

The coupling between DEM and FEM is done in a partitioned manner, which allows the combination of the respective best-suited solution strategies for each subproblem and the transfer of information in-between.

Accordingly, the user is not restricted to a code which includes both participants but instead can couple any existing DEM and FEM software by creating a suitable interface. This publication concentrates on the discussion of spatial mapping with cable structures. The coupling ultimately also allows the use of blackbox solvers for each participant (e.g., symplectic Euler [21] for the DEM and generalized alpha method [22] for the FEM). In order to advance the state of the art, a strong coupling algorithm is developed for the DEM-FEM impact problems.

To investigate its potential and superior performance in the underlying application case, a weak coupling algorithm is presented and used for comparison. It is known from the field of fluid-structure interaction [23, 24] that a strong coupling algorithm typically allows larger time steps compared to a weak coupling approach. The aim of this work is to investigate the properties of a strong coupling algorithm for DEM-FEM coupling and assess its usability in this setup.

From a formal point of view, the structure of the paper is as follows:

- (i) Section 2 describes the FEM notation including an introduction to the applied cable formulation
- (ii) Section 3 gives an overview of DEM
- (iii) Section 4 introduces the equilibrium required for the coupling and depicts the spatial mapping
- (iv) Section 5 explains the staggered weak coupling approach
- (v) Section 6 depicts the strong coupling approach, which adds additional complexity
- (vi) Section 7 demonstrates the advantages of the proposed coupling algorithm and investigates the influence of a variety of different input parameters
- (vii) Sections 7.1 and 7.2 show and investigate the novel coupling approaches
- (viii) Sections 7.3 and 7.4 present sensitivity analyses of the important parameters
- (ix) Sections 7.5 and 7.7 demonstrate large-scale problems
- (x) Section 8 gives a conclusion and outlook on future research
- (xi) Appendix A provides a more detailed discussion of the calculation of contact forces for the DEM
- (xii) Appendix B provides references to the software used in this study and provides scripts for reproduction of results

## 2. The Finite Element Method

The finite element method (FEM) [25] is used to numerically solve partial differential equations. For this purpose, a domain is discretized into finite elements for which an approximated solution is known.

As described in [22, 26–28], kinematic relations describe the possible movement of such elements. The current configuration  $\mathbf{x}$  can be described with the help of a time-



dependent map (noted as  $t$ ) from the reference configuration  $\mathbf{X}$ , which can be obtained from the displacement vector  $\mathbf{u}$  (additionally see Figure 1):

$$\mathbf{x}(t) = \mathbf{X} + \mathbf{u}(t), \quad (1)$$

the bold letters indicate tensors and vectors.

**2.1. Virtual Work.** The momentum equation can be described by applying the divergence theorem [22, 27, 29, 30]:

$$\text{div } \boldsymbol{\sigma} + \mathbf{b} = \rho \ddot{\mathbf{u}}, \quad (2)$$

with  $\boldsymbol{\sigma}$  being the first Cauchy stress, the body forces  $\mathbf{b}$ , the acceleration  $\ddot{\mathbf{u}}$ , and the density  $\rho$ . Multiplying the momentum equation (2) with the virtual displacement field  $\delta \mathbf{u}$  and integrating over the physical domain  $\Omega$  leads to the weak form, respectively:

$$\delta W_{\text{int}} - \delta W_{\text{ext}} + \delta W_{\text{kin}} = 0. \quad (3)$$

The three virtual work contributions: the internal work (equations (4), respectively (5)), the external work (equation (6)), and the kinetic work (equation (7)), are obtained by the partial integration:

$$\delta W_{\text{int}} = \int_{\Omega} \boldsymbol{\sigma} : \delta \mathbf{e} \, d\Omega, \quad (4)$$

$$\delta W_{\text{int}} = \int_{\Omega_0} \mathbf{S} : \delta \mathbf{E} \, d\Omega_0, \quad (5)$$

$$\delta W_{\text{ext}} = \int_{\Omega} \mathbf{b} \cdot \delta \mathbf{u} \, d\Omega + \int_{\Gamma_{\sigma}} \boldsymbol{\sigma} \mathbf{n} \cdot \delta \mathbf{u} \, d\Gamma_{\sigma}, \quad (6)$$

$$\delta W_{\text{kin}} = \int_{\Omega} \rho \ddot{\mathbf{u}} \cdot \delta \mathbf{u} \, d\Omega, \quad (7)$$

with the Almansi strain  $\mathbf{e}$ , the normal direction of  $\Omega$ ,  $\mathbf{n}$ , and the Neumann boundary  $\Gamma_{\sigma}$ . From equation (4), one can obtain equation (5) (for detailed information, see [22, 27]), which describes the internal virtual work with the use of the Piola–Kirchhoff 2 (PK2) stress tensor  $\mathbf{S}$  and the Green–Lagrange strain tensor  $\mathbf{E}$  within the initial domain  $\Omega_0$ .

**2.2. Cable Element.** With regard to the cable element, a cable or a “truss element formulation” having two nodes ( $\mathbf{n}_k$  and  $\mathbf{n}_l$ ) considering geometrical nonlinear behaviour is used. The kinematics is outlined in Figure 1. Each node requires three (or for 2D, two) displacement degrees of freedom (dofs), but no further dofs are required.

As the bases for the structural analysis and to introduce relevant notations, the internal forces and the tangent stiffness matrix are briefly noted.

Due to the one-dimensional nature of the element, only one parametric coordinate  $\xi$  [ $-1 \leq \xi \leq +1$ ] is used to describe the geometry [25] with linear shape functions.

By virtue of equation (5), the internal forces  $\mathbf{F}_{\text{int}}$  read for each degree of freedom  $r$  as follows:

$$F_{r,\text{int}} = A \int_0^L (\mathbf{S} + \mathbf{S}_{\text{pre}}) : \frac{\partial \mathbf{E}}{\partial u_r} \frac{dX}{(L/2)d\xi}, \quad (8)$$

for the constant crosssection  $A$ , the reference length  $L$ , and a given prestress  $\mathbf{S}_{\text{pre}}$ . The tangent stiffness matrix  $\mathbf{K}$  can be expressed as

$$K_{rs} = A \cdot \frac{L}{2} \int_{-1}^{+1} \left( \frac{\partial (\mathbf{S} + \mathbf{S}_{\text{pre}})}{\partial u_s} : \frac{\partial \mathbf{E}}{\partial u_r} + (\mathbf{S} + \mathbf{S}_{\text{pre}}) : \frac{\partial^2 \mathbf{E}}{\partial u_r \partial u_s} \right) d\xi, \quad (9)$$

$$K_{rs} = A \cdot \frac{L}{2} \int_{-1}^{+1} \left( \mathbf{D} : \frac{\partial \mathbf{E}}{\partial u_r} : \frac{\partial \mathbf{E}}{\partial u_s} + (\mathbf{S} + \mathbf{S}_{\text{pre}}) : \frac{\partial^2 \mathbf{E}}{\partial u_r \partial u_s} \right) d\xi. \quad (9)$$

The constitutive law used in this work is the St. Venant–Kirchhoff hyperelastic material model [29, 30] described by the strain-energy functional  $\Psi_{\text{sv}}$ . Its first and second derivatives w.r.t.  $\mathbf{E}$  describe the PK2-stress  $\mathbf{S}$  and the material tangent modulus  $\mathbf{D}$ , respectively [30]:

$$\mathbf{S} = \frac{\partial \Psi_{\text{sv}}}{\partial \mathbf{E}}, \quad (10)$$

$$\mathbf{D} = \frac{\partial^2 \Psi_{\text{sv}}}{\partial \mathbf{E} \partial \mathbf{E}}.$$

The prestress  $\mathbf{S}_{\text{pre}}$  is a stress, which is initially applied and added to the internal forces of the structure. It is a second-order tensor; however, for the truss kinematics, only a scalar is required. If a stress state, in equilibrium to the initial prestress, is required within a complex structure, form-finding procedures need to be applied beforehand. In contrast to standard structural analysis, form-finding solves an inverse engineering problem. This inverse problem is to find a geometry which corresponds to an equilibrium configuration, whose stress state is identical to the given prestress. The force density method is one approach used to realize this [24, 31]. The described kinematic relation is capable to model either a cable or a truss formulation. To model a realistic behaviour of cable structures, it needs to be ensured that no compression stresses are carried by the structure. With an additional check if a cable is under compression, stiffness contributions and internal forces are avoided. In the following, using the applied naming, trusses would allow compression stresses, whereas cables do not.

The element mass matrix  $\mathbf{M}$  for a dynamic simulation results from the virtual kinetic work as depicted in equation (7). With  $\mathbf{N}(\xi)$  being the shape functions and the reference density  $\rho_0$ ,  $\mathbf{M}$  is defined as follows:

$$\mathbf{M} = A \cdot \frac{L}{2} \cdot \rho_0 \int_{-1}^{+1} \mathbf{N}(\xi)^T \mathbf{N}(\xi) d\xi. \quad (11)$$

The damping matrix  $\mathbf{C}$  is expressed via the Rayleigh damping as a linear combination of the mass matrix  $\mathbf{M}$  and the stiffness matrix  $\mathbf{K}$  (for more information, see [32]):

$$\mathbf{C} = \tau \mathbf{M} + \kappa \mathbf{K}, \quad (12)$$

with  $\tau$  and  $\kappa$  as the scaling factors.

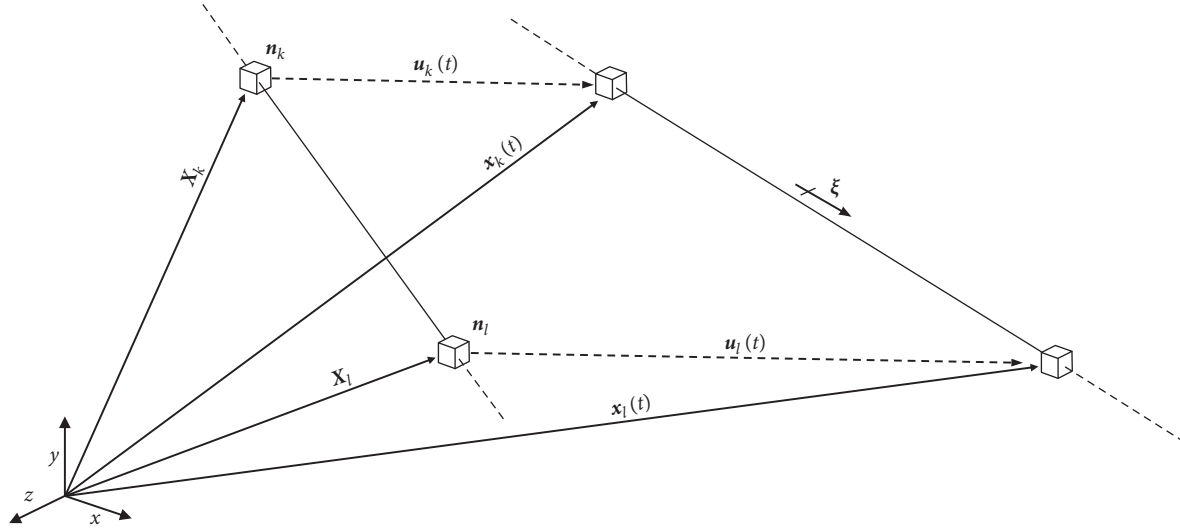


FIGURE 1: Spatial mapping of cable element kinematics between the nodes  $\mathbf{n}_k$  and  $\mathbf{n}_l$ .

### 3. The Discrete Element Method

This section describes the fundamentals of the discrete element method (DEM), with a focus towards the DEM-FEM coupling (following Sections 4–7).

The DEM used within this scope models the dynamics of spherical particles, considering external forces such as gravity and contact with other particles or contact with differently described objects. DEM can be used for many different particle shapes such as rectangles, cones, spheres, and more. However, only spherical particles are considered in this publication. To describe more complex shapes, a set of spheres is connected within clusters. A cluster consists of multiple particles which are used for contact detection and force evaluation. The mass and centre of gravity are described within the cluster shape and independent of the masses of the particles (for further information, see [33]).

The basic steps in a DEM simulation are as follows (also [21]):

- (i) Contact detection
- (ii) Evaluation of contact forces
- (iii) Integration of motion

These steps will be briefly described in the following.

**3.1. Contact Detection.** Within the scope of this publication, certain contact scenarios are of interest. The centre of spheres is described with  $\mathbf{C}_i$ , and their respective radius is  $R_i$ . The distance to contacted edges is deciphered with  $d_i$  (Figure 2).

Two spheres  $\mathbf{C}_i$  and  $\mathbf{C}_j$ :

$$\|\mathbf{C}_i - \mathbf{C}_j\| < R_i + R_j. \quad (13)$$

Sphere  $\mathbf{C}_i$  and vertex  $\mathbf{n}_k$ :

$$\|\mathbf{C}_i - \mathbf{n}_k\| < R_i. \quad (14)$$

Sphere  $\mathbf{C}_i$  and  $d_i$  to edge:

$$d_i < R_i. \quad (15)$$

**3.2. Evaluation of Contact Forces.** The contact forces can be evaluated using different contact laws and rheological models. For a detailed description of contact models, see [6, 21, 34, 35]. A more detailed description of the evaluation of contact forces is included in Appendix A. The coefficient of restitution (COR),  $\epsilon_{\perp}$  (see equation (A.7)), is an essential part in the contact and is further investigated in Section 7.4.

**3.3. Integration of Motion.** The integration of motion is described by Newton's second law of motion. The translational acceleration  $\ddot{\mathbf{u}}$  is described via the force  $\mathbf{F}$  and the mass of the particle  $m$ . The angular acceleration  $\dot{\boldsymbol{\omega}}$  is expressed by the moments  $\mathbf{T}$  and the tensor of rotational inertia  $\mathbf{I}$  [21]:

$$\begin{aligned} m\ddot{\mathbf{u}} &= \mathbf{F}, \\ \mathbf{I}\dot{\boldsymbol{\omega}} &= \mathbf{T}. \end{aligned} \quad (16)$$

The forces and torques at each particle  $i$  are described as follows [6, 19, 21]:

$$\begin{aligned} \mathbf{F}_i &= \mathbf{F}_i^{\text{ext}} + \sum_{j=1}^n \widehat{\mathbf{F}}^{ij} + \mathbf{F}_i^{\text{damp}}, \\ \mathbf{T}_i &= \mathbf{T}_i^{\text{ext}} + \sum_{j=1}^n \mathbf{r}_c^{ij} \times \mathbf{F}^{ij} + \mathbf{T}_i^{\text{damp}}. \end{aligned} \quad (17)$$

The resulting forces and torques depend on the following components:

$\mathbf{F}_i^{\text{ext}}, \mathbf{T}_i^{\text{ext}}$ : external loads (e.g., gravity)

$\mathbf{F}^{ij}$ : contact interactions between neighbouring particles or boundaries as the contact  $\mathbf{F}_{\text{contact}}$  (see Appendix A for description of the components  $F_n$  and  $F_t$ )

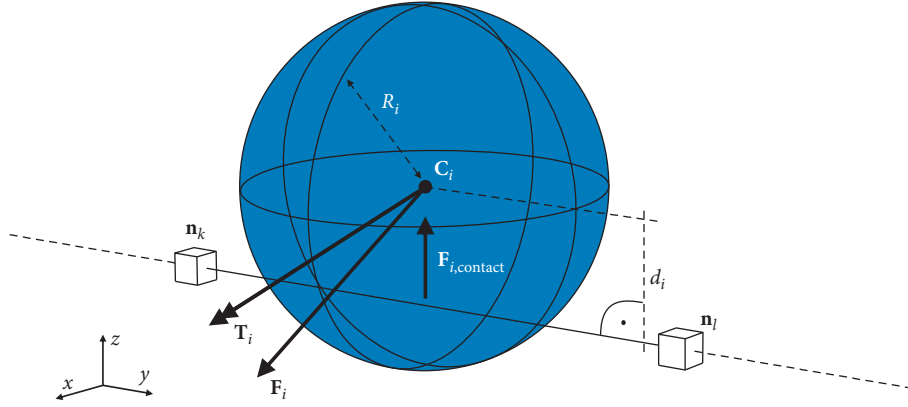


FIGURE 2: Spherical DEM particle  $i$  in contact with cable structure between the nodes  $\mathbf{n}_k$  and  $\mathbf{n}_l$ .

$\mathbf{F}_i^{\text{damp}}, \mathbf{T}_i^{\text{damp}}$ : external damping boundaries  
 $\mathbf{n}^{ij}, \mathbf{t}^{ij}$ : normal and tangential vectors at the respective contact point  
 $\mathbf{r}_c^{ij}$ : vector connecting the particle centre and the respective contact point

#### 4. Staggered Coupling of DEM and FEM

To couple two standalone physically independent interacting numerical problems such as the simulation of particles and structures, a suitable interface condition to achieve equilibrium is needed to be found.

**4.1. Structure-Particle Equilibrium.** To put the two independent physics, the DEM and the FEM, into an equilibrium state, the following force equilibrium at the structure needs to be achieved:

$$\begin{aligned} & \mathbf{F}_{\text{contact}}(\mathbf{u}^{\Omega_{S,\Gamma}}(t), \dot{\mathbf{u}}^{\Omega_{S,\Gamma}}(t), \mathbf{u}^P(t), \dot{\mathbf{u}}^P(t)) \\ & - \mathbf{F}_{\text{int}}^{\Omega_{S,\Gamma}}(\mathbf{u}^{\Omega_{S,\Gamma}}(t), \dot{\mathbf{u}}^{\Omega_{S,\Gamma}}(t), \ddot{\mathbf{u}}^{\Omega_{S,\Gamma}}(t)) = 0, \end{aligned} \quad (18)$$

where  $\mathbf{u}$  describes the displacements,  $\dot{\mathbf{u}}$  represents the velocities,  $\Omega_S$  represents the structural domain, while  $\Gamma$  of  $\Omega_S$  includes all nodes which are in interaction with the DEM particles,  $P$ .

With respect to equation (18), the contact forces  $\mathbf{F}_{\text{contact}}$  of the particles, which are dependent on its displacements and the velocities, need to be in equilibrium with the internal forces  $\mathbf{F}_{\text{int}}^{\Omega_{S,\Gamma}}$  of the structure, which are dependent on its displacements, velocities, and accelerations (equation (8) and additional including inertia effects). The equilibrium of both DEM and FEM simulation is graphically depicted in Figure 3.

The basic idea of the proposed partitioned coupling simulation is the interchange of primary (such as the displacement) and secondary (e.g., forces) interface variables which are obtained as the solution of the respective components of the simulation.

**4.2. Spatial Mapping.** In the following, the DEM problem is solved independently from the structural problem. To do

this, the displacements and velocities of the structure at the given time step are transferred to DEM, and this structure is further seen as the DEM wall, described by the domain  $\Omega_D$ . The wall is used to calculate contact forces with the DEM particles  $P$ , which are depending on its displacements and velocities (see Appendix A for contact laws and force calculations). After solving the DEM problem, the resulting contact forces are transferred to the structural analysis problem. With the contact forces, seen as external forces, the dynamic structural problem is solved, resulting in new displacements and velocities on the domain  $\Omega_S$ . This procedure is outlined in Figure 4.

Following this, the contact forces  $\mathbf{F}_{\text{contact}}$  are now dependent on the displacements and velocities of  $\Omega_D$  and not directly on  $\Omega_S$  and are defined as the external forces coming from the DEM:

$$\mathbf{F}_{\text{ext}}^{\Omega_{S,\Gamma}} = \mathbf{F}_{\text{contact}}(\mathbf{u}^{\Omega_{D,\Gamma}}(t), \dot{\mathbf{u}}^{\Omega_{D,\Gamma}}(t), \mathbf{u}^P(t), \dot{\mathbf{u}}^P(t)). \quad (19)$$

The equilibrium within the structural mechanics problem is given as follows:

$$\mathbf{F}_{\text{ext}}^{\Omega_{S,\Gamma}} - \mathbf{F}_{\text{int}}^{\Omega_{S,\Gamma}}(\mathbf{u}^{\Omega_{S,\Gamma}}(t), \dot{\mathbf{u}}^{\Omega_{S,\Gamma}}(t), \ddot{\mathbf{u}}^{\Omega_{S,\Gamma}}(t)) = 0. \quad (20)$$

After solving both domains, the two interface conditions, for the displacements and the velocities between both fields, are not fulfilled anymore:

$$\mathbf{u}^{\Omega_{D,\Gamma}}(t) - \mathbf{u}^{\Omega_{S,\Gamma}}(t) = 0, \quad (21)$$

$$\dot{\mathbf{u}}^{\Omega_{D,\Gamma}}(t) - \dot{\mathbf{u}}^{\Omega_{S,\Gamma}}(t) = 0. \quad (22)$$

Resulting from this, the contact forces  $\mathbf{F}_{\text{contact}}$  computed within  $\Omega_D$  and the contact forces which would be computed within  $\Omega_S$  are not the same anymore, and thus, the equilibrium expression is not fulfilled:

$$\begin{aligned} & \mathbf{F}_{\text{contact}}(\mathbf{u}^{\Omega_{D,\Gamma}}(t), \dot{\mathbf{u}}^{\Omega_{D,\Gamma}}(t), \mathbf{u}^P(t), \dot{\mathbf{u}}^P(t)) \\ & - \mathbf{F}_{\text{contact}}(\mathbf{u}^{\Omega_{S,\Gamma}}(t), \dot{\mathbf{u}}^{\Omega_{S,\Gamma}}(t), \mathbf{u}^P(t), \dot{\mathbf{u}}^P(t)) = 0. \end{aligned} \quad (23)$$

For small time steps, resulting into smaller contact forces, the tracking of the interface equilibrium can be negligible. However, for ill-conditioned systems and large time steps, the resulting difference will lead to inaccuracies

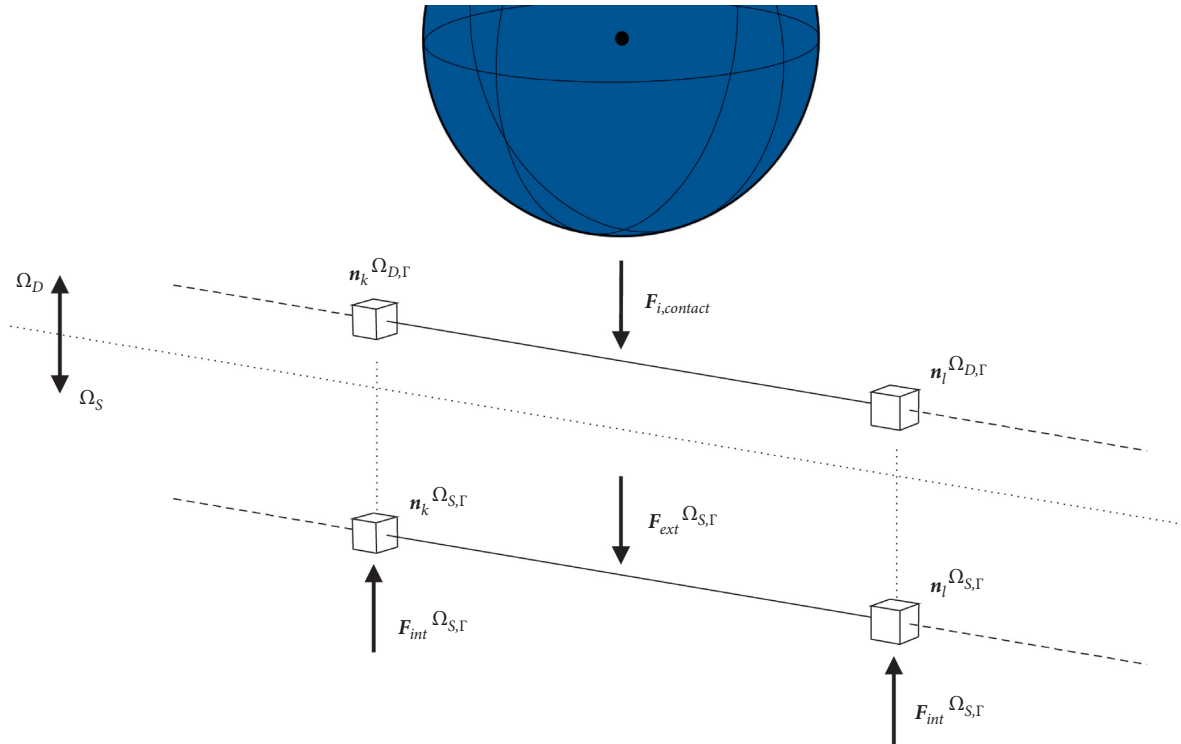


FIGURE 3: Domain definition and force equilibrium in DEM and FEM simulation.

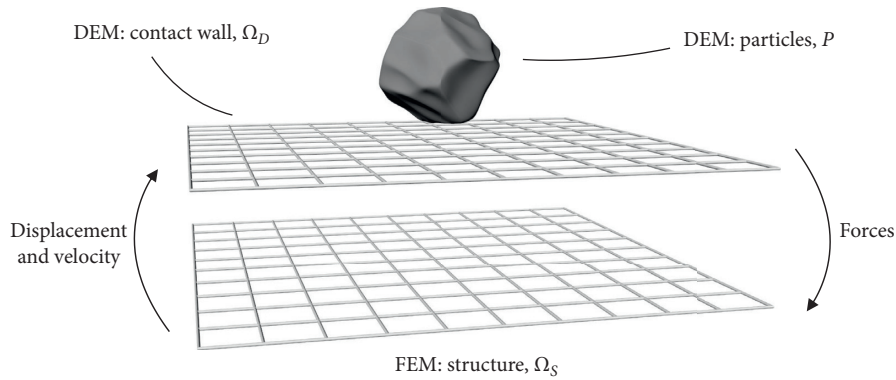


FIGURE 4: Transfer of forces and displacements and velocities between different applications.

and makes the solution unstable. To solve this problem, a possible approach is presented in Section 6.

4.3. *Influence of Coefficient of Restitution (COR).* Large contact forces will result in difficult fulfilment of interface conditions (equations (21)–(23)). Section 6 proposes a remedy for that problem. One major factor influencing the magnitude of the contact forces is the DEM particle property COR. This value must be defined by the user and heavily influences the stability of the coupled simulation (see example in Section 7.4).

The coefficient represents the ratio of initial speed and final speed after impact [21] (equation (A.6)) and is further discussed in Appendix A. Since this coefficient is determined

manually for each simulation, it is important to be careful when doing the calibration.

4.4. *Mesh Dependency for Cable Structures.* For the specific application of highly flexible cable structures in this study, such as rockfall protection nets or any other kind of cable-like structures, the DEM wall condition  $\Omega_D$  discretization and the FEM  $\Omega_S$  discretization on  $\Gamma$  must exactly coincide (conforming meshes). The respective meshes represent a physical mesh which must be correctly described in order to model the exact contact positions. To demonstrate this behaviour, Figure 5(a) visualizes the DEM part of the simulation. A cable net is modelled and impacted by two spheres. A large sphere finds contact and deforms the boundary, while a smaller sphere penetrates an opening. In

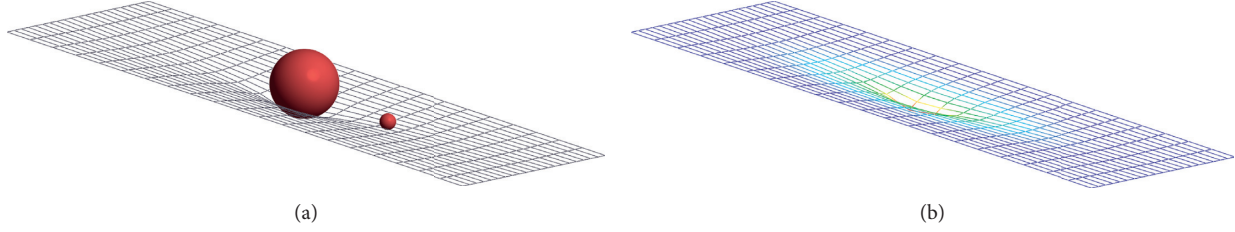


FIGURE 5: Modelling of impact with cable-structured boundaries. (a) Discretized  $\Omega_D$ . (b) Discretized  $\Omega_S$ .

addition, Figure 5(b) represents the respective FEM structure which is used to calculate the adequate structural response.

If surface elements such as shells or membranes, which do not possess physically the predetermined discrete contact positions, are used within a coupled simulation, arbitrary meshes can be used. In that case, a mapper [36] will be responsible for the correct data transfer.

## 5. Staggered Weak Coupling

The fundamental idea of the weak coupling (sometimes also called explicit coupling [24]) follows a single exchange of coupling data in each time step. The communication pattern is depicted in Figure 6. The important steps at each time, including this communication pattern, can be summarized as follows:

- (1) Solve DEM (results:  $\mathbf{u}^P$ ,  $\dot{\mathbf{u}}^P$ , and  $\mathbf{F}_{\text{contact}}$ )
- (2) Map  $\mathbf{F}_{\text{contact}}$  from DEM to Structure
- (3) Solve Structure (results:  $\mathbf{u}^{\Omega_{S,\Gamma}}$ ,  $\dot{\mathbf{u}}^{\Omega_{S,\Gamma}}$ , and  $\ddot{\mathbf{u}}^{\Omega_{S,\Gamma}}$ )
- (4) Map *displacements* and *velocities* from Structure to DEM
- (5) Advance in time (not explicitly shown)

The interface variables are accordingly updated (see Steps (2) and (4)):

Displacement:

$${}^{k+1}\mathbf{u}^{\Omega_{D,\Gamma}} = {}^k\mathbf{u}^{\Omega_{S,\Gamma}}. \quad (24)$$

Velocity:

$${}^{k+1}\dot{\mathbf{u}}^{\Omega_{D,\Gamma}} = {}^k\dot{\mathbf{u}}^{\Omega_{S,\Gamma}}. \quad (25)$$

Contact force:

$${}^{k+1}\mathbf{F}_{\text{ext}}^{\Omega_{S,\Gamma}} = {}^k\mathbf{F}_{\text{contact}}. \quad (26)$$

This algorithm is comparatively easy to implement and typically does not require any deep interaction. Standard DEM and FEM simulation environments provide the exchange data as an output. Therefore, different software can

also be efficiently applied here. Furthermore, it was shown that the algorithm can be applied if the time steps do not become too large (see examples in Sections 7.1 and 7.2). However, the behaviour of this procedure can become unstable as soon as the differences in stiffness, mass, and velocity between the two physics become very high. The procedure is then very prone to the time step size used. Decreasing the time step size will lead to inefficient and numerically costly simulations.

To gain a deeper understanding of the underlying procedure, this approach is further detailed in Algorithm 1. In order to facilitate the reproduction of the results, the *Python* script used, including all comments, is provided in Appendix B.

In this procedure, two additional features will be discussed. They are independent of the coupling approach used but improve the performance significantly. They are added in Algorithm 1 and highlighted as follows:

- (i) *particle\_near\_wall* (line 3–6): if the respective particles are in the vicinity of the structural model to adjust the time step is checked. A particle moving freely in space can be simulated with a time step larger than it would be required for the simulation of the DEM-FEM interaction.
- (ii) *forces ≠ 0.0* (line 12–15): this is an additional check used only to solve the structure when contact forces are present. This is only valid if the self-weight of the structure or any other loads (except impact loads) are neglected. Otherwise, a preliminary simulation or a form finding [24, 31] of the structure is needed.

## 6. Staggered Strong Coupling

As known from other coupled multiphysics problems, such as fluid-structure interaction (FSI) [24, 37], the direct explicit transfer of the interface data (forces, velocities, and displacements) can lead to divergence problems in the staggered simulation. This problem is caused by large contact forces due to differences in velocities, acceleration, and highly different masses on both sides. In contrast to the weak coupling approach, the strong coupling (in the literature also called implicit coupling [24] or a conventional serial staggered approach within the context of loose coupling [38, 39]) adds an additional iteration loop in each time step, which solves for the equilibrium between both numerical physics. This requires a Gauss–Seidel loop between DEM and FEM, which might need to be solved multiple



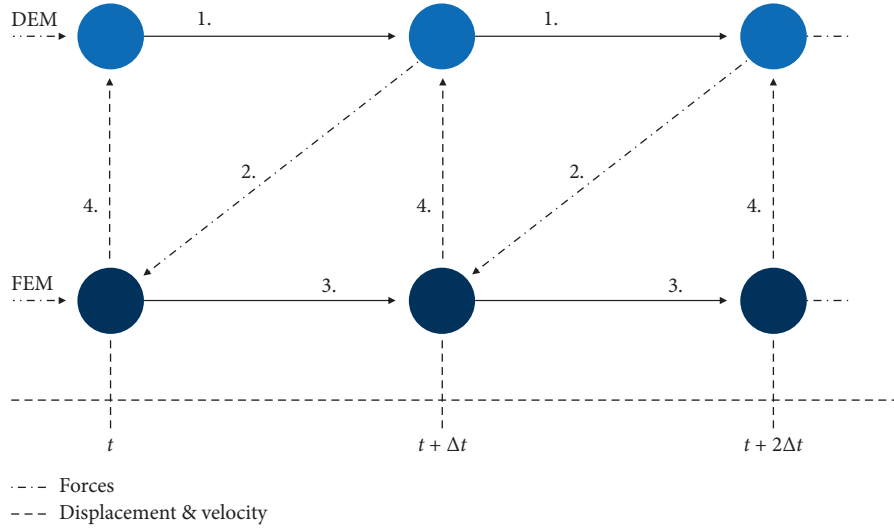


FIGURE 6: Staggered weak coupling procedure, between DEM and FEM.

```

(1) Initialize
(2) While time < end_time do
(3)   If particle _ near _ wall then
(4)     use predefined time step
(5)   Else
(6)     use increased time step
(7)   t = t + Δt
(8)   Search nearest neighbours and find contact → equations (13)–(15)
(9)   Calculate contact forces → equation (A.5)
(10)  Time integration of DEM part → equation (16)
(11)  Map forces on Γ from ΩD to ΩS
(12)  If forces ≠ 0.0 then
(13)    Solve structure (FEM)
(14)    Map velocity and displacement on Γ from ΩS to ΩD
(15)    Update position of ΩD to ΩS → equation (1)
(16) Finalize
  
```

ALGORITHM 1: Weak coupling.

times within one time step [23, 24, 38, 39]. This strategy enforces the coupling conditions (equations (4)–(6)) to be fulfilled. Convergence is considered to be achieved, as soon as the interface residual is below a user-defined tolerance  $\epsilon$ . The residual formulation is defined by using equation (27)

The steps of this approach are shown in Figure 7 and summarized in the following, using the respective numbering in the abovementioned Figure 7:

- (1) Solve DEM (results:  $\mathbf{u}^P$ ,  $\dot{\mathbf{u}}^P$ , and  $\mathbf{F}_{\text{contact}}$ )
- (2) Map  $\mathbf{F}_{\text{contact}}$  from DEM to Structure
- (3) Solve Structure (results:  $\mathbf{u}^{\Omega_{S,\Gamma}}$ ,  $\dot{\mathbf{u}}^{\Omega_{S,\Gamma}}$ , and  $\ddot{\mathbf{u}}^{\Omega_{S,\Gamma}}$ )
- (4) Map *displacements* and *velocities* from Structure to DEM
- (5) Calculate interface residual  $\epsilon$  (equation (27))

- (6) Repeat Steps 1–5 until the interface residual reaches a given tolerance

- (7) Advance in time

The weak coupling algorithm, described in the preceding Section 5 expresses single iteration in the strong coupling scheme (Steps (1)–(4)). The additional interface loop (Step (6), being controlled by the breaking criteria in Step (5)) which adds complexity to the solution procedure and significantly increases the computation costs as the system now needs to be solved multiple times within one time step. However, it allows more accurate results and higher simulation stability. It can be noted that the number of solving iterations is typically still lower than if the time step would be reduced to a value where the weak coupling approach would still be applicable. This is especially due to the property that



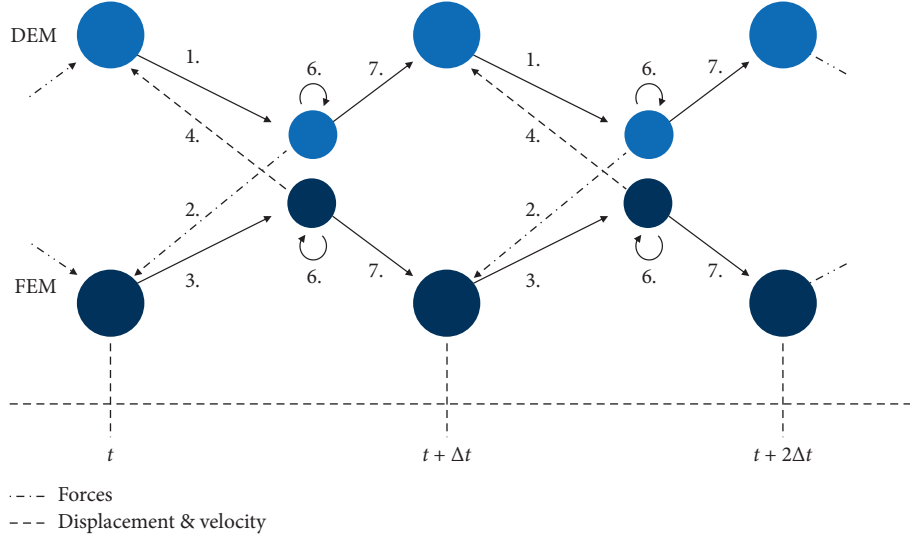


FIGURE 7: Strong coupling communication diagram.

many coupling iterations are typically not required throughout the simulation, but only at specific time steps. The comparison of the two procedures, including a view on the performance, is outlined in Section 7.

The residual criteria within the strong coupling loop are defined by

$$\epsilon < \frac{\|{}^k \mathbf{r}\|}{\sqrt{n_{\text{eq}}}}, \quad (27)$$

where  $\epsilon$  is the user-defined breaking tolerance. It is checked after each iteration  $k$  by scaling the norm of the residuum  ${}^k \mathbf{r}$  with the square root of the number of degrees of freedom  $n_{\text{eq}}$  at the interface  $\Gamma$  [40]. It is important to note that the interface tolerance should be larger than the convergence tolerances of the respective individual solvers within the coupled system; otherwise the convergence criteria cannot be reached. The residuum can either be obtained by the displacements, the velocities, or the contact forces. By subtracting the current solutions on the boundary  $\Gamma$  from the previous solutions of Step  $k-1$ , the residuum of each variable can be noted as follows:

Displacement residuum:

$${}^k \mathbf{r}_u = {}^k \mathbf{u}^{\Omega_{S,\Gamma}} - {}^{k-1} \mathbf{u}^{\Omega_{S,\Gamma}}. \quad (28)$$

Velocity residuum:

$${}^k \mathbf{r}_{\dot{u}} = {}^k \dot{\mathbf{u}}^{\Omega_{S,\Gamma}} - {}^{k-1} \dot{\mathbf{u}}^{\Omega_{S,\Gamma}}. \quad (29)$$

Contact force residuum:

$${}^k \mathbf{r}_F = {}^k \mathbf{F}_{\text{contact}} - {}^{k-1} \mathbf{F}_{\text{contact}}. \quad (30)$$

Furthermore, large time steps typically lead to large differences in the interface velocities and displacements, and thus the result can be nonphysical large contact forces. If those forces are too high, small time steps still can lead to unstable simulations, even with the use of the proposed strong coupling algorithm. As a remedy, the transferred data can be gradually applied, which is also called relaxation. The outcome is that this permits a faster interface convergence. The so-called *convergence acceleration* [24] can be achieved by numerous methods and is discussed in the following.

Two different strategies can be chosen for the relaxation: either the relaxation of the displacements and velocities or the relaxation of the contact forces. The relaxation is done w.r.t. the residual (equations (28)–(30)), respectively:

Relaxed displacements:

$${}^k \mathbf{u}_{\text{rel}}^{\Omega_{S,\Gamma}} = {}^{k-1} \mathbf{u}_{\text{rel}}^{\Omega_{S,\Gamma}} + {}^k \alpha_u {}^k \mathbf{r}_u. \quad (31)$$

Relaxed velocities:

$${}^k \dot{\mathbf{u}}_{\text{rel}}^{\Omega_{S,\Gamma}} = {}^{k-1} \dot{\mathbf{u}}_{\text{rel}}^{\Omega_{S,\Gamma}} + {}^k \alpha_{\dot{u}} {}^k \mathbf{r}_{\dot{u}}. \quad (32)$$

Relaxed contact forces:

$${}^k \mathbf{F}_{\text{contact,rel}} = {}^{k-1} \mathbf{F}_{\text{contact,rel}} + {}^k \alpha_F {}^k \mathbf{r}_F. \quad (33)$$

Each variable is subsequently updated from the previous solution (Step  $k-1$ ) using the respective interface residuum scaled by relaxation factor  $\alpha$ .

There are different approaches to obtain the scaling factor  $\alpha$  [39]. The relaxation factor can be set to a user-defined constant value, which is very simple and helps to

improve the quality of the simulation. Another approach is to use the *Aitken* method [41]. The *Aitken* method optimizes  $\alpha$  in every iteration w.r.t. the current residuum  ${}^k\mathbf{r}$  and the previous residuum  ${}^{k-1}\mathbf{r}$ :

$${}^k\alpha(\mathbf{r}) = {}^{k-1}\alpha \frac{{}^{k-1}\mathbf{r} \cdot ({}^k\mathbf{r} - {}^{k-1}\mathbf{r})}{\|{}^k\mathbf{r} - {}^{k-1}\mathbf{r}\|}, \quad (34)$$

respectively,  $\alpha_u = \alpha(\mathbf{r}_u)$ ,  $\alpha_{ii} = \alpha(\mathbf{r}_{ii})$ , and  $\alpha_F = \alpha(\mathbf{r}_F)$ . The influence of the relaxation factor  $\alpha$  is studied in the example in Section 7.3.

In this study, either the displacement and the velocity field or the contact forces are independently relaxed and subsequently mapped. However, in the case of displacements and velocities, both residua have to be achieved to ensure that both solution fields still coincide on both sides. Thus, the resulting residuum for both relaxing procedures is given as follows:

Displacement and velocity residua:

$${}^k\mathbf{r} = \max({}^k\mathbf{r}_u, {}^k\mathbf{r}_{ii}). \quad (35)$$

Contact force residuum:

$${}^k\mathbf{r} = {}^k\mathbf{r}_F. \quad (36)$$

The interface variables are updated accordingly (see Steps 2 and 4 in Figure 7). The following variables are exchanged within the interface:

*Without relaxation*

Displacements:

$${}^{k+1}\mathbf{u}^{\Omega_{D,\Gamma}} = {}^k\mathbf{u}^{\Omega_{S,\Gamma}}. \quad (37)$$

Velocities:

$${}^{k+1}\dot{\mathbf{u}}^{\Omega_{D,\Gamma}} = {}^k\dot{\mathbf{u}}^{\Omega_{S,\Gamma}}. \quad (38)$$

Contact forces:

$${}^{k+1}\mathbf{F}_{\text{ext}}^{\Omega_{S,\Gamma}} = {}^k\mathbf{F}_{\text{contact}}. \quad (39)$$

*With relaxation*

Displacements:

$${}^{k+1}\mathbf{u}^{\Omega_{D,\Gamma}} = {}^k\mathbf{u}_{\text{rel}}^{\Omega_{S,\Gamma}}. \quad (40)$$

Velocities:

$${}^{k+1}\dot{\mathbf{u}}^{\Omega_{D,\Gamma}} = {}^k\dot{\mathbf{u}}_{\text{rel}}^{\Omega_{S,\Gamma}}. \quad (41)$$

Contact forces:

$${}^{k+1}\mathbf{F}_{\text{ext}}^{\Omega_{S,\Gamma}} = {}^k\mathbf{F}_{\text{contact,rel}}. \quad (42)$$

In summary, both solution strategies are described within Algorithms 2 and 3 in pseudocode. They are both further elaborated on in Appendix B.3.

## 7. Systematic Assessment of the DEM-FEM Coupling

This section presents some examples which systematically analyse the difference between the herein introduced coupling approaches and their application within the simulation of relevant industrial applications. The examples show problems of impacting objects on highly flexible lightweight cable structures, such as protection nets. These interaction problems typically have numerical stability issues within the simulations, as the net structures have a low mass, whereas the rocks are typically heavy. This instability leads to the problem that especially when the first impact occurs, the forces might become very large. Thus, due to the different masses, this may lead to convergence problems, especially if the chosen time step is large, which can lead to inaccuracies in the simulation.

In the first academic problem 7.1, a cable structure is modelled to evaluate the influence of different time step values. Section 7.2 subsequently uses a cable structure with a large prestress while also showing the influence of the COR in order to analyse the influence of larger contact forces on the required time step. Section 7.2 investigates the difference between relaxing forces (Algorithm 3) and relaxing displacements and velocities (Algorithm 2). The proper choice of a relaxation factor is further discussed in the example in 7.3. The influence of the COR, which scales the contact forces, is then analysed in Section 7.4. Finally, a practical application of a rockfall into a cable net, using the herein explained approaches, is presented in Section 7.5.

*7.1. Impact on a Compliant Cable: Large Deformations.* In this example, a single DEM particle with perfect spherical dimensions impacts on a prestressed cable, which is discretized with three finite elements. Here, the contact point on the structure is known, and thus it can be focused on the performance of the coupling algorithms. The setup of this academic example can be found in Figure 8(a), with  $E$  as Young's Modulus and Poisson's ratio  $\nu$ . It demonstrates the necessity of a strong coupling algorithm; since for larger time steps, the phenomena of artificial contact loss, due to large initial contact forces, occur.

Within empirical tests, the time step  $\Delta t = 10^{-3}$  s is found to be the highest possible time step for which the weak coupling algorithm can resolve to an appropriate solution.

```

(1) Initialize
(2) While  $time < end\_time$  do
(3)   While  $interface\_res \geq tolerance\_interface$  do
(4)     Search nearest neighbours and find contact  $\rightarrow$  equations (13)–(15)
(5)     Calculate contact forces  $\rightarrow$  equation (A.5)
(6)     Time integration of DEM part  $\rightarrow$  equation (16)
(7)     Map forces on  $\Gamma$  from  $\Omega_D$  to  $\Omega_S$ 
(8)     Solve structure (FEM)
(9)     Map velocity and displacement on  $\Gamma$  from  $\Omega_S$  to  $\Omega_D$ 
(10)    Calculate residuals for velocity and displacement  $\rightarrow$  equations (28) and (29)
(11)    Relax velocity and displacement  $\rightarrow$  equations (31) and (32)
(12)    Update position of  $\Omega_D$   $\rightarrow$  equation (1)
(13)     $interface\_res = \max(displacement\_residual, velocity\_residual)$ 
(14)    Update position of  $\Omega_S$   $\rightarrow$  equation (1)
(15) Finalize
    
```

ALGORITHM 2: Strong coupling: relaxed displacement and velocity.

```

(1) Initialize
(2) While  $time < end\_time$  do
(3)   While  $interface\_res \geq tolerance\_interface$  do
(4)     Search nearest neighbours and find contact  $\rightarrow$  equations (13)–(15)
(5)     Calculate contact forces  $\rightarrow$  equation (A.5)
(6)     Time integration of DEM part  $\rightarrow$  equation (16)
(7)     Map forces on  $\Gamma$  from  $\Omega_D$  to  $\Omega_S$ 
(8)     Calculate residuals for forces  $\rightarrow$  equation (30)
(9)     Relax forces  $\rightarrow$  equation (33)
(10)    Solve structure (FEM)
(11)    Map velocity and displacement on  $\Gamma$  from  $\Omega_S$  to  $\Omega_D$ 
(12)    Update position of  $\Omega_D$   $\rightarrow$  equation (1)
(13)     $interface\_res = force\_residual$ 
(14)    Update position of  $\Omega_S$   $\rightarrow$  equation (1)
(15) Finalize
    
```

ALGORITHM 3: Strong coupling: relaxed forces.

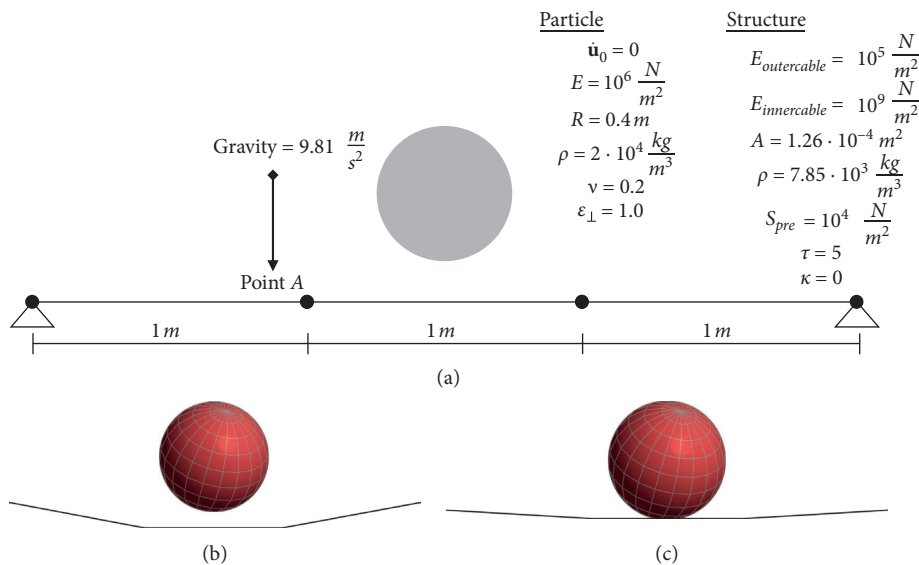


FIGURE 8: Problem setup, including all geometrical and physical input parameters for the simulation. Results after impact with time step of  $\Delta t = 10^{-2}$  s. (a) Problem setup. (b) Weak coupling after impact. (c) Strong coupling after impact.

Here, the coefficient of restitution (COR) is set to be 1.0. Implicit time integration is used for the structure, as the chosen time step is too large for an appropriate solution with an explicit time integration scheme. Figures 8(b) and 8(c) show the behaviour of the cable after impact, for the time step size of  $\Delta t = 10^{-2}$  s. Using the weak coupling approach, a “jump” can be outlined as shown in Figure 8(b). Due to the large time step, a greater indentation and higher velocities occur. Consequently, the interacting force is too large, so that the sphere and cable do not continuously stay in contact during the entire time. This leads to a nonphysical behaviour of the coupled problem, as shown in Figure 9.

By adding the additional interface loop to solve for the contact force, the convergence of the problem can be achieved for a larger time step of  $\Delta t = 10^{-2}$  s.

In the following, the time step of the first contact is discussed in detail. It can be seen (Figure 10(d)) that the contact force is relatively large in the first inner iteration (coming from the relatively large time step) and decreases within the interface iteration to a converged solution, due to the application of the *Aitken* relaxation, introduced in equation (34). This exemplarily demonstrates the advantages of the strong coupling scheme, presented in this article. The large discrepancy in the contact force would lead to an unstable coupled simulation when using a standard weak coupling algorithm. The same accounts for the deflections of the impacting sphere as shown in Figures 10(a)–10(c) presenting a visual description of the interface condition in equations (21) and (22). It can be seen that the positions of  $\Omega_D$  and  $\Omega_S$  do converge to a common value to fulfil the interface displacement/velocity equilibrium (equations (21) and (22)).

As an example, the converging contact force for each iteration in time step  $t = 1.2$  s and the total number of inner iterations for each time step are shown in Figures 11(a) and 11(b). It shows that the force at the first iteration is almost 4 times higher than it is after the converged solution. Figure 11(b) shows that the number of inner iterations can vary greatly (between 1, if there is no contact, and 9 iterations) within each time step. However, it can be noted that the number of contact simulations is still lower than if the time step would be decreased to  $\Delta t = 10^{-3}$  s, which is the limit for which the weak coupling approach still converges.

### 7.2. Comparison to Position of Rest with Different Time Steps.

In this section, a setup similar to the previous example (Section 7.1 and Figure 8(a)) with an increased prestress ( $S_{\text{pre}} = 10^6$  N/m<sup>2</sup>) and a homogeneous Young’s Modulus ( $E = 10^9$  N/m<sup>2</sup>) in the cable structure is used with the following changes for the impacting sphere:  $R = 0.12$  m and  $\rho = 3.5 \cdot 10^4$  kg/m<sup>3</sup>. The result of the transient analysis will be compared to the static solution, considering the particle as an external force. This static force is defined as follows:

$$F_{\text{static}} = \frac{\overbrace{\frac{4}{3}\pi R_{\text{sphere}}^3}^{m_{\text{sphere}}}}{\underbrace{V_{\text{sphere}}}} \cdot \rho_{\text{sphere}} \cdot \underbrace{9.81 \frac{\text{m}}{\text{s}^2}}_{\text{gravity}}. \quad (43)$$

The resulting static deflection of Point A (Figure 8(a)) is shown in Figure 12. This comparison proves that the transient analysis approaches the static solution after a certain time.

Furthermore, the sensitivity of the time step within each coupling algorithm is also studied in this example. The results of all solutions are presented and compared in Figure 12. It shows that the weak coupling approach provides an accurate performance for a time step of  $\Delta t = 10^{-3}$  s, whereas the solution for  $\Delta t = 10^{-2}$  s is very unstable. It turns out that for large time steps, the result oscillates around the expected solutions.

The measured solutions for time steps of  $\Delta t = 10^{-2}$  s and  $\Delta t = 3 \cdot 10^{-2}$  s show that the strong coupling algorithm still allows for good convergence for rather large time steps. However, by increasing the time steps, the number of interface iterations subsequently increase, which is shown in Figures 13(a) and 13(b). Especially when the impact occurs, the large difference in interface velocities leads to an increased number of interface iterations (Figure 13(b)). Within the scope of coupled simulations, this difference is decreased by the proposed algorithm leading to a smaller number of iterations.

The influence if either displacements and velocities or forces are relaxed is examined in the following. Both options are described in Algorithms 2 and 3, respectively.

Comparing Figures 13(a) and 13(b), it can be noted that relaxing the forces facilitates slightly faster convergence than relaxing displacements and velocities.

In this specific case at hand, clear and marked off points of load application (impact position) do exist. In different cases, for example in the following Section 7.5, where a variety of possible impact nodes exist, relaxing displacements and velocities are shown to be the better choice. In those cases, which appear more frequently, the impacting spheres can rapidly change the impacting position and thus lead to a slow converging force residual.

### 7.3. Influence of the Relaxation Factor.

In this example, the influence of the relaxation factor  $\alpha$  in the case of relaxed displacements and velocities is investigated by comparing the *Aitken* relaxation (equation (34)) and a set of constant relaxation factors. For this purpose, the COR is set to 1.0 (which physically describes a perfectly elastic impact on a rigid obstacle) to neglect the influence of the wall velocity and thus concentrate solely on the relaxation factor. The same problem setup as in Section 7.2 is used.

As Figure 14 shows, a constant relaxation factor can be used as long as it is smaller than 1.0.  $\alpha = 1.0$  describes a nonrelaxed system and does not find a proper solution for

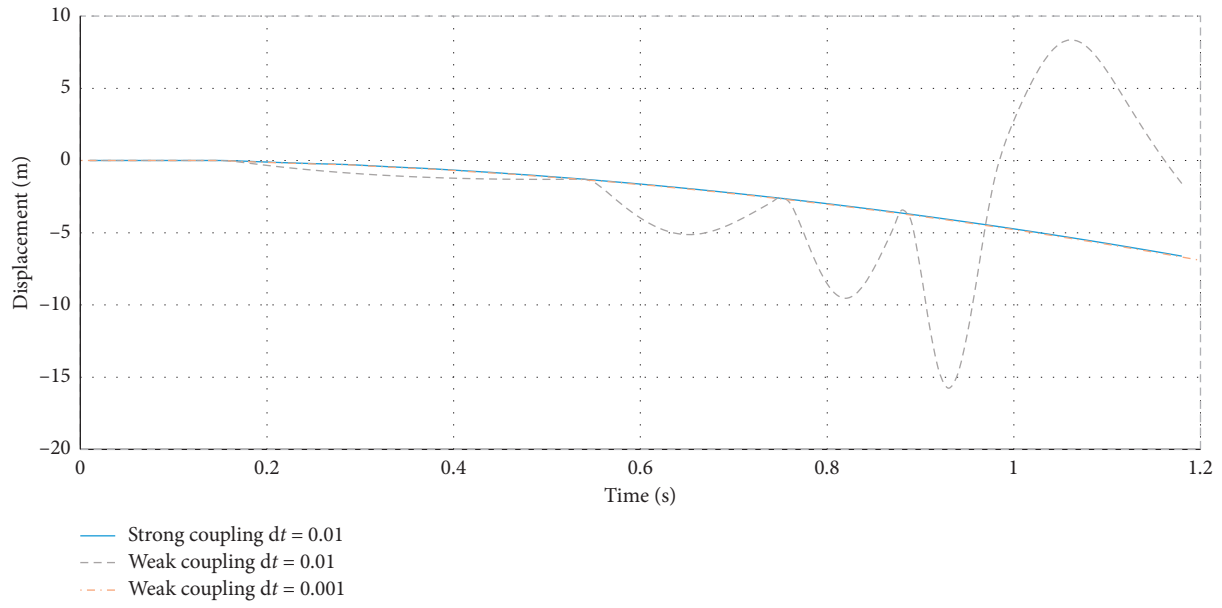
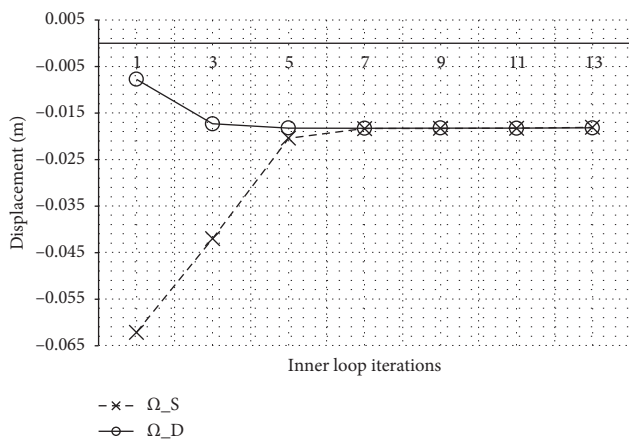
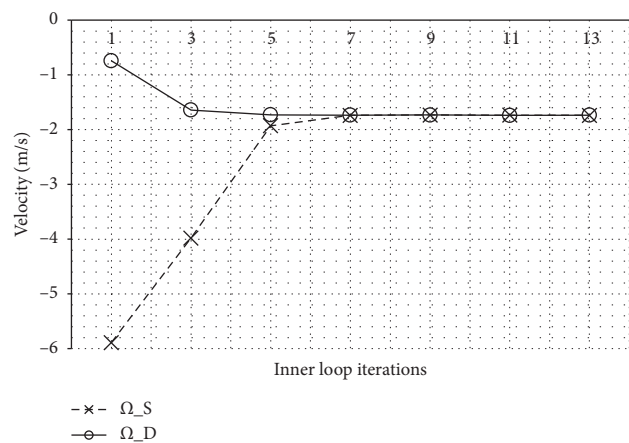


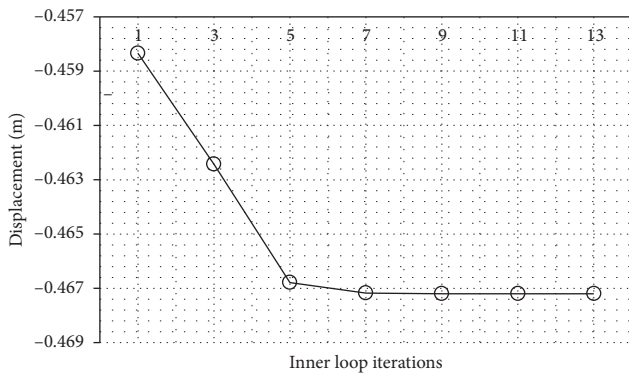
FIGURE 9: Comparison of weak coupling approach with  $\Delta t = 10^{-2}$  s and  $\Delta t = 10^{-3}$  s against the strong coupling approach with  $\Delta t = 10^{-2}$  s for the vertical displacements of node (A) (Figure 8(a)).



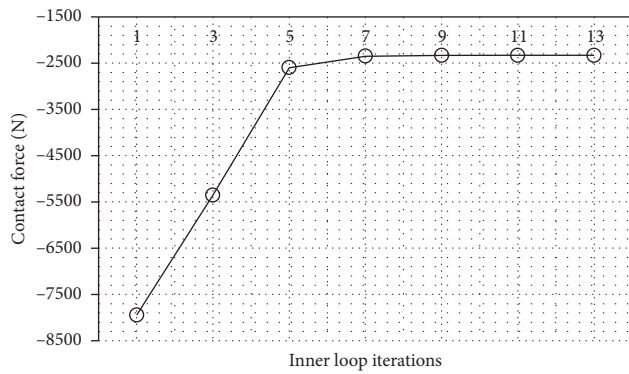
(a)



(b)



(c)



(d)

FIGURE 10: Simulation results within one time step over inner coupling iterations. (a) Interface displacement. (b) Interface velocity. (c) Displacement of impacting sphere. (d) Contact forces on  $\Omega_D$ .

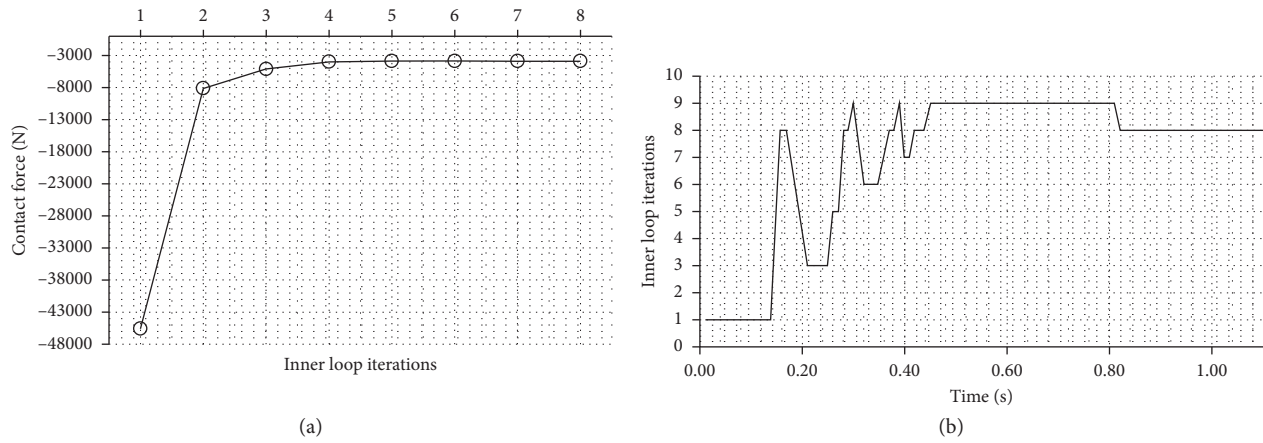


FIGURE 11: Interface simulation results. (a) Contact force at  $t = 1.2$  s. (b) Number of interface iterations per time step.

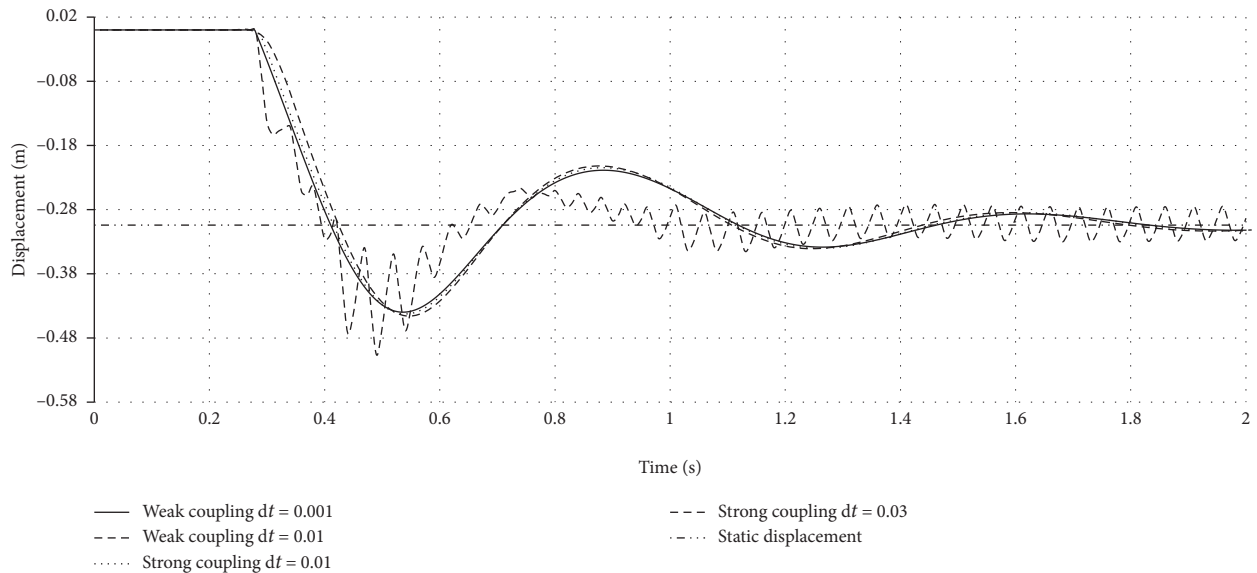


FIGURE 12: Comparison of weak coupling approach with  $\Delta t = 10^{-2}$  s and  $\Delta t = 10^{-3}$  s against the strong coupling approach with  $\Delta t = 10^{-2}$  s and  $\Delta t = 3 \cdot 10^{-3}$  s for the vertical displacements of node A (Figure 8(a)). Furthermore, the static solution of the problem is provided to show which value the results should approach.

this given example. Manually finding a suitable constant relaxation factor is cumbersome and is dependent on the system setup. In addition, it heavily influences the solving time, as Table 1 demonstrates. For a constant  $\alpha$  and the Aitken  $\alpha$  (equation (34)), the comparison is performed with respect to computation time. It can be noted that although constant relaxation factors provide good results, the optimized Aitken relaxation factor facilitates faster convergence to the residual.

**7.4. Influence of the Coefficient of Restitution.** Another important entity within the multiphysics problem is the COR  $\varepsilon_{\perp}$  (Section 3). As Figure 15(b) shows, the COR directly influences the contribution of the DEM rigid wall velocity to the contact force. Current state-of-the-art publications such as [42–44] express the importance of the COR value for

impact simulations. For a case study, different COR values are used, while the time step is kept constant.

As can be seen in Figure 16(a) (zoomed in Figure 16(b)), the interface coupling becomes unstable as soon as the COR reaches a small value. This instability can be overcome by using the strong coupling algorithm presented in Section 6 and is a result of the increased contact force in the system [34]. Additionally, Figure 16(a) describes another important feature: the choice of COR does not influence the final damped solution of the structure (see “static” in the graph in Figure 12) but only the maximum transient solution. Figure 17 visualizes the progression of the maximum interface iterations over the simulation time and indicates the advantages of the proposed coupling algorithm. The large number of iterations at the time of first contact ( $t \approx 0.25$  s) calls for a small time step due to the increased difference in interface velocities. This can be overcome with the help of



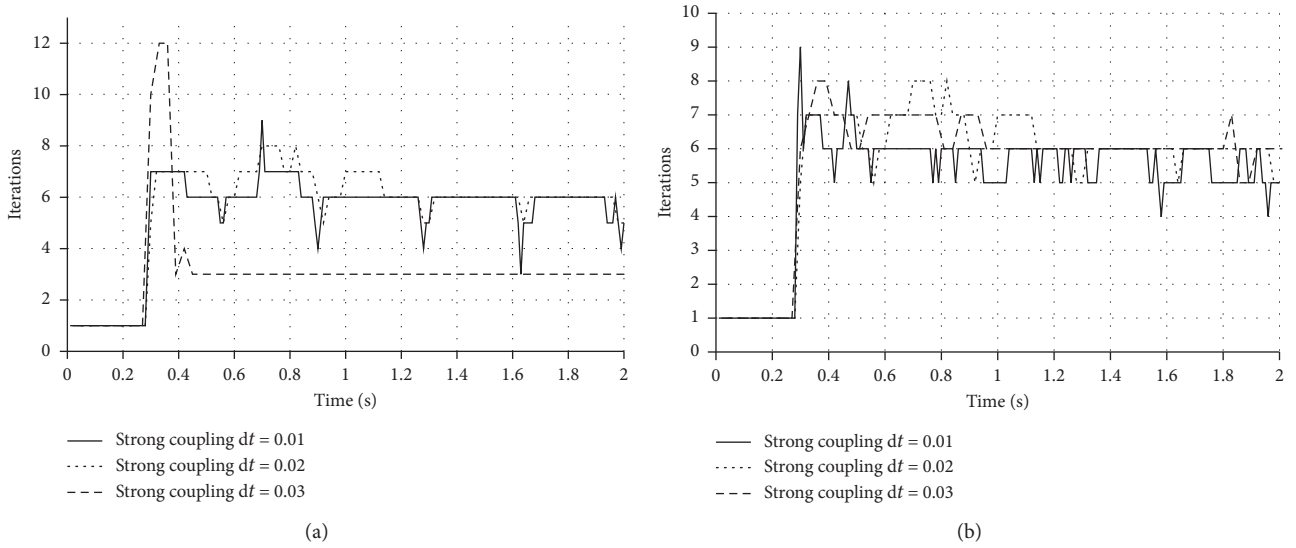


FIGURE 13: Number of interface iterations per time step, for either (a) relaxed displacements and velocities or (b) relaxed forces.

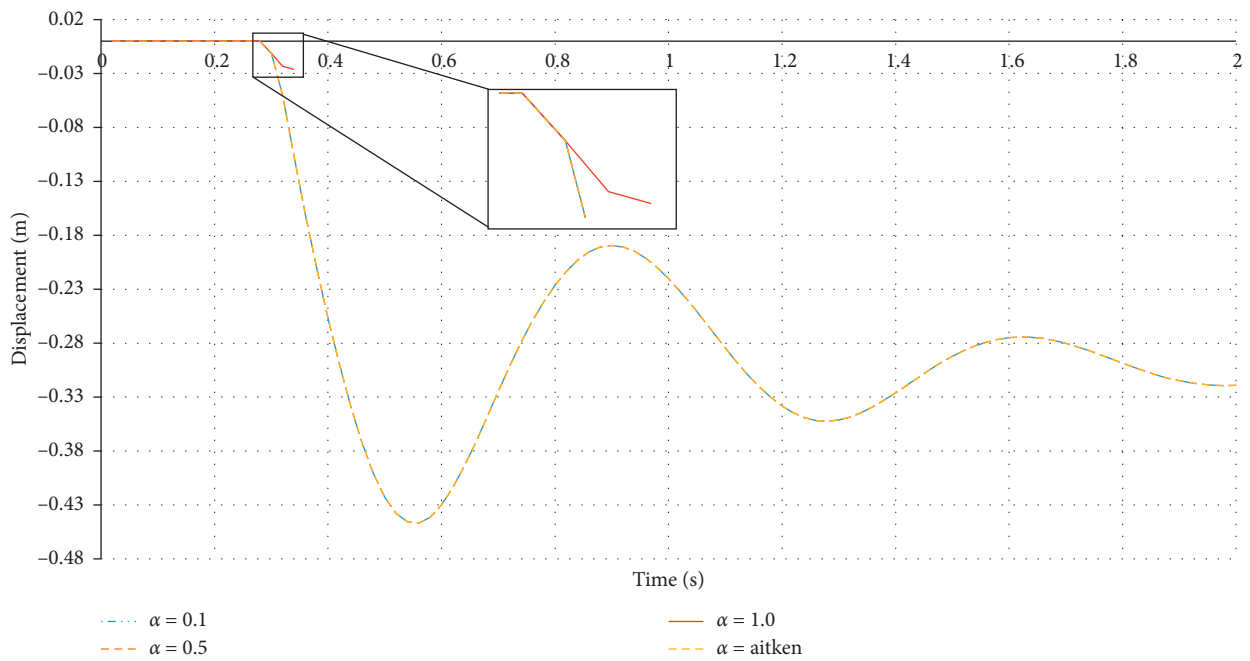


FIGURE 14: Comparison of displacement over time for different relaxation factors  $\alpha$ . With  $\alpha = 1.0$ , the simulation becomes unstable shortly after the first contact is detected. Underrelaxation of  $\alpha < 1.0$  leads to stable simulations too. However, this is more computationally costly than using the optimized Aitken relaxation factor.

TABLE 1: Comparison of computation time with different relaxations and the Aitken relaxation.

Relaxation factor $\alpha$	Relative computation time (%)
0.1	100.0
0.2	54.1
0.5	20.4
0.7	28.5
Aitken	18.7

additionally introduced interface iterations. As the simulation proceeds and the initial velocity difference is properly controlled, fewer iterations are needed to enforce the interface conditions.

7.5. *Practical Application: Angled Protection Net.* One prominent practical application case of highly flexible structures can be found in mountainous regions. As an

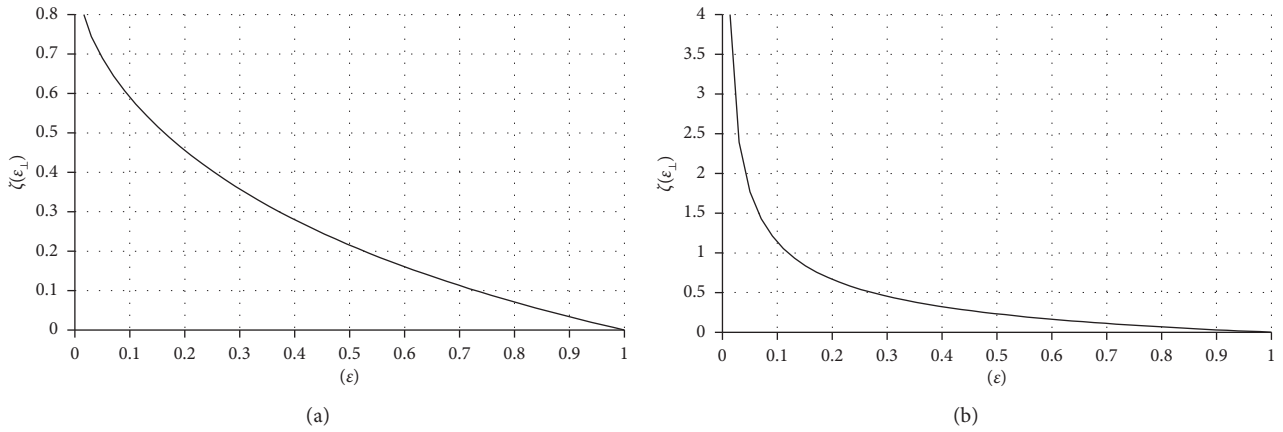


FIGURE 15: Damping coefficient  $\zeta(\varepsilon_{\perp})$ , see [34, 35] for more information. (a) Influence of COR w.r.t. equation (A.7). (b) Influence of COR w.r.t. equation (A.8).

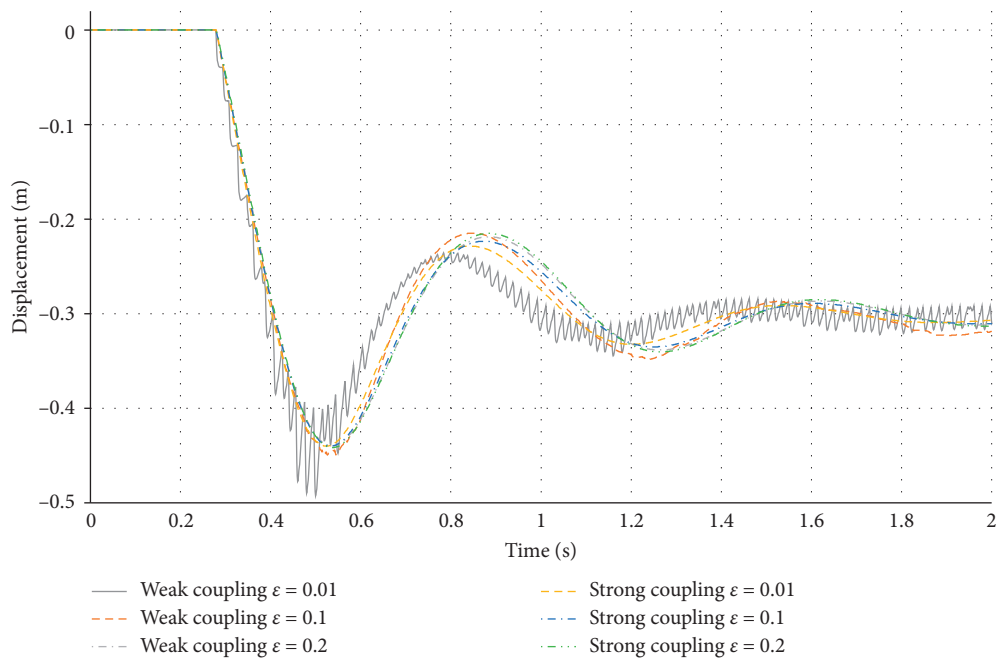


FIGURE 16: Continued.

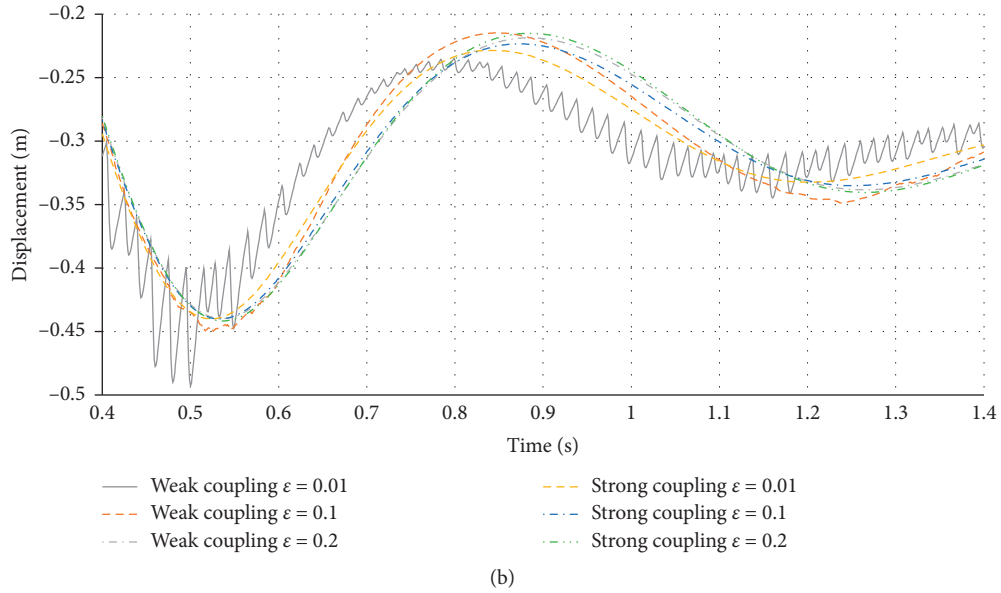


FIGURE 16: Comparison of different COR values. (a)  $t_0 = 0.0 - t_1 = 2.0$ . (b) Scaling to  $t_0 = 0.4 - t_1 = 1.4$ .

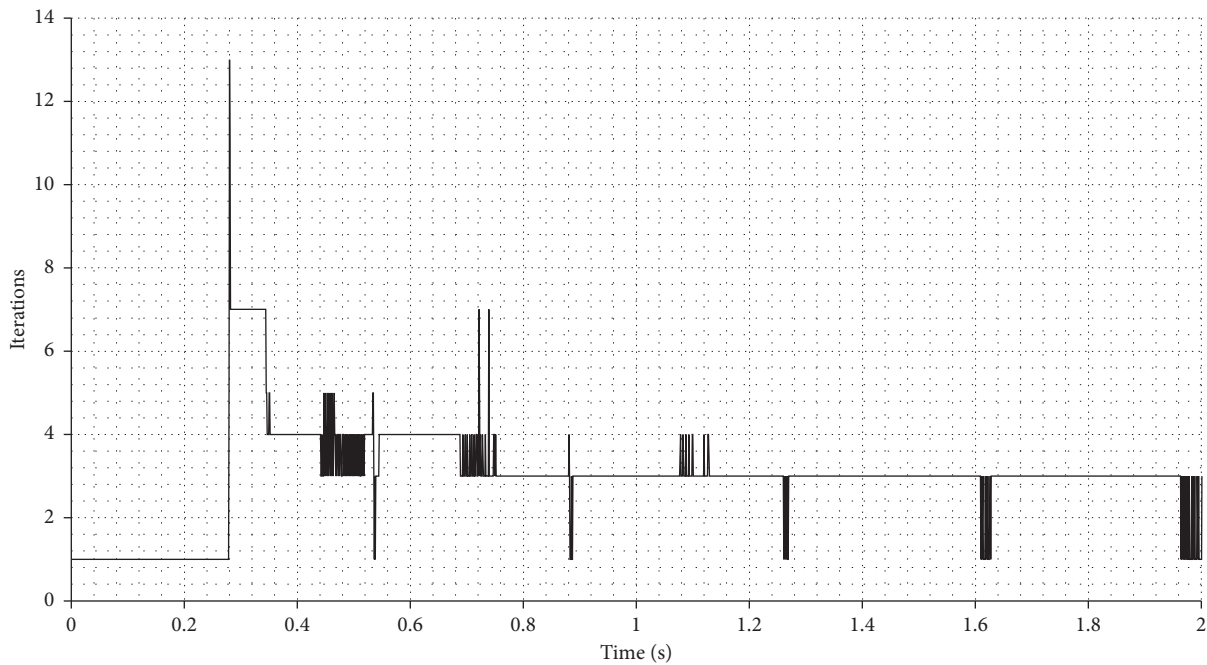


FIGURE 17: Strong coupling interface iterations for  $\epsilon_{\perp} = 0.2$ .

alternative to protection nets used to catch rocks, angled nets can also be spanned over roads to direct impacting objects to a safe spot, as shown in Figure 18(a).

To test the limits of the presented algorithms, in this study, the same system as shown in Figure 18(b) is modelled without prestressing the cable structure, leading to a very compliant structure (compare Table 2). Additionally, a small COR of  $\epsilon_{\perp} = 0.2$  and a high impact velocity are chosen to introduce even more difficulties due to an increased contact force.

Using a time step of  $2 \cdot 10^{-4}$  s, the different behaviours after impact are presented in the incidental Figures 19(a) and 19(b).

Similar to the example from Section 7.1, the weakly coupled problem experiences too large contact forces and loses contact between the impacting object and the structure, whereas the strong coupling algorithm manages to keep the contact for the given time step (Figure 20(a)).

The considerably large number of interface iterations (Figure 20(b)) is a result of the system setup. This example



FIGURE 18: Picture of protection net and corresponding numerical model, including the net as cable structure and two impacting rocks modelled as single DEM particles. The one particle is chosen to be so small that it falls through the net, to verify the correct coupling detection. (a) Route Chalais-Vercorin, Valais [45]. (b) Numerical DEM-FEM coupled model.

TABLE 2: Properties of FEM and DEM parts of example in Section 7.5.

FEM		DEM	
$E$ [N/m <sup>2</sup> ]	$7 \cdot 10^5$	$E$ [N/m <sup>2</sup> ]	$1 \cdot 10^5$
$A$ [m <sup>2</sup> ]	$1.26 \cdot 10^{-5}$	$\dot{u}_0$ [m/s]	[0.0, -5.54, -5.54]
$\rho$ [kg/m <sup>3</sup> ]	$7.85 \cdot 10^3$	$\rho$ [kg/m <sup>3</sup> ]	$2.5 \cdot 10^3$
$S_{\text{pre}}$	0	$R_i$ [m]	[0.21, 0.05]
$\tau$	20	$\nu$	$2 \cdot 10^{-1}$
$\kappa$	0	$\epsilon_{\perp}$	$2 \cdot 10^{-1}$

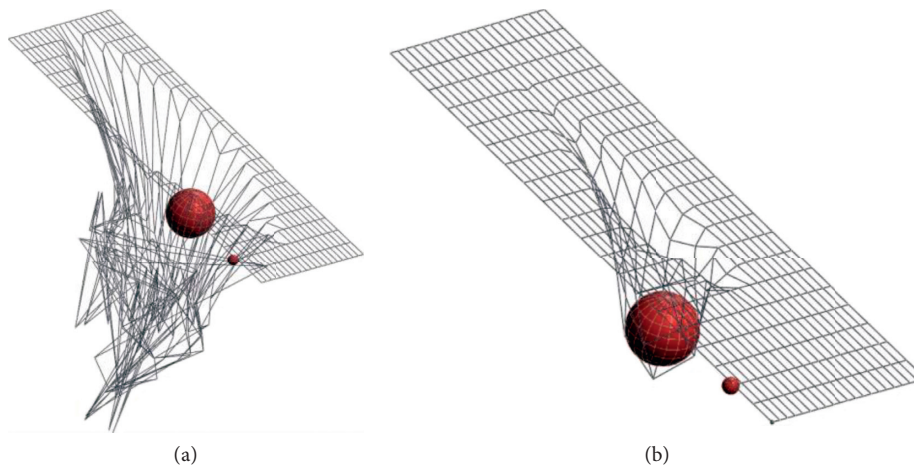


FIGURE 19: Comparison of the (a) weak coupling to the (b) strong coupling approach with the same time step  $\Delta t = 2 \cdot 10^{-4}$  s.

tries to push the time step to a maximum and represents the largest possible time step, which cannot even be used for weak coupling anymore, describing a complex problem.

**7.6. Arbitrary Boundary Conditions.** Another advantage of this procedure is the possibility to use arbitrary boundary conditions for the problem. As can be seen in Figures 21(a)–22(e), the arbitrary triangular and quadrilateral meshes can be used to simulate any boundary condition, for instance, a mountainous region. As it is the state of the art in industrial applications, \*.stl files can be used. If only point clouds are

available, standard tools can be used to create a triangulated mesh. The structural part can be subsequently put into this domain to easily capture the interaction of different terrain models and loading scenarios.

As an example, Figures 21(a)–21(i) demonstrate a plane boundary with a curtain-like structure in the middle and a cable net protection net at the end of the slope.

In contrast to the plane boundary, Figures 22(a)–22(e) show the use of an arbitrarily shaped boundary, obtained from a \*.stl mesh. The effortless integration of a deformable FEM structure into the arbitrary boundary is indicated in this example.

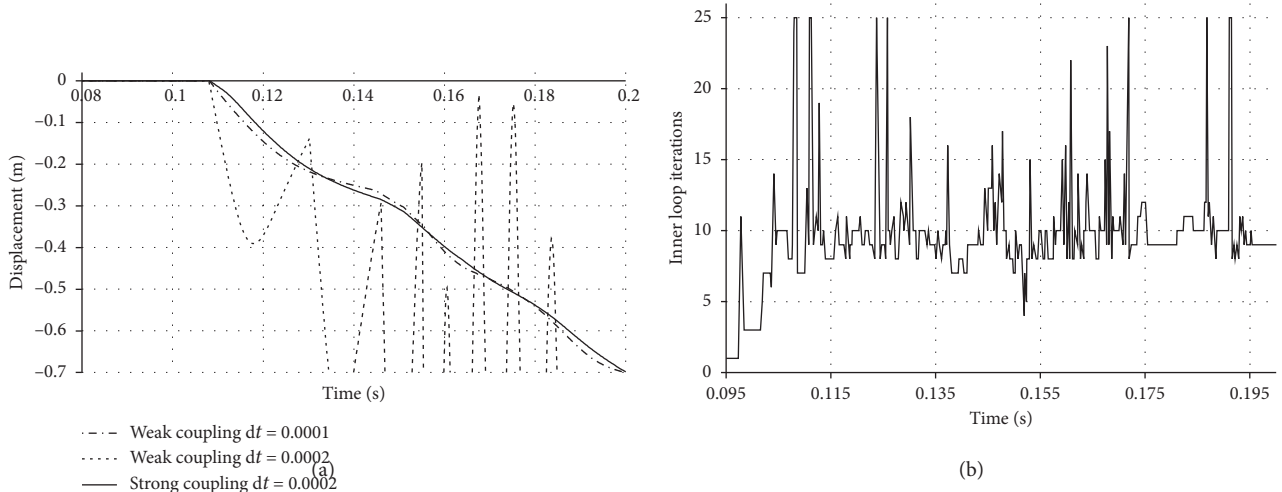


FIGURE 20: Simulation results. (a) Weak vs. strong coupling-displacement of centre node. (b) Interface iterations over simulation time.

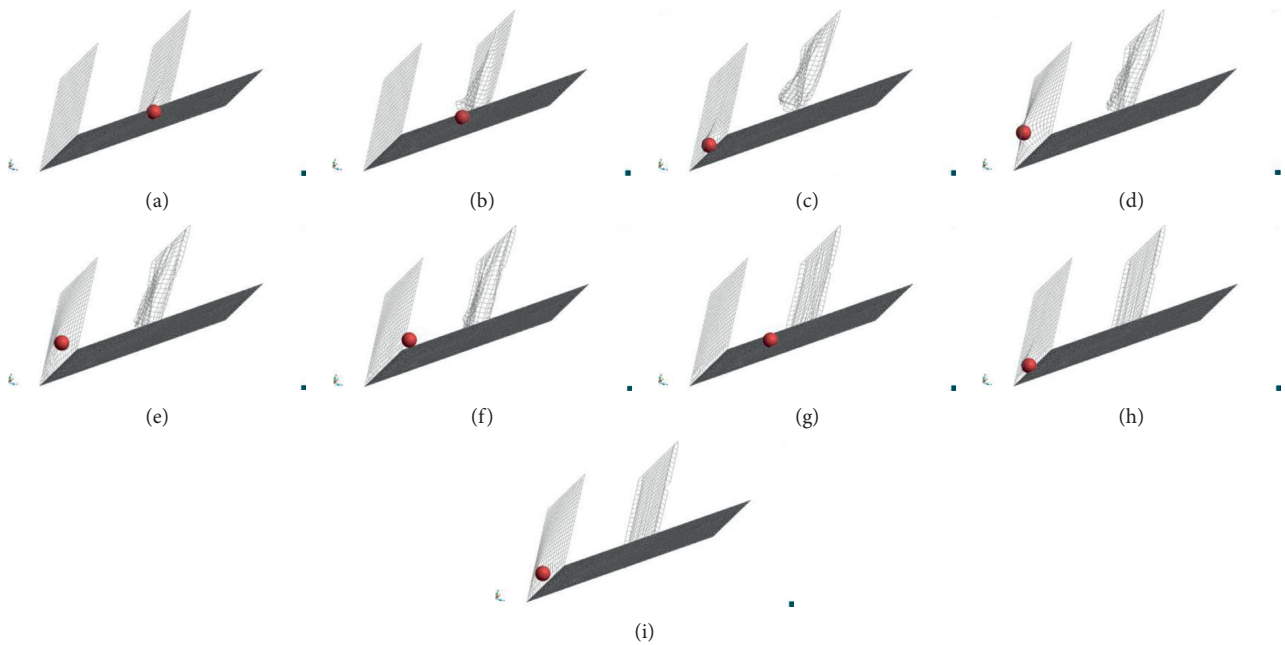


FIGURE 21: Plane boundary rigid with one impacting sphere and two protection nets. The first net (right) is not connected on the lower edge, and the other is coupled to the ground. (a)  $t = 1.3$  s. (b)  $t = 1.5$  s. (c)  $t = 1.9$  s. (d)  $t = 2.2$  s. (e)  $t = 2.4$  s. (f)  $t = 2.5$  s. (g)  $t = 3.6$  s. (h)  $t = 4.4$  s. (i)  $t = 4.7$  s.

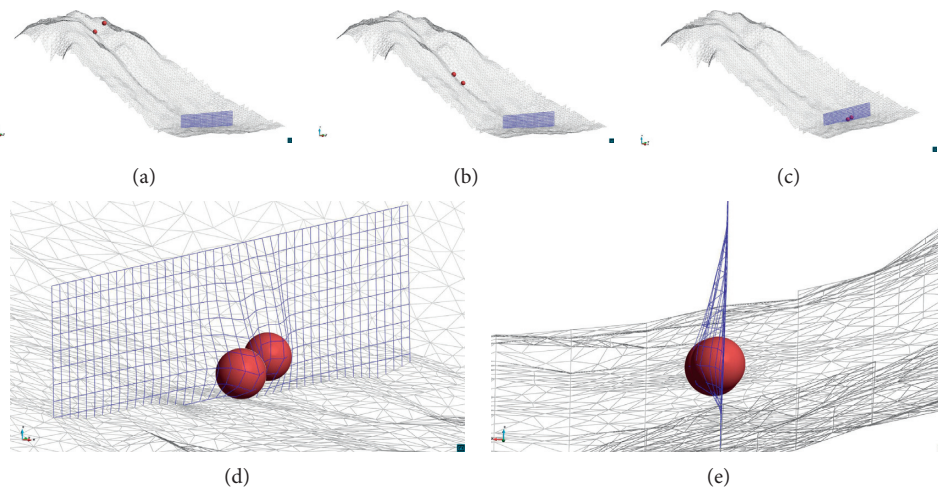


FIGURE 22: Triangulated terrain model, showing the downward rolling of the rocks, which are being slowed and stopped by the protection net. (a)  $t = 1.2$  s. (b)  $t = 4.5$  s. (c)  $t = 6.8$  s. (d) Net impact  $t = 6.8$  s. (e) Net impact: side view  $t = 6.8$  s.

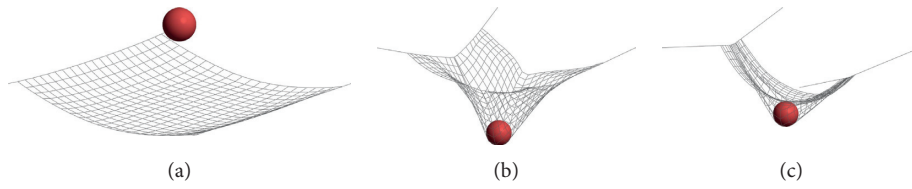


FIGURE 23: Sliding node within the FEM model. It allows us to model a more accurate behaviour of the cable structure nets. (a)  $t = 0.0$  s. (b)  $t = 2.7$  s. (c)  $t = 4.5$  s.

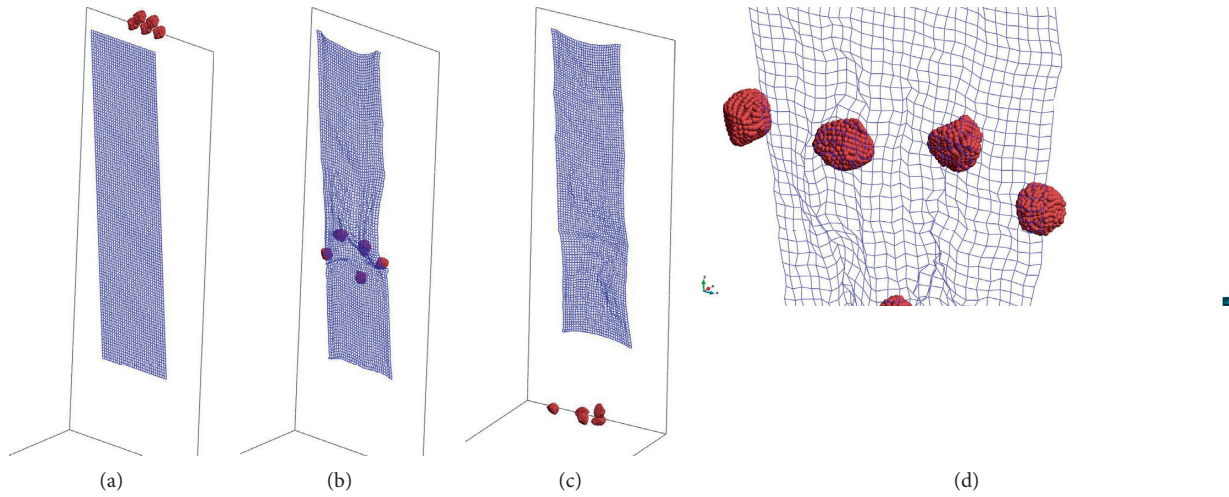


FIGURE 24: Impact problem with more complex shape of impacting objects. Moving impact rocks are discretized as particles which are clustered to allow any arbitrary shapes. (a)  $t = 0.0$  s. (b)  $t = 1.3$  s. (c)  $t = 3.0$  s. (d) Impact of DEM clusters,  $t = 1.3$  s.

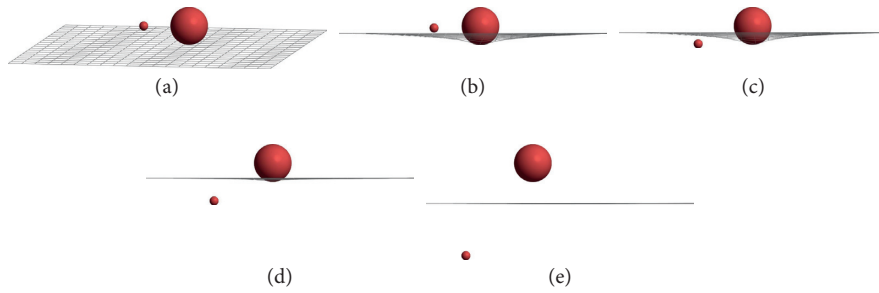


FIGURE 25: Small particle is penetrating and falling through the coarse cable net. Big particle collides with cable structure and is stopped and thrown back by the protection structure. (a)  $t = 0.0$  s. (b)  $t = 0.05$  s. (c)  $t = 0.1$  s. (d)  $t = 0.15$  s. (e)  $t = 0.2$  s.

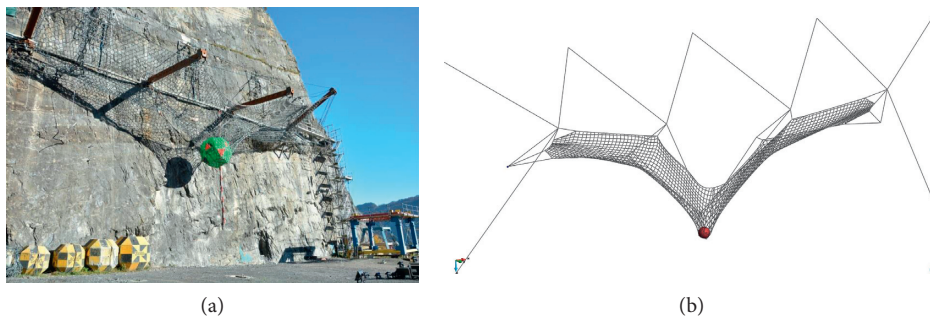


FIGURE 26: Protection net test setup in Walenstadt, Switzerland. (a) Testing area in Walenstadt, St. Gallen, Switzerland [45]. (b) FEM mesh.



**7.7. Special Modelling Possibilities.** Using two standalone solution techniques, such as the DEM and structural mechanics FEM, enables the user to benefit from the full range of capabilities and strengths of both participants, such as sliding nodes on cable elements (including friction) [1, 4] (Figures 23(a)–23(c)), custom ring elements [1, 4, 46], plasticity laws to model energy dissipation elements, choice of multiple time integration schemes, and clusters of particles (Figures 24(a)–24(d)) to model arbitrarily shaped objects such as rocks, which is an advantage over state-of-the-art rockfall protection simulations as discussed in [1, 47].

Using rigid bodies to model impacting objects has the disadvantage of neglecting damage and deformation of the object itself and adding additional complexity when handling arbitrarily shaped objects. The DEM offers the possibility to simulate breakup of impacting objects [21]; however, the simulation of the continuum with DEM particles can be very costly, and calibration can be elaborate.

The possibility to model  $\Omega_D$  with line wall conditions suitable to the FEM mesh additionally allows for small rocks to penetrate the protection net (Figures 25(a)–25(e)). In summary, the combination of the DEM and the FEM allows the user to model any possible object impacting in a highly flexible structure modelled by any suitable structural finite element types. Any conceivable combination (Figure 26) is possible as long as a suitable algorithm, as presented in this paper, is available.

## 8. Conclusions and Outlook

The numerical analysis of lightweight structures coupled with impacting heavy objects proves to be a complex problem and leads to instabilities within the simulation, especially due to the different masses of the participants. To overcome this problem, this publication presents several staggered coupling approaches and presents a sensitivity study with respect to certain crucial parameters.

The procedure suggested herein uses FEM with cable element formulations for flexible lightweight structures (Section 2) and DEM for the interacting objects (Section 3). Furthermore, Section 4 shows the procedure for reaching the equilibrium between both physics. First, the procedure is explained with a single interface calculation within each time step (Section 5). In many examples, this approach proved to be unstable, specifically at initial contacts (indicating large velocity differences). Additionally, the simulation needs small time steps, which might be required only at certain steps. Thus, to overcome this problem, an additional iteration between the physics was explained in Section 6. This allows time steps to be increased significantly and improves the efficiency of the simulation (see examples in 7.1, 7.2, and 7.3). Additionally, the sensitivity of the quality of the simulation is tested by varying the relaxation factor (equation (34) in combination with example in 7.3) and the coefficient of restitution (COR) (see Appendix A in combination with example in 7.4). While the underlying algorithms are abstractly presented in the preceding sections, more detailed versions can be found in the following appendix to allow the interested reader to independently reproduce the results.

The novel approaches make it possible to efficiently simulate the correct behaviour of complex existing structures. The example in 7.5 shows net structures interacted with rocks which are based on existing structures in the Austrian and Swiss Alps. The stability is heavily influenced by a restricting time step (Figures 19(a) and 20(a)) if the interface is not controlled by a suitable algorithm as presented in this study.

In addition, the use of two standalone applications in this study, the so-called “blackbox solvers” allows for a variety of advantageous features. As described in Section 7.6, any given terrain model can be integrated into the simulation process to efficiently capture environmental influences on the results (Figures 22(a)–22(e)). Furthermore, Section 7.7 demonstrates the advantages of an independent FEM application which is capable of modelling numerous structural details, such as energy dissipation elements or sliding nodes on cable elements. Accordingly, DEM can be used to model arbitrarily shaped impacting objects (Figures 24(a)–24(d)). This allows for independent work in the respective application without changing the coupling strategy, which especially proves beneficial in an open-source software environment such as KRATOS [48].

In future research, different FEM formulations [2, 3] can be tested for the simulation of the protection nets. Furthermore, if rocks cannot be explicitly described, other particle approaches such as the material point method (MPM [5]) could be applied with the proposed coupling approach. By the way of example, conceivable application cases include the simulation of mud-flow barriers as well as avalanche barriers. Furthermore, the influence of the time integration scheme is additionally a significant factor which will require deeper investigations.

## Abbreviations

FEM: Finite element method  
 DEM: Discrete element method  
 COR: Coefficient of restitution  
 MPM: Material point method  
 FSI: Fluid-structure interaction.

## Appendix

### A. DEM Force Derivation

A detailed description of the evaluation of forces described in Section 3 is provided in order to further discuss the necessary quantities in the underlying coupling scheme. As soon as a contact is detected, the forces can be evaluated using various contact laws and rheological models in which the normal indentation  $\delta_n$  [21] is as follows:

$$\delta_n = R_i + R_j - (\mathbf{C}_j - \mathbf{C}_i) \cdot \mathbf{n}^{ij}, \quad \text{with } \mathbf{n}^{ij} = \frac{\mathbf{C}_j - \mathbf{C}_i}{\|\mathbf{C}_j - \mathbf{C}_i\|}, \quad (\text{A.1})$$

and its time derivative  $\dot{\delta}_n$ , the normal vector  $\mathbf{n}^{ij}$ , and the increment of tangential displacement  $\Delta s$  are used.

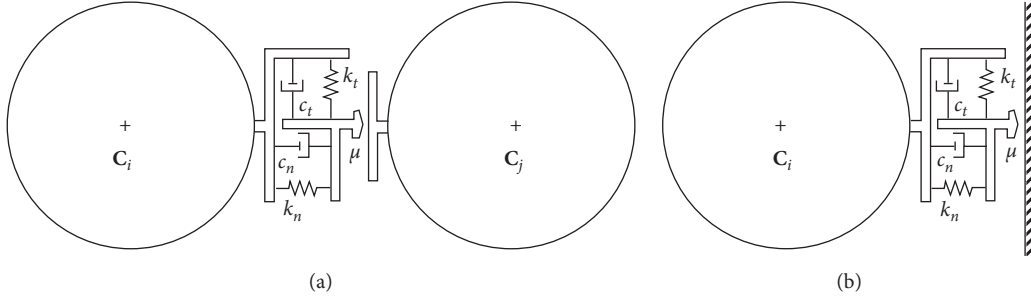


FIGURE 27: DEM-DEM and DEM-FEM rheological models. (a) DEM-DEM [21]. (b) DEM-FEM [21].

TABLE 3: Stiffness values for sphere-sphere and sphere-wall contact [21].

	Sphere $i$ -Sphere $j$	Sphere $i$ -Wall $j$
$k_n$	$(4/3(((1-\nu_i^2)/E_i) + ((1-\nu_j^2)/E_j)))\sqrt{(R_i R_j/(R_i+R_j))\delta_n}$	$(4/3(((1-\nu_i^2)/E_i) + ((1-\nu_j^2)/E_j)))\sqrt{R_i\delta_n}$
$k_t$	$(8/(((2-\nu_i)/G_i) + ((2-\nu_j)/G_j)))\sqrt{(R_i R_j/(R_i+R_j))\delta_n}$	$(8G_i/(2-\nu_i))\sqrt{R_i\delta_n}$
$c_n$	$(2(\zeta_i + \zeta_j)/2)\sqrt{((m_i m_j)/(m_i + m_j))k_n}$	$2\zeta_i\sqrt{m_i k_n}$
$c_t$	$(2(\zeta_i + \zeta_j)/2)\sqrt{((m_i m_j)/(m_i + m_j))k_t}$	$2\zeta_i\sqrt{m_i k_t}$

In order to obtain  $\Delta s$ , the tangent unit vector  $\mathbf{t}^{ij}$  must be derived by splitting the velocity at the contact point  $\mathbf{v}_c^{ij}$  into normal  $\mathbf{v}_{c,n}^{ij}$  and tangential  $\mathbf{v}_{c,t}^{ij}$  components. First, the contact point velocity is expressed with the aid of the respective element velocity  $\mathbf{v}_i$ , element angular velocity  $\boldsymbol{\omega}_i$ , and the vector  $\mathbf{r}_c^{ij}$  connecting the particle centre and the contact point:

$$\mathbf{v}_c^{ij} = (\boldsymbol{\omega}_j \times \mathbf{r}_c^{ji} + \mathbf{v}_j) - (\boldsymbol{\omega}_i \times \mathbf{r}_c^{ij} + \mathbf{v}_i), \quad (\text{A.2})$$

and then, split up

$$\begin{aligned} \mathbf{v}_{c,n}^{ij} &= (\mathbf{v}_c^{ij} \cdot \mathbf{n}^{ij})\mathbf{n}^{ij}, \\ \mathbf{v}_{c,t}^{ij} &= \mathbf{v}_c^{ij} - \mathbf{v}_{c,n}^{ij}, \end{aligned} \quad (\text{A.3})$$

which allows us to express  $\Delta s$  using the tangent unit vector, the element displacement  $\mathbf{u}_i$ , and the element rotation  $\boldsymbol{\Theta}_i$ :

$$\begin{aligned} \Delta s &= \|\mathbf{u}^{ij} \cdot \mathbf{t}^{ij}\|, \\ \mathbf{t}^{ij} &= \frac{\mathbf{v}_{c,t}^{ij}}{\|\mathbf{v}_{c,t}^{ij}\|}, \\ \mathbf{u}^{ij} &= (\boldsymbol{\Theta}_j \times \mathbf{r}_c^{ji} + \mathbf{u}_j) - (\boldsymbol{\Theta}_i \times \mathbf{r}_c^{ij} + \mathbf{u}_i). \end{aligned} \quad (\text{A.4})$$

For a Hertz–Mindlin spring-dashpot contact model (denominated as HM + D in [34]), as shown in Figures 27(a) and 27(b), the normal  $F_n$  and tangential  $F_t$  contact forces [21, 34] for the case of two spheres colliding,

$$\begin{aligned} F_n &= k_n \delta_n + c_n \dot{\delta}_n, \\ F_{te}^n &= F_{te}^{n-1} + k_t^n \Delta s^n, \quad \text{if } \Delta F_n \geq 0, \\ F_{te}^n &= F_{te}^{n-1} \frac{k_t^n}{k_t^{n-1}} + k_t^n \Delta s^n, \quad \text{if } \Delta F_n < 0, \\ F_t^n &= \min[F_{te}^n + c_t v_{c,t}^{ij}, \mu F_n]. \end{aligned} \quad (\text{A.5})$$

are calculated with the aid of the normal and tangential stiffness  $k_n$  and  $k_t$ , respectively, and the damping coefficients  $c_n$  and  $c_t$  [21], considering the maximum tangential force restricted to the Coulomb's friction limit [34] with the coefficient of friction  $\mu$ . The tangential forces are consequently updated from the last step, indicated by the superscript  $n$ .

The material parameters in Table 3 (Young's modulus  $E$ , particle mass  $m$ , shear modulus  $G$ , and Poisson's ratio  $\nu$ ) are typically obtained by calibration from experiments [49].

As a scaling factor in Table 3, the dashpot coefficient  $\zeta$  [21, 34] is frequently expressed using the normal coefficient of restitution (COR)  $\varepsilon_\perp$  as shown in the following equation:

$$\varepsilon_\perp = \frac{\delta_n^{\text{after}}}{\delta_n^{\text{before}}}, \quad (\text{A.6})$$

$$\zeta = \frac{\ln \varepsilon_\perp}{\sqrt{\pi^2 + (\ln \varepsilon_\perp)^2}}. \quad (\text{A.7})$$

Based on our experience, which is as well as supported by [34, 35], a more realistic modelling of the dashpot coefficient  $\zeta$  is given by the following equation [34, 35]:

$$\zeta = \sqrt{\frac{1.0}{1.0 - (1.0 + \varepsilon_\perp)^2} \cdot e^\Lambda} - 1.0, \quad (\text{A.8})$$

$$\begin{aligned} \Lambda &= \varepsilon_\perp \cdot (h_1 + \varepsilon_\perp \cdot (h_2 + \varepsilon_\perp \cdot (h_3 + \varepsilon_\perp \cdot (h_4 + \varepsilon_\perp \cdot (h_5 + \varepsilon_\perp \\ &\quad \cdot (h_6 + \varepsilon_\perp \cdot (h_7 + \varepsilon_\perp \cdot (h_8 + \varepsilon_\perp \cdot (h_9 + \varepsilon_\perp \cdot h_{10})))))))). \end{aligned} \quad (\text{A.9})$$

```

(1) ### Import Applications ####
(2) # Structural Mechanics Application is for FEM analysis, in this scope used for the cable structures.
(3) from KratosMultiphysics.StructuralMechanicsApplication import structural_mechanics_analysis as structural_analysis
(4) # DEM Application is for DEM analysis; in this scope, it holds certain expressions for walls and can also deal with clustered
    particles.
(5) from KratosMultiphysics.DEMApplication import KratosDEMAnalysis as dem_analysis
(6) # Mapping Application is to allow a mapping between certain spaces; it is used to handle certain interfaces to make the procedures
    more generic.
(7) import KratosMultiphysics.MappingApplication as KratosMapping
(8) ### Define Problem Setup ###
(9) # model part for all faces/boundary walls
(10) mp_dem = dem_analysis.rigid_face_model_part
(11) # model part for all DEM particles
(12) mp_dem_particle = dem_analysis.spheres_model_part
(13) # Analysis model and model part for structural elements
(14) model = KratosMultiphysics.Model()
(15) mp_struct = model["Structure.computing_domain"]
(16) # Create mapper and define relations. It relates the model parts of the walls in DEM to the cable structures in FEM
(17) mapper = KratosMapping.MapperFactory.CreateMapper(mp_dem, mp_struct, mapper_settings)
(18) # Create utility to optimize contact detection
(19) dem_mesh_moving_utility = DEMApplication.MoveMeshUtility()
(20) ### Initialize Application Setup ###
(21) # Initialize all necessary variables within the applications
(22) structural_analysis.Initialize()
(23) dem_analysis.Initialize()

```

ALGORITHM 4: Problem setup.

```

(1) ### Start Time Loop ###
(2) while dem_analysis.time < dem_analysis.end_time:
(3)     # increase time step if particles are not near to the interface
(4)     if not dem_mesh_moving_utility.CheckIsNearToWall(mp_dem_particle.Nodes):
(5)         dem_analysis.SetDeltaTime(multiply = 100.0)
(6)     # reset time step if particles are near to the interface
(7)     else:
(8)         dem_analysis.SetDeltaTime(multiply = 1.0)
(9)     ### Solve DEM Problem ###
(10)    # update time parameters
(11)    dem_analysis._UpdateTimeParameters()
(12)    # search and find neighbouring elements/particles which are in contact
(13)    dem_analysis.SearchOperations()
(14)    # calculate contact forces
(15)    dem_analysis.ForceOperations()
(16)    # integrate in time to obtain new position and velocity of DEM particles
(17)    dem_analysis.IntegrationOfMotion()
(18)    # finalize time step by updating state variables
(19)    dem_analysis.FinalizeSingleTimeStep()
(20)    # check for contact forces and solve FEM part if contact forces exist
(21)    if dem_mesh_moving_utility.CheckContact(mp_dem.Nodes):
(22)        ### Map Contact Forces ###
(23)        # DEM to Structure
(24)        mapper.Map(DEMApplication.CONTACT_FORCES, StructuralMechanicsApplication.POINT_LOAD)
(25)        ### Solve Structural Mechanics Problem ###
(26)        structural_analysis.AdvanceInTime()
(27)        # set the previous configuration as the current configuration
(28)        structural_analysis.InitializeSolutionStep()
(29)        # prediction step for solution scheme if necessary

```

ALGORITHM 5: Continued.

```

(30) structural_analysis.Predict()
(31) # solve the FEM system of equations or explicitly integrate in time
(32) structural_analysis.SolveSolutionStep()
(33) # finalize time step by updating state variables and spatial position
(34) structural_analysis.FinalizeSolutionStep()
(35) ### Map Velocity and Displacement ####
(36) # Structure to DEM
(37) mapper.InverseMap(VELOCITY)
(38) mapper.InverseMap(DISPLACEMENT)
(39) # update position of DEM wall condition
(40) dem_analysis.MoveMesh()
(41) ### Finalize Applications ####
(42) # e.g., free memory, make output, ...
(43) dem_analysis.Finalize()
(44) structural_analysis.Finalize()

```

ALGORITHM 5: Weak coupling.

```

(1) ### Start Time Loop ####
(2) while dem_analysis.time < dem_analysis.end_time:
(3) # update time parameters
(4) dem_analysis.AdvanceInTime()
(5) structural_analysis.AdvanceInTime()
(6) # save the current position, forces, velocity, etc., of the DEM wall condition and particles
(7) dem_analysis.SaveCurrentData()
(8) # initialize time step
(9) structural_analysis.InitializeSolutionStep()
(10) # initial interface residuals
(11) InitializeResiduals()
(12) while interface_residual > interface_tolerance:
(13) ### Solve DEM Problem ####
(14) # reset the previous saved data of the particle to keep it at the same reference position in each inner loop step
(15) dem_analysis.SetOldDataParticles()
(16) # search and find neighbouring elements/particles which are in contact
(17) dem_analysis.SearchOperations()
(18) # calculate contact forces
(19) dem_analysis.ForceOperations()
(20) # integrate in time to obtain new position and velocity of DEM particles
(21) dem_analysis.IntegrationOfMotion()
(22) ### Map Contact Forces ####
(23) # DEM to Structure
(24) mapper.Map(DEMApplication.CONTACT_FORCES, StructuralMechanicsApplication.POINT_LOAD)
(25) ### Solve Structural Mechanics Problem ####
(26) # prediction step for solution scheme (if necessary)
(27) structural_analysis.Predict()
(28) # solve the FEM system of equations or explicitly integrate in time
(29) structural_analysis.SolveSolutionStep()
(30) ### Map Velocity and Displacement ####
(31) # Structure to DEM
(32) mapper.InverseMap(VELOCITY)
(33) mapper.InverseMap(DISPLACEMENT)
(34) ### Calculate Interface Residuals ####
(35) calculate_displacement_residual()
(36) calculate_velocity_residual()
(37) # use the maximum residual for the convergence check
(38) interface_residual = max(displacement_residual, velocity_residual)
(39) ### Relax Exchange Data ####
(40) dem_analysis.RelaxDisplacementAndVelocity()

```

ALGORITHM 6: Continued.

```

(41) dem_analysis.SetRelaxedDisplacementAndVelocity()
(42) ### Update DEM ####
(43) # update position of DEM wall
(44) dem_analysis.MoveMesh()
(45) # use the current position of the DEM wall condition and the last converged position to calculate the difference in
displacement, which is used to calculate contact force
(46) dem_analysis.CalculateDeltaDispFromIntermediatePos()
(47) # finalize time step by updating state variables and spatial position
(48) structural_analysis.FinalizeSolutionStep()
(49) dem_analysis.FinalizeSingleTimeStep()
(50) ### Finalize Applications ####
(51) dem_analysis.Finalize()
(52) structural_analysis.Finalize()

```

ALGORITHM 6: Strong coupling: relax displacements and velocities.

```

(1) ### Start Time Loop ####
(2) while dem_analysis.time < dem_analysis.end_time:
(3) # update time parameters
(4) dem_analysis.AdvanceInTime()
(5) structural_analysis.AdvanceInTime()
(6) # save the current position, forces, velocity, etc., of the DEM wall condition and particles
(7) dem_analysis.SaveCurrentData()
(8) # initialize time step
(9) structural_analysis.InitializeSolutionStep()
(10) # initial interface residuals
(11) InitializeResiduals()
(12) while interface_residual > interface_tolerance:
(13) ### Solve DEM Problem ####
(14) # reset the previous saved data of the particle to keep it at the same reference position in each inner loop step
(15) dem_analysis.SetOldDataParticles()
(16) # search and find neighbouring elements/particles which are in contact
(17) dem_analysis.SearchOperations()
(18) # calculate contact forces
(19) dem_analysis.ForceOperations()
(20) # integrate in time to obtain new position and velocity of DEM particles
(21) dem_analysis.IntegrationOfMotion()
(22) ### Map Contact Forces ####
(23) # DEM to Structure
(24) mapper.Map(DEMApplication.CONTACT_FORCES, StructuralMechanicsApplication.POINT_LOAD)
(25) ### Calculate Interface Residual ####
(26) interface_residual = calculate_force_residual()
(27) ### Relax Exchange Data ####
(28) dem_analysis.RelaxForces()
(29) dem_analysis.SetRelaxedForces()
(30) # prediction step for solution scheme (if necessary)
(31) structural_analysis.Predict()
(32) # solve the FEM system of equations or explicitly integrate in time
(33) structural_analysis.SolveSolutionStep()
(34) ### Map Velocity and Displacement ####
(35) # Structure to DEM
(36) mapper.InverseMap(VELOCITY)
(37) mapper.InverseMap(DISPLACEMENT)
(38) ### Update DEM ####
(39) # update position of DEM wall
(40) dem_analysis.MoveMesh()

```

ALGORITHM 7: Continued.

```

(41) # use the current position of the DEM wall condition and the last converged position to calculate the difference in
      displacement, which is used to calculate
(42) dem_analysis.CalculateDeltaDispFromIntermediatePos()
(43) # finalize time step by updating state variables and spatial position
(44) structural_analysis.FinalizeSolutionStep()
(45) dem_analysis.FinalizeSingleTimeStep()
(46) ### Finalize Applications ####
(47) dem_analysis.Finalize()
(48) structural_analysis.Finalize()

```

ALGORITHM 7: Strong coupling: relax forces.

$$\mathbf{h} = [-6.918798, -16.41105, 146.8049, -796.4559, 2928.711, -7206.864, 11494.29, -11342.18, 6276.757, -1489.915]. \quad (\text{A.10})$$

The difference can be observed in Figures 15(a) and 15(b). For further information about this topic, the reader is redirected to [21, 34, 35].

With respect to [21, 35], the COR expresses the ratio between the velocity after  $\delta_n^{\text{after}}$  and the velocity before  $\delta_n^{\text{before}}$  impact. A maximum of  $\varepsilon_{\perp} = 1.0$  will model a perfectly elastic impact, whereas  $\varepsilon_{\perp} = 0.0$  models a perfectly plastic impact. A smaller COR increases the influence of the impact velocity in the contact force calculation [21, 34] (equation (A.5)) and is thus critical for the coupled simulation in this study, in which a Hertz–viscous–Coulomb contact law is used [21].

For frictional cohesion-less contact as used in this study, the normal force must be constrained to always be  $\geq 0.0$  [21], since no traction in normal direction is allowed. To correctly capture this behaviour, Cummins et al. [34] describe how to modify the contact duration calculation by using the dashpot coefficient as described by equation (A.8). For further discussion on the contact forces, additional contact laws, and specific DEM-related topics such as contact duration, etc., see [21, 34, 35, 50, 51].

## B. Code Scripts and Development Environment

To give the interested reader a better understanding and the possibility to reproduce the results, the algorithms are presented with the notation used. The open-source multi-physics software *KRATOS* [48] was used for this study. It can be downloaded [52]. An installation guideline is provided there, too. *KRATOS* is designed in C++ and includes a *Python* interface to facilitate the advanced development and simulation. Documentation for the *Python* scripts used in this study is provided in the following. To run the simulation, the structural mechanics application, the discrete element application, and the mapping application are required.

**B.1. Problem Setup.** The script to define the problem setup is shown in the following. This initialization script is for both the weak and the strong coupling approach, which are described in the following appendices (Algorithm 4).

**B.2. Weak Coupling Algorithm.** First, the *Python* script to run the weak coupling algorithm (Section 5) is provided. This code sequence describes two possibilities to improve the efficiency of the simulation: one by increasing the time step if particles are far away from the interface and the other by solving the FEM part only if contact forces have been detected. These two features are omitted in Appendix B.3 for simplicity purposes. However, they can be used to optimize computation time (Algorithm 5).

**B.3. Strong Coupling Algorithm.** The two strong coupling approaches described in Section 6 are depicted in the following algorithms. First, the procedure to relax displacements and velocities is explained, followed by the procedure to relax the transferred forces (Algorithms 6 and 7).

**B.3.1. Relax Displacements and Velocities algorithm 7**

**B.3.2. Relax Forces**

## Data Availability

No data were used to support the findings of the study.

## Conflicts of Interest

The authors declare that they have no conflicts of interest.

## Authors' Contributions

All the authors prepared the manuscript. All the authors read and approved the final manuscript.

## Acknowledgments

This work was supported by the Technical University of Munich (TUM).

## References

- [1] A. Volkwein, *Numerische Simulation von flexiblen Steinschlagschutzsystemen*, ETH, Zurich, Switzerland, 2004.
- [2] A. Mentani, L. Govoni, A. Giacomini, G. Gottardi, and O. Buzzi, "An equivalent continuum approach to efficiently model the response of steel wire meshes to rockfall impacts," *Rock Mechanics and Rock Engineering*, vol. 51, no. 9, pp. 2825–2838, 2018.



- [3] S. Tahmasbi, A. Giacomini, C. Wendeler, and O. Buzzi, "On the computational efficiency of the hybrid approach in numerical simulation of rockfall flexible chain-link mesh," *Rock Mechanics and Rock Engineering*, vol. 52, no. 10, pp. 3849–3866, 2019.
- [4] R. Boulaud and C. Douthe, "A sliding cable model for rockfall barrier simulations using dynamic relaxation," in *Proceedings of the IASS Annual Symposium*, Hamburg, Germany, September 2017.
- [5] X. Zhang, Z. Chen, and Y. Liu, *The Material Point Method: A Continuum-Based Particle Method for Extreme Loading Cases*, Academic Press, Cambridge, MA, USA, 2016.
- [6] M. Santasusana, Miquel, J. Irazábal, E. Oñate, and J. M. Carbonell, "The Double Hierarchy Method. A parallel 3D contact method for the interaction of spherical particles with rigid FE boundaries using the DEM," *Computational Particle Mechanics*, vol. 3, no. 3, pp. 407–428, 2016.
- [7] J. Stransky and M. Jirásek, "Open source DEM-FEM coupling," in *Proceedings of the Engineering Mechanics*, Stuttgart, Germany, May 2012.
- [8] H. Haddad, M. Guessasma, and J. Fortin, "A DEM-FEM coupling based approach simulating thermomechanical behaviour of frictional bodies with interface layer," *International Journal of Solids and Structures*, vol. 81, pp. 203–218, 2016.
- [9] J. Denape, "Third body concept and wear particle behavior in dry friction sliding conditions," *Tribological Aspects in Modern Aircraft Industry*, pp. 1–12, 2014.
- [10] L. Cao, F. Sadeghi, and L.-E. Stacke, "A combined EFEM-DEM dynamic model of rotor-bearing-housing system," *Journal of Tribology*, vol. 139, no. 6, 2017.
- [11] B. Baskaran, S. M. Srinivasan, B. Maffeo et al., "Shot peening simulation using discrete and finite element methods," *Advances in Engineering Software*, vol. 41, no. 12, pp. 1266–1276, 2010.
- [12] K. Kovthaman, S. Utili, and N. Petrinic, "A combined DEM-FEM numerical method for Shot Peening parameter optimization," *Advances in Engineering Software*, vol. 79, pp. 13–26, 2015.
- [13] A. Ashtekar and F. Sadeghi, "A new approach for including cage flexibility in dynamic bearing models by using combined explicit finite and discrete element methods," *Journal of Tribology*, vol. 134, no. 4, 2012.
- [14] C. Bovet and L. Zamponi, "An approach for predicting the internal behaviour of ball bearings under high moment load," *Mechanism and Machine Theory*, vol. 101, pp. 1–22, 2016.
- [15] J. Takabi and M. M. Khonsari, "On the dynamic performance of roller bearings operating under low rotational speeds with consideration of surface roughness," *Tribology International*, vol. 86, pp. 62–71, 2015.
- [16] K. A. Kounoudji, M. Renouf, G. Mollon, and Y. Berthier, "Role of third body on bolted joints' self-loosening," *Tribology Letters*, vol. 61, no. 3, 2016.
- [17] S. Liu, H. Li, S. Shen, and S. Wu, "Simulation of particle rebounding from the slider air bearing surface," *Microsystem Technologies*, vol. 22, no. 6, pp. 1475–1481, 2016.
- [18] N. T. Ngo, B. Indraratna, and C. Rujikiatkamjorn, "Coupled DEM-FEM analysis for simulating ballasted rail tracks," in *Proceedings of the 15th IACMAG*, Wuhan, China, October 2017.
- [19] E. Oñate, F. Zárata, M. A. Celigueta et al., "Advances in the DE and coupled DEM and FEM techniques in non linear solid mechanics," *Advances in Computational Plasticity: A Book in Honour of D. Roger J. Owen*, Scipedia, Barcelona, Spain, 2018.
- [20] E. Oñate, M. A. Celigueta, S. Latorre et al., "Lagrangian analysis of multiscale particulate flows with the particle Finite Element Method," *Computational Particle Mechanics*, vol. 1, no. 1, pp. 85–102, 2014.
- [21] M. Santasusana, *Numerical Techniques for Non-linear Analysis of Structures Combining Discrete Element and Finite Element Methods*, CIMNE, Barcelona, Spain, 2016.
- [22] T. Belytschko, W. Liu, B. Moran, and K. Elkhodary, *Nonlinear Finite Elements for Continua and Structures*, Wiley, Hoboken, NJ, USA, 2013.
- [23] U. Küttler, *Effiziente Lösungsverfahren für Fluid-Struktur-Interaktions-Probleme*, TUM, Munich, Germany, 2009.
- [24] R. Wüchner, *Mechanik und Numerik der Formfindung und Fluid-Struktur-Interaktion von Membrantragwerken*, TUM, Munich, Germany, 2006.
- [25] G. Strang and G. Fix, *An Analysis of the Finite Element Method*, Wellesley-Cambridge Press, Wellesley, MA, USA, 2008.
- [26] E. A. de Souza Neto, D. Peric, and D. R. J. Owen, *Computational Methods for Plasticity: Theory and Applications*, Wiley, Hoboken, NJ, USA, 2011.
- [27] J. Bonet and R. D. Wood, *Nonlinear Continuum Mechanics for Finite Element Analysis*, Cambridge University Press, Cambridge, UK, 2008.
- [28] G. A. Holzapfel, *Nonlinear Solid Mechanics: A Continuum Approach for Engineering*, Wiley, Hoboken, NJ, USA, 2000.
- [29] A. M. Widhammer, *Variation of Reference Strategy*, TUM, Munich, Germany, 2015.
- [30] Y. Basar and D. Weichert, *Nonlinear Continuum Mechanics of Solids: Fundamental Mathematical and Physical Concepts*, Springer, Berlin Heidelberg, 2000.
- [31] T. Drieseberg, *Ein Beitrag zur Formfindung von Tensegrity-Systemen mit der Kraftdichtemethode*, Kassel University Press, Kassel, Germany, 2007.
- [32] A. Alipour and F. Zareian, "Study Rayleigh damping in structures; uncertainties and treatments," in *Proceedings of the 14th World Conference on Earthquake Engineering*, Beijing, China, October 2008.
- [33] B. Smeets, T. Odenthal, S. Vanmaercke, and H. Ramon, "Polygon-based contact description for modeling arbitrary polyhedra in the Discrete Element Method," *Computer Methods in Applied Mechanics and Engineering*, vol. 290, pp. 277–289, 2015.
- [34] S. Cummins, C. Thornton, and C. Cleary, "Contact force models in inelastic collisions," in *Proceedings of the Ninth International Conference on CFD in the Minerals and Process*, Melbourne, Australia, December 2012.
- [35] T. Schwager and T. Pöschel, "Coefficient of restitution and linear-dashpot model revisited," *Granular Matter*, vol. 9, no. 6, pp. 465–469, 2007.
- [36] T. Wang, *Development of Co-simulation Environment and Mapping Algorithms*, TUM, Munich, Germany, 2016.
- [37] A. Winterstein, C. Lerch, K.-U. Bletzinger, and R. Wüchner, "Partitioned simulation strategies for fluid-structure-control interaction problems by Gauss-Seidel formulations," *Advanced Modeling and Simulation in Engineering Sciences*, vol. 5, no. 1, 2018.
- [38] C. Farhat, K. G. van der Zee, and P. Geuzaine, "Provably second-order time-accurate loosely-coupled solution algorithms for transient nonlinear computational aeroelasticity," *Computer Methods in Applied Mechanics and Engineering*, vol. 195, no. 17–18, pp. 1973–2001, 2006.
- [39] S. Sicklinger, *Stabilized Co-simulation of Coupled Problems Including Fields and Signals*, TUM, Munich, Germany, 2014.
- [40] U. Küttler and W. Wall, "Fixed-point fluid-structure interaction solvers with dynamic relaxation," *Computational Mechanics*, vol. 43, no. 1, pp. 61–72, 2008.

- [41] C. Aitken, "XXV.—on Bernoulli's numerical solution of algebraic equations," in *Proceedings of the Royal Society of Edinburgh*, Edinburgh, UK, 1927.
- [42] N. Sabatakakis, N. Depountis, and N. Vagenas, "Evaluation of rockfall restitution coefficients," *Engineering Geology for Society and Territory*, vol. 2, pp. 2023–2026, 2015.
- [43] A. Pavlos, H. Saroglou, and G. Tsiambaos, "Rockfall: scaling factors for the coefficient of restitution," in *Proceedings of the Eurock 2013 Rock Mechanics for Resources, Energy & Environment*, Wroclaw, Poland, September 2013.
- [44] K. T. Chau, R. H. C. Wong, and J. J. Wu, "Coefficient of restitution and rotational motions of rockfall impacts," *International Journal of Rock Mechanics and Mining Sciences*, vol. 39, no. 1, pp. 69–77, 2002.
- [45] Geobruigg, <https://www.geobruigg.com/>.
- [46] J. P. E. Osorio, *Simulation of Flexible Steel Wire-Net Rock-Fall Barriers via Finite Element Model Updating*, ETH, Zurich, Switzerland, 2015.
- [47] A. Volkwein, "Numerical simulation of flexible rockfall protection systems," *Computing in Civil Engineering*, 2005.
- [48] KRATOS Multi-Physics, <https://www.cimne.com/kratos/>.
- [49] C. J. Coetzee and D. N. J. Els, "Calibration of granular material parameters for DEM modelling and numerical verification by blade–granular material interaction," *Journal of Terra-mechanics*, vol. 46, no. 1, pp. 15–26, 2009.
- [50] G. Casas, D. Mukherjee, M. A. Celigueta, T. I. Zohdi, and E. Oñate, "A modular, partitioned, Discrete Element framework for industrial grain distribution systems with rotating machinery," *Computational Particle Mechanics*, vol. 4, no. 2, pp. 181–198, 2017.
- [51] H. A. Navarro and M. P. de Souza Braun, "Determination of the normal spring stiffness coefficient in the linear spring–dashpot contact model of discrete element method," *Powder Technology*, vol. 246, pp. 707–722, 2013.
- [52] KRATOS Multi-Physics - GitHub Repository, <https://github.com/KratosMultiphysics/Kratos>.

## Research Article

# Investigation on Influences of Two Discrete Methods on Galloping Characteristics of Iced Quad Bundle Conductors

Xiaohui Liu <sup>1</sup>, Guangyun Min <sup>2</sup>, Chuan Wu <sup>3</sup>, and Mengqi Cai <sup>4</sup>

<sup>1</sup>State Key Laboratory of Mountain Bridge and Tunnel Engineering, Chongqing Jiaotong University, Chongqing 400074, China

<sup>2</sup>School of Civil Engineering, Chongqing Jiaotong University, Chongqing 400074, China

<sup>3</sup>State Grid Henan Electric Power Research Institute, Zhengzhou 450052, China

<sup>4</sup>School of Architecture and Civil Engineering, Chengdu University, Chengdu 610106, China

Correspondence should be addressed to Xiaohui Liu; [cqdxlxh@126.com](mailto:cqdxlxh@126.com)

Received 19 May 2020; Revised 10 October 2020; Accepted 17 October 2020; Published 5 November 2020

Academic Editor: Chiara Bedon

Copyright © 2020 Xiaohui Liu et al. This is an open access article distributed under the Creative Commons Attribution License, which permits unrestricted use, distribution, and reproduction in any medium, provided the original work is properly cited.

The partial differential galloping equation of iced quad conductors can be transformed into an ordinary differential galloping equation by two discrete methods: one is a direct discrete method and the other is an indirect discrete method. The two discrete methods are reasonable and effective and have their own advantages and disadvantages, but whether the two different discrete methods would cause the differences in galloping characteristics of the iced quad conductor has not been studied. Based on this concept, this paper studies this problem systematically. Firstly, based on the variational principle for Hamiltonian, the partial differential galloping equation with 3DOFs of the iced quad bundle conductor is derived and then two discrete methods are used to transform the partial differential galloping equation into an ordinary differential galloping equation. One is to use a direct method to transform partial differential galloping equation into an ordinary differential galloping equation, while the other is to use an indirect method to transform partial differential galloping equation into an ordinary differential galloping equation. Secondly, based on the wind tunnel test, the three-component aerodynamic coefficients of each subconductor of the iced quad conductor are obtained, and the equivalent aerodynamic coefficients at the central axis of the quad bundle conductor are obtained by using a reasonable method. Then, the aerodynamic coefficients are fitted by Taylor rules and the aerodynamic coefficients of wind angle of attack which is  $55^\circ$  are used in the analysis of galloping characteristics of the iced quad conductor. Finally, based on the numerical method, the displacement response of the two discrete methods is obtained. By comparing the differences of the displacement response obtained by the two discrete methods, it is found that the two discrete methods have certain influences on the phase, frequency, and amplitude of the iced quad bundle conductor. By comparing the calculation process of these two discrete methods, it can be obtained that the calculation process of the direct discrete method is more complex and the calculation process of the indirect discrete method is simpler. By comparing the calculation results of these two discrete methods, the amplitude obtained by the indirect discrete method is bigger than that obtained by the direct discrete method, especially the amplitude in the torsional direction. The research conclusion of this paper can offer some guidance to civil and electric engineering.

## 1. Introduction

With the rapid development of power grid, the galloping characteristics of iced transmission lines have attracted the attention of most scholars [1–5]. In fact, the span length of transmission lines is far larger than its diameter, which belongs to the flexible cable structure. For cable structure, Irvine firstly studied the statics and linear and nonlinear dynamics of the suspension cable structure and proposed

important Irvine parameters [6]. Perkins divided the external excitation of elastic suspension cable into two types, parametric excitation and periodic excitation, and studied the interaction between mode shapes and mode shapes of elastic suspension cable [7]. Rega firstly systematically expounded the mechanical modeling, response, and non-linear phenomena of the suspension cable from the theoretical analysis, then verified the correctness of the theoretical analysis from the experiment, and found lots of

valuable guidance and suggestions for civil and electric engineering [8]. Some scholars also have made many contributions to the study of suspension structure. Lilien and Havard established the finite element model of conductor with 6-DOF joints based on the space curved beam theory, then used the Newton–Raphson method to solve the static nonlinear problem, and found some very meaningful conclusions [9]. Based on the existing research, Yan et al. considered the influences of bending stiffness on the suspension cable and modified the error of bending stiffness not considered in the existing literature [10]. According to the variational principle for Hamiltonian, Xiao et al. deduced the nonlinear dynamic equation with 3DOFs considering bending stiffness of suspension cable, then analyzed the possible internal resonance modes of the cable by the multiscale method, and studied the influences of bending stiffness on internal resonance by the numerical method [11].

Although the existing papers are based on the cable structure to analyze the vibration characteristics of iced transmission lines, the galloping of iced transmission lines is different from the vibration of cable. Because the galloping characteristics of transmission lines are related to ice type, ice thickness, and other factors, the galloping of transmission lines is essentially a fluid-structure coupling vibration. Because the galloping of iced transmission lines is affected by aerodynamic loads, the top priority of studying the galloping characteristics is to obtain the three-dimensional aerodynamic coefficients of transmission lines. Zhao et al. analyzed the actual galloping data of a single conductor, two-bundle conductor, three-bundle conductor, and quad bundle conductor and then obtained some valuable results, which can provide some references for the study of the galloping characteristics of conductor [12]. Kimura et al. made the static wind tunnel test and dynamic wind tunnel test on the crescent iced conductor and then analyzed the differences between static aerodynamic characteristics and dynamic aerodynamic characteristics [13]. Lou et al. investigated the influences of iced thickness, initial iced accretion angle, and subconductor on the aerodynamic properties [14], and Cai et al. measured the aerodynamic coefficients of the iced 8-bundle conductor under different turbulence intensities flow by the wind tunnel experiment [15].

In order to study the galloping characteristics of the iced quad conductor, the partial differential galloping equation of iced quad conductor is firstly required; then the partial differential galloping equation should be transformed into an ordinary differential galloping equation by the reasonable method. While according to existing literature, it can be found that some scholars are used to choose the direct discrete method to transform the partial differential galloping equation into ordinary differential galloping equation, while others are used to select the indirect discrete method to transform partial differential galloping equation into ordinary differential galloping equation. These two discrete methods both are correct and effective, but whether these two discrete methods would affect the galloping characteristics of the iced quad bundle conductor has not been studied by anyone. Based on this concept, this paper systematically studies the influences of the two different

discrete methods on galloping characteristics of the iced quad bundle conductor. In this paper, the partial differential galloping equation of iced quad conductor with 3DOFs is established firstly, then two different methods are used to transform the partial differential galloping equation into an ordinary differential galloping equation. Then, through the wind tunnel test, the three-component aerodynamic coefficients of the quad bundle conductor are measured, and the equivalent aerodynamic coefficients at the central axis of the quad bundle conductor are obtained by a reasonable method. Finally, the galloping characteristics of the iced quad conductor are studied, and the influences of two different discrete methods on the displacement response of the iced quad conductor are also investigated.

## 2. Galloping Equation of the Iced Conductor

**2.1. Mathematical Model and Galloping Equation.** The mathematical model of transmission lines is established as shown in Figure 1. The two ends of the conductor are constrained by fixed supports.  $\Gamma_1$  is the equilibrium configuration under the action of gravity and  $\Gamma_2$  is the dynamic configuration under the action of gravity and other external loads.

In order to obtain the galloping equation of the conductor, the Cartesian coordinate system has been established and the left support of the conductor has been taken as the origin of the Cartesian coordinate system, which can be seen in Figure 1.

Because of the influences of iced, the cross-sectional area of the conductor would become noncircular, so its center of mass is not at the center of the circle. The variational principle for Hamiltonian belongs to the energy method, which is essentially the conservation of energy in the system. Although the conductor would rotate eccentrically due to the influences of iced, the variational principle for Hamiltonian would be also suitable for the derivation of the galloping equation of the conductor. Since it can be obtained from the variational principle for Hamiltonian,

$$\int \delta k^v - \int \delta \Pi + \int \delta w' = 0, \quad (1)$$

where  $\delta k^v$  is the kinetic energy of the iced conductor,  $\delta \Pi$  is the potential energy of the iced conductor, and  $\delta w'$  is the virtual work associated with gravity, external, and damping forces.

Kinetic energy, potential energy, and virtual work of the conductor are, respectively, as follows:

$$\int_0^l k^v ds = \int_0^l \frac{1}{2} m \dot{u}_i^2 ds + \frac{1}{2} \int_0^l J \dot{\theta}^2 ds + \int_0^l s_z \dot{u}_3 \dot{\theta} ds - \int_0^l s_y \dot{u}_2 \dot{\theta} ds, \quad (2a)$$

$$\int_0^l \Pi ds = \int_0^l \left( T \varepsilon + \frac{1}{2} EA \varepsilon^2 \right) ds + \frac{1}{2} \left[ \int_0^l EI \left( \frac{\partial^2 u_i}{\partial s^2} \right)^2 ds + \int_0^l GI_p \varepsilon_\theta^2 ds \right], \quad (2b)$$

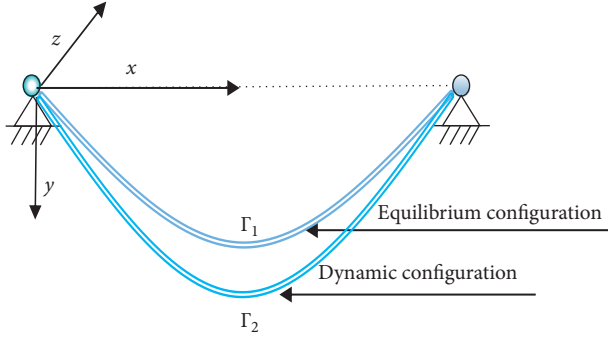


FIGURE 1: The mathematical model of the conductor.

$$\int_0^l \delta w' ds = \left( \sum_{i=1}^3 p_i - c_i \dot{u}_i \right) + (p_\theta - c_\theta \dot{\theta}), \quad (2c)$$

where  $S_z$  and  $S_y$  are static moments,  $EI$  is bending stiffness,  $EA$  is tensile stiffness,  $GI_p$  is torsional stiffness,  $\varepsilon$  is tensile strain,  $J$  is moment of inertia,  $\theta$  is torsional angle,  $u_i$  is dynamic displacement,  $\varepsilon_\theta$  is torsional strain,  $p_i$  and  $p_\theta$  are external aerodynamic forces,  $c_i$  and  $c_\theta$  are damping coefficients,  $T$  is static tension, and  $l$  is span length.

Substituting equations (2a)–(2c) into equation (1), can obtain that

$$\begin{aligned} \frac{\partial}{\partial s} \left\{ H \left( \frac{dx_i}{ds} + \frac{\partial u_i}{\partial s} \right) + EA\Theta \right\} &= (J\ddot{\theta} + S_z\ddot{u}_3 - S_y\ddot{u}_2)\delta_{i\theta} \\ &+ (S_z\delta_{i3} - S_y\delta_{i2})\ddot{\theta} + EI \frac{\partial^4 u_i}{\partial s^4} \\ &- GI_p \frac{\partial^2 \theta}{\partial x_1} \delta_{i\theta} + m u_{i,} \end{aligned} \quad (3)$$

where

$$\Theta = \left[ \frac{dx_i}{ds} \frac{\partial u_i}{\partial s} + \frac{1}{2} \left( \frac{\partial u_i}{\partial s} \right)^2 \right] \left( \frac{dx_i}{ds} + \frac{\partial u_i}{\partial s} \right). \quad (4)$$

Only considering the vertical ( $u_2$ ), transverse ( $u_3$ ), and torsional ( $\theta$ ) movement of the conductor and ignoring the horizontal ( $u_1$ ) movement of the conductor and then substituting equation (4) into equation (3), the partial differential galloping equation of the conductor in vertical ( $u_2$ ), transverse ( $u_3$ ), and torsional direction ( $\theta$ ) can be obtained as follows:

$$\frac{\partial}{\partial x} \left\{ EA \left[ \frac{dy}{dx} \frac{\partial u_2}{\partial x} + \frac{1}{2} \left[ \left( \frac{\partial u_2}{\partial x} \right)^2 + \left( \frac{\partial u_3}{\partial x} \right)^2 \right] \right] \left( \frac{dy}{dx} + \frac{\partial u_2}{\partial x} \right) + H \frac{\partial u_2}{\partial x} \right\} = m\ddot{u}_2 - S_y\ddot{\theta} + EI \frac{\partial^4 u_2}{\partial x^4} + f_2\dot{u}_2 - p_2, \quad (5a)$$

$$\frac{\partial}{\partial x} \left\{ EA \left[ \frac{dy}{dx} \frac{\partial u_2}{\partial x} + \frac{1}{2} \left[ \left( \frac{\partial u_2}{\partial x} \right)^2 + \left( \frac{\partial u_3}{\partial x} \right)^2 \right] \right] \left( \frac{\partial u_3}{\partial x} \right) + H \frac{\partial u_3}{\partial x} \right\} = m\ddot{u}_3 + S_z\ddot{\theta} + EI \frac{\partial^4 u_3}{\partial x^4} + f_3\dot{u}_3 - p_3, \quad (5b)$$

$$(J\ddot{\theta} + S_z\ddot{u}_3 - S_y\ddot{u}_2) - GI_p \frac{\partial^2 \theta}{\partial x} + f_\theta \dot{\theta} - p_\theta = 0. \quad (5c)$$

**2.2. Direct Discrete Method.** The experts represented by Lou et al. [16, 17] generally transformed the partial differential galloping equation into an ordinary differential galloping equation by direct discrete method; that is, equation (4) is directly substituted into equation (3).

The detailed steps of the direct discrete method are given below. The dynamic displacements can be expressed as

$$u_2(x, t) = \psi_2(x)q_2(t), \quad (6a)$$

$$u_3(x, t) = \psi_3(x)q_3(t), \quad (6b)$$

$$\theta(x, t) = \psi_\theta(x)q_\theta(t), \quad (6c)$$

where  $\psi_2$ ,  $\psi_3$ , and  $\psi_\theta$  are mode shapes and  $q_2$ ,  $q_3$ , and  $q_\theta$  are vibration functions.

Substituting equations (6a)–(6c) into equations (5a)–(5c), then it can be obtained that

$$\frac{\partial}{\partial x} \{ H\psi_2'q_2 + EA \ell (y' + \psi_2'q_2) \} = m\psi_2\ddot{q}_2 - S_y\psi_\theta\ddot{q}_\theta + EI\psi_2''''q_2 + f_2\psi_2\dot{q}_2 - p_2, \quad (7a)$$

$$\frac{\partial}{\partial x} \{ H\psi_3'q_3 + EA \ell (\psi_3'q_3) \} = m\psi_3\ddot{q}_3 + S_z\psi_\theta\ddot{q}_\theta + EI\psi_3''''q_3 + f_3\psi_3\dot{q}_3 - p_3, \quad (7b)$$

$$(J\psi_\theta\ddot{q}_\theta - S_z\psi_3\ddot{q}_3 + S_y\psi_2\ddot{q}_2) = GI_p\psi_\theta'q_\theta - f_\theta\psi_\theta\dot{q}_\theta + p_\theta, \quad (7c)$$



where

$$\ell = y' \psi_2' q_2 + \frac{1}{2} (\psi_2'^2 q_2^2 + \psi_3'^2 q_3^2). \quad (8)$$

Using the Galerkin method for equation (7a), then it can be obtained that

$$b_1 \ddot{q}_2 + b_2 \dot{q}_2 + b_4 q_2 + b_5 q_2^2 + b_6 q_3^2 + b_8 q_2^3 + b_9 q_2 q_3^2 + b_{10} \ddot{q}_\theta = PP_2. \quad (9a)$$

Using the Galerkin method for equation (7b), then it can be obtained that

$$c_1 \ddot{q}_3 + c_2 \dot{q}_3 + c_3 q_3 + c_5 q_2 q_3 + c_6 q_2^2 q_3 + c_7 q_3^3 + c_8 \ddot{q}_\theta = PP_3. \quad (9b)$$

Using the Galerkin method for equation (7c), then it can be obtained that

$$d_1 \ddot{q}_\theta + d_2 \dot{q}_\theta + d_3 \ddot{q}_3 + d_4 \ddot{q}_2 + d_5 q_\theta = PP_4. \quad (9c)$$

Equations (9a)–(9c) are the three-degree-of-freedom coupling ordinary differential galloping equation of iced conductor obtained by the direct discrete method, and the expression of the coefficients involved in equations (9a)–(9c) is shown in the appendix.

**2.3. Indirect Discrete Method.** Some experts [18, 19] thought that the axial galloping of the iced conductor is very weak, so the influences of its axial inertia force can be ignored. Based on this concept, equation (4) can be averaged along the span length; that is,

$$\Theta^m = \frac{1}{l} \int_0^l \left[ \frac{dx_i}{ds} \frac{\partial u_i}{\partial s} + \frac{1}{2} \left( \frac{\partial u_i}{\partial s} \right)^2 \right] \left( \frac{dx_i}{ds} + \frac{\partial u_i}{\partial s} \right) dx. \quad (10)$$

Substituting equation (10) into equations (5a)–(5c), then it can be obtained that

$$\frac{\partial}{\partial x} \left\{ \frac{EA}{l} \int_0^l \frac{dy}{dx} \frac{\partial u_2}{\partial x} + \frac{1}{2} \left[ \left( \frac{\partial u_2}{\partial x} \right)^2 + \left( \frac{\partial u_3}{\partial x} \right)^2 \right] dx \left( \frac{dy}{dx} + \frac{\partial u_2}{\partial x} \right) + H \frac{\partial u_2}{\partial x} \right\} = m \ddot{u}_2 - S_y \ddot{\theta} + EI \frac{\partial^4 u_2}{\partial x^4} + f_2 \dot{u}_2 - p_2, \quad (11a)$$

$$\frac{\partial}{\partial x} \left\{ \frac{EA}{l} \int_0^l \frac{dy}{dx} \frac{\partial u_2}{\partial x} + \frac{1}{2} \left[ \left( \frac{\partial u_2}{\partial x} \right)^2 + \left( \frac{\partial u_3}{\partial x} \right)^2 \right] dx \left( \frac{\partial u_3}{\partial x} \right) + H \frac{\partial u_3}{\partial x} \right\} = m \ddot{u}_3 + S_z \ddot{\theta} + EI \frac{\partial^4 u_3}{\partial x^4} + f_3 \dot{u}_3 - p_3, \quad (11b)$$

$$(J \ddot{\theta} + S_z \dot{u}_3 - S_y \dot{u}_2) - GI_p \frac{\partial^2 \theta}{\partial x^2} + f_\theta \dot{\theta} - p_\theta = 0. \quad (11c)$$

Substituting equations (6a)–(6c) into equation (11a) and using the Galerkin method, then it can be obtained that

$$b_1' \ddot{q}_2 + b_2' \dot{q}_2 + b_4' q_2 + b_5' q_2^2 + b_6' q_3^2 + b_8' q_2^3 + b_9' q_2 q_3^2 + b_{10}' \ddot{q}_\theta = PP_2'. \quad (12a)$$

Substituting equations (6a)–(6c) into equation (11b) and using the Galerkin method, then it can be obtained that

$$c_1' \ddot{q}_3 + c_2' \dot{q}_3 + c_3' q_3 + c_5' q_2 q_3 + c_6' q_2^2 q_3 + c_7' q_3^3 + c_8' \ddot{q}_\theta = PP_3'. \quad (12b)$$

Substituting equations (6a)–(6c) into equation (11c) and using the Galerkin method, then it can be obtained that

$$d_1' \ddot{q}_\theta + d_2' \dot{q}_\theta + d_3' \ddot{q}_3 + d_4' \ddot{q}_2 + d_5' q_\theta = PP_4'. \quad (12c)$$

Equations (12a)–(12c) are the three-degree-of-freedom coupling ordinary differential galloping equation of the iced conductor obtained by the indirect discrete method.

**2.4. Aerodynamic Loads on the Iced Conductor.** The mathematical model of aerodynamic load on the iced conductor is established as shown in Figure 2. The iced model is crescent,  $F_L$  is aerodynamic lift,  $F_D$  is aerodynamic drag,  $U$  is true wind speed,  $Ur$  is relative wind speed, and  $D$  is the diameter of the conductor.

$p_2$  is aerodynamic load in the vertical direction,  $p_3$  is aerodynamic load in the transverse direction,  $p_\theta$  is the aerodynamic load in the torsional direction; then,

$$p_2 = F_L \cos(\alpha_t) - F_D \sin(\alpha_t) = 0.5 \rho U^2 DC_y(\alpha), \quad (13a)$$

$$p_3 = F_L \sin(\alpha_t) + F_D \cos(\alpha_t) = 0.5 \rho U^2 DC_z(\alpha), \quad (13b)$$

$$p_\theta = 0.5 \rho U^2 D^2 C_M(\alpha), \quad (13c)$$

where  $C_y(\alpha)$ ,  $C_z(\alpha)$ , and  $C_M(\alpha)$  are aerodynamic coefficients,  $\alpha$  is instantaneous wind angle of attack, and  $\rho$  is air density. The aerodynamic coefficients can be fitted by a cubic curve; that is,

$$C_y(\alpha) = \alpha_1 \alpha + \alpha_2 \alpha^2 + \alpha_3 \alpha^3, \quad (14a)$$

$$C_z(\alpha) = \beta_1 \alpha + \beta_2 \alpha^2 + \beta_3 \alpha^3, \quad (14b)$$

$$C_M(\alpha) = \gamma_1 \alpha + \gamma_2 \alpha^2 + \gamma_3 \alpha^3, \quad (14c)$$

where  $\alpha_i$ ,  $\beta_i$ , and  $\gamma_i$  are the three-component coefficients determined by wind tunnel test, which are related to the initial wind angle of attack, torsional angle, and relative wind speed.



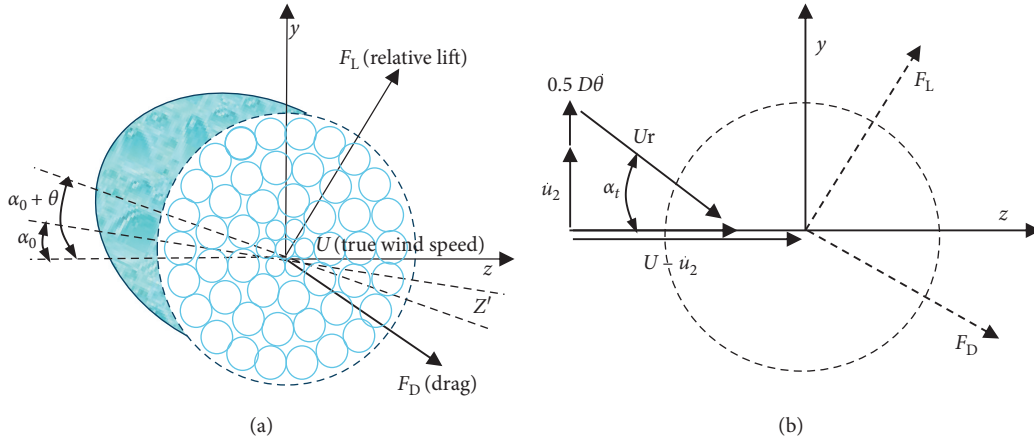


FIGURE 2: Cross-sectional model of the iced conductor and relative flow. (a) Cross-sectional model of the iced conductor. (b) Relative flow in the quasi-steady assumption.

According to equations (13a)–(13c) and equations (14a)–(14c), then using the Galerkin method, it can be obtained that

$$pp_2 = pp'_2(t) = \int_0^l \frac{1}{2} \rho U^2 D \left( \left( -\frac{\alpha_1}{U} \right) \psi_2(x) \dot{q}_2(t) + \left( \frac{\alpha_2}{U^2} \right) [\psi_2(x) \dot{q}_2(t)]^2 - \left( \frac{\alpha_3}{U^3} \right) [\psi_2(x) \dot{q}_2(t)]^3 \right) \psi_2(x) dx, \quad (15a)$$

$$pp_3 = pp'_3(t) = \int_0^l \frac{1}{2} \rho U^2 D \left( \left( -\frac{\beta_1}{U} \right) \psi_2(x) \dot{q}_2(t) + \left( \frac{\beta_2}{U^2} \right) [\psi_2(x) \dot{q}_2(t)]^2 - \left( \frac{\beta_3}{U^3} \right) [\psi_2(x) \dot{q}_2(t)]^3 \right) \psi_3(x) dx, \quad (15b)$$

$$pp_4 = pp'_4(t) = \int_0^l \frac{1}{2} \rho U^2 D^2 \left( \left( -\frac{\gamma_1}{U} \right) \psi_2(x) \dot{q}_2(t) + \left( \frac{\gamma_2}{U^2} \right) [\psi_2(x) \dot{q}_2(t)]^2 - \left( \frac{\gamma_3}{U^3} \right) [\psi_2(x) \dot{q}_2(t)]^3 \right) \psi_3(x) dx. \quad (15c)$$

By substituting equations (15a)–(15c) into equations (9a)–(9c), the ordinary differential equation with considering the influences of aerodynamic loads on the iced

conductor under direct discrete method can be obtained as follows:

$$\begin{cases} b_1 \ddot{q}_2 + (b_2 + b^*) \dot{q}_2 + b_4 q_2 + b_5 \dot{q}_2^2 + b_6 \dot{q}_2^3 + b_8 q_2^3 + b_9 q_2 \dot{q}_2^2 + b_{10} \ddot{q}_\theta + b_{11} \dot{q}_2^2 + b_{12} \dot{q}_2^3 = 0, \\ c_1 \ddot{q}_3 + c_2 \dot{q}_3 + c_3 q_3 + c_5 q_2 q_3 + c_6 \dot{q}_2^2 q_3 + c_7 \dot{q}_2^3 + c_8 \ddot{q}_\theta + c_9^* \dot{q}_2 + c_{10}^* \dot{q}_2^2 + c_{11}^* \dot{q}_2^3 = 0, \\ d_1 \ddot{q}_\theta + d_2 \dot{q}_\theta + d_3 \ddot{q}_3 + d_4 \dot{q}_2 + d_5 q_\theta + d_6^* \dot{q}_2 + d_7^* \dot{q}_2^2 + d_8^* \dot{q}_2^3 = 0, \end{cases} \quad (16)$$

where the expression of the coefficients involved in equation (16) is shown in the appendix.

By substituting equations (15a)–(15c) into equations (12a)–(12c), the ordinary differential equation with



FIGURE 3: Wind tunnel with low wind speed (1.4 m × 1.4 m).



FIGURE 4: Iced model.

considering the influences of aerodynamic loads on the iced conductor under indirect discrete method can be obtained as follows:

$$\begin{cases} b_1''\ddot{q}_2 + (b_2' + b^*)\dot{q}_2 + b_4'q_2 + b_5'q_2^2 + b_6'q_3^2 + b_8'q_2^3 + b_9'q_2q_3^2 + b_{10}'\ddot{q}_\theta + b_{11}^*\dot{q}_2^2 + b_{12}^*\dot{q}_2^3 = 0, \\ c_1'\dot{q}_3 + c_2'\dot{q}_3 + c_3'q_3 + c_5'q_2q_3 + c_6'q_2^2q_3 + c_7'q_3^3 + c_8'\ddot{q}_\theta + c_9^*\dot{q}_2 + c_{10}^*\dot{q}_2^2 + c_{11}^*\dot{q}_2^3 = 0, \\ d_1'\ddot{q}_\theta + d_2'\dot{q}_\theta + d_3'\ddot{q}_3 + d_4'\ddot{q}_2 + d_5'q_\theta + d_6^*\dot{q}_2 + d_7^*\dot{q}_2^2 + d_8^*\dot{q}_2^3 = 0, \end{cases} \quad (17)$$

where the expression of the coefficients involved in equation (17) is shown in the appendix.

### 3. Wind Tunnel Tests

In order to obtain the three-component aerodynamic coefficients of the crescent iced quad bundle conductor, the wind tunnel test was carried out in China Aerodynamics Research and Development center. The quasi-static method is used to test the aerodynamic coefficients of a cross-sectional model of the iced conductor. The picture of 1.4 m × 1.4 m wind tunnel with low wind speed is shown in

Figure 3, the picture of the iced model is shown in Figure 4, and the picture of the force-measuring model is shown in Figure 5.

After measuring the aerodynamic loads, the top motor of force-measuring model would drive force-measuring model to rotate 5°; then, the aerodynamic load is measured again and the range of measurement is 0°~180°. The aerodynamic coefficients of the iced quad bundle conductor measured by the wind tunnel test include aerodynamic drag, lift, and moment coefficients; then, the dimensionless aerodynamic parameters are defined as follows:



FIGURE 5: Force-measuring model.

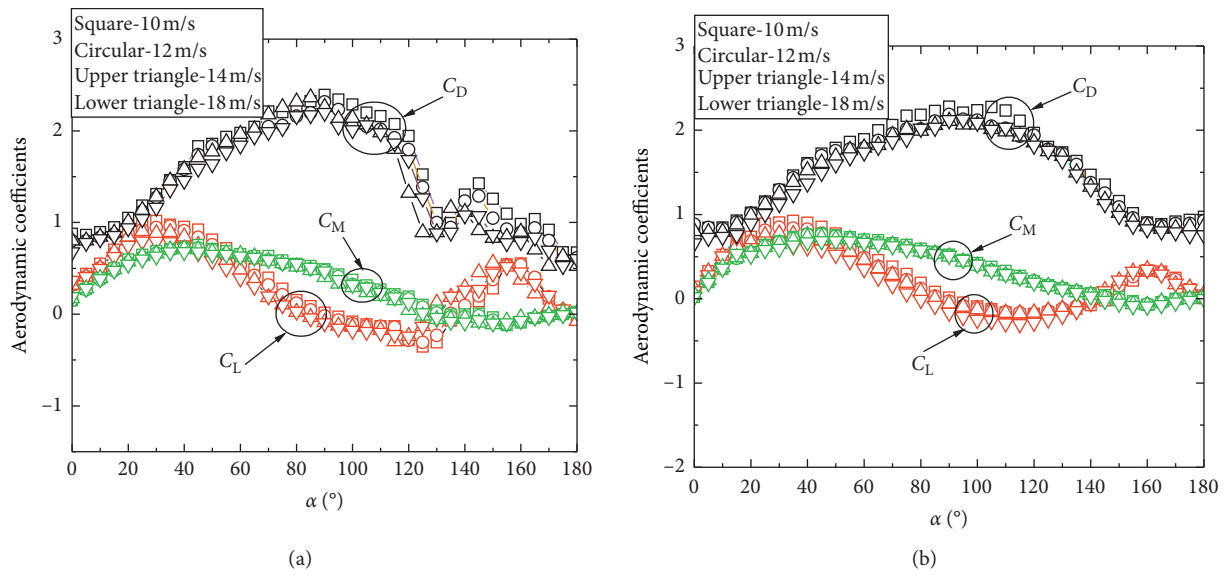


FIGURE 6: Continued.

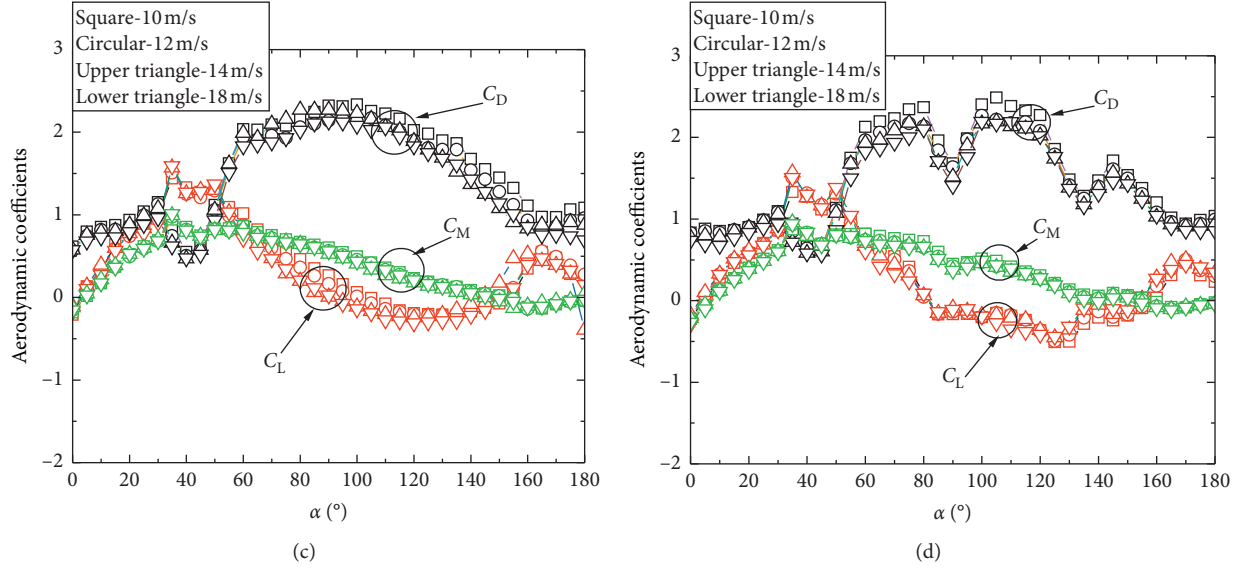


FIGURE 6: Aerodynamic coefficients under various wind velocities. (a) Aerodynamic coefficients of subconductor 1. (b) Aerodynamic coefficients of conductor 2. (c) Aerodynamic coefficients of subconductor 3. (d) Aerodynamic coefficients of subconductor 4.

$$\begin{aligned} C_D &= \frac{F_D}{0.5\rho U^2 L D}, \\ C_L &= \frac{F_L}{0.5\rho U^2 L D}, \\ C_M &= \frac{M_L}{0.5\rho U^2 L D^2}, \end{aligned} \quad (18)$$

where  $L$  is the effective length of the conductor,  $F_D$  is the lift load of the conductor,  $F_L$  is the drag load, and  $M_L$  is the torque of the conductor, respectively.

According to the wind tunnel test, the aerodynamic coefficients of crescent iced quad bundle conductor with 12 mm iced thickness under the wind speed of 10 m/s, 12 m/s, 14 m/s, and 18 m/s are shown in Figure 6.

From Figure 6, when  $\alpha$  is less than  $40^\circ$ , the curves of the aerodynamic lift coefficients show an upward trend. When  $\alpha$  is in the range of  $40^\circ \sim 120^\circ$ , the curves of the aerodynamic lift coefficients show a downward trend. When  $\alpha$  is in the range of  $120^\circ \sim 160^\circ$ , the curves of the aerodynamic lift coefficients have another downing range, but its downward trend is more obvious than that of  $\alpha$  being in the range of  $40^\circ \sim 120^\circ$ . When  $\alpha$  is in the range of  $160^\circ \sim 180^\circ$ , the curves of aerodynamic lift coefficients show an upward trend again.

The aerodynamic drag coefficients of subconductor 1 are affected by the wake of subconductor 2 when  $\alpha$  is  $135^\circ$ . The aerodynamic drag coefficients of subconductor 3 drop suddenly influenced by the wake of subconductor 2 when  $\alpha$  is near  $45^\circ$ . The aerodynamic drag coefficients of subconductor 4 are affected by the wake effect of subconductor 1, subconductor 2, and subconductor 3 when  $\alpha$  is about  $45^\circ$ ,  $90^\circ$ , and  $135^\circ$ , respectively.

When  $\alpha$  is less than  $45^\circ$ , the curves of the aerodynamic torque coefficients increase with  $\alpha$ . When  $\alpha$  is greater than  $45^\circ$ , the curves of the aerodynamic torque coefficients decrease with  $\alpha$ .

Because the subconductor of the iced quad bundle would be effect by wake effects, it is not reasonable to choose the aerodynamic coefficients of one subconductor to study the galloping characteristics of the iced quad bundle conductor. In practical civil engineering, the galloping of the quad bundle conductor usually is expressed as the whole vibration of the quad bundle conductor, so the aerodynamic coefficients at the central axis of the quad bundle conductor are obtained by choosing a reasonable method in this paper.

In order to obtain the three-component aerodynamic coefficients at the central axis of the quad bundle, the equivalent aerodynamic lift coefficients and drag coefficients at the central axis of the quad bundle are defined as follows:

$$C_L^N = \frac{1}{N} \sum_{i=1}^N C_L^i, \quad (19a)$$

$$C_D^N = \frac{1}{N} \sum_{i=1}^N C_D^i, \quad (19b)$$

where  $C_L^i$  and  $C_D^i$ , respectively, represent the aerodynamic lift coefficients and aerodynamic drag coefficients of each subconductor of the quad bundle conductor and  $N$  represents the number of each subconductor.

The equivalent aerodynamic moment coefficients at the central axis of the quad bundle are defined as follows:

$$C_M^N = \frac{1}{N} [C_{M,S}^N + C_{M,D}^N + C_{M,L}^N], \quad (19c)$$

where the physical meaning of  $C_{M,S}^N$ ,  $C_{M,D}^N$ , and  $C_{M,L}^N$  is the contribution of the torque, drag, and lift of the subconductor to the quad bundle conductor.

According to equations (19a)–(19c), it can be obtained that three-component aerodynamic coefficients at the central axis of the quad bundle under the wind speed of 18 m/s are shown in Figure 7.

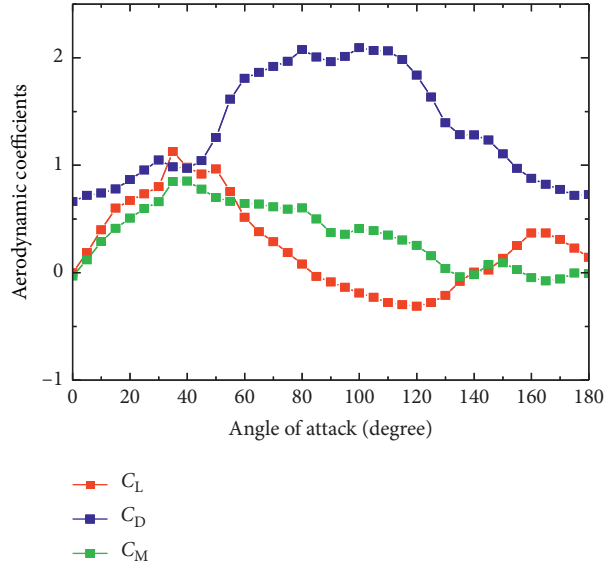


FIGURE 7: Aerodynamic coefficients at the central axis of the quad bundle.

It can be seen from Figure 7 that the curve of the equivalent aerodynamic lift coefficient of the quad bundle has a negative slope when  $\alpha$  is in the ranges of  $40^\circ$ – $120^\circ$  and

$160^\circ$ – $180^\circ$  and it would be easy to gallop. Selecting the three-component aerodynamic coefficients when  $\alpha$  is  $55^\circ$ , then according to Taylor's rules, it can be obtained that

$$C_y(\alpha) = (C_y|\alpha=0) + \left(\frac{\partial C_y}{\partial \alpha}|\alpha=0\right)\alpha + \left(\frac{\partial^2 C_y}{\partial \alpha^2}|\alpha=0\right)\alpha^2 + \left(\frac{\partial^3 C_y}{\partial \alpha^3}|\alpha=0\right)\alpha^3 + O(\alpha^4), \quad (20a)$$

$$C_z(\alpha) = (C_z|\alpha=0) + \left(\frac{\partial C_z}{\partial \alpha}|\alpha=0\right)\alpha + \left(\frac{\partial^2 C_z}{\partial \alpha^2}|\alpha=0\right)\alpha^2 + \left(\frac{\partial^3 C_z}{\partial \alpha^3}|\alpha=0\right)\alpha^3 + O(\alpha^4), \quad (20b)$$

$$C_M(\alpha) = (C_M|\alpha=0) + \left(\frac{\partial C_M}{\partial \alpha}|\alpha=0\right)\alpha + \left(\frac{\partial^2 C_M}{\partial \alpha^2}|\alpha=0\right)\alpha^2 + \left(\frac{\partial^3 C_M}{\partial \alpha^3}|\alpha=0\right)\alpha^3 + O(\alpha^4), \quad (20c)$$

where the right items of equation (20a) can be expressed as

$$(C_y|\alpha=0) = C_L \cos(\alpha) + C_D \sin(\alpha) = (C_L|\alpha=0), \quad (21a)$$

$$\left(\frac{\partial C_y}{\partial \alpha}|\alpha=0\right) = \left(\left(\frac{\partial C_L}{\partial \alpha} \cos \alpha - C_L \sin \alpha + \frac{\partial C_D}{\partial \alpha} \sin \alpha + C_D \cos \alpha\right)|\alpha=0\right) = \frac{\partial C_L}{\partial \alpha} + C_D, \quad (21b)$$

$$\left(\frac{\partial^2 C_y}{\partial \alpha^2}|\alpha=0\right) = \left(\left(\frac{\partial^2 C_L}{\partial \alpha^2} \cos \alpha - 2\frac{\partial C_L}{\partial \alpha} \sin \alpha - C_L \cos \alpha + \frac{\partial^2 C_D}{\partial \alpha^2} \cos \alpha + 2\frac{\partial C_D}{\partial \alpha} \sin \alpha - C_D \sin \alpha\right)|\alpha=0\right) = \frac{\partial^2 C_L}{\partial \alpha^2} - C_L + 2\frac{\partial C_D}{\partial \alpha}, \quad (21c)$$

$$\begin{aligned} \left(\frac{\partial^3 C_y}{\partial \alpha^3}|\alpha=0\right) &= \left(\left(\frac{\partial^3 C_L}{\partial \alpha^3} \cos \alpha - 3\frac{\partial^2 C_L}{\partial \alpha^2} \sin \alpha - 3\frac{\partial C_L}{\partial \alpha} \cos \alpha + C_L \sin \alpha + \frac{\partial^3 C_D}{\partial \alpha^3} \sin \alpha + 3\frac{\partial^2 C_D}{\partial \alpha^2} \cos \alpha - 3\frac{\partial C_D}{\partial \alpha} \sin \alpha - C_D \cos \alpha\right)|\alpha=0\right) \\ &= \frac{\partial^3 C_L}{\partial \alpha^3} - 3\frac{\partial C_L}{\partial \alpha} + 3\frac{\partial^2 C_D}{\partial \alpha^2} - C_D. \end{aligned} \quad (21d)$$

For the constant term in equations (21a)–(21d) is a fixed value, which would not affect the galloping characteristics of the iced quad bundle conductor, then by ignoring the

constant term and substituting equations (21a)–(21d) into equation (20a), it can be obtained that

$$C_y = \left( \frac{\partial C_L}{\partial \alpha} + C_D \right) \alpha + \left( \frac{\partial^2 C_L}{\partial \alpha^2} - C_L + 2 \frac{\partial C_D}{\partial \alpha} \right) \alpha^2 + \left( \frac{\partial^3 C_L}{\partial \alpha^3} - 3 \frac{\partial C_L}{\partial \alpha} + 3 \frac{\partial^2 C_D}{\partial \alpha^2} - C_D \right) \alpha^3 + O(\alpha^4). \quad (22a)$$

In the same way, the aerodynamic coefficients in the transverse and torsional direction can be expressed as

$$C_z = \left( \frac{\partial C_D}{\partial \alpha} + C_L \right) \alpha + \left( \frac{\partial^2 C_D}{\partial \alpha^2} - C_D - 2 \frac{\partial C_L}{\partial \alpha} \right) \alpha^2 + \left( \frac{\partial^3 C_D}{\partial \alpha^3} - 3 \frac{\partial C_D}{\partial \alpha} - 3 \frac{\partial^2 C_L}{\partial \alpha^2} + C_L \right) \alpha^3 + O(\alpha^4), \quad (22b)$$

$$C_z(\alpha) = \frac{\partial C_M}{\partial \alpha} \alpha + \frac{\partial^2 C_M}{\partial \alpha^2} \alpha^2 + \frac{\partial^3 C_M}{\partial \alpha^3} \alpha^3 + O(\alpha^4). \quad (22c)$$

Let the coefficients of the primary term, the coefficient of the secondary term, and the coefficient of the tertiary term of  $\alpha$  in equation (22a) be  $\alpha_1$ ,  $\alpha_2$ , and  $\alpha_3$ , respectively; that is,

$$\frac{\partial C_L}{\partial \alpha} + C_D = \alpha_1,$$

$$\frac{\partial^2 C_L}{\partial \alpha^2} - C_L + 2 \frac{\partial C_D}{\partial \alpha} = \alpha_2, \quad (23)$$

$$\frac{\partial^3 C_L}{\partial \alpha^3} - 3 \frac{\partial C_L}{\partial \alpha} + 3 \frac{\partial^2 C_D}{\partial \alpha^2} - C_D = \alpha_3.$$

Then,  $C_y(\alpha)$  can be expressed as

$$C_y = \alpha_1 \alpha + \alpha_2 \alpha^2 + \alpha_3 \alpha^3. \quad (24a)$$

In the same way,  $C_z(\alpha)$  and  $C_M(\alpha)$  can be expressed as

$$C_z = \beta_1 \alpha + \beta_2 \alpha^2 + \beta_3 \alpha^3, \quad (24b)$$

$$C_M = \gamma_1 \alpha + \gamma_2 \alpha^2 + \gamma_3 \alpha^3. \quad (24c)$$

Finally, it can be obtained that

$$C_y = -0.96060\alpha - 1.40716\alpha^2 + 97.62315\alpha^3, \quad (25a)$$

$$C_z = 2.39795\alpha - 7.00826\alpha^2 - 119.95612\alpha^3, \quad (25b)$$

$$C_M = 2.6744\alpha + 22.30868\alpha^2 - 132.0081\alpha^3. \quad (25c)$$

#### 4. Numerical Analysis

The galloping characteristics of the iced quad bundle conductor are investigated and the galloping characteristics of the iced quad bundle conductor obtained by these two discrete methods will be compared in this paper. Since the physical parameters of the iced quad bundle conductor are involved, the parameters of the quad bundle conductor are listed in Table 1 [20].

By substituting the physical parameters into equations (16) and (17) and combining the three-component aerodynamic coefficients in equation (25), the displacement response of the iced quad bundle conductor under direct discrete method and indirect discrete method can be obtained by using the Runge–Kutta method, as shown in Figures 8 and 9.

From Figures 8 and 9, it can be seen that the iced quad bundle conductor gradually tends to be stable at 400 s under these two discrete methods; that is, the differences in the discrete method would not change the time when the iced quad bundle conductor reaches the steady state. It also can be found that the amplitudes obtained by these two discrete methods are different to some extent, and the most obvious differences are amplitude in the torsional direction.

In order to compare the differences of the displacement response obtained by these two discrete methods more clearly, selecting the data as the iced quad bundle conductor is in the steady state to obtain the local curves of displacement response, which are shown in Figure 10.



TABLE 1: Physical parameters of the conductor.

Parameters	Notation	Units	For line
Axial rigidity	$AE$	$10^6 \text{ N}$	13.30
Torsional rigidity	$GI_P$	$\text{Nm}^2 \text{rad}^{-1}$	101
Diameter	$D$	$10^{-3} \text{ m}$	18.80
Tension	$H$	$10^3 \text{ N}$	21.73
Damping ( $y$ )	$\zeta_y$	$10^{-2}$	0.067
Damping ( $z$ )	$\zeta_z$	$10^{-3}$	0.067
Damping ( $\theta$ )	$\zeta_\theta$	$10^{-2}$	0.253
Mass per unit length	$M$	$\text{kg m}^{-1}$	1.53
The moment of inertia	$J$	$10^{-4} \text{ kg m}^2 \text{m}^{-1}$	57.02
The static moment	$S_y$	$\text{kg m m}^{-1}$	0.000459
The static moment	$S_z$	$\text{kg m m}^{-1}$	-0.000145

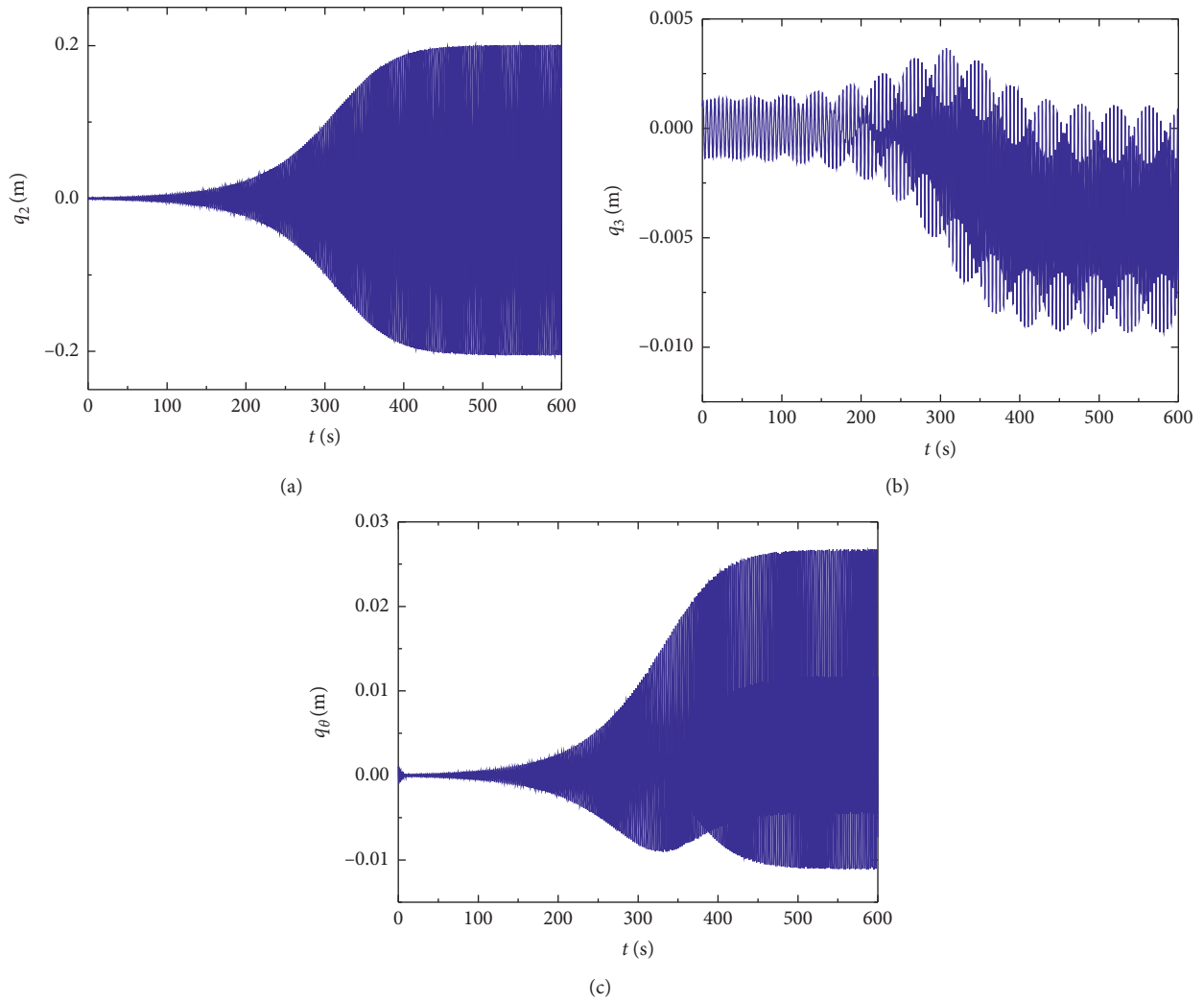


FIGURE 8: Displacement response under direct discrete method. (a) Vertical displacement. (b) Transverse displacement. (c) Torsional displacement.

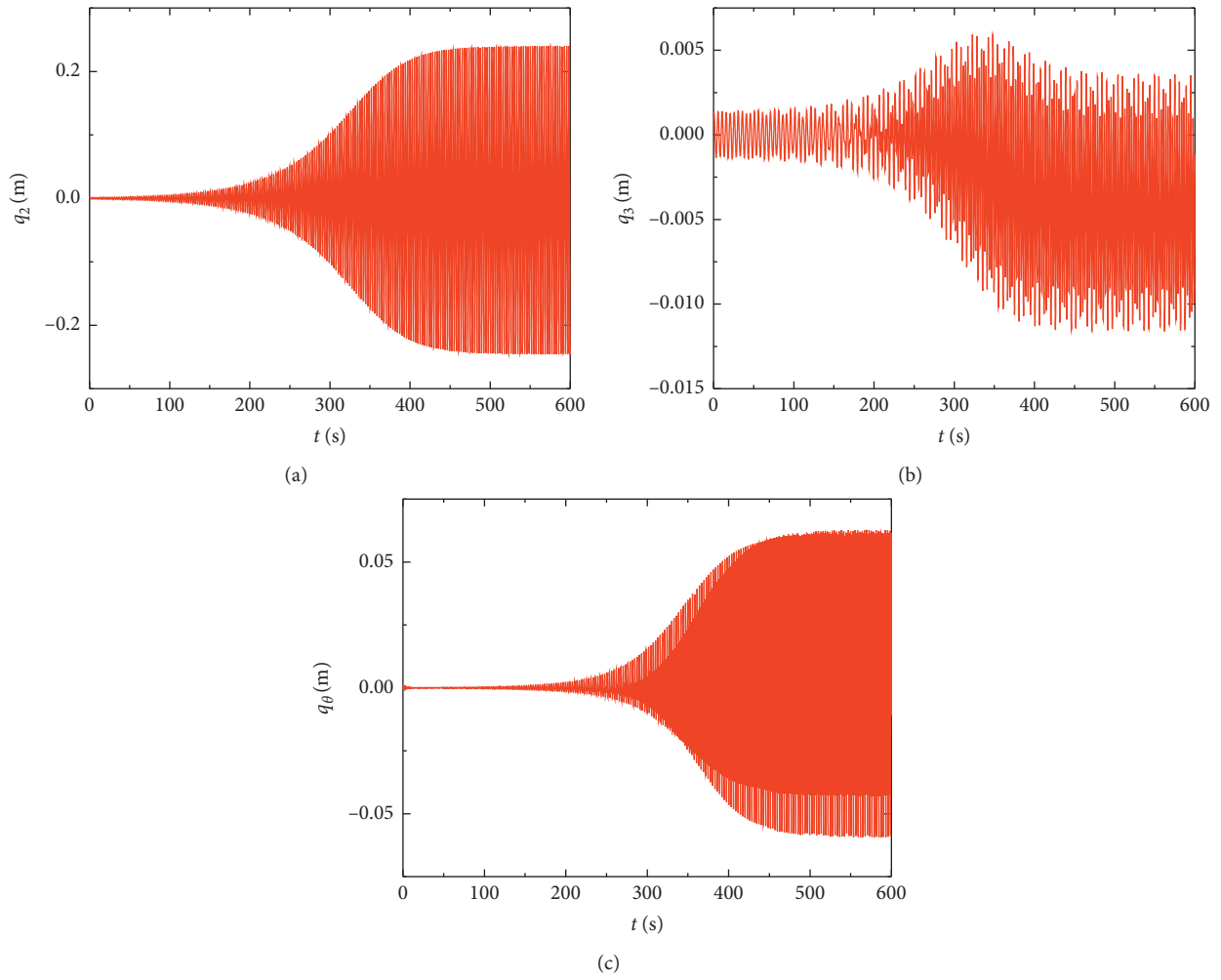


FIGURE 9: Displacement response under indirect discrete method. (a) Vertical displacement. (b) Transverse displacement. (c) Torsional displacement.

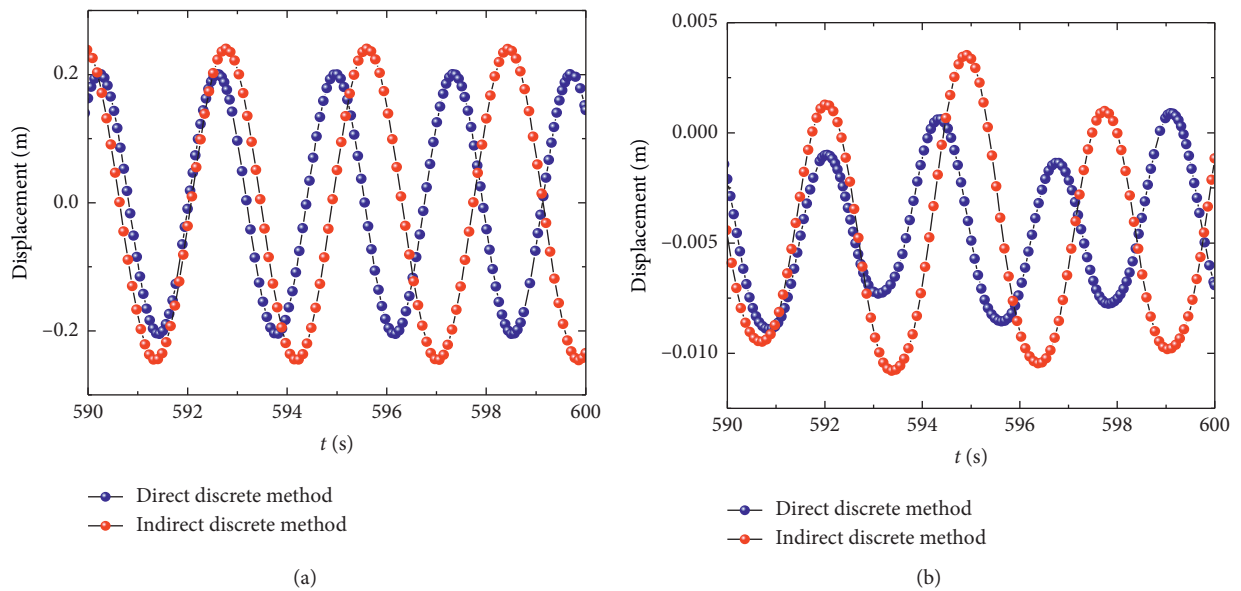


FIGURE 10: Continued.

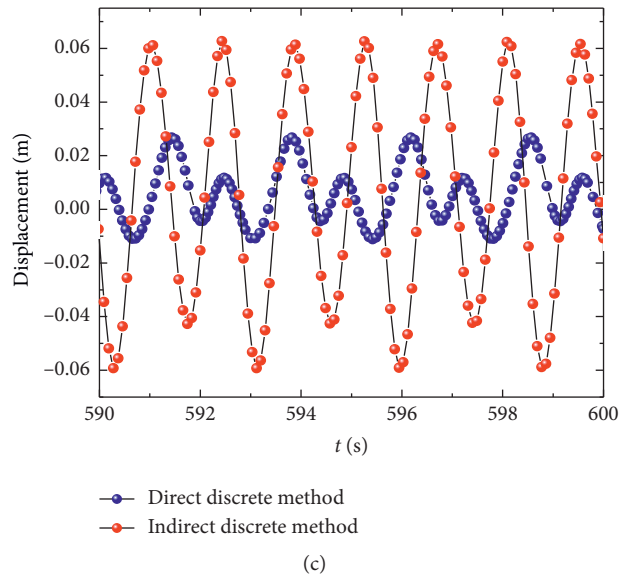


FIGURE 10: Local displacement. (a) Vertical displacement, (b) Transverse displacement, (c) Torsional displacement.

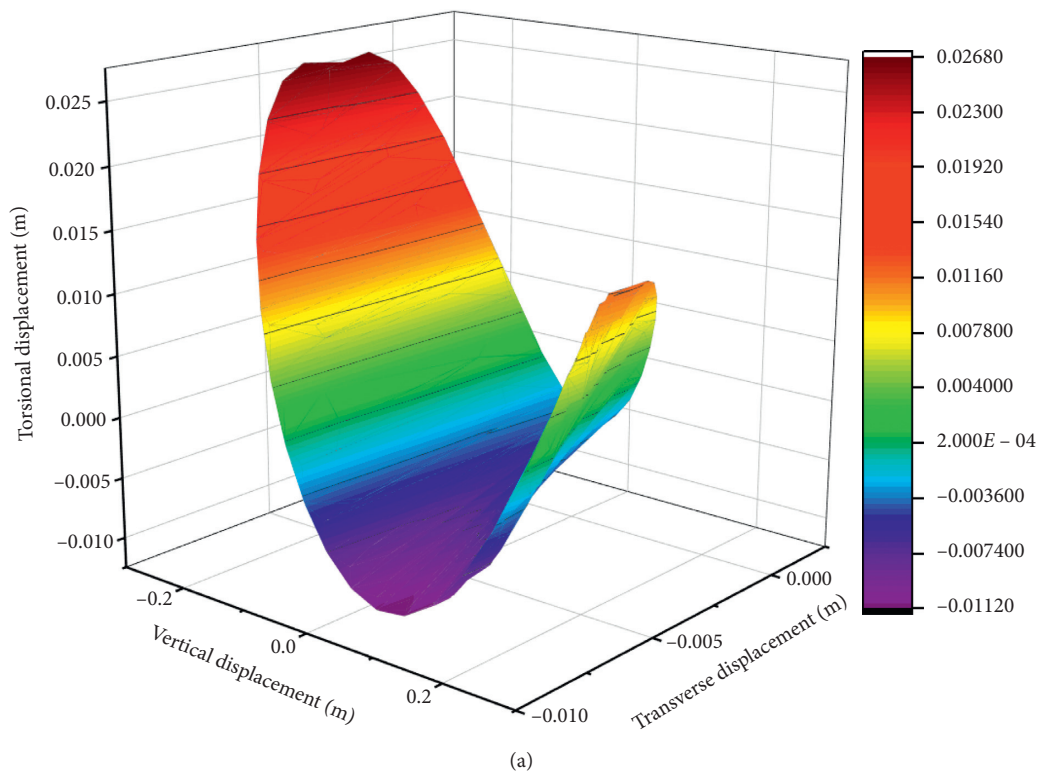


FIGURE 11: Continued.

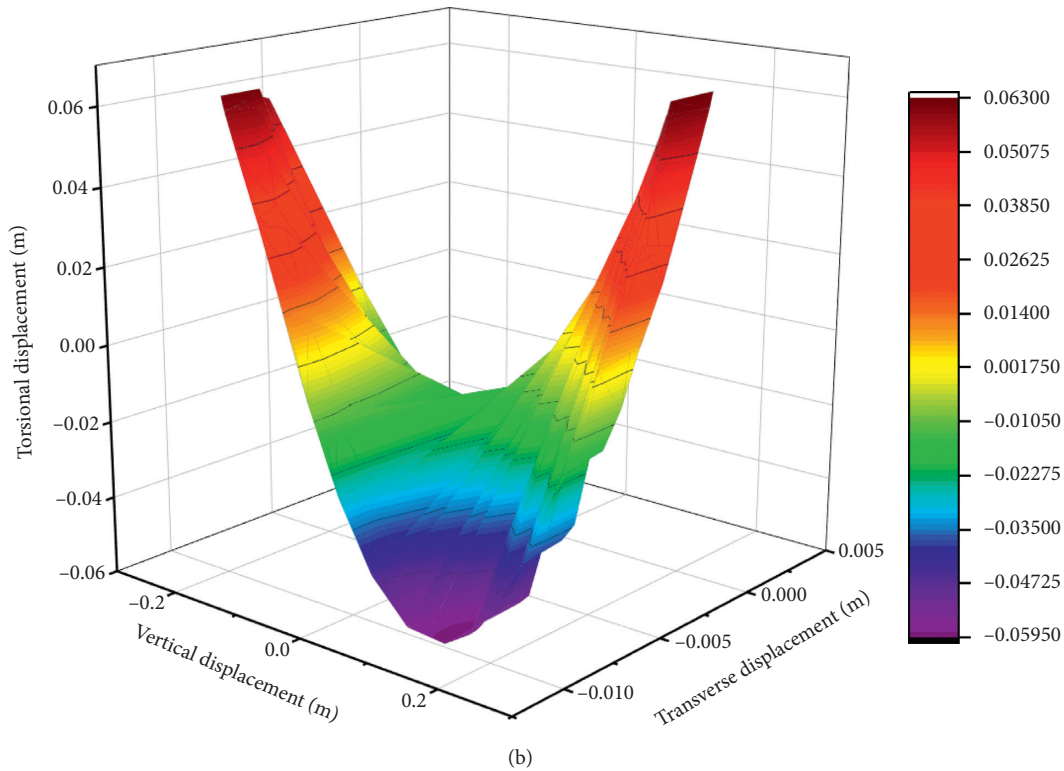


FIGURE 11: Amplitude diagrams. (a) Direct discrete method. (b) Indirect discrete method.

It can be seen from Figure 10 that, in the transverse and torsional directions, the amplitude of the indirect discrete method is greater than that of the direct discrete method, and the differences of the amplitude in the torsional direction are particularly obvious. The frequency, phase, and amplitude of the iced quad bundle conductor obtained by the two discrete methods are different to some extent. Different discrete methods may lead to some errors between the theoretical results and the actual conditions, which is a noteworthy phenomenon.

When the iced quad bundle conductor is galloping, the amplitude is one of the most concerned parameters for the studying of galloping characteristics. Because the amplitude in the torsion direction obtained by the two discrete methods has obvious differences, in order to compare the amplitude in the torsion direction obtained by the two discrete methods more clearly, amplitude diagrams below are obtained which are shown in Figure 11.

Form Figure 11, the maximum amplitude in the torsion direction obtained by the direct discrete method is 0.02680 m, while the maximum amplitude in the torsion direction obtained by the indirect discrete method is 0.06300 m. This is because the indirect discrete method ignores the axial inertial force of the iced quad bundle conductor, which leads to the increase of the amplitude in the torsional direction compared with the amplitude in the torsional direction obtained by the direct discrete method.

## 5. Conclusions

Firstly, based on the variational principle for Hamiltonian, the partial differential galloping equation with 3DOFs of the iced quad bundle conductor is derived; then two discrete methods are used to transform the partial differential galloping equation into an ordinary differential galloping equation. Secondly, based on the wind tunnel test, the three-component aerodynamic coefficients of each sub-conductor of the iced quad conductor are obtained; then, the equivalent aerodynamic coefficients at the central axis of the quad bundle conductor are obtained by using a reasonable method. Finally, based on the numerical method, the displacement responses of the two discrete methods are obtained. The following conclusions can be listed:

- (1) Based on the wind tunnel test, it can obtain that each sub-conductor of the iced quad bundle conductor would be effect by wake effects, so it is not reasonable to choose the aerodynamic coefficients of one sub-conductor to investigation on the galloping characteristics of the iced quad bundle conductor. For studying the galloping characteristics of the iced quad bundle conductor, three-component aerodynamic coefficients at the central axis of the quad bundle should be obtained firstly.

- (2) Based on the numerical method, it can be obtained that the amplitude of the indirect discrete method is greater than that of the direct discrete method, and the differences of the amplitude in the torsional direction are particularly obvious. The frequency and phase of the galloping of the iced quad bundle conductor obtained by the two discrete methods are also different to some extent. This is because the indirect discrete method ignores the axial inertial force of the iced quad bundle conductor, which leads to the increase of the amplitude in the torsional direction compared with the amplitude in the torsional direction obtained by the direct discrete method.
- (3) Based on the fact that the calculation process of the partial differential galloping equation is transformed into an ordinary differential galloping equation, it can be obtained that the calculation process of the direct discrete method is more complex and the calculation process of the indirect discrete method is simpler. However, based on the calculation results of the galloping characteristics, the amplitude obtained by the indirect discrete method is bigger than that obtained by the direct discrete method, especially the amplitude in the torsional direction. This is because the indirect discrete method ignores the axial inertial force of the iced quad bundle conductor since the amplitude in the torsional direction obtained by it is worthy of further discussion.

## Appendix

$$b_1 = \int_0^l m\psi_2^2 dx,$$

$$b_2 = \int_0^l f_2\psi_2^2 dx,$$

$$b_4 = \int_0^l \left\{ EI\psi_2' - \frac{\partial}{\partial x} (H\psi_2' + EA y'^2 \psi_2') \right\} \psi_2 dx, \quad (A.1)$$

$$b_5 = - \int_0^l \frac{\partial}{\partial x} \left( \frac{3EA}{2} y' \psi_2'^2 \right) \psi_2 dx,$$

$$b_6 = - \int_0^l \frac{\partial}{\partial x} \left( \frac{EA}{2} y' \psi_3'^2 \right) \psi_2 dx,$$

$$b_8 = - \int_0^l \frac{\partial}{\partial x} \left( \frac{EA}{2} y' \psi_3'^3 \right) \psi_2 dx,$$

$$b_9 = - \int_0^l \frac{\partial}{\partial x} \left( \frac{EA}{2} \psi_2' \psi_3'^2 \right) \psi_2 dx, \quad (A.2)$$

$$b_{10} = - \int_0^l S_y \psi_\theta \psi_2 dx,$$

$$pP_2 = \int_0^l p_2 \psi_2 dx,$$

$$b_1' = \int_0^l m\psi_2^2 dx,$$

$$b_2' = \int_0^l f_2 \psi_2^2 dx,$$

$$b_4' = \int_0^l \left( EI\psi_2'''' - \frac{EA}{l} y'''' \int_0^l y' \psi_2' dx - H\psi_2'' \right) \psi_2 dx, \quad (A.3)$$

$$b_5' = - \int_0^l \left\{ \left( \frac{EA}{2l} y'' \int_0^l \psi_2'^2 dx \right) + \int_0^l \left( \frac{EA}{l} \psi_2'''' \int_0^l y' \psi_2' dx \right) \right\} \psi_2 dx,$$

$$b_6' = - \int_0^l \frac{EA}{2l} y'' \int_0^l \psi_3'^2 dx \psi_2 dx, \quad (A.4)$$

$$b_{10}' = - \int_0^l S_y \psi_\theta \psi_2 dx,$$

$$b_8' = - \int_0^l \left( \frac{EA}{2l} \psi_2'' \int_0^l \psi_2'^2 dx \right) \psi_2 dx,$$

$$b_9' = - \int_0^l \left( \frac{EA}{2l} \psi_2'' \int_0^l \psi_3'^2 dx \right) \psi_2 dx,$$

$$pP_2' = \int_0^l f_2 \psi_2^2 dx, \quad (A.5)$$

$$c_1 = \int_0^l m\psi_3^2 dx,$$

$$c_2 = \int_0^l f_3 \psi_3^2 dx,$$

$$c_3 = \int_0^l \left[ EI\psi_3'''' - \frac{\partial}{\partial x} (H\psi_3') \right] \psi_3 dx,$$

$$c_5 = - \int_0^l \frac{\partial}{\partial x} (EA\psi_3' \psi_2' y') \psi_3 dx, \quad (A.6)$$

$$c_6 = - \int_0^l \frac{\partial}{\partial x} \left( \frac{EA}{2} \psi_3' \psi_2'^2 \right) \psi_3 dx,$$

$$c_7 = - \int_0^l \frac{\partial}{\partial x} \left( \frac{EA}{2} \psi_3'^3 \right) \psi_3 dx,$$

$$c_8 = \int_0^l S_z \psi_\theta \psi_3 dx,$$

$$pP_3 = \int_0^l p_3 \psi_3 dx, \quad (A.7)$$

$$c_1' = \int_0^l m\psi_3^2 dx,$$

$$c_2' = \int_0^l f_3 \psi_3^2 dx,$$

$$\begin{aligned}
 c'_3 &= \int_0^l \left( EI\psi_3'''' - H\psi_3'' \right) \psi_3 dx, \\
 c'_5 &= - \int_0^l \left( \frac{EA}{I} \psi_3'' \int_0^l y' \psi_2' dx \right) \psi_3 dx, \\
 c'_6 &= - \int_0^l \left( \frac{EA}{I} \psi_3'' \int_0^l \psi_2'^2 dx \right) \psi_3 dx,
 \end{aligned} \tag{A.8}$$

$$\begin{aligned}
 c'_7 &= - \int_0^l \left( \frac{EA}{2I} \psi_3'' \int_0^l \psi_3'^2 dx \right) \psi_3 dx, \\
 c'_8 &= \int_0^l S_z \psi_\theta \psi_3 dx, \\
 pp'_3 &= \int_0^l p_3 \psi_3 dx, \\
 d_1 &= \int_0^l J \psi_\theta^2 dx, \\
 d_2 &= \int_0^l f_\theta \psi_\theta^2 dx,
 \end{aligned} \tag{A.9}$$

$$\begin{aligned}
 d_3 &= \int_0^l S_z \psi_3 \psi_\theta dx, \\
 d_4 &= - \int_0^l S_y \psi_2 \psi_\theta dx, \\
 d_5 &= - \int_0^l GI_p \psi_\theta'' \psi_\theta dx, \\
 pp_4 &= \int_0^l p_\theta \psi_\theta dx, \\
 d'_1 &= \int_0^l J \psi_\theta^2 dx,
 \end{aligned} \tag{A.10}$$

$$\begin{aligned}
 d'_2 &= \int_0^l f_\theta \psi_\theta^2 dx, \\
 d'_3 &= \int_0^l S_z \psi_3 \psi_\theta dx, \\
 d'_4 &= - \int_0^l S_y \psi_2 \psi_\theta dx, \\
 d'_5 &= - \int_0^l GI_p \psi_\theta'' \psi_\theta dx, \\
 pp'_4 &= \int_0^l p_\theta \psi_\theta dx,
 \end{aligned} \tag{A.11}$$

$$\begin{aligned}
 b^* &= \int_0^l \frac{1}{2} \rho U^2 D \left( \frac{\alpha_1}{U} \right) \psi_2(x)^2 dx, \\
 b_{11}^* &= \int_0^l \frac{1}{2} \rho U^2 D \left( \frac{\alpha_2}{U^2} \right) \psi_2(x)^3 dx, \\
 b_{12}^* &= \int_0^l \frac{1}{2} \rho U^2 D \left( \frac{\alpha_3}{U^3} \right) \psi_2(x)^4 dx,
 \end{aligned} \tag{A.12}$$

$$\begin{aligned}
 c_9^* &= \int_0^l \frac{1}{2} \rho U^2 D \left( \frac{\beta_1}{U} \right) \psi_2(x) \psi_3(x) dx, \\
 c_{10}^* &= \int_0^l \frac{1}{2} \rho U^2 D \left( \frac{\beta_2}{U^2} \right) [\psi_2(x)]^2 \psi_3(x) dx,
 \end{aligned} \tag{A.13}$$

$$\begin{aligned}
 c_{11}^* &= \int_0^l \frac{1}{2} \rho U^2 D \left( \frac{\beta_3}{U^3} \right) [\psi_2(x)]^3 \psi_3(x) dx, \\
 d_6^* &= \int_0^l \frac{1}{2} \rho U^2 D^2 \left( \frac{\gamma_1}{U} \right) \psi_2(x) \psi_\theta(x) dx,
 \end{aligned} \tag{A.14}$$

$$\begin{aligned}
 d_7^* &= \int_0^l \frac{1}{2} \rho U^2 D^2 \left( \frac{\gamma_2}{U^2} \right) [\psi_2(x)]^2 \psi_\theta(x) dx, \\
 d_8^* &= \int_0^l \frac{1}{2} \rho U^2 D^2 \left( \frac{\gamma_3}{U^3} \right) [\psi_2(x)]^3 \psi_\theta(x) dx.
 \end{aligned} \tag{A.15}$$

## Data Availability

The data used to support this study are available from the corresponding author upon request.

## Conflicts of Interest

The authors declare that there are no conflicts of interest regarding the publication of this paper.

## Acknowledgments

This work was financially supported by the National Natural Science Foundation of China (51507106 and 51308570), Cutting Edge Project of Chongqing Science and Technology Commission (cstc2017jcyjAX0246), Graduate Research and Innovation Project of Chongqing (cys19240), China Postdoctoral Science Foundation (2020M672238), Chengdu International Science and Technology Cooperation Support Funding (2020-GH02-00059-HZ), and Technology Research Project of Chongqing Education Commission (KJ201600712182).

## References

- [1] X. Li, D. Yu, and Z. Li, "Parameter analysis on wind-induced vibration of UHV cross-rope suspension tower-line," *Advances in Civil Engineering*, vol. 2017, Article ID 8756019, 9 pages, 2017.
- [2] X. H. Liu, Y. Hu, and M. Q. Cai, "Free vibration analysis of transmission lines based on the dynamic stiffness method," *Royal Society Open Science*, vol. 6, no. 3, Article ID 181354, 2019.
- [3] X. Liu, L. Liu, M. Cai, and B. Yan, "Free vibration of transmission lines with multiple insulator strings using refined models," *Applied Mathematical Modelling*, vol. 67, pp. 252–282, 2019.
- [4] M. Cai, L. Zhou, H. Lei, and H. Huang, "Wind tunnel test investigation on unsteady aerodynamic coefficients of iced 4-bundle conductors," *Advances in Civil Engineering*, vol. 2019, Article ID 2586242, 12 pages, 2019.



- [5] J. Li, M. Zhang, and G. Zhao, "Nonlinear dynamic analysis of high-voltage overhead transmission lines," *Shock and Vibration*, vol. 2018, Article ID 1247523, 2018.
- [6] H. M. Irvine, *Cable Structures*, The MIT Press, London, UK, 1981.
- [7] N. C. Perkins, "Modal interactions in the non-linear response of elastic cables under parametric/external excitation," *International Journal of Non-Linear Mechanics*, vol. 27, no. 2, pp. 233–250, 1992.
- [8] G. Rega, *Theoretical and Experimental Nonlinear Vibrations of Sagged Elastic Cables//Nonlinear Dynamic Phenomena in Mechanics*, Springer Netherlands, Dordrecht, Netherlands, 2011.
- [9] J. L. Lilien and D. G. Havard, "Galloping data base on single and bundle conductors prediction on maximum amplitudes," *IEEE Transactions on Power Delivery*, vol. 15, no. 2, pp. 670–674, 2000.
- [10] Z. Yan, E. Savory, Z. Li, and W. E. Lin, "Galloping of iced quad-conductors bundles based on curved beam theory," *Journal of Sound and Vibration*, vol. 333, no. 6, pp. 1657–1670, 2014.
- [11] Y. Xiao, W. D. Zhou, and L. C. Fan, "Analytical solution of in-plane free vibration of suspension cables considering bending stiffness," *Journal of Earthquake Engineering and Engineering Vibration*, vol. 33, no. 4, pp. 75–80, 2013, in Chinese.
- [12] Y. Y. Zhao, H. B. Zhou, B. Jin, and W. C. Liu, "Internal response of inclined cable considering bending rigidity," *Journal of Hunan University (Natural Sciences)*, vol. 34, no. 05, pp. 1–5, 2007, in Chinese.
- [13] K. M. Kimura, Y. Inoue, T. Fujino et al., "Unsteady forces on an ice-accreted four-conductor bundle transmission line," in *Proceedings of the 10th International Conference on Wind Engineering*, pp. 467–472, Copenhagen: Denmark, June 1999.
- [14] W. J. Lou, J. Lv, M. F. Huang, L. Yang, and D. Yan, "Aerodynamic force characteristics and galloping analysis of iced bundle conductors" *Wind and Structures*, vol. 18, no. 2, pp. 135–154, 2014.
- [15] M. Cai, Q. Xu, L. Zhou, X. Liu, and H. Huang, "Aerodynamic characteristics of iced 8-bundle conductors under different turbulence intensities," *KSCE Journal of Civil Engineering*, vol. 23, no. 11, pp. 4812–4823, 2019.
- [16] W. J. Lou, L. Yang, M. F. Huang, M. Asce, and X. H. Yang, "Two-parameter bifurcation and stability analysis for non-linear galloping of iced transmission lines," *Journal of Engineering Mechanics*, vol. 140, no. 11, Article ID 04014081, 2014.
- [17] Y. Y. Zhao, L. H. Wang, D. L. Chen, and L. Z. Jiang, "Three-dimensions nonlinearity dynamics analysis of inclined-cable," *Journal of Hunan University (Natural Science)*, vol. 2011, no. 3, pp. 90–96, 2001, in Chinese.
- [18] A. Luongo, D. Zulli, and G. Piccardo, "Analytical and numerical approaches to nonlinear galloping of internally-resonant suspended cable," *Journal of Sound and Vibration*, vol. 315, no. 3, pp. 375–393, 2008.
- [19] L. H. Wang and Y. Y. Zhao, "Large amplitude motion mechanism and non-planar vibration character of stay cables subject to the support motions," *Journal of Sound and Vibration*, vol. 327, no. 1, pp. 121–133, 2009.
- [20] Y. M. Desai, P. Yu, N. Popplewell, and A. H. Shah, "Finite element modeling of transmission line galloping" *Computers and Structures*, vol. 57, no. 3, pp. 407–420, 1995.

## Research Article

# Experimental Investigation of Unloading-Induced Red Sandstone Failure: Insight into Spalling Mechanism and Strength-Weakening Effect

Yong Luo <sup>1,2</sup>, Fengqiang Gong <sup>2,3,4</sup> and Dongqiao Liu<sup>3</sup>

<sup>1</sup>School of Resources Environment and Safety Engineering, University of South China, Hengyang 421001, China

<sup>2</sup>School of Resources and Safety Engineering, Central South University, Changsha 410083, China

<sup>3</sup>State Key Laboratory for Geomechanics and Deep Underground Engineering, China University of Mining and Technology (Beijing), Beijing 100083, China

<sup>4</sup>School of Civil Engineering, Southeast University, Nanjing 211189, China

Correspondence should be addressed to Fengqiang Gong; [fengqiangg@126.com](mailto:fengqiangg@126.com)

Received 2 May 2020; Revised 8 September 2020; Accepted 19 October 2020; Published 31 October 2020

Academic Editor: Yanchao Shi

Copyright © 2020 Yong Luo et al. This is an open access article distributed under the Creative Commons Attribution License, which permits unrestricted use, distribution, and reproduction in any medium, provided the original work is properly cited.

To study the effect of excavation unloading on hard rock failure, a series of true-triaxial compression tests, biaxial compression tests, and true-triaxial unloading compression tests (two different unloading rates) at different confining pressures was conducted on red sandstone cube samples. The strength and failure characteristics and their relationship for red sandstone unloading at different unloading rates and confining pressures were analyzed. Based on the test results, the effects of the unloading rate and confining pressure on the strength and failure characteristics of hard rock were explored, and a reasonable explanation for unloading-induced spalling in hard rock tunnels was presented. The results show the stress-strain curve of highly stressed red sandstone exhibits a stress step during unloading, and the higher the unloading rate, the lower the stress level required for a stress step. The rock strength-weakening effect induced by unloading was confirmed. The mechanical properties of red sandstone become more unstable and complicated after unloading. After the red sandstone is unloaded to a two-dimensional stress state, with increasing confining pressure, the strength increases first and then decreases; the failure mode changes from a low-confining pressure tensile-shear failure to a high-confining pressure tensile failure; and the geometries of the slabs change from large thick plates and wedges to medium- and small-sized thin plates. At equal confining pressures, the higher the unloading rate, the lower the strength (i.e., the strength-weakening effect is more pronounced), the thinner the slab, and the lower the confining pressure required for the failure mode to change from tensile-shear failure to tensile failure. The unloading rate and confining pressure affect the strength and failure characteristics by affecting the crack initiation type and propagation direction in hard rock. For deep hard rock tunnels with high unloading rate and axial stress, neglecting the effects of unloading rate and axial stress will lead to a dangerous support design. For deep hard rock ore, if the maximal horizontal principal stress exceeds the critical confining pressure, the mining surface should be perpendicular to the direction of the minimal horizontal principal stress. The results of this study are of great engineering significance for guiding deep hard rock tunnel construction and mining.

## 1. Introduction

Deep rock mass is in the original three-dimensional (3D) geo-stress environment and exhibits generally a stable state without failure before excavation. After its excavation, the

stress environment changes from 3D to two-dimensional (2D, such as those of tunnels and caverns) or one-dimensional (such as those of pillars). During excavation, the rock mass experiences the unloading of confining pressure. The confining pressure at the excavation surface is reduced to

zero, which results in a significant decrease in the strength of the rock mass and, eventually, its failure. For hard rock, when the concentrated stress around the excavation surface exceeds the strength of the surrounding rock, brittle failure of varying severity will occur, such as spalling and rockburst [1–10]. Studies have shown that the rock mass strength and failure mode depend mainly on the confining pressure [11–15]. Generally, the strength of rocks increases gradually with increasing confining pressure, indicating an evident positive correlation. The failure mode changes with the change in the confining pressure, thereby transitioning from a tensile failure at low confining pressure to a shear failure at high confining pressure [16–19]. The harder the rock, the higher its strength, and the more significantly the failure mode is affected by the confining pressure [20]. In addition to the influence of the confining pressure on rock failure, the magnitude of the unloading rate caused by excavation will affect the rock failure. Many studies have shown that the unloading effect degrades rock, which leads to different degrees of damage inside the rock [21–25], and altered mechanical properties of the rock. The influence of the unloading effect on the rock failure is related to the unloading rate during excavation; and it is generally believed that the higher the unloading rate is, the more significant the influence is [26–30]. For high-stress hard rock, the greater the unloading rate during excavation, the more severe the failure. Hard rocks are more likely to experience rockburst at high unloading rates, and nonviolent spalling is more likely to occur at relatively low unloading rates [31, 32].

However, excavation causes the hard rock to transition from a 3D to a 2D stress state. The confining pressure of the vertical excavation surface is unloaded, while the confining pressure parallel to the excavation surface (such as the axial stress of tunnels, roadways, and caverns) is not unloaded. After the excavation, the confining pressure parallel to the excavation surface and tangential stress affect simultaneously the deformation and failure of the surrounding rock. Experimental research results have shown that a confining pressure parallel to the excavation surface affects the strength and failure mode of the surrounding rock, such as the severity of the hard rock failure [33–35]. Currently, traditional conventional triaxial unloading tests are mainly used to study the effect of the unloading rate on the strength and failure of hard rock. After unloading the confining pressure, the samples are in a uniaxial compression state, which differs from the 2D stress state of the rock surrounding the deep tunnel. In fact, during the excavation process, the hard rock is simultaneously affected by the confining pressure parallel to the excavation surface and the unloading rate. Therefore, when studying the effect of unloading on the strength and failure of hard rock, the effects of the confining pressure and unloading rate should be considered simultaneously.

In this study, a series of true-triaxial compression tests (TCTs), biaxial compression tests (BCTs), and true-triaxial unloading compression tests (including true-triaxial unloading compression tests at a low unloading rate (TLU) and at a high unloading rate (THU)) was performed on red sandstone cube samples to analyze the effects of the

unloading rate and confining pressure on hard rock failure. Through a detailed analysis and summary of the test results, the strength and failure characteristics and their relationship for red sandstone unloading at different unloading rates and confining pressures were determined. Therefore, the effects of the unloading rate and confining pressure on the strength and failure characteristics of hard rock were revealed, and a reasonable explanation for unloading-induced spalling in hard rock tunnels (or caverns) is presented in this paper.

## 2. Experimental Method

**2.1. Rock Description and Sample Preparation.** The red sandstone used in this experiment originates from Linyi, China. This sandstone has a uniaxial compressive strength (UCS) of 97.5 MPa, a uniaxial tensile strength (UTS) of 3.9 MPa (ratio of UCS to UTS is approximately 25), an elastic modulus of 18.6 GPa, a density of 2.43 g/cm<sup>3</sup>, and a longitudinal wave velocity of 3108 m/s, and it exhibits a moderate rockburst tendency [36, 37]. Thus, the red sandstone is a typical hard rock with high strength and strong brittleness. Visually, the red sandstone is reddish-brown with a uniform texture, no evident structural weak surface, and medium-fine-grained sand-like texture, as shown in Figure 1(a). A thin section of the red sandstone was examined under a polarizing microscope, and the microstructure of the red sandstone was recorded under plane- and orthogonally polarized light, as shown in Figures 1(b) and 1(c). The red sandstone is mainly composed of quartz (42%), K-feldspar (5%), zeolite (8%), plagioclase (35%), calcite (9%), and opaque minerals (1%) [38].

In this study, the red sandstone was processed into cube samples (50 mm × 50 mm × 50 mm), as shown in Figure 1(d). The six faces of the cube samples were polished to obtain parallel faces with deviations within the range of ±0.05 mm and perpendicular adjacent faces within angle deviations within the range of ±0.25°. In addition, the six faces were evenly coated with Vaseline before the test, to mitigate the end effect.

**2.2. Test Equipment.** The employed TRW-3000 rock true-triaxial test system (Figure 2) consists of six independent loading systems, and the X, Y, and Z directions can be independently loaded to obtain unequal 3D stress conditions. The maximal loading capacity in the horizontal X and Y directions is 2000 kN, and the maximal loading capacity in the vertical Z direction is 3000 kN. During the test, the deformation in the three directions was measured with an extensometer, and then the strain in the corresponding direction was calculated based on the deformation. Thus, the TRW-3000 rock true-triaxial test system can realistically simulate a deep geo-stress environment and an excavation unloading process of rock mass.

- (i) TCT: first, the test machine loading device was used to perform simultaneous true-triaxial loading on the cube samples at a loading rate of 1 kN/s in the X, Y, and Z directions. Subsequently, the load was maintained for 5 min after the set confining



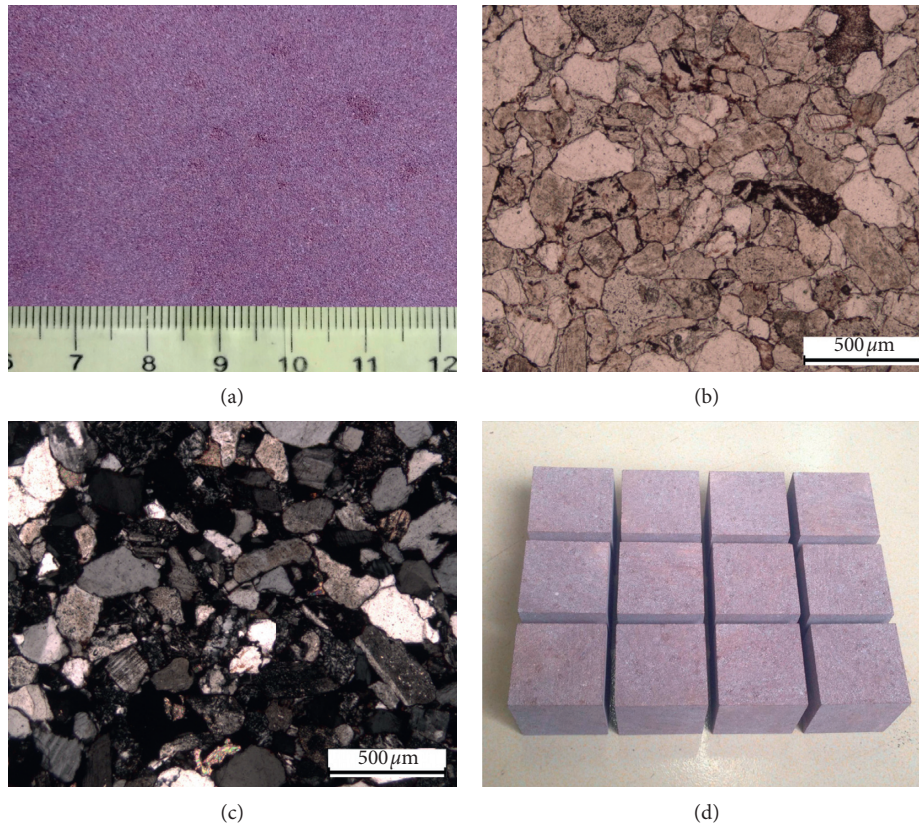


FIGURE 1: Red sandstone material and samples: (a) naked-eye observation, (b) plane-polarized light, (c) cross-polarized light [36], and (d) cube samples.

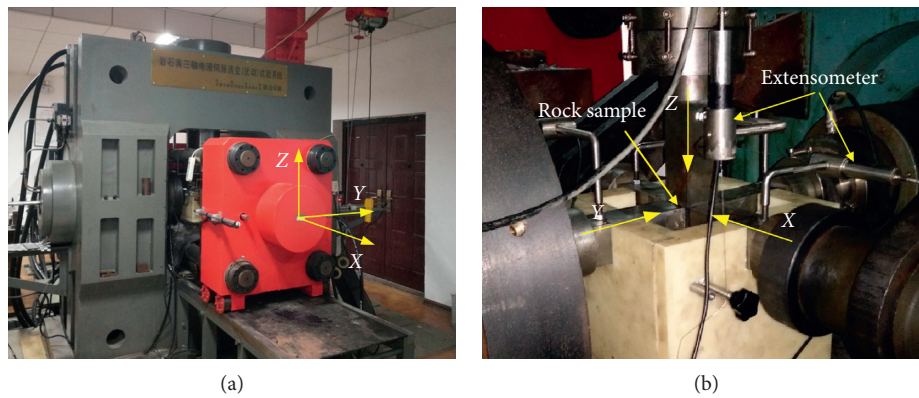


FIGURE 2: TRW-3000 rock true-triaxial test system: (a) overall appearance and (b) internal loading device.

pressure level was reached. In the next step, the loads in the  $X$  and  $Y$  directions remained constant, while the load in the  $Z$  direction continued to increase at a loading rate of  $1 \text{ kN/s}$  until the sample finally suffered overall failure; the loading was then stopped. A schematic of the loading path is shown in Figure 3(a).

(ii) BCT: first, the  $Y$  and  $Z$  directions of the testing machine loading device were used to load the cube samples at a loading rate of  $1 \text{ kN/s}$ . When the load in both directions reached the set confining pressure

level, the load was maintained for 5 min. Subsequently, the load in the  $Y$  direction was maintained constant, while the load in the  $Z$  direction increased at  $1 \text{ kN/s}$  until the sample finally suffered overall failure, and the loading was stopped. A schematic of the loading path is shown in Figure 3(b).

(iii) TLU (or THU): first, the  $X$ ,  $Y$ , and  $Z$  directions of the testing machine loading device were used to perform true-triaxial loading on the cube samples at a loading rate of  $1 \text{ kN/s}$ . After the load in the three directions reached the set confining pressure level, it

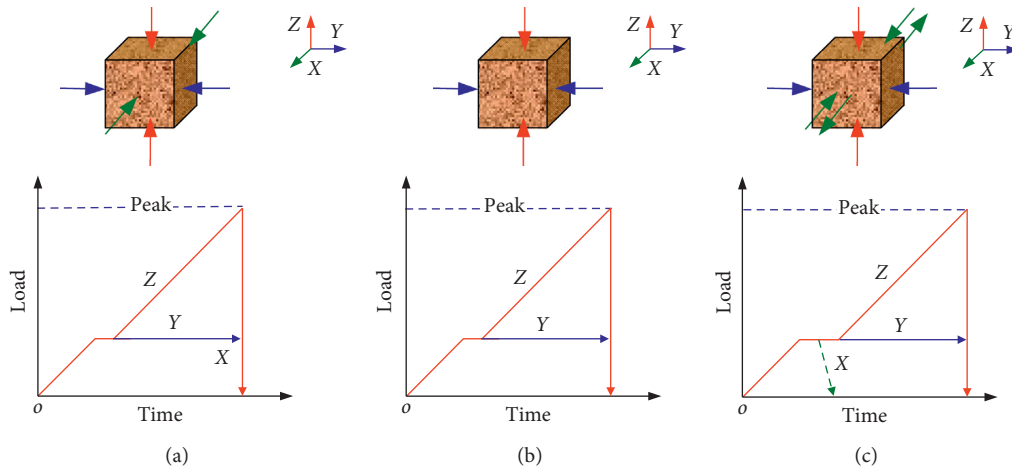


FIGURE 3: Test loading path: (a) TCT, (b) BCT, and (c) TLU (or THU).

remained constant for 5 min. Subsequently, the loads in the Y and Z directions remained constant, while the load in the X direction decreased at an unloading rate of 0.2 kN/s (or 10 kN/s). After the unloading, the loads in the Y and Z directions were kept constant for 5 min. Subsequently, the Y-direction load remained constant, while the Z-direction load increased at 1 kN/s until the sample suffered overall failure, and the loading stopped. A schematic of the loading path is shown in Figure 3(c).

**2.3. Experimental Scheme.** To study the effects of the unloading rate and confining pressure on the strength and failure characteristics of hard rock during unloading, two unloading rates (0.2 and 10 kN/s) and seven confining pressure levels (5, 10, 20, 30, 40, 50, and 60 MPa) were applied in the true-triaxial unloading compression tests (including TLU (unloading rate of 0.2 kN/s) and THU (unloading rate of 10 kN/s)). In addition, TCTs and BTCs were conducted at seven confining pressure levels to compare their results with those of the TLU and THU. To simplify the test scheme, the confining pressures in both horizontal directions were equal. The specific experimental scheme is as follows:

### 3. Test Results and Analysis

Based on the test scheme in Section 2.2, the TCTs, BCTs, TLU, and THU were conducted on cube samples at different confining pressures. To reduce the influence of accidental errors on the test results, tests with large differences in the results were repeated. In the subsequent analysis, only the test results with a peak strength close to the average peak strength are presented owing to the limited manuscript length.

**3.1. Stress-Strain Curve.** In this study, only the Z direction stress-strain curve ( $\sigma_z - \varepsilon_z$ ) was analyzed. Figure 4 shows the

Z direction stress-strain curve for each test. For the TCTs (Figure 4(a)), the stress-strain curves exhibit a significant yielding stage before the peak strength, and the curves do not drop rapidly when the stresses increase to the peak strength. Thus, the brittleness of the red sandstone is significantly reduced in the 3D stress state. As the confining pressure increases, the elastic modulus increases. For the BCTs (Figure 4(b)), the stress-strain curves are similar to the uniaxial compressive stress-strain curve of a cylindrical sample. When loaded to the peak strength of the corresponding confining pressure, the curves drop rapidly and show strong brittleness. With increasing confining pressure, the elastic modulus increases first and then decreases. For the TLU and THU (Figures 4(c) and 4(d)), as the confining pressure increases, the elastic modulus increases first and then decreases, and some stress-strain curves include a stress step during the unloading process. For example, when the unloading rate is 0.2 kN/s and the confining pressure exceeds 30 MPa, the strain increases continuously during unloading, and a stress step is formed in the curve. The higher the stress level during unloading, the longer the stress step (Figure 4(c)). When the unloading rate is 10 kN/s, the stress-strain curves show a significant stress step at a confining pressure of 20 MPa, and the sample experiences overall failure during the unloading process at a confining pressure of 60 MPa (Figure 4(d)). In addition, according to Figures 4(a)–4(d), the stress-strain curves of the TCTs are smooth, and the differences in the stress-strain curves at different confining pressures are small. For the BCTs, TLU, and THU, the stress-strain curves at different confining pressures are quite different and rough, and the higher the unloading rate, the more evident the difference.

It can be concluded that, in the 3D stress environment, the crack propagation and coalescence of red sandstone are relatively stable; the plasticity is improved; and the mechanical properties remain relatively stable. In the 2D stress environment, particularly for red sandstone in an unloading process, the cracks are prone to unstable propagation and coalescence, and the mechanical properties are unstable. The higher the unloading rate, the lower the stress level required

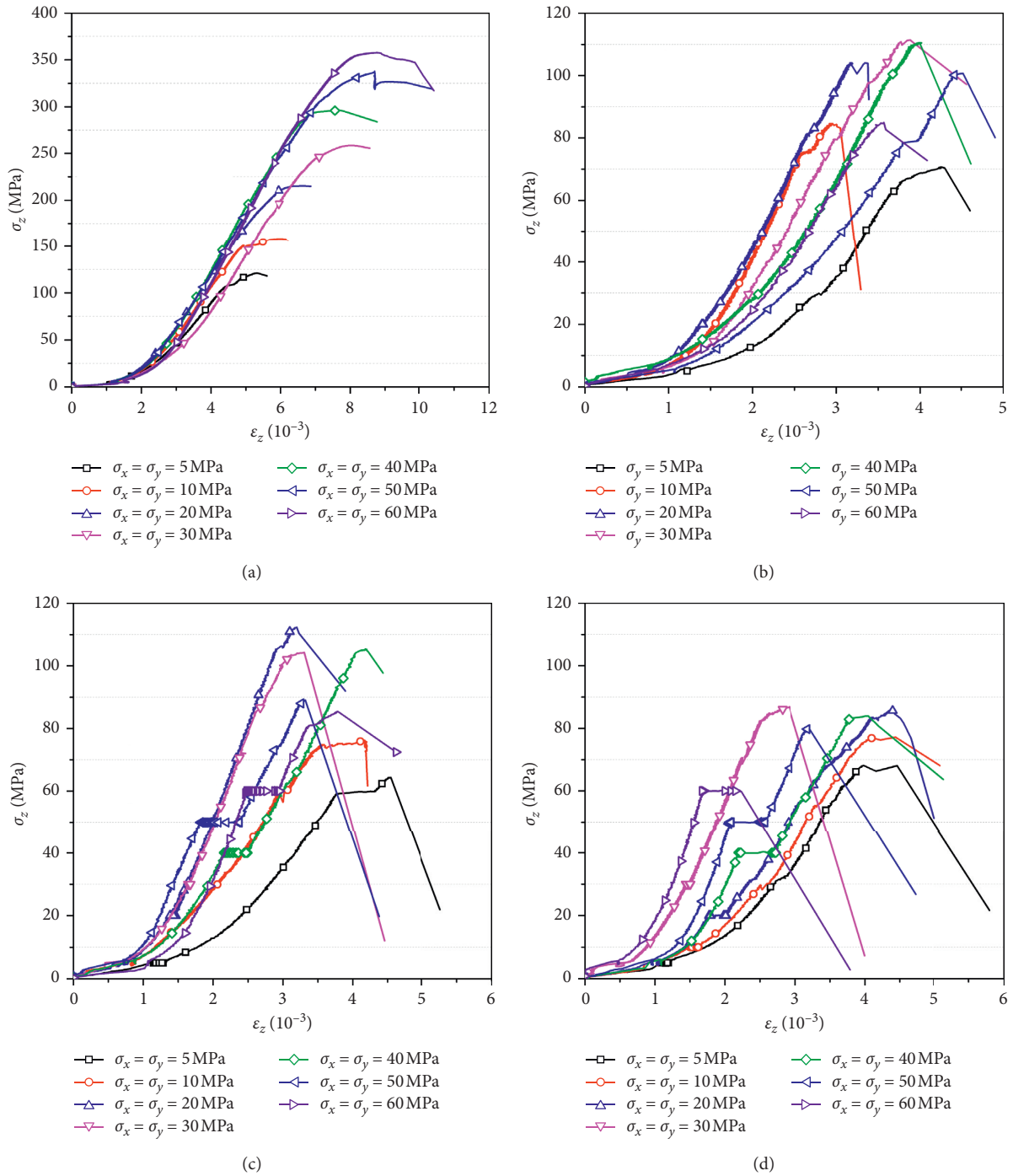


FIGURE 4: The Z direction stress-strain curve: (a) TCT, (b) BCT, (c) TLU, and (d) THU ( $\sigma_x$ ,  $\sigma_y$ , and  $\sigma_z$  are the stresses in the Z, Y, and X directions, respectively).

for significant deformation. As a result, the mechanical properties of hard rock experiencing unloading become more complicated.

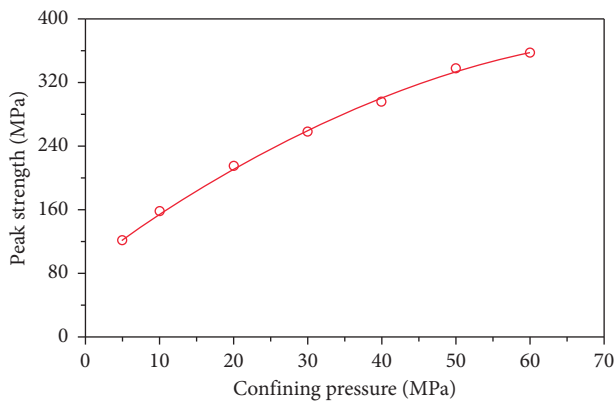
**3.2. Strength Properties.** Owing to the large difference in the peak strength at some confining pressures, the tests were repeated. The peak strength observed during each test at different confining pressures is shown in Table 1.

Accordingly, the relationship between the peak strength of each test and confining pressure was determined (Figure 5). For the TCTs, the peak strength increases significantly with increasing confining pressure; however, the higher the confining pressure is, the smaller the positive slope is (Figure 5(a)). For the BCTs, TLU, and THU, the peak strength increases with increasing confining pressure when the confining pressure is below 30 MPa; however, the positive slope decreases gradually. When the confining pressure



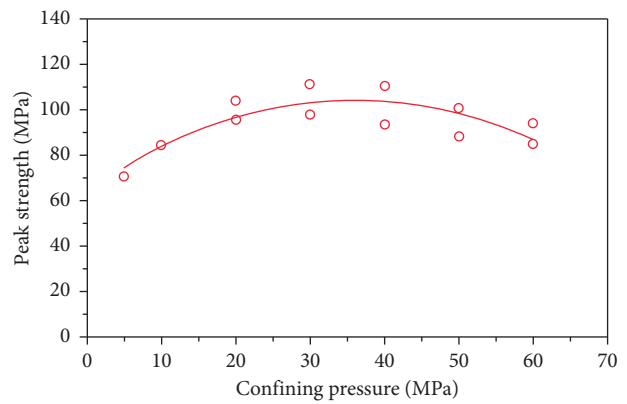
TABLE 1: Peak strength of each test at different confining pressures.

Confining pressure (MPa)	5	10	20	30	40	50	60
Peak strength of TCT (MPa)	121.1	158.5	215.3	258.5	296.0	337.7	357.7
Peak strength of BCT (MPa)	70.7	84.6	104.0	111.4	93.4	88.5	84.9
Average	70.7	84.6	99.8	104.7	102.0	94.6	89.5
Peak strength of TLU (MPa)	64.3	76.2	97.9	113.9	110.1	89.0	85.4
			77.0	68.3	101.5	76.5	
			112.3	120.3	105.4		
				110.3			
				104.3			
Average	64.3	76.2	95.7	97.2	103.5	91.9	85.4
Peak strength of THU (MPa)	68.1	77.2	85.8	78.6	84.0	80.1	84.3
			93.3	97.6	114.3	89.2	60.0
				86.8	73.1		
Average	68.1	77.2	89.6	87.7	90.4	84.7	72.2



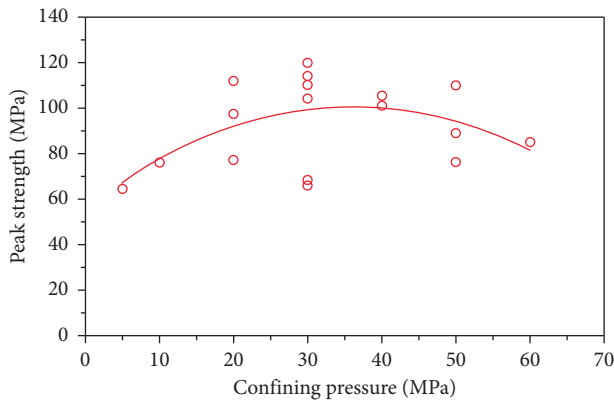
○ Test data  
— Fitting curve

(a)



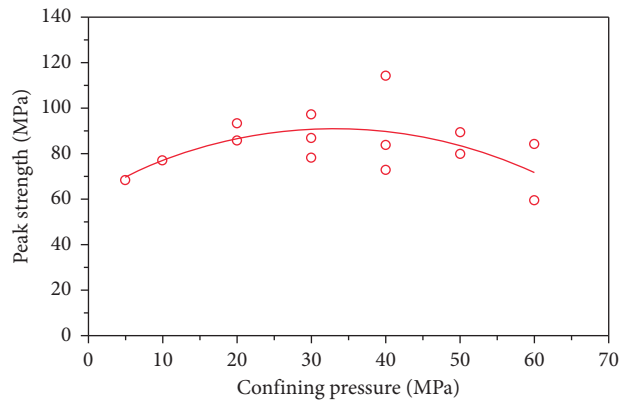
○ Test data  
— Fitting curve

(b)



○ Test data  
— Fitting curve

(c)



○ Test data  
— Fitting curve

(d)

FIGURE 5: Relationship between the peak strength and confining pressure: (a) TCT, (b) BCT, (c) TLU, and (d) THU.

increases from 30 to 40 MPa, the peak strength experiences a small decrease. When the confining pressure is over 40 MPa and continues to increase, the peak strength decreases

continuously with gradually increasing negative slope. By comparing the peak strengths of the BCTs, TLU, and THU, it can be observed that the peak strength distribution of the

samples undergoing unloading processes at equal confining pressures is more discrete, particularly when the confining pressure is close to 30–40 MPa (Figures 5(b)–5(d)).

The previously presented results indicate that the peak strength increases monotonously with increasing confining pressure when the hard rock is in a 3D stress state (the two confining pressures are equal). There is a critical confining pressure for a hard rock in a 2D stress state, and the peak strength increases first and then decreases with increasing confining pressure (i.e., the peak strength is maximal at the critical confining pressure). The peak strength of the hard rock undergoing unloading is more unstable. It can be concluded that when the axial stress is below the critical confining pressure, the higher the axial stress, the higher the strength of the surrounding rock for deep hard rock tunnels. When the axial stress is greater than the critical confining pressure, the greater the axial stress, the lower the strength of the surrounding rock. Therefore, the axial stress should be considered in the support design of deep hard rock tunnels, and immediate support should be provided after excavation. For deep hard rock ore, if the maximal horizontal principal stress is higher than the critical confining pressure of the ore, the minimal horizontal principal stress should be unloaded during mining to reduce the strength of the ore and improve the mining efficiency.

To investigate the influence of the unloading rate and confining pressure on the strength of red sandstone further, the average peak strength is used in the following analysis. Figure 6 shows the relationship between the average peak strength and confining pressure for each test. The peak strength of the TCT is significantly higher than that of the BCT, TLU, and THU at equal confining pressures; in addition, the higher the confining pressure, the greater the difference in the peak strength. The peak strengths of the BCT, TLU, and THU increase first and then decrease with increasing confining pressure, and the critical confining pressures are within 30–40 MPa. Their peak strength difference is relatively small at the same confining pressure, particularly when the unloading rate is low. Hence, the transformation of the red sandstone stress state from 3D to 2D is the main reason for its strength reduction. That is, the confining pressure increases (or decreases) by the same value, and the strength increase (or decrease) is much higher in the 3D than in the 2D stress state, particularly when the unloading rate is high. For example, the confining pressure of the BCT decreases from  $\sigma_y = 60$  to 10 MPa, thereby resulting in a decrease in the peak strength of 4.9 MPa, while the confining pressure of the TCT decreases from  $\sigma_y = \sigma_x = 50$  MPa to  $\sigma_y = 50$  MPa and  $\sigma_x = 0$  MPa, which results in a reduction in the peak strength of 243.1 MPa.

Figure 7 presents the relationship between the peak strength and unloading rate at different confining pressures. The order of the peak strengths at a specific confining pressure is approximately as follows: BCT > TLU > THU. Within the range of the confining pressure variation investigated in this study, the peak strength difference between the BCT and TLU is small; however, their difference is more significant at a low than at a high confining pressure. The possible reason for this result is that the unloading rate of the

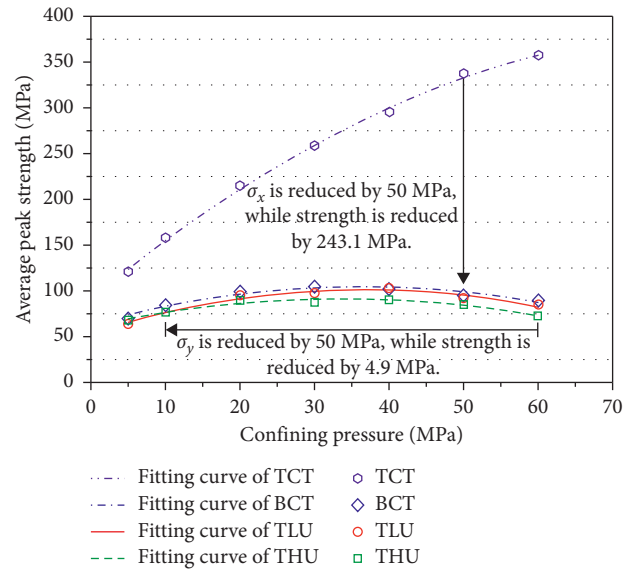


FIGURE 6: Relationship between the average peak strength and confining pressure.

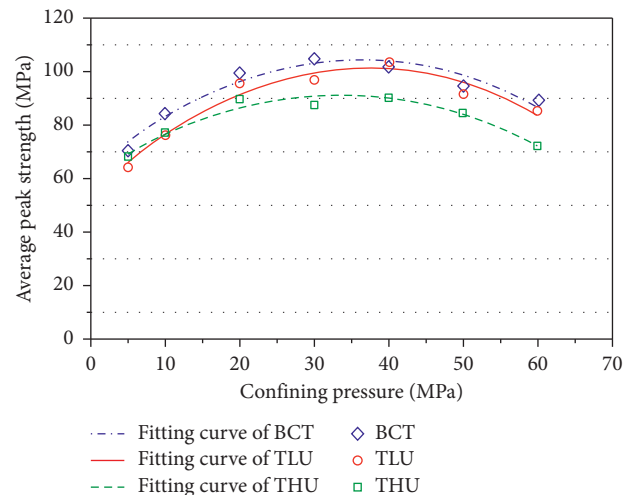


FIGURE 7: Relationship between the average peak strength and unloading rate.

TLU is very low, and its impact is limited. Consequently, its influence becomes weaker relative to the confining pressure at a high confining pressure. However, at a high unloading rate, the strength difference between the BCT and THU is relatively evident at a high confining pressure. This indicates that the high unloading rate exhibits a significant strength-weakening effect on the hard rock under high confining pressure.

In summary, the unloading rate and confining pressure affect the strength of red sandstone, and the effect of the confining pressure on the strength is significantly greater than that of the unloading rate. Therefore, the decreasing confining pressure caused by excavation is the most important reason for the decrease in the strength and failure of hard rock. A low unloading rate has no significant effect on

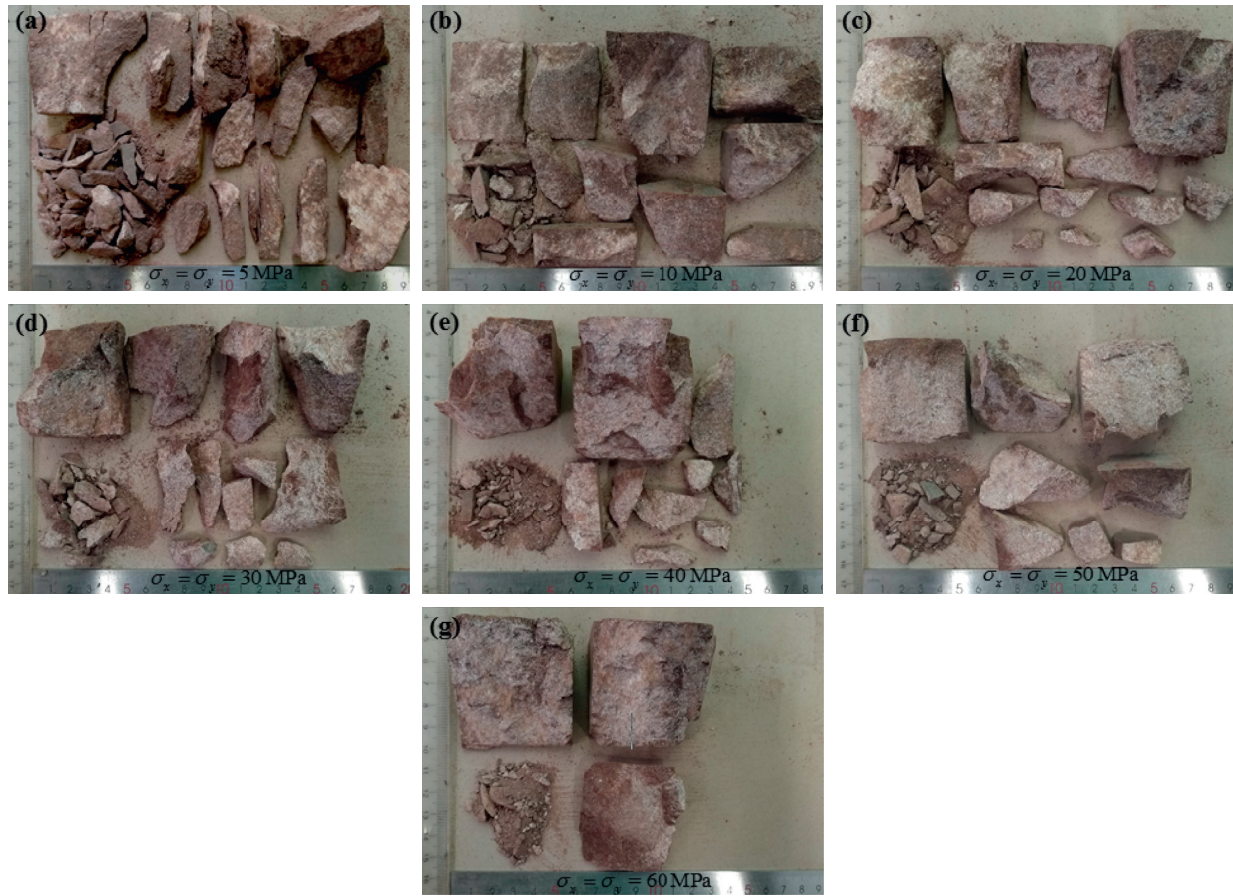


FIGURE 8: Failure characteristics of TCT at different confining pressures.

the strength of hard rock, whereas a high unloading rate does a significant strength-weakening effect on hard rock at a high confining pressure.

**3.3. Failure Characteristics.** The failure characteristics (including failure geometry and failure mode) of the samples in the TCTs, BCTs, TLU, and THU at different confining pressures are shown in Figures 8–11, respectively. In general, the failure characteristics of the BCT, TLU, and THU are similar and differ significantly from those of the TCT. The specific failure characteristics of each test are as follows:

- (i) Failure geometry. As shown in Figure 8, at a low confining pressure, the samples of the TCT are severely broken, and the slabs are mostly long and columnar. With increasing confining pressure, the fragmentation of the sample is reduced, and the blockiness and thickness of the slabs increase continuously. At high confining pressure, the slabs are large wedges. For example, at  $\sigma_y = \sigma_x = 60$  MPa, only three large wedge-shaped slabs are formed (Figure 8(g)). As shown in Figures 9–11, the size of most slabs produced by the BCT, TLU, and THU in the  $X$  (thickness) direction is shorter than those produced in the  $Y$  and  $Z$  directions (blockiness). Thus, slabs that are approximately parallel to the  $Y$ - $Z$  plane are dominant. At a low confining pressure, the

slabs are thick, their blockiness is large, the degree of fragmentation is relatively low, and their geometries are mainly plate and wedge shapes. With increasing confining pressure, the slabs become thinner; their blockiness decreases; and the degree of fragmentation becomes more severe. At a high confining pressure, the fragmentation of the samples is severe; the thickness and blockiness of the slabs are significantly reduced; and the slabs become mainly plate-shaped, with a low thickness and low blockiness. Furthermore, owing to the effect of the unloading rate, the failure geometry of the samples at equal confining pressures is different in the BCT, TLU, and THU. The higher the unloading rate, the smaller the blockiness, the thinner the slabs, and the more severe the fragmentation of the samples. Within the investigated confining pressure range, the difference in the failure geometries of the BCT and TLU is not significant, whereas that of the failure geometries of the BCT and THU is remarkable. Hence, a high unloading rate promotes the fragmentation of red sandstone and the formation of thin plate-shaped slabs; thus, the red sandstone is more prone to spalling.

- (ii) Failure mode. As shown in Figure 8, at a low confining pressure, the samples of the TCT experience mainly columnar splitting and conjugate shearing of





FIGURE 9: Failure characteristics of BCT at different confining pressures.

multiple fracture surfaces along the direction of the maximal principal stress (i.e., Z direction). At a moderate confining pressure, the failure mode of samples is an inclined shear failure with multiple fracture surfaces, and at a high confining pressure, the failure mode is an inclined shear failure with a single fracture surface. As shown in Figures 9–11, in general, as the confining pressure increases, the friction powder on the surface of the slabs decreases in the BCT, TLU, and THU. Thus, the shear failure becomes gradually weaker with increasing confining pressure. At a low confining pressure, the friction powder on the surface of the slabs near the unloading surface of the BCT is not significant, and the dominant failure mode is tension. Moreover, a considerable amount of friction powder is generated on the surface of the slabs near the sample center, and the dominant failure mode is shear failure. With increasing confining pressure, the tensile characteristics of the slabs near the unloading surface become more significant, and the friction powder amount on the slab surfaces in the sample center decreases continuously. In particular, when the confining pressure exceeds 30–40 MPa, the shear characteristics become significantly weaker. At a high confining pressure, the slabs near the unloading

surface and in the sample center exhibit evident tensile characteristics; i.e., the dominant failure mode of the sample is tensile failure. Owing to the effect of the unloading rate, the TLU and THU have more significant effects on the tensile characteristics of the slabs than the BCT at the same confining pressure. At a high unloading rate (i.e., THU) and at a low and high confining pressure, the dominant failure mode is tensile failure.

The following two conclusions can be drawn: (i) at low confining pressures, hard rock is prone to tensile failure in both 3D (columnar splitting) and 2D (plate-shaped splitting) stress states; in addition, shear failures occur in local areas. With increasing confining pressure, in the 3D stress state, the hard rock failure converts from a multiple-fracture surface tension-shear mixed failure to a single-fracture surface shear failure; the shear characteristics improve continuously, and the degree of fragmentation decreases. In the 2D stress state, the shear characteristics are continuously weakened; the failure state transforms gradually into a thin-plate-shaped tensile failure (i.e., spalling); the range of the tensile failure increases; and the fragmentation is more serious. (ii) The influence of the unloading rate on the failure characteristics of hard rock is related to the magnitudes of the confining pressure and unloading rate. The tensile

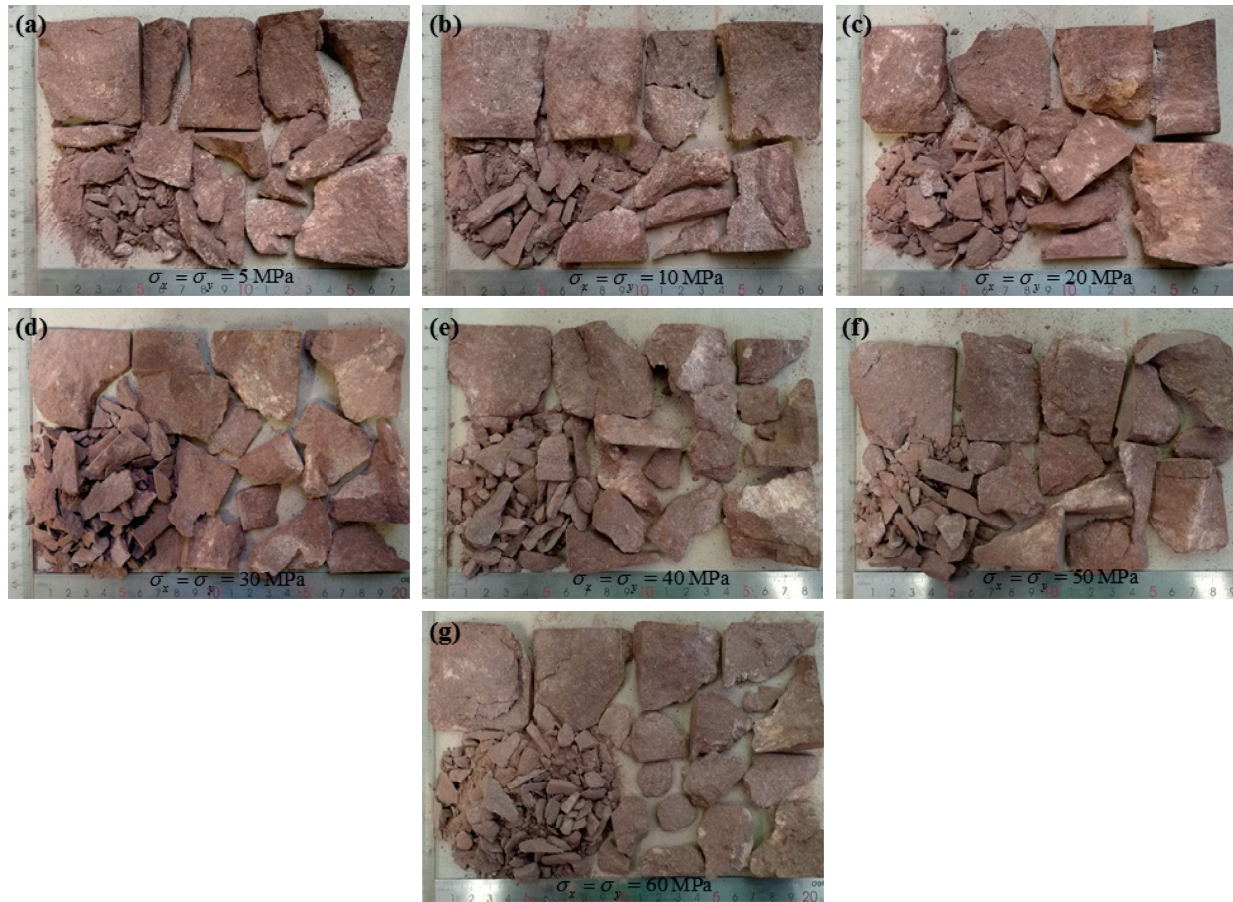


FIGURE 10: Failure characteristics of TLU at different confining pressures.

characteristics are more evident when the hard rock experiences unloading; thin plate splitting (i.e., spalling) is more likely to occur, and the fragmentation is more serious. The higher the unloading rate and confining pressure, the deeper the range of the hard rock tensile failure. When the unloading rate is low, the effect is not significant. Therefore, the effect of the unloading rate on the hard rock failure manifests itself mainly in enhanced tensile characteristics, which reduces the confining pressure required for a tensile failure in hard rock. That is, the increasing unloading rate accelerates the transition of the failure mode from shear to tensile failure and the change of the slab geometry from a thick plate or wedge to a thin plate.

In summary, after the excavation of high-stress hard rock, if the confining pressure of the parallel excavation surface is low, the tensile failure depth near the excavation surface is shallow, the fracture surface is approximately parallel to the excavation surface, and the slabs are large, thick plates. With increasing confining pressure, the depth of the tensile failure near the excavation surface increases, and the blockiness and thickness of the slabs become smaller and thinner, respectively. Simultaneously, the higher the unloading rate during excavation, the greater the depth of the tensile failure near the excavation surface, and the smaller and thinner the slab blockiness and thickness, respectively. Therefore, for deep hard rock tunnels or caverns, the higher the axial stress and

unloading rate during excavation, the higher the possibility of spalling in the surrounding rock, and a rockburst disaster may occur in severe cases. Thus, for deep hard rock ore, mining methods with high unloading rates and unloading the minimal horizontal principal stress enhance ore fragmentation.

#### 4. Discussion

In general, the shear strength of rock material is greater than the tensile strength, and the more evident the shear characteristics, the higher the corresponding strength. This is proved by the TCT results presented herein. According to Section 3, hard rock that experiences unloading exhibits weaker shear characteristics and decreased strength. Figure 12 shows the relationship between the peak strength and failure characteristics of each test. With increasing confining pressure, the failure mode of the TCT shows that the shear failure and the corresponding peak strength increase continuously. The failure modes of the BCTs, TLU, and THU show that the shear failure weakens gradually, and the corresponding peak strength increases first and then decreases. To determine the effects of the unloading rate and confining pressure on the strength and failure characteristics of hard rock, the experimental results in this paper are explained based on crack initiation and propagation.



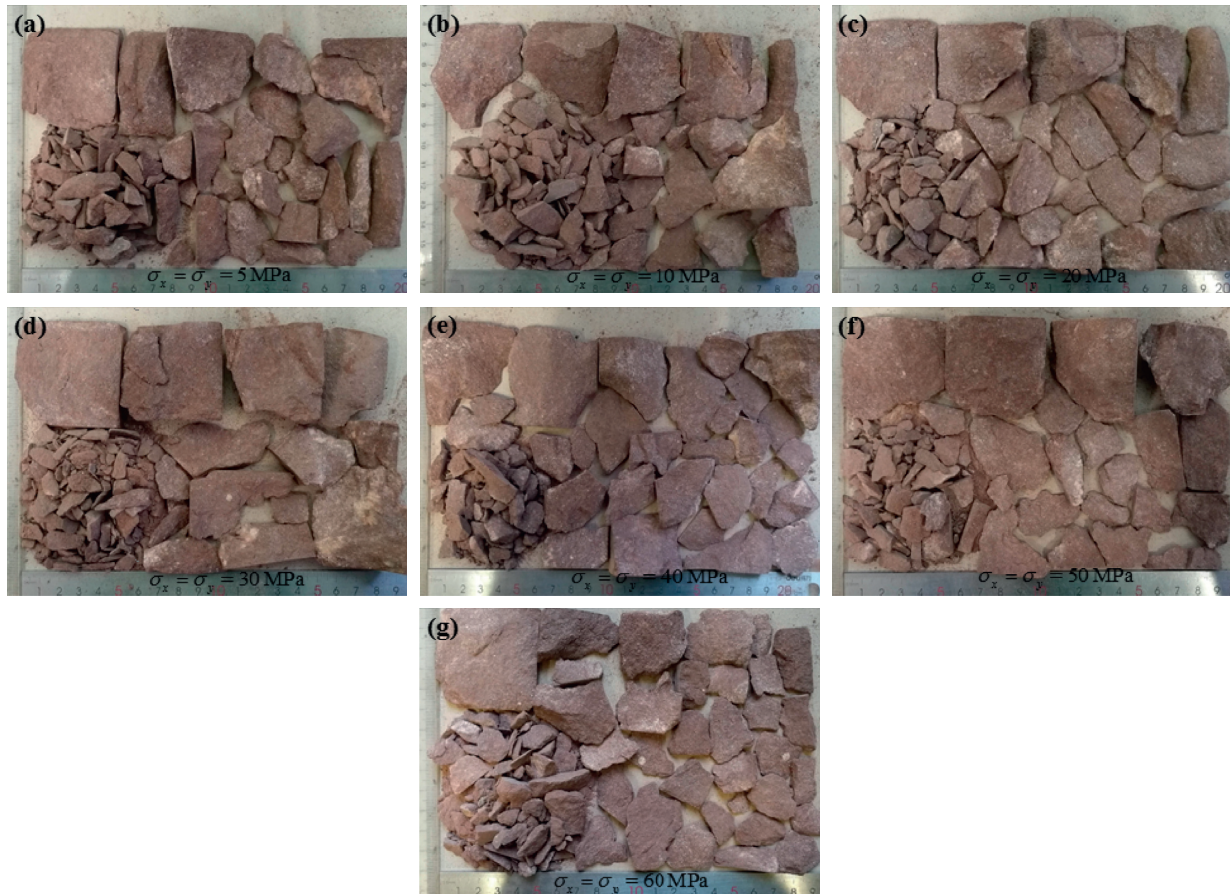


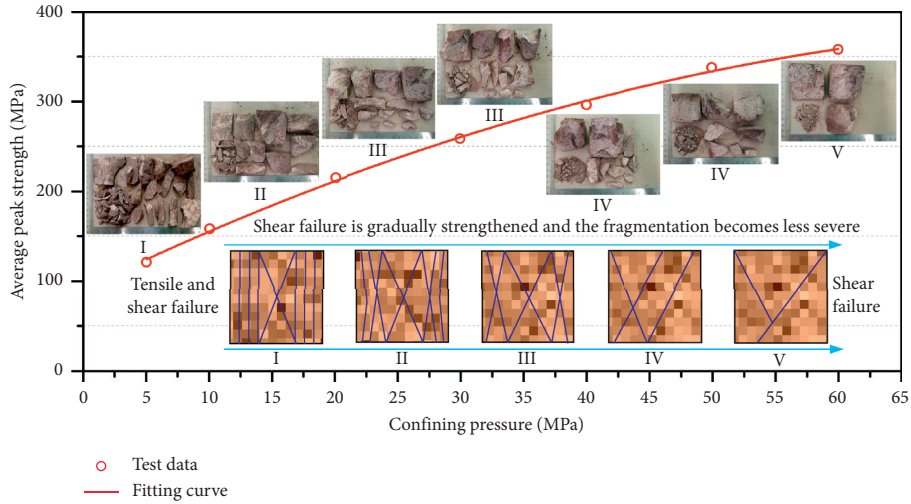
FIGURE 11: Failure characteristics of THU at different confining pressures.

The reason for rock failure is the macroscopic manifestation of continuous initiation, propagation, and coalescence of internal cracks [39–41]. Hence, the strength and failure characteristics during rock failure are closely related to the initiation, propagation, and coalescence of internal cracks. According to Section 3.3, for the TCT, as the confining pressure increases, the fragmentation of the sample decreases, and the wedge-shaped slab becomes thicker. For the BCTs, TLU, and THU, when the confining pressures are equal, the higher the unloading rate, the more serious the fragmentation of the samples, the more plate-shaped slabs parallel to the unloading surface are produced, and the thinner the slabs. When the unloading rate is constant, the higher the confining pressure, the more severe the fragmentation of the sample, the more plate-shaped slabs parallel to the unloading surface are produced, and the thinner the slabs. The severe fragmentation of the sample indicates that a great number of cracks have been created during the failure, while the great number and thin thickness of slabs parallel to the unloading surface indicate that a great number of cracks have propagated and coalesced in a direction parallel to the 2D stress plane (i.e., the Y-Z plane). It can be concluded that the changes in the confining pressure and unloading rate affect the initiation, propagation, and coalescence of cracks in hard rock.

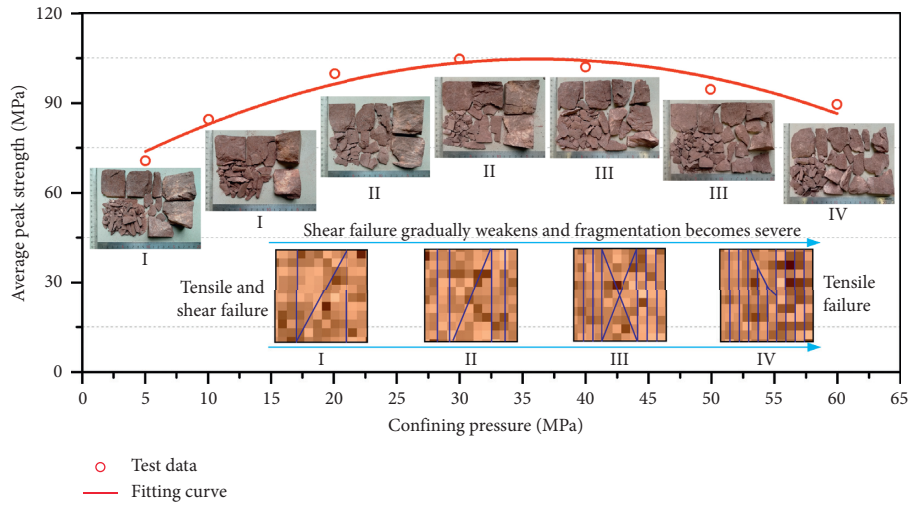
Regarding the confining pressure, Sahouryeh et al. [42] believed that, in the 2D stress state, the effect of intermediate

principal stress will cause the internal cracks of the rock to propagate continuously and coalesce in direction parallel to the 2D stress (i.e., the intermediate principal stress and maximal principal stress) plane, which results in a tensile failure. Cai [43] used a numerical simulation method to study the effect of intermediate principal stress on the surrounding rock failure around caverns. The main reasons for the spalling of rock around the caverns are the minimal principal stress (which is close to zero), the relatively high intermediate principal stress, and rock heterogeneity. The increasing confining pressure in the 2D stress state promotes crack propagation and coalescence in the direction of the 2D stress plane, which results in tensile failure. However, below the critical confining pressure, the confining pressure has a dual effect on the hard rock failure. First, the increasing confining pressure causes the cracks to propagate in the direction of the 2D stress plane, which promotes a tensile failure in the hard rock. Second, an increasing confining pressure increases the frictional resistance required to overcome hard rock fracture [44]; that is, an increasing crack initiation stress delays the hard rock failure [33], which increases the strength. When the critical confining pressure is exceeded, an increasing confining pressure facilitates the propagation of tensile cracks along the 2D plane stress direction, reduces the crack initiation stress, and decreases the strength of the hard rock. In addition, the increasing

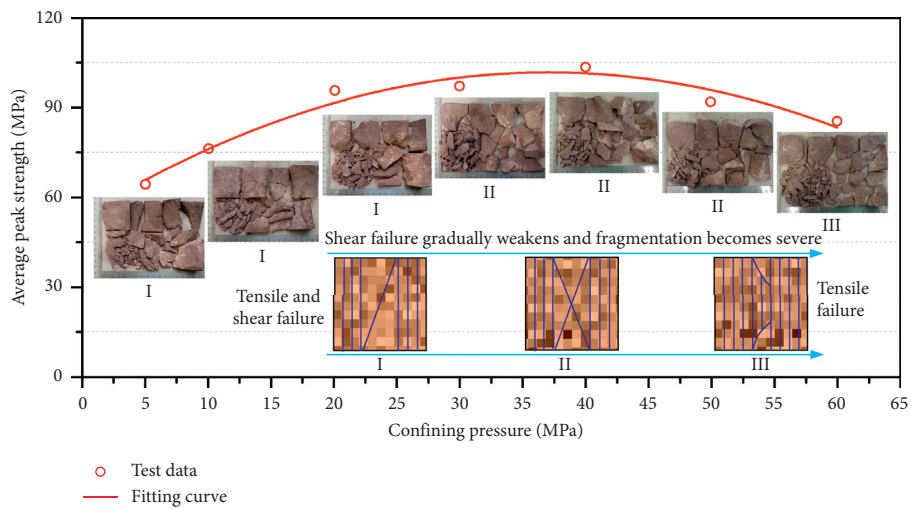




(a)

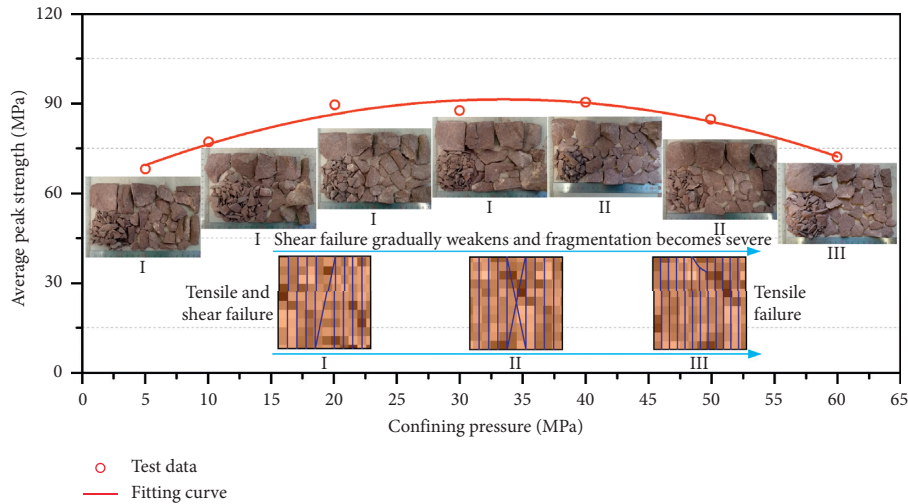


(b)



(c)

FIGURE 12: Continued.



(d)

FIGURE 12: Corresponding relationship between peak strength and failure characteristics: (a) TCT, (b) BCT, (c) TLU, and (d) THU.

confining pressure causes severe hard rock fragmentation, which is mainly due to the promoted initiation, propagation, and coalescence of more cracks in the hard rock failure process. Therefore, in the 2D stress state, with increasing confining pressure, the strength of the hard rock increases first and then decreases, the shear failure becomes gradually weaker, and the fragmentation becomes more severe. In the 3D stress state, the increasing confining pressure suppresses the initiation and propagation of tensile cracks parallel to the stress plane or in the direction of the maximal principal stress [45] and increases the crack initiation stress. As a result, the rock failure is delayed; the shear failure becomes enhanced; the strength is increased; and fragmentation is reduced.

Regarding the unloading rate, some studies have shown that hard rock exhibits strong tensile fracture characteristics during unloading (verified by the test results in this paper), and tensile cracks will be generated inside the rock [46–50]. The higher the unloading rate, the more developed the tensile cracks [51]. Therefore, when hard rock under unloading fails, more tensile cracks propagate and coalesce in the direction of the 2D stress plane under the combined effect of the confining pressure and maximal principal stress. Thus, the shear failure is weakened; the strength is reduced (i.e., strength-weakening effect); and the fragmentation becomes severe. Moreover, the higher the unloading rate is, the more significant these effects are.

In summary, the unloading rate and confining pressure affect the strength and failure characteristics by affecting the crack initiation type and propagation direction in hard rock. The influence of the confining pressure on hard rock depends on the stress state. In a 3D stress state, the confining pressure mainly inhibits the initiation and propagation of tensile cracks and increases the crack initiation stress. After unloading to a 2D stress state, the increasing confining pressure promotes mainly the initiation and propagation of tensile cracks parallel to the 2D stress plane. The unloading rate promotes mainly the initiation of tension cracks in hard

rock, thereby allowing more tension cracks to propagate and coalesce during hard rock failure, which leads to a strength-weakening effect on the hard rock. Therefore, during the excavation of deep high-stress hard rock tunnels (or caverns), affected by the unloading rate, numerous tensile cracks are generated in the surrounding rock within a certain range around the tunnel. Under the combined action of high tangential and axial stresses, the tensile cracks propagate and coalesce approximately parallelly to the excavation surface, which results in spalling.

## 5. Conclusions

- (1) The order of the peak strengths of the different tests at equal confining pressure is  $TCT > BTC > TLU > THU$ . During unloading, the stress-strain curve of red sandstone exhibits a stress step, and its mechanical properties become more unstable and complicated after unloading. After unloading to the 2D stress state, cracks in red sandstone are prone to unstable propagation, and the failure exhibits strong brittleness. The higher the unloading rate, the greater the difference between the mechanical properties, and the lower the stress level required for a stress step in the stress-strain curve.
- (2) A critical confining pressure (within 30–40 MPa) exists after the red sandstone is unloaded to a 2D stress state. With increasing confining pressure, the strength increases first and then decreases (the strength is maximal at the critical confining pressure), and the failure mode changes from a low-confining pressure tension-shear mixed failure to a high-confining pressure tension failure. In addition, fragmentation becomes more severe, and the geometries of the slabs change from large thick plates and wedges to medium- and small-sized thin plates. The change of the red sandstone stress state from 3D to 2D is the main reason for its strength decrease.

- (3) The influence of the unloading rate on the failure of red sandstone is related to the magnitudes of the confining pressure and unloading rate. The rock strength-weakening effect induced by unloading was confirmed. At equal confining pressures, the higher the unloading rate, the lower the strength (i.e., the strength-weakening effect is more pronounced), the weaker the shear failure, the more severe the fragmentation, and the easier the formation of thin-plate slabs. Increasing the unloading rate reduces the confining pressure required for the red sandstone failure mode to change from tensile-shear mixed failure to tensile failure. The effect of the high unloading rate on the failure of red sandstone is evident, particularly at high confining pressures, whereas a low unloading rate has no significant effect on the failure of red sandstone.
- (4) The unloading rate and confining pressure affect the strength and failure characteristics of hard rock by affecting the type of crack initiation and direction of crack propagation. The effect of the unloading rate causes mainly tension cracks in the hard rock parallel to the unloading surface, which leads to an easier propagation and coalescence of tensile cracks when the hard rock is damaged. In the 2D stress state, the increasing confining pressure promotes the initiation and propagation of tensile cracks parallel to the stress plane. When the confining pressure is below the critical confining pressure, it will increase the crack initiation stress and delay the hard rock failure; in addition, the crack initiation stress decreases when the confining pressure exceeds the critical confining pressure.
- (5) A reasonable explanation for spalling in deep hard rock tunnels (or caverns) was provided. During the excavation of deep hard rock tunnels, under the influence of the unloading rate, numerous tensile cracks are generated in the surrounding rock within a certain range around the tunnel. Under the combined action of high tangential and axial stresses, these tensile cracks propagate and coalesce approximately parallelly to the excavation surface, which induces spalling. The greater the unloading rate and axial stress, the greater the failure depth of spalling.
- (6) The effects of the unloading rate and axial stress should be considered for deep hard rock tunnels. Neglecting the effect of the unloading rate affects the safety of the support design, particularly at high unloading rates. When the axial stress is lower or higher than the critical confining pressure of the surrounding rock, neglecting the axial stress will lead to a conservative or dangerous support design, respectively. For deep hard rock ore, if the maximal horizontal principal stress exceeds the critical confining pressure, the mining surface should be perpendicular to the direction of the minimal horizontal principal stress to reduce the strength and improve the fragmentation of ore.

## Data Availability

The data used to support the findings of this study are included within the article.

## Conflicts of Interest

The authors declare that they have no conflicts of interest.

## Acknowledgments

This work was supported by the Project of the National Natural Science Foundation of China (Grant no. 41877272), the State Key Laboratory for GeoMechanics and Deep Underground Engineering, China University of Mining & Technology, Beijing (Grant no. SKLGDUEK1827), and University of South China Research Fund (190XQD091).

## References

- [1] M. S. Diederichs, "The 2003 Canadian geotechnical colloquium: mechanistic interpretation and practical application of damage and spalling prediction criteria for deep tunneling," *Canadian Geotechnical Journal*, vol. 44, no. 9, pp. 1082–1116, 2007.
- [2] F. Q. Gong, X. F. Si, X. B. Li, and S. Y. Wang, "Experimental investigation of strain rockburst in circular caverns under deep three-dimensional high-stress conditions," *Rock Mechanics and Rock Engineering*, vol. 52, no. 2, pp. 1459–1474, 2019.
- [3] F. Q. Gong, W. X. Wu, T. B. Li, and X. F. Si, "Experimental simulation and investigation of spalling failure of rectangular tunnel under different three-dimensional stress states," *International Journal of Rock Mechanics and Mining Sciences*, vol. 122, Article ID 104081, 2019.
- [4] Y. Luo, F. Q. Gong, D. Q. Liu, S. Y. Wang, and X. F. Si, "Experimental simulation analysis of the process and failure characteristics of spalling in D-shaped tunnels under true-triaxial loading conditions," *Tunnelling and Underground Space Technology*, vol. 90, pp. 42–61, 2019.
- [5] A. Mazaira and P. Konicek, "Intense rockburst impacts in deep underground construction and their prevention," *Canadian Geotechnical Journal*, vol. 52, no. 10, pp. 1426–1439, 2015.
- [6] A. Manouchehrian and M. Cai, "Numerical modeling of rockburst near fault zones in deep tunnels," *Tunnelling and Underground Space Technology*, vol. 80, pp. 164–180, 2018.
- [7] H. Wu, P. H. S. W. Kulatilake, G. Zhao, W. Liang, and E. Wang, "A comprehensive study of fracture evolution of brittle rock containing an inverted U-shaped cavity under uniaxial compression," *Computers and Geotechnics*, vol. 116, p. 103219, 2019.
- [8] A. Keneti and B. A. Sainsbury, "Review of published rockburst events and their contributing factors," *Engineering Geology*, vol. 246, pp. 361–373, 2018.
- [9] Y. Luo, F. Q. Gong, X. B. Li, and S. Y. Wang, "Experimental simulation investigation of influence of depth on spalling characteristics in circular hard rock tunnel," *Journal of Central South University*, vol. 27, no. 3, pp. 891–910, 2020.
- [10] F. Q. Gong, W. X. Wu, and L. Zhang, "Experimental investigation on strength weakening effect of red sandstone tensile failure under high pre-static load induced by dynamic disturbance," *Journal Central South University*, 2020.

- [11] K. Du, C. Z. Yang, R. Su, M. Tao, and S. F. Wang, "Failure properties of cubic granite, marble, and sandstone specimens under true triaxial stress," *International Journal of Rock Mechanics and Mining Sciences*, vol. 130, p. 104309, 2020.
- [12] E. L. Liu and S. M. He, "Effects of cyclic dynamic loading on the mechanical properties of intact rock samples under confining pressure conditions," *Engineering Geology*, vol. 125, pp. 81–91, 2012.
- [13] S. Q. Yang, T. Xu, L. He, H. W. Jing, S. Wen, and Q. L. Yu, "Numerical study on failure behavior of brittle rock specimen containing pre-existing combined flaws under different confining pressure," *Archives of Civil and Mechanical Engineering*, vol. 15, no. 4, pp. 1085–1097, 2015.
- [14] J. Cui, H. Hao, Y. C. Shi, X. B. Li, and K. Du, "Experimental study of concrete damage under high hydrostatic pressure," *Cement and Concrete Research*, vol. 100, pp. 140–152, 2017.
- [15] M. Hokka, J. Black, D. Tkalich et al., "Effects of strain rate and confining pressure on the compressive behavior of Kuru granite," *International Journal of Impact Engineering*, vol. 91, pp. 183–193, 2016.
- [16] S. Q. Yang, H. W. Jing, and S. Y. Wang, "Experimental investigation on the strength, deformability, failure behavior and acoustic emission locations of red sandstone under triaxial compression," *Rock Mechanics and Rock Engineering*, vol. 45, no. 4, pp. 583–606, 2012.
- [17] P. K. Kaiser and B.H. Kim, "Characterization of strength of intact brittle rock considering confinement-dependent failure processes," *Rock Mechanics and Rock Engineering*, vol. 48, no. 1, pp. 107–119, 2015.
- [18] X. F. Si and F. Q. Gong, "Strength-weakening effect and shear-tension failure mode transformation mechanism of rockburst for fine-grained granite under triaxial unloading compression," *International Journal of Rock Mechanics and Mining Sciences*, vol. 131, p. 104347, 2020.
- [19] X. B. Li, F. Q. Gong, M. Tao et al., "Failure mechanism and coupled static-dynamic loading theory in deep hard rock mining: a review," *Journal of Rock Mechanics and Geotechnical Engineering*, vol. 9, no. 4, pp. 767–782, 2017.
- [20] M. Ohnaka, "The quantitative effect of hydrostatic confining pressure on the compressive strength of crystalline rocks," *Journal of Physics of the Earth*, vol. 21, no. 2, pp. 125–140, 1973.
- [21] H. B. Li, J. Zhao, and T. J. Li, "Triaxial compression tests on a granite at different strain rates and confining pressures," *International Journal of Rock Mechanics and Mining Sciences*, vol. 36, no. 8, pp. 1057–1063, 1999.
- [22] F. Feng, S. J. Chen, D. Y. Li, S. T. Hu, W. P. Huang, and B. Li, "Analysis of fractures of a hard rock specimen via unloading of central hole with different sectional shapes," *Energy Science & Engineering*, vol. 7, no. 6, pp. 2265–2286, 2019.
- [23] S.L. Qiu, X.T. Feng, J.Q. Xiao, and C.Q. Zhang, "An experimental study on the pre-peak unloading damage evolution of marble," *Rock Mechanics and Rock Engineering*, vol. 47, no. 2, pp. 401–419, 2014.
- [24] J. D. Qiu, D. Y. Li, X. B. Li, and Q. Q. Zhu, "Numerical investigation on the stress evolution and failure behavior for deep roadway under blasting disturbance," *Soil Dynamics and Earthquake Engineering*, vol. 137, p. 106278, 2020.
- [25] J. H. Yang, Q. H. Jiang, Q. B. Zhang, and J. Zhao, "Dynamic stress adjustment and rock damage during blasting excavation in a deep-buried circular tunnel," *Tunnelling and Underground Space Technology*, vol. 71, pp. 591–604, 2018.
- [26] W. B. Lu, M. Chen, Z. G. Shan, and X. R. Chen, "Energy release process of surrounding rocks of deep tunnels with two excavation methods," *Journal of Rock Mechanics and Geotechnical Engineering*, vol. 4, no. 2, pp. 160–167, 2012.
- [27] X. P. Zhou and Y. D. Shou, "Excavation-induced zonal disintegration of the surrounding rock around a deep circular tunnel considering unloading effect," *International Journal of Rock Mechanics and Mining Sciences*, vol. 64, pp. 246–257, 2013.
- [28] X. Huang, Q. S. Liu, B. Liu, X. W. Liu, Y. C. Pan, and J. P. Liu, "Experimental study on the dilatancy and fracturing behavior of soft rock under unloading conditions," *International Journal of Civil Engineering*, vol. 15, no. 6, pp. 921–948, 2017.
- [29] H. Y. Wang, A. Dyskin, P. Dight, E. Pasternak, and A. Hsieh, "Review of unloading tests of dynamic rock failure in compression," *Engineering Fracture Mechanics*, vol. 225, Article ID 106289, 2018.
- [30] K. Duan, Y. L. Ji, W. Wu, and C. Y. Kwok, "Unloading-induced failure of brittle rock and implications for excavation-induced strain burst," *Tunnelling and Underground Space Technology*, vol. 84, pp. 495–506, 2019.
- [31] X. G. Zhao, J. Wang, M. Cai et al., "Influence of unloading rate on the strainburst characteristics of Beishan granite under true-triaxial unloading conditions," *Rock Mechanics and Rock Engineering*, vol. 47, no. 2, pp. 467–483, 2014.
- [32] S. Akdag, M. Karakus, A. Taheri, G. Nguyen, and H. Manchao, "Effects of thermal damage on strain burst mechanism for brittle rocks under true-triaxial loading conditions," *Rock Mechanics and Rock Engineering*, vol. 51, no. 6, pp. 1657–1682, 2018.
- [33] P.Z. Pan, X.T. Feng, and J. A. Hudson, "The influence of the intermediate principal stress on rock failure behaviour: a numerical study," *Engineering Geology*, vol. 124, pp. 109–118, 2012.
- [34] G. S. Su, J. Q. Jiang, S. B. Zhai, and G. L. Zhang, "Influence of tunnel axis stress on strainburst: an experimental study," *Rock Mechanics and Rock Engineering*, vol. 50, no. 6, pp. 1551–1567, 2017.
- [35] X. F. Si, L. Q. Huang, X. B. Li, C. D. Ma, and F. Q. Gong, "Experimental investigation of spalling failure of D-shaped tunnel under three-dimensional high-stress conditions in hard rock," *Rock Mechanics and Rock Engineering*, 2020.
- [36] F. Q. Gong, Y. Luo, X.B. Li, X. F. Si, and M. Tao, "Experimental simulation investigation on rockburst induced by spalling failure in deep circular tunnels," *Tunnelling and Underground Space Technology*, vol. 81, pp. 413–427, 2018.
- [37] F. Q. Gong, J. Y. Yan, S. Luo, and X. B. Li, "Investigation on the linear energy storage and dissipation laws of rock materials under uniaxial compression," *Rock Mechanics and Rock Engineering*, vol. 52, no. 11, pp. 4237–4255, 2019.
- [38] Y. Luo, "Influence of water on mechanical behavior of surrounding rock in hard-rock tunnels: an experimental simulation," *Engineering Geology*, vol. 277, p. 105816, 2020.
- [39] F. Q. Gong, D. H. Lu, X. B. Li, Q. H. Rao, and Z. T. Fu, "Toughness increasing or decreasing effect of hard rock fracture with pre-static loading under dynamic disturbance," *Chinese Journal of Rock Mechanics and Engineering*, vol. 33, no. 9, pp. 1905–1915, 2014, in Chinese.
- [40] H. Zhou, J. J. Lu, R. C. Xu, C. Q. Zhang, and F. Z. Meng, "Critical problems of study of slabbing failure of surrounding rock in deep hard rock tunnel and research progress," *Rock and Soil Mechanics*, vol. 36, no. 10, pp. 2737–2749, 2015, in Chinese.
- [41] Q. S. Bai, S. H. Tu, and C. Zhang, "DEM investigation of the fracture mechanism of rock disc containing hole(s) and its



- influence on tensile strength,” *Theoretical and Applied Fracture Mechanics*, vol. 86, pp. 197–216, 2016.
- [42] E. Sahouryeh, A. V. Dyskin, and L. N. Germanovich, “Crack growth under biaxial compression,” *Engineering Fracture Mechanics*, vol. 69, no. 18, pp. 2187–2198, 2002.
- [43] M. Cai, “Influence of intermediate principal stress on rock fracturing and strength near excavation boundaries-Insight from numerical modeling,” *International Journal of Rock Mechanics and Mining Sciences*, vol. 45, no. 5, pp. 763–772, 2008.
- [44] K. Mogi, “Effect of the intermediate principal stress on rock failure,” *Journal of Geophysical Research*, vol. 72, no. 20, pp. 5117–5131, 1967.
- [45] F. Feng, X. B. Li, J. Rostami, D. X. Peng, D. Y. Li, and K. Du, “Numerical investigation of hard rock strength and fracturing under polyaxial compression based on Mogi-Coulomb failure criterion,” *International Journal of Geomechanics*, vol. 19, no. 4, Article ID 04019005, 2019.
- [46] T. B. Li and L. S. Wang, “An experimental study on the deformation and failure features of a basalt under unloading condition,” *Chinese Journal of Rock Mechanics and Engineering*, vol. 12, no. 4, pp. 321–327, 1993, in Chinese.
- [47] K. Du, M. Tao, X. B. Li, and J. Zhou, “Experimental study of slabbing and rockburst induced by true-triaxial unloading and local dynamic disturbance,” *Rock Mechanics and Rock Engineering*, vol. 49, no. 9, pp. 3437–3453, 2016.
- [48] H. A. Amundsen, A. Emdal, and V. Thakur, “Field and laboratory study of stress relief due to unloading in block samples of sensitive clay,” *Géotechnique*, vol. 70, no. 6, pp. 503–517, 2020.
- [49] R. Q. Huang and D. Huang, “Evolution of rock cracks under unloading condition,” *Rock Mechanics and Rock Engineering*, vol. 47, no. 2, pp. 453–466, 2014.
- [50] K. Wang and F. Du, “Experimental investigation on mechanical behavior and permeability evolution in coal-rock combined body under unloading conditions,” *Arabian Journal of Geosciences*, vol. 12, p. 422, 2019.
- [51] Y. Cong, Z. Q. Wang, Y. R. Zheng, and L. M. Zhang, “Effect of unloading stress levels on macro-and microfracture mechanisms in brittle rocks,” *International Journal of Geomechanics*, vol. 20, no. 6, Article ID 04020066, 2020.

## Research Article

# Numerical Evaluation of Reinforced Concrete Columns Retrofitted with FRP for Blast Mitigation

Jing Dong , Junhai Zhao , and Dongfang Zhang 

School of Civil Engineering, Chang'an University, Xi'an 710061, China

Correspondence should be addressed to Junhai Zhao; zhaojh@chd.edu.cn

Received 7 April 2020; Revised 10 August 2020; Accepted 7 September 2020; Published 16 September 2020

Academic Editor: Chiara Bedon

Copyright © 2020 Jing Dong et al. This is an open access article distributed under the Creative Commons Attribution License, which permits unrestricted use, distribution, and reproduction in any medium, provided the original work is properly cited.

Fiber reinforced polymer (FRP) material is commonly applied in retrofitting structures due to the advantages of high strength and well corrosion resistance. Previous studies indicated that retrofitting with FRP sheet was an effective way for protecting the existing structures to resist the blast loads, but little research made comprehensive comparison study on the blast response of RC columns with different retrofitting strategies. This paper proposed a series of FRP retrofitting strategies and evaluated their effect on blast mitigation using numerical analysis approach. Comparison studies were conducted on the effect of FRP type, FRP thickness, and retrofitting mode on blast mitigation. A finite element model of RC columns retrofitted with FRP under blast loading was developed. The model considered the strain rate effect of steel and concrete and the orthotropic property of FRP composites. The reliability of the proposed model was validated against the data from a field blast test. Based on the verified model, the blast responses of RC columns with different retrofitting strategies were numerically investigated. According to the result analysis, appropriate FRP type, FRP thickness, retrofitting mode, and retrofitting length were recommended.

## 1. Introduction

Blast accidents caused by deliberate terrorist attacks and improper operations occur frequently. The blast accidents and their secondary disasters may bring about casualties and economic losses. Additionally, structures easily damage or even collapse when exposed to severe blast loading. For reducing the damage after explosion, the blast protection of buildings should be taken into consideration in the design phase. Besides, it is an urgent and significant task to retrofit the existing structures for blast mitigation.

In order to enhance the blast resistance of the existing building structures, previous studies provide valuable achievements on the retrofitting strategies with some high strength or high stiffness materials bonding on the surface of the structure, such as fiber reinforced polymer (FRP), steel plates, and aluminium foam. These retrofitting schemes can improve the blast resistance performance of the structures in different degrees [1]. Among those retrofitting materials, FRP is the most commonly used material [2]. FRP is a high performance and low weight composite material with well

corrosion resistance [3]. Reinforced concrete (RC) structure is widely applied in civil engineering. Recently, many researchers have made attempts to utilize FRP materials for blast mitigation of RC structures. Researchers in Karagozian & Case Science and Engineering Consulting Firm initially investigated the use of composite material to resist blast effects [4–6]. Buchan and Chen [7] and Zhao et al. [8] presented reviews on blast resistance of reinforced concrete structures retrofitted with FRP composites. The reviews pointed out that the blast resistance of a structure was obviously enhanced with FRP. In terms of type of FRP material studied, there are many research papers on carbon fiber reinforced polymer (CFRP) and glass fiber reinforced polymer (GFRP), but few on other types of FRP material. From the perspective of research approach, scaled blast test and numerical simulation are the common research methods, while few studies utilize the theoretical analysis due to the complication of blast load. Some representative studies are as follows. For the RC slabs and walls retrofitted with FRP, Silva and Lu [9] carried out blast tests on RC slabs strengthened with CFRP. The strengthening schemes of



slabs included one-side retrofitting and two-side retrofitting. The two-side retrofitting scheme could significantly increase the blast resistance while the one-side retrofitting scheme showed little effect on blast protection of the RC slab. Nam et al. [10, 11] proposed the numerical model of GFRP-retrofitted RC slab and CFRP-retrofitted RC wall subjected to blast loading. The numerical model considered the strain rate effect and FRP debonding failure and was validated against the previous experimental data. Tanapornraweekit et al. [12, 13] conducted two independent blast tests and numerical simulation on GFRP and CFRP strengthened RC slabs. Based on this study, Lin and Zhang [14] numerically studied the effect of thickness of GFRP sheets on blast mitigation. The results indicated that the deflections of RC slabs under blast loading decreased with the increase of GFRP thickness. Kong et al. [15] numerically analyzed the blast response of RC slabs strengthened with aramid fiber reinforced polymer (AFRP). The effects of AFRP layers and four different strengthening modes were discussed. Three AFRP layers was recommended in the study as the appropriate retrofitting number of layers. Additionally, wholly strengthened RC slabs showed better blast resistance than strip-like and crosswise strengthened RC slabs. For the RC columns retrofitted with FRP, Crawford et al. [4] experimentally and numerically studied the blast effect of conventional RC column, RC column retrofitted with steel, and RC column retrofitted with FRP. In most of the cases studied, retrofitting the column with steel or FRP wraps can effectively prevent collapse. Mutalib and Hao [16] investigated the P-I diagrams of RC columns strengthened with CFRP. The different FRP strengthening modes were innovatively studied, including strip, wrap, and both wrap and strip strengthening. Rodriguez-Nikl et al. [17] tested nine rectangular RC columns with and without FRP. Load-deflection curves of the column and stain of FRP were obtained. Nevertheless, the test was performed in the laboratory with lateral quasi-static load, which simulated the blast loading. Similarly, Jacques et al. [18] implemented RC columns retrofitted with GFRP under simulated blast loading. Different from the above research, shock-tube test setup was adopted to generate the simulated blast loading. Full-scale field blast test of RC column retrofitted with GFRP was carried out by Qasrawi et al. [19]. Results indicate that retrofitting with GFRP is reliable to reduce the residual displacement and local damage of the column. Liu et al. [20, 21] studied the RC piers retrofitted with CFRP under contact and noncontact explosion. The specimen in the field blast test included unretrofitted column, one-layer CFRP-retrofitted column, two-layer CFRP-retrofitted column, and three-layer CFRP-retrofitted column. With the increase of the CFRP layers, the blast resistance of the columns performs better. In summary, all the previous research results demonstrated that the RC structures retrofitted with FRP exhibited better blast resistance compared with conventional RC structures. However, the blast responses of RC structures retrofitted with CFRP, GFRP, and AFRP were experimentally or numerically studied separately. Parametric analysis substantially focused on the material strength, reinforcement ratio, and scaled distance. Only some studies

mentioned the effect of thickness or strengthening modes of a particular FRP material. The comparative studies on different FRP retrofitting strategies were still insufficient, especially for FRP-retrofitted RC columns. It is necessary to implement a comprehensive investigation on the blast performance of RC columns retrofitted with different retrofitting schemes including FRP type, FRP thickness, and retrofitting modes.

In this study, a series of retrofitting strategies were proposed for improving the blast resistance of reinforced concrete columns. Different FRP types, FRP thicknesses, and retrofitting modes were considered in the proposed retrofitting designs. The blast responses of these retrofitting strategies were evaluated and compared using the numerical analysis method. First, a finite element model of the RC columns retrofitted with FRP under blast loading was developed with the consideration of strain rate effect. The numerical analysis was conducted by the explicit nonlinear finite element program LS-DYNA. The reliability of the proposed numerical model was verified against the relevant experimental results. Furthermore, a series of RC columns retrofitted with FRP under identical blast condition were numerically investigated based on the verified model. The blast responses of the columns were compared, and the effect of different retrofitting strategies was discussed. The reported findings in this study can serve as available reference for blast mitigation of structural design and retrofitting.

## 2. Design of RC Columns Retrofitted with FRP

In order to investigate the effect of RC columns with different retrofitting strategies on blast mitigation, this paper presents a series of FRP retrofitting schemes, including different FRP types, FRP thicknesses, and retrofitting modes. In view of broader application in the engineering practice, all the designed columns for this comparative study are of square section. Of all the investigated columns, S-1 is a conventional RC column as a control member. Each column consists of a 300 mm × 300 mm square cross section and a height of 3000 mm. The columns are reinforced with four 20 mm longitudinal bars and 10 mm stirrups. As depicted in Figure 1, the reinforcement ratio is 1.4%. The geometry and reinforcement of the RC column come from a column in the actual project, which is designed based on the Chinese code for concrete structures (GB50010-2010). The material properties for concrete and steel are obtained from the material test and are described in Table 1.

The retrofitted columns are designed from the following three aspects. Firstly, as the commonly used strengthening materials, CFRP, GFRP, AFRP are selected to be the retrofitting materials for comparative study. Table 2 lists the properties of the three types of FRP materials. The material properties are obtained from previous research on FRP retrofitting [13, 16, 22]. Secondly, the structures are often strengthened with multi-layer FRP material in engineering reinforcement application. This study also investigates the effect of FRP

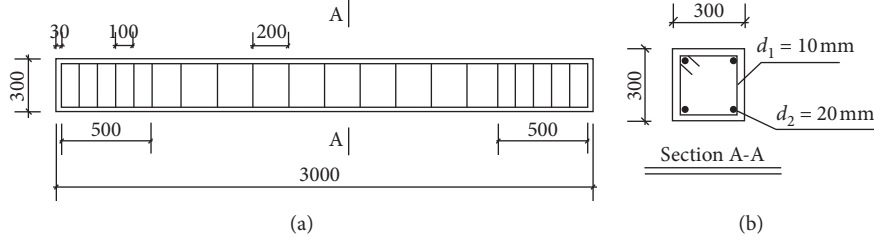


FIGURE 1: Geometry and reinforcement of the column. (a) Reinforcement configuration. (b) Cross section.

TABLE 1: Material properties for steel reinforcement and concrete.

Material	Parameters	Magnitude
Steel reinforcement	Mass density	7830 kg/m <sup>3</sup>
	Young's modulus	208 GPa
	Poisson's ratio	0.3
	Yield stress	450 MPa
Concrete	Mass density	2400 kg/m <sup>3</sup>
	Compressive strength	40 MPa
	Shear modulus	14.86 GPa

thickness or layers on blast protection. The thicknesses of 0.17 mm, 0.34 mm, 0.51 mm, 0.68 mm, and 0.85 mm (namely, 1 layer, 2 layers, 3 layers, 4 layers, and 5 layers) are considered. Thirdly, four retrofitting modes were designed in this study. Under blast loading, RC columns may suffer flexural damage, shear damage, and flexural-shear damage. The vulnerable parts are mainly concentrated in the middle and two ends of the column [23]. Among the four retrofitting modes shown in Figure 2, Mode A is the wholly FRP wrapped mode, and the others are partially wrapped modes. Mode B is 1800 mm length FRP wrapped at the midspan of the column. Mode C is every 600 mm FRP wrapped at both midspan and two ends of the column. Mode D is two 900 mm length FRP sheets wrapped at two ends of the column. The total length of FRP material used in the three partial retrofitting designs is 1800 mm.

Each investigated column is given a specific number in this study so as to describe the columns in the following parts conveniently. Except the unretrofitted column S-1, all the retrofitted columns in this study are assigned as "XX-X." The first capital refers to the abbreviation of FRP type, the second capital is the retrofitting layer of FRP, and the last capital represents the retrofitting mode. For example, G3-C is the column retrofitted with 3-layer GFRP material and the retrofitting mode is Mode C.

### 3. Finite Element Model

Numerical simulation is an effective approach to analyzing the blast response of structures. Some data and phenomena that are difficult to be observed from the experiment can be easily obtained in the numerical simulation. Moreover, this method can significantly save the research expenses. A well-known explicit dynamic program, LS-DYNA, is adopted in numerical analysis.

#### 3.1. Material Model

**3.1.1. Steel Reinforcement Model.** For the material model of both longitudinal bars and stirrups, kinematic hardening plasticity model is chosen to model the steel reinforcement. In LS-DYNA, this model is implemented as keyword MAT\_PLASTIC\_KINEMATIC (MAT003). The yield stress function of steel is given by

$$\sigma_y = \left[ 1 + \left( \frac{\dot{\epsilon}}{C} \right)^{1/p} \right] (\sigma_0 + \beta E_p \epsilon_p^{\text{eff}}), \quad (1)$$

where  $\sigma_0$  is the initial yield stress,  $C$  and  $p$  are strain rate parameters,  $\beta$  is the hardening parameter,  $\dot{\epsilon}$  and  $\epsilon_p^{\text{eff}}$  are strain rate and effective plastic strain, respectively, and  $E_p$  is plasticity hardening modulus. As shown in Figure 3,  $E_t$  is the slope of the bilinear stress-strain curve, and  $l$  and  $l_0$  are the undeformed and deformed lengths of uniaxial tension specimen. By varying the hardening parameter  $\beta$ , kinematic hardening, isotropic hardening, and combination hardening could be specified.

The strength of steel materials increases under the high strain rate impact. Based on the Cowper-Symonds model [24], the strain rate effect of steel reinforcement is considered as the dynamic increase factor (DIF) of  $1 + (\dot{\epsilon}/C)^{1/p}$ . This material model is particularly suitable for modeling the dynamic behavior of steel under blast loading [25].

**3.1.2. Concrete Model.** Currently, the concrete material models that are commonly used in the impact issues mainly include the Johnson-Holmquist-Cook (JHC) model [26], Riedel-Hiermaier-Thoma (RHT) model [27], and Malvar model [28]. In this study, MAT\_JOHNSON\_HOLMQUIST\_CONCRETE (MAT 111) in LS-DYNA is selected to model the concrete material. This model is applicable to simulate concrete under high pressure, high strain, and high strain rate [29]. The advantage of JHC model is the comprehensive consideration of strain rate effect and accumulated damage effect [30]. As depicted in Figure 4, the equivalent yield strength of the model is given by

$$\sigma^* = [A(1 - D) + Bp^{*N}] \left[ 1 + \text{Cln} \left( \frac{\dot{\epsilon}}{\dot{\epsilon}_0} \right) \right], \quad (2)$$

where  $\sigma^* = \sigma/f'_c$  denotes the normalized equivalent stress, in which  $\sigma$  is the actual equivalent stress and  $f'_c$  is the quasi-static uniaxial compressive strength;  $A$  represents the normalized cohesive strength;  $B$  represents the normalized

TABLE 2: Material properties for FRP.

Parameters	Magnitude		
	CFRP	GFRP	AFRP
Mass density	1580 kg/m <sup>3</sup>	1600 kg/m <sup>3</sup>	1440 kg/m <sup>3</sup>
Young's modulus-longitudinal direction	138 GPa	75.6 GPa	67 GPa
Young's modulus-transverse direction	9.65 GPa	17.7 GPa	4.7 GPa
Poisson's ratio	0.021	0.025	0.028
Shear modulus	5.24 GPa	2.8 GPa	2.0 GPa
Longitudinal tensile strength	2280 MPa	1330 MPa	1420 MPa
Transverse tensile strength	57 MPa	69 MPa	36 MPa
Shear strength	71 MPa	70 MPa	53 MPa

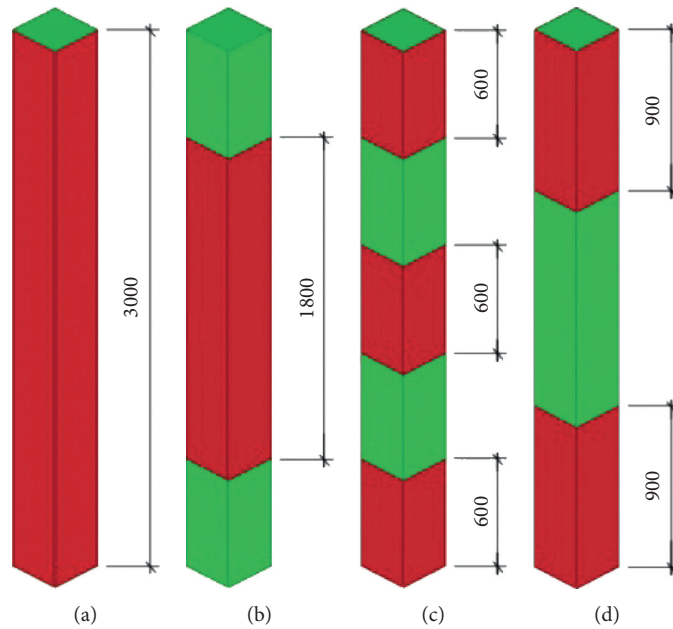


FIGURE 2: Four retrofitting modes. (a) Mode A. (b) Mode B. (c) Mode C. (d) Mode D.

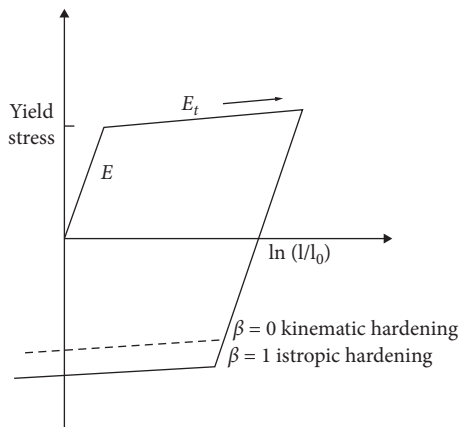


FIGURE 3: Stress-strain relationship of hardening material.

pressure hardening;  $C$  represents the strain rate coefficient;  $N$  represents the pressure hardening exponent;  $p^* = p/f'_c$  denotes the normalized pressure, in which  $p$  is the hydrostatic pressure;  $\dot{\epsilon}$  and  $\dot{\epsilon}_0 = 1.0 \text{ s}^{-1}$  are the strain rate and

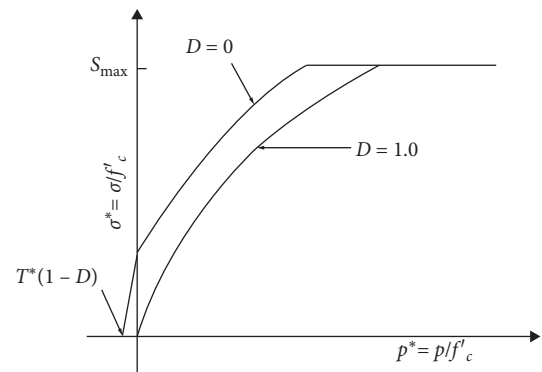


FIGURE 4: Constitutive law of JHC model.

reference strain rate, respectively; and  $D$  ( $0 \leq D \leq 1$ ) represents the damage parameter and is expressed as

$$D = \sum \frac{\Delta \epsilon_p + \Delta \mu_p}{D_1 (p^* + T^*)^{D_2}}, \quad (3)$$

where  $\Delta\varepsilon_p$  is the equivalent plastic strain increment and  $\Delta\mu_p$  is the plastic volumetric strain increment;  $T^* = T/f'_c$  denotes the normalized largest tensile hydrostatic pressure, in which  $T$  is the maximum tensile hydrostatic pressure; and  $D_1$  and  $D_2$  are damage constants.

In JHC model, the relationship between pressure and volume is described as equation of state in three response regions as follows. The curve of hydrostatic pressure and volumetric strain is also illustrated in Figure 5.

$$P = K\mu \text{ (elastic region)}, \quad (4)$$

where  $P$  is the hydrostatic pressure,  $K$  is the elasticity modulus, and  $\mu$  is volumetric strain.

$$P = \frac{P_{\text{crush}} + (\mu - \mu_{\text{crush}})(P_{\text{lock}} - P_{\text{crush}})}{(\mu_{\text{lock}} - \mu_{\text{crush}})} \text{ (plastic transition region)}, \quad (5)$$

where  $P_{\text{crush}}$  and  $\mu_{\text{crush}}$  are the crushed pressure and volumetric strain in the uniaxial compression test of concrete;  $P_{\text{lock}}$  and  $\mu_{\text{lock}}$  are the locking pressure and volumetric strain.

$$P = K_1\bar{\mu} + K_2\bar{\mu}^2 + K_3\bar{\mu}^3 \text{ (fully dense region)}, \quad (6)$$

where  $\bar{\mu} = (\mu - \mu_{\text{lock}})/(1 + \mu_{\text{lock}})$  is the modified volumetric strain;  $K_1$ ,  $K_2$ , and  $K_3$  are material constants.

**3.1.3. FRP Model.** MAT\_ENHANCED\_COMPOSITE\_DAMAGE (MAT054) in LS-DYNA is applied to model the behavior of FRP composite. This material model can effectively simulate the composite materials especially orthotropic materials. The failure criterion of this material model is based on Chang–Chang model. It includes the failure criteria for the tensile fiber mode, compressive fiber mode, tensile matrix mode, and compressive matrix mode [31]. The strength enhancement of FRP under high strain is relatively insignificant and negligible [32, 33], so the strain rate effect of CFRP is ignored in this study.

**3.2. Mesh Size.** The numerical results are affected by the mesh size especially when the nonlinear material models are adopted in simulation [34]. With a larger mesh size, the computing time is applicable while the accuracy of the results is lower. On the contrary, if the mesh size is too small, even though the computing accuracy is guaranteed, the computing efficiency is rather low. In order to ensure the efficiency and accuracy in numerical analysis, trial simulation tests were carried out with 10 mm being selected as the mesh size in this study. Moreover, the simulation converged well when the mesh size is 10 mm.

**3.3. Generation of Blast Loading.** The press-time history curve of typical blast load is shown in Figure 6(a).  $P_0$  is the initial atmospheric pressure. After detonation, the press of blast wave reaches the peak press  $P_{SO}$  quickly at the time of  $t_A$ . Then the press drops gradually to the initial atmospheric press through the positive press duration  $t_0$ . During the time

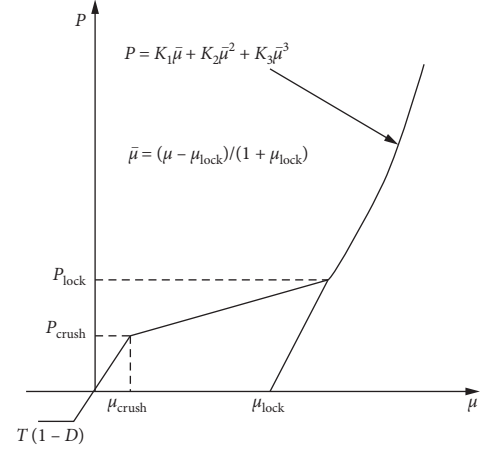


FIGURE 5: Relationship of hydrostatic pressure and volumetric strain in JHC model.

of  $t_0^-$ , the press keeps on decreasing to the peak value of  $P_{SO}^-$  in the negative phase and then finally returns to the initial atmospheric pressure. In LS-DYNA, blast loading can be generated by three approaches. (1) As shown in Figure 6(b), the blast loading is simplified to triangle load by neglecting the negative phase of blast wave. The load curve is defined using the keyword LOAD\_CURVE. This approach is quite easy to implement and high in computational efficiency, but the accuracy is relatively low due to the simplification of blast loading. (2) Another approach is to develop the model of air domain, explosive, and structures according to the actual geometry. The blast loading is generated by detonating the explosive using the keyword INITIAL\_DETONATION. As to the numerical results of this approach, even the propagation of blast wave within the air is feasible to be observed. However, the computational amount is extremely large especially for a small mesh size or a large standoff distance case. (3) The third way is to utilize the built-in function CONWEP air blast model. CONWEP is an empirical blast function based on the data from various blast tests. By employing the keyword LOAD\_BLAST and LOAD\_SEGMENT\_SET, the blast loading is generated. This blast function shows a high computational accuracy within an acceptable computational efficiency [35]. In this study, the blast loading is generated by CONWEP approach.

**3.4. Boundary Conditions and Erosion.** The reinforcement bars are modeled with beam elements, concrete is employed with solid elements, and FRP is adopted with shell elements. Separate model is utilized to develop the RC column wrapped with FRP. In order to be consistent with the fixed ends condition in the following blast tests, translational and rotational constraints for  $x$ ,  $y$ , and  $z$  directions are implemented at the head and the foot of the column using the keyword BOUNDARY\_SPC\_SET. Perfect bond is assumed in this study as the slip between concrete and rebar can be neglected under the instantaneous load [29]. In order to veritably simulate the crush and fracture of the concrete under impulsive loading, the erosion algorithm is employed.



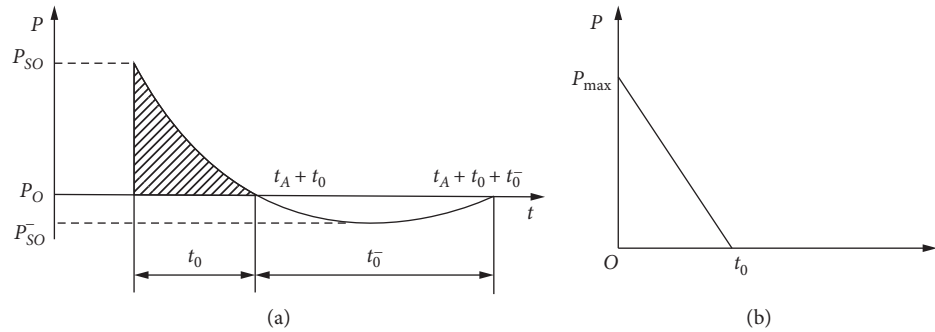


FIGURE 6: Press-time curve of blast loading. (a) Typical blast loading. (b) Simplified blast loading.

By adding the keyword `MAT_ADD_EROSION`, the elements in finite element model are deleted when the erosion criterion reaches the given value. In this study, a principle tensile strain of 0.001 is adopted for the primary criterion of concrete [36].

**3.5. Verification of Numerical Modeling.** The above-mentioned numerical modeling should be validated against the relevant blast tests. The test implemented in laboratory with simulated blast loading is inappropriate for verification because the strain rate of simulated blast loading is different from the strain of real blast loading in explosion. The available data are limited in the relevant blast test. In this paper, the finite element model is validated against the blast test of RC circular column retrofitted with CFRP carried out by Liu [20]. Since the specimens in blast test are circular columns while the investigated columns in this paper are square, the proposed numerical model was also compared with the numerical results of RC square column retrofitted with CFRP analyzed by Crawford [4].

The column in the field blast test was a circular section column with a diameter of 400 mm and a length of 3500 mm. The concrete strength grade was C40 and the reinforcement ratio was 0.9%. The column was wholly retrofitted with one-layer CFRP sheet. As to Case 26 in the blast test, the explosive was 2 kg TNT and was detonated at a standoff distance of 1500 mm. The numerical model is generated by the proposed model mentioned above, and the geometry of column and material properties are in accordance with the blast test. Figure 7 displays finite element model of the RC column retrofitted with FRP after meshing. Since the field blast test was very dangerous, only limited data were observed in the test. The numerical results are compared with those available test data. The deformation of the column exported from numerical analysis is compared with the deformation observed from the test. It can be seen from Figure 8 that the column is almost intact from both test and numerical results, and no obvious rupture of FRP is noticed. That is because the scaled distance in this case is  $1.5 \text{ m/kg}^{1/3}$ , which is classified as far blast event. One acceleration sensor was set on the backside of the column with a height of 300 mm. Figure 9 illustrates the comparison between the test result and numerical result on the acceleration history curve of the column. The comparison shows that the numerical result is

essentially in agreement with the test result. As to Case 25 in the field test, the weight of TNT is 1 kg, and the standoff distance between explosive and the column is still 1500 mm. Two strain gauges were stuck at the longitudinal bar and stirrup separately with a height of 330 mm. One pressure transducer was arranged at the height of 1330 mm. Table 3 compares the numerical results and the data collected from the test. The deviation rate of the strain of longitudinal bar and stirrup is only  $-4\%$  and  $-4.4\%$ . The numerical result is very close to the test data. The deviation rate of the arrival time of the peak pressure is  $-10.19\%$ , and the deviation rate of the peak pressure is  $-0.94\%$ . This is mainly because field blast tests are highly sensitive to the environment and other external factors. The actual environment of the test site cannot be completely simulated in the numerical analysis, but the deviation rate is still in a rational range.

Moreover, in order to verify the proposed numerical approach further, a finite element model is developed and compared with the results analyzed in [4]. The column is a square RC column with a section of  $750 \text{ mm} \times 750 \text{ mm}$  and a height of 3650 mm. Eight longitudinal bars with a diameter of 32 mm and stirrups with a diameter of 10 mm at 450 mm are reinforced. The reinforcements are ASTM A615 Grade 60 steel bars. The strength and elasticity modulus are 34.5 MPa and 29 GPa, respectively. The RC column is retrofitted with six-layer CFRP sheets, and the total thickness of CFRP sheets is 0.5 m. The finite element model is developed according to the approach proposed in this study. Table 4 compares the numerical results in this paper and those in [4]. Additionally, the displacement history curve at midspan of the column in Case 2 is compared in Figure 10.

From the above validation and comparison, the proposed finite element proved to be a reliable approach to simulate the performance of RC columns retrofitted with FRP under blast loading. In addition, the verified numerical model is suitable for evaluating the blast response of RC columns retrofitted with FRP in different blast situation or different retrofitting scheme.

## 4. Results and Discussion

Based on the verified finite element model, a series of RC columns retrofitted with different strategies are numerically analyzed. The details of the column and the design of retrofitting schemes are described in Section 2. The material

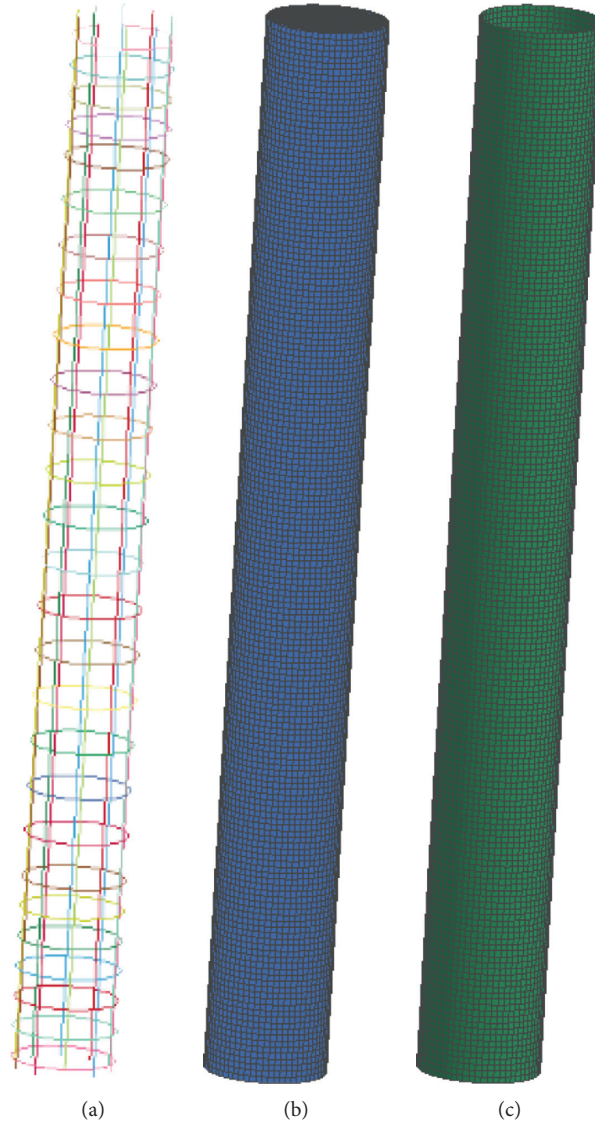


FIGURE 7: Finite element model of tested column. (a) Rebar. (b) Concrete. (c) FRP.

model and analysis setting of the investigated columns are developed based on Section 3. The explosives of all investigated cases are 8 kg TNT with a standoff distance of 0.8 m, and the scaled distance is  $0.4 \text{ m/kg}^{1/3}$ . After being solved by LS-DYNA, the numerical results of the numerical models are postprocessed by LS-PrePost, and available data are exported.

Deformation is an important index to measure the blast resistance performance of the structural members. According to the numerical results, the columns mainly suffer flexural deformation. The maximum displacement occurs at the midspan of the member. Therefore, the displacements of midspan of the columns under blast loading are exported to measure the blast performance. Additionally, damage assessment is chosen to evaluate the damage degree of the structure. Based on the Unified Facilities Criteria (UFC 3-340-02), support rotation angle is usually used as a failure criterion for structural members. The support

rotation angle is a combination of the maximum deflection of a given column and the length of the column. This angle is usually used in damage assessment of the structure under blast loading and blast resistance design. The support rotation angle  $\theta$  is calculated by the maximum midspan deflection and half-span length, which is given by [37]

$$\theta = \tan^{-1}\left(\frac{2x_m}{l}\right), \quad (7)$$

where  $x_m$  refers to the maximum displacement of the column and  $l$  denotes the length of the column. According to the limited rotation values given by standards, the local damage level can be classified into three categories: (1) slight damage ( $\theta < 2^\circ$ ); (2) moderate damage ( $2^\circ \sim 4^\circ$ ); (3) severe damage ( $\theta > 4^\circ$ ) [38]. All the retrofitting schemes and main results of the investigated columns are listed in Table 5.

The mass of explosive in the numerical analysis is relatively small, and the scaled distance is  $0.4 \text{ m/kg}^{1/3}$ . The blast





FIGURE 8: Deformation of tested column. (a) Test result. (b) Numerical result.

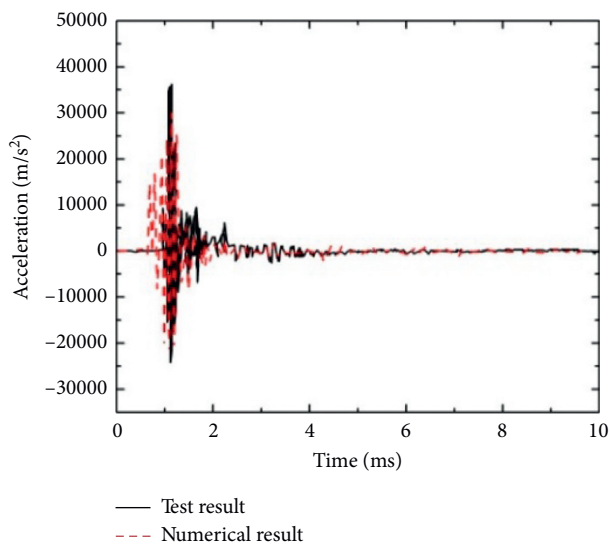


FIGURE 9: Acceleration history curve of the test point on the column.

event is identified as the intermediate class, so the given columns all suffer slight damage based on the results of support rotation angle. As a whole, the retrofiting of FRP

TABLE 3: Comparison of numerical results and test data.

	Test	Simulation	Deviation rate (%)
Strain of longitudinal bar	150 $\mu\epsilon$	144 $\mu\epsilon$	-4.0
Strain of stirrup	273 $\mu\epsilon$	261 $\mu\epsilon$	-4.4
Arrival time of peak pressure	2.56 ms	2.299 ms	-10.19
Peak pressure	0.32 MPa	0.317 MPa	-0.94

material can reduce the deformation and damage of the columns under blast loading. However, under the same blast condition, the dynamic responses of columns retrofitted with different strategies are not uniform. It is necessary to find out the effect of different retrofiting strategies on blast mitigation. The details are discussed from the following aspects.

**4.1. FRP Thickness.** The RC columns retrofitted with different thicknesses of FRP were initially reported to simulate the blast resistance of RC columns retrofitted with different layers of FRP material. Figure 11 describes the displacement history curve at midspan of columns retrofitted with different thicknesses of FRP. In columns wholly retrofitted with CFRP, for

TABLE 4: Comparison of the maximum deflection in the analysis.

Case	Charge weight (kg)	Standoff distance (m)	Maximum deflection (mm)		Deviation rate (%)
			Crawford et al. [4]	Present analysis	
1	682	3.05	132	146.25	10.80
2	682	3.05	18	19.13	6.28
3	1364	6.1	88	91.47	3.94

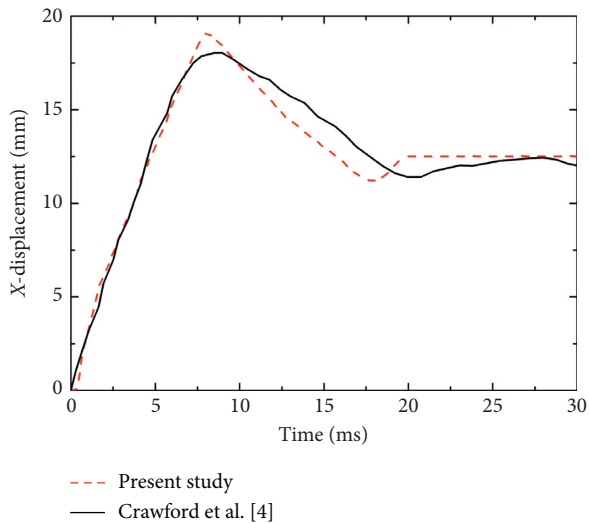


FIGURE 10: Displacement history curve at midspan of the column in Case 2.

example, when the thickness of CFRP is 0.17 mm, 0.34 mm, 0.51 mm, 0.68 mm, and 0.85 mm (namely 1, 2, 3, 4, and 5 layers, respectively), the maximum deflection of the column is 28.56 mm, 23.91 mm, 20.79 mm, 18.08 mm, and 17.90 mm. The deformation reduced obviously compared with the unreinforced column. The blast resistance performance improves with the increase of FRP thickness. Compared with S-1, the maximum displacement of C1-A, C2-A, C3-4, C4-A, and C5-A reduces by 22.20%, 34.86%, 43.37%, 50.75%, and 51.24%, respectively. It should be noticed that the decrease does not present a linear change. Instead, the blast mitigation effect weakens with the increase of FRP thickness or layers. When the FRP thickness reaches a certain value, it is of little significance to further increase the thickness of FRP for blast protection. The deformations of C4-A and C5-A are very approximate. In these cases, if the thickness of FRP is above 0.68 mm (4 layers), the retrofitting scheme is uneconomical. Columns retrofitted with AFRP and GFRP exhibit the same pattern as columns retrofitted with CFRP.

**4.2. FRP Type.** The blast responses of RC columns retrofitted with different types of FRP material were also studied. For expressing the blast mitigation effect of FRP materials, the unreinforced column S-1 was also included in the comparative study. Figure 12 shows the deformation and damage distribution of S-1, A1-A, C1-A, and G1-A. As can be seen from Figure 12(a), since the midspan of the column S-1 is closest to the explosive, obvious crushing damage of concrete at the midspan can be found. With the propagation of

blast wave, local concrete at the back surface of the column dilates and spalls. Cracks can also be observed at the top and bottom of the column due to the increase of the shear stress. Some of the longitudinal bars and stirrups slightly bend without any breakage. The maximum effective stress of the reinforcement at the midspan of the column is 512 MPa, which exceeds the yield stress of the steel reinforcement. For the retrofitted columns, the damage modes of the retrofitted column are quite different from that of conventional RC column. Minor cracks and no obvious spall phenomenon of the concrete can be observed. Partial ruptures of the FRP are noticed at two ends of the column. However, the wrapping of FRP can efficiently prevent the spalling and splashing of the concrete. Additionally, the bending deformations of the retrofitted columns are smaller than that of S-1. For the structural members that are not severely damaged, the deformation of the column is an important indicator to evaluate their blast resistance. The displacement history curves of midspan of S-1, A1-A, C1-A, and G1-A are illustrated in Figure 13. Under the blast loading, the deformations of all columns reach the peak rapidly and then drop to a certain value. The maximum deformation of S-1, A1-A, C1-A, and G1-A is 36.71 mm, 33.82 mm, 28.56 mm, and 31.73 mm, respectively. Compared with S-1, the deflection of A1-A, C1-A, and G1-A reduces by 7.87%, 22.20%, and 13.57%. The FRP material effectively restrains the lateral expansion of the concrete inside, so that the concrete is under three-dimensional compression. Thus, the deformation performance of the column is enhanced, and the blast resistance is improved. Among the three types of FRP materials mentioned in this study, the deflection of the column retrofitted with CFRP is relatively the least. This indicates that CFRP is the best retrofitting material for blast protection. However, from an economic perspective, CFRP is the most expensive among the three materials. If the cost of retrofitting is considered, GFRP is a preferable choice because its cost is almost 1/4 that of CFRP. For example, the maximum displacement of G2-A and C1-A is 26.93 and 28.56, respectively. It can be noticed that the G2-A has better blast resistance effect and less cost than C1-A.

### 4.3. Retrofitting Mode

**4.3.1. Dynamic Response.** In addition to full FRP retrofitting, three local retrofitting methods are also designed in this paper. The details of the four retrofitting strategies are described in Section 2. Figure 14 shows the deflection-history curves of one-layer FRP-retrofitted column with different strengthening modes. The variation tendency of the deflection of the columns with time is basically the same. The

TABLE 5: Information and main results of investigated columns.

Column no.	FRP type	FRP thickness (mm)	Retrofitting mode	Max deflection (mm)	$\theta$ (°)
S-1	—	—	—	36.71	1.40
C1-A	CFRP	0.17	Mode A	28.56	1.09
C1-B	CFRP	0.17	Mode B	31.57	1.21
C1-C	CFRP	0.17	Mode C	31.09	1.19
C1-D	CFRP	0.17	Mode D	32.44	1.24
C2-A	CFRP	0.34	Mode A	23.91	0.91
C3-A	CFRP	0.51	Mode A	20.79	0.79
C3-B	CFRP	0.51	Mode B	23.17	0.88
C3-C	CFRP	0.51	Mode C	22.93	0.88
C3-D	CFRP	0.51	Mode D	23.85	0.91
C4-A	CFRP	0.68	Mode A	18.08	0.69
C5-A	CFRP	0.85	Mode A	17.90	0.68
A1-A	AFRP	0.17	Mode A	33.82	1.29
A1-B	AFRP	0.17	Mode B	35.74	1.36
A1-C	AFRP	0.17	Mode C	35.13	1.34
A1-D	AFRP	0.17	Mode D	35.96	1.37
A2-A	AFRP	0.34	Mode A	29.55	1.13
A3-A	AFRP	0.51	Mode A	25.76	0.98
A3-B	AFRP	0.51	Mode B	27.69	1.06
A3-C	AFRP	0.51	Mode C	27.03	1.03
A3-D	AFRP	0.51	Mode D	28.04	1.07
A4-A	AFRP	0.68	Mode A	22.79	0.87
A5-A	AFRP	0.85	Mode A	22.03	0.84
G1-A	GFRP	0.17	Mode A	31.73	1.21
G1-B	GFRP	0.17	Mode B	34.61	1.32
G1-C	GFRP	0.17	Mode C	34.15	1.30
G1-D	GFRP	0.17	Mode D	35.12	1.34
G2-A	GFRP	0.34	Mode A	26.93	1.03
G3-A	GFRP	0.51	Mode A	23.11	0.88
G3-B	GFRP	0.51	Mode B	24.98	0.95
G3-C	GFRP	0.51	Mode C	24.27	0.93
G3-D	GFRP	0.51	Mode D	25.86	0.99
G4-A	GFRP	0.68	Mode A	20.92	0.80
G5-A	GFRP	0.85	Mode A	20.38	0.78

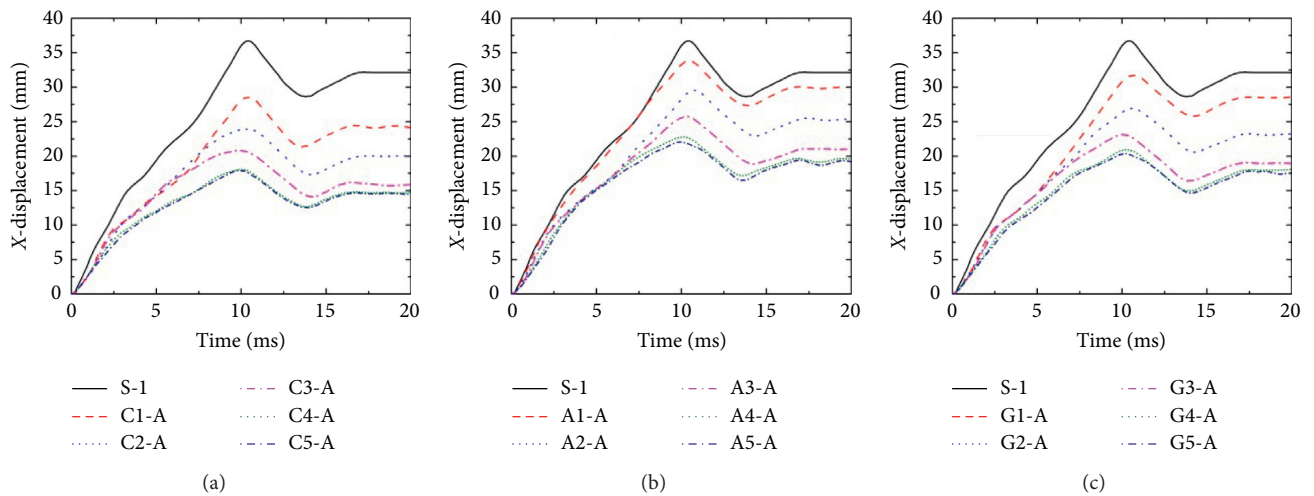


FIGURE 11: Displacement history curve at midspan of the column retrofitted with different FRP thicknesses. (a) CFRP. (b) AFRP. (c) GFRP.

maximum displacement at the midspan of the column is also used as a comparison indicator. For the one-layer CFRP-retrofitted columns, the maximum displacement of C1-A, C1-B, C1-C, and C1-D is 28.56 mm, 31.57 mm,

31.09 mm, and 32.44 mm, respectively. Compared with unretrofitted column S-1, the deflection of the above-mentioned four columns reduces by 22.20%, 14.00%, 15.31%, and 11.63%, respectively. For the one-layer AFRP-

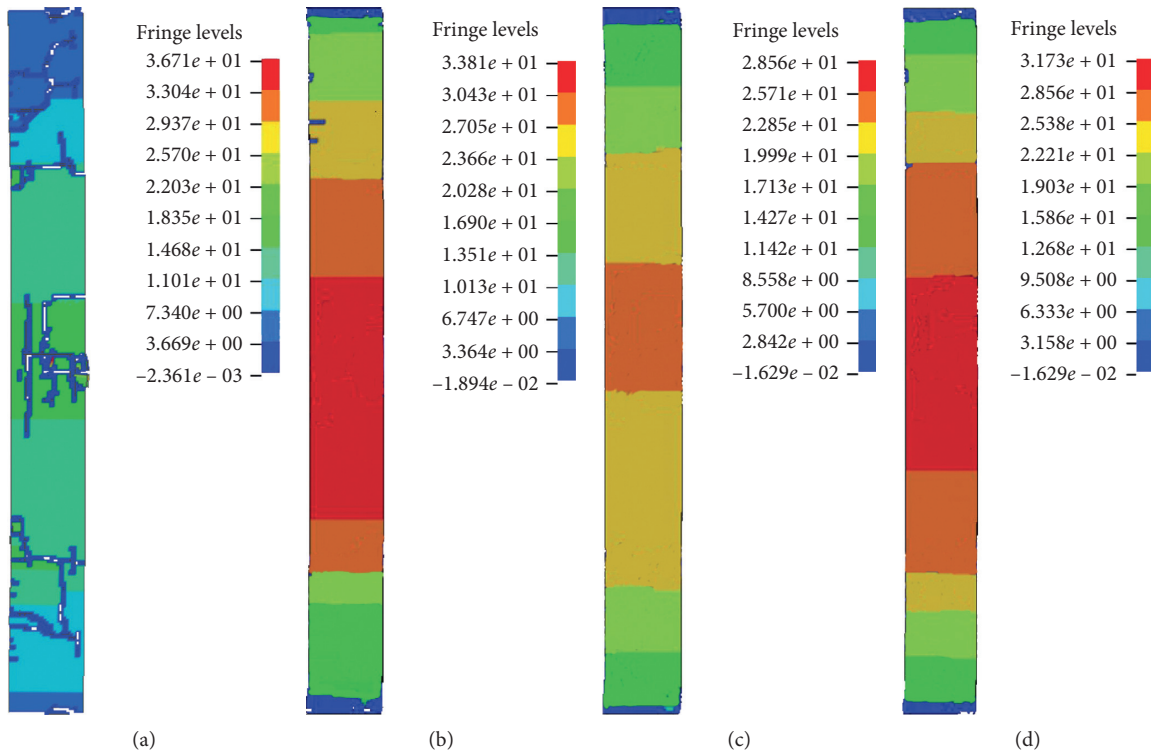


FIGURE 12: Damage distribution of columns retrofitted with different types of FRP (left view). (a) S-1. (b) A1-A. (c) C1-A. (d) G1-A.

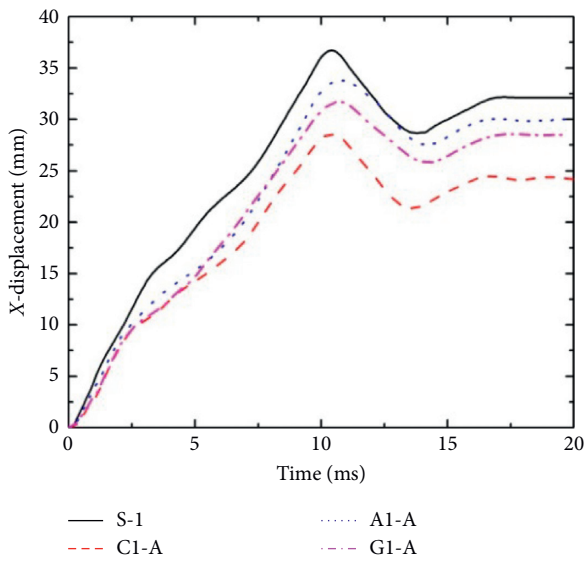


FIGURE 13: Displacement history curve at midspan of the column retrofitted with different FRP types.

retrofitted columns, the maximum deflection of A1-A, A1-B, A1-C, and A1-D is 33.82 mm, 35.74 mm, 35.13 mm, and 35.96 mm, respectively. Compared with the maximum deflection of S-1, the deflection of the four columns decreases by 7.87%, 2.64%, 4.30%, and 0.68%, respectively. It is found that retrofitting the column with one-layer AFRP at two ends of the column has little effect on blast mitigation. For the one-layer GFRP-retrofitted columns, the maximum deflection of G1-A, G1-B, G1-C, and G1-D reduces by 13.57%,

5.72%, 6.97%, and 4.33%, respectively, compared with that of S-1. Figure 15 illustrates a comparison of the maximum deflection of columns retrofitted with different modes. No matter what the type of the FRP is and how many FRP layers are there, the effects of different retrofitting modes on blast mitigation are almost the same. For the performance of the column to resist deformation under blast loading, the wholly retrofitting mode is still the most effective strategy, while the effect of only two-end retrofitting mode is relatively the worst. The effects of Mode B and Mode C are close to each other in terms of maximum displacement and residual displacement. For the columns retrofitted with the same FRP material and thickness, the antiexplosion performance of wholly retrofitted column is better than that of locally retrofitted columns. Moreover, the protection of FRP wraps could mitigate the spalling of the inner concrete. However, the amount of FRP sheets used for local retrofitting is 60% of the amount of FRP materials used for full retrofitting in this paper. The method of partial retrofitting at middle and two ends of the column has also a good effect on lessening the deformation of RC columns under blast loading. Therefore, if the structure is inconvenient for whole retrofitting, it is recommended to apply this retrofitting strategy.

**4.3.2. Retrofitting Length.** According to the above research, Mode C exhibits the best blast resistance performance among all partial retrofitting modes. In Mode C, the influence of retrofitting length on blast mitigation is further studied. As can be seen from Figure 16, in addition to the above retrofitting length of 600 mm for each section, numerical modes of

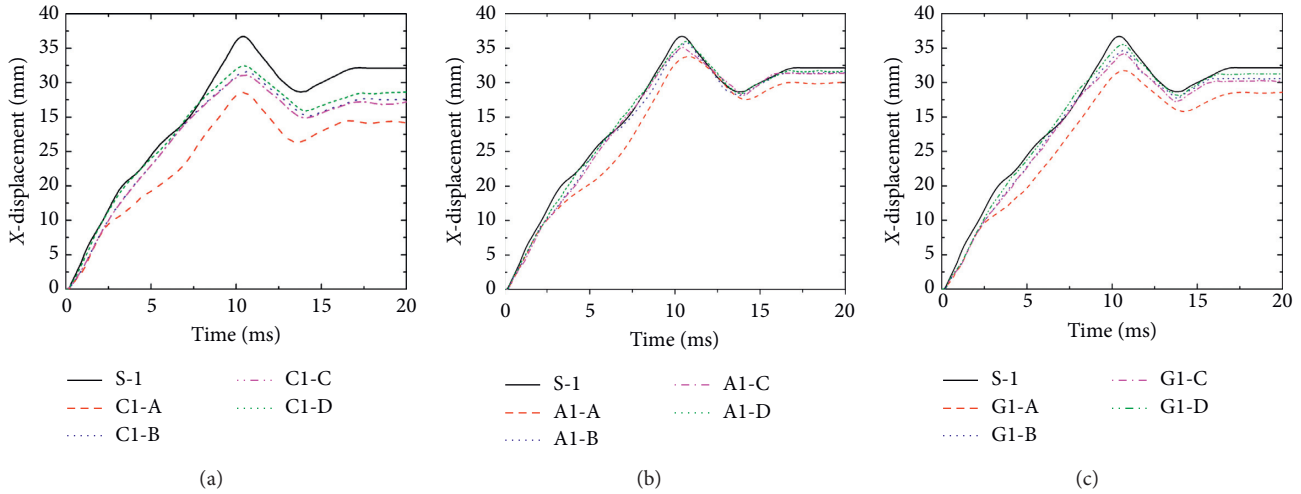


FIGURE 14: Displacement history curve at midspan of the columns retrofitted with different modes. (a) CFRP. (b) AFRP. (c) GFRP.

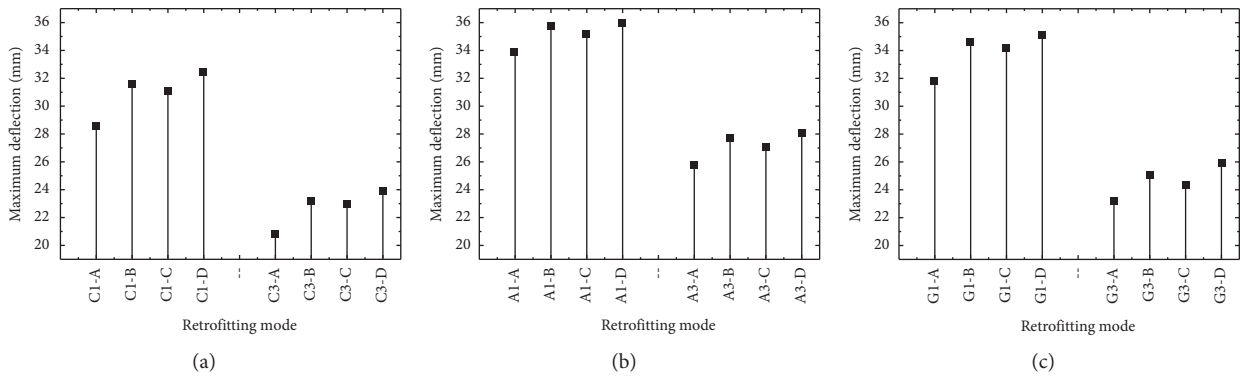


FIGURE 15: Maximum deflection of the columns retrofitted with different modes. (a) CFRP. (b) AFRP. (c) GFRP.

300 mm, 400 mm, 500 mm, 700 mm, 800 mm, and 900 mm for each section are developed. The dynamic responses of these columns under the same blast condition are investigated. Figure 17 depicts the maximum displacement of columns retrofitted with different retrofitting lengths in Mode C. The deformation becomes smaller under blast loading with the longer retrofitting length and larger wrapping area. With the increase of retrofitting length, the stiffness of the column increases, but the improvement for blast resistance does not show a linear relationship with the increase of retrofitting length. Similar to the phenomenon studied in FRP thickness, the growth rate of the blast mitigation effect slows down gradually when the length reaches a certain value. In this case, 400~700 mm for each section is deemed as the proper retrofitting length range for Mode C.

### 5. Conclusions

In this paper, the dynamic response of reinforced concrete columns retrofitted with FRP is investigated using the numerical analysis approach. The main findings are summarized as follows.

- (i) A finite element model of RC columns retrofitted with FRP under blast loading is developed. The strain rate

effect of concrete and steel and orthotropic property of FRP material are considered in the finite element model. The proposed model is validated against the relevant test data. The numerical analysis corresponds well with the previous results.

- (ii) A series of RC columns retrofitted with FRP are numerically analyzed using this reliable finite element model. The retrofitted columns are designed with different FRP types, FRP thicknesses, and retrofitting modes. Compared with conventional RC column, retrofitting with FRP can effectively mitigate the damage and deformation of the columns under blast loading.
- (iii) The deformation of the column decreases with the increase of FRP thickness, but not in the same proportion. The blast mitigation effect weakens with the increase of the FRP material. In the investigated cases, when the thickness of FRP is above 0.68 mm, adding the thickness of FRP has little effect in terms of improving the blast resistance of the column. Thus the maximum thickness for FRP retrofitting suggested in this study is 0.68 mm (namely, 4 layers).



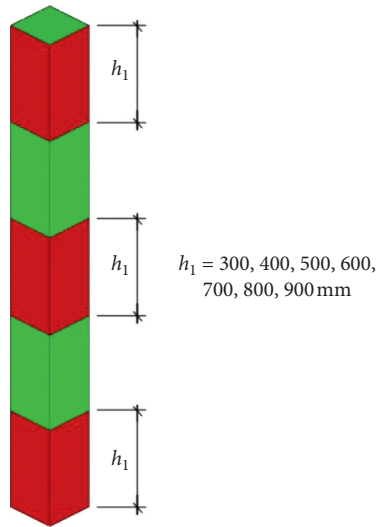


FIGURE 16: Design of retrofitting length.

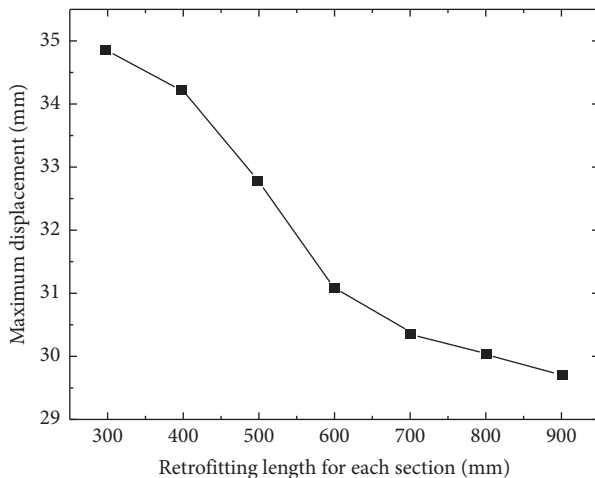


FIGURE 17: Maximum displacement of columns retrofitted with different retrofitting lengths.

- (iv) In the three FRP types studied, CFRP is the best retrofitting material for improving the blast resistance of RC columns. GFRP is recommended as the retrofitting material if the cost of material is considered.
- (v) A full retrofitting mode and three local retrofitting modes are designed in this study. The full retrofitting mode performs the best in terms of blast mitigation while the material amount is more than others. Among the three local retrofitting modes, retrofitting at both two ends and middle part of the column is suggested. 400~700 mm retrofitting length for each section is regarded as the proper length for this retrofitting mode.

## Data Availability

The data used to support the findings of this study are available from the corresponding author upon request.

## Conflicts of Interest

The authors declare that they have no conflicts of interest regarding the publication of this paper.

## Acknowledgments

This study was financially supported by the National Natural Science Foundation of China (NSFC) (Grant no. 51878056), the Social Development Foundation for Science and Technology Planning Project of Shaanxi Province (Grant no. 2019SF-256), and the Fundamental Research Funds for the Central Universities, CHD (Grant nos. 300102280203 and 300102289105).

## References

- [1] L. Chen, Q. Fang, J. Fan, Y. Zhang, H. Hao, and J. Liu, "Responses of masonry infill walls retrofitted with CFRP, steel wire mesh and laminated bars to blast loadings," *Advances in Structural Engineering*, vol. 17, no. 6, pp. 817–836, 2014.
- [2] H. Draganić, G. Gazić, and D. Varevac, "Experimental investigation of design and retrofit methods for blast load mitigation—a state-of-the-art review," *Engineering Structures*, vol. 190, pp. 189–209, 2019.
- [3] L. V. D. Einde, L. Zhao, and F. Seible, "Use of FRP composites in civil structural applications," *Construction and Building Materials*, vol. 17, no. 6, pp. 389–403, 2007.
- [4] J. E. Crawford, L. J. Malvar, J. W. Wesevich, J. Valancius, and A. D. Reynolds, "Retrofit of reinforced concrete structures to resist blast effects," *ACI Structural Journal*, vol. 94, no. 4, pp. 371–377, 1997.
- [5] L. J. Malvar, K. B. Morrill, and J. E. Crawford, "Numerical modeling of concrete confined by fiber-reinforced composites," *Journal of Composites for Construction*, vol. 8, no. 4, pp. 315–322, 2004.
- [6] L. J. Malvar, J. E. Crawford, and K. B. Morrill, "Use of composites to resist blast," *Journal of Composites for Construction*, vol. 11, no. 6, pp. 601–610, 2007.
- [7] P. A. Buchan and J. F. Chen, "Blast resistance of FRP composites and polymer strengthened concrete and masonry structures—a state-of-the-art review," *Composites Part B: Engineering*, vol. 38, no. 5–6, pp. 509–522, 2007.
- [8] J. H. Zhao, J. Dong, and D. F. Zhang, "Research status of dynamic responses of RC structure confined with FRP under blast loading," *World Earthquake Engineering*, vol. 35, no. 1, pp. 97–109, 2019.
- [9] P. F. Silva and B. Lu, "Improving the blast resistance capacity of RC slabs with innovative composite materials," *Composites Part B: Engineering*, vol. 38, no. 5–6, pp. 523–534, 2007.
- [10] J.-W. Nam, H.-J. Kim, S.-B. Kim, N.-H. Yi, and J.-H. J. Kim, "Numerical evaluation of the retrofit effectiveness for GFRP retrofitted concrete slab subjected to blast pressure," *Composite Structures*, vol. 92, no. 5, pp. 1212–1222, 2010.
- [11] J.-W. Nam, I.-S. Yoon, and S.-T. Yi, "Numerical evaluation of FRP composite retrofitted reinforced concrete wall subjected to blast load," *Computers and Concrete*, vol. 17, no. 2, pp. 215–225, 2016.
- [12] G. Tanapornraweekit, N. Haritos, P. Mendis, and T. Ngo, "Finite element simulation of FRP strengthened reinforced concrete slabs under two independent air blasts," *International Journal of Protective Structures*, vol. 1, no. 4, pp. 469–488, 2010.

- [13] G. Tanapornraweekit, N. Haritos, and P. Mendis, "Behavior of FRP-RC slabs under multiple independent air blasts," *Journal of Performance of Constructed Facilities*, vol. 25, no. 5, pp. 433–440, 2011.
- [14] X. S. Lin and Y. X. Zhang, "Nonlinear finite element analysis of FRP-strengthened reinforced concrete panels under blast loading," *International Journal of Computational Methods*, vol. 13, no. 4, Article ID 1641002, 2016.
- [15] X. Kong, X. Qi, Y. Gu, I. A. Lawan, and Y. Qu, "Numerical evaluation of blast resistance of RC slab strengthened with AFRP," *Construction and Building Materials*, vol. 178, pp. 244–253, 2018.
- [16] A. A. Mutalib and H. Hao, "Development of P-I diagrams for FRP strengthened RC columns," *International Journal of Impact Engineering*, vol. 38, no. 5, pp. 290–304, 2011.
- [17] T. Rodriguez-Nikl, C.-S. Lee, G. A. Hegemier, and F. Seible, "Experimental performance of concrete columns with composite jackets under blast loading," *Journal of Structural Engineering*, vol. 138, no. 1, pp. 81–89, 2012.
- [18] E. Jacques, A. Lloyd, P. Imbeau et al., "GFRP-Retrofitted reinforced concrete columns subjected to simulated blast loading," *Journal of Structural Engineering*, vol. 141, no. 11, Article ID 04015028, 2015.
- [19] Y. Qasrawi, P. J. Heffernan, and A. Fam, "Performance of concrete-filled FRP tubes under field close-in blast loading," *Journal of Composites for Construction*, vol. 19, no. 4, Article ID 04014067, 2015.
- [20] L. Liu, "Experimental study of differently protective RC piers under blast loading," Master Thesis, Southeast University, Nanjing, China, 2016.
- [21] L. Liu, Z. H. Zong, C. Gao, S. Yuan, and F. Lou, "Experimental and numerical study of CFRP protective RC piers under contact explosion," *Composite Structures*, vol. 234, Article ID 111658, 2020.
- [22] L. Yang, Y. Yan, and N. Kuang, "Experimental and numerical investigation of aramid fibre reinforced laminates subjected to low velocity impact," *Polymer Testing*, vol. 32, no. 7, pp. 1163–1173, 2013.
- [23] Y. Shi, H. Hao, and Z.-X. Li, "Numerical derivation of pressure-impulse diagrams for prediction of RC column damage to blast loads," *International Journal of Impact Engineering*, vol. 35, no. 11, pp. 1213–1227, 2008.
- [24] G. R. Cowper and P. S. Symonds, *Strain Hardening and Strain Rate Effect in the Impact Loading of Cantilever Beams*, Report in Brown University, Providence, RI, USA, 1957.
- [25] X. Lin, Y. X. Zhang, and P. J. Hazell, "Modelling the response of reinforced concrete panels under blast loading," *Materials & Design (1980–2015)*, vol. 56, pp. 620–628, 2014.
- [26] T. J. Holmoquist, G. R. Joshson, and W. H. Cook, "A computational constitutive model for concrete subjected to large strains, high strain rates, and high pressure," in *Proceedings of the 14th International Symposium on Ballistics*, Quebec, Canada, September 1993.
- [27] W. Riedel, K. Thoma, S. Hiermaier et al., "Penetration of reinforced concrete by BETA-B-500 numerical analysis using a new macroscopic concrete model for hydrocodes," in *Proceedings of 9th International Symposium on Interaction of the Effect of Munitions with Structures*, Berlin, Germany, May 1999.
- [28] L. J. Malvar, J. E. Crawford, J. W. Wesevich, and D. Simons, "A plasticity concrete material model for DYNA3D," *International Journal of Impact Engineering*, vol. 19, no. 9-10, pp. 847–873, 1997.
- [29] Y. S. Tai, T. L. Chu, H. T. Hu, and J. Y. Wu, "Dynamic response of a reinforced concrete slab subjected to air blast load," *Theoretical and Applied Fracture Mechanics*, vol. 56, no. 3, pp. 140–147, 2011.
- [30] J. Dong, J. H. Zhao, D. F. Zhang, and Y. Li, "Research on dynamic response of concrete-filled steel tube columns confined with FRP under blast loading," *Shock and Vibration*, vol. 2019, Article ID 8692310, 18 pages, 2019.
- [31] LS-DYNA, *Keyword User's Manual, Version 971*, Livermore Software Technology Corporation, Livermore, CA, USA, 2006.
- [32] H. Kimura, M. Itabashi, and K. Kawata, "Mechanical characterization of unidirectional CFRP thin strip and CFRP cables under quasi-static and dynamic tension," *Advanced Composite Materials*, vol. 10, no. 2-3, pp. 177–187, 2012.
- [33] A. A. Mutalib, M. H. Mussa, and H. Hao, "Effect of CFRP strengthening properties with anchoring systems on P-I diagrams of RC panels under blast loads," *Construction and Building Materials*, vol. 200, pp. 648–663, 2019.
- [34] H. Draganić and D. Varevac, "Analysis of blast wave parameters depending on air mesh size," *Shock and Vibration*, vol. 2018, Article ID 3157457, 18 pages, 2018.
- [35] F. Zhang, C. Wu, H. Wang, and Y. Zhou, "Numerical simulation of concrete filled steel tube columns against blast loads," *Thin-Walled Structures*, vol. 92, pp. 82–92, 2015.
- [36] J. L. Pan, M. Luo, and J. J. Zhou, "Dynamic responses and failure mechanism of reinforced concrete cylindrical column wrapped with CFRP under blast loading," *Journal of Tianjin University*, vol. 43, pp. 755–761, 2010.
- [37] UFC 3-340-02, *Structures to Resist the Effects of Accidental Explosion*, US Department of Defence (USDOD), Washington, DC, USA, 2008.
- [38] M. Momeni, M. A. Hadianfard, C. Bedon, and A. Baghlani, "Numerical damage evaluation assessment of blast loaded steel columns with similar section properties," *Structures*, vol. 20, pp. 189–203, 2019.

## Research Article.

# A Method for Determining Feasibility of Mining Residual Coal above Out-Fashioned Goaf under Variable Load: A Case Study

**Yuxia Guo,<sup>1,2</sup> Honghui Yuan,<sup>1,2</sup> Xiaogang Deng,<sup>3</sup> Yujiang Zhang<sup>1,2,3,4</sup>, Yunlou Du,<sup>1,2</sup> Hui Liu,<sup>3</sup> Guorui Feng,<sup>1,2</sup> Jiali Xu,<sup>4</sup> Renle Zhao,<sup>2</sup> and Dao Viet Doan<sup>5</sup>**

<sup>1</sup>College of Mining Engineering, Taiyuan University of Technology, Taiyuan 030024, China

<sup>2</sup>Shanxi Engineering Research Center for Green Mining, Taiyuan 030024, China

<sup>3</sup>Shandong Energy Linyi Mining Group Co., Ltd., Linyi 276017, China

<sup>4</sup>Postdoctoral Centre, Shandong Energy Group Co., Ltd., Jinan 250014, China

<sup>5</sup>Department of Underground and Mining Construction, Hanoi University of Mining and Geology, Hanoi 100803, Vietnam

Correspondence should be addressed to Yujiang Zhang; [ylczyj@yeah.net](mailto:ylczyj@yeah.net)

Received 25 March 2020; Revised 18 July 2020; Accepted 12 August 2020; Published 27 August 2020

Academic Editor: Chiara Bedon

Copyright © 2020 Yuxia Guo et al. This is an open access article distributed under the Creative Commons Attribution License, which permits unrestricted use, distribution, and reproduction in any medium, provided the original work is properly cited.

Out-fashioned goaf is the protective structure for mining the upper residual coal, and its stability is the core problem in mining the upper residual coal. According to the upward mining demand for No. 5 coal seam above the out-fashioned goaf in Baizi Coal Mine, a new method is proposed to determine the upward mining safety. According to the analysis of the actual situation of the mine, the coal pillar and suspended roof in the out-fashioned goaf are taken as the objects. Furthermore, a “coal pillar-suspended roof” system model based on the variable load induced by abutment pressure of upper coal seam mining is established. After the mechanical model was solved, the parameter acquisition method of the model was established. The basic parameters of Baizi Coal Mine were considered to determine the feasibility of mining residual coal above out-fashioned goaf. And the effects of variable load on the coal pillar and suspended roof stability were analyzed. The results show that the upper No. 5 coal seam in Baizi Coal Mine can be mined safely. Compared to the traditional method, which simplifies all the upper loads to uniform loads, the new method is safer. The system stability of the suspended roof and coal pillar is influenced by “ $a/L$ ” and “ $L$ .” Axial stress curves of the coal pillar and suspended roof appear nearly parabolic with “ $a/L$ ” varying. Their maximum values are obtained when the “ $a/L$ ” value is around 0.5~0.6. In this situation, the combination structure is most easy to be damaged. The ratio  $q'/q$  has a linear relationship with all stresses of the system model. The failure sequence of the system model is determined by analyzing the relationship between the tensile strength of the suspended roof and compressive strength of the coal pillar. This study provides a reference case for coal resources upward mining under similar conditions.

## 1. Introduction

The amount of residual coal exceeds 1.2 Gt [1, 2], with a great majority resulting from the utilization of the out-fashioned coal mining method. It mainly includes the reamer-pillar coal mining, roadway pillar mining, and top-coal caving mining of the lane pillar. These goafs could be called as the out-fashioned goafs. According to statistical findings, it is observed that there are abundant coal resources left in out-fashioned goafs, and the recovery ratio is from 10% to 20% [3]. These out-fashioned mining methods are used for

mining high-quality coal resources in many mines for a long time. In the 1950s to 1980s, in order to ensure coal supply and short-term economic benefits, massive lower high-quality thick coal seams have been mined in preference to the upper coal seams. Because of this fact, lots of coal resources above the out-fashioned goafs are abandoned, which is widespread in China, especially in Shanxi and Shaanxi provinces [4, 5]. If the upper residual coal remains unmined until the mine is closed, it will remain forever in the ground, resulting in wastage of resources. Currently, due to shortage of energy resources, we need to exploit them to improve the

recovery rate of coal resources. However, the upper residual coal distinguishes from the common coal in mining conditions. The upper residual coal is supported by pillars and suspended roofs in the out-fashioned goaf. When the upper residual coal working face goes across the coal pillar or the suspended roof, it is very likely to cause the coal pillar instability or the suspended roof rupture, causing the collapse of personnel or equipment. Hence, the stability of the coal pillar and suspended roof is the key technique problem in upper residual coal mining above the out-fashioned goaf. We must ensure the stability of the lower coal pillar and its suspended roof during mining upper coal seams.

Many researchers analyzed the integrity of the upper coal seam and its surrounding rock stability, proposing corresponding methods for determining the feasibility of upward mining. These methods mainly include the rational analytical method, the “three-zone” method, mathematical statistics method, and the method of equilibrium surrounding rock. Their determination formulas and application conditions are shown in Table 1.

These methods are proposed after statistically analyzing the field measured data, which are derived from longwall mining conditions. But, the out-fashioned mining differentiates from the longwall mining. In the out-fashioned goaf, compared with the longwall goaf, coal pillars with irregular size and shape were left to support the roof, which results in a limited roof caving or even no caving. The upper coal seam and its surrounding rock are integral and stable. So, if these methods are adopted to determine the feasibility of the mining upper residual coal seam above the out-fashioned goaf, plentiful coal resources will be wasted due to limitations on the applicability of these methods.

Analyzing the stability of the system composed of coal pillars and suspended roofs in the out-fashioned goaf is preferred to determine the feasibility of mining the upper residual coal seam above the out-fashioned goaf. A large number of scholars have been studying these relative issues. The residual coal pillar and its roof in the lower out-fashioned goaf were simplified to the mechanical model of beam and plate by using elastic theory. In the reference, the suspended roof was simplified as a simply supported beam and clamped beam [12]. And the limited spans were calculated to judge the feasibility of mining the upper coal above the out-fashioned goaf. If the maximum length of the suspended roof exceeds the limit span, the suspended roof would be judged to be unstable. Xie et al. [17] established a math analysis model of coal pillars and suspended roofs in goaf to study the out-fashioned goaf stability through researching the bearing character of the coal pillar. The suspended roof above the lane mining goaf was simplified as a consecutive deep seam mechanical model under uniformly distributed load [18]. From the mechanical model, two failure modes of antishearing and antistretching exist and the suspended roof stability determines the feasibility of upward mining. He et al. [19] established the interaction system model of “coal pillar-roof.” In the system, the hard roof and coal pillar were, respectively, regarded as elastic slabs and continuous support spring. A strain-softening model considering the damage constituent was established

to describe coal pillar mechanical characteristics. Furthermore, the model was utilized to study the instability mechanism of the “coal pillar-roof” interaction system in goaf. Finally, mechanical conditions and system stability were confirmed according to the engineering condition of Majiliang Coal Mine.

Furthermore, the influence of abutment pressure on the upper coal seam has been considered in upward mining. Li et al. [20] studied the damage evolution and failure mechanism of the suspended floor under concentrated load and uniformly distributed load and put forward a floor rock fracture criterion. Based on the experiment and field measurement in Qiuci Mine, Wu et al. [21] verified that abutment pressure induced by upper coal seam mining had specific effect on the stability of the lower goaf suspended roof in upward mining. Stability conditions of the suspended roof in lower goaf were calculated through simplifying abutment pressure as uniformly distributed constant load [22]. Based on elastic-plastic theory and practical engineering condition in Shirengou Iron Mine, China, a two-dimensional fixed beam mechanical model was built to analyze the stability of bi-level goafs and isolated pillars. And the result shows that a variety of stress transmit caused by incomplete overlapping of bilevel goafs gives rise to difference in different isolated pillar zones, causing stress and displacement mutation of goafs.

In the above studies, beam or slab models were built to study the stability of the system consisting of suspended roofs and coal pillars. And abutment pressure induced by upper coal seam mining was simplified to static additional load. The system stability of the “suspended roof and coal pillar” is a criterion determining whether the upper coal seam could be mined.

These research studies solve the problem of upward mining to some extent and promote the recovery and utilization of upper coal resources above the out-fashioned goaf [23]. However, coal mining is a dynamic process. With the advance of the upper coal seam working face, its abutment pressure will change periodically. The abutment pressure induced by upper coal seam mining simplified to static additional load is a gross oversimplification. The destructive effects on the coal pillar and suspended roof caused by shifting variable abutment pressure were ignored. This may lead to a decline in the accuracy of stability judgment, which may cause the judgment to be inconsistent with the actual engineering conditions, leading to the occurrence of suspended roof collapse accident, causing damage to personnel and equipment in upper coal seam mining.

In order to ensure the safety of upper residual coal above the out-fashioned goaf, a method for determining the feasibility of upward mining considering upward mining effects was proposed first. The method is used to judge the feasibility of upward mining by judging the stability of the out-fashioned goaf. Then, taking the coal pillar and suspended roof in out-fashioned goaf as an integral object, a stability mechanical model focusing on the variable load induced by abutment pressure of upper coal seam mining was established. And the parameter acquisition method of the model was established. Thirdly, the basic parameters of Baizi Coal



TABLE 1: Stability determination methods of the upward mining of longwall goaf.

Methods	Calculation formula and application condition
Rational analytical method [6, 7]	$K > 6$ (single seam) $K > 6.3$ (multiple seam)
Mathematical statistics method [8]	$H > 1.14h^2 + 4.14 + h$
The “three-zone” method [6, 9–13]	Caving zone 1: $H_c = (h - S_c)/(b - 1)$ Caving zone 2: $H_c = 1000h/(c_1h + c_2)$ Fracture zone 1: $H_f = 1000h/(c_3h + c_4)$ Fracture zone 2: $H_f = m + \sum_{i=1}^{n-1} h_i$ (here (a) strong and hard: $c_1 = 2.1, c_2 = 16, c_3 = 1.2, c_4 = 2$ ; (b) medium strong: $c_1 = 4.7, c_2 = 19, c_3 = 1.6, c_4 = 3.6$ ; (c) soft and weak: $c_1 = 6.2, c_2 = 32, c_3 = 3.1, c_4 = 5$ ) (here $m$ is the mining thickness and $h_i$ is the stratum thickness $i$ )
The method of equilibrium surrounding rock [14–16]	$H_p = M/(K_1 - 1) + h_p$ (here $K_1, M,$ and $h_p$ are, respectively, the bulking coefficient, mining thickness, and equilibrium surrounding rock thickness)

Mine were considered to determine the feasibility of upward mining residual coal above the out-fashioned goaf. And the effects of variable load on the coal pillar and suspended roof stability were analyzed.

## 2. Engineering Situations

**2.1. Geological Conditions.** As shown in Figure 1, Baizi Coal Mine is located in Xunyi County, Shaanxi Province. The width of the coal mine is 1.5 kilometers from west to east, and the length is 2.0 kilometers from south to north [17].

As shown in Figure 2, No. 5 coal seam and No. 8 coal seam are commercial seams in Baizi Coal Mine. The coal seams and their roof and floor occurrence conditions are followed. The coal bed pitches from 1° to 5°. The buried depth of No. 5 coal seam is 115 m to 190 m. The thickness of No. 5 coal seam is from 0.8 m to 2.5 m, and the average thickness is 1.6 m. And the thickness of No. 8 coal seam is from 0.8 m to 5.5 m, and the average thickness is 3.2 m. The distance between No. 5 coal seam and No. 8 coal seam is from 20 m to 40 m, and its average distance is 25 m. The detailed roof and floor occurrence condition distributions are shown in Figure 2.

**2.2. Physical and Mechanical Parameters.** The physical and mechanical parameters of the rock strata of the roof and floor are essential for determining the feasibility of ascending mining. The elasticity, volume weight, cohesion, and tensile strength of lithology are acquired in Table 2.

**2.3. Mining Conditions.** For historical reasons, No. 8 coal seam has been mined using the reamer-pillar coal mining method, which is one of the out-fashioned mining methods. The 4 m wide coal was mined, and 4 m wide coal pillars were left in No. 8 coal seam with this method. But the coal pillar is irregular in size and shape (Figure 3). The mining height of No. 8 coal seam is 2.4 m, and the coal resources of No. 8 coal seam have been used up. So, No. 5 coal seam was planned to be mined. The longwall mining method was planned to utilize to mine No. 5 coal seam above No. 8 coal seam out-fashioned goafs. The mining engineering plan is shown in Figure 3.

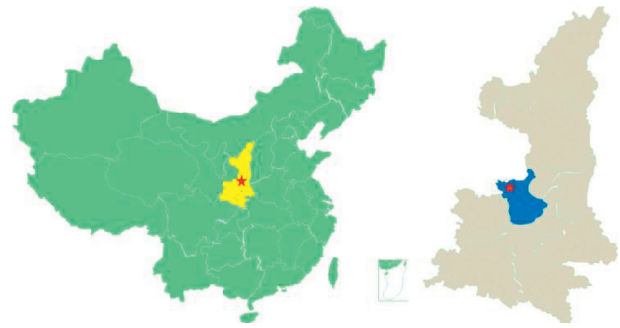


FIGURE 1: Location plan of Baizi Coal Mine.

Lithology	Rock type	Thickness (m)
	Medium sandstone	19
	Mudstone	4.0
	Charcoal mudstone	0.5
	#5 coal seam	1.6
	Charcoal mudstone	5.2
	Mudstone	3.6
	Siltite	6.7
	Charcoal mudstone	4.5
	#8 coal seam	3.2
	Charcoal mudstone	2.0
	Alumina mudstone	6.0

FIGURE 2: Bar chart of coal seam geology of the coal seam.

## 3. The Determination Method

Briefly, the method is to judge the feasibility of upward mining by judging the stability of lower out-fashioned goafs consisting of the coal pillar and their suspended roof. The stability of the coal pillar and suspended roof is determined by using the theoretical analysis method, based on structural mechanics and elastic theory [24]. Firstly, the pressure above



TABLE 2: Physical and mechanical parameters of lithology.

Lithology	Elasticity modulus, $E$ (GPa)	Volume weight, $\rho$ ( $\text{kg}\cdot\text{m}^{-3}$ )	Cohesion, $C$ (MPa)	Tensile strength, $\sigma_t$ (MPa)	Friction angle, $\varphi$ ( $^\circ$ )
No. 5 coal seam	5.1	14.00	3.0	1.2	30
Charcoal mudstone	10.3	24.83	5.5	4.1	32
Mudstone	12.4	23.69	3.5	3.5	35
Siltite	14.5	25.34	12.2	5.1	38
Charcoal mudstone	17.1	24.63	3.6	3.2	32
No. 8 coal seam	5.5	14.30	2.8	1.3	29

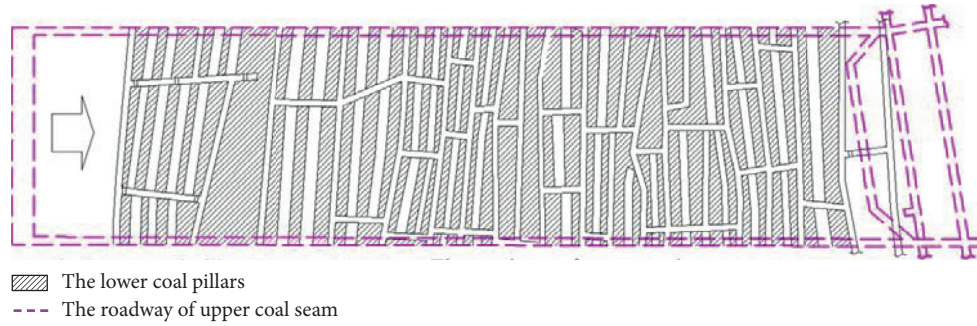


FIGURE 3: Mining engineering plan schematic map.

the suspended roof is simplified as a constant load and the abutment pressure during mining the upper coal seam is simplified as a triangular distributed load, which is the main difference with other methods. Then, the mechanical model is established by using the theoretical analysis method; the model is utilized to study the stability of the system consisting of the coal pillar and their suspended roof of the lower out-fashioned goaf. The feasibility of mining the upper residual coal seam above the out-fashioned goaf is determined based on unstable conditions under combined action.

**3.1. Model Establishment.** Figure 4 provides a profile along the advancing direction of the upper longwall working face according to Figure 3. It indicates the relationship among the upper coal seam, lower residual coal pillar, and suspended roofs [25]. The suspended roofs bear the overburden load and varied distributed load induced by upper coal seam mining. An integral system model of the residual coal pillar and suspended roof is built to study the stability of the system model under combined action of overburden load and the lead abutment pressure of upper working face. In the system model, the roof is simplified as a girder which can bear axial force, shearing force, and bending moment, and coal pillar as elastic fixed support that only bears axial force, overburden load as uniformly distributed constant load, and the lead abutment pressure of upper working face as the triangular distributed load which is varied in length and scale. It is supposed that the coal pillar only bears axial force, and the simplified mechanical model of the suspended roofs and coal pillars is obtained (shown in Figure 4(b)).

**3.2. Model Solution.** The model was solved by using mechanics of materials and structural mechanics [24, 26]. The solution procedures are as follows: first, the results bearing only overburden load are calculated, and then, the results bearing only varied triangular load are calculated; finally, the final results utilizing the superposition principle are calculated.

The structure and load of the model are symmetrical when only overburden load acts. Half of the model was used to simplify the calculation and solve the mechanical model. The model before and after simplification is shown in Figure 5. According to the potential failure form of the coal pillar and suspended roof, the axial force and shearing force of the coal pillar and its roof need to be solved. So based on the static equilibrium, moment equilibrium, and deformation coordination conditions, the displacement equation of the simplified model is obtained as follows:

$$\begin{cases} X_1 \frac{l^3}{3E_2 I_2} + X_2 \frac{l^2}{2E_2 I_2} + \frac{qL^2 l^2}{8E_2 I_2}, \\ X_1 \frac{l^2}{2E_2 I_2} + X_2 \left( \frac{l}{E_2 I_2} + \frac{l'}{E_2 I_2} \right), \end{cases} \quad (1)$$

where  $X_1$  is the axial force of the suspended roof;  $M_Z$  is the bending moment of the suspended roof;  $X_3$  is the maximal shearing force of the suspended roof;  $F_N$  is the axial force of the coal pillar;  $I_1$  is the inertia moment of the suspended roof;  $I_2$  is the inertia moment of the coal pillar;  $L$  is the distance of two adjacent pillars;  $l'$  is the height of the pillar;  $q$  is the load intensity of the overburden load of the suspended

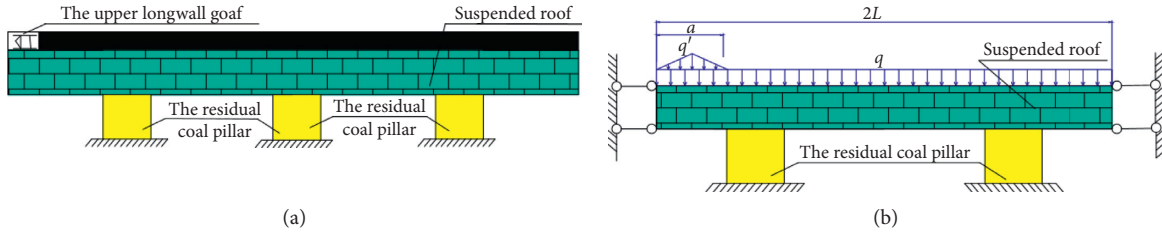


FIGURE 4: Diagrammatic figure and simplified mechanical model.

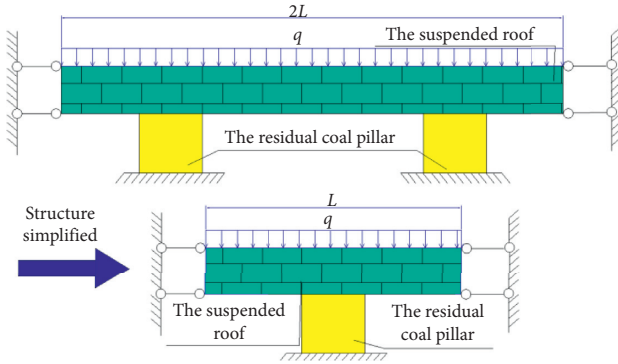


FIGURE 5: Model simplification bearing only overburden load.

roof;  $q'$  is the load intensity of the varied triangular load; and  $a$  is the range of the varied triangular load.

The simultaneous equation (1) is solved, and the results are as follows:

$$X_1 = \frac{qE_2I_2L^3}{(8E_1I_1l'^2 - 4E_2I_2l')}, \quad (2)$$

$$X_2 = \frac{qL^3E_2I_2}{(24E_1I_1l'^2 - 12E_2I_2l')}.$$

According to the force balance in the vertical direction, utilizing the above results, the axial force of the coal pillar  $F_{NC}$  is calculated using the following formula:

$$F_{NC} = \frac{qL}{2}. \quad (3)$$

As shown in Figure 6, when the model only bears varied triangular load, the models before and after simplification are given. In order to obtain the axial stress, bending moment, and shearing stress of the suspended roof, the displacement equation of the simplified model is obtained as follows:

$$\begin{cases} X_3' = \left( \frac{L^3}{24E_1I_1} + \frac{L^2l'}{8E_2I_2} \right) = 0, \\ F_{NC} = X_3' + \frac{q'a}{2}, \end{cases} \quad (4)$$

where  $X_3$  is the maximal shearing force of the suspended roof and  $F_{NC}$  is the axial force of the coal pillar under uniform load.

The simultaneous equations (4) are solved, and the results are shown below:

$$\begin{cases} X_3' = \frac{2E_1I_1q'aL^2l'}{((3E_1I_1L + 8E_2I_2l')L^2)}, \\ F_{NC}' = \frac{2E_1I_1q'aL^2l'}{((3E_1I_1L + 8E_2I_2l')L^2)} + q'a. \end{cases} \quad (5)$$

Then, the methods of moment distribution are utilized to obtain the torque equilibrium equation to solve the moments of coal and the suspended roof:

$$\begin{cases} M_1 \left( \frac{L}{2E_1I_1} + \frac{l'}{E_2I_2} \right) + M_2 \frac{l'}{E_2I_2} = \frac{q'aL(L-a)}{32E_1I_1} + \frac{q'l'a(L-a)}{16E_2I_2}, \\ M_1 \frac{l'}{E_2I_2} + M_2 \left( \frac{L}{2E_1I_1} + \frac{l'}{E_2I_2} \right) = \frac{q'al'(L-a)}{8E_2I_2}, \\ M_1 = 2M_{ZR} = 2M_{ZL}, \end{cases} \quad (6)$$

where  $M_{ZR}$  is the bending moment of the right suspended roof;  $M_{ZL}$  is the bending moment of the left suspended roof; and  $M_M$  is the bending moment of the coal pillar.

The simultaneous equations (5) and (6) are solved, and the result is shown as follows:

$$\begin{cases} M_{ZL} = \frac{q'a(L-a) [E_2^2I_2^2L + 4E_1^2I_1^2l']}{2(8E_2^2I_2^2L^2 + 32E_1E_2I_1I_2Ll')}, \\ M_{ZR} = \frac{q'a(L-a) [E_2^2I_2^2L^2 + 4E_1^2I_1^2l']}{(8E_2^2I_2^2L^2 + 32E_1E_2I_1I_2Ll')}. \end{cases} \quad (7)$$

As shown in Figure 6, we calculate the stress, bending moment, and shearing force of the suspended roof when it bears inverse varied triangular load. The mechanics equilibrium equations are given as shown below:

$$\begin{cases} X_3'' = F_N'' = \frac{q'a}{2}, \\ M_M'' = \frac{q'a(L-a)}{4}, \end{cases} \quad (8)$$

where  $X_3''$  is the maximal shearing force of the rock stratum of the roof;  $F_N''$  is the axial force of the coal pillar under

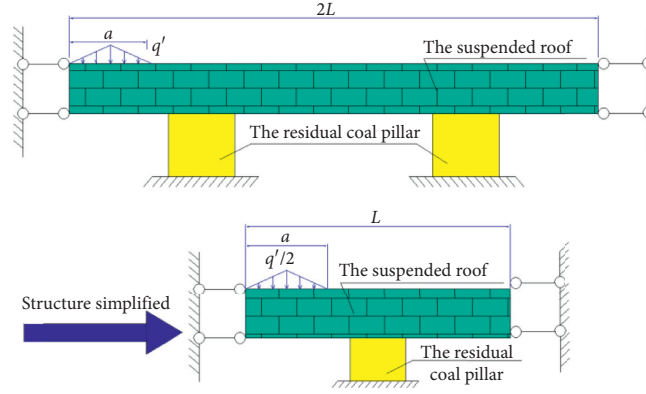


FIGURE 6: Model simplification bearing only varied triangular load.

triangular load; and  $M''_M$  is the bending moment of the coal pillar.

So far, the mechanical equation of the coal pillar and the suspended roof in the situation of bearing variable triangular load is obtained. According to equations (2), (5), (7), and (8), the superposition principle is utilized to calculate the results of the system model:

$$\begin{cases} X_1 = \frac{qE_2I_2L^3}{8E_1I_1l'^2 - 4E_2I_2Ll'}, \\ X_3 = \frac{2q'aE_1I_1L^2l'}{3E_1I_1L^3 - 8E_2I_2L^2l'} + \frac{qL}{2} + \frac{qa}{2}, \\ F_N = \frac{2q'aE_1I_1L^2l'}{3E_1I_1L^3 - 8E_2I_2L^2l'} + \frac{qL}{2} + q'a, \end{cases} \quad (9)$$

$$\begin{cases} M_Z = \frac{qL^3E_2I_2}{24E_1I_1l' - 12E_2I_2L} + \frac{q'a(L-a)L^2E_2I_2^2 + 4l'^2E_1I_1^2}{8E_2I_2^2L^2 + 32E_1E_2I_1I_2Ll'}, \\ M_M = \frac{q'a(L-a)}{4} + \frac{q'a(L-a)L^2E_2I_2^2 + 4l'^2E_1I_1^2}{16E_2I_2^2L^2 + 64E_1E_2I_1I_2Ll'}, \end{cases} \quad (10)$$

where  $M_Z$  is the moment of the suspended roof;  $M_M$  is the moment of the coal pillars; and  $F_N$  is the combined axial force of coal pillars.

In order to determine the stability of the model, the maximal axial stress and shearing stress should be calculated [26]. Considering the bending stress derived from force and bending moment, the maximal axial stress and shearing stress are acquired using the following equation:

$$\begin{cases} \sigma_{\max} = \frac{M_{\max}}{W}, \\ \tau_{\max} = \frac{F_Q S_{Z,\max}^*}{I_z b}, \end{cases} \quad (11)$$

where  $\sigma_{\max}$  is the maximal axial stress;  $\tau_{\max}$  is the maximal shearing stress;  $W$  is the section modulus in bending moment of the suspended roof,  $W = bh^3/6$ ;  $M_{\max}$  is the maximal moment of beam, such as the moment of the suspended roof  $M_Z$ ;  $F_Q$  is the shearing force of the beam, the suspended roof  $X_3$ ;  $S_{Z,\max}^*$  is the static moment of the suspended roof,  $S_{Z,\max}^* = bh^2$ ; and  $I_p$  is the moment of inertia of the suspended roof.

The stress of axial and shearing is correlated with the moment of the beam, and the detailed relationship is shown in formula (11). The moment of the suspended roof is the moment of the beam. The axial stress and shearing stress of the suspended roof and axial stress of the coal pillar (formula (12)) are derived from formulas (9), (10), and (11):

$$\begin{cases} \tau_{\max}^R = \frac{2E_1I_1q'aL(L-a)l'}{(3E_1I_1L^3 + 8E_2I_2L^2l')b_1h_1} + \frac{qL}{2b_1h_1} + \frac{qa}{2b_1h_1}, \\ \sigma_{\max}^R = \frac{1}{b_1h_1} \left( \frac{qL^3E_2I_2}{(4E_1I_1l' - 2E_2I_2L)b_1} + \frac{qE_2I_2L^3}{l'(8E_1I_1l' - 4E_2I_2L)b_1} + \frac{3q'(L-a)a(L^2E_2I_2^2 + 12l'^2E_1I_1^2)}{4E_2I_2L(E_2I_2L + 16E_1I_1l')b_1} \right), \end{cases} \quad (12)$$

$$\sigma_{\max}^C = \frac{1}{b_2h_2} \left( \frac{3q'a(L-a)}{2b_2h_2} + \frac{q'a(L-a)(3E_2I_2^2L^2 + 12E_1I_1^2l'^2)}{E_2I_2L(8E_2I_2L + 32E_1I_1l')b_2h_2} + \frac{2q'aE_1I_1L^2l'}{(3E_1I_1L^3 + 8E_2I_2L^2l') + q'l' + qL} \right) \quad (13)$$

where  $\tau_{\max}^R$  is the maximal shearing stress of the suspended roof;  $\sigma_{\max}^R$  is the maximal normal stress of the suspended roof;  $b_1$  is the width of the transverse section of the suspended roof;  $h_1$  is the height of the transverse section of the suspended roof;  $\sigma_{\max}^C$  is the bearing normal stress of the coal pillar;  $b_2$  is the width of the transverse section of the coal pillar; and  $h_2$  is the height of the transverse section of the coal pillar.

The shearing stress of the coal pillar has little influence on the strength stability of the out-fashioned goaf. So when we utilized the abovementioned results of the system stability of the coal pillar and the suspended roof, the effect of shearing stress on the coal pillar can be ignored.

**3.3. Model Parameters Determination Method.** The basic parameters of the determination model are acquired by engineering geologic reports, operational rules, and rock mechanical tests. In addition, the suspended roof, load, and compression strength of the coal pillar are determined by the following methods [27].

**3.3.1. Suspended Roof.** In the system model, the suspended roof is a key rock stratum. The suspended roof is the main structure that bears overburden load and abutment load. According to the theory of the key rock stratum [28], the key rock stratum is the stratum bearing the overburden load and

varied distributed load induced by upper coal seam mining. The stability of the key rock stratum is a key question to studying ascending mining feasibility. So, the identification of the key rock stratum of No. 8 coal seam should be implemented. According to the theory of key stratum, the method of identifying the key rock stratum is given in the following formula:

$$\begin{cases} q_1(x)_n = \frac{E_1 d_1^3 \sum_{i=1}^n \rho_i d_i}{\sum_{i=1}^n E_i d_i^3}, \\ q_1(x)_n = q_1(x)_{n+1}, \end{cases} \quad (14)$$

where  $q_1(x)_n$  is the load of the  $n$ th stratum;  $q_1(x)_{n+1}$  is the load of the  $(n+1)$ th stratum;  $E_1$  is the elasticity modulus of the first stratum;  $E_i$  is the elasticity modulus of the  $i$ th stratum;  $d_i$  is the thickness of the first stratum; and  $\rho_i$  is the density of the  $i$ th stratum.

**3.3.2. Load.** The loads of overburden and abutment pressure are the key parameters [5]. Solving the vital parameters has two steps. Firstly, the pressure of overburden and abutment should be obtained. The methods of obtaining the pressure are similar to the stimulated test and field measurements [9, 29]. And then the load can be calculated by

$$\begin{cases} q = P_q \times L, \\ q' = q_z \times L, \end{cases} \quad (15)$$

$$q_z = 0.637(P_Q - P_q) \left[ \arctan \frac{x_0 l_0}{z \sqrt{4x_0^4 + l_0^2 + 4z^2}} + \frac{l_0 z \left( \sqrt{4x_0^4 + l_0^2 + 4z^2} - \sqrt{l_0^2 + 4z^2} \right)}{2x_0 (l_0^2 + 4z^2)} \right], \quad (16)$$

where  $q$  is the load of the overburden;  $q'$  is the load of the abutment pressure;  $P_q$  is the mine ground pressure when mining upper coal seam;  $P_Q$  is the mine ground pressure when periodic weighting of ascending mining occurs;  $x_0$  and  $l_0$ , respectively, are the width and length of the load of overburden; and  $z$  is the depth of floor rock strata.

**3.3.3. Compression Strength of Coal Pillar.** The compression strength of the coal pillar correlates with uniaxial compressive strength and coal pillar size [30]. The uniaxial strength of the laboratory coal sample was converted into the uniaxial strength of the critical cube by using the Hustrulid method. The Hustrulid method estimates the size effect of the coal pillar in the field. The formula of the Hustrulid method is shown below:

$$\sigma_m = \sigma_c \sqrt{\frac{D}{d}}, \quad (17)$$

where  $D$  is the sample diameters;  $d$  is the sample height;  $\sigma_c$  is the compression strength of the coal sample; and  $\sigma_m$  is the uniaxial strength of the critical cube.

Furthermore, the strength of the coal pillar in the field is calculated using the relationship of uniaxial strength of the critical cube and coal pillar [31]. The representative strength converting formula is as follows:

$$\begin{cases} \sigma_{s1} = \sigma_m \left[ 0.778 + 0.222 \left( \frac{W}{h} \right) \right], \\ \sigma_{s2} = \sigma_m \frac{W^{0.446}}{h^{0.66}}, \\ \sigma_s = \min\{\sigma_{s1}, \sigma_{s2}\}, \end{cases} \quad (18)$$

where  $W$  is the width of the coal pillar;  $h$  is the height of the coal pillar; and  $\sigma_s$  is the uniaxial compression strength of the coal pillar.

## 4. Results and Discussion

**4.1. Parameters.** The study data of Baizi Coal Mine [32] are utilized to verify the validity of theoretical formulas in the following. According to engineering situation, the fundamental data are followed. The distance of two adjacent coal pillars  $L$  is 4 m; the mining height of No. 8 coal seam  $l'$  is 2.4 m. Physical and mechanical parameters, derived from Table 2, are shown in Table 3.

The key rock stratum of No. 8 coal seam, the load of overburden and abutment pressure, and uniaxial compression strength of the coal pillar are vital for the feasibility determination of mining upper coal seam. So, the vital parameters of the suspended roof, load, and coal pillar are solved in the following.

Firstly, combining the geological data in Table 1 and the key stratum determination formula (13), the key stratum is determined. The cohesion of siltite in No. 8 coal seam roof is 12.2 MPa; the tensile strength is 5.1 MPa. The siltite is the key rock strata. So, the siltite is the suspended roof. Parameters of the key rock strata were determined. The thickness of siltite  $h_1$  is 6.7 m. So, the parameters of the suspended roof are shown in Table 3.

Furthermore, the vertical pressure data of No. 5 coal seam floor, measured by stress sensor, are collected and analyzed. We find that the pressure of No. 5 coal seam floor is equal when the first pressure is approaching; the vertical pressure  $P_q$  is 2.67 MPa. No. 8 periodic pressure significantly occurs in the procedure of mining upper coal seams. The maximum pressure  $P_Q$  is 4.3 MPa. According to formula (14), the load intensities  $q$  and  $q'$  are calculated in Table 3.

Finally, the compression strength of the coal pillar correlates with uniaxial compressive strength and coal pillar size. The test specimens are round; specimen diameter is  $D = 5$  centimeters, and specimen height is  $d = 10$  centimeters. The laboratory experiment was carried out on the coal sample of No. 8 coal seam to get the uniaxial compressive strength  $\sigma_c = 15.7$  MPa [17]. The uniaxial strength of the critical cube is converted by using formula (17) and formula (18). The compression strength of the coal pillar  $\sigma_s$  is 11.8 MPa.

**4.2. Judgment.** The maximal shearing stress of the suspended roof is  $\tau_{\max}^R = 1.595$  MPa, and it is under the shearing strength of suspended roof  $[\tau] = 8.92$  MPa. The maximal tensile stress of the suspended roof is  $\sigma_{\max}^R = 3.98$  MPa, and it is under the uniaxial tensile strength of the suspended roof  $[\sigma_1] = 5.1$  MPa. The maximal axial stress of the coal pillar is  $\sigma_{\max}^C = 10.2$  MPa, and it is under the axial strength of the coal pillar  $[\sigma_2] = 11.1$  MPa. These data mean that the system strength of the suspended roof and coal pillar is more than the stress on the system. Hence, the system of the coal pillar and suspended roof is stable which is determined by this method. And the results corresponded with the practical engineering projects.

**4.3. Effects of Variable Load.** The varying values of “ $a/L$ ” are used to measure the influence of load movement on axial force and shear force in the model. The range of varied

triangular load “ $a$ ” is associated with the distance of the adjacent coal pillar. According to formulas (11) and (12) and the Baizi coal mine’s conditions, when “ $a/L$ ” is 0.1, 0.2, 0.3, . . . , 1, the effect of the varied triangular load for the maximal axial stress and shearing stress of determined formulas on system stability is analyzed. With varying “ $a/L$ ,” the maximal stress of rock and coal pillar is shown in Figure 7.

As shown in Figure 7, the variation trend of axial stress of the residual coal pillar and suspended roof is similar. As “ $a/L$ ” increases, these stresses first go up and then go down. But with the increase of “ $a/L$ ,” the peak value of shear stress in the coal pillar appears later than that in the suspended roof. Synchronous changes in the position and size of variable loads are the reason.

As shown in Figure 7, in order to analyze the effects of the varied load, we used  $(q + q')$  as the uniform load calculation stress of the model when “ $a/L$ ” = 0. The maximal shear and axial stress of the suspended roof as well as the maximal axial stress of the coal pillar are calculated as 1.07 MPa, 0.026 MPa, and 3.6 MPa. Without considering the varied load, the maximal stress of the model is much smaller than when considering the varied load. This indicates that whether the load movement considered has a great influence on the stress when the load value is the same. Obviously, the results obtained by this method are more secure.

In general, the compressive strength of coal and rock mass is vital in all strength [33]. The shearing strength is greater than the tensile strength. Furthermore, the shearing stress of the suspended roof is small and increases slowly. So, the suspended roof is not subject to shear failure. Whether the suspended roof tensile failure or coal pillar compression failure occurs firstly? The calculated stress in the pillar is greater than that of the rock. However, for coal and rock mass, failure sequence cannot be ensured from the curves. It is determined by the relationship between the tensile strength of the suspended roof and the compressive strength of the coal pillar.

**4.3.1. Load Range Effect for Suspended Roof.** From practical ascending mining engineering project cases [19, 21, 22], it is not difficult to find that the system strength stability of the residual coal pillar and suspended roof can be mainly influenced by the parameters “ $L$ ” and “ $a/L$ .” Hence, the regulations of system stability are studied through the control variables approach. The influence of regulations of the stability of the suspended roof is studied in detail firstly in the following.

According to formulas (11) and (12) and Table 3, the relationship of stress of the suspended roof and coal pillar with “ $a/L$ ” and “ $L$ ” was analyzed. When  $L = 4, 8, 12, 16, 20$  meters and “ $a/L$ ” is 0.1, 0.2, . . . , 1.0, the shear stress and axial stress of the suspended roof and coal pillar are, respectively, calculated and displayed in Figures 8–10.

As shown in Figure 8, the shearing stress of the suspended roof has a positive correlation with “ $a/L$ .” When “ $L$ ” is larger, the shearing stress curves of the suspended roof are steeper. It indicates that when the length of the suspended roof is longer, the system strength stability of the



TABLE 3: Detailed values of parameters in Baizi Coal Mine.

$q'$ (MN/m)	$q$ (MN/m)	$l'$ (m)	$L$ (m)	$b_1$ (m)	$b_2$ (m)	$h_1$ (m)	$h_2$ (m)	$I_1$ (m <sup>4</sup> )	$I_2$ (m <sup>4</sup> )	$E_1$ (GPa)	$E_2$ (GPa)
3.72	10.68	2.4	4	4	4	6.7	4	133	5.3	14	5.5

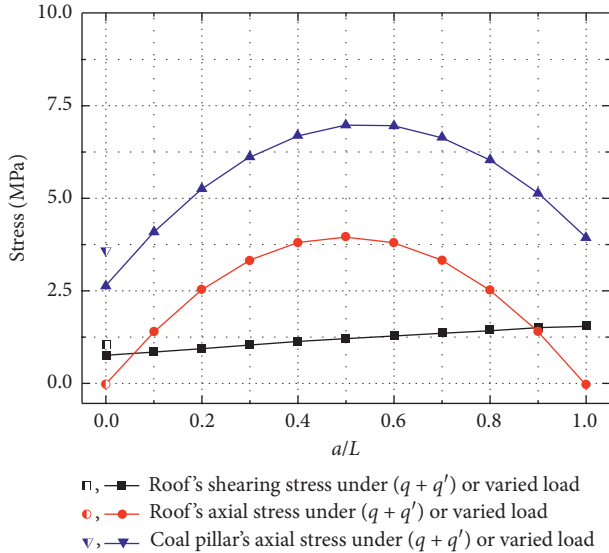


FIGURE 7: The relationship between stresses and “ $a/L$ ” in Baizi Coal Mine.

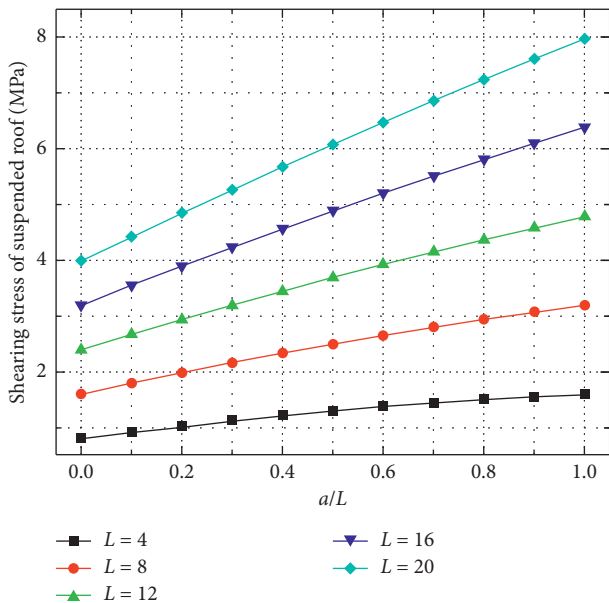


FIGURE 8: Shearing stress of the suspended roof with “ $a/L$ ”.

suspended roof and coal pillar is lower, whereas other facts are equal.

In practical mining engineering projects, when the length of the suspended roof gets wider, the system strength stability will be destroyed more easily. And the shearing stress of the suspended roof increases with the increase of the varied load range on the suspended roof. Based on the abovementioned analysis results, engineers in coal mine can

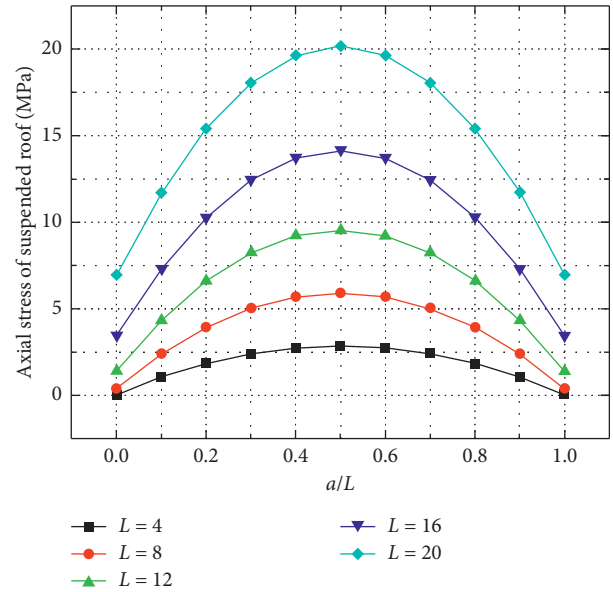


FIGURE 9: Axial stress of the suspended roof with “ $a/L$ ”.

calculate the maximal length and the varied load range to determine whether the suspended roof can be fractured.

The relationship of axial stress of the suspended roof with “ $a/L$ ” is shown in Figure 9. The curves show a parabolic shape with downward opening. For different “ $L$ ,” the axial stress curves are higher and steeper with increasing “ $L$ .” All axial stress curves of the suspended roof have a positive correlation with “ $L$ .” When “ $L$ ” increases, the curves converge more. It is indicated that the axial stress increases more and more quickly than the shear stress. For all curves in Figure 9, when “ $a/L$ ” is about 0.5, the axial stress of the suspended roof is the maximum. For practical engineering project cases, when “ $a/L$ ” is about 0.5, the stability of the system of the coal pillar and suspended roof will be destroyed more easily. Hence, this situation should be avoided in the process of ascending mining.

4.3.2. Load Range Effect for Coal Pillar. The relationship curves of axial stress of the coal pillar with “ $a/L$ ” are shown in Figure 10. The curves show a parabolic shape with downward opening which have a similar trend with the curves of axial stress of the suspended roof. The axial stress of the coal pillar has a positive correlation with the value of “ $L$ .” Hence, the distance of two adjacent coal pillars should be given priority consideration.

Furthermore, when all values of “ $a/L$ ” is about 0.5, the axial stress curves reach maximum. These results can instruct practical engineering operations. For practical mining engineering projects, when “ $a/L$ ” equals to about 0.5, the strength stability of the system of the suspended roof and

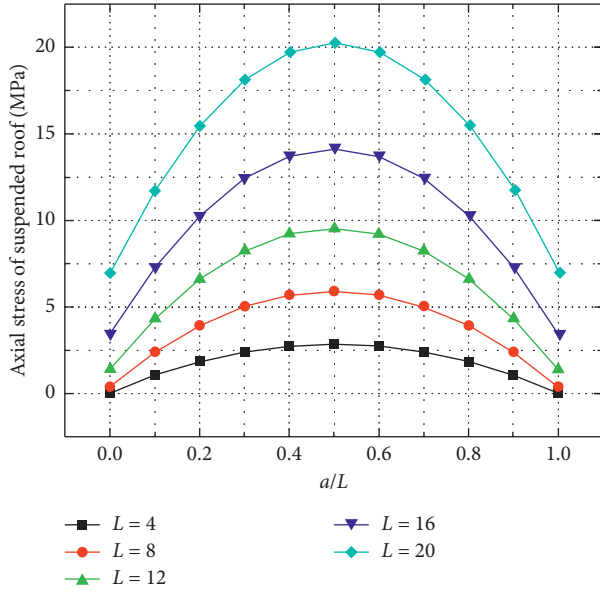


FIGURE 10: Axial stress of the residual coal pillar with “ $a/L$ ”.

coal pillar is used to determine the feasibility of upward mining above the out-fashioned goaf.

**4.3.3. Load Magnitude Effect for the System Model.** With all other conditions being equal, we changed the value of variable load  $q'$  (such as  $0.2q$ ,  $0.4q$ ,  $0.6q$ ,  $0.8q$ , and  $1.0q$ ). And the stress curves of the system model are derived with the varying ratio of  $q'/q$  (Figure 11).

Figure 11 shows that the ratio of  $q'/q$  has a linear relationship with all stresses of the system model. The slope of shearing stress curves is the smallest. The ratio of  $q'/q$  has least effect on shearing stress of the suspended roof, which is consistent with the conclusion that shearing force does not affect roof failure [34]. When the ratio of “ $a/L$ ” is the same, the slopes of the curves between axial stress of the suspended roof and coal pillar are very close, indicating that the axial force of the suspended roof and coal pillar increases nearly synchronously with the change of ratio of  $q'/q$ . The failure sequence of the system model depends on the relationship between the tensile stress of the suspended roof and the compressive strength of the coal pillar. According to the linear relationship shown in Figure 11, the failure sequence of the system model is calculated using the following formula:

$$\frac{\sigma_s}{\sigma_t} = f\left(\frac{q'}{q}\right) = \frac{k_c(q'/q) + \sigma_{sI}}{k_r(q'/q) + \sigma_{tI}}, \quad (19)$$

where  $\sigma_{sI}$  and  $\sigma_{tI}$  are, respectively, the axial stress of the suspended roof and coal pillar when  $q'$  equals to zero;  $k_c$  and  $k_r$  are, respectively, axial stress curve slopes of the suspended roof and coal pillar;  $\sigma_s$  is the compression strength of the coal pillars; and  $\sigma_t$  is the tensile strength of the suspended roof.

For cases of varying ratio of ( $q'/q$ ), the relationship between  $f(q'/q)$  and the ratio of  $\sigma_s/\sigma_t$  are compared to

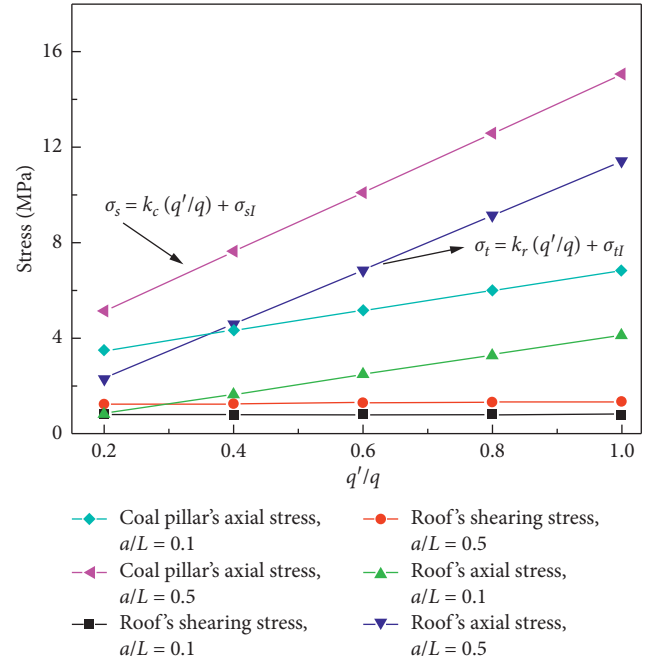


FIGURE 11: The relationship of the stress ratio  $q'/q$ .

determine whether the coal pillar or suspended roof will be damaged first, which is more advantageous for field technicians.

## 5. Conclusions

A method for determining the feasibility of upward mining residual coal above the out-fashioned goaf was studied, and the following conclusions were obtained:

- (1) Variable additional load is mainly considered to simulate the influence of abutment pressure caused by upper coal seam mining. On this basis, the suspended roof and coal pillar in the lower out-fashioned goaf are taken as objects to establish the mechanical model. The mechanical model solution and parameter acquisition method were also established. The practical engineering data of Baizi Coal Mine were utilized to analyze the relationship of stress with “ $a/L$ ” and “ $L$ ”.
- (2) Compared with the system without variable load, the ultimate stresses obtained by the system model considering the variable load are much higher. Therefore, compared with this method, the traditional method, which simplifies upper loads to uniform loads, leaves a greater safety factor to ensure the safe mining of the upper coal seam above the out-fashioned goaf.
- (3) Through the analyses of determining formula of key parameters, the system stability of the suspended roof and coal pillar is influenced by “ $a/L$ ” and “ $L$ ,” and the effect of “ $a/L$ ” is significant for axial and shearing stress. Axial stress curves of the coal pillar and suspended roof appear nearly parabolic with

varying “ $a/L$ .” Their maximum values are obtained when the values of “ $a/L$ ” are 0.5~0.6. In this situation, the combination system consisted of the coal pillar and suspended roof is most easy to be damaged. With the increase of the distance  $L$  between the two adjacent coal pillars, the stress of the model increases, and the axial stress of the coal pillar increases the fastly. The ratio of  $q'/q$  has a linear relationship with all stresses of the system model. The failure sequence of the system model is determined by analyzing the relationship between the tensile strength of the suspended roof and compressive strength of the coal pillar.

- (4) Under the action of variable load caused by No. 5 coal seam mining in Baizi Coal Mine, the suspended roof and coal pillar of the lower out-fashioned goaf remain stable, which is consistent with the results of engineering practice. This study provides a reference for the mining of coal resources under similar conditions.

## Data Availability

The method was validated by the data provided in Ref. [32].

## Conflicts of Interest

The authors declare that they have no conflicts of interest.

## Acknowledgments

This work was funded by the Joint Research Fund under cooperative agreement between the National Natural Science Foundation of China (NSFC) and Funds for Coal-Based Low-Carbon Technology of Shanxi (No. U1710258), Shanxi Province Applied Basic Research Program (No. 201801D221342), the National Natural Science Foundation of China (Nos. 51422404 and 51574172), Science and Technology Innovation Project of Shanxi Colleges and Universities (2019L0181), Program for Key Research Project of Shanxi Province in the Field of Social Development (No. 201803D31044), Yan'an Industry Key Core Technology Innovation Project (2019ZCGY-025), Program for “1331” Key Team of Scientific and Technology Innovation in Shanxi Province, Program for the Excellent Innovation Team of Higher Learning Institutions of Shanxi Province, Program for the Leading Talents of Emerging Industry of Shanxi Province, and Shanxi Province Technology Innovation Program for the Key Team.

## References

- [1] Y. Zhang, G. Feng, M. Zhang et al., “Residual coal exploitation and its impact on sustainable development of the coal industry in China,” *Energy Policy*, vol. 96, pp. 534–541, 2016.
- [2] G. R. Feng, Y. J. Zhang, T. Y. Qi, and L. X. Kang, “Status and research progress for residual coal mining in China,” *Journal of China Coal Society*, vol. 45, pp. 151–159, 2020.
- [3] Y. J. Zhang, G. R. Feng, and T. Y. Qi, “Experimental research on internal behaviors of caved rocks under the uniaxial confined compression,” *Advances In Materials Science And Engineering*, vol. 2017, Article ID 6949264, 8 pages, 2017.
- [4] L. Tang and S. Liang, “Study on the feasibility of the upward mining above the goaf of the irregular roadway mining under the influence of hard and thick strata,” *Geotechnical and Geological Engineering*, vol. 37, no. 6, pp. 5035–5043, 2019.
- [5] D. F. Zhu, X. M. Song, H. C. Li, Z. H. Liu, C. Wang, and Y. M. Huo, “Cooperative load-bearing characteristics of a pillar group and a gob pile in partially caved areas at shallow depth,” *Energy Science & Engineering*, vol. 8, no. 1, 2020.
- [6] W. B. Sun, “The ascending mining technology of closed multiple-seams with a large mining depth,” *Electronic Journal of Geotechnical Engineering*, vol. 21, pp. 6337–6346, 2016.
- [7] L. Wang, “The technology and application of ascending mining in coal seams,” in *Proceedings of the 21st Century Efficient Intensive Mine Symposium*, pp. 76–79, Shaowu, China, June 2012.
- [8] G. R. Feng, *Basic Theory and Practice of Upward Mining in Coal Mine Residual Area*, Taiyuan University Of Technology, Beijing, China, 2010.
- [9] S. S. Peng, *Longwall Mining*, p. 818, Springer, Berlin, Germany, 2014.
- [10] M. Bai, F. Kendorski, and D. Roosendaal, “Chinese and North American high-extraction underground coal mining strata behaviour and water protection experience and guidelines,” in *Proceedings of the 14th International Conference on Ground Control in Mining*, pp. 209–217, Morgantown, WV, USA, August 1995.
- [11] Y. Xu, J. Li, S. Liu, and L. Zhou, “Calculation formula of “two-zone” height of overlying strata and its adaptability analysis,” *Coal Mining Technology*, vol. 16, pp. 4–11, 2011.
- [12] W. Guo, G. Zhao, G. Lou, and S. Wang, “A new method of predicting the height of the fractured water-conducting zone due to high-intensity longwall coal mining in China,” *Rock Mechanics and Rock Engineering*, vol. 52, pp. 2789–2802, 2018.
- [13] D. Zhang, W. Sui, and J. Liu, “Overburden failure associated with mining coal seams in close proximity in ascending and descending sequences under a large water body,” *Mine Water And the Environment*, vol. 37, no. 2, pp. 322–335, 2018.
- [14] F. Xue, “Feasibility study on ascending mining of near coal seam group,” *Coal Mine Modernization*, vol. 1, pp. 19–21, 2013.
- [15] S. F. Wang, X. B. Li, J. R. Yao et al., “Experimental investigation of rock breakage by a conical pick and its application to non-explosive mechanized mining in deep hard rock,” *International Journal Of Rock Mechanics And Mining Sciences*, vol. 122, Article ID 104063, 2019.
- [16] K. Du, C. Z. Yang, R. Su, M. Tao, and S. F. Wang, “Failure properties of cubic granite, marble, and sandstone specimens under true triaxial stress,” *International Journal Of Rock Mechanics And Mining Sciences*, vol. 130, Article ID 104309, 2020.
- [17] X. Z. Xie, “Study on stability of roof-coal pillar in room and pillar mining goaf in shallow depth seam,” *Coal Science and Technology*, vol. 42, pp. 1–9, 2014.
- [18] Y. D. Jiang, Y. M. Yang, Z. Q. Ma, and Y. W. Li, “Breakage mechanism of roof strata above widespread mined-out area with roadway mining method and feasibility analysis of upward mining,” *Meitan Xuebao/Journal of the China Coal Society*, vol. 41, pp. 801–807, 2016.
- [19] G. L. He, D. C. Li, Z. W. Zhai, and G. Y. Tang, “Analysis of instability of coal pillar and stiff roof system,” *Journal of the China Coal Society*, vol. 32, pp. 897–901, 2007.
- [20] H. L. Li, *Study on Coal Seam Floor Failure Rule under Mining Dynamic Loading Effect and Control Technique of Water-*

- Inrush*, China University of mining and technology, Xuzhou, China, 2016.
- [21] B. Y. Wu, Z. G. Deng, Y. F. Feng, and F. Li, "Analysis of the influence of interlayer rock on ascending mining under special conditions," *Journal of the China Coal Society*, vol. 42, pp. 842–848, 2017.
- [22] J. X. Fu, W. D. Song, and Y. Y. Tan, "Study on influence of overlapping rate of double layer gobs on stability of isolation roof and its mechanical model," *Journal of Mining and Safety Engineering*, vol. 35, pp. 58–63, 2018.
- [23] N. Jiang, C. X. Wang, H. Y. Pan, D. W. Yin, and J. B. Ma, "Modeling study on the influence of the strip filling mining sequence on mining-induced failure," *Energy Science & Engineering*, vol. 8, no. 6, pp. 1–17, 2020.
- [24] Y. Q. Long and S. H. Bao, *Structural Mechanics*, Higher Education Press, Beijing, China, 2000.
- [25] B.-Y. Jiang, S.-T. Gu, L.-G. Wang, G.-C. Zhang, and W.-S. Li, "Strainburst process of marble in tunnel-excavation-induced stress path considering intermediate principal stress," *Journal of Central South University*, vol. 26, no. 4, pp. 984–999, 2019.
- [26] H. W. Liu and J. X. Lin, *Mechanics of Materials*, Higher Education Press, Beijing, China, 1998.
- [27] B. H. G. Brady and E. T. Brown, *Rock Mechanics for Underground Mining*, Allen & Unwin, Crows Nest, Australia, 1985.
- [28] M. G. Qian, X. X. Miu, and J. L. Xu, "Theoretical study of key stratum in ground control," *Journal of China Coal Society*, vol. 3, pp. 2–7, 1996.
- [29] H. Moomivand, "Effect of size on the compressive strength of coal," in *Proceedings of the 99th International Symposium on Mining Science and Technology*, pp. 399–404, Beijing, China, 1999.
- [30] C. X. Wang, B. T. Shen, J. T. Chen et al., "Compression characteristics of filling gangue and simulation of mining with gangue backfilling: an experimental investigation," *Geomech Engineering*, vol. 20, no. 6, pp. 485–495, 2020.
- [31] Z. T. Bieniawali and H. H. Sun, *Strata Control in Mineral Engineering*, China MiningUniversity Press, Beijing, China, 1990.
- [32] X. P. Shao, E. S. Liu, X. L. Cai, J. T. Wu, and J. Zhang, "Experimental study on stability of pillar in upward mining in pillar mined out area," *Coal Engineering*, vol. 50, pp. 5–9, 2018.
- [33] D. Zhu, Y. Wu, Z. Liu, X. Dong, and Y. Jin, "Failure mechanism and safety control strategy for laminated roof of wide-span roadway," *Engineering Failure Analysis*, vol. 111, pp. 1–14, 2020.
- [34] Q. Wang, B. Jiang, L. Wang et al., "Control mechanism of roof fracture in no-pillar roadways automatically formed by roof cutting and pressure releasing," *Arabian Journal of Geosciences*, vol. 13, p. 10, 2020.

## Research Article

# Assessment of Cascading Accidents of Frostbite, Fire, and Explosion Caused by Liquefied Natural Gas Leakage

Chengjun Yue <sup>1</sup>, Li Chen <sup>1</sup>, Hengbo Xiang <sup>2</sup>, Linfeng Xu,<sup>1</sup> Shigang Yang,<sup>2</sup> Zhan Li,<sup>2</sup> Chenxi Xia,<sup>2</sup> and Qin Fang<sup>1,2</sup>

<sup>1</sup>Engineering Research Center of Safety and Protection of Explosion & Impact of Ministry of Education, Southeast University, Nanjing 211189, China

<sup>2</sup>State Key Laboratory of Disaster Prevention & Mitigation of Explosion & Impact, Army Engineering University of PLA, Nanjing 210007, China

Correspondence should be addressed to Li Chen; [li.chen@seu.edu.cn](mailto:li.chen@seu.edu.cn) and Hengbo Xiang; [xhb3188@163.com](mailto:xhb3188@163.com)

Received 25 March 2020; Revised 27 July 2020; Accepted 8 August 2020; Published 26 August 2020

Academic Editor: Chiara Bedon

Copyright © 2020 Chengjun Yue et al. This is an open access article distributed under the Creative Commons Attribution License, which permits unrestricted use, distribution, and reproduction in any medium, provided the original work is properly cited.

Liquefied natural gas (LNG) leaks often lead to cascading accident disasters, including vapor cloud release, explosion, fire, and toxic gas release. The origin and evolution of each accidental disaster must be considered when assessing safety. This paper discusses the safety assessment project of an LNG gas storage station in Xuzhou, China. Multiple conceivable disasters due to the leakage of LNG storage tanks are simulated and analyzed using the computational fluid dynamic software FLACS. We studied different wind speeds interacting with the flammable vapor cloud area and creating frostbite in areas of low temperature. Diffusion simulations of vapor cloud explosion (VCE), thermal radiation, and the distribution of toxic substances were performed. The overpressure-impulse criterion was used to calculate the influence range of VCE. Heat flux, heat dose, and heat flux-heat dose criteria were used to calculate the safe distance for personnel in the event of fire. Based on the calculation results of the three latter criteria, this paper recommends using the heat flux criterion to evaluate fire accidents. The danger zone of each accident was compared. VCE accidents yielded the largest area.

## 1. Introduction

Liquefied natural gas (LNG) is an efficient, clean, and relatively inexpensive energy source and widely used in every daily life, industrial production, and other fields [1]. It has become one of the three pillars of the world's energy with the volatile international oil price and the rapid growth of the demand for clean energy [2]. Ensuring people's safety is a paramount concern due to the flammable and explosive nature of LNG, with leakage causing many serious accidents and enormous loss. For example, in 1944, an LNG leakage explosion occurred at an LNG station in Cleveland, USA. The explosion spread over 14 blocks, killed 136 people, and injured 225. The damage extended to 0.75 square miles [3]. In 1997, a spherical tank at an oil refinery in India leaked and exploded, resulting in 25 storage tanks and 19 buildings burned down. More than 60 people were killed, and the

damage was nearly \$150 million [4]. In 2004, an LNG receiving terminal in Algeria leaked and caused a fire, resulting in 27 deaths, 74 injuries, and over 1 billion U.S. dollars in damages [5]. In 2011, an LPG cylinder leakage accident at a restaurant in Xi'an China resulted in 11 deaths and 31 injuries and also affected 12 shops and severely damaged 53 vehicles with a direct economic loss of 9.9 million Yuan [6].

The diffusion and explosion models and the combustion fireball from LNG leakage are studied by many researchers. Kim et al. [7] proposed a new semianalytical method to estimate the evaporation rate of the LNG liquid pool based on the heat conduction equation and diffusion data. Wang et al. [8] introduced the atmospheric transmission rate  $\tau$  in the original TNO dynamic model. The optimization model of theoretical predictions fully agrees with the experimental data. Yi et al. [9] established a fire spread model based on the fire dynamics simulator (FDS) and analyzed the fire spread



results for a fire scenario in different functional places under the same conditions and the spread of fire outside of the room. The results showed that visibility was a more influential factor in determining the critical time required for fire to become a hazard comparing with CO mass fraction and temperature. Dadashzadeh et al. [10] proposed a methodology for toxicity risk assessment during an LNG fire. It is announced that high concentrations of combustion products and longer exposure time at the process facility increase risks. However, the direct consequence of fire was not considered.

Baalisampang et al. [11] developed an evaluation method for cascade accidents caused by LNG leakage. This method uses computational fluid dynamics (CFD) software FLACS simulation of LNG leakage on a series of disasters and considers the evolving scenario, namely, from a liquid pool after LNG evaporation followed by combustion, explosion, and yielding combustion products. Lv et al. [12] established a reduced model of 160,000 m<sup>3</sup> LNG storage tank according to the ratio of 1:100, carried out LNG explosion tests, and simulated the explosion process with FLACS. They then established the correlation between the test model and the full-size model explosion overpressure to evaluate the maximum explosion overpressure of large LNG storage tanks. Li et al. [13] used FLACS to simulate the development of a flame, overpressure after leakage, and an explosion of a natural gas pipeline. It was found that the length of natural gas chambers and different ignition positions had little influence on overpressure. This finding supported stronger structural designs and a division of the fire prevention zone. Ren [14] studied the changing law of temperature in the process of large-area LNG leakage and explosion using numerical methods. Moreover, the numerical model considered the influence of wind speed on the temperature of the escaped liquefied natural gas. Hu et al. [15] proposed a topological network model and inversion method for LNG tank fire accidents. They established a topological model for LNG tank fire inversion and found the shortest path, according to the weighted edge topological network structure and to determine the fire location. The location of the fire source obtained by this method was identical to the actual accident location. Bao et al. [16] carried out experimental research on the deflagration of unrestricted methane-air mixture. The impacts of methane concentration and volumetric on the deflagration loads were demonstrated. They also proposed a new model for the prediction of deflagration loads of borderless methane-air mixture. Li et al. [17–20] studied the performances of infilled masonry walls under vented gas explosion by filed blast tests and proposed corresponding retrofitting techniques, such as bonding with CFRP, BFRP, and GFRP materials.

The calculated value by the theoretical model often differs significantly from the actual value of the project due to the influences of obstacle distribution, block rate, type of environment, and other site-specific factors. LNG leakage accidents are often accompanied by a series of cascading accidents such as gas leakage, explosion, fire, and flash fire. The accidents that may happen during the LNG storage tank leakage and the corresponding conditions are shown in

Table 1. It is necessary to analyze the accident types accurately and establish a refined model for specific cases to obtain more accurate calculation results. Taking an LNG storage station in Xuzhou, China, as the engineering background, this paper studied the disastrous consequences of LNG storage tank leakage and explosion by using the CFD software FLACS and divided the safe distance of personnel by the probability method, providing guidance and reference for engineering construction and disaster prevention.

## 2. Evaluation Methods

The evaluation method in this study was developed based on the evaluation process reported by Baalisampang et al. [11]. The original process can be basically divided into five steps:

- (1) The LNG leakage formed a liquid pool. The commercially available software FLACS was used to model and simulate the evaporation of LNG.
- (2) A series of potential transition phenomena, such as LNG vapor diffusion, pool fires, and steam cloud explosions, were considered. The phenomenological changes in LNG leakage, as well as the effects of atmospheric and thermal radiation, were used to assess potential cascading events. The heat load obtained from the pool fire had to be used as the ignition source of the VCE to meet the minimum ignition energy for the transition to occur.
- (3) The heat released by the pool fire was assumed as a potential ignition source to ignite and consume the vapor cloud at that location. It is because that VCE [21, 22] might be produced if the ignition delay is between 5 and 10 minutes.
- (4) The probability function was used to analyze the consequences of fire, explosion, or combustion products and the impacts of thermal radiation on property and personnel.
- (5) Comprehensive assessment with disasters of fire, explosion, and combustion.

This original process above introduced the progression of LNG leakage accidents, however, with some deficiencies yet. Four of these deficiencies were improved in this study.

- (1) The storage temperature of LNG is around  $-160^{\circ}\text{C}$ , and vaporization absorbs a large amount of heat, with a sharp thermal drop in the surrounding space. Frostbite can be caused [14] when the temperature of human skin tissue drops below the freezing point (273 K). Rescue personnel must take rescue measures within a safe temperature range. Therefore, the impacts of LNG leakage on the ambient temperature were considered in this study.
- (2) The wind speed can directly affect the distribution of LNG vapor clouds and combustion products, as well as the thermal load of the pool fire, which in turn indirectly affects the explosion load distribution of the vapor cloud. Wind speed is, therefore, an important factor in LNG leakage accidents.

TABLE 1: Possible accidents and conditions caused by LNG storage tank leakage.

Accident	Accident conditions					Type of accident
	Leak	Ignition source	Formation of vapor cloud or pool	Ignite	Open space	
LNG storage tank leak	Uninterrupted	x	√	x	x	Jet fire
			√	x	√	Flash fire
			√	Vapor cloud	x	VCE
			x	√	x	No accident
			x	Pool	√	Pool fire
	Transient	x	√	x	N	No accident
			√	x	x	BLEVE
			√	Vapor cloud	√	Flash fire
			x	√	x	VCE
			x	Pool	√	Pool fire
			x	x	No accident	

- (3) The impact of explosion overpressure is insufficient. Impulse is also an important evaluation factor. A comprehensive consideration of overpressure and impulse can more accurately assess the impact of an explosion. The improved evaluation process is shown in Figure 1.
- (4) We evaluated fire accidents from three aspects of heat flux, heat measurement, and their comprehensive influences, respectively, and compare the calculation results of the three and finally found out the most optimal evaluation index.

### 3. Mathematical Model

**3.1. Basic Assumptions.** Obstacles on the ground make the wind field structure nearby irregular, resulting in extraordinarily complex atmospheric turbulences and high uncertainty regarding leakage and diffusion of combustible gasses. We simplified the calculation through the following assumptions [23]:

- (1) The movement of air-born particles can be regarded as the movement of incompressible fluid when the wind speed in the lower atmosphere is about 10 m/s.
- (2) Turbulence is random in space and time but can be described statistically. This can be used as the starting point to model turbulence motion. Variables such as wind speed are the sum of their average and disturbance quantities according to the Reynolds hypothesis. This applies to the horizontal component of wind speed  $u = \bar{u} + u'$ .
- (3) The turbulence viscosity coefficient  $\nu_t$  characterizes the properties of atmospheric turbulence according to the Boussinesq hypothesis. The two-equation turbulence model, namely,  $k$ - $\varepsilon$  turbulence model, was used to solve the value of  $\nu_t$ .

**3.2. Governing Equation.** The three-dimensional equations of turbulent diffusion of gas in the atmosphere can be derived as follows.

Mass conservation equation (continuity equation):

$$\frac{\partial u_i}{\partial x_i} = 0. \quad (1)$$

Momentum conservation equation:

$$\frac{\partial}{\partial t} (\rho u_i) + \frac{\partial}{\partial x_j} (\rho u_i u_j) = -\frac{\partial p}{\partial x_i} + \frac{\partial}{\partial x_j} \left( u \frac{\partial u_i}{\partial x_j} - \rho \bar{u}'_i \bar{u}'_j \right). \quad (2)$$

Energy conservation equation:

$$\frac{\partial}{\partial t} (\rho E) + \frac{\partial}{\partial x_i} (\rho u_i E) = \frac{\partial}{\partial x_i} \left( k_{\text{eff}} \frac{\partial T}{\partial x_i} - \sum_j h_j J_j \right), \quad (3)$$

where  $T$  is the temperature (K),  $p$  is the gas pressure (Pa),  $u$  is the velocity (m/s),  $\rho$  is the air density ( $\text{kg/m}^3$ ),  $\mu$  is the turbulent fluid viscosity, and  $k_{\text{eff}}$  is the effective conduction coefficient. For turbulence conditions, the widely used  $k$ - $\varepsilon$  turbulence model was adopted.

The concentration distribution of continuous leakage can be calculated according to one of the following three formulae based on wind speed  $u$ , the relationship between the height of atmospheric mixing layer  $H_0$ , and the diffusion coefficient of vertical wind direction [24–27]:

- (1) When the wind speed is  $1 \text{ m/s} < u \leq 1.6 H_0$ , the gas diffusion concentration at a point  $(x, y, z)$  in the spatial coordinate system with the leakage source as the origin and the wind direction as the  $X$ -axis is

$$C(x, y, z) = \frac{Q}{2\pi u \sigma_y \sigma_z} \exp\left(-\frac{y^2}{2\sigma_y^2}\right) \cdot \left\{ \exp\left[-\frac{(z-H)^2}{2\sigma_z^2}\right] + \exp\left[-\frac{(z+H)^2}{2\sigma_z^2}\right] \right\}, \quad (4)$$

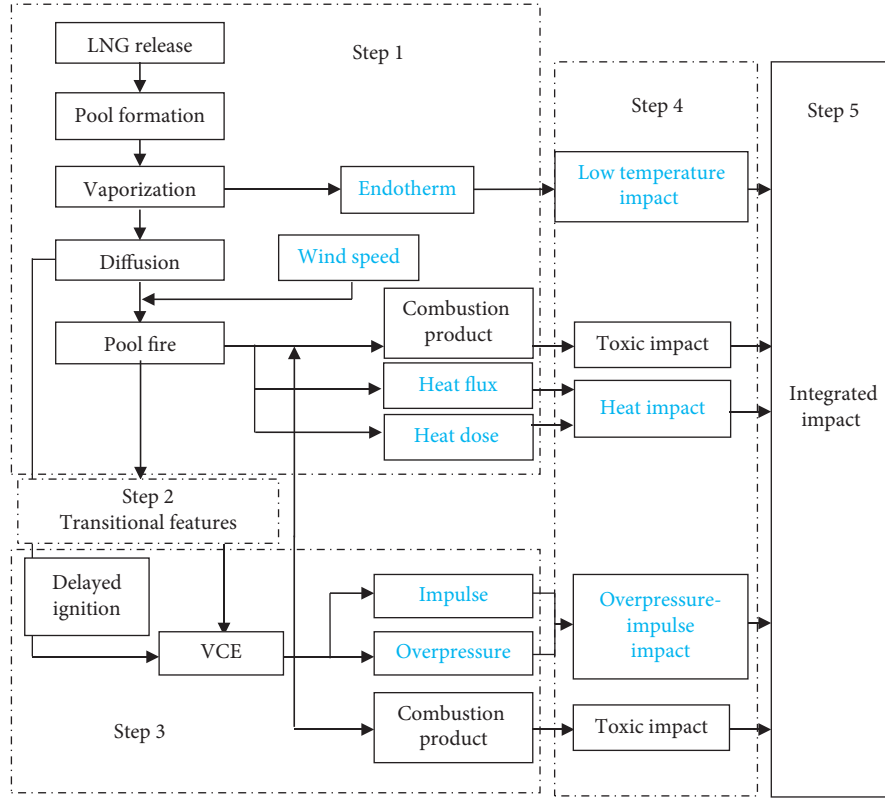


FIGURE 1: Comprehensive assessment process of LNG leakage accident.

where  $C(x, y, z)$  is the average concentration of the leakage gas at a certain point downwind  $(x, y, z)$  ( $\text{kg}/\text{m}^3$ );  $Q$  is the leakage source strength ( $\text{kg}/\text{s}$ );  $u$  is the average wind speed ( $\text{m}/\text{s}$ );  $H$  is the effective height of the leakage source ( $\text{m}$ );  $\sigma_x$ ,  $\sigma_y$ , and  $\sigma_z$  are the diffusion parameters in the direction of  $X$ ,  $Y$ , and  $Z$  axis, respectively ( $\text{m}$ );  $x$  is the distance downwind ( $\text{m}$ );  $y$  is the wind distance ( $\text{m}$ ); and  $z$  is the height above the ground ( $\text{m}$ ).

- (2) When the wind speed is  $u < 0.5 \text{ m/s}$ , assuming that the steam is evenly distributed around the leakage source in all directions, the concentration  $c(r)$  from the leakage source is as follows:

$$c(r) = \frac{2Q}{(2\pi)^{(3/2)}} \cdot \frac{b}{b^2 r^2 + a^2 H^2} \cdot \exp\left[-\frac{b^2 r^2 + a^2 H^2}{2a^2 b^2 (m\Delta)^2}\right], \quad (5)$$

where  $c(r)$  is the concentration at the distance  $r$  from the leakage source ( $\text{kg}/\text{m}^3$ );  $a$  and  $b$  are diffusion coefficients ( $\text{m}$ ); and  $m\Delta$  is the duration of static wind,  $\Delta = 3600 \text{ s}$ , and  $m$  is 1, 2, 3, ...

- (3) When the wind speed  $u$  is  $0.5 \text{ m/s} < u < 1 \text{ m/s}$ , continuous leakage is described by the superposition of instantaneous air mass leakage quantity  $Q\Delta t$  in time  $\Delta t$ . The concentration at point  $(x, y, z)$  with the leakage source as the origin of the coordinate system and the downwind direction as the  $X$ -axis is

$$C(x, y, z) = \int_0^\infty C'(x, y, z) dt,$$

$$C'(x, y, z) = \frac{2Q}{(2\pi)^{(3/2)} \sigma_x \sigma_y \sigma_z} \exp\left(-\frac{y^2}{2\sigma_y^2}\right) \exp\left[-\frac{(x-ut)^2}{2\sigma_x^2}\right] \cdot \left\{ \exp\left[-\frac{(z-H)^2}{2\sigma_z^2}\right] + \exp\left[-\frac{(z+H)^2}{2\sigma_z^2}\right] \right\}. \quad (6)$$

## 4. Numerical Modeling

**4.1. Geometric Model.** The size and distribution of objects in the actual scene were determined based on the satellite topographic map, as shown in Figure 2(a). Figure 2(c) is the physical map of the LNG storage tank. The numerical model of the LNG storage tank and its surrounding buildings was established by using FLACS, as shown in Figure 2(c), where the wind direction, leakage position, and ignition position in the developed model were also indicated. The monitor point was set every 3 m near the ignition position, designated from 1 to 30.

**4.2. Grid Sensitivity Analysis.** The mesh size affects the accuracy of the calculation results although FLACS was usually verified in the calculation of microscale model. The results corresponding to mesh sizes can differ more than 10-fold.



FIGURE 2: Developed numerical model of the LNG accidents: (a) satellite topographic map; (b) LNG storage tank; (c) information of numerical model.

The sensitivity of the mesh size must be analyzed before the numerical calculation. As the number of grids increases, the calculation accuracy improves, but the calculation scale also increases. Five grid size models of 2.0 m, 1.5 m, 1.25 m, 1.0 m, and 0.5 m were used to calculate the explosion scenario. The results are shown in Figure 3. Overpressure value increases gradually with the decrease in the grid size. The difference between the overpressure values corresponding to the 1.0 m and 0.5 m grids does not exceed 4.3%; it is much smaller than other grid sizes. When the grid size is under 1.0 m, the calculation results barely change. The core diffusion area is set to 1.0 m, and the extended area is set to 2.0 m. The entire area is divided into 1.0 m uniform grids to calculate gas explosion, as shown in Figure 4.

**4.3. Parameter Determination.** The LNG storage tank volume was  $157.9 \text{ m}^3$ , the initial inside pressure 0.6 MPa, and the LNG temperature was  $-162^\circ\text{C}$ . The atmospheric pressure was assumed as  $1.01 \times 10^5 \text{ Pa}$ , the atmospheric temperature was set to  $20^\circ\text{C}$ , and the wind speed was 0 m/s, 4 m/s, and 8 m/s, respectively. This allowed the discussion of the influence of wind speed on the gas diffusion. The relative turbulence intensity was 0.1, and the turbulence length scale was 0.01 m. The leakage hole diameter of LNG storage tank was 100 mm, and the leakage hole was assumed circular. The leak rate was calculated using the leak module of FLACS with an initial leak rate of 38.25 kg/s.

We used the preference wind to set up the wind outflow boundary and the others by using nozzle, as provided in Table 2.



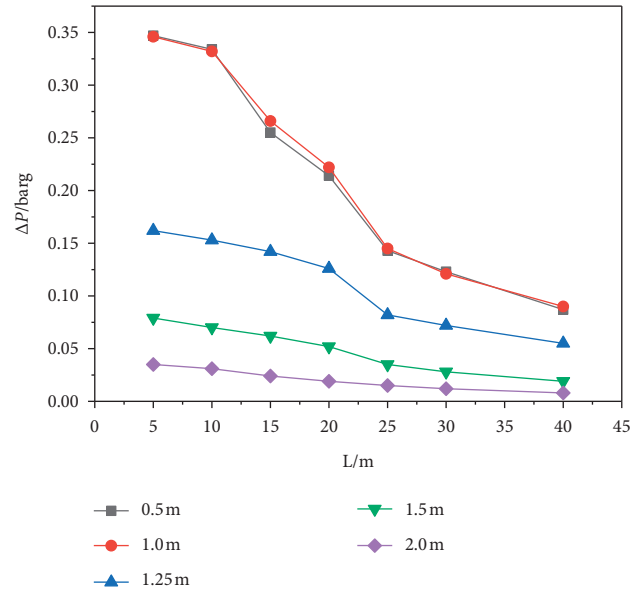


FIGURE 3: Relationship between overpressure and distance with different grid sizes.

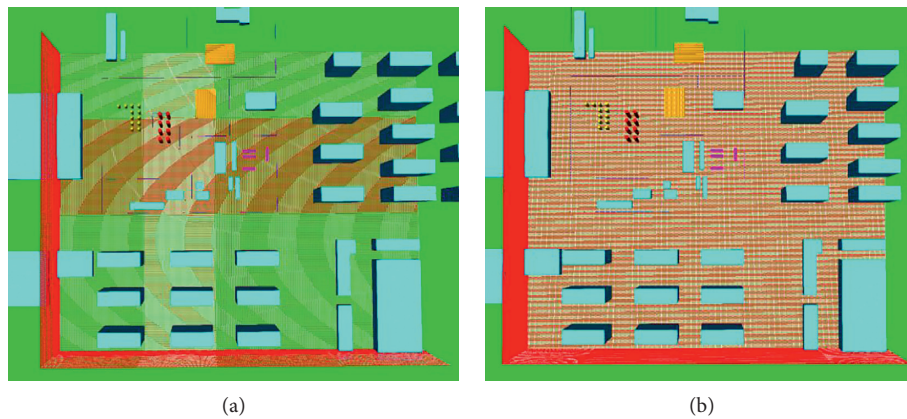


FIGURE 4: LNG diffusion and explosion meshing: (a) gas leak and fire grid; (b) gas explosion grid.

TABLE 2: Boundary conditions.

Name	Type
XLO	Nozzle
XHI	Wind
YLO	Wind
YHI	Nozzle
ZLO	Wind
ZHI	Nozzle

The gas diffusion velocity was related to the surface roughness  $Z_0$ . Higher surface roughness will yield slower gas diffusion. The ground roughness was set to 1.0 according to the suggested standard value provided in Table 3 [28].

The atmospheric stability was determined by factors like wind speed, radiation amount, and cloud cover. According to the Pasquill–Gifford classification standard of atmospheric stability in Table 4, the atmospheric stability corresponding to the four wind speeds is B, C, and D, respectively. The initial condition parameters are listed in Table 5.

## 5. Results and Discussion

**5.1. Analysis of Diffusion Results.** LNG leakage and diffusion were simulated under three wind conditions with a wind speed of 0 m/s, 4 m/s, and 8 m/s. Figure 5 shows the flammable zone of LNG under each wind condition at the time of 190 s, where the methane flammable concentration was between 5.0% and 15.0%. The combustible area was 12409 m<sup>2</sup>, 5097 m<sup>2</sup>, and 870 m<sup>2</sup>. Clouds travel faster and spread more widely with the wind. However, wind also hastens the dilution of fuel in the air. Explosions are prevented when the methane concentration falls below 5%. Therefore, the presence of actually wind reduces the LNG diffusion risk; the higher the wind speed is, the smaller the combustible area is.

The combustible area reaches a dynamic equilibrium and remains unchanged with time when the fuel vapor cloud speed equals the lost speed. The combustible product has reached its dynamic equilibrium at wind speeds of 4 m/s and 8 m/s at the time of 190 s, while when  $v=0$  m/s, the



TABLE 3: Values of the ground roughness.

Ground type	Flat and open	Scattered tall and low buildings	Dense tall and low buildings
$Z_0/m$	$\leq 0.1$	1~4	4

TABLE 4: Classification of atmospheric stability.

Wind speed (m/s)	Daylight			Clouds at night	
	Strong	Medium	Weak	>50%	<50%
<2	A	A~B	B	E	F
2~3	A~B	B	C	E	E
3~4	B	B~C	C	D	E
4~6	C	C~D	D	D	D
>6	C	D	D	D	D

TABLE 5: Initial conditions used.

Parameters	Value
Values of characteristic velocity	0/4/8 m/s
Relative turbulence intensity	0.01
Turbulence length scale	0.1 m
Temperature	20°C
Ambient pressure	100 kPa
Ground roughness	1.0 m
Reference height	10 m

combustible zone is still progressing even after 500 s, as shown in Figure 6. It is found that the wind speed is a key factor in the dilution rate, diffusion rate, and influence range of the combustible region. Wind turbines can be added to speed up dilution of the steam cloud and reduce the risk of explosion in addition to controlling the leakage source to prevent LNG leakage-related disasters.

The evaporation of LNG causes the temperature of the surrounding space to drop rapidly, so rescuers must pay attention to the potential of frostbite during emergency repairs. Although the influence range of low temperature is smaller than that of diffusion, its impact lasts longer. Once a leakage accident occurs, it is accompanied by low-temperature injury. The occurrence of fire and VCE requires certain ignition conditions to be presented. The risk of frostbite is higher than that of fire and VCE. Figure 7 shows a diagram of the temperature distribution on-site under different wind speeds at 190 s of leakage. In the absence of wind, diffusion of LNG is slow, and the fuel is rather concentrated around the storage tank, which decreases the temperature in the whole site rapidly. The area of frostbite ( $T \leq 273$  K) is significantly larger than that at wind speeds of 4 m/s and 8 m/s. The temperature in the lower air inlet decreases in the whole station when the wind speed is 8 m/s, leading to an area of frostbite up to 7 m around the leaking tank. Wind can effectively accelerate the diffusion of LNG and reduce the frostbite area and the duration of low temperature.

**5.2. Risk Assessment of Fire Accident.** The commonly used thermal radiation assessment criteria include the thermal dose, the heat flux, and the heat flux-heat dose criteria. The heat flux criterion stipulates that the critical heat flux value of possible burns for personnel is 4 kW/m<sup>2</sup>. The critical heat dose for a

one-time burn affecting personnel is 125 kJ/m<sup>2</sup> [23]. The criterion holds that whether the target can be harmed is not determined by either heat dose or heat flux alone but in conjunction. If heat dose and heat flux are used as abscissa and ordinate, respectively, the critical state of target damage corresponds to a critical curve, as shown in Figure 8. The lower left of the curve is the safe area; the upper left is the harmful zone. The asymptotes are  $q = q_{cr}$  and  $Q = Q_{cr}$ , respectively, corresponding to critical heat flux and critical heat dose.

Based on the burns of exposed skin, Lees [29] obtained the critical heat flux-time curve of exposed skin under the action of thermal radiation, as shown in Figure 9. Unbearable pain is experienced when the temperature below the skin at a depth of 0.1 mm exceeds 44.80°C. Pain increases sharply and then gradually subsides until it completely disappears with increasing temperature, indicating that the exposed skin has been completely burned out. At a less than 40 s exposure time, the curve is an inclined line with a constant heat dose between 60 and 70 kJ/m<sup>2</sup>, which is consistent with the recommended value of 65 kJ/m<sup>2</sup> in the literature [30]. Beyond an exposure time of 120 s, the curve is basically a horizontal line, and the corresponding heat flux is constant at 1.4 to 1.5 kW/m<sup>2</sup>. When the heat flux is less than or equal to 1.4 kW/m<sup>2</sup>, there is no tissue damage regardless of the exposure time. Normal blood flow reduces the possibility for the local temperature to reach or exceed 44.80°C.

The fire accident started at 300 s after the leakage of LNG, and it can be known from the simulation results that the influence range of heat radiation reached the maximum after 25 s of flame combustion, as shown in Figure 10, and the radius of the danger is 43.82 m. In addition, the heat dose value was measured through the monitor points, and Figure 11 shows the heat dose values of points 21 to 30.

Buettner provided the empirical formula, assuming that 20% of the skin is exposed. Pietersen proposed the current common probability equation of thermal radiation injury in 1990 [31–33].

The probability of death when the skin is exposed is

$$P_r = -36.38 + 2.56 \ln(tI^{(4/3)}). \quad (7)$$

Probability of death with clothing protection (20% skin exposed) is

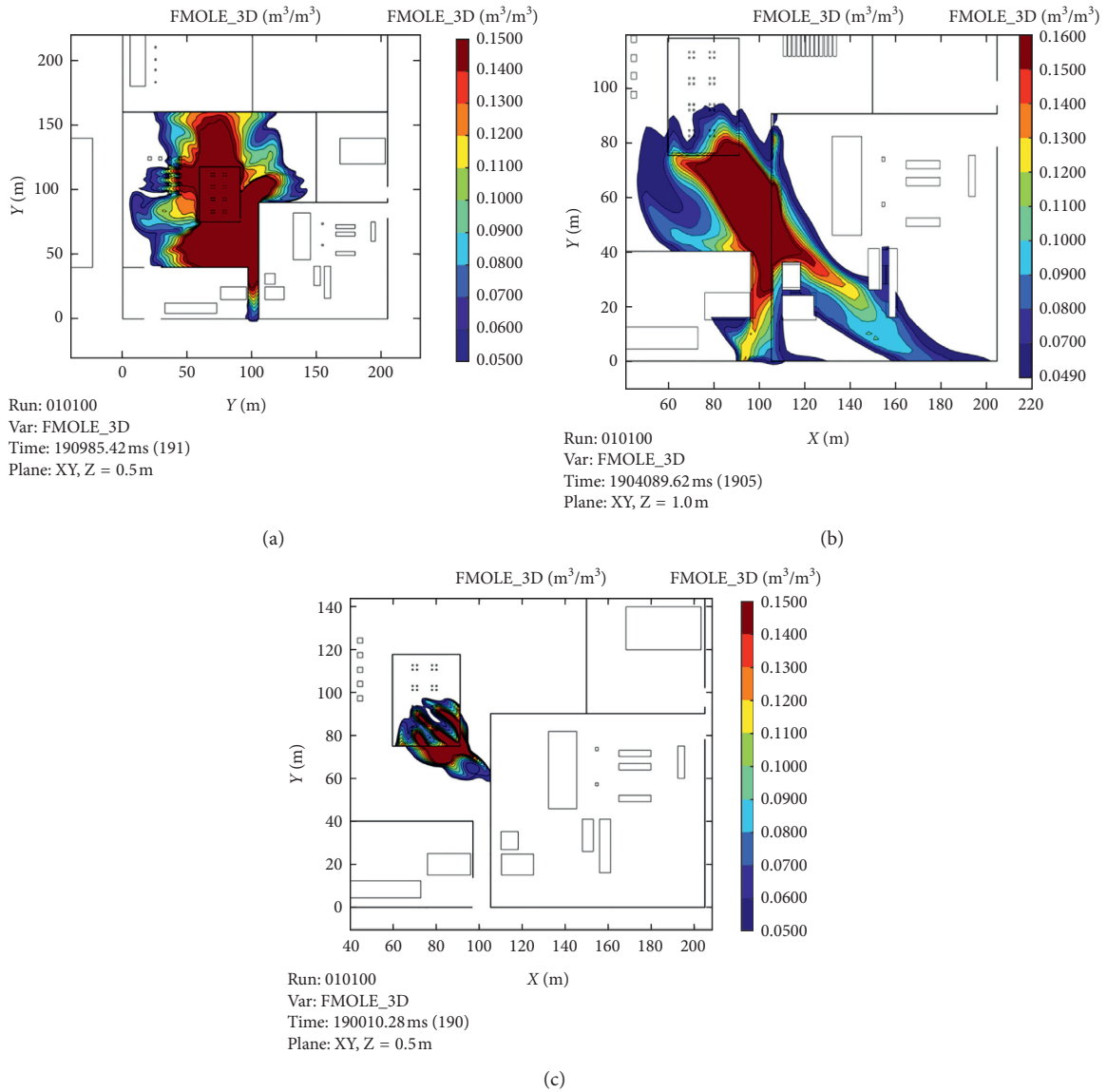


FIGURE 5: Diffusion diagrams at different wind speeds: (a)  $v = 0 \text{ m/s}$ ; (b)  $v = 4 \text{ m/s}$ ; (c)  $v = 8 \text{ m/s}$ .

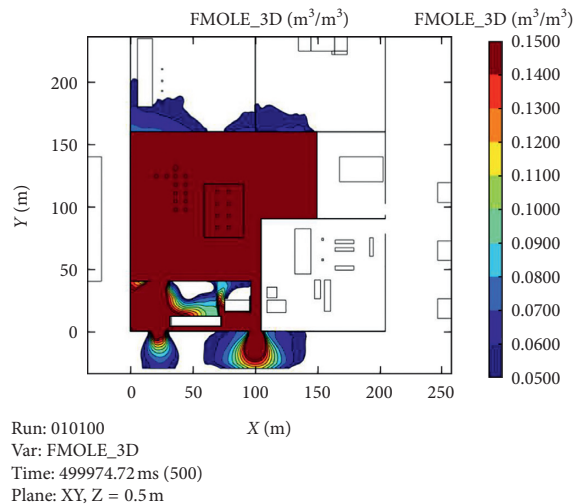


FIGURE 6: Varying process of LNG vapor cloud without wind ( $t = 500 \text{ s}$ ).

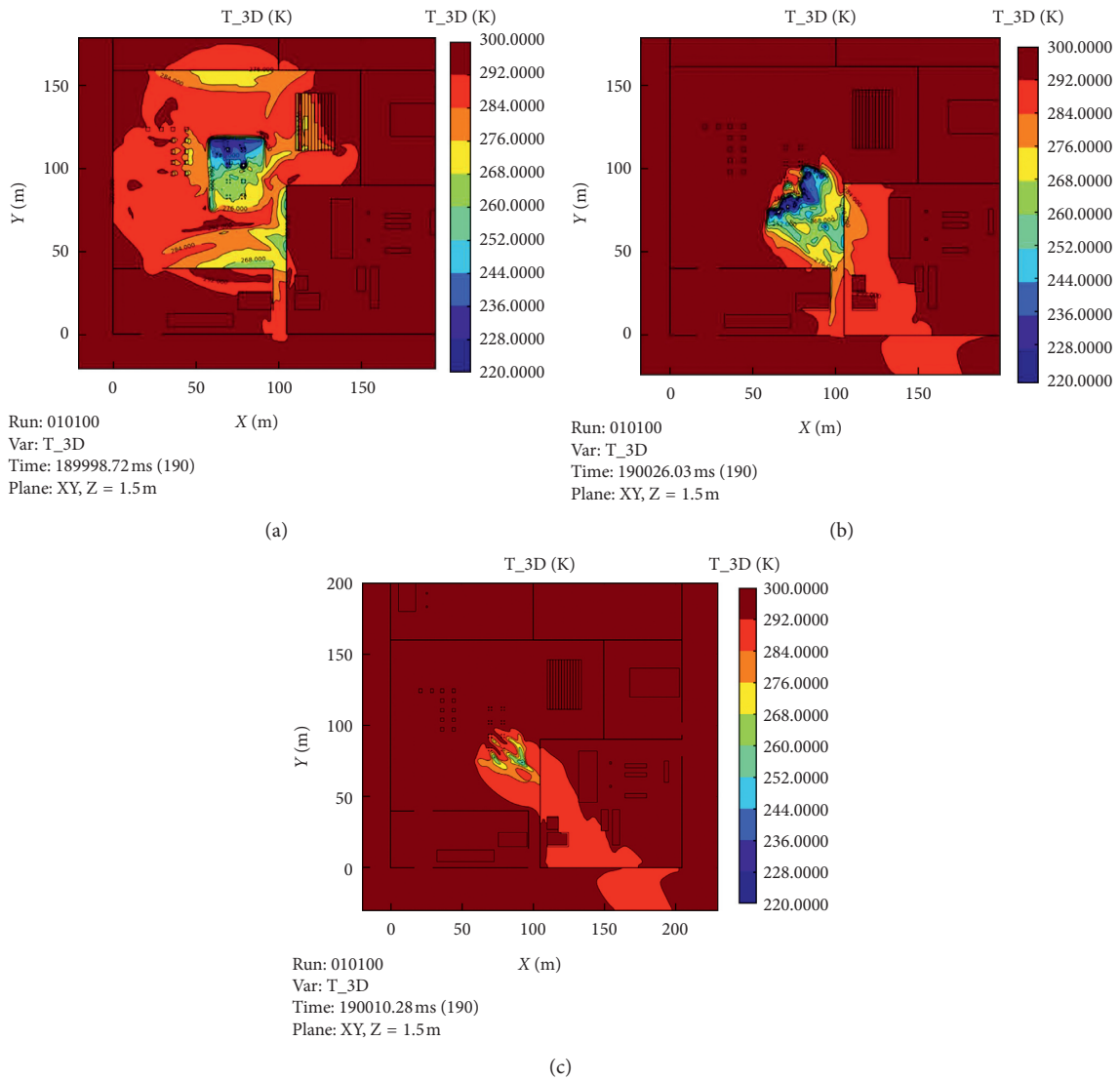


FIGURE 7: Temperature profile of LNG leakage: (a)  $v=0$  m/s; (b)  $v=4$  m/s; (c)  $v=8$  m/s.

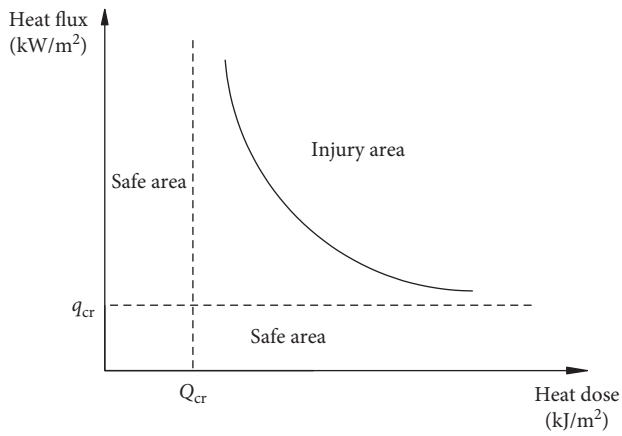


FIGURE 8: Heat flux-heat dose curve of heat radiation damage [22].

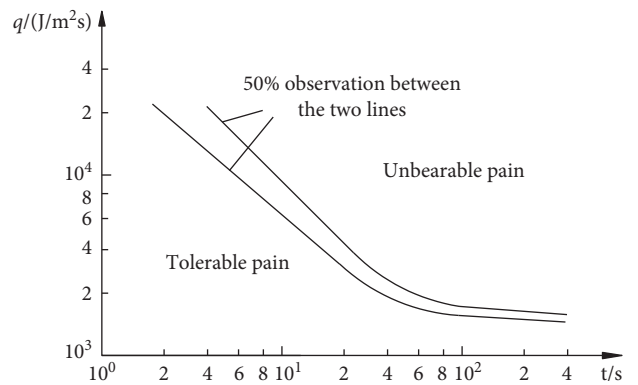


FIGURE 9: The critical curve of exposed skin under thermal radiation [22].

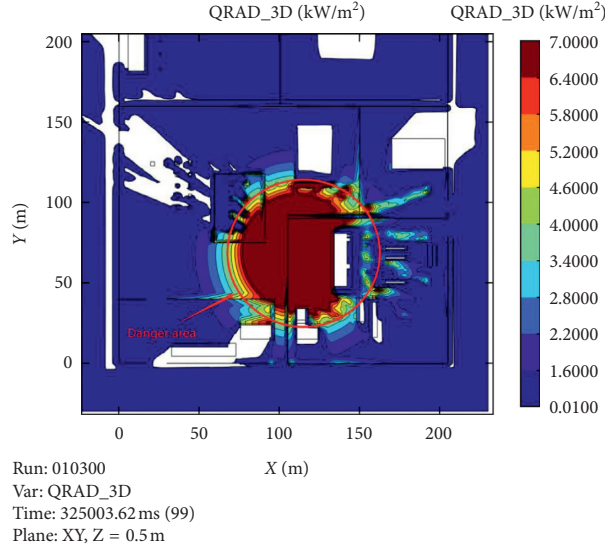


FIGURE 10: Heat flux influence range.

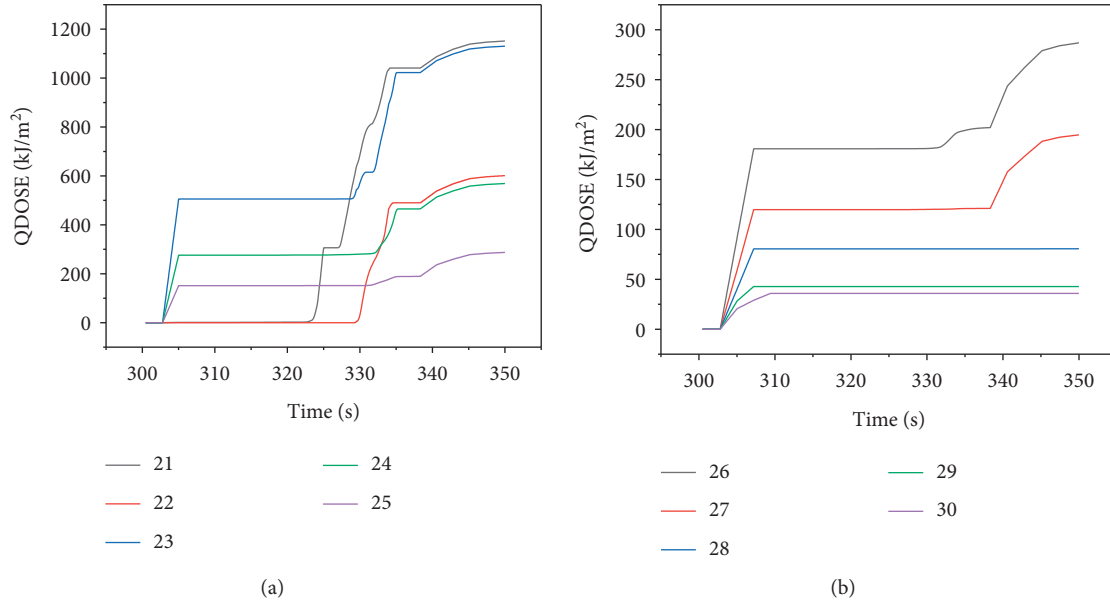


FIGURE 11: Heat dose calculation value.

$$P_r = -37.23 + 2.56 \ln(tI^{(4/3)}). \quad (8)$$

Probability of second-degree burn (serious injury) with clothing protection (20% skin exposed) is

$$P_r = -43.14 + 3.0186 \ln(tI^{(4/3)}). \quad (9)$$

Probability of first-degree burns (minor injuries) with clothing protection (20% skin exposed) is

$$P_r = -39.83 + 3.0186 \ln(tI^{(4/3)}), \quad (10)$$

where  $I$  is the heat flux received by the human body ( $w/m^2$ );  $t$  is the exposure time (s); and  $P_r$  is the damage probability

variable. When  $P_r = 5$ , the corresponding damage percentage is 50%.

We used the principle of exposure time of 10 s and 50% probability and determined the radius  $R_1$  of death, the radius  $R_2$  of serious injury, and the radius  $R_3$  of minor injury, as listed in Table 6. The influence radius of the heat flux-heat dose criterion is 45 m, the influence radius of the heat dose criterion is only 30.4 m, as shown in Figure 12. The calculation of heat flux-heat dose criterion is more complicated than the heat flux criterion. Therefore, we propose to use the heat flux criterion to evaluate the heat of combustion in the fire and explosion scenarios.

TABLE 6: Damage range calculated by heat flux-heat dose criterion (m).

Damage types	Dangerous distance (m)	Calculated thermal radiation flux (kW/m <sup>2</sup> )	Thermal radiation damage threshold (kW/m <sup>2</sup> )
Die radius	19.25	41.99	37.5
Serious injury radius	24	27.81	25
Minor radius	45	12.23	12.5

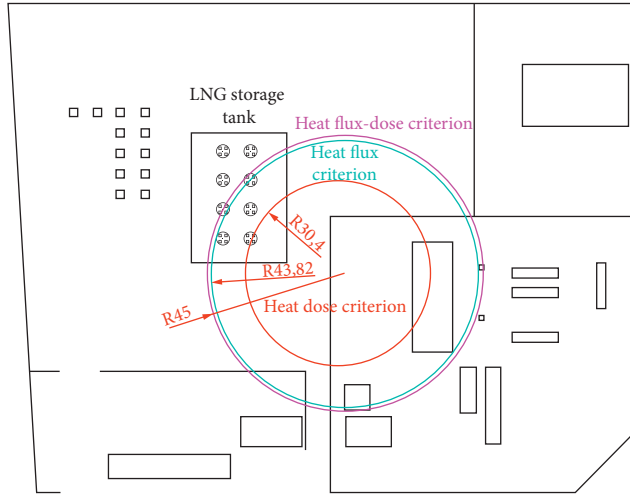


FIGURE 12: Influence range of heat dose, heat flux, and heat flux-heat dose criteria.

5.3. *VCE Analysis and Risk Assessment.* The range of combustible zone can be determined with the results of leakage. The simulated 3D cloud image of the VCE is shown in Figure 13.

In the 1970s, the United States ballistic research laboratory (BRL) and the naval weapons laboratory (NOL) proposed a set of damage criteria of blast wave, namely, the overpressure-impulse criteria [31]. They state that the overpressure and impulse of the detonation wave together determine whether and to what extent the target is damaged. If different combinations of overpressure and impulse satisfy certain conditions, they can cause the same degree of damage to the target. In this paper, the damage range of VCE was evaluated by using this criterion. The ordinate in Figure 14 [23] is the peak overpressure of the propagated blast wave, and the abscissa is the respective impulse. The curve is the equal-damage curve of the target, where the lines  $i_s = i_{s,cr}$  and  $\Delta P_s = \Delta P_{s,cr}$  are the asymptote of the equal-damage curve and  $i_{s,cr}$  and  $\Delta P_{s,cr}$  represent the critical impulse and critical overpressure of the target damage, respectively. The damage-free zone is to the left of the vertical asymptote and below the horizontal asymptote, while the damage zone is to the right of the vertical asymptote and above the horizontal asymptote. Based on the  $\Delta P - I$  damage criterion, Yan [34] fitted the  $P - I$  curves of severe injury, moderate injury, and minor injury according to the biological test results, and the corresponding calculation formula is as follows:

$$(\Delta P_s - 20)(i_s - 85)^{1.02} = C, \quad (11)$$

where  $C$  is a constant value and  $C$  values corresponding to serious injury, injury, and minor injury are  $4.9 \times 10^4$ ,  $2.3 \times 10^4$ , and  $1.0 \times 10^4$ , respectively. Critical overpressure is  $\Delta P_{s,cr} = 20 \text{ kPa}$ , and critical impulse is  $i_{s,cr} = 85 \text{ kPa} \cdot \text{s}$ .

The most vulnerable nonfatal organ of human body impacted by a blast wave is the ear, and the most vulnerable fatal organ is the lung [35]. The consequences of ear and lung injury can be analyzed based on the blast wave. For the probability variables of death from eardrum rupture and pulmonary hemorrhage, the formula which takes impulse into account was used [36]:

$$P_r = -12.6 + 1.524 \ln(\Delta P_s) \quad (\text{eardrum rupture}),$$

$$P_r = 5 - 5.74 \ln\left(\frac{4.2e^5}{P_{ef}} + \frac{1694}{I}\right) \quad (\text{pulmonary hemorrhage}), \quad (12)$$

where  $\Delta P_s$  is the peak overpressure,  $P_a$ ;  $P_r$  is the damage probability variable;  $I$  is the peak impulse,  $\text{Pa} \cdot \text{s}$ ; and  $P_{ef}$  is the effective overpressure, which is determined jointly with the body posture  $P_a$ . The calculation formula is as follows [31]:

$$P_{ef} = \Delta P_s + \frac{5(\Delta P_s)^2}{2\Delta P_s + 1.4 \times 10^6}. \quad (13)$$

Possible casualties can be projected for a steam cloud explosion by dividing the injury area into dead, serious, and minor area. The classification of explosion-related injuries is shown in Table 7.

The radius of eardrum rupture of 1% of the personnel is used as the dangerous distance of VCE to guide the reinforcement of key parts and the emergency evacuation of personnel. The calculated personnel damage radius is shown in Table 8. With the explosion point as the center, the dead areas, severely injured areas, and lightly injured areas were indicated, respectively, in the storage station, as shown in Figure 15. It can be found that almost the entire site is in the danger zone, and its influence range is greater than steam cloud diffusion and fire accidents.

5.4. *Combustion Product Impact.* The main component of LNG is methane, and the main toxic gas produced in the event of VCE and fire accident is carbon monoxide, which will kill people within 2-3 minutes if its concentration reaches 1.28% [37]. Compared with VCE and thermal radiation accident, the carbon monoxide impact lasts longer and is not easily detected by human body, which is a more dangerous accident. The distribution of carbon monoxide in VCE accident was simulated. The distribution is shown in



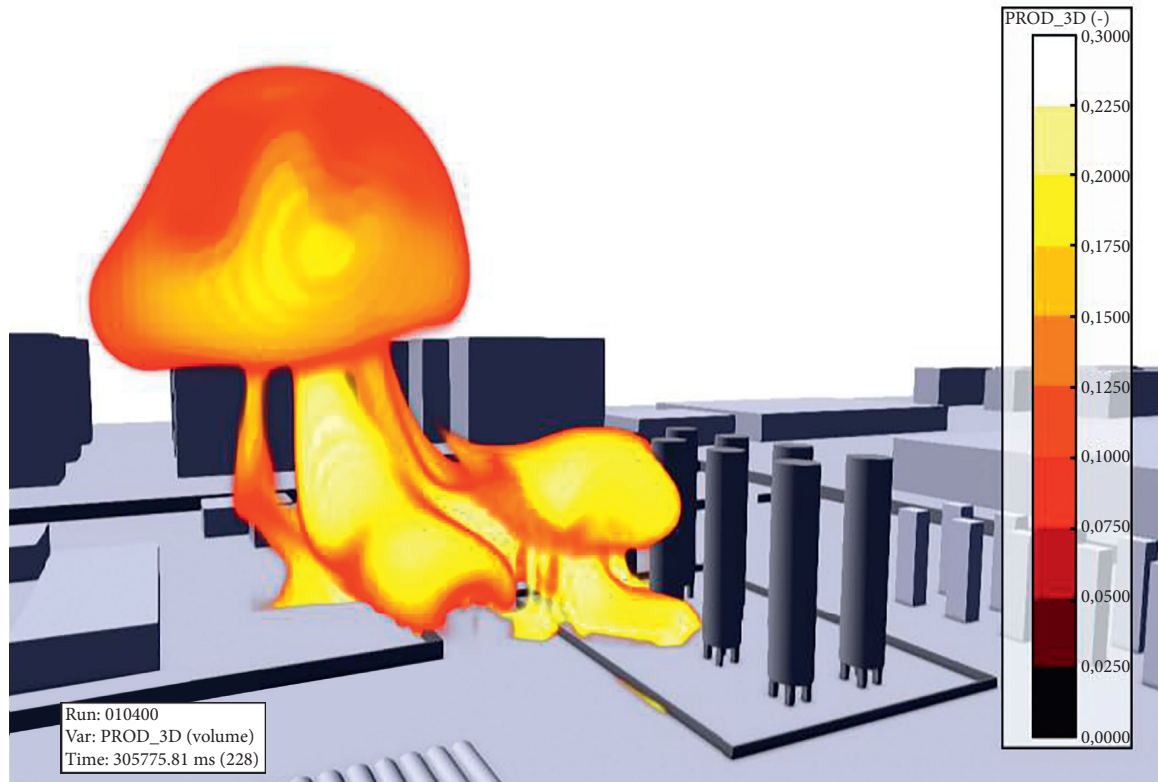


FIGURE 13: VCE effect image.

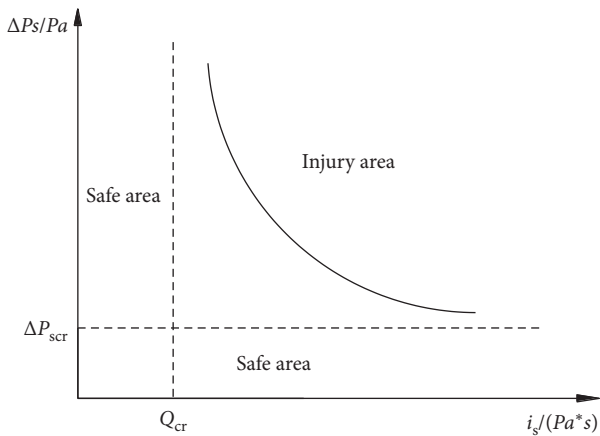


FIGURE 14: Overpressure-impulse criterion of blast wave damage.

TABLE 7: Classification of injuries caused by explosions.

Damage level	Personal injury
Death	Over 50% of people die from pulmonary hemorrhage
Seriously injured	Over 50% of people eardrums rupture
Minor injury	1% of people eardrums rupture

TABLE 8: Steam cloud explosion damage zone.

Type of damage	Dangerous distance/m
Personal injury radius	22.00
Death radius	39.70
Minor injury radius	106.98

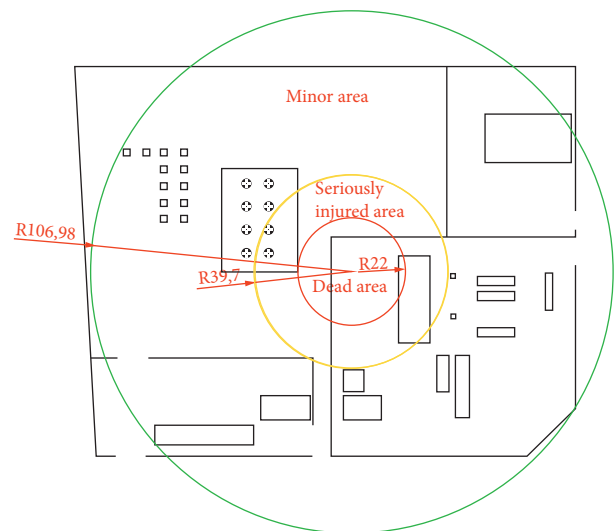


FIGURE 15: Explosion damage range calculated by overpressure-impulse criterion.

Figure 16. It can be seen that carbon monoxide can affect the area outside the station, the office building in the downwind is vulnerable, and the exit 2 is covered by the toxic. The

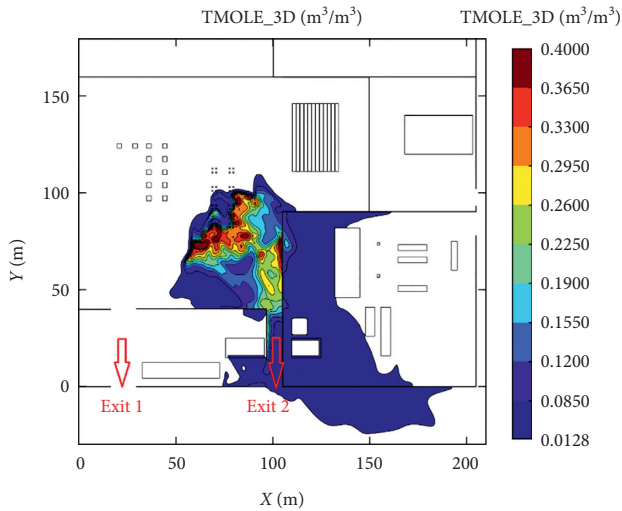


FIGURE 16: Distribution of toxic mole fraction (CO).

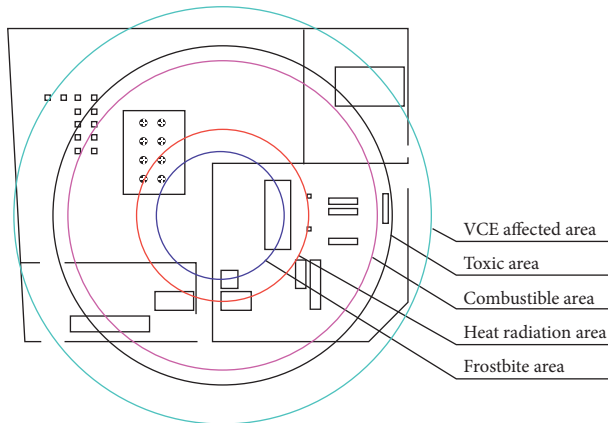


FIGURE 17: Comparison map of the impact scope of each disaster.

evacuation route should be determined according to the wind direction when organizing personnel to evacuate.

**5.5. Scope of Each Disaster.** Using comprehensive comparison VCE, toxic mole fraction, vapor cloud diffusion, heat radiation, and frostbite, we can see from Figure 17 that the VCE's sphere of influence is the largest of these five harms in this type of accident, followed by toxic mole fraction and vapor cloud diffusion, and the frostbite area the smallest. The impact of the VCE is the primary factor in formulating preventive measures and emergency plans.

## 6. Summary

LNG leakage will lead to a series of cascading accidents, such as cryogenic frostbite caused by factors such as LNG evaporation, steam cloud diffusion, explosion, fire, and toxic gas. The cascading accidents often have greater impact than the single disaster, so the assessment of LNG leakage requires a comprehensive analysis of all types of harmful events. We further improved the LNG leak assessment

method proposed by Baalisampan et al. Considering the wind speed, cryogenic frostbite, and the new personnel injury assessment method, the safety assessment method was applied to an LNG storage station in Xuzhou, China. Some conclusions are drawn as follows:

- (1) Wind can effectively accelerate the spread of LNG and reduce the areas of combustion and frostbite. A higher wind speed leads to a more obvious reduction. When the wind speed is 4 m/s, the combustible area reduces by 58.9% compared with that of 0 m/s, while when the wind speed reaches 8 m/s, the combustible area reduces by 93.0%, which shows that the wind speed is an important factor affecting diffusion.
- (2) Three criteria, heat flux, heat dose, and heat flux-heat dose, were employed to calculate the distances for personal injury in a fire. The range determined by the heat dose criterion is dangerous. The heat flux and the heat flux-heat dose criterion yield similar distances. Given the tedious calculation of the latter and the equivalent result, the heat flux method was recommended to use for the evaluation.
- (3) The overpressure-impulse criterion was employed and combined with the probability assessments. The radius in which 1% of the personnel experience eardrum rupture is denoted as the VCE dangerous distance.
- (4) The influence range of VCE, toxic mole fraction, vapor cloud diffusion, heat radiation, and frostbite were comprehensively compared. The influence range of VCE was the largest of all the cascade accidents.

## Data Availability

No additional data are available.

## Conflicts of Interest

The authors declare that they have no conflicts of interest.

## Acknowledgments

The authors acknowledge the financial support from the National Natural Science Foundation of China (Grant no. 51978166 and 51738011), the Fundamental Research Funds for the Central Universities, and Natural Science Foundation of Jiangsu Province of China (Grant no. BK20180081).

## References

- [1] C. Gao, B. Su, M. Sun, X. Zhang, and Z. Zhang, "Interprovincial transfer of embodied primary energy in China: a complex network approach," *Applied Energy*, vol. 215, pp. 792–807, 2018.
- [2] X. Q. Zhuang, *Numerical Simulation of Leakage Diffusion of Large Liquefied Natural Gas Storage Tank*, Wuhan University of Technology, Wuhan, China, 2012.
- [3] J. Wuertz, J. Bartzis, A. Venetsanos, S. Andronopoulos, J. Statharas, and R. Nijsing, "A dense vapour dispersion code

- package for applications in the chemical and process industry,” *Journal of Hazardous Materials*, vol. 46, pp. 273–284, 1996.
- [4] M. H. Faber and M. G. Stewart, “Risk assessment for civil engineering facilities: critical overview and discussion,” *Reliability Engineering & System Safety*, vol. 80, no. 2, pp. 173–184, 2003.
  - [5] P. H. Bittelberghs, “Risk analysis and safety policy developments in The Netherlands”” *Journal of Hazardous Materials*, vol. 71, no. 1-3, pp. 59–84, 2000.
  - [6] F. Ting, “Network communication analysis of emergencies in the new media era—a case study of “Xi’an 11-14 catering store explosion,”” *News Lovers*, no. 6, pp. 13–14, 2012.
  - [7] M. Kim, K. Chung, L.-D. Nguyen, B. Choi, and T. Kim, “New measurement method for vaporization velocity for spreading cryogenic liquid,” *Process Safety and Environmental Protection*, vol. 133, pp. 97–103, 2020.
  - [8] K. Wang, Y. He, Z. Liu, and X. Qian, “Experimental study on optimization models for evaluation of fireball characteristics and thermal hazards induced by LNG vapor cloud explosions based on colorimetric thermometry,” *Journal of Hazardous Materials*, vol. 366, pp. 282–292, 2019.
  - [9] X. Yi, C. Lei, J. Deng et al., “Numerical simulation of fire smoke spread in a super high-rise building for different fire scenarios,” *Advances in Civil Engineering*, vol. 2019, Article ID 1659325, 11 pages, 2019.
  - [10] M. Dadashzadeh, F. Khan, R. Abbassi, and K. Hawboldt, “Combustion products toxicity risk assessment in an offshore installation,” *Process Safety and Environmental Protection*, vol. 92, no. 6, pp. 616–624, 2014.
  - [11] T. Baalisampang, R. Abbassi, V. Garaniya, F. Khan, and M. Dadashzadeh, “Modelling an integrated impact of fire, explosion and combustion products during transitional events caused by an accidental release of LNG,” *Process Safety and Environmental Protection*, vol. 128, pp. 259–272, 2019.
  - [12] D. Lv, W. Tan, L. Liu, G. Zhu, and L. Peng, “Research on maximum explosion overpressure in LNG storage tank areas,” *Journal of Loss Prevention in the Process Industries*, vol. 49, pp. 162–170, 2017.
  - [13] Z. Li, J. Wu, M. Liu, Y. Li, and Q. Ma, “Numerical analysis of the characteristics of gas explosion process in natural gas compartment of utility tunnel using FLACS,” *Sustainability*, vol. 12, no. 1, p. 153, 2020.
  - [14] S. Ren, “The leakage, low temperature diffusion and explosion of liquefied natural gas in open space,” *Baozha Yu Chongji*, vol. 38, pp. 891–897, 2018.
  - [15] J.-Q. Hu, R.-H. Wang, and L.-B. Zhang, “Topological network inversion method of fire source location for liquefied natural gas (LNG) storage,” *Procedia Engineering*, vol. 211, pp. 247–255, 2018.
  - [16] Q. Bao, Q. Fang, S. Yang et al., “Experimental investigation on the deflagration load under unconfined methane-air explosions,” *Fuel*, vol. 185, pp. 565–576, 2016.
  - [17] Z. Li, L. Chen, Q. Fang, W. Chen, H. Hao, and Y. Zhang, “Experimental and numerical study of basalt fiber reinforced polymer strip strengthened autoclaved aerated concrete masonry walls under vented gas explosions,” *Engineering Structures*, vol. 152, pp. 901–919, 2017.
  - [18] Z. Li, L. Chen, Q. Fang et al., “Study of autoclaved aerated concrete masonry walls under vented gas explosions,” *Engineering Structures*, vol. 141, pp. 444–460, 2017.
  - [19] Z. Li, L. Chen, Q. Fang et al., “Experimental and numerical study of unreinforced clay brick masonry walls subjected to vented gas explosions,” *International Journal of Impact Engineering*, vol. 104, pp. 107–126, 2017.
  - [20] Z. Li, L. Chen, Q. Fang et al., “Experimental and numerical study on CFRP strip strengthened clay brick masonry walls subjected to vented gas explosions,” *International Journal of Impact Engineering*, vol. 129, pp. 66–79, 2019.
  - [21] “Fires, explosions, and toxic gas dispersions: effects calculation and risk analysis 2010,” *Process Safety Progress*, vol. 31, no. 3, p. 319, 2012.
  - [22] A. Soman and G. Sundararaj, “Consequence assessment of vapour cloud explosion involving hydrogen release,” *International Journal of Emerging Technology and Advance Engineering*, vol. 11, no. 2, pp. 291–296, 2012.
  - [23] S. G. Yang, *Theoretical and Numerical Simulation Research on the Risk of Leakage of Salt Rock Gas Reservoir*, PLA Army Engineering University, Nanjing, China, 2013.
  - [24] Z. P. Meng, S. L. Wang, and X. W. Ding, “Three-dimensional numerical simulation of combustible gas leakage and diffusion near obstacles,” *Chemical Equipment Technology*, vol. 28, no. 02, pp. 74–78, 2007.
  - [25] J. C. Jiang and X. H. Pan, *Theory and Application of Chemical Process Safety*, Chemical Industry Press, Beijing, China, 2006.
  - [26] Z. Q. Wang, *Study on Leakage Model of High-Pressure Gas Pipeline and Regional Analysis of its Consequences*, China University of Geosciences, Beijing, China, 2009.
  - [27] J. M. Hao, G. D. Ma, and S. X. Wang, *Air Pollution Control Engineering*, Higher Education Press, Beijing, China, 2010.
  - [28] X. H. Cui, *The Risk Analysis of Natural Gas Tank Leakage and Diffusion and Numerical Simulation*. Xi’an, Xi’an University of Science and Technology, 2017.
  - [29] F. P. Lees, *Loss Prevention in the Process Industries-Hazard Identification, Assessment, and Control*, Vol. 2, Butterworth-Heinemann, Oxford, UK, 2nd edition, 1996.
  - [30] R. Huo, Z. H. Yang, and J. X. Liu, *Fire and Explosion Prevention and Control Engineering*, Machinery Industry Press, Beijing, China, 2007.
  - [31] D. M. Yu, *Quantitative Risk Assessment of Storage and Transportation of Inflammable, Explosive and Toxic Dangerous Goods*, China Railway Publishing House, Beijing, China, 2000.
  - [32] R. Pula, F. I. Khan, B. Veitch, and P. R. Amyotte, “A grid based approach for fire and explosion consequence analysis,” *Process Safety and Environmental Protection*, vol. 84, no. B2, pp. 79–91, 2006.
  - [33] J. LaChance, A. Tchouvelev, and A. Engebo, “Development of uniform harm criteria for use in quantitative risk analysis of the hydrogen infrastructure,” *International Journal of Hydrogen Energy*, vol. 36, no. 3, pp. 2381–2388, 2011.
  - [34] F. Yan, *Power Evaluation and Temperature Field Measurement of Fuel Air Explosives*, Nanjing University of Science and Technology, Nanjing, China, 2005.
  - [35] W. E. Baker, P. A. Cox, P. S. Westine, J. J. Kulesz, and R. A. Strehlow, *Explosion Hazards and Evaluation*, Elsevier Scientific Publishing Company, New York, NY, USA, 1983.
  - [36] F. D. Alonso, E. G. Ferradás, T. D. J. J. Sánchez, A. M. Aznar, J. R. Gimeno, and J. M. Alonso, “Consequence analysis to determine the damage to humans from vapour cloud explosions using characteristic curves,” *Journal of Hazardous Materials*, vol. 150, no. 1, pp. 146–152, 2008.
  - [37] T. Struttman, A. Scheerer, T. S. Prince, and L. A. Goldstein, “Unintentional carbon monoxide poisoning from an unlikely source,” *The Journal of the American Board of Family Medicine*, vol. 11, no. 6, pp. 481–484, 1998.

## Research Article

# Experimental Investigation on Strength and Deformation Characteristics of Red Sandstone at Strain Rates of $10^{-2} \sim 55 \text{ s}^{-1}$

Jie Shi,<sup>1</sup> Zongmu Luo ,<sup>2</sup> Huachao Liu ,<sup>1</sup> Dan Wang,<sup>1</sup> Haipeng Shen,<sup>3</sup> and Zeng Li<sup>2</sup>

<sup>1</sup>National Defense School, Army Engineering University of PLA, Nanjing 210007, China

<sup>2</sup>State Key Laboratory of Disaster Prevention and Mitigation of Explosion and Impact, Army Engineering University of PLA, Nanjing 210007, China

<sup>3</sup>School of Field Engineering, Army Engineering University of PLA, Nanjing 210007, China

Correspondence should be addressed to Zongmu Luo; [langdon0114@163.com](mailto:langdon0114@163.com) and Huachao Liu; [273750748@qq.com](mailto:273750748@qq.com)

Received 6 May 2020; Revised 11 June 2020; Accepted 3 August 2020; Published 13 August 2020

Academic Editor: Yanchao Shi

Copyright © 2020 Jie Shi et al. This is an open access article distributed under the Creative Commons Attribution License, which permits unrestricted use, distribution, and reproduction in any medium, provided the original work is properly cited.

The mechanical properties of rocks under low to intermediate strain rate are of great importance for seismic engineering, rock impact, and blasting excavation. To study the strength and deformation characteristics of sandstone subjected to low-medium speed impact loading, the complete stress-strain relationships of uniaxial compression at strain rates of  $10^{-2} \sim 55 \text{ s}^{-1}$  were obtained utilizing MTS and drop weight impact test devices. It is indicated that the dynamic compressive strength of sandstone in the range of intermediate strain rate increases approximately linearly with the strain rate under the quasi-static loading condition, while increasing nonlinearly under the dynamic loading condition. The deformation and fracture process of sandstone still consists of pore compaction stage, elastic deformation stage, instable microcrack propagation stage, and brittle fracture stage. The peak stress, critical strain, and residual strain increase with an increase in the strain rate, and the corresponding fracture mode changes from shear failure to split failure. The evolution law of total absorbed strain energy with deformation coincides with that of stored elastic strain energy for sandstone at the intermediate strain rate. The effect of the strain rate on elastic strain energy is more significant than that of dissipated strain energy. Furthermore, both the brittleness and fracture degree of sandstone become more remarkable with the strain rate increasing.

## 1. Introduction

Dynamic rock mechanics involves the strength and deformation behavior of rock-like materials (e.g., rock and concrete) subjected to dynamic impacts. In general, the mechanical properties and fracture behavior of materials change with an increase in the loading rate. The sources of dynamic loads originate from explosion, shock, and earthquake vibration. In fact, rock engineering often involves the dynamic loading scenarios, such as excavation engineering, civil engineering, blasting engineering, projectile impact, seismic events, and rock collapse. The loading rate is an important index corresponding to different velocities of impacts for rock medium. It is well recognized that different rocks may exhibit diverse mechanical responses with the change of the strain rate [1]. The range of the strain

rate can be roughly divided into low strain rate (LSR:  $10^{-5} \sim 10^{-2} \text{ s}^{-1}$ ), intermediate strain rate (ISR:  $10^{-2} \sim 10^2 \text{ s}^{-1}$ ), high strain rate (HSR:  $10^2 \sim 10^4 \text{ s}^{-1}$ ), and ultrahigh strain rate (UHSR: higher than  $10^4 \text{ s}^{-1}$ ). Figure 1 shows a variety of experimental equipment for the application of the above strain rate range. For decades, considerable efforts have been made on the strain rate effect on mechanical properties of various rocks and its underlying physical mechanisms. Huang and Liu [2] carried out low loading rate loading experiments on coal and rock. The results showed that the increase of the strain rate caused more serious damage to the internal structure of coal and rock. Grote et al. [3], Zhang and Zhao [4], and Ma et al. [5, 6] performed low-speed and high-speed impact tests on rocks in the strain rate ranges of  $10^{-5} \sim 10^{-2} \text{ s}^{-1}$  and  $10^1 \sim 10^2 \text{ s}^{-1}$  with the hydraulic testing machine and the large-diameter SHPB test apparatus,



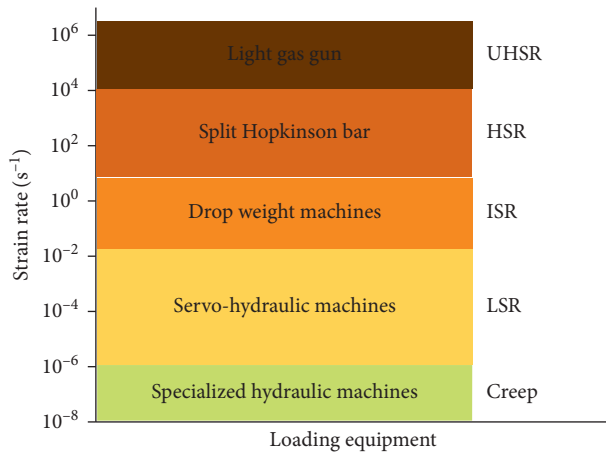


FIGURE 1: Classification of strain rate and loading equipment.

respectively. It is indicated that rock materials present obvious strain rate hardening effect, that is, the peak strength, strain, and elastic modulus of the rock constantly increase with the strain rate increasing. Shang et al. [7] obtained the material state equation of granite by conducting plate impact test on granite at ultrahigh strain rate of  $10^5 \sim 10^6 \text{ s}^{-1}$ .

It is of great significance for the prevention and control of underground engineering disasters such as blasting shock, rock burst, and mine vibration in sandstone medium. It is generally believed that the dynamic strength and cohesion of sandstone are positively correlated with the loading strain rate and the internal friction angle is negatively correlated with the loading strain rate, whereas the effect of the strain rate on elastic modulus is not evident [8–10]. Under the condition of biaxial stress, the dynamic compressive strength of sandstone increases with the increase of strain rate and prestress  $\sigma_2$ , while it decreases with the increase of prestress  $\sigma_1$  [11]. In the case of triaxial stress, the dynamic compressive strength of sandstone increases linearly with the increase of confining pressure, and the secant modulus also increases with the increase of confining pressure [9]. In addition, Zhou et al. [12] explored the effect of saturated water on dynamic fracture of sandstone. The study showed that free water had a delayed effect on crack propagation speed. Under the same loading rate, the dynamic initiation toughness and expansion toughness of saturated samples were significantly lower than that of dry samples, while the energy absorbed by them was also lower than that of dry samples. Zhang et al. [13] and Luo et al. [14] analyzed the dynamic mechanical characteristics of sandstone under cyclic freezing-thawing conditions. It is indicated that the dynamic compressive strength decreases exponentially with an increase in freezing-thawing times, while it increases linearly with the strain rate increasing. The brittleness of sandstone increases with an increase in freezing-thawing times. Liu and Xu [15] investigated the effect of the strain rate on dynamic compression mechanical behavior of sandstone at high temperature. The results prove that the enhancement of the strain rate on dynamic compressive strength, critical strain, and energy absorption ratio still exists at high temperature, but the effect on elastic modulus

is not obvious. Liu et al. [16] investigated the propagation of shock wave in wet and dry sandstone. The study reveals that the velocity of shock wave in sandstone increases linearly with an increase in impact velocity under the same water content. Free water increases the velocity of the shock wave in the material.

As aforementioned, current research on the mechanical properties of rock-like materials in the high strain rate and the low strain rate regime is relatively systematic, while there are few reports regarding the mechanical behavior of rocks in the range of the intermediate strain rate due to the limitations of experimental devices and technologies. In this paper, uniaxial compression loading experiments within the strain rate range of  $10^{-2} \sim 55 \text{ s}^{-1}$  were carried out on sandstone samples using MTS hydraulic test and INSTRON drop weight impact test apparatus. The complete stress-strain relationships of red sandstone at different strain rates are obtained to estimate the effect of the loading strain rate on the peak strength, deformation, failure mode, energy dissipation, and brittleness.

## 2. Experimental Procedure

**2.1. Sample Preparation.** The tested sandstone were derived from a quarry in Linyi, Shandong province, China. To facilitate transportation, the sandstone was exploited at a depth of 20 m and cut into plate with the sizes of  $1000 \times 400 \times 100 \text{ mm}^3$ . The cylinder samples with diameters of 50 mm and 30 mm were then cored with a rock coring machine. The end face and circumference of the samples were carefully polished with a grinding machine to make the end face parallel error and side vertical error meet the experimental requirements. Finally, the standard cylinder sample [17] with dimensions of  $\Phi 50 \text{ mm} \times 100 \text{ mm}$  and  $\Phi 30 \text{ mm} \times 60 \text{ mm}$  were prepared for the quasi-static uniaxial compression test and dynamic impact compression test.

**2.2. Experimental Equipment and Program.** The quasi-static uniaxial compression test was carried out with the MTS647.250 servo-hydraulic material testing device (Figure 2(a)). The maximum axial loading force is 2500 kN, and the measurement error of deformation and loading force is less than 1%. The displacement loading mode was adopted and the loading speed was set at 1 mm/s and 10 mm/s in quasi-static compression test, respectively. According to the time-history curves of force and displacement monitored by the testing system, the stress-strain curves of the samples under quasi-static compression can be obtained. The INSTRON (CEAST 9350) drop weight impact apparatus (Figure 2(b)) was used for dynamic compression test. The initial height of the hammer can be set between 0.3 m and 1.1 m to achieve an impact speed range between 0.77 m/s and 24 m/s. In the impact loading test, two different hammers of 16.175 kg and 21.175 kg were selected with impact velocities of 2.5 m/s, 3 m/s, 3.5 m/s, and 4 m/s, respectively. In the center of the sample, the resistance strain gauges connected to the dynamic strain instrument were pasted along the axial and circular direction. The stress-strain curve of the



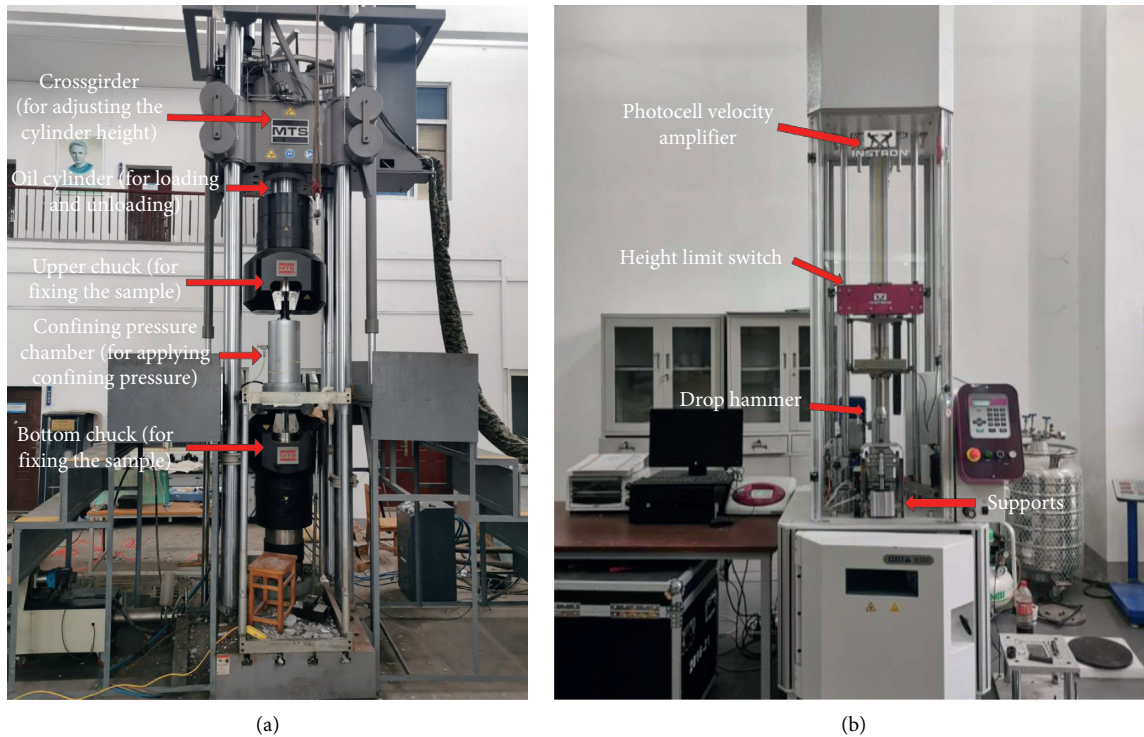


FIGURE 2: Experiment apparatus. (a) MTS 647.250 testing machine. (b) Drop weight impact testing machine.

specimen under dynamic compression can be derived by combining the stress time-history curve collected by the force sensor on the hammer and the strain time-history curve collected by the dynamic strain instrument. Meanwhile, a high-speed camera was used to record the macroscopic crack development process of samples under impact loads. Sandstone samples with similar density and porosity were chosen to reduce the discreteness of experimental data.

### 3. Results and Discussion

**3.1. Characteristics of Stress-Strain Curve.** Figure 3 presents the complete stress-strain relationships of sandstone samples selected for the quasi-static compression test at the strain rate of  $10^{-2} \text{ s}^{-1}$  and  $10^{-1} \text{ s}^{-1}$ . Figure 4 depicts the stress-strain curves of eight sandstone samples selected for the drop weight impact compression test with different hammer weights at different intermediate strain rates.

It can be seen from Figure 3 that the deformation process of sandstone under compression has undergone pore compaction stage, elastic deformation stage, instable fracture propagation stage before failure, and the descending stage after failure. By comparing the curves at two loading strain rates, it can be found that the pore compaction stages basically coincide under quasi-static loading since the samples were prepared with similar initial density, porosity, and other physical properties. Meanwhile, the elastic deformation stage of different samples is also similar, implying the strain rate has no remarkable influence on the elastic modulus of sandstone in the range of

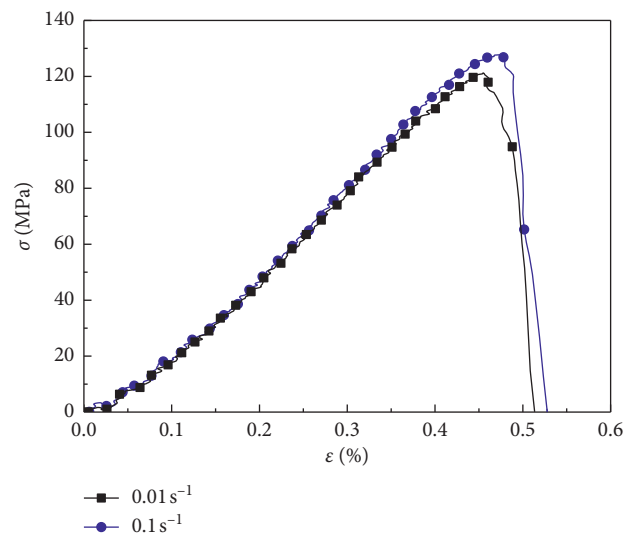


FIGURE 3: Stress-strain curves at different strain rates under quasi-static compression.

$10^{-2} \sim 10^{-1} \text{ s}^{-1}$ . The peak strength of sandstone at strain rate of  $10^{-1} \text{ s}^{-1}$  is about 6.5 MPa higher than that of at strain rate of  $10^{-2} \text{ s}^{-1}$ . The critical strain of sandstone at strain rate of  $10^{-1} \text{ s}^{-1}$  is also 1.8% larger than that of at strain rate of  $10^{-2} \text{ s}^{-1}$ . As can be seen in Figure 4, the elastic deformation stage under impact load is discrete. The average measured elastic modulus is about 18.13 GPa, which is smaller than that under quasi-static compression. This may be because the measured axial strain is

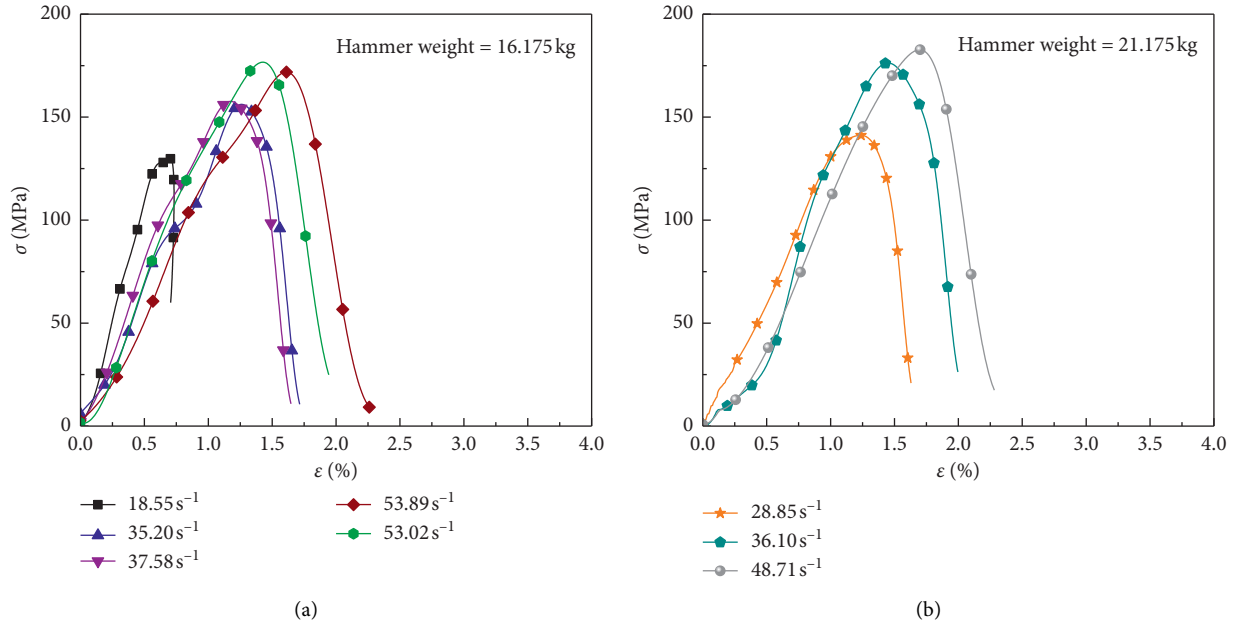


FIGURE 4: Stress-strain curves at different strain rates under dynamic compression.

larger than the actual one, resulting in a smaller elastic modulus. The steep descent section after failure demonstrates the brittle failure characteristics of sandstone. The peak stress exhibits an obvious rising trend with an increase in the strain rate, which indicates that the compressive strength also has a significant rate effect in intermediate strain rate zone. Compared with Figures 4(a) and 4(b), hammer weight also affects the peak stress of sandstone. Under similar strain rate, the increase of hammer weight leads to an increase in peak stress, which is because the greater the weight of the hammer is, the more energy is transferred to the sample.

**3.2. Effect of Strain Rate on Compressive Strength.** Figure 5 shows the relation of the compressive strength of sandstone and loading strain rate in the range of  $10^{-2} \sim 55 \text{ s}^{-1}$ . It can be seen that the compressive strength gradually increases with an increase in the strain rate, indicating that the compressive strength has an obvious strain rate effect, which is consistent with the findings by [18–20]. With the increase of the strain rate, the number of cracks in the failure process increases and the absorbed energy increases, while the crack propagation lags behind the loading speed. According to the impulse theorem, the delayed deformation leads to stress enhancement, which leads to the final improvement of dynamic compressive strength. The underlying physical mechanisms of the strain rate effect of materials are from the perspectives of inertia effect [21], Stefan viscosity effect [22], dynamic fracture effect [23], and thermal activation effect [24].

The ratio of dynamic compressive strength to uniaxial compressive strength at  $10^{-2} \text{ s}^{-1}$  strain rate was defined as the dynamic increase factor (DIF). The strength data tested at the intermediate strain rate was plotted in the monologarithmic coordinate, as shown in Figure 6. It is seen that, with the increase of the strain rate, the dependence of

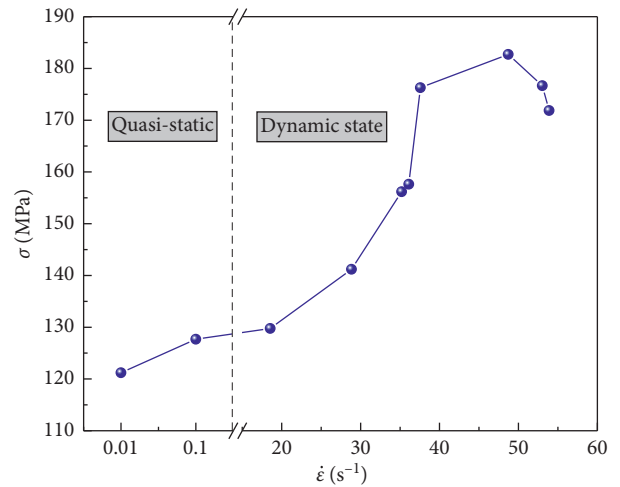


FIGURE 5: Relationship between compressive strength and strain rates.

compressive strength on the strain rate gradually increases. As the strain rate exceeds  $10^1 \text{ s}^{-1}$ , the DIF value rapidly increases from 1.08 to 1.47. Considering that the different rate sensitivity of DIF under quasi-static condition and dynamic condition, the linear and binomial functions are utilized to describe the relationship:

$$\begin{cases} \text{DIF} = 1.06 + 0.02 \lg \dot{\epsilon}, & 10^{-2} \text{ s}^{-1} \leq \dot{\epsilon} < 18.55 \text{ s}^{-1}, \\ \text{DIF} = 0.74 - 0.15 \lg \dot{\epsilon} + 0.33 (\lg \dot{\epsilon})^2, & 18.55 \text{ s}^{-1} \leq \dot{\epsilon} < 53.89 \text{ s}^{-1}. \end{cases} \quad (1)$$

**3.3. Effect of Strain Rate on Failure Mode.** Figure 7 shows the development law of the deformation with the change of the strain rate. Most of the critical strain and residual strain

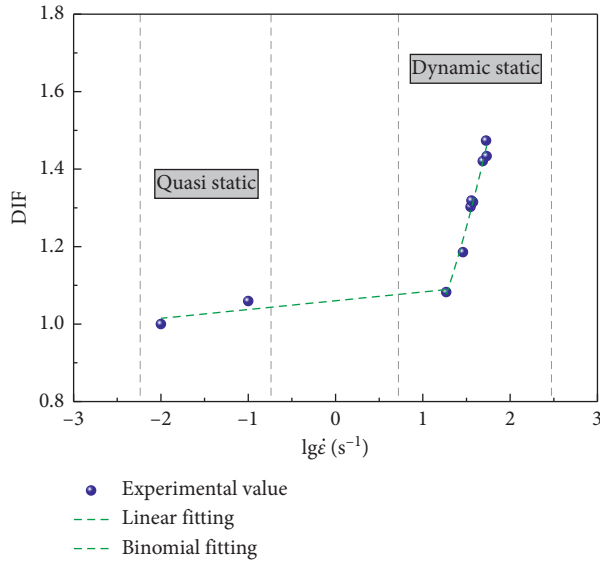


FIGURE 6: Strain rate effect on the uniaxial compressive strength.

under dynamic impact exceed 1%. The strain increases nonlinearly with the increase of the strain rate, which is consistent with the considerable experimental results summarized by Bischoff and Perry [25]. To be more specific, the critical strain increases from 0.46% to 1.71%, while the residual strain increases from 0.5% to 2.36%.

The failure mode of rock under compression is a complex phenomenon which has not yet been properly explained with a standard mechanical model. Szwedzicki [26] divided rock failure into five modes: single tensile, single shear, multitensile, multishear, and complex fracture. Through considerable experimental studies, Ramsey and Chester [27] believe that rock compression failure can be divided into five modes: splitting failure, tensile shear failure, shear failure, dilatation failure, and bulging failure. They point out that rock failure mode transforms with the change of loading condition. That is, the failure mode of sandstone is affected by the strain rate.

Figure 8 depicts the failure modes of sandstone samples at different strain rates. Figures 8(a)–8(c) show that the failure mode of sandstone under quasi-static compression is mainly shear failure. At strain rate of  $10^{-2} \text{ s}^{-1}$ , the sample presents unilateral conjugate oblique shear failure, and there are several unpenetrated fractures in the longitudinal direction, and the failure block is relatively complete. At the strain rate of  $10^{-1} \text{ s}^{-1}$ , the sample presents x-shaped conjugate oblique shear failure, and the sample forms failure cones on the upper and lower part. The peeling part is relatively broken. Figures 8(d)–8(e) show that the failure mode of sandstone under dynamic compression is mainly split failure. Besides, the higher the failure strain rate is, the higher the failure degree is. It is also founded that, as the loading state changes from quasi-static to dynamic compression, the failure mode changes from shear failure to split failure.

**3.4. Effect of Strain Rate on Energy Evolution.** The process of rock deformation and failure is essentially the process of energy evolution in rock. The energy absorbed by the rock

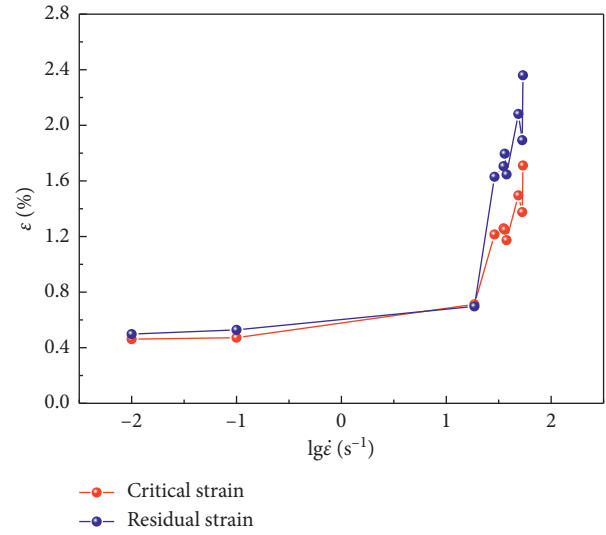


FIGURE 7: Relationship between deformation and logarithmic form of the strain rate.

during compression can be divided into recoverable elastic strain energy and unrecoverable dissipated strain energy, of which the elastic strain energy is for the elastic deformation, while the dissipated strain energy mainly consumes for the generation and development of internal microcracks [28, 29]. Under uniaxial compression, the strain energy density of each component is calculated as follows [29]:

$$\begin{aligned}
 U &= \int_0^{\varepsilon} \sigma(\varepsilon) d\varepsilon, \\
 U_E &= \frac{1}{2E} \sigma^2, \\
 U_D &= \int_0^{\varepsilon} \sigma(\varepsilon) d\varepsilon - \frac{1}{2E} \sigma^2,
 \end{aligned} \tag{2}$$

where  $U$ ,  $U_E$ , and  $U_D$  are the total strain energy density, elastic strain energy density, and dissipated strain energy density, respectively.  $\sigma(\varepsilon)$  is a stress-strain function.  $E$  is the unloading modulus, which is replaced by the elastic modulus when calculating.

Figure 9 presents the evolution law of each component strain energy development of sandstone at strain rates of  $10^{-2} \text{ s}^{-1}$ ,  $10^{-1} \text{ s}^{-1}$ ,  $18.55 \text{ s}^{-1}$ , and  $53.89 \text{ s}^{-1}$  with respect to deformation. It indicated that the elastic strain energy stored in the sample increases continuously with the compression process before failure, while the dissipated strain energy changes little at a low level. When the stress reached its peak, the stored elastic strain energy is released abruptly and dissipated strain energy increases rapidly. Different from quasi-static compression, the dissipated strain energy before failure displays an obvious trend of growth in the dynamic compression process, which indicates that the stage of fracture instability is more obvious in the dynamic compression. By observing Figure 9(c), one may find that the stored elastic strain energy was not fully released after the compression process due to the incomplete failure of the sample. It is consistent with the monitored stress-strain curve.

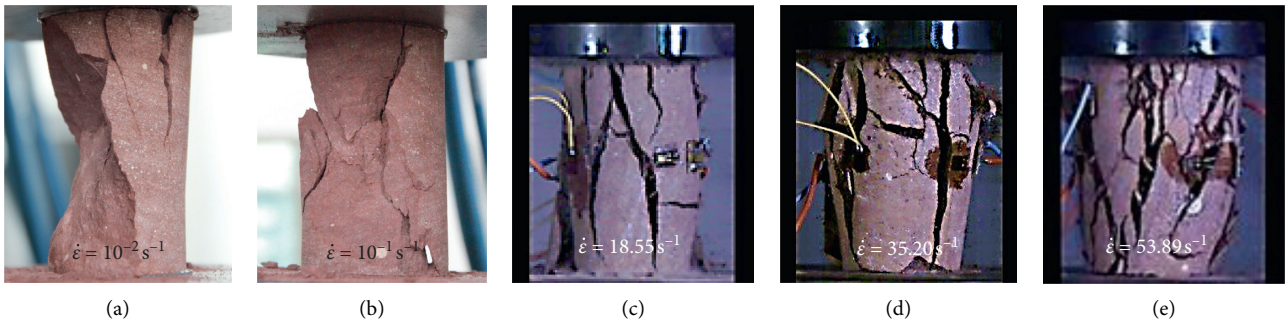


FIGURE 8: Failure mode of sandstone at different strain rates.

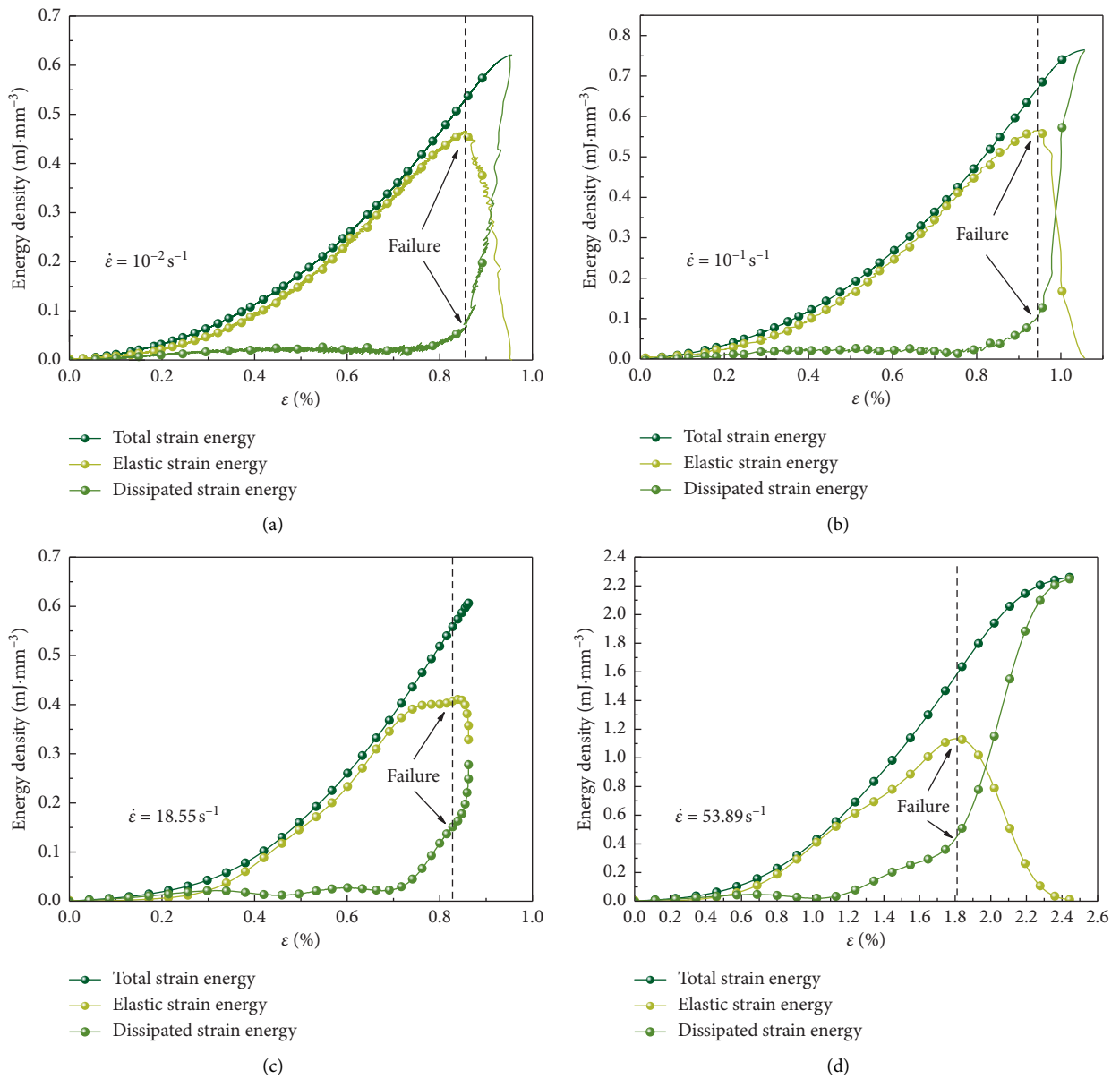


FIGURE 9: Energy evolution curves of sandstone samples at different strain rates.



Figure 10 shows the total strain energy, elastic strain energy, and dissipated strain energy of sandstone at failure time at different strain rates. It can be seen that, in the strain rate range of  $10^{-2} \sim 55 \text{ s}^{-1}$ , the total strain energy and elastic strain energy increase significantly with the increase of the strain rate. Specifically, the total strain energy and elastic strain energy increase from  $0.53 \text{ mJ/mm}^3$  and  $0.44 \text{ mJ/mm}^3$  to  $1.69 \text{ mJ/mm}^3$  and  $1.43 \text{ mJ/mm}^3$ , respectively. With the increase of the loading rate, the total energy absorbed in the sample increases and the elastic unit number stored in the sample also increases abruptly, resulting in the increase of elastic strain energy [30]. The effect of the strain rate on dissipated strain energy is not obvious. The value of dissipated strain energy fluctuates in the range of  $0 \sim 0.4 \text{ mJ/mm}^3$ . Furthermore, the proportion of elastic strain energy and dissipated strain energy is depicted in Figure 11. It is found that the ratio of elastic strain energy and dissipated strain energy to total strain energy reflects strong discreteness at the intermediate strain rate. However, in general, with an increase in the strain rate, the proportion of elastic strain energy decreases while that of dissipated strain energy increases. Specifically, the proportion of dissipated strain energy fluctuates between 10% and 30%, indicating that when the lithology and fracture conditions of the samples are similar, the strain rate has little influence on it.

**3.5. Effect of Strain Rate on Brittleness.** Brittleness is one of the important mechanical indexes of rock medium, whereas the evaluation standard of brittleness is not uniform. Many scholars put forward more than 20 brittleness indexes in total from the perspectives of mineral composition, strength ratio, and energy dissipation. To assess the brittleness of sandstone under impact loads, the brittleness index proposed by Baron [31] from the perspective of energy is adopted for its calculation as follows:

$$B = \frac{W_E}{W}, \quad (3)$$

where  $W$  is the total energy in the compression process and  $W_E$  is the recoverable elastic energy. The smaller the ratio of elastic energy to total energy is, the more energy is used for destruction, which leads to the more obvious brittleness of rocks.

Figure 12 displays the change of brittleness index with the strain rate under impact loading. It can be seen that the brittleness index of sandstone decreases with the increase of strain rate within the range of  $15 \sim 55 \text{ s}^{-1}$ , indicating that the brittleness is more obvious with the strain rate increasing. The effect of the strain rate on brittleness is closely related to energy dissipation and release during deformation and failure. With an increase in the loading strain rate, the energy consumed for fracture development increases, and the

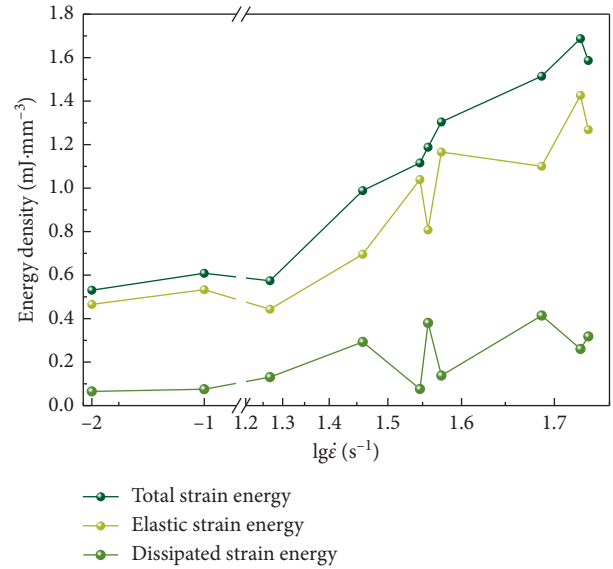


FIGURE 10: Strain rate effect on the strain energy of tested sandstone.

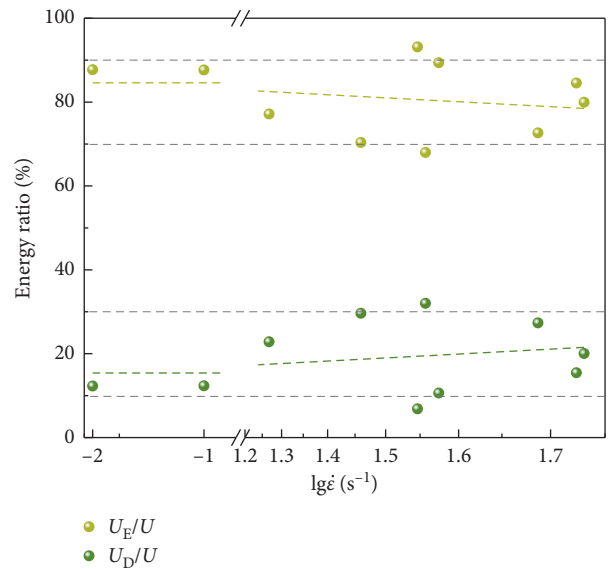


FIGURE 11: Relationship between the energy ratio and strain rate.

energy is released more dramatically during the failure, resulting in the increase of fracture degree. By fitting the experimental data, the empirical formula for the brittle index with respect to the strain rate at the intermediate strain rate is formulated:

$$B = 0.73 - 2.99 \times 10^{-4} e^{(\dot{\epsilon}/10.87)} - 2.99 \times 10^{-4} e^{(\dot{\epsilon}/12.08)} - 2.99 \times 10^{-4} e^{(\dot{\epsilon}/13.29)}. \quad (4)$$



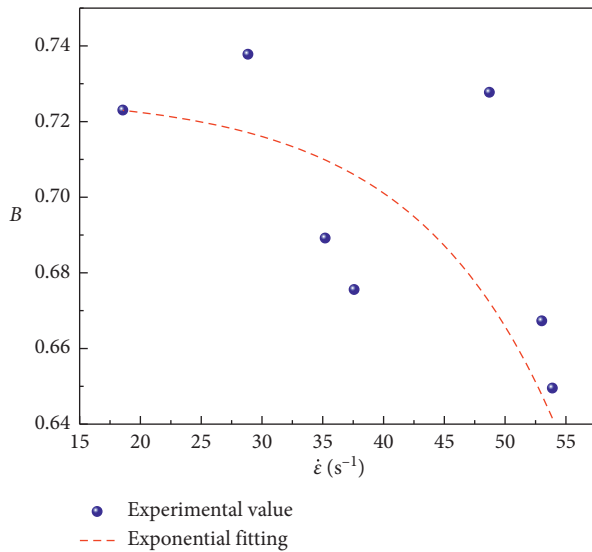


FIGURE 12: Strain rate effect on the brittleness index.

#### 4. Conclusion

The uniaxial compression tests were carried out with MTS and drop weight impact testing machine on sandstone in the medium strain rate range of  $10^{-2} \sim 55 s^{-1}$ . The following main conclusions were obtained as follows.

The deformation and failure of sandstone under compression at the intermediate strain rate undergoes pore compaction stage, elastic deformation stage, instable fracture prepeak propagation stage, and postpeak descending stage. The critical strain and residual strain exhibit an increasing trend with the increase of the strain rate.

The strain rate has an evident effect on the compressive strength of sandstone. The compressive strength increases linearly with the strain rate under the quasi-static condition and increases under the dynamic condition. The failure mode of sandstone is closely related to the loading strain rate. As the loading mode changes from quasi-static to dynamic, the failure mode turns from shear failure to split failure.

The strain rate has an effect on the elastic strain energy and dissipated strain energy at failure time during energy evolution. Both elastic strain energy and dissipated strain energy increase with an increase in the strain rate, and the elastic strain energy is more sensitive to the loading strain rate than the dissipated strain energy. When the lithology and fracture conditions are similar, the strain rate has little influence on the proportion of dissipated strain energy to total strain energy.

The failure of sandstone is a typical brittle failure. The brittle characteristics of sandstone become more remarkable with the increase of the strain rate, accompanied with a higher degree of fracture.

#### Data Availability

All data used to support the findings of this study are available from the first author upon request.

#### Disclosure

Jie Shi and Zongmu Luo are first authors.

#### Conflicts of Interest

The authors declare that there are no conflicts of interest regarding the publication of this paper.

#### Acknowledgments

This work was financed and fully supported by the National Natural Science Foundation of China (Grant nos. 51774295 and 51808551), which are greatly appreciated by the authors.

#### References

- [1] Q. B. Zhang and J. Zhao, "A review of dynamic experimental techniques and mechanical behaviour of rock materials," *Rock Mechanics and Rock Engineering*, vol. 47, no. 4, pp. 1411–1478, 2014.
- [2] B. Huang and J. Liu, "The effect of loading rate on the behavior of samples composed of coal and rock," *International Journal of Rock Mechanics and Mining Sciences*, vol. 61, pp. 23–30, 2013.
- [3] D. L. Grote, S. W. Park, and M. Zhou, "Dynamic behavior of concrete at high strain rates and pressures: I. experimental characterization," *International Journal of Impact Engineering*, vol. 25, no. 9, pp. 869–886, 2001.
- [4] Q. B. Zhang and J. Zhao, "Quasi-static and dynamic fracture behaviour of rock materials: phenomena and mechanisms," *International Journal of Fracture*, vol. 189, no. 1, pp. 1–32, 2014.
- [5] L. Ma, Z. Li, J. Liu, L. Duan, and J. Wu, "Mechanical properties of coral concrete subjected to uniaxial dynamic compression," *Construction and Building Materials*, vol. 199, pp. 244–255, 2019.
- [6] L. Ma, J. Wu, M. Wang, L. Dong, and H. Wei, "Dynamic compressive properties of dry and saturated coral rocks at high strain rates," *Engineering Geology*, vol. 272, p. 105615, 2020.
- [7] J. L. Shang, L. T. Shen, and J. Zhao, "Hugoniot equation of state of the Bukit Timah granite," *International Journal of Rock Mechanics and Mining Sciences*, vol. 37, no. 4, pp. 705–713, 2000.
- [8] X. Li, F. Gong, M. Tao et al., "Failure mechanism and coupled static-dynamic loading theory in deep hard rock mining: a review," *Journal of Rock Mechanics and Geotechnical Engineering*, vol. 9, no. 4, pp. 767–782, 2017.
- [9] F.-Q. Gong, X.-F. Si, X.-B. Li, and S.-Y. Wang, "Dynamic triaxial compression tests on sandstone at high strain rates and low confining pressures with split Hopkinson pressure bar," *International Journal of Rock Mechanics and Mining Sciences*, vol. 113, pp. 211–219, 2019.
- [10] X. Si, F. Gong, X. Li, S. Wang, and S. Luo, "Dynamic Mohr-Coulomb and Hoek-Brown strength criteria of sandstone at high strain rates," *International Journal of Rock Mechanics and Mining Sciences*, vol. 115, pp. 48–59, 2019.
- [11] K. Liu, J. Zhao, G. Wu, A. Maksimenko, A. Haque, and Q. Zhang, "Dynamic strength and failure modes of sandstone under biaxial compression," *International Journal of Rock Mechanics and Mining Sciences*, vol. 128, p. 104260, 2020.
- [12] Z. Zhou, X. Cai, D. Ma et al., "Water saturation effects on dynamic fracture behavior of sandstone," *International*

- Journal of Rock Mechanics and Mining Sciences*, vol. 114, pp. 46–61, 2019.
- [13] J. Zhang, H. Deng, A. Taheri, B. Ke, and C. Liu, “Deterioration and strain energy development of sandstones under quasi-static and dynamic loading after freeze-thaw cycles,” *Cold Regions Science and Technology*, vol. 160, pp. 252–264, 2019.
- [14] Y. Luo, D. Qu, G. Wang, X. Li, and G. Zhang, “Degradation model of the dynamic mechanical properties and damage failure law of sandstone under freeze-thaw action,” *Soil Dynamics and Earthquake Engineering*, vol. 132, p. 106094, 2020.
- [15] S. Liu and J. Xu, “Effect of strain rate on the dynamic compressive mechanical behaviors of rock material subjected to high temperatures,” *Mechanics of Materials*, vol. 82, pp. 28–38, 2015.
- [16] C. Liu, Y. Wu, X.-f. Zhang et al., “Propagation of shock waves in dry and wet sandstone: experimental observations, theoretical analysis and meso-scale modeling,” *Defence Technology*, vol. 14, no. 5, pp. 513–521, 2018.
- [17] R. Ulusay, *The ISRM Suggested Methods for Rock Characterization, Testing and Monitoring: 2007–2014*, Springer, Berlin, Germany, 2014.
- [18] M. Cai, P. K. Kaiser, F. Suorineni, and K. Su, “A study on the dynamic behavior of the Meuse/Haute-Marne argillite,” *Physics and Chemistry of the Earth, Parts A/B/C*, vol. 32, no. 8–14, pp. 907–916, 2007.
- [19] C. Qi, M. Wang, and Q. Qian, “Strain-rate effects on the strength and fragmentation size of rocks,” *International Journal of Impact Engineering*, vol. 36, no. 12, pp. 1355–1364, 2009.
- [20] P. Rossi and F. Toutlemonde, “Effect of loading rate on the tensile behaviour of concrete: description of the physical mechanisms,” *Materials and Structures*, vol. 29, no. 2, pp. 116–118, 1996.
- [21] M. E. Kipp, D. E. Grady, and E. P. Chen, “Strain-rate dependent fracture initiation,” *International Journal of Fracture*, vol. 16, no. 5, pp. 471–478, 1980.
- [22] P. Rossi, “A physical phenomenon which can explain the mechanical behaviour of concrete under high strain rates,” *Materials and Structures*, vol. 24, no. 6, pp. 422–424, 1991.
- [23] D. E. Grady, “Local inertial effects in dynamic fragmentation,” *Journal of Applied Physics*, vol. 53, no. 1, pp. 322–325, 1982.
- [24] Q. Qian, C. Qi, and M. Wang, “Dynamic strength of rocks and physical nature of rock strength,” *Journal of Rock Mechanics and Geotechnical Engineering*, vol. 1, no. 1, pp. 1–10, 2009.
- [25] P. H. Bischoff and S. H. Perry, “Compressive behaviour of concrete at high strain rates,” *Materials and Structures*, vol. 24, no. 6, pp. 425–450, 1991.
- [26] T. Szwedzicki, “A hypothesis on modes of failure of rock samples tested in uniaxial compression,” *Rock Mechanics and Rock Engineering*, vol. 40, no. 1, pp. 97–104, 2007.
- [27] J. M. Ramsey and F. M. Chester, “Hybrid fracture and the transition from extension fracture to shear fracture,” *Nature*, vol. 428, no. 6978, pp. 63–66, 2004.
- [28] P. Wang, J. Xu, X. Fang, and P. Wang, “Energy dissipation and damage evolution analyses for the dynamic compression failure process of red-sandstone after freeze-thaw cycles,” *Engineering Geology*, vol. 221, pp. 104–113, 2017.
- [29] H. Xie, L. Li, R. Peng, and Y. Ju, “Energy analysis and criteria for structural failure of rocks,” *Journal of Rock Mechanics and Geotechnical Engineering*, vol. 1, no. 1, pp. 11–20, 2009.
- [30] Y. Jiang, H. Li, and Y. Zhao, “Effect of loading rate on energy accumulation and dissipation in rocks,” *Journal of China University of Mining & Technology*, vol. 43, no. 3, in China, 2014.
- [31] L. I. Baron, *Determination of Properties of Rocks*, Gostekhizdat, Moscow, Russia, in Russian, 1962.

## Research Article

# Experimental and Mathematical Modeling of Monotonic Behavior of Calcareous Sand

Haotian Zhang,<sup>1</sup> Zongmu Luo ,<sup>1</sup> Yanyu Qiu,<sup>1</sup> Huachao Liu ,<sup>1</sup> Juan Gu,<sup>1</sup> and Jian Tang<sup>2</sup>

<sup>1</sup>State Key Laboratory of Disaster Prevention & Mitigation of Explosion & Impact, Army Engineering University of PLA, Nanjing 210007, China

<sup>2</sup>31619 PLA Troops, Zhenjiang 212421, China

Correspondence should be addressed to Zongmu Luo; [langdon0114@163.com](mailto:langdon0114@163.com) and Huachao Liu; [273750748@qq.com](mailto:273750748@qq.com)

Received 12 May 2020; Revised 22 June 2020; Accepted 13 July 2020; Published 31 July 2020

Academic Editor: Li Chen

Copyright © 2020 Haotian Zhang et al. This is an open access article distributed under the Creative Commons Attribution License, which permits unrestricted use, distribution, and reproduction in any medium, provided the original work is properly cited.

The prominent performance of wave elimination and energy absorption makes calcareous sand important and useful in infrastructure construction and protection engineering. Due to the high compressibility induced by remarkable intragranular void and irregular shape, calcareous sand presents different mechanical behaviors from common terrestrial sands. Considerable efforts have been made to explore the static and dynamic mechanical properties of calcareous sand. In this paper, a series of monotonous experiments have been performed on calcareous sand utilizing the electrohydraulic servo-controlled test apparatus designed by the Global Digital Systems Ltd (GDS). The effects of confining pressure and relative density on the mechanical properties of dry, drained, and undrained saturated sand were studied, and the underlying micromechanism of deformation and failure was discussed. It can be found that the residual stress of dry calcareous sand is independent of the relative density, while the peak stress and residual stress of drainage saturated sand have a positive correlation with the relative density. The increase of confining pressure makes the strain softening more remarkable and heightens the peak stress and residual stress. The stress-strain curve of calcareous sand can be divided into two portions: prepeak portion and postpeak softening portion. For the dry sand and drainage saturated sand, the softened part can be partitioned into three phases, i.e., accelerated phase, steady phase, and degradation phase, while the undrained saturated sand tends to hyperbolic softening. A mathematical model composed of a hyperbolic function and an inverted S-shaped function was formulated to describe the multiphase characteristic, in which the setting of parameter  $p$  expands its applicability. The experimental result validated the model, showing that the model can better describe the monotonic stress-strain relationship of calcareous sand. Besides, the physical meanings of model parameters were discussed.

## 1. Introduction

In the past few decades, sea-sand as a building material has been getting more attention. Many countries, such as the UK [1] and Japan [2, 3], regard sea-sand as an alternative material for river sand. The geological origin of sea-sand is similar to that of river sand [4, 5], but the surface texture affecting the interlocking effect is different [6–8]. Besides, there is more salt and debris of marine creature (like sea shell) in sea-sand [9]. The debris of marine creature is even deemed to the key difference between river sand and sea-sand [10]. Therefore, the mechanical performance of sea-sand is quite different from that of river sand.

Calcareous sand is a special kind of sea-sand, mainly distributed in the marine area between N30° and S30°. It has been widely used in the construction on islands and reefs. On the one hand, calcareous sand is the main material for marine reclamation land and protective engineering [11–18]. On the other hand, calcareous sand is also an important raw material for fine concrete aggregate [19, 20]. It should be noted that calcareous sand has different mechanical properties from terrestrial sands such as silica sand. The main reason is that the skeleton of calcareous sand is formed by the fragments of marine life (such as corals, shells, and mollusks), and its particles have significant internal void spaces and various irregular shapes [21, 22]. The difference

in mechanical properties leads to the foundation stability, strength, and durability of calcareous sand concrete buildings different from those of general concrete buildings. Furthermore, as a typical loose granular material, calcareous sand is widely used in protective engineering, which often involves the dynamic loading scenarios. Based on the impact test by the split Hopkinson pressure bar (SHPB) device, the law of stress wave attenuation in calcareous sand has been revealed. By measuring variables such as stress wave propagation speed and peak stress, it is found that the wave attenuation effect and the energy absorption properties of calcareous sand was better than those of terrestrial sand [14–17]. Hence, calcareous sand is of great importance in infrastructure construction and protection engineering. The mechanical properties of calcareous sand under monotonic loading are the basis for investigating its dynamic mechanical response, which can provide a beneficial reference for impact load experiment, explosion effect research, and protection engineering design. Meanwhile, it is significant to establish an effective and simple model that can accurately describe the mechanical characteristics of calcareous-sand under monotonic loading.

There are considerable constitutive models for sand at monotonic loadings in the available literatures. These models have been proposed under the premise of simplification and assumption with limitation of application scope in essence. Therefore, the advantages and disadvantages of the models should be clarified when applying these theoretical models. Among them, the hyperbolic elastic model of Duncan and Chang [23] is widely used for granular materials due to its simplicity and convenience. Nevertheless, it cannot reflect the strain-softening behavior. It appears that the models are more and more satisfactory in describing the essential behavior features of sand, but the theoretical framework and the application still need to be further investigated.

- (i) Nonlinear elastic model [23–25]: this kind of model can be consistent with the experimental results as long as the model parameters are enough. The nonlinear nature of the soil can be reflected, and the model parameters with distinct physical significance can be determined by conventional tests. The models have been widely used in practical engineering and are generally suitable for strain hardening materials such as footings on sand and clay. However, they cannot be applied to geotechnical materials with strain softening characteristics due to relatively large deviation of calculation results. In addition, the models cannot reflect the influence of intermediate principal stress and the dilatancy of soil, so their scope of application are limited.
- (ii) Elastic-plastic model [26–31]: this kind of model has a more rigorous theory framework, which can predict the soil properties under various load conditions, thus have a wider application field. The results of research on cohesionless soils such as river sand show that the model can be used to predict the soil performance of drained and undrained conditions from typical dense sand to typical loose

sand. The postpeak behaviors of strain hardening and strain softening are also modeled correctly. But, there are some difficulties in determining up to fourteen model parameters. In addition, these models are sometimes not practical in practice because the theoretical description is too complex.

- (iii) Hypoplastic model [32–35]: in these models, the relationship between stress rate and strain rate is directly constructed at the framework of thermodynamic theory. The constitutive relations established can be expressed by simple mathematical expression, and the influence of stress path can be considered. Since the concepts such as double yield surface and anisotropic hardening criterion are introduced, the practical ability of the models is strengthened, and the complex constitutive characteristics of soil are described. Although the theoretical complexity is decreased, the model parameters are not easy to be obtained.
- (iv) Critical state model [36–40]: in this type of model, a state parameter is achieved based on the critical state theory. The introduction of the state parameter enables these constitutive models to take into account the mechanical behavior related to the change of material state during loading. Therefore, the deficiency of treating loose and dense sandy soil as different media has been overcome. Some of these models even fit for both sand and clay. However, there are more model parameters such as confining pressure and load path, and the parameter determination is also complex.

In fact, it is very difficult to completely and accurately describe the complex deformation characteristics of the sand under any conditions. The various kinds of models aforementioned demonstrate that there is a contradiction between the accurate description and application complexity. Therefore, a balance between accuracy and complexity should be reached in a model based on the user demands. In this paper, a series of monotonous experiments have been performed on calcareous sand, and the corresponding stress-strain curves are obtained and analyzed. A mathematical model describing the complete stress-strain curves is proposed, and its feasibility is verified by the test results. Moreover, the physical meanings of model parameters are discussed.

## 2. Monotonic Behavior of Calcareous Sand

*2.1. Sand Samples Tested.* The calcareous sand used in this study was obtained from the South China Sea between N4° and N16°. It was mainly medium-fine sand and consists of coral fragments. The energy-dispersive X-ray spectroscopy was used for elemental analysis of sand sample, showing that the mineral composition is composed of as high as 97% calcium carbonate with specific gravities of 2.7–2.85 and is mainly composed of 33%–47% aragonite and 53%–67% high magnesian calcite [41]. The surface texture was observed by scanning electron microscopy (SEM), as shown in Figure 1. The SEM images indicate that there are many pores distributed around the particle surface. The porous characteristic leads to more interlocking parts between angular grains in calcareous sand than those in ordinary terrestrial sands.

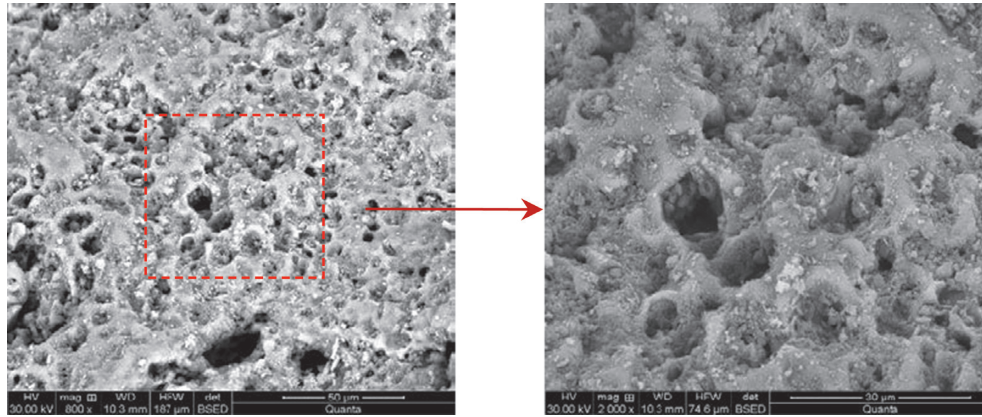


FIGURE 1: SEM image of calcareous sand.

In this study, the grains coarser than 2 mm were removed and the corresponding grain size distribution curve is shown in Figure 2. Considering the effect of relative density, the specific gravity and the maximum and minimum dry densities were measured according to ASTM standard D5550 and D5253, respectively [42, 43]. The results are summarized in Table 1.

**2.2. Test Equipment and Methods.** The electrohydraulic servo-controlled dynamic triaxial test system (DYNTTS) developed by GDS has been used in this study, as shown in Figure 3. It integrates the triaxial cell and the axial pressure driver. Axial load and axial deformation are controlled by the bottom of the triaxial cell. The standard pressure/volume controllers are used for confining pressure and back pressure, respectively. By means of high accuracy transducers and a powerful data collector, the axial force, vertical displacement, and pore pressure are measured and recorded. The built-in software of the computer control system is utilized to precisely control the test conditions and receive data in real time.

The samples were all cylindrical with a diameter of 50 mm and a height of 100 mm. According to the relative density designed by the test scheme, the samples were arranged by the layered packing method. For saturated calcareous sand, the confining pressure and back pressure were increased every 20 minutes while maintaining an effective confining pressure of 5 kPa. Each increase was 100 kPa until the pore pressure parameter  $B$  exceeded 0.98, where  $B$  is the ratio of the increment of internal pore water pressure to the increment of back pressure. In the experiment, the sand samples were fully saturated after the back pressure reached 500 kPa. After that, the specimens were isotropic consolidated under certain values of effective confining pressure. For dry sand, the confining pressure directly increased to the preset value and remained constant. The consolidation was completed when the deformation of the sand sample stabilized. Finally, monotonic triaxial tests were performed on calcareous dry sand and calcareous saturated sand under undrained/drainage condition. All the tests were controlled by axial displacement. For dry sand and saturated sand under undrained condition, the loading rate was 0.5 mm/min. For saturated sand under drainage condition, the loading rate was 0.01 mm/min.

For the calcareous sand with the relative density of 30%, 45%, and 60%, respectively, the monotonic triaxial tests were carried out under the initial effective confining pressure of 100 kPa, 200 kPa, and 300 kPa, respectively. The specific test scheme is shown in Table 2.

**2.3. Typical Stress-Strain Curves.** Figure 4 shows the test result of dry calcareous sand with the relative densities of  $D_r = 30\%$ , 45%, and 60%. The confining pressures were all 200 kPa. From Figure 4, it can be found that the loose calcareous sand presents a similar complete stress-strain curve with the denser calcareous sand. The stress-strain curves can be divided into two portions: the prepeak portion (OA section) and the postpeak portion (AD section). After the axial stress reaches the peak point, calcareous sand presents a state of strain-softening, which is a process of progressive failure. The negative tangent slope of stress-strain curve can be used to characterize the softening rate. The larger the tangent slope is, the smaller the softening rate is. Based on the change of softening rate, the postpeak strain-softening portion can be further divided into three phases:

- (i) Accelerated phase (section  $AB$ ): in this phase, the tangent slope gradually decreases from zero, which means that the corresponding softening rate continuously increases. Therefore, the first phase can be called accelerated phase. The starting point  $A$  (peak stress) is related to the relative density.
- (ii) Steady phase (section  $BC$ ): when the tangent slope decreases to the minimum, the stress-strain curve develops into the secondary phase. In this phase, the softening rate is the largest and maintained constant. Thus, the secondary phase  $BC$  can be called steady phase.
- (iii) Degradation phase (section  $CD$ ): in this phase, the tangent slope begins to increase until to zero. It means that the corresponding softening rate continuously decreases. Based on this, section  $CD$  is the degradation phase. The ending point  $D$  (residual stress) is independent of relative density.



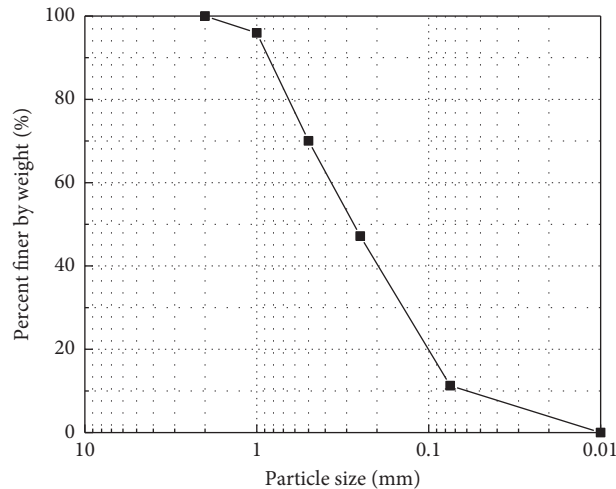


FIGURE 2: Grain size distribution curve of sand samples tested.

TABLE 1: Physical properties of test calcareous sand.

Property	$G_s$	$D_{10}$ (mm)	$Cu/(D_{60}/D_{10})$	$\rho_{dmin}$ ( $\text{g}\cdot\text{cm}^{-3}$ )	$\rho_{dmax}$ ( $\text{g}\cdot\text{cm}^{-3}$ )
Calcareous sand	2.807	0.055	7.3	1.14	1.48

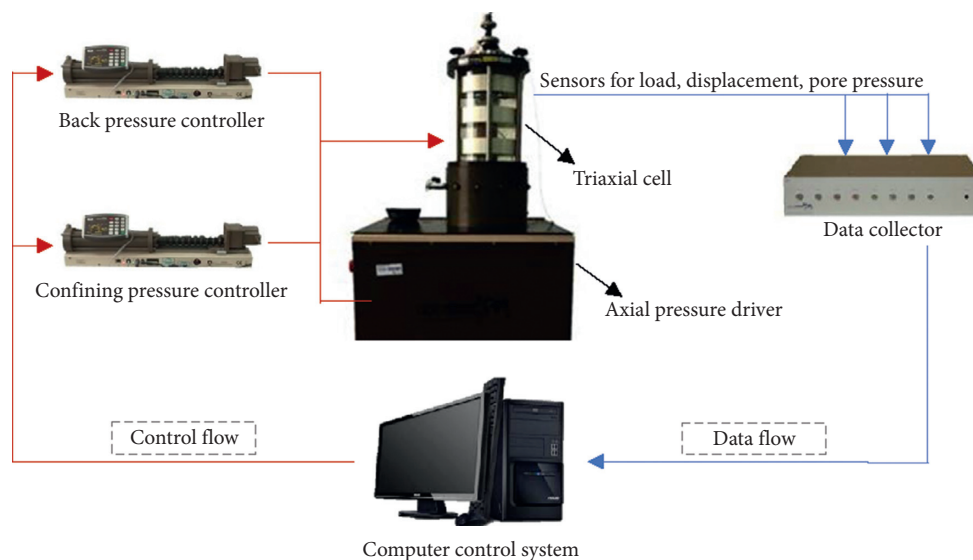


FIGURE 3: GDS dynamic triaxial test system.

The stress-strain curves of dry calcareous sand with a relative density of 30% under different confining pressure are shown in Figure 5. It is found that both of the stress-strain curves at low and high confining pressure can be divided into two portions: prepeak portion and postpeak portion of three phases. Especially, the larger the confining pressure is, the more obvious the strain-softening of three phases is. The starting and terminal points of postpeak portion are both related to the confining pressure. Specifically, the larger confining pressure corresponds to the higher starting and terminal points.

The stress-strain curves of saturated calcareous sand at drained triaxial compression are shown in Figure 6. The test

results indicate that the stress-strain curves of saturated calcareous sand at drained compression can also be divided into prepeak portion and postpeak portion of three phases. The starting and terminal points of strain-softening are both related to the relative density and the initial effective confining pressure. The accelerated phase occupies a higher proportion in the total deformation process, exceeding the steady phase in this test condition, while the deformation during the accelerated phase is less than that during the steady phase for dry sand.

Saturated Nevada sand and saturated Toyoura sand (data from [44]) have been compared, of which some physical properties are presented in Table 3. Compared with the two sands, calcareous sand presents a larger strain-softening, as

TABLE 2: Scheme of the monotonic triaxial tests.

Test number	Condition	Relative density (%)	Confining pressure (kPa)
D-01	—	30	100
D-02	—	30	200
D-03	—	30	300
D-04	—	45	200
D-05	—	60	200
S-01	Undrained	30	100
S-02	Undrained	30	200
S-03	Undrained	30	300
S-04	Undrained	45	200
S-05	Undrained	60	200
S-06	Drainage	30	100
S-07	Drainage	30	200
S-08	Drainage	30	300
S-09	Drainage	45	200
S-10	Drainage	60	200

In the column of the test number, *D* represents dry sand and *S* represents saturated sand. For each case, the experiment was repeated two times. The average value was taken as the final result under the premise of good repeatability.

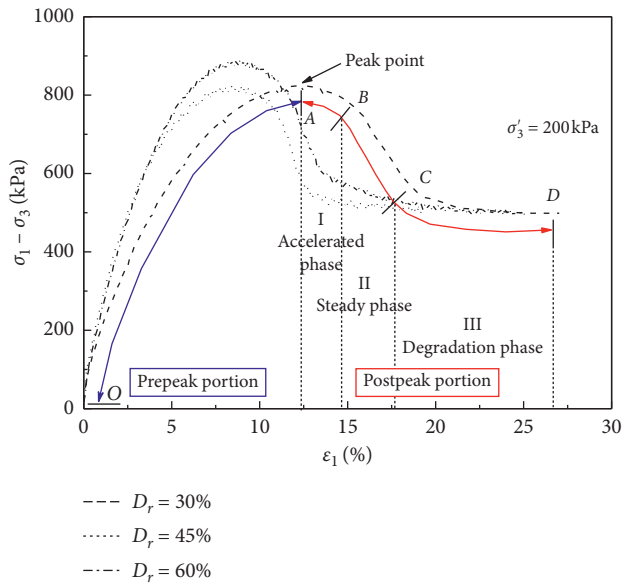


FIGURE 4: Stress-strain curves of dry calcareous sand with different relative densities.

shown in Figure 7. The postpeak portion of calcareous sand is three-phased, while that of Nevada sand is two-phased. For Toyoura sand, the strain-softening portion is even approximately linear. The larger strain-softening is due to the higher compressibility of calcareous sand. Besides, the multiphase characteristic is closely related to the contact between particles. Considering the porous property, the more interlocking parts in calcareous sand may be the main cause of the three-phase softening.

The stress-strain curve of saturated calcareous sand at undrained triaxial compression is different from that of dry calcareous sand, but it is similar to that of other sands, as shown in Figure 8. When the initial effective confining

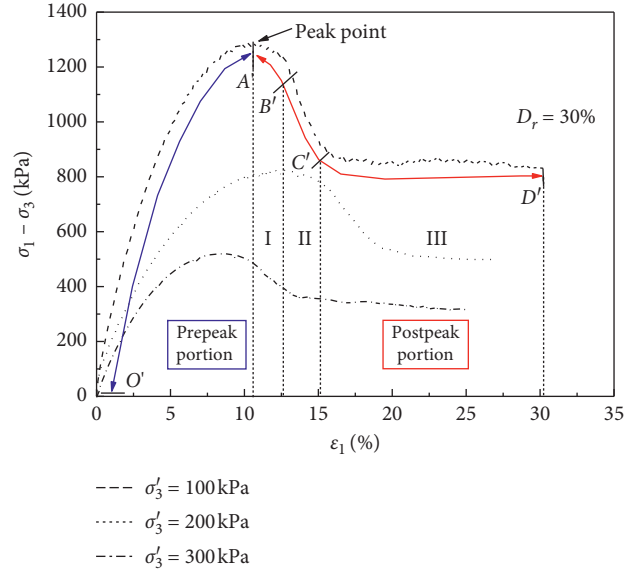


FIGURE 5: Stress-strain curves of dry calcareous sand at different confining pressures.

pressure is relatively low, the stress-strain curve of calcareous sand presents hyperbolic relationship without strain-softening phase under undrained compression. The stress-strain curve at a high initial effective confining pressure is composed of two portions: prepeak portion and postpeak portion. However, the postpeak portion is not three-phased but behaves as a hyperbolic softening like Toyoura sand.

**2.4. Micromechanism of Deformation and Failure.** The deformation of calcareous sand is mainly a process of coupled development between particle slip and breakage [45], as shown in Figure 9. During the slip process, particles mainly resist deformation by friction, while the crushing process is accompanied by interlocking effect. When the stress reaches the strength of the particles, the crushing occurs and causes deformation. At the initial stage of loading, the contact between particles is not close, so the slippage is relatively easy. At this time, the pressure bearing mainly depends on the interlocking between particles. With the increase of axial pressure, the particles are gradually broken and the occlusal structure is increased. However, the breakage and abrasion of the sharp corners reduce the roughness of the particle surface, which weakens the interlocking effect. Meanwhile, the overall contact between particles becomes tighter as the test progresses, resulting in a more prominent friction effect. Moreover, particle crushing releases internal pores, increases the friction area, and further enhances the friction effect. In general, under the cooperation of interlocking and friction, monotonic experiments of calcareous sand show the phenomenon of strain hardening and multiphase strain softening, which is more complicated than the samples with better roundness and less breakage, such as the Nevada sand and the Toyoura sand. Under undrained conditions, pore water changes the relative motion of particles and weakens the softening degree of calcareous sand.

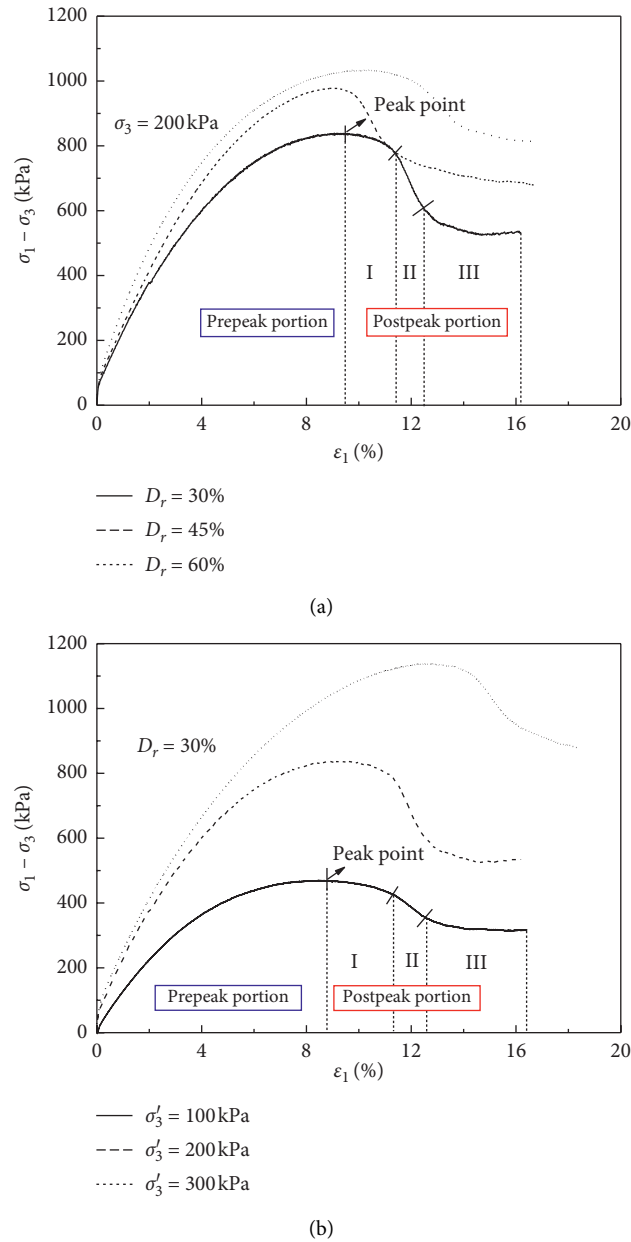


FIGURE 6: Stress-strain curve of saturated calcareous sand at drained compression. Tests on specimens (a) with different relative densities and (b) at different confining pressures.

TABLE 3: Physical properties of Nevada sand and Toyoura sand.

Property	$G_s$	$D_{50}/\text{mm}$	$Cu/(D_{60}/D_{10})$	$\rho_{dmin}$ ( $\text{g}\cdot\text{cm}^{-3}$ )	$\rho_{dmax}$ ( $\text{g}\cdot\text{cm}^{-3}$ )
Nevada sand	2.67	0.15	—	1.387	1.733
Toyourea sand	2.65	0.17	1.7	1.340	1.659

From the perspective of force chain evolution, the mechanism of deformation and failure can be further explained. When pressure is applied to calcareous sand, the relative positions of the particles are adjusted. The particles aggregate to form the initial load-bearing structure, and a series of force chains are formed in the direction of the principal stress. The form of the force chain network is

determined by the contact and interaction between particles, which affects the deformation. Through microscopic observation [46], it can be found that there are mainly three ways of contact between particles, namely, point-like contact, extended contact, and contact L-S (a large grain in contact with many small grains). The schematic diagram is shown in Figure 10. Point-like contacted particles are prone

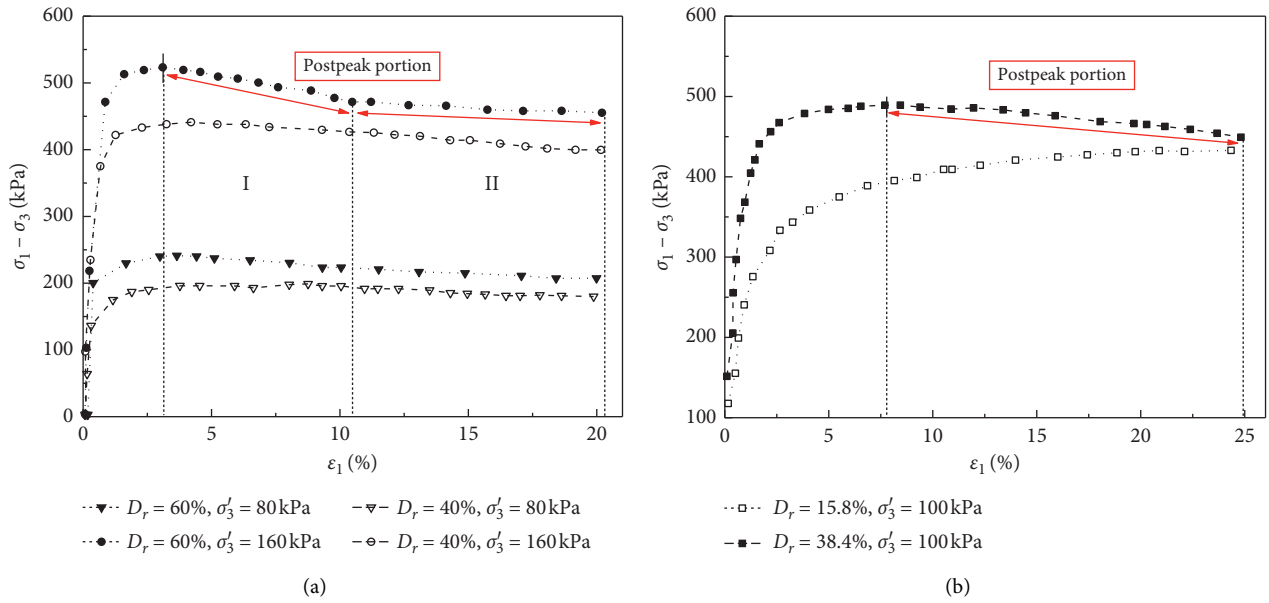


FIGURE 7: Stress-strain curves of sand at drained compression (data from [44]). (a) Nevada sand. (b) Toyoura sand.

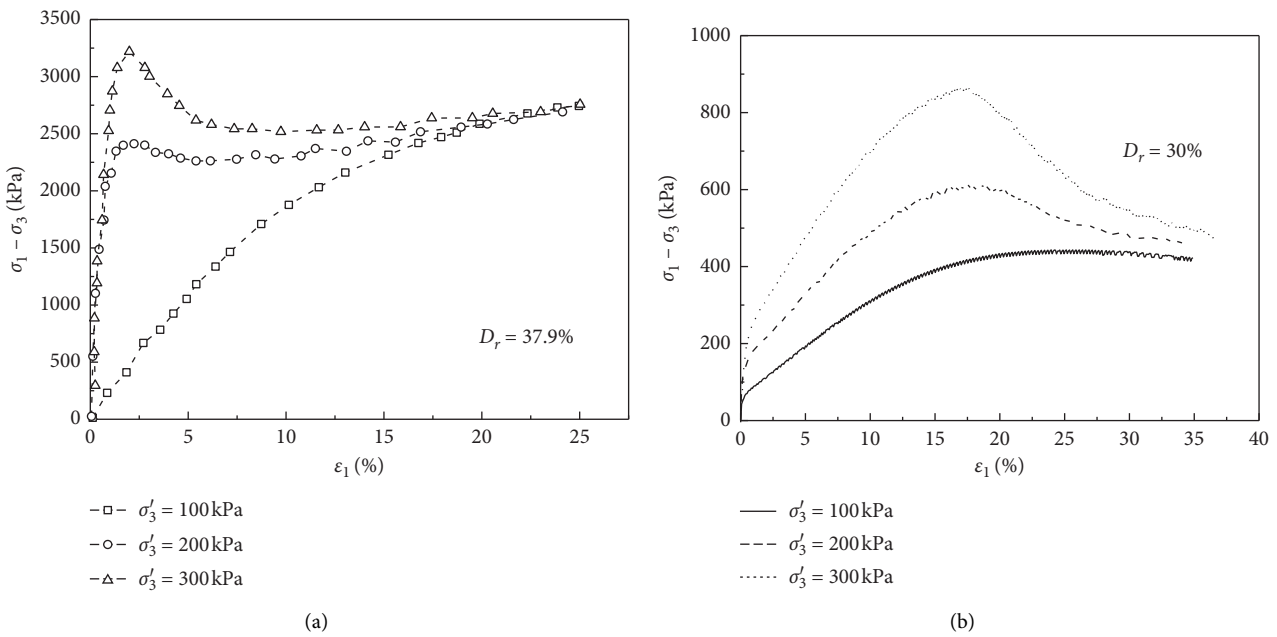


FIGURE 8: Stress-strain curves of sand at undrained compression. (a) Calcareous sand. (b) Toyoura sand (data from [44]).

to wear and damage under the effect of stress concentration, causing preliminary strain softening; meanwhile, the sharp corners with higher strength cause the particles in contact with them to split, and the slippage of the new fine particles accelerate the strain softening; particle fragmentation promotes the development from point-like contacts to extended contact. At this time, the contact area between the particles is larger, and the particles are hard to be destroyed. In addition, the breakage of particles makes the grading better, then contact L-S is easily formed when large particles are surrounded by small particles. Small particles support large

particles well and produce a confining pressure-like effect, reducing the degree of particle fragmentation and suppressing softening.

### 3. Formulation of Constitutive Model

Based on the monotonic test results of calcareous sand, it can be realized that the prepeak portion of stress-strain curve is hyperbolic shaped. The postpeak portion of dry calcareous sand and drained saturated calcareous sand is both three-phased, while that of undrained saturated calcareous sand is

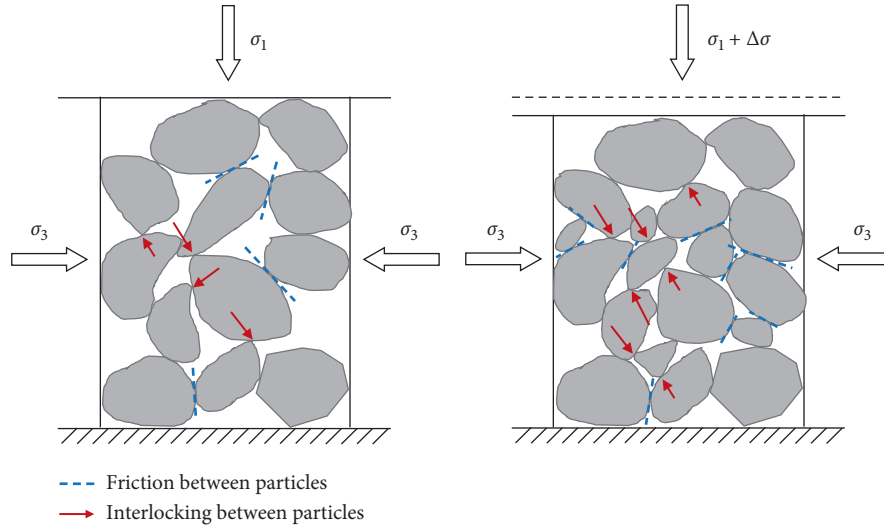


FIGURE 9: Sketch of deformation mechanism of calcareous sand.

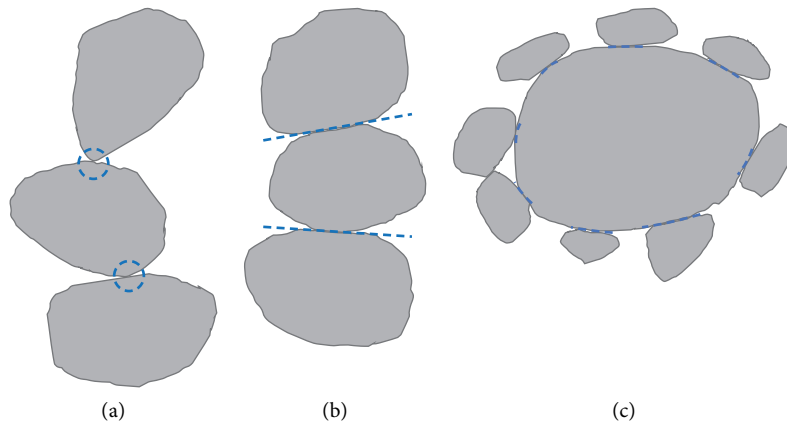


FIGURE 10: Typical contact patterns of calcareous sand particles. (a) Point-like contact. (b) Extended contact. (c) Contact L-S.

hyperbolic. Therefore, the model for calcareous sand should reflect the hyperbolic prepeak portion and the three-phase postpeak portion or the hyperbolic postpeak portion.

For the prepeak portion, the stress-strain relationship can be regarded as hyperbolic. Based on the hyperbolic elastic model of Duncan and Chang [23], the stress-strain relationship can be written as

$$\sigma = \frac{\varepsilon_1}{a + b\varepsilon_1}, \quad (1)$$

where  $\varepsilon_1$  is the axial strain, (%),  $\sigma$  is the principal stress difference,  $\sigma = \sigma_1 - \sigma_3$ , (kPa), and  $a$  and  $b$  are the experimental parameters.

For the postpeak portion, the three-phase stress-strain curve is inverted S-shaped. It can be expressed with the following function:

$$\sigma = \sigma_p - A \left[ 1 - \frac{1}{1 + ((\varepsilon_1/m) - (\varepsilon_p/m))^p} \right], \quad (2)$$

where  $\varepsilon_1$  is the axial strain, (%),  $\sigma$  is the principal stress difference,  $\sigma = \sigma_1 - \sigma_3$ , (kPa), and the parameters  $\varepsilon_p$  and  $\sigma_p$  correspond the abscissa and ordinate values of the starting point of equation (2), respectively. The parameter  $A$  decides the ordinate value of terminal point of equation (2). Combined with the characteristic of postpeak stress-strain curve, it can be deduced that  $\sigma_p$  is the peak stress (kPa),  $\varepsilon_p$  is the critical strain (%), and  $A$  is the difference between peak stress and residual stress (kPa).

The value of the peak stress is related to the confining pressure and can be determined conveniently by Mohr-Coulomb failure criterion as

$$\sigma_p = \frac{2c \cdot \cos \varphi + 2\sigma_3 \cdot \sin \varphi}{1 - \sin \varphi}, \quad (3)$$

which has been described by Duncan and Chang [23], where  $c$  is the cohesion and  $\varphi$  is the angle of internal friction. Substituting the result into equation (1), the critical strain can be expressed by



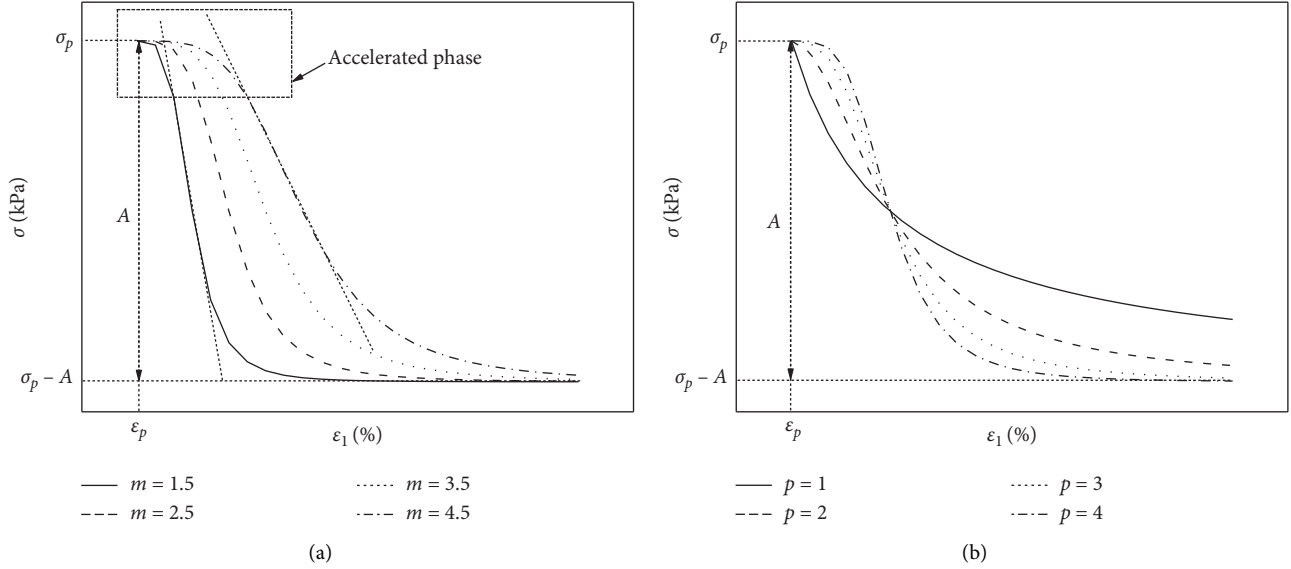


FIGURE 11: The influence of model parameters on the postpeak curve. Influence of (a) parameter  $m$  and (b) parameter  $p$ .

$$\epsilon_p = \frac{2a(c \cdot \cos \varphi + \sigma_3 \cdot \sin \varphi)}{1 - \sin \varphi - 2b(c \cdot \cos \varphi + \sigma_3 \cdot \sin \varphi)} \quad (4)$$

In equation (2), the parameter  $m$  is the softening rate factor. As shown in Figure 11(a),  $m$  affects the softening rate of the accelerated phase and steady phase. The value of  $m$  ranges effectively from 0 to positive infinity. The larger the  $m$ , the lower the softening rate on the accelerated phase and steady phase.

As shown in Figure 11(b), the parameter  $p$  is a phase factor, which affects the amount of deformation required for the acceleration phase. The greater the  $p$ , the more the strain experienced during the acceleration phase. Especially, when the parameter  $p$  is equal to 1, there would be no acceleration phase. In this case, equation (2) reduces to

$$\sigma = (\sigma_p - A) + A \frac{m}{m + (\epsilon_1 - \epsilon_p)} \quad (5)$$

Meanwhile, the curve for the postpeak portion transforms from an inverted S-shaped curve to a hyperbolic one. This means that equation (2) not only fits for the dry calcareous sand and drained saturated calcareous sand but also fits for the undrained saturated calcareous sand by adjusting the value of parameter  $p$ . The  $p$  value is valid when it is not less than 1. The curve described by the model is more similar

to the hyperbolic softening when  $p$  is closer to 1. As  $p$  increases, the three-phase softening characteristic becomes more obvious.

Therefore, the mathematical model for the monotonic stress-strain relationship of calcareous sand can be expressed as

$$\sigma = \begin{cases} \frac{\epsilon_1}{a + b\epsilon_1}, & (\sigma < \sigma_p), \\ \sigma_p - A \left[ 1 - \frac{1}{1 + \left( \frac{\epsilon_1}{m} - \frac{\epsilon_p}{m} \right)^p} \right], & (\sigma > \sigma_p). \end{cases} \quad (6)$$

Furthermore, in order to extend the above mathematical model to three dimensions, the generalized Hooke's law is introduced:

$$\epsilon_1 = \frac{1}{E_t} [\sigma_1 - \nu_t(\sigma_2 + \sigma_3)] = \frac{1}{E_t} (\sigma_1 - 2\nu_t\sigma_3), \quad (7)$$

where  $E_t$  and  $\nu_t$  are the elastic modulus and Poisson's ratio, respectively. Equation (7) is substituted into equation (6), and a three-dimensional mathematical model can be obtained by combining the Duncan-Chang  $E$ - $\nu$  model:

$$\sigma_1 - \sigma_3 = \begin{cases} \frac{1}{(E_t a / (\sigma_1 - 2\nu_t \sigma_3)) + b}, & (\sigma < \sigma_p), \\ \sigma_p - A \left[ 1 - \frac{1}{1 + \left( \frac{(\sigma_1 - 2\nu_t \sigma_3) / E_t}{m} - \frac{\epsilon_p}{m} \right)^p} \right], & (\sigma > \sigma_p), \end{cases} \quad (8)$$

where  $E_t$  and  $\nu_t$  are represented as:

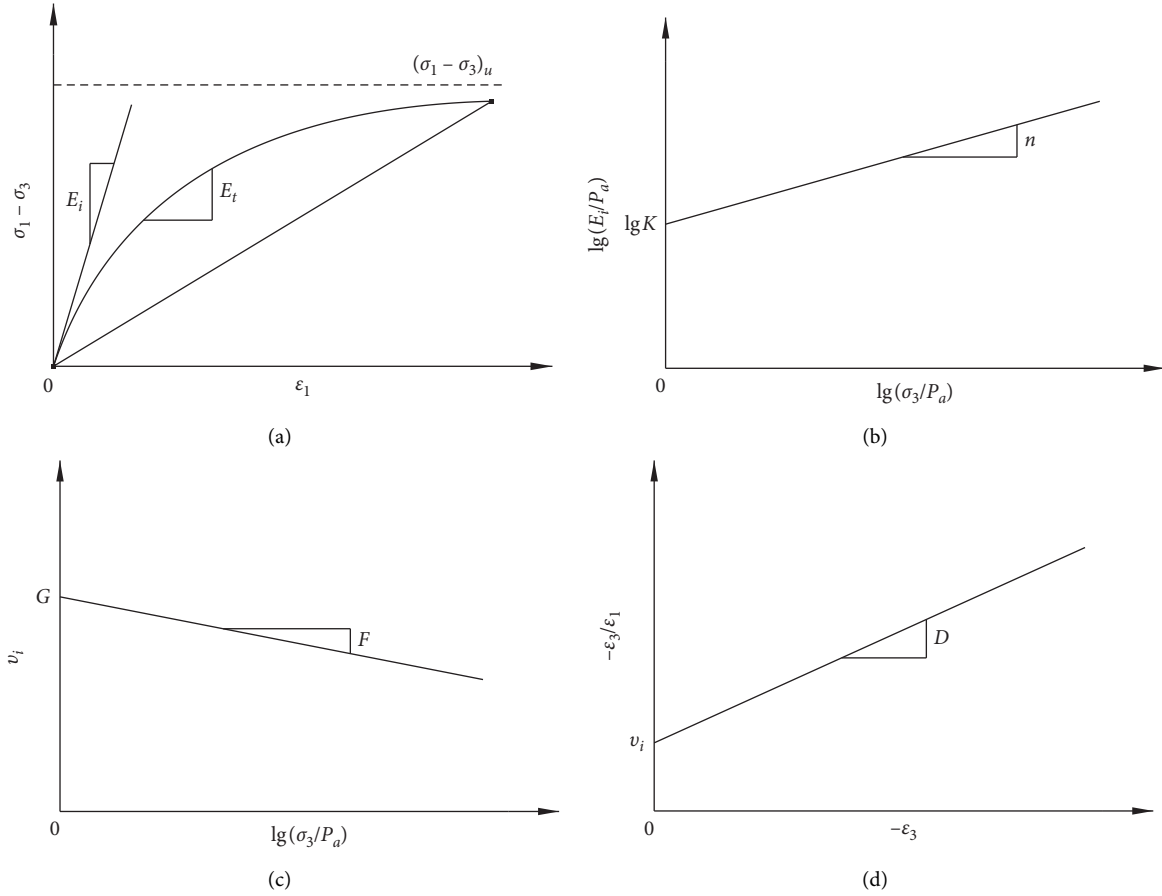


FIGURE 12: Determination of model parameters. Relation curve of (a)  $(\sigma_1 - \sigma_3) - \varepsilon_1$ , (b)  $\lg(E_i/P_a) - \lg(\sigma_3/P_a)$ , (c)  $\nu_i - \lg(\sigma_3/P_a)$ , and (d)  $(-\varepsilon_3/\varepsilon_1) - (-\varepsilon_3)$ .

$$\left\{ \begin{array}{l} E_t = \left[ 1 - R_f \frac{(1 - \sin \varphi)(\sigma_1 - \sigma_3)}{2c \cos \varphi + 2\sigma_3 \sin \varphi} \right]^2 K P_a \left( \frac{\sigma_3}{P_a} \right)^n, \\ \nu_t = \frac{G - F \lg(\sigma_3/P_a)}{(1 - X)^2}, \\ X = \frac{D(\sigma_1 - \sigma_3)}{K P_a (\sigma_3/P_a)^n \left[ 1 - \left( \frac{R_f (1 - \sin \varphi)(\sigma_1 - \sigma_3)}{2c \cos \varphi + 2\sigma_3 \sin \varphi} \right) \right]} \end{array} \right. \quad (9)$$

where  $R_f$  is the failure ratio, which is the ratio between the deviatoric stress value at failure and the ultimate deviatoric stress value, and its calculation formula and schematic diagram are followed as equation (10) and Figure 12(a);  $c$  is the cohesion;  $\varphi$  is the angle of internal friction;  $P_a$  is the atmospheric pressure;  $K$  and  $n$  are the experimental constants, respectively, representing the intercept and slope of the  $\lg(E_i/P_a) - \lg(\sigma_3/P_a)$  curve, in which  $E_i$  is the initial elastic modulus (Figure 12(b));  $G$  and  $F$  are material constants respectively, representing the intercept and slope of the  $\nu_i - \lg(\sigma_3/P_a)$  curve, in which  $\nu_i$  is the initial Poisson's ratio

(Figure 12(c)); and  $D$  is the experimental constant, which is the reciprocal of the slope of the  $(-\varepsilon_3/\varepsilon_1) - (-\varepsilon_3)$  curve (Figure 12(d)):

$$R_f = \frac{(\sigma_1 - \sigma_3)_f}{(\sigma_1 - \sigma_3)_u}. \quad (10)$$

#### 4. Model Validation

To validate the feasibility of the mathematical model, the calculated and measured results are compared. fd1Equations

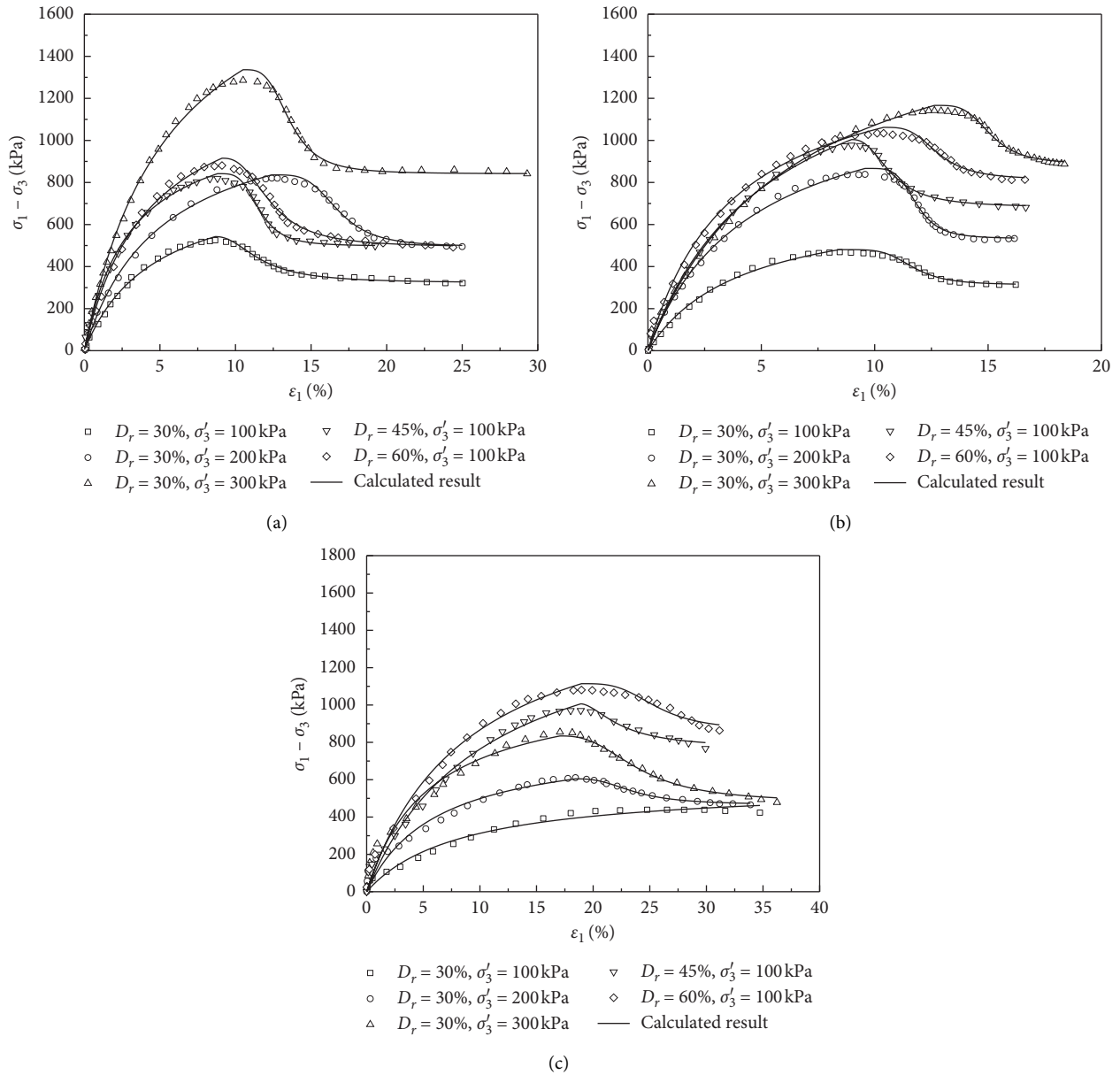


FIGURE 13: Comparison between test data and calculated results. (a) Dry calcareous sand. Saturated calcareous sand at (b) drained compression and (c) undrained compression.

(1) and (2)fd2 were used to fit with the prepeak portion and the postpeak portion of stress-strain curve, respectively. The value of parameters  $a$  and  $b$  in equation (1) were obtained through fitting with the test data of prepeak portion. To ensure the continuity of the piecewise function, the parameters  $\epsilon_p$  and  $\sigma_p$  were approximated as the terminal points of the prepeak fitting result, and  $A$  was determined to be the difference value between the substituted  $\sigma_p$  and residual stress. Then, the value of parameters  $m$  and  $p$  in equation (2) were obtained through fitting with the test data of postpeak portion. The calculated results are shown in Figure 13. The values of the corresponding model parameters are shown in Table 4.

From Figure 13, it can be obviously seen that the model can well describe the monotonic stress-strain relationship of

calcareous sand. Furthermore, the model parameters can be easily determined and their physical meanings are clear. Therefore, the mathematical model can be easily applied in the engineering practice.

In Section 2, the postpeak stress-strain curve of undrained saturated calcareous sand is regarded as hyperbolic. Whereas, the value of parameter  $p$  is not equal to 1, indicating that the fitting result with the hyperbolic function is not as good as that with the inverted S-shaped model. For the Toyoura sand, when the parameter  $p$  is equal to 1, the hyperbolic postpeak softening curve can be well described by the mathematical model. Compared with the unified model put forward by Jin et al. [44], the mathematical model has a better description, as shown in Figure 14. The unified model can be applied for both sand and clay, but the model has

TABLE 4: Values of model parameters.

Parameter	$D_r$ (%)	$\sigma'_3$ (kPa)	$a$ ( $10^{-3}$ )	$b$ ( $10^{-3}$ )	$\varepsilon_p$ (%)	$\sigma_p$ (kPa)	$A$ (kPa)	$m$	$\rho$
Dry calcareous sand	30	100	5.54	1.20	8.66	542.55	221.11	3.06	2.18
	30	200	4.29	0.85	12.40	836.06	341.28	4.41	3.84
	30	300	2.73	0.49	10.50	1336.31	495.01	3.12	3.44
	45	200	2.67	0.88	8.81	841.81	343.71	2.78	3.83
	60	200	3.16	0.75	9.11	915.34	423.81	3.25	2.59
Drained saturated calcareous sand	30	100	5.77	1.4	9.51	480.58	167.02	3.24	4.56
	30	200	3.59	0.78	10.40	866.54	333.22	2.26	4.58
	30	300	3.6	0.57	12.93	1166.31	278.99	2.49	3.81
	45	200	3.38	0.62	8.98	1003.88	322.64	1.77	2.47
	60	200	2.61	0.69	10.39	1061.89	248.52	2.42	3.39
Undrained saturated calcareous sand	30	100	14.54	1.75	—	—	—	—	—
	30	200	7.68	1.24	18.44	604.49	138.79	5.24	2.66
	30	300	5.04	0.90	17.07	834.28	356.21	7.03	2.59
	45	200	6.7	0.64	18.91	1006.29	239.41	3.69	1.72
	60	200	5.43	0.61	18.97	1114.28	250.82	6.70	3.32

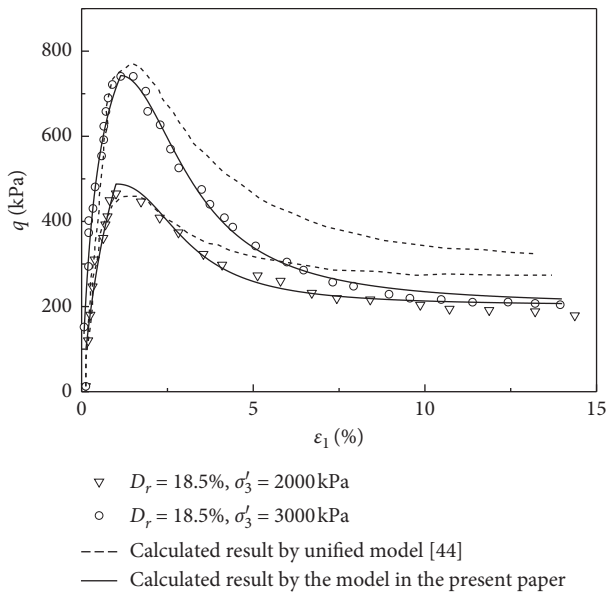


FIGURE 14: Comparison between test data and calculated result for undrained Toyoura sand.

thirteen parameters and their determination is also relatively complicated. In contrast, there are only seven parameters in the mathematical model in this paper. And, the parameters can be determined quickly based on the triaxial compression test result. Therefore, the mathematical model here is easier to be applied in engineering.

The prepeak stress-strain curves are almost all hyperbolic for various sands, so the hyperbolic function seems to be universal for sands. But, the postpeak softening of sand is different. For the sand with a characteristic of high compressibility, like calcareous sand, its postpeak softening presents an obvious three-phase shape. For the less compressible sand like Toyoura sand, the postpeak softening is hyperbolic, or even approximately linear. The obvious advantage of the mathematical model here is that it can well describe the stress-strain relationship, especially the postpeak multiphase softening characteristic. With the aid of this model, the effects of variables such as density and confining

pressure as well as the mechanism of deformation and failure can be better understood.

## 5. Conclusions

According to the results of the triaxial compression test, the monotonic stress-strain curve of calcareous sand can be divided into two portions: prepeak portion and postpeak portion. For the dry sand and saturated calcareous sand under drainage condition, the postpeak softening portion can be further divided into three phases from the perspective of softening rate, i.e., accelerated phase, steady phase, and degradation phase. For the undrained saturated calcareous sand, the postpeak softening tendency appears as a two-phase hyperbolic shape. Moreover, it can be found that the residual stress is independent of the relative density for dry sand. The increase of confining pressure makes the strain softening more obvious and heightens the peak stress and residual stress; the starting and terminal points of strain softening under drainage compression are related to relative density and initial effective confining pressure. In addition, the amount of deformation required for the acceleration phase to total deformation is greater than that of dry sand; under undrained triaxial compression, increased initial confining pressure can enhance strain-softening.

Based on the monotonic characteristic of calcareous sand, a mathematical model has been proposed, in which a hyperbolic function and an inverted S-shaped function were used to describe the prepeak portion and the postpeak portion, respectively. It is worth noting that the application of parameter  $p$  enables the model to describe not only inverted S-shaped softening but also hyperbolic softening. The established model was validated with experiment results, showing that it can better describe the monotonic stress-strain relationship of calcareous sand. Besides, the physical meanings of the model parameters are clear and not hard to determine, making the model convenient to apply.

## Data Availability

All data used to support the findings of this study are available from the first author upon request.

## Disclosure

Haotian Zhang and Zongmu Luo are regarded as co-first authors.

## Conflicts of Interest

The authors declare that there are no conflicts of interest regarding the publication of this paper.

## Authors' Contributions

Haotian Zhang and Zongmu Luo contributed equally to the work.

## Acknowledgments

This work was financed and fully supported by the National Natural Science Foundation of China (Grant nos. 51774295 and 51808551), which is greatly appreciated by the authors.

## References

- [1] G. P. Chapman, "The sea-dredged sand and gravel industry of Great Britain," in *Proceedings of a Symposium: Sea-Dredged Aggregates for Concrete*, Slough, UK, December 1968.
- [2] K. Yamazaki, "Viewpoints on using sea sand in concrete as fine aggregates in Japan," *Cement and Concrete Research*, vol. 12, pp. 72–76, 1974.
- [3] J. Zheng and C. Bian, "A review of the present situation of the development and utilization of fine aggregate in Japan," *Early-Mixed Concrete*, vol. 3, pp. 27–29, 2014, in Chinese.
- [4] W. Gutt and R. J. Collins, "Sea-dredged aggregates in concrete," *Building Research Establishment Information Paper*, vol. 7, 1987.
- [5] W. Liu, "Study on characteristics of dredged marine sand and the mechanical properties of concrete made with dredged marine sand," *Bulletin of the Chinese Ceramic Society*, vol. 33, pp. 15–22, 2014.
- [6] S. Hasdemir, A. Tugrul, and M. Yilmaz, "The effect of natural sand composition on concrete strength," *Construction & Building Materials*, vol. 112, pp. 940–948, 2016.
- [7] A. Katz and H. Baum, "Effect of high levels of fines content on concrete properties," *ACI Materials Journal*, vol. 103, no. 6, p. 474, 2006.
- [8] Md Safiuddin, S. N. Raman, and M. F. M. Zain, "Utilization of quarry waste fine aggregate in concrete mixtures," *Journal of Applied Sciences Research*, vol. 3, pp. 202–208, 2007.
- [9] J. Xiao, C. Qiang, A. Nanni, and K. Zhang, "Use of sea-sand and seawater in concrete construction: current status and future opportunities," *Construction and Building Materials*, vol. 155, pp. 1101–1111, 2017.
- [10] K. Newman, "Aspects of workability, strength, shrinkage and creep, sea dredged aggregates for concrete," in *Proceedings of a Symposium, Sand and Gravel Association of Great Britain*, Buckinghamshire, UK, December 1968.
- [11] W. Deng and Y. Wang, "Investigating the factors affecting the properties of coral sand treated with microbially induced calcite precipitation," *Advances in Civil Engineering*, vol. 2018, Article ID 9590653, 6 pages, 2018.
- [12] T. Feng, Y. Tang, Q. Wang, J. Zhang, and J. Song, "Experimental investigation of dynamic characteristics of subsea sand-silt mixtures," *Advances in Civil Engineering*, vol. 2019, Article ID 5619039, 9 pages, 2019.
- [13] L. Ma, J. Wu, M. Wang, L. Dong, and H. Wei, "Dynamic compressive properties of dry and saturated coral rocks at high strain rates," *Engineering Geology*, vol. 272, p. 105615, 2020.
- [14] Y. Xiao, L. Chen, and F. Qin, "Experimental study on the attenuation of stress wave in coral sand," *Chinese Journal of Rock Mechanics and Engineering*, vol. 37, pp. 1520–1529, 2018, in Chinese.
- [15] X. Yu, L. Chen, Q. Fang, J. Zhang, D. Guo, and X. Hou, "Determination of attenuation effects of coral sand on the propagation of impact-induced stress wave," *International Journal of Impact Engineering*, vol. 125, pp. 63–82, 2019.
- [16] Y. Xiao, L. Chen, and F. Qin, "A testing method on the attenuation of stress waves in loose porous media and its application to coral sand," *Engineering Mechanics*, vol. 36, no. 1, pp. 44–52, 2019, in Chinese.
- [17] Y. Lv, X. Li, and Y. Wang, "Particle breakage of calcareous sand at high strain rates," *Powder Technology*, vol. 366, pp. 776–787, 2020.
- [18] Y. Lv, J. Liu, and Z. Xiong, "One-dimensional dynamic compressive behavior of dry calcareous sand at high strain rates," *Journal of Rock Mechanics and Geotechnical Engineering*, vol. 11, no. 1, pp. 192–201, 2019.
- [19] L. Wang, J. Mei, J. Wu, X. He, H. Li, and Q. Ding, "Mechanical properties and microscopic mechanism of coral sand-Cement mortar," *Advances in Materials Science and Engineering*, vol. 2020, Article ID 4854892, 11 pages, 2020.
- [20] L. Ma, Z. Li, J. Liu, L. Duan, and J. Wu, "Mechanical properties of coral concrete subjected to uniaxial dynamic compression," *Construction and Building Materials*, vol. 199, pp. 244–255, 2019.
- [21] M. Salem, H. Elmamlouk, and S. Agaiby, "Static and cyclic behavior of North Coast calcareous sand in Egypt," *Soil Dynamics and Earthquake Engineering*, vol. 55, pp. 83–91, 2013.
- [22] Q. Fang, J. Zhang, L. Chen, J. Liu, J. Fan, and Y. Zhang, "An algorithm for the grain-level modelling of a dry sand particulate system," *Modelling and Simulation in Materials Science and Engineering*, vol. 22, Article ID 055021, 2014.
- [23] J. M. Duncan and C.-Y. Chang, "Nonlinear analysis of stress and strain in soils," *Journal of Soil Mechanics & Foundations Division*, vol. 96, 1970.
- [24] L. Domaschuk and P. Valliappan, "Nonlinear settlement analysis by finite element," *Computer-Aided Design*, vol. 8, 1976.
- [25] H. Izumi, K. Kamemura, and S. Sato, "Finite element analysis of stresses and movements in excavations," in *Proceedings of the Numerical Methods in Geomechanics (Papers to 2nd International Conference)*, Blacksburg, VA, USA, June 1976.
- [26] P. V. Lade and J. M. Duncan, "Elastoplastic stress-strain theory for cohesionless soil," *Journal of Geotechnical and Geoenvironmental Engineering*, vol. 101, no. 10, pp. 1037–1053, 1975.
- [27] P. V. Lade, "Elasto-plastic stress-strain theory for cohesionless soil with curved yield surfaces," *International Journal of Solids and Structures*, vol. 13, no. 11, pp. 1019–1035, 1977.
- [28] M. K. Kim and P. V. Lade, "Single hardening constitutive model for frictional materials: I. Plastic potential Function,"



- International Journal of Rock Mechanics and Mining Sciences & Geomechanics Abstracts*, vol. 26, 1989.
- [29] F. L. DiMaggio, "Material model for granular soils," *Journal of Engineering Mechanics*, vol. 97, 1971.
- [30] L. Resende and J. B. Martin, "Formulation of drucker-prager cap model," *Journal of Engineering Mechanics*, vol. 111, no. 7, pp. 855–881, 1985.
- [31] H. Matsuoka, "A stress-strain model for granular materials considering the mechanism of fabric change," *Studies in Applied Mechanics*, vol. 7, 1983.
- [32] Dafalias and F. Yannis, "Bounding surface plasticity. I: mathematical foundation and hypoplasticity," *Journal of Engineering Mechanics*, vol. 112, no. 9, pp. 966–987, 1986.
- [33] Z. L. Wang, Y. F. Dafalias, and C. K. Shen, "Bounding surface hypoplasticity model for sand," *Journal of Engineering Mechanics*, vol. 116, no. 5, pp. 983–1001, 1990.
- [34] J. P. Bardet, "Hypoplastic model for sands," *Journal of Engineering Mechanics*, vol. 116, no. 9, pp. 1973–1994, 1990.
- [35] W. Wu and E. Bauer, "A simple hypoplastic constitutive model for sand," *International Journal for Numerical and Analytical Methods in Geomechanics*, vol. 18, no. 12, pp. 833–862, 1994.
- [36] M. G. Jefferies, "Nor-Sand: a simple critical state model for sand," *Géotechnique*, vol. 43, no. 1, pp. 91–103, 1993.
- [37] W. Wu, E. Bauer, and D. Kolymbas, "Hypoplastic constitutive model with critical state for granular materials," *Mechanics of Materials*, vol. 23, no. 1, pp. 45–69, 1996.
- [38] X. S. Li, "A sand model with state-dependent dilatancy," *Géotechnique*, vol. 52, no. 3, pp. 173–186, 2002.
- [39] M. T. Manzari and Y. F. Dafalias, "A critical state two-surface plasticity model for sands," *Géotechnique*, vol. 47, no. 2, pp. 255–272, 1997.
- [40] H. S. Yu, "CASM: a unified state parameter model for clay and sand," *International Journal for Numerical and Analytical Methods in Geomechanics*, vol. 22, no. 8, pp. 621–653, 1998.
- [41] L. Ma, Z. Li, M. Wang, H. Wei, and P. Fan, "Effects of size and loading rate on the mechanical properties of single coral particles," *Powder Technology*, vol. 342, pp. 961–971, 2019.
- [42] ASTM Standard, "Test method for specific gravity of soil solids by gas pycnometer. ASTM standard D5550–14," *Annual Book of ASTM Standards, 04.08*, ASTM, West Conshohocken, PA, USA, 2014.
- [43] ASTM Standard, "Test methods for maximum index density and unit weight of soils using a vibratory table," *ASTM Standard D4253–16*, ASTM, West Conshohocken, PA, USA, 2016.
- [44] Y. Jin, Z. Yin, D. Zhang, and H. Huang, "Unified modeling of the monotonic and cyclic behaviors of sand and clay," *Acta Mechanica Sinica*, vol. 28, no. 2, pp. 111–132, 2015.
- [45] Y. Wang, "Investigation on the deformation mechanism of calcareous sand," *Protective Engineering*, vol. 40, pp. 35–39, 2018, in Chinese.
- [46] J. Fonseca, P. Bésuelle, and G. Viggiani, "Micromechanisms of inelastic deformation in sandstones: an insight using X-ray micro-tomography," *Géotechnique Letters*, vol. 3, no. 2, pp. 78–83, 2013.

## Research Article

# Computation Method for the Settlement of a Vertically Loaded Pile in Sloping Ground

Chong Jiang , Wen-yan Wu, Jia-li He, and Lu-jie Chen

*School of Resources and Safety Engineering, Central South University, Changsha 410083, Hunan, China*

Correspondence should be addressed to Chong Jiang; [jiang4107@sohu.com](mailto:jiang4107@sohu.com)

Received 16 February 2020; Accepted 16 June 2020; Published 23 July 2020

Academic Editor: Xihong Zhang

Copyright © 2020 Chong Jiang et al. This is an open access article distributed under the Creative Commons Attribution License, which permits unrestricted use, distribution, and reproduction in any medium, provided the original work is properly cited.

Based on the hyperbolic curve tangent modulus method and the wedge stress theory, this paper proposes a calculation method for the settlement of a vertically loaded single pile in sloping ground. By establishing the relationship between the initial tangent modulus and the compression modulus of the slope soil, the tangent modulus of the slope soil is obtained combining with Mindlin-Geddes solution and Hansen formula, and the solution of the pile settlement in sloping ground is derived. Then, a series of numerical analyses are carried out to examine the feasibility of the proposed method. Finally, the effect of parameters is discussed in detail, including the slope angle, the distance of the pile from the slope crest, and the soil properties around the pile. The results show that the pile settlement will increase by increasing the slope angle or decreasing the distance of the pile from the slope crest, and the effect of the two parameters on the pile settlement is coupling-related. Besides, the compression modulus, cohesion, and internal friction angle of the soil around the pile are negatively related to the pile settlement and it is found that the compression modulus of the soil is the more influential parameter.

## 1. Introduction

Pile foundations are one of the widely used foundations, which are often used in the transmission tower, high-rise building, bridge engineering, and other structures. These structures are often built in or near the slope. The calculation of the pile settlement is an important part of the pile foundation design in sloping ground [1].

At present, the majority of studies focus on the theoretical calculation methods of the pile settlement in flat ground, mainly including the elastic theory method [2, 3], the shearing displacement method [4], the load transfer method [5], and the layerwise summation method. In recent years, based on the above theoretical methods, many researchers have carried out further research on the nonlinear calculation of the pile settlement [6–8]. For example, Zhao et al. [9] used the energy method to calculate the pile settlement with a high bearing platform. According to the cylindrical cavity expansion theory and the load-transfer models, Zhang et al. [10] established the nonlinear deformation calculation method of the pile foundation in sand. In

addition, a series of optimization calculation methods of the pile settlement under different conditions in flat ground are proposed [11–13]. However, the pile behavior in sloping ground is different from that in flat ground. First, the stress state of the soil in sloping ground changes because the soil around the pile is in an asymmetric space which is different from the semi-infinite space in flat ground. Second, the lack of soil in a slope reduces the constraint of the soil on the pile and the Earth pressure on the pile side will inevitably decrease; therefore, the ultimate bearing capacity of the pile tip in sloping ground decreases. Finally, the slope effect is generated; that is, the pile displacement in sloping ground is larger than that in flat ground under the same load. As a result, the calculation methods of the pile settlement in flat ground are no longer suitable for piles in sloping ground. However, the research on the calculation method of the pile settlement in sloping ground is limited. Most of the researchers have investigated the lateral response [14–16], lateral deformation [17, 18], and lateral bearing capacity [19–21] of pile foundations or the load transfer law of pile foundations under vertical load [22] in sloping ground.

Therefore, it is necessary to establish the calculation method of the pile settlement in sloping ground.

Based on the hyperbolic curve tangent modulus method, considering the slope effect, this paper establishes the calculation method of the pile settlement in sloping ground and performs parametric studies. Firstly, based on the wedge stress theory, the three-direction stress relationship of soil in sloping ground under the self-weight is studied, and the relationship between the initial tangent modulus  $E_0$  and the compression modulus  $E_s$  is deduced. Then, combined with the tip resistance ratio of the pile in sloping ground, Mindlin-Geddes solution is improved to calculate the additional stress of the pile tip. Besides, Hansen formula is used to calculate the ultimate resistance at the pile tip, which can consider the inclination of the ground. Finally, the pile settlement in sloping ground is calculated by combining with the layerwise summation method. In addition, the theoretical results are compared with the numerical simulation results. The influential parameters including the slope angle, the distance of the pile from the slope crest, the compression modulus, cohesion, and internal friction angle of the soil around the pile are analyzed.

## 2. Calculation Method of the Pile Settlement in Sloping Ground Based on the Hyperbolic Curve Tangent Modulus Method

**2.1. Basic Assumptions.** The schematic of the model analyzed is illustrated in Figure 1.  $(r, \theta)$  is the polar coordinate system,  $(x, z)$  is the rectangular coordinate system, and the  $y$  direction is perpendicular to the  $x$ - $z$  plane. The stress of the soil around the pile under the self-weight is  $\rho g$ . The basic assumptions are made as follows for simplicity:

- (1) The pile is rigid without compression deformation. The settlement at the pile tip is equal to the settlement at the pile top.
- (2) Both soil and pile are homogeneous and isotropic.
- (3) The slope is stable without instability and damage.

**2.2. Calculation Method of the Pile Settlement in Sloping Ground.** Based on the hyperbolic curve tangent modulus method [23], the load-settlement curve of the pile is assumed to be a hyperbolic curve:

$$P = \frac{S}{a + bS}, \quad (1)$$

where  $a$  and  $b$  are fitting parameters of the hyperbolic curve, which can be obtained by curve fitting.

Then the tangent modulus of the soil at any depth under the pile tip is

$$E_t = \left(1 - R_f \frac{P_z}{P_u}\right)^2 E_0. \quad (2)$$

Combined with the layerwise summation method, it can be obtained that, under the load increment  $P_i$ , the compression  $\Delta S_{ij}$  of the soil layer  $\Delta h_j$  at a certain depth under the pile is

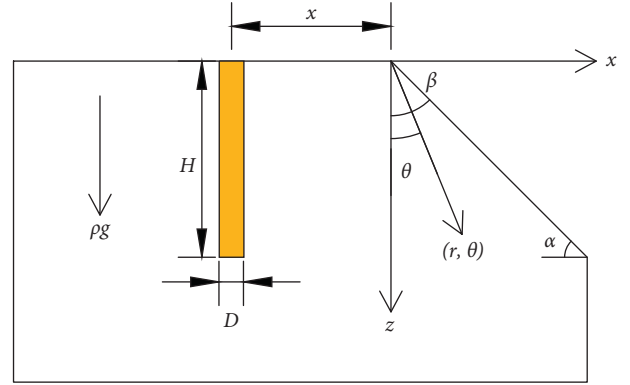


FIGURE 1: Schematic view of the model.

$$\Delta S_{ij} = \frac{P_i \Delta h_j}{E_t}. \quad (3)$$

After obtaining the compression of each layered soil, the total settlement  $S_i$  of the pile tip under each load level can be obtained:

$$S_i = \sum_{j=1}^n \Delta S_{ij}. \quad (4)$$

In order to consider the slope effect on the pile settlement, based on the wedge stress theory, the initial tangent modulus equation of the soil in a slope is derived. Then, by introducing Mindlin-Geddes solution and Hansen formula, the tangent modulus of the pile in sloping ground is obtained according to equation (2), and the calculation method of the pile settlement in sloping ground is finally established by combining equation (3) with equation (4).

**2.2.1. Initial Tangent Modulus Equation of the Pile in Sloping Ground Based on Wedge Theory.** In order to study the three-dimensional stress relationship of the soil in a slope, the elastic stress solution of the soil in a slope under the self-weight in [24] is introduced:

$$\sigma_r = \frac{1}{4} \rho g r \left[ \frac{3 \cos^2 \beta - 2}{\cos^2 \beta} (\cos \theta - \cos 3\theta) + t g \beta (\sin \theta - 3 \sin 3\theta) \right] + \rho g r \cos \theta, \quad (5)$$

$$\sigma_\theta = \frac{1}{4} \rho g r \left[ \frac{3 \cos^2 \beta - 2}{\cos^2 \beta} (3 \cos \theta + \cos 3\theta) + t g \beta (\sin \theta + 3 \sin 3\theta) \right] + \rho g r \cos \theta, \quad (6)$$

$$\tau_{r\theta} = \frac{1}{4} \rho g r \left[ \frac{3 \cos^2 \beta - 2}{\cos^2 \beta} (\sin \theta + \sin 3\theta) + t g \beta (\cos \theta + 3 \cos 3\theta) \right], \quad (7)$$

where  $\sigma_r$ ,  $\sigma_\theta$ , and  $\tau_{r\theta}$  are the elastic stress solutions of the soil in the polar coordinate system.

Equations (5)~(7) in the polar coordinate are transformed to elastic stress solution in rectangular coordinate system as equations (8)~(10) for simplicity:

$$\sigma_z = \frac{\sigma_r + \sigma_\theta}{2} + \frac{\sigma_r - \sigma_\theta}{2} \cos 2\theta - \tau_{r\theta} \sin 2\theta, \quad (8)$$

$$\sigma_x = \frac{\sigma_r + \sigma_\theta}{2} - \frac{\sigma_r - \sigma_\theta}{2} \cos 2\theta + \tau_{r\theta} \sin 2\theta, \quad (9)$$

$$\tau_{zx} = \frac{\sigma_r - \sigma_\theta}{2} \sin 2\theta + \tau_{r\theta} \cos 2\theta, \quad (10)$$

where  $\sigma_z$ ,  $\sigma_x$ , and  $\tau_{zx}$  are the elastic stress solutions of the soil in the rectangular coordinate system.

The soil mass on the central axis of the pile body includes

$$r \cos \theta = z, \quad (11)$$

$$r \sin \theta = x. \quad (12)$$

In the rectangular coordinate system, the elastic stress solution of the soil in a slope under the self-weight stress can be obtained by equations (5)~(12):

$$\sigma = \rho g z, \quad (13)$$

$$\sigma_x = -\rho g \left( z \frac{2 \cos^2 \beta - 2}{\cos^2 \beta} + x t g \beta \right), \quad (14)$$

$$\tau_{zx} = \rho g z t g \beta. \quad (15)$$

According to equation (16), which is the principal stress transformation equation, the maximum principal stress  $\sigma_1$  and the minimum principal stress  $\sigma_2$  can be obtained:

$$\left. \begin{array}{l} \sigma_1 \\ \sigma_2 \end{array} \right\} = \frac{\sigma_z + \sigma_x}{2} \pm \sqrt{\left( \frac{\sigma_z - \sigma_x}{2} \right)^2 + \tau_{zx}^2}. \quad (16)$$

Suppose that this is a plane strain problem and the longitudinal strain  $\sigma_x = k_1 \sigma_z$ , combined with Hooke's law:

$$\varepsilon_y = \frac{1}{E_0} [\sigma_y - \nu(\sigma_z + \sigma_x)]. \quad (17)$$

The third principal stress can be calculated:

$$\sigma_y = \nu(\sigma_z + \sigma_x). \quad (18)$$

Therefore, based on equations (13)~(18), the three-dimensional stress solution of soil in a slope can be obtained. The three-dimensional stress relationship of soil in a slope under self-weight is expressed in equations (19) and (20).

$$\sigma_x = k_1 \sigma_z, \quad (19)$$

$$\sigma_y = k_2 \sigma_z, \quad (20)$$

where  $k_1$  and  $k_2$  are the ratio of horizontal stresses  $\sigma_x$  and  $\sigma_y$  and vertical stress  $\sigma_z$ .

In the confining compression test, the relationship between soil stress, strain, and compression modulus  $E_s$  is as follows:

$$\varepsilon_z = \frac{\sigma_z}{E_s}. \quad (21)$$

Under the condition of triaxial test, according to the generalized Hooke's law, the vertical strain of soil is as follows:

$$\varepsilon_z = \frac{\sigma_z}{E_0} - \nu \frac{\sigma_x}{E_0} - \nu \frac{\sigma_y}{E_0}. \quad (22)$$

Assuming that the initial state of the soil is the same under different test conditions [25], the relationship between the initial tangent modulus  $E_0$  and the compression modulus  $E_s$  can be obtained by combining equations (21) and (22), that is, the initial tangent modulus equation of the pile in sloping ground:

$$E_0 = E_s (1 - \nu k_1 - \nu k_2). \quad (23)$$

### 2.2.2. Additional Stress Solution of the Soil at the Pile Tip.

In order to consider the slope effect on the additional stress of the soil at the pile tip, the resistance ratio  $\delta$  (end resistance ratio  $\delta =$  pile end resistance/pile top load) of the pile tip in sloping ground is introduced to improve the Mindlin-Geddes solution [26]. In this solution, the vertical load  $P$  on the pile top is divided into two parts: the pile end resistance  $\delta P$  and the pile side friction  $(1 - \delta)P$ . It is assumed that pile side friction resistance is a triangular distribution with linear increase along the pile depth, as shown in Figure 2.

Then the additional stress of the soil under the pile tip is produced by the pile tip resistance and the pile side friction resistance:

$$p_z = p_{zp} + p_{zs}. \quad (24)$$

The pile tip resistance and pile side friction are assumed to be the internal concentrated force of soil, and the additional stress produced by the pile tip resistance is

$$p_{zp} = \frac{\delta P}{H^2} I_p, \quad (25)$$

$$I_p = \frac{1}{8\pi(1-\nu)} \left\{ \frac{(1-2\nu)(m-1)}{A^3} - \frac{(1-2\nu)(m-1)}{B^3} + \frac{3(m-1)}{A^5} + \frac{3(3-4\nu)m(m+1)^2 - 3(m+1)(5m+1)}{B^5} + \frac{30m(m+1)^3}{B^7} \right\}. \quad (26)$$

The additional stress caused by the pile side friction is

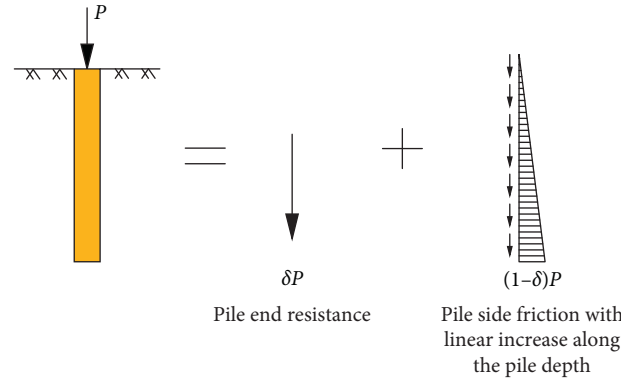


FIGURE 2: Decomposition of pile load in Mindlin-Geddes solution [26].

$$P_{zs} = \frac{P}{H^2} (1 - \delta) I_s, \quad (27)$$

$$I_s = \frac{1}{4\pi(1-\nu)} \left\{ \frac{2(2-\nu)}{A} - \frac{2(2-\nu)(4m+1) - 2(1-2\nu)(1+m)m^2/n^2}{B} - \frac{2(1-2\nu)m^3/n^2 - 8(2-\nu)m}{F} \right. \\ \left. - \frac{mn^2 + (m-1)^3}{A} - \frac{4\nu n^2 m + 4m^3 - 15n^2 m - 2(5+2\nu)(m/n)^2(m+1)^3}{B^3} \right. \\ \left. - \frac{12(m/n)^2 m^5 + 6m^3 + 2(5+2\nu)(m/n)^2 m^3}{F^3} - \frac{6mn^2(n^2 - m^2) + 12(m/n)^2(m+1)^5}{B^5} \right. \\ \left. + \frac{12(m/n)^2 m^5 + 6mn^2(n^2 - m^2)}{F^5} + 2(2-\nu) \ln \left( \frac{A+m-1}{F+m} \times \frac{B+m+1}{F+m} \right) \right\}, \quad (28)$$

where  $A^2 = n^2 + (m-1)^2$ ;  $B^2 = n^2 + (m+1)^2$ ;  $F^2 = n^2 + m^2$ ;  $n = x/H$ ; and  $m = z/H$ .

Therefore, according to equations (24)~(28), the additional stress on the soil at any depth of the pile tip under the vertical load  $P$  can be calculated. The pile tip resistance ratio  $\delta$  is generally determined by the actual measurement data of local engineering [26]. In this paper, the Mindlin-Geddes solution is improved by using the pile tip resistance ratio in sloping ground obtained from numerical simulation.

**2.2.3. Solution of the Ultimate Resistance at the Pile Tip.** In order to consider the slope effect on the ultimate resistance of the pile tip, Hansen solution [25] is used to calculate the ultimate resistance of the pile tip:

$$p_u = \frac{1}{2} \gamma DN_r s_r d_r g_r b_r + qN_q s_q d_q i_q g_q b_q + cN_c s_c d_c i_c g_c b_c. \quad (29)$$

In this paper, since load inclination and foundation bottom inclination are not considered,  $i_r$ ,  $i_q$ ,  $i_c$ ,  $b_r$ ,  $b_q$ , and  $b_c$  are all taken as 1.

**2.3. Determination of Calculation Parameters.** The method of parameter determination [25, 26] is shown in Table 1.

### 3. Validation of Settlement Calculation Method

The finite element software is used to simulate the pile settlement under vertical load in sloping ground. By comparing the results of numerical simulation and theoretical calculation, the reliability of the proposed method is verified.

**3.1. Numerical Simulation.** Most of the available researches are focused on the lateral response of the pile under the lateral load in slopes and the settlement characteristics of the pile under vertical load in slopes are rarely analyzed. Therefore, the data of  $\alpha = 45^\circ$  in [27] was used to verify the correctness of the modeling method. The pile length is  $H = 12$  m and the pile diameter is  $D = 0.6$  m. Soil and pile properties are summarized in Table 2.

The comparison results between the simulation in this paper and those in [27] are shown in Figure 3. A good compatibility could be seen, which proves the correctness of the numerical modeling method in this paper.

The rigid pile is defined as [28]  $H \leq 2.5/\eta$ , where  $\eta$  is the deformation coefficient of pile body ( $m^{-1}$ ). The length diameter ratio of pile is calculated by combining the "m" method. Therefore, in this simulation,  $H = 8m$ ,  $D = 1$  m, and distance of the pile from the slope crest is the normalized value of  $x = (n + 0.5)D$ . Parameters in Table 2 are used for soil and pile properties.



TABLE 1: Determination of calculation parameters.

Parameters	Determination method	Parameters	Determination method
$a, b$	Obtained from P-S curve fitting	$s_r$	$S_c = 1 - 0.4(D/H)$
$R_f$	According to experience value, generally between 0.85 and 1.00	$s_q$	$S_q = 1 + (D/H)\tan\phi$
$P, c, v, \gamma, \phi, Es$	Determination by laboratory test or field test	$s_c$	$S_c = 1 + 0.2(D/H)$
$\delta$	Statistical determination of measured data of local projects	$g_c$	$g_c = 1 - (\alpha/147^\circ)$
$N_q$	$N_q = e^{\pi \tan\phi} \tan^2(45^\circ + (\phi/2))$	$g_a$	$g_a = (1 - 0.5 \tan\alpha)^5$
$N_c$	$N_c = (N_q - 1)\cot\phi$	$g_r$	$g_r = (1 - 0.5 \tan\alpha)^5$
$N_r$	$N_r = 1.5(N_q - 1)\tan\phi$	$d_r$	$d_r = 1.0$
$d_q$	$d_q = 1 + 2 \tan\phi(1 - \sin\phi)^2(H/D)$	$d_c$	$d_c = 1 + 0.4(H/D)$

TABLE 2: Soil and pile properties.

Material	Young's modulus (Pa)	Poisson's ratio	Density ( $\text{kg}\cdot\text{m}^{-3}$ )	Cohesion (Pa)	Friction angle ( $^\circ$ )	Dilatation angle ( $^\circ$ )
Pile	$3.0 \times 10^{10}$	0.1	2500	—	—	—
Soil	$1.2 \times 10^7$	0.40	1800	$3.0 \times 10^4$	$35^\circ$	$5^\circ$

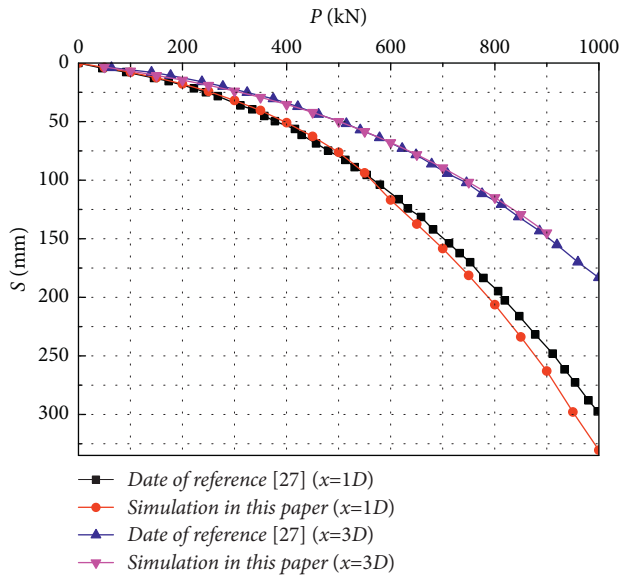


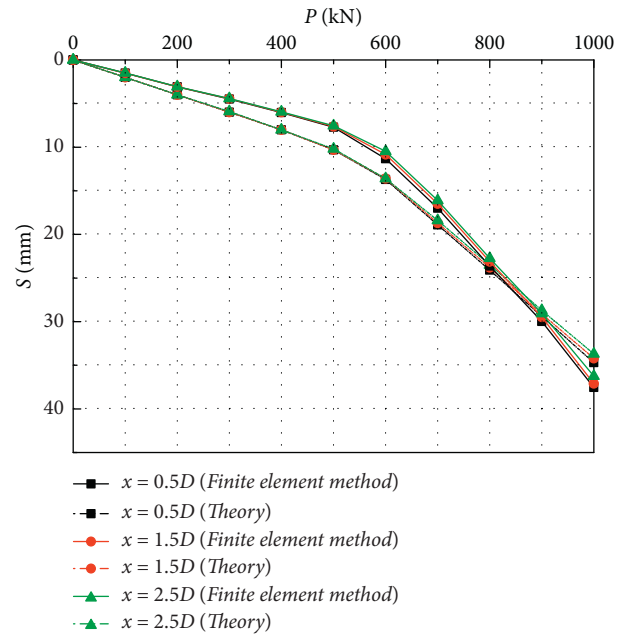
FIGURE 3: Comparison of simulation results between this paper and literature.

3.2. *Validation of the Settlement Calculation Method.* The ratio of pile tip resistance and pile top load obtained by numerical simulation is applied to the parameter  $\delta$  in theoretical calculation. The comparison between numerical simulation results and theoretical calculation results is shown in Figures 4 and 5.

A good fit of P-S curve could be seen and the settlement law of the pile is consistent. Comparing the settlement of theoretical calculation and simulation results under the same conditions, the maximum error values in Figures 4 and 5 are 8.78% and 5.65%, respectively, which are within the reasonable error range, proving the correctness of the theoretical calculation method.

#### 4. Parametric Analysis

The slope angle, the distance of the pile from the slope crest, the compression modulus, cohesion, and friction angle of

FIGURE 4: Comparison of P-S curve under  $\alpha = 15^\circ$ .

the soil are important parameters that influence the pile settlement in sloping ground. Based on the calculation method of the pile settlement in sloping ground under vertical load, parametric studies are carried out. The values of these parameters are shown in Table 2.

4.1. *Effect of the Slope Angle.* Figures 6 and 7 show the P-S curve of the pile with 7 different slope angles when the distance of the pile from the slope crest  $x$  is  $0.5D$  and  $10.5D$ , respectively, which shows the following:

- (1) Under the same load, the pile settlement increases with the increase of slope angle. When the slope angle gets larger, the increase of the pile settlement is more obvious.

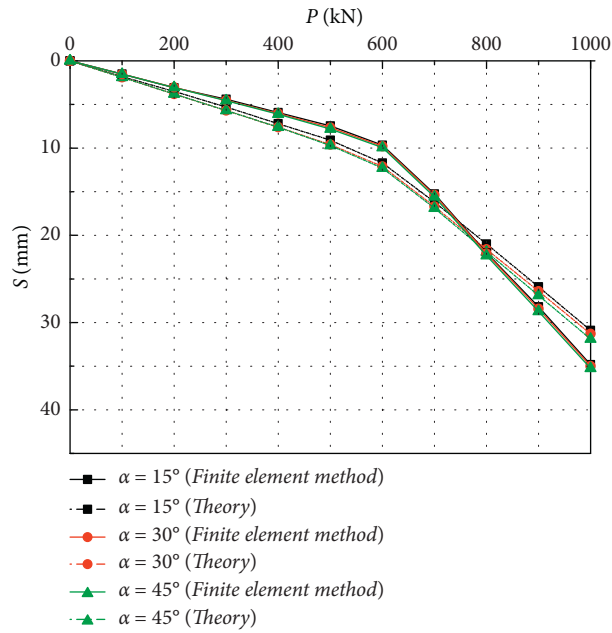


FIGURE 5: Comparison of P-S curve under  $x = 10.5D$ .

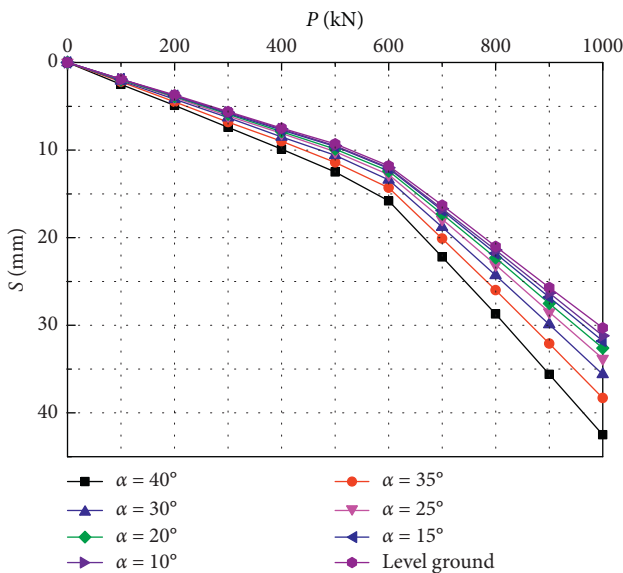


FIGURE 6: Effect of slope angle on P-S curve with different slope proximity under  $x = 0.5D$ .

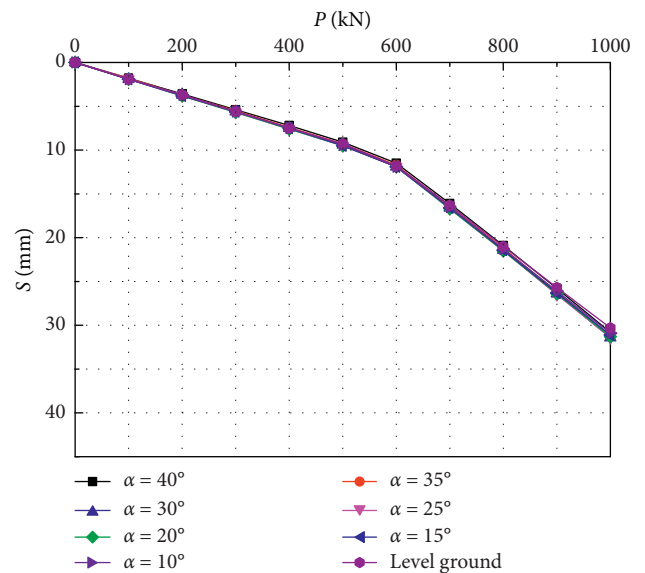


FIGURE 7: Effect of slope angle on P-S curve with different slope proximity under  $x = 10.5D$ .

(2) The effect of slope angle on the pile settlement is weakened by the increase of distance of the pile from the slope crest. When  $x = 0.5D$ , the growth rate of the pile settlement is between 2.97% and 40.26% with the increase of slope angle, compared with that of pile in flat ground under the maximum load. When  $x = 10.5D$ , the growth rate of the pile settlement is between 1.98% and 3.63%.

4.2. Effect of the Distance of the Pile from the Slope Crest. Figures 8 and 9 show the P-S curve of the pile under 10 different slope proximities with slope angle of  $15^\circ$  and  $60^\circ$ , respectively, which shows the following:

- (1) With the decrease of slope proximity, the settlement of pile foundation increases gradually under the same load. The smaller the slope proximity is, the more significantly the tendency of pile foundation settlement increases.
- (2) With the increase of slope angle, the effect of slope proximity on slope effect is strengthened. Compared with the pile in flat ground, when  $\alpha = 15^\circ$ , the growth rate of the pile settlement approaches 0 with the decrease of  $x$  and when  $\alpha = 60^\circ$ , the maximum growth rate of the pile settlement reaches 47.84% with the decrease of  $x$ .

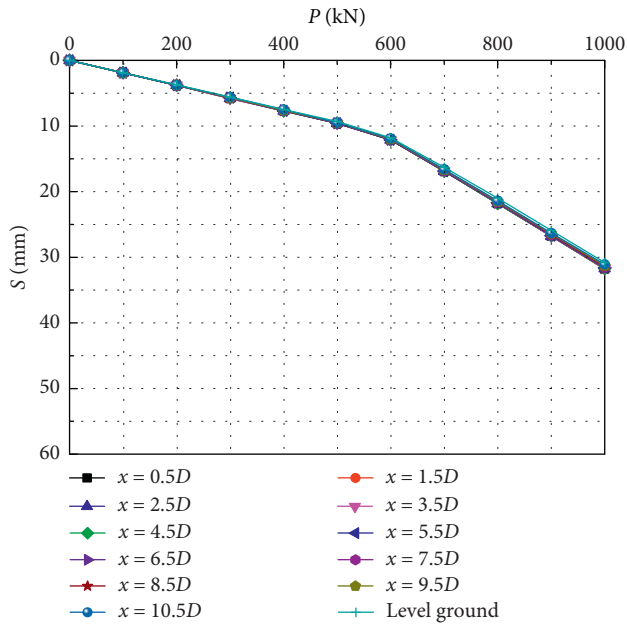


FIGURE 8: Effect of slope proximity on P-S curve with different slope angle under  $\alpha = 15^\circ$ .

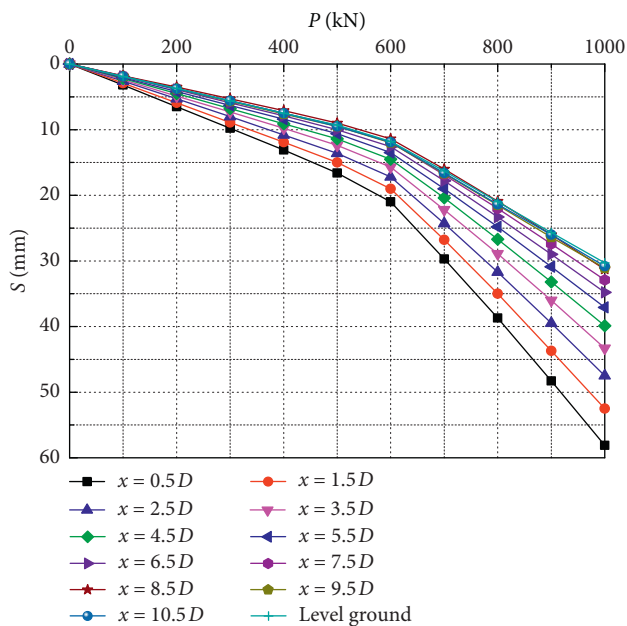


FIGURE 9: Effect of slope proximity on P-S curve with different slope angle under  $\alpha = 60^\circ$ .

- (3) When  $x \geq 8.5D$ , the pile settlement tends to be stable, which is very close to the settlement of pile in flat ground, and the effect of slope is negligible.

4.3. Effect of Compression Modulus. Figures 10 and 11 show the  $E_s$ -S curve under different conditions when  $P = 1000$  kN, which shows the following.

The settlement of pile foundation decreases with the increase of compression modulus  $E_s$ , and the decrease range

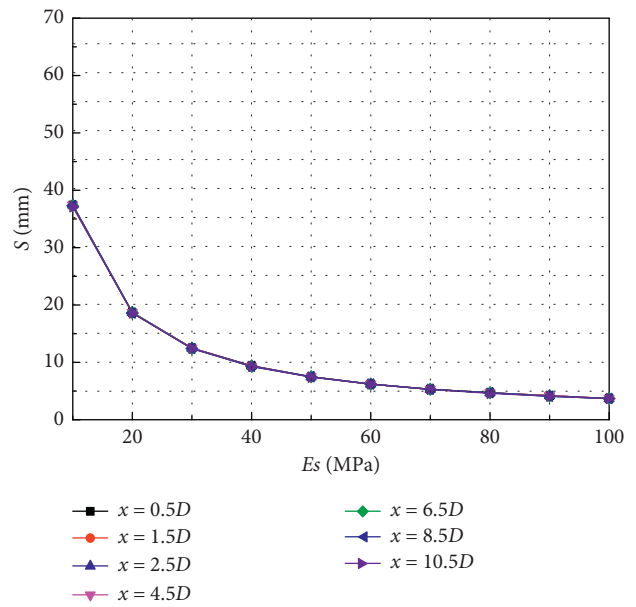


FIGURE 10:  $E_s$ -S curve under  $P = 1000$  kN and  $\alpha = 15^\circ$ .

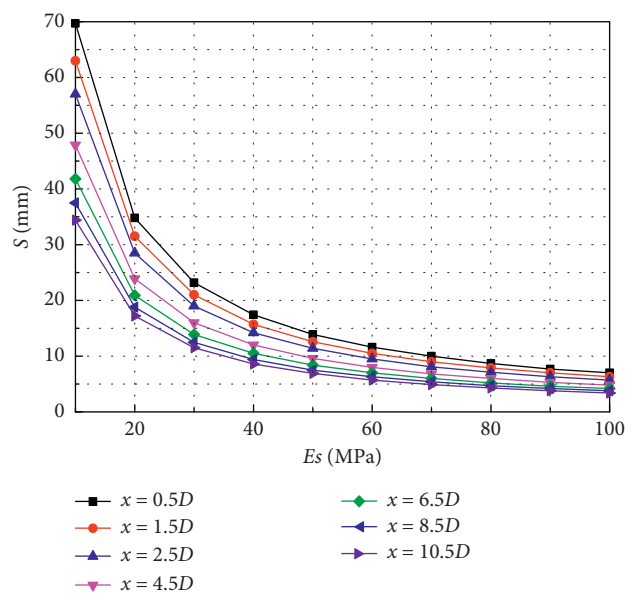


FIGURE 11:  $E_s$ -S curve under  $P = 1000$  kN and  $\alpha = 60^\circ$ .

is related to slope effect. When  $\alpha = 15^\circ$ , with the increase of  $E_s$  from 10 MPa to 40 MPa, the settlement of pile foundation decreases sharply, with the decrease range reaching 74.87%; when  $E_s$  is between 40 MPa and 60 MPa, the rate of settlement decrease gradually slows down; when  $E_s$  is more than 60 MPa, the settlement of pile foundation tends to be stable. However, when  $\alpha = 60^\circ$ , the range of pile foundation settlement changes with  $E_s$  increases with the decrease of  $x$ , which shows that the more prominent the slope effect, the greater the influence of  $E_s$  on the settlement of pile foundation.

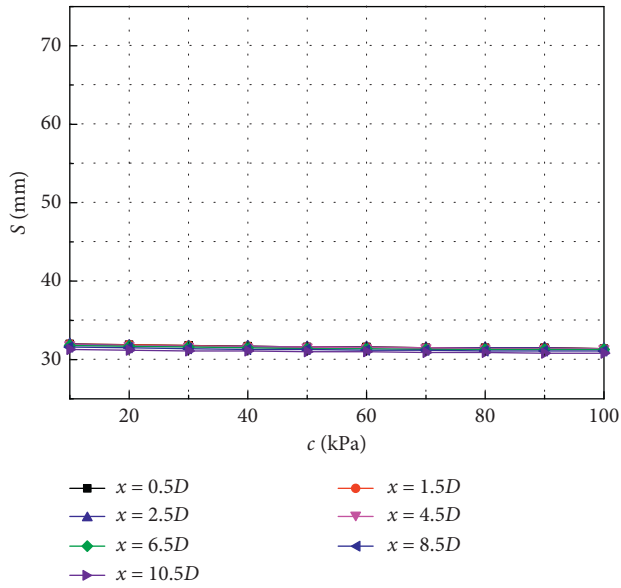


FIGURE 12: c-S curve under  $P=1000$  kN and  $\alpha=15^\circ$ .

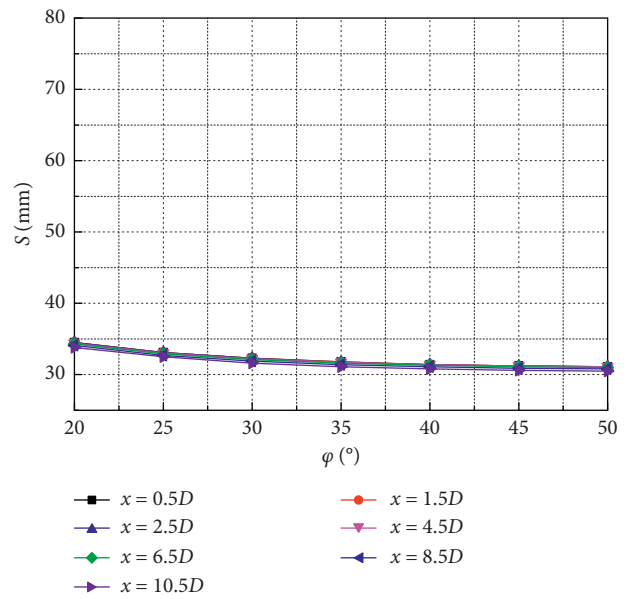


FIGURE 14:  $\phi$ -S curve under  $P=1000$  kN and  $\alpha=15^\circ$ .

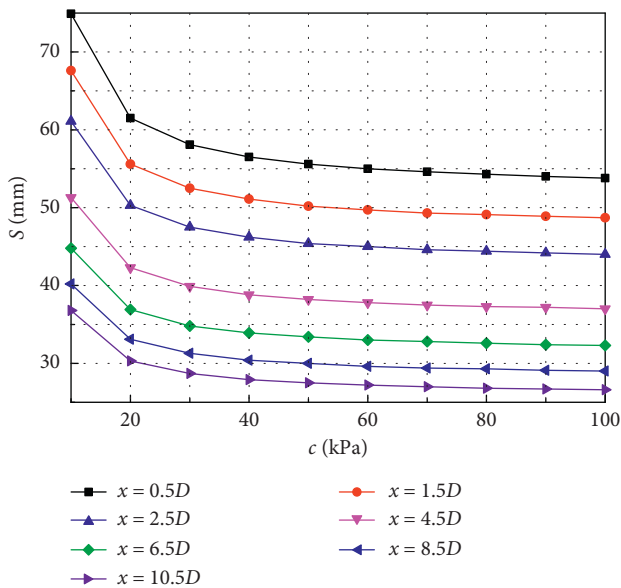


FIGURE 13: c-S curve under  $P=1000$  kN and  $\alpha=60^\circ$ .

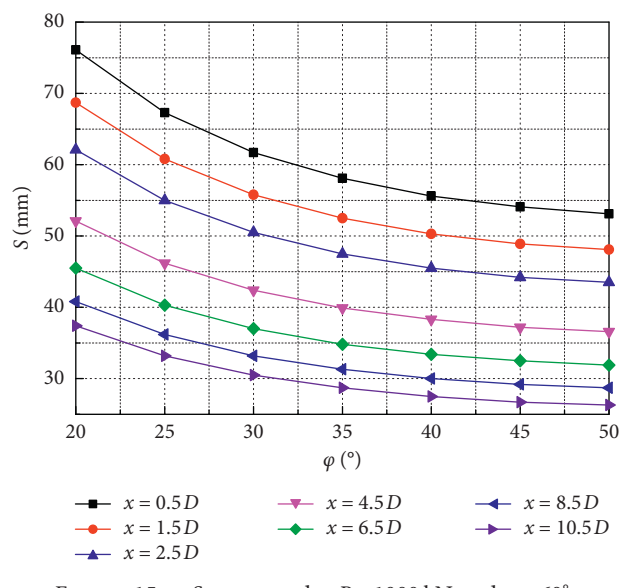


FIGURE 15:  $\phi$ -S curve under  $P=1000$  kN and  $\alpha=60^\circ$ .

4.4. Influence of Cohesion. Figures 12 and 13 show the c-S curve under different conditions when  $P=1000$  kN. The pile settlement decreases with the increase of cohesion and the decrease is related to the slope effect. When  $\alpha=15^\circ$ , the variation of the pile settlement with  $c$  is very small; however, when  $\alpha=60^\circ$ , with the increase of  $c$  from 10 kPa to 20 kPa, the pile settlement decreases sharply and the decrease range is between 17.66% and 17.89% with the difference of  $x$ . When  $c$  is between 20 kPa and 60 kPa, the decrease rate of settlement slows down and when  $c$  is over 60 kPa, the settlement of pile foundation tends to be stable.

4.5. Effect of the Friction Angle. Figures 14 and 15 show the  $\phi$ -S curve under different conditions when  $P=1000$  kN. The pile settlement decreases with the increase of the friction angle and the decrease rate is related to the slope effect. When  $\alpha=15^\circ$ , the pile settlement varies less with  $\phi$ ; however, when  $\alpha=60^\circ$ , the pile settlement changes greatly with  $\phi$ . As  $\phi$  increases from  $20^\circ$  to  $50^\circ$ , the pile settlement decreases by 30%, indicating that increase of slope angle enhances the effect of  $\phi$  on the pile settlement. However, under the same angle, with the change of  $x$ , the rate of the pile settlement changing with  $\phi$  is basically the same, indicating that the effect of  $\phi$  on pile foundation settlement is almost not affected by  $x$ .

## 5. Conclusion

Based on the hyperbolic curve tangent modulus method, this paper studies the calculation method of the pile settlement under vertical load in sloping ground, and conclusions are drawn as follows:

- (1) Based on hyperbolic curve tangent modulus method, the calculation method of the pile settlement in sloping ground is proposed. The P-S curve obtained by this method is consistent with the numerical simulation results and the deformation law of the pile is consistent, which proves the feasibility of this method in calculating the pile settlement in sloping ground.
- (2) The effect of the slope angle and the distance of the pile from the slope crest on the pile settlement is coupled. With the increase of  $\alpha$ , the effect of  $x$  on the pile settlement is enhanced and, with the increase of  $x$ , the effect of  $\alpha$  on settlement is weakened.
- (3) The compression modulus, cohesion, and friction angle of the soil are all negatively related to the pile settlement. It was found that the pile settlement changes more obviously with the compression modulus, indicating that the compression modulus has a more significant effect on the pile settlement.

## Nomenclature

$b_r, b_q, b_c$ :	Correction factor of foundation bottom tilt
$c$ :	Cohesion of soil
$d_r, d_q, d_c$ :	Depth correction factor considering soil strength
$D$ :	Pile diameter
$E_s$ :	Compression modulus
$E_t$ :	Tangent modulus
$E_0$ :	Initial tangent modulus
$g$ :	Acceleration of gravity
$g_r, g_q, g_c$ :	Correction factor of ground tilt
$H$ :	Pile length
$i_r, i_q, i_c$ :	Correction factor of load inclination
$I_p$ :	Stress influence coefficient of pile tip resistance
$I_s$ :	Stress influence coefficient of pile side friction
$N_q, N_c, N_r$ :	Bearing capacity coefficient of foundation
$P$ :	Vertical load
$P_u$ :	Ultimate resistance of pile tip
$P_z$ :	Additional stress of soil at pile tip
$P_{zp}$ :	Additional stress caused by pile tip resistance
$P_{zs}$ :	Additional stress caused by pile side friction
$q$ :	Self-weight stress of soil at pile tip
$R_f$ :	Failure ratio
$S$ :	Settlement of pile top
$s_r, s_q, s_c$ :	Correction factor of pile foundation shape
$x$ :	Distance of the pile from the slope crest
$\alpha$ :	Slope angle
$\beta$ :	Opposite angle of the slope angle
$\gamma$ :	Bulk density of soil at pile tip
$\rho$ :	Soil density
$\varphi$ :	Friction angle of soil

$\nu$ :	Poisson's ratio
$\delta$ :	Tip resistance ratio.

## Data Availability

The data used to support the findings of this study are available from the corresponding author upon request.

## Conflicts of Interest

The authors declare that there are no conflicts of interest regarding the publication of this paper.

## Acknowledgments

This work was supported by the National Natural Science Foundation of China (Grant no. 51678570).

## References

- [1] J. Q. Mao and Y. Jiang, "Settlement calculation of pile group foundation based on results of vertical static load test on single pile," *Journal of the China Railway Society*, vol. 39, no. 1, pp. 97–103, 2017.
- [2] H. G. Poulos and E. H. Davis, *Piles Foundation Analysis and Design*, Wiley, New York, NY, USA, 1980.
- [3] H. G. Poulos and E. H. Davis, "The settlement behaviour of single axially loaded incompressible piles and piers," *Géotechnique*, vol. 18, no. 3, pp. 351–371, 1968.
- [4] R. W. Cooke, "The settlement of friction pile foundation," in *Proceedings of the Conference of Tall Building Kuala Lumpur*, Kuala Lumpur, Malaysia, 1974.
- [5] H. B. Seed and L. C. Reese, "The action of soft clay along friction piles," *Transactions, ASCE*, vol. 122, no. SM11, pp. 731–754, 1957.
- [6] L. Li and W. B. Gong, *Prediction of Nonlinear Vertical Settlement of a Pile Group Consisting of New and Existing Displacement Piles in Clay Strata*, Soils and Foundations, Tokyo, Japan, 2019.
- [7] Y. Jia, F. G. Song, B. L. Wang, and L. C. Long, "Modified load transfer method for calculation of foundation pile settlement due to dewatering," *Rock and Soil Mechanics*, vol. 36, no. 1, pp. 68–82, 2015.
- [8] W. J. Jun, D. Y. Yan, M. M. Wang et al., "Load-settlement rules and calculation of foundation piles in Karst cave, Chinese," *Journal of Geotechnical Engineering*, vol. 39, no. S2, pp. 67–70, 2017.
- [9] M. H. Zhao, Y. Q. Yang, P. B. Yin, and J. Long, "Settlement calculation of pile foundation with elevated caps by energy method," *Journal of Central South University (Science and Technology)*, vol. 46, no. 2, pp. 670–675, 2015.
- [10] Q. Q. Zhao, R. F. Feng, Y. L. Yu, S. W. Liu, and J. G. Qian, *Simplified Approach for Prediction of Nonlinear Response of Bored Pile Embedded in Sand*, Soils and Foundations, Tokyo, Japan, 2019.
- [11] M. H. Zhao, S. Q. Ma, Y. Xiao, and C. W. Yang, "Calculation on settlement of geogrid-encased stone columns based on thick-walled cylinder model," *Journal of Hunan University (Natural Sciences)*, vol. 46, no. 5, pp. 86–93, 2019.
- [12] D. D. Xin, L. W. Zhang, and C. X. Su, "Settlement research of pile groups in layered soil based on virtual soil-pile model," *Rock and Soil Mechanics*, vol. 38, no. 8, pp. 2368–2394, 2017.



- [13] Z. J. Wang, X. Y. Xie, and J. C. Wang, "A new nonlinear method for vertical settlement prediction of a single pile and pile groups in layered soils," *Computers and Geotechnics*, vol. 45, pp. 118–116, 2012.
- [14] H. Sharafi, Y. S. Maleki, and M. K. Fard, "Three-dimensional finite difference modeling of static soil-pile interactions to calculate p-y curves in pile-supported slopes," *Arabian Journal of Geosciences*, vol. 9, no. 1, pp. 1–16, 2016.
- [15] K. S. Beena, P. E. Kavitha, and K. P. Narayanan, "Model studies on laterally loaded piles in sloping clay bed," *Indian Geotechnical Journal*, vol. 48, no. 5, pp. 1–11, 2017.
- [16] Z. Fu, G. Jiang, S. Yuan, and A. Li, "Lateral behavior of piled bridge foundation and stabilizing piles on steep slope," *KSCE Journal of Civil Engineering*, vol. 23, no. 10, pp. 4223–4236, 2019.
- [17] C. Jiang, Z. C. Zhao, and J. L. He, "Nonlinear analysis of combined loaded rigid piles in cohesionless soil slope," *Computers and Geotechnics*, vol. 117, 2020.
- [18] Z. Muszyński and J. Rybak, "Horizontal displacement control in course of lateral loading of a pile in a slope," *IOP Conference Series: Materials Science and Engineering*, vol. 245, no. 3, Article ID 032002, 2017.
- [19] N. Nimityongskul, Y. Kawamata, D. Rayamajhi et al., "Full-scale tests on effects of slope on lateral capacity of piles installed in cohesive soils," *Journal of Geotechnical and Geoenvironmental Engineering*, vol. 144, no. 1, Article ID 04017103, 2018.
- [20] K. Georgiadis, M. Georgiadis, and C. Anagnostopoulos, "Lateral bearing capacity of rigid piles near clay slopes," *Soils and Foundations*, vol. 53, no. 1, pp. 144–154, 2013.
- [21] M. H. Yang, B. Deng, and M. H. Zhao, "Experimental and theoretical studies of laterally loaded single piles in slopes," *Journal of Zhejiang University-Science A (Applied Physics & Engineering)*, vol. 20, no. 11, pp. 838–851, 2019.
- [22] M. Jesmani, A. Kasrania, and M. Kamalzare, "Finite element modelling of undrained vertical bearing capacity of piles adjacent to different types of clayey slopes," *International Journal of Geotechnical Engineering*, vol. 12, no. 1, pp. 1–8, 2016.
- [23] G. H. Yang, "New computation method for soil foundation settlements," *Chinese Journal of Rock Mechanics and Engineering*, vol. 27, no. 4, 2007.
- [24] J. M. Gao and Z. L. Dun, *Wedge Stress Theory and its Application in Engineering*, Coal Industry Publishing House, Beijing, China, 2011.
- [25] G. X. Li, B. Y. Zhang, and Y. Z. Yu, *Soil Mechanics*, Tsinghua University Press, Beijing, China, 2013.
- [26] J. X. Zhou, G. X. Li, J. H. Zhang, S. M. Yu, and H. J. Wang, *Foundation Works*, Tsinghua University Press, Beijing, China, 2015.
- [27] C. Jiang, J. L. He, L. Liu et al., "Effect of loading direction and slope on laterally loaded pile in sloping ground," *Advances in Civil Engineering*, vol. 2018, Article ID 7569578, 12 pages, 2018.
- [28] P. D. Shi, *Pile and Pile Foundation Handbook*, China Communications Press Co., Ltd., Beijing, China, 2015.

## Research Article

# Physical Modelling of Roll and Pitch Motions of Travelling or Stationary Ship in Large-Scale Landslide-Generated Waves

Pei-yin Yuan <sup>1</sup>, Ping-yi Wang,<sup>2</sup> and Yu Zhao<sup>2,3</sup>

<sup>1</sup>College of Shipping and Naval Architecture, Chongqing Jiaotong University, Chongqing 400074, China

<sup>2</sup>College of River and Ocean Engineering, Chongqing Jiaotong University, Chongqing 400074, China

<sup>3</sup>College of Architecture and Urban Planning, Chongqing Jiaotong University, Chongqing 400074, China

Correspondence should be addressed to Pei-yin Yuan; yuan\_pei\_yin@163.com

Received 10 March 2020; Revised 18 May 2020; Accepted 30 June 2020; Published 21 July 2020

Academic Editor: Yanchao Shi

Copyright © 2020 Pei-yin Yuan et al. This is an open access article distributed under the Creative Commons Attribution License, which permits unrestricted use, distribution, and reproduction in any medium, provided the original work is properly cited.

Large-scale landslides often occur in river-type reservoirs, and landslide-generated waves affect navigation channels and the navigation of ships. Thus, such waves cause widespread regional disasters. This study establishes a mechanical model of landslide-generated waves via field investigations and data collection, reveals the mechanism and process of landslide-generated waves, and investigates the propagation characteristics of landslide-generated waves along a sloping wave. The feasibility of the model is verified via (i) regularity analysis, (ii) comparative analysis of the effect of landslide-generated waves of mountain river channel reservoirs on the movement characteristics of navigation vessels and stationary vessels, (iii) deviation from the equilibrium position, and (iv) an in-depth study of the influence of large-scale landslide-generated waves on ships in different navigation positions in a river channel. Countermeasures are proposed for a sailing ship to tackle a sudden landslide-generated wave; these measures can provide a theoretical basis for ships to sail safely through large-scale landslide-generated waves.

## 1. Introduction

Bank slopes are affected by water immersion, water erosion, wave impacts, water level fluctuation, and earthquakes. The unfavourable geological phenomena of high-density rock mass collapse and slip occur frequently, causing large-scale high-density rock mass to move at high speeds. Landslides into water trigger large waves, causing devastating damage to life and property in the landslide area and the surrounding areas. The formation of a landslide-generated wave is generally divided into three stages. In the first stage, the landslide body slides into the water along the bank slope at a high speed and interacts with the water body; then, the water quality points move, and landslide-generated waves are triggered [1]. The second stage is the landslide-generated wave. In the horizontal propagation and diffusion phase of the opposite bank, the propagation phase interacts with structures in the river channel. In the third stage, the landslide-generated wave propagates along the bank slope and offshore [2]. Current research focuses on the

characteristics of landslide-generated wave formation and the characteristics of the interaction between landslide-generated waves and structures.

Recent research efforts into landslide-generated waves have been productive. Heller [3] reviewed existing experiments on subaerial landslide-produced impulse waves. Huang et al. [4] established a source model of landslide-generated waves in shallow water. Viroulet et al. [5] described extreme events to obtain related scaling laws. Yavari-Ramshe and Ataie-Ashtiani [6] presented a new landslide-generated wave model to design a granular type of model. Jeevan et al. [7] revealed that the submergence time scaling of distortable two-stage debris significantly differs from that of a nondeformable solid.

Different theories have been utilized to predict ship responses, such as those of Cummins [8] and Hatecke [9], and research efforts into the prediction of ship roll motion have been productive. Liu and Papanikolaou [10] applied a three-dimensional frequency-domain panel code, Ibrahim and Grace [11] studied the impact of large-amplitude ship

motions and ocean wave loads, and Liu and Papanikolaou [10] presented an online model to predict the roll motion of a ship during manoeuvring. Many researchers also have assessed the navigation safety of ships. Szlapczynski and Szlapczynska [13] presented a way to show data on ship collision avoidance, Yuan et al. [14] proposed a methodology to investigate ship-to-ship safety via the forward speed problem, and Pitana and Kobayashi [15] researched several vessel-related issues regarding pending tsunamis. Chalkias [16] and Tannuri et al. [17] discussed the viability of estimating the on-site directional wave spectrum by measuring stationary ship motion. Some researchers also have begun to propose models of moored ship motion due to the preliminary occurrence of severe tsunamis, such as Uzaki et al. [18], Shigeki and Masayoshi [19], and Sakakibara et al. [20].

This paper is based in part on a large-scale physical model test. The study analyses the results of the model test, derives the empirical formula for the propagation of landslide-generated waves, and compares the characteristics of roll and pitch motions of moving and stationary ships. The conclusions can provide some guidance for the navigation safety of vessels in the Three Gorges Reservoir.

## 2. Physical Model

Although landslide accidents are common, field data from these types of events are unfortunately very limited; such data include rare field measurements of landslide scarp, landslide deposit, tsunami run-up, and eyewitness accounts. Critically important data related to landslide motion and both spatial and temporal tsunami evolution are lacking [21]. Therefore, this paper applies a large-scale model test to collect such data.

**2.1. Ship Model.** The test vessel was a 3500T river-to-sea container ship. Thin wood was used for the hull plate, various types of wood strips composed the skeleton structure, and the ship model was designed according to a scale ratio of 1:70. Further, geometric, kinematic, and dynamic similarity were satisfied in the design process. Iron weights of differing mass were used to control the different load conditions of the ship, such that the draft, gravity centre position, moment of inertia, and natural period of roll and pitch motion were similar to the prototype. The ship model is shown in Figure 1.

In this test, the ship was assumed to be fully loaded. An MG996R servo was used. Based on the servo motor control theory, the propeller speed could be adjusted to accurately control the ship speed. During the test, we could control the rotation speed of the propeller by controlling the rotation speed of the DC motor. Generally, we used a combination of GPS positioning speed measurement and interval speed measurement, and the navigation speed of the ship model was ensured to be 0.6 m/s. This paper focuses on two states of the ship: sailing in still water at 0.6 m/s and sitting relatively stationary in still water. Table 1 lists all the main parameters of the ship.

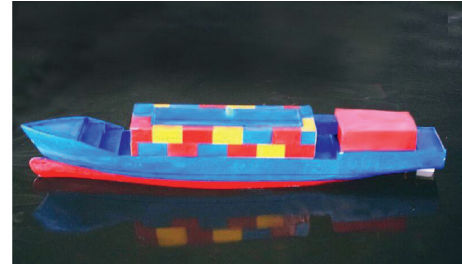


FIGURE 1: Ship model.

TABLE 1: Ship-type parameters.

Ship-type parameter	Real ship	Ship model
Length of ship (m)	94.5	1.350
Type width (m)	15.1	0.216
Deep (m)	9.0	0.129
Design draught (m)	5.6	0.080
Block coefficient	0.7	0.7
Full load displacement (t/g)	3500	10,150

**2.2. Landslide Model.** The landslide body was a slider comprising cement, sand, and stone as the raw materials. According to the preliminary investigation and statistics, the landslide body density mortar was reasonably arranged, and different sizes of block moulds were produced. The block body slid along a prefabricated chute comprising ferrous materials. Parameters such as width, height, and inclination were adjustable. The shape of the landslide body was a rectangular parallelepiped. Considering the smaller angle between the direction of action of the landslide body and the water body and the direction of the landslide body, the power of the landslide body on the water body increased, and the landslide inclination angle was selected as  $40^\circ$  [22]. The length, width, and height of the chute were 1 m, 1.5 m, and 0.6 m, respectively. The chute was flexibly affixed onto the carriage. The carriage comprised No. 20 channel steel. The height of the carriage was 2 m, the width was 2 m, and the length was 3 m. The landslide was 1 m in length, 1.5 m in width, and 0.2 m in thickness. The corresponding prototype landslide size was  $102,900 \text{ m}^2$ . The landslide water depth was 0.74 m, corresponding to a water depth of 51.8 m, and the landslide body was symmetrical. During the test, the slider was forced from the water surface along the landslide direction and was accelerated downward at the specified speed in advance. Frictional resistance and external environmental factors such as wind were not applicable during the sliding process. Figure 2 shows the test chute.

**2.3. Channel Model.** To produce similar physical phenomena for the prototype and the model, the geometric, kinematic, and dynamic similarities must be satisfied. Considering the conditions of the experiment, the scale of the model was selected as 1:70, such that the water depth and Reynolds number met the requirements. The channel model was built by the mean of cross section, and the monitoring points were arranged in the channel to set the water level. The cross section is shown in Figure 3.

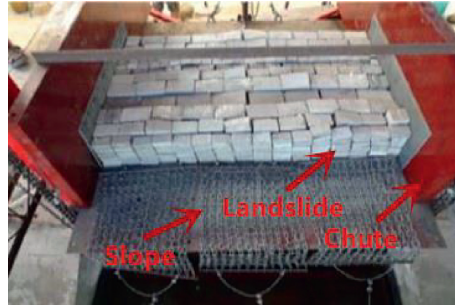


FIGURE 2: Test chute.

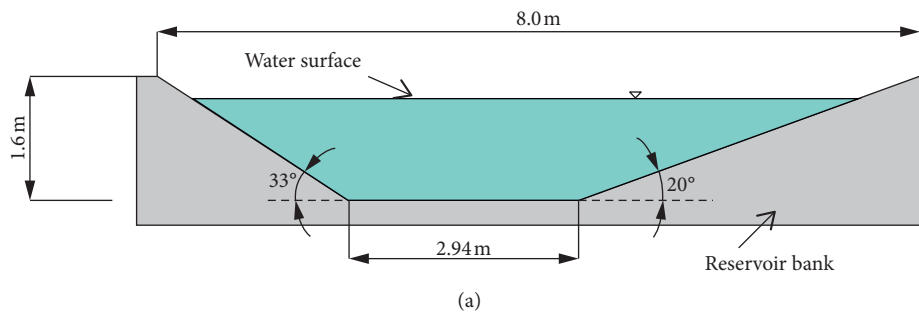


FIGURE 3: Cross section. (a) Global diagram. (b) Local diagram.

To monitor the initial height of the landslide-generated wave, the distance between the entry point and collector was selected as 0.5 m. The channel was divided into river course (#1), landslide water (#2), and curved water (#3), as shown in Figure 4.

**2.4. Uncertainty in Measurements.** System error and random error are the main causes of uncertainty in test measurement. System errors, such as the friction resistance and air resistance of a landslide, cannot be avoided. During the test, after each group of working conditions was tested, the bottom and side of the chute were polished until they became smooth. After the researcher removed the landslide from the river, the chute was dried to reduce the system error as much as possible. In order to reduce the random error, the test was repeated. Four repeated orthogonal tests were conducted for each working condition. Through image recording, it was ensured that the

position, length, width, height, and other parameters of the landslide were consistent, and the front end of the landslide at the water interface was readjusted. The first test determined the position of the measurement instrument, and the second test determined the height of the landslide surge. The results of the third and fourth tests were compared. If the resulting error was greater than 5%, the tests were repeated. If the test result error was less than 5%, the average value of the two groups of tests was taken as the result, to minimize the random error.

**2.5. Free Decay Test.** When the ship was in still water, the researchers gave the ship a certain roll amplitude and released it smoothly. Through the motion acquisition and analysis device loaded on the ship, the researchers could analyse the ship's roll motion damping and motion law while comprehensively studying the ship's recovery characteristics of freedom in the vertical plane. When the ship deviated from



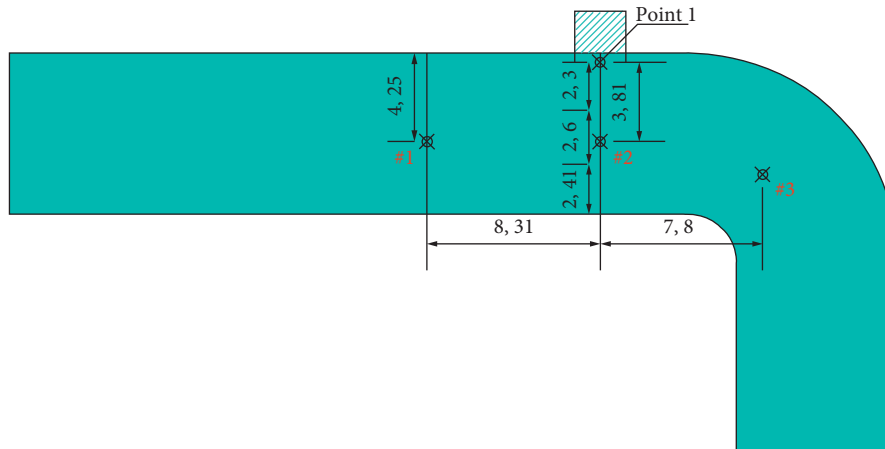


FIGURE 4: Channel model and measuring points.

the balance position under the action of external force, if the external force disappeared, the ship either returned or did not return to the original balance position depending on its own recovery characteristics. During the free-attenuation test, the ship model was released when it deviated from a certain angle in still water. The rolling period of the ship model depended on the angle of inclination at the beginning. This test further verified the accuracy of the model. The test results revealed that the amplitude attenuation law of ship roll motion met the test requirements. The hydrodynamic characteristics, natural roll period, roll damping, and inertia moment of the ship could be further adjusted through the free attenuation test. The free attenuation test curve of the ship is shown in Figure 5.

### 3. Water Level of Landslide-Generated Wave

The wave parameters, such as the water level, wave height, and period, were measured. An ultrasonic wave acquisition and analysis instrument designed through independent research and development was used to arrange seven measurement points in the river channel to measure the initial landslide-generated wave height. Monitoring point 1 was the position of the centre point of the landslide body after entering the water. The acquisition time and acquisition frequency were 50 s and 50 Hz, respectively.

Figure 6 shows a time history curve of the initial wave height after a large volume of landslide body entered the water. The initial waveform of the rock mass landslide was complex, exhibiting random waves with strong asymmetry. After the landslide body accelerated to a slide, the landslide body and water contact area formed a cavity. As shown from the time history curve of the initial wave height, the peak of the initial wave was higher, the trough was lower, and nonlinearity and wave climbing phenomena were obvious. After the peak maximum value, the trough maximum value appeared. The wave amplitude was rapidly attenuated. The maximum wave height of the initial was observed after the landslide body entered the water, and the water body was squeezed to raise the free liquid surface. The energy of the slider was converted to kinetic energy of the surrounding medium, and the vortex strength was attached near the

landslide body. The landslide body entered the channel at high speed in the form of a large amplitude wave, and all the energy was released. At this time, the kinetic energy of the water body reached the maximum value; the nonlinearity of the water wave increased and, in turn, suppressed the increase in the peak height of the landslide-generated wave. As time progressed, the landslide-generated wave decayed; the asymmetry of the wave gradually disappeared; and the water surface gradually returned to a stable state. During the model test, the water surface was in a relatively stable state 7.5 s before the landslide body entered the water. The landslide-generated wave was transmitted to the monitoring point at 7.5 s. The peak value of the wave was 4.082 cm, and the maximum value of the trough was 1.212 cm. The landslide-generated wave height and period are shown in Table 2.

### 4. Maximum Wave Amplitude and Height

After the landslide body entered the water, the water surface fluctuated sharply, and the free surface was broken. The degree of fluctuation was related to the width–thickness ratio of the landslide body, the shape of the leading edge of the landslide body, and the shape of the channel. The wave height of the landslide-generated wave was attenuated by analysing the wave height contour of the curved channel, which was divided into four areas: the curve attenuation area, the attenuation area after cornering, the attenuation area within the width of the landslide body, and the attenuation area outside the width of the landslide body. The environmental load considered herein was a ship that was stationary or sailing straight toward the landslide body. The attenuation area within the width range—that is, the section area of the landslide body—met the conditions of a landslide-generated wave.

The height of a landslide-generated wave is affected by the coupling of the initial wave height, water depth, energy exchange adequacy, and river section morphology. Regression analysis was used to determine the empirical calculation formula for the wave height.

This paper primarily considers the propagation characteristics of a landslide-generated wave along the



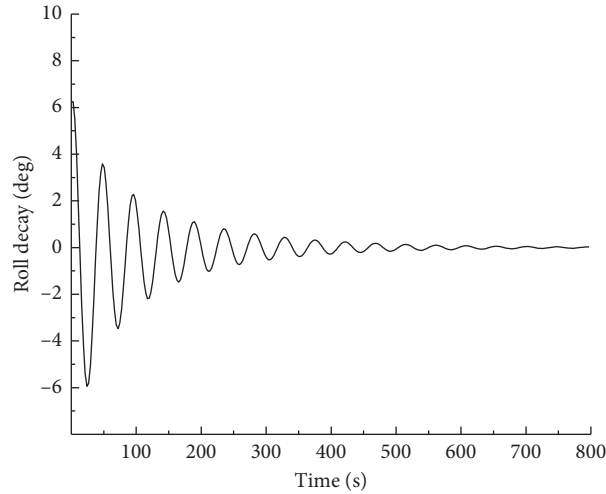


FIGURE 5: Free decay test of roll.

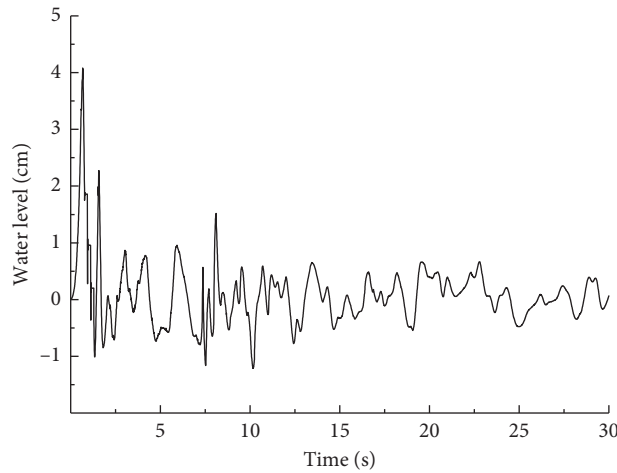


FIGURE 6: Time history curve of first wave height.

TABLE 2: Initial wave height and period statistics.

Wave number	Maximum wave height (cm)	Effective wave height (cm)	Maximum period (s)	Effective period (s)
35	4.082	1.870	1.028	1.023

water inlet section of the landslide body. The primary factors are the initial wave height, the propagation distance  $x$ , the water depth  $h$ , and the slip angle. Through a dimensionless analysis of the parameters, the attenuation coefficient of the landslide-generated wave propagation under this condition is obtained:

$$K = 11.94 \left( \frac{H_{FW}}{h} \right)^{1.067} \left( \frac{x}{h} \right)^{-0.94} \beta^{-1.23}. \quad (1)$$

The formula for calculating the wave height is determined by the attenuation coefficient of the power function regression:

$$H_a = K \cdot H_{FW}. \quad (2)$$

This formula applies to the first wave height in the range of 0–15 m.

By deriving the landslide-generated wave formula along the course, we found that energy loss occurred in the interaction between the landslide body and the water body. As the distance of the landslide-generated wave increased, the wave period increased, the wavelength of the landslide-generated wave increased, and the wave steepness decreased. Because the same landslide quantity and landslide conditions were applied, the velocities of the landslide-generated waves were fixed, as was the time when the landslide-generated wave reached the ship.

## 5. Experimental Result of Landslide-Generated Waves

The impact of a landslide-generated wave on ship motion is nonlinear, especially for large-scale landslides, which

produce strong landslide-generated waves. The influencing factors are related to the wave height, period, wave angle of incidence, water depth, and other factors. The ship was stationary or moving at a speed of 0.6 m/s in the straight waters, landslide waters, and curved waters. The landslide induced a parameter change. The width of the river model was 8 m, which was generalized to a right-angled curve. The radius of the arc was 7 m, the distance between the navigation position of the ship and the navigation centreline was 0.5 m, the distance between the remote water course and the curved water area monitoring point was 8.94 m from the landslide entry point, and the landslide water monitoring point was 3.3 m from the landslide entry point. The monitoring points of the end waters and the curved waters focused on the influence of the shape of the river section on the propagation characteristics of the landslide-generated waves. The monitoring points of the landslide waters were on the landslide section, and the landslide-generated waves were compared to the roll and pitch motions of stationary ships and sailing ships. The law of amplitude variation proposes countermeasures for a sudden landslide by ships and provides certain guidelines for engineering practice. The interaction process between the ship and landslide-induced wave is shown in Figure 7.

#### 5.1. Experimental Result in Remote Waters of River Course.

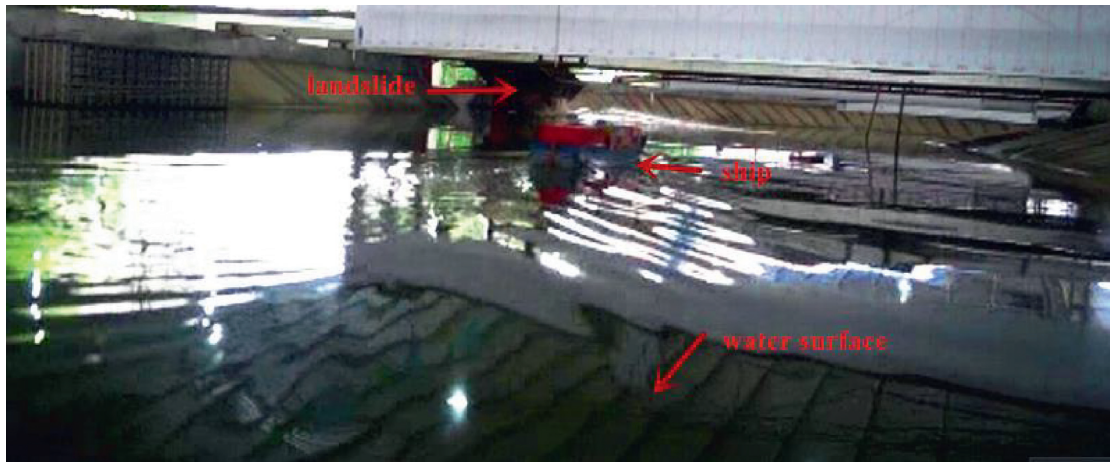
Figure 8 shows the effects of the landslide-induced wave in terms of ship roll when the ship was stationary or sailing at a speed of 0.6 m/s through the straight waters at the far end of the river. The navigation direction of the ship was opposite to that of the landslide-generated wave. The sailing ship was first subjected to the landslide and then subjected to roll motions owing to the additional ship and quality. Owing to damping, the oblique wave incident angle, reflow, splash, breaking waves, etc., the amplitude of the roll motion of the sailing ship was larger than that of the stationary ship, and the safety factor was low. The rolling motion amplitude of the sailing ship was 5–10 s. A peak was present in each of the 13- to 16-second intervals. Based on research and analysis, the initial direction of rolling is related to wave elements. When a wave crest reaches the ship first, the ship will incline in the direction of wave propagation; when a wave trough arrives first, the ship will incline in the direction of wave propagation. In this process, the landslide-generated waves impacted the hull. No wave was observed on the deck, but a liquid splash occurred. During the landslide, the hull was partially subjected to extreme pressure and the amplitude of the rolling motion. After the occurrence of the peak, the ship gradually settled to a stable state by its own resilience. After the landslide and the hull contact with the wave, the energy of the landslide-generated wave continued to propagate owing to the viscous effect of the water body, and the energy of the landslide-generated wave continued to dissipate. The wave should focus not only on the impact of the sloping first wave on the ship after entering the water but also on the decrease in the

ship's roll amplitude. The instant at which the peak of the secondary wave occurred, the ship was still in the water. After the sudden landslide, the amplitude of the rolling motion changed, and the fluctuation range was primarily concentrated at 9–18 s. The variation of the rolling change was strong, and the change in amplitude due to rolling was small. There was no evident liquid splash, but a wave on the deck was observed.

Figure 9 shows the effects of the landslide-induced wave in terms of ship pitch when the ship was stationary or sailing at a speed of 0.6 m/s through the straight waters at the far end of the river. The waves exerted fluctuating pressure on the ship, and the amplitude of the pitching motion of the ship changed. The peak value of the pitching motion of the sailing ship occurred at 1–8 s. The energy was primarily concentrated during that period, and the maximum pitching motion amplitude was 1.5°. The danger period was high; the ship was stationary in the straight waters at the far end of the river, and the peak value of the pitching motion of the sailing ship occurred at 3–18 s. In that period, the landslide-generated wave had little effect on the ship's pitch, and the maximum pitching motion amplitude was 0.7°; the landslide-generated wave propagated slightly while the ship was sailing, and the ship's navigation direction was opposite to the direction of the landslide-generated wave. A landslide-generated wave has different impacts on the pitching motion of a sailing ship and a stationary ship. The height of a landslide-generated wave decreases with increasing propagation distance. The wave slams the ship, and the ship's motion response increases over time. The amplitude of motion gradually decreases and eventually becomes stable.

#### 5.2. Experimental Result in Landslide Water.

Figure 10 shows the effects of the landslides in terms of ship roll when the ship was stationary or sailing at a speed of 0.6 m/s through the waters in the landslide section. Landslides have adverse effects on both stationary ships and sailing ships. Under the continuous action of the original wave, the roll angle reached the maximum value in a short period and then decayed rapidly. Because the applied force and resistance were nonlinear, the attenuation law also was nonlinear. The impact of the landslides on the ships sailing at 0.6 m/s was divided into two stages; the first stage occurred within 1–5 s. When the landslide body entered the water, the impact created landslide-generated waves, and the liquid splashed significantly, accompanied by waves on the deck. Because the ship had been sailing straight, the landslide wave acted on the middle and rear parts of the ship. Thus, large-amplitude swaying motion was easily produced, and the rate of change of the motion amplitude was steep. The second stage occurred at 11–18 s and was caused by the landslide-generated wave. The direction was transmitted and finally reached the end of the river, thereby impacting the bank slope, forming reflection, reflow, and superimposing the impact of the synthetic wave on the sailing ship. The maximum amplitude of the rolling motion of the first stage was 10°. The maximum rolling motion of the second-stage ship was 9°. When a ship encounters a landslide in actual



(a)



(b)



(c)

FIGURE 7: Continued.

navigation, it should focus on controlling the navigation speed and instability of the water field to prevent the landslide-generated wave from causing “secondary injury” to the ship. For the stationary ship in the waters of the landslide section, the landslide body generated a landslide-generated wave after entering the water. The roll motion amplitude of the ship appeared at 1–14 s, showing a single

peak state, and the wave energy of the landslide gradually decreased along the landslide. The ship relied on its own recovery torque and recovery damping. The amplitude of the rolling motion gradually decreased and eventually stabilised. The ship was stationary in the sluice waters. It is necessary to focus on the starting moment of the landslide to prevent the landslide from occurring. The impact of the first wave on the





FIGURE 7: Interaction process between ship and landslide-induced wave.

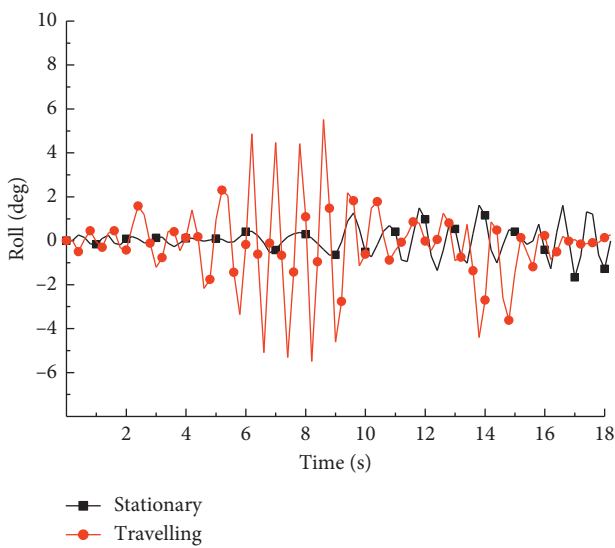


FIGURE 8: Time history curve of ship roll in straight section.

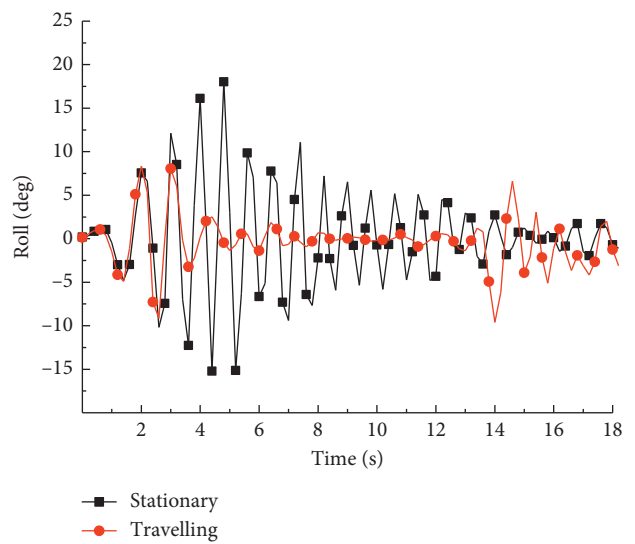


FIGURE 10: Time history curve of ship roll in landslide section.

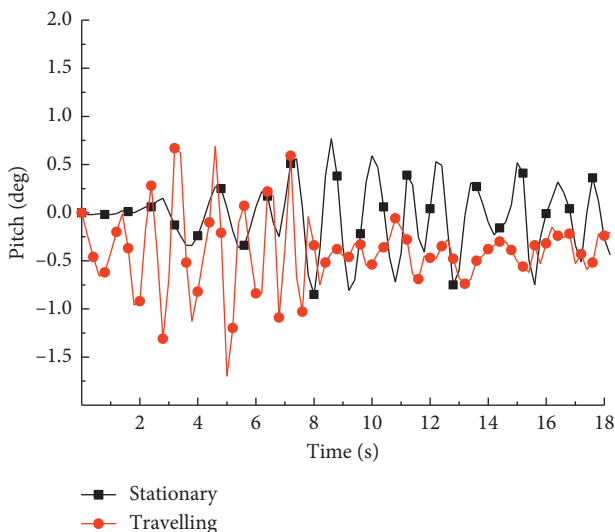


FIGURE 9: Time history curve of ship pitch in straight section.

ship, as well as reasonable and effective disaster prevention and mitigation procedures, should be considered.

Figure 11 shows the effects of the landslides in terms of ship pitch when the ship was stationary or sailing at a speed of 0.6 m/s through the waters in the landslide section. The amplitude of the pitching motion of the ship changed, and two large fluctuations occurred. The first fluctuation period was from 0 s to 5 s. During this period, the landslide body entered the water, and the impulse wave directly interacted with the sailing vessel. The maximum pitch angle was 2.5°; the second fluctuation period was from 13 s to 15 s. The larger amplitude fluctuation was due to the wave propagation along the path, attenuation, and ship wave. The reflected and diffracted wave superimposed on the wave interaction with the ship, and the maximum pitch angle was 2°. The influence of the rock mass landslide on the stationary ship in the landslide section was consistent with the propagation characteristics of the landslide. Further, the pitch motion amplitude was small: the maximum pitch angle in the still water was 0.5°, and the ship gradually returned to a stable equilibrium state by relying on its own recovery torque.

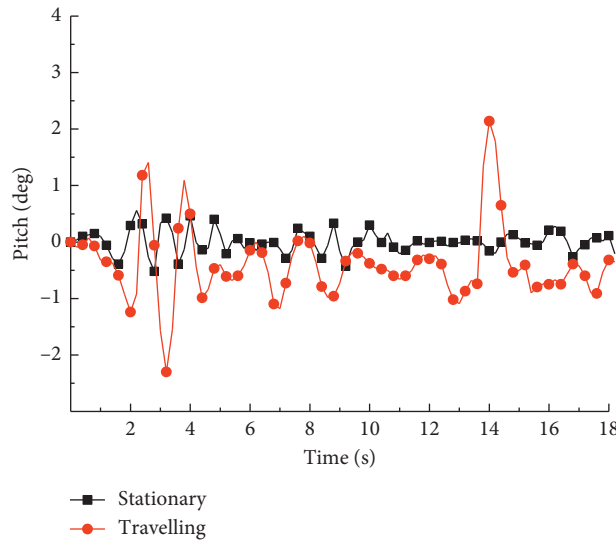


FIGURE 11: Time history curve of ship pitch in landslide section.

5.3. *Experimental Result in Curved Water.* A landslide-generated wave in the river channel is affected by the meandering characteristics of the channel. The speed of the landslide-generated wave caused by the high-speed landslide body was limited, i.e., less than the ship’s navigation speed of 0.6 m/s and that of the landslide-generated wave. The sailing vessel was in a chasing state and did not influence the ship’s motion response amplitude during the measurement time. Therefore, the curved river waters focused the impact of the landslide-generated wave on the motion characteristics of the stationary ship.

Figures 12 and 13 show the results of stationary ships suddenly encountering landslide-generated waves in a curved river. Owing to the influence of landslide-generated waves on curved river channels caused by topography, shore walls, and shallow water, landslide-generated waves show areas of obvious turbulence during propagation, accompanied by strong irregularities and pulses. Under the action of pressure, the stationary ship produced a large-amplitude motion, i.e., the amplitude of the roll motion and the amplitude of the pitch motion. The maximum roll angle was  $5.5^\circ$ , and the maximum pitch angle was  $0.9^\circ$ . After the landslide body entered the water, the first interaction between the first wave and the ship was generated. When the ship was inclined to the left at the beginning, the roll amplitude on the left side of the ship was greater than that on the right side; when the ship was inclined to the right at the beginning, the roll amplitude on the right side of the ship was greater than that on the left side. The landslide-generated waves flowed along the ship climbing, the side waves of the ship, and the forward flow of the ship and continued to spread to the other side. With the gradual reduction in the energy of the landslide-generated wave, the ship’s roll motion amplitude and pitch motion amplitude also gradually decreased. The ship relied on its own restoring force and damping and gradually stabilised. In this process, the

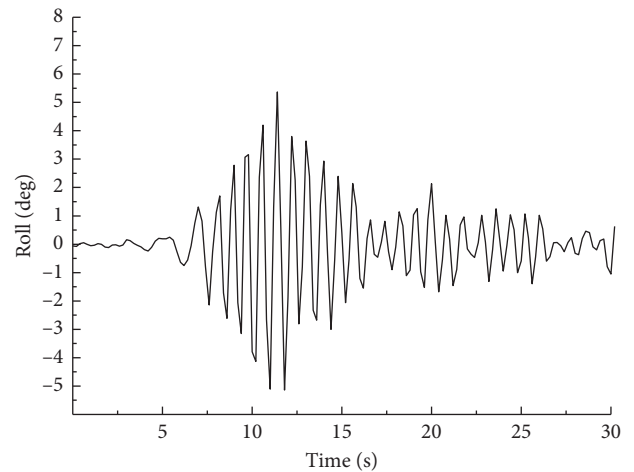


FIGURE 12: Time history curve of ship roll in curved section.

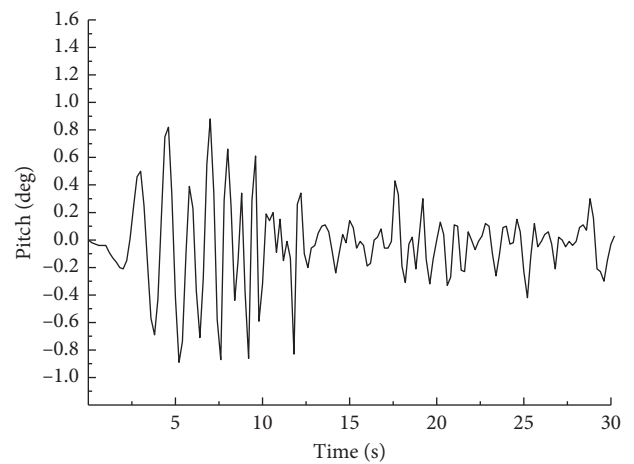


FIGURE 13: Time history curve of ship pitch in curved section.



ship interacted with the landslide-generated wave. During the process, the phenomena of sloshing and splashing were not obvious. The landslide-generated wave propagated along the same distance, and the influence of the curved channel on the amplitude of the pitching motion of the ship was the same.

## 6. Discussion and Conclusion

Based on collected data, statistical analysis, and on-site measurement of rock mass landslides in the reservoir area, combined with the actual engineering of the navigation channel, a combination of theoretical analysis and physical model tests was used to study the characteristics and spread of landslides in channel rivers. The law and its influence on the amplitude of the motion of stationary ships and sailing ships in the river channel is summarized as follows:

- (1) The initial wave of the landslide was a complex wave comprising an undulating wave and an oscillating wave. The height of the first wave of the landslide was directly related to the landslide volume, water inlet angle, and length-to-width ratio of the landslide body. The landslide-generated wave height decreased with increasing propagation distance. The initial wave showed obvious asymmetry; the peak was high, the trough was low, and the nonlinearity was strong. As time passed, the energy of the landslide-generated wave gradually decreased.
- (2) The propagation of landslide-generated waves was related to the shape of the river, the distance of propagation, and the depth of the water. The ship sailed at a constant speed in the straight waters, the landslide waters, and the waters in the bends of the river channel. The same type of landslide-generated wave spread to the vicinity of the ship, causing varying degrees of liquid splashing, breaking waves, and backflow. Additionally, the variation in the ship's motion amplitude varied.
- (3) If a landslide occurs in the rear of a ship, the ship should accelerate forward to avoid the sluice waters, thus effectively suppressing the peak height and minimizing the landslide with the free attenuation of the landslide energy.
- (4) The control of the ship roll angle must be emphasized to prevent a landslide body from entering the water and causing the first wave of the landslide. The incident, reflection, radiation, reflow, and side of the landslide must also be considered. Waves and the slamming of secondary waves responded to the motion of the ship.
- (5) To effectively prevent the occurrence of slamming, the design of ships sailing in landslide-affected waters should appropriately increase the deck height and initial clearance to control the shape of the longitudinal section of the ship.

## Data Availability

The data are available in this manuscript. The data in this manuscript were obtained through a series of analyses. The related data used to support the findings of this study are available from the corresponding author upon request.

## Conflicts of Interest

The authors declare that there are no conflicts of interest regarding the publication of this paper.

## Acknowledgments

This study was financially supported by the National Natural Science Foundation (51479015), Social Science and Technology Innovation Program for People's Livelihood in Chongqing (cstc2019jscx-msxmX0302, cstc2018jscx-msybX0233, and cstc2019jscx-lyjsAX0008), and the Science and Technology Program of the Chongqing Education Commission (KJQN201900735).

## References

- [1] H. M. Fritz, *Initial phase of landslide generated impulse waves*, Ph.D. thesis, Eidgenössische Technische Hochschule Zürich, Zürich, Switzerland, 2002.
- [2] P. Yuan, P. Wang, and Y. Zhao, "Model test research on the propagation of tsunamis and their interaction with navigating ships," *Applied Sciences*, vol. 9, no. 3, p. 475, 2019.
- [3] Heller, "Landslide generated impulse waves experimental results," *Coastal Engineering*, vol. 38, no. 4, pp. 1313–1325, 2008.
- [4] B. Huang, S. C. Wang, and Y. B. Zhao, "Impulse waves in reservoirs generated by landslides into shallow water," *Coastal Engineering*, vol. 123, no. 5, pp. 52–61, 2017.
- [5] S. Viroulet, D. Cébron, O. Kimmoun, and C. Kharif, "Shallow water waves generated by subaerial solid landslides," *Geophysical Journal International*, vol. 193, no. 2, pp. 747–762, 2013.
- [6] S. Yavari-Ramshe and B. Ataie-Ashtiani, "A rigorous finite volume model to simulate subaerial and submarine landslide-generated waves," *Landslides*, vol. 14, no. 1, pp. 203–221, 2017.
- [7] K. Jeevan, P. R. Puskar, K. B. Khattri, P. Kattel, B. M. Tuladhar, and S. P. Pudasaini, "Landslide-generated tsunami and particle transport in mountain lakes and reservoirs," *Annals of Glaciology*, vol. 57, no. 71, pp. 232–244, 2016.
- [8] W. E. Cummins, "The impulse response function and ship motions," *Schiffstechnik*, no. 9, pp. 101–109, 2010.
- [9] H. Hatecke, "The impulse response fitting and ship motions," *Ship Technology Research*, vol. 62, no. 2, pp. 97–106, 2015.
- [10] S. Liu and A. Papanikolaou, "Prediction of parametric rolling of ships in single frequency regular and triple frequency group waves," *Ocean Engineering*, vol. 120, no. 7, pp. 274–280, 2016.
- [11] R. A. Ibrahim and I. M. Grace, "Modeling of ship roll dynamics and its coupling with heave and pitch," *Mathematical Problems in Engineering*, pp. 242–256, 2010.
- [12] J.-c. Yin, Z.-j. Zou, and F. Xu, "On-line prediction of ship roll motion during maneuvering using sequential learning RBF neural networks," *Ocean Engineering*, vol. 61, no. 6, pp. 139–147, 2013.
- [13] R. Szlapczynski and J. Szlapczynska, "A method of determining and visualizing safe motion parameters of a ship

- navigating in restricted waters,” *Ocean Engineering*, vol. 129, no. 1, pp. 363–373, 2017.
- [14] Z.-M. Yuan, A. Incecik, S. Dai, D. Alexander, C.-Y. Ji, and X. Zhang, “Hydrodynamic interactions between two ships travelling or stationary in shallow waters,” *Ocean Engineering*, vol. 108, no. 21, pp. 620–635, 2015.
- [15] T. Pitana and E. Kobayashi, “Assessment of ship evacuations in response to pending tsunamis,” *Journal of Marine Science and Technology*, vol. 15, no. 3, pp. 242–256, 2010.
- [16] D. Chalkias, “Moonpool behavior of a stationary vessel in waves and a method to increase operability,” in *Proceedings of the ASME International Conference on Ocean*, Trondheim, Norway, June 2017.
- [17] E. A. Tannuri, J. V. Sparano, A. N. Simos, and J. J. Da Cruz, “Estimating directional wave spectrum based on stationary ship motion measurements,” *Applied Ocean Research*, vol. 25, no. 5, pp. 243–261, 2003.
- [18] K.-i. Uzaki, N. Matsunaga, Y. Nishii, and Y. Ikehata, “Cause and countermeasure of long-period oscillations of moored ships and the quantification of surge and heave amplitudes,” *Ocean Engineering*, vol. 37, no. 2-3, pp. 155–163, 2010.
- [19] S. Shigeki and K. Masayoshi, “Initial attack of large-scaled tsunami on ship motions and mooring loads,” *Ocean Engineering*, vol. 36, no. 2, pp. 145–157, 2009.
- [20] S. Sakakibara, S. Takeda, Y. Iwamoto, and M. Kubo, “A hybrid potential theory for predicting the motions of a moored ship induced by large-scaled tsunami,” *Ocean Engineering*, vol. 37, no. 17-18, pp. 1564–1575, 2010.
- [21] B. C. McFall, *Physical Modelling of Landslide Generated Tsunamis in Various Scenarios from Fjords to Conical Islands*, Georgia Institute of Technology, Atlanta, GA, USA, 2014.
- [22] L. Chen, *Experimental Study on Characteristics of Rock-type Landslide Surge and Impact for Navigable Conditions of the River-Channel Type Reservoir in Mountainous Area*, Chongqing Jiaotong University, Chongqing, China, 2014.

## Research Article

# Experimental and Theoretical Analysis for Isolation Performance of New Combined Isolation Devices under Blast Loading

Yang Liu,<sup>1</sup> Zhen Liao ,<sup>1</sup> Yulong Xue ,<sup>2</sup> Zhizhong Li ,<sup>1</sup> Luzhong Shao,<sup>1</sup> and Degao Tang<sup>1</sup>

<sup>1</sup>State Key Laboratory for Disaster Prevention & Mitigation of Explosion & Impact, Army Engineering University of PLA, Nanjing 210000, Jiangsu, China

<sup>2</sup>Research Institute for National Defense Engineering of Academy of Military Science PLA China, Beijing 100850, China

Correspondence should be addressed to Zhen Liao; ccess027@163.com, Yulong Xue; karl\_xue88@outlook.com, and Zhizhong Li; lizz0607@163.com

Received 10 February 2020; Accepted 2 May 2020; Published 15 May 2020

Academic Editor: Xihong Zhang

Copyright © 2020 Yang Liu et al. This is an open access article distributed under the Creative Commons Attribution License, which permits unrestricted use, distribution, and reproduction in any medium, provided the original work is properly cited.

The strong shock and vibration effect caused by explosion may pose a serious threat to the surrounding environment and the safety of personnel and equipment. This also makes the problem of vibration isolation and absorption of the structures subjected to blast loading increasingly prominent. In this paper, three kinds of new combined isolation devices with high resistance are designed and manufactured, and the characteristic parameters such as natural vibration period, frequency, and damping ratio are obtained through drop hammer impact test. Based on the Duhamel integral principle, analytical solutions of dynamic response of the combined isolation devices under rectangular pulse blast loading are derived, and the calculation expressions of transmissibility and vibration isolation rate are proposed. Combined with the test results, the isolation performance of three kinds of combined isolation devices under blast loading is obtained by using the theoretical calculation formula, and the influencing factors of isolation performance are further analyzed parametrically. The research results provide a reference for the application of combined isolation devices in isolation and shock absorption of structures under blast loading.

## 1. Introduction

In recent years, more and more attentions have been attracted to the field of vibration isolation and absorption of structures [1–3]. As early as 1976, Harris Cyril et al. [4] compiled the handbook of impact and vibration, which comprehensively and systematically discussed all aspects of impact and vibration problems, including the theoretical basis of impact and vibration, measurement means, shock absorption and isolation technology, and the impact of vibration on human body. Shang et al. [5] studied the variation law of horizontal stiffness of three-dimensional isolated piers by carrying out quasi-static tests, established the isolation and nonisolation models of frame structures, and conducted time-history analysis to study the isolation performance of three-dimensional isolated piers. The results

show that the horizontal acceleration can be attenuated by more than 40% and the internal force of the beam can be reduced by more than 30% under different ground motions. Li and Xue [6] conducted a shaking table test and study on the three-dimensional tribo-disc spring combined isolation bearing suitable for long-span structures. By applying simple harmonic excitation load and ground motion excitation load in the horizontal direction, they analyzed the influence of load change and ground motion intensity on the isolation performance of the isolation bearing. The results show that the tribo-disc spring combined isolation has good hysteresis performance in both horizontal and vertical direction, and the vertical equivalent damping ratio is between 0.10 and 0.15. Zeng [7] conducted an experimental study on the vertical and horizontal stiffness characteristics of lead-core isolation combined supports and analyzed the influence of

different combined supports on the isolation effect of the superstructure under the same ground motion. The results show that the lead in lead-core rubber bearings increases the shear stiffness of the bearings to some extent, but the effect on the bending stiffness can be neglected. Xiang et al. [8] adopted simulation software MATLAB Simulink to analyze the antiexplosion and isolation performance of the isolation system with MR damper. The results show that MR damper can effectively reduce displacement, acceleration, and vibration dose value (VDV) response of the structures subjected to blast loading, showing better isolation performance. Based on Runge-Kutta method, Yan et al. [9] calculated the dynamic response of double-layer isolation system and studied the isolation performance of the system under blast loading according to VDV isolation standard. Xia [10] analyzed the vibration response of large-scale storage tank under the earthquake action by using the finite element method. After using the combination of rubber bearing and sliding bearing, it can significantly improve the isolation efficiency for the structure. The results show that the combination of lead-core rubber isolation bearing and sliding bearing can bring better isolation effect to the structure after the earthquake, and the isolation efficiency increases with the increase of oil storage, with the maximum close to 50%. In order to explore the mechanism of continuous collapse of isolated structures during explosions in underground chambers, Du and Zeng [11] used LS-DYAN to establish a computational model for the isolated structures with reinforced concrete frames. The results show that the main reason for the continuous collapse of the structure is the failure of the transmission path caused by the initial damage of adjacent members after the failure of the target member, and the degree of initial damage is the key factor affecting the collapse scale of the structure.

At present, many research results have been obtained on the isolation performance of isolation devices under general seismic load or earthquake load, but few researches on the isolation performance of isolation devices subjected to explosion and impact loads. The strong vibration effect of the structure or the surrounding environment caused by the explosion load put forward higher requirements for the isolation performance of the isolation device. For this reason, three new kinds of combined isolation devices with high resistance are developed in this paper, and the isolation performance of the combined isolation device is studied experimentally and theoretically, so as to provide a reference for the application of the new combined isolation device developed in this paper in the field of structural antiexplosion.

The experimental research and experimental results of the combined isolation devices are described in Section 2. The formula for calculating the isolation performance of combined isolation system under explosion load is theoretically derived, and the vibration isolation rate of three kinds of combined isolation devices is calculated in Section 3. The parametric analysis for isolation performance of the isolation device is developed in Section 4, while Section 5 contains the conclusions.

## 2. Experimental Study on Combined Isolation Devices

*2.1. Test Model Design.* Three kinds of combined isolation devices are developed, each of which is composed of four steel springs with the same specification and symmetrical arrangement and a damping body. According to the selected damping material, the isolation device is named as spring-cylinder isolation device, spring-rubber isolation device, and spring-aluminum foam isolation device successively, as shown in Table 1. In order to obtain reliable and effective test results, 2 models were made for each kind of isolation device. The schematic diagrams and physical diagrams of the three kinds of combined isolation devices are shown in Figure 1.

Table 2 lists the major specifications parameters of single steel spring, from which we can find that the maximum bearing capacity of the selected steel springs can reach 45.22 kN while the allowable maximum deformation is 340 mm. These steel springs have the characteristics of high bearing capacity and large deformation. As the major energy dissipation unit in the isolation devices, the rubber and aluminum foam damping are made of chlorinated butyl rubber and aluminum foam, respectively, whereas the cylinder damping is filled with the air at normal temperature. The cylinder damping compresses or absorbs air through lateral holes during the deformation to consume the vibration energy.

*2.2. Experimental Scheme.* The test was carried out on the hard and flat ground by the drop hammer impact loading method, as shown in Figure 2. The square steel counterweight was fixed on the top of the isolation device, with a side length of 70 cm and a thickness of 5 cm. A weight of 4.0 t was suspended at a certain height directly above the isolation device. When the isolation device was in a static state, the shock load was applied to the isolation device by releasing the hammer suddenly and making it fall freely. Two acceleration sensors were arranged on the lower surface of the upper plate of the isolation device. The vibration acceleration signal of each test isolation device was obtained by dynamic signal test system. The two sensors were arranged at the midpoint of the two sides of the square top plate, with a distance of 5 cm from the respective edges of the plate. Each isolation device underwent several tests until reasonable and effective acceleration signals were acquired.

*2.3. Test Results and Analysis.* In order to eliminate the burr phenomenon in the acceleration signal, five-point cubic smoothing method [12, 13] was used to smooth the original acceleration vibration signal, and then the frequency domain integration method [14, 15] to integrate the smoothed acceleration signal to obtain the displacement time-history curve of the isolation devices.

The time-history curve of free vibration for typical low-damping system is shown in Figure 3. Since the real damping characteristics of structure are very complex and difficult to determine, the equivalent viscous damping ratio  $\xi$  with the same attenuation rate under free vibration is usually used to



TABLE 1: Type and quantity of combined isolation devices.

Name	Abbreviation	Damping material	Quantity
Spring-cylinder isolation device	TQGG	Cylinder damping	2
Spring-rubber isolation device	TXJG	Rubber damping	2
Spring-aluminum foam isolation device	TPMLG	Aluminum foam damping	2

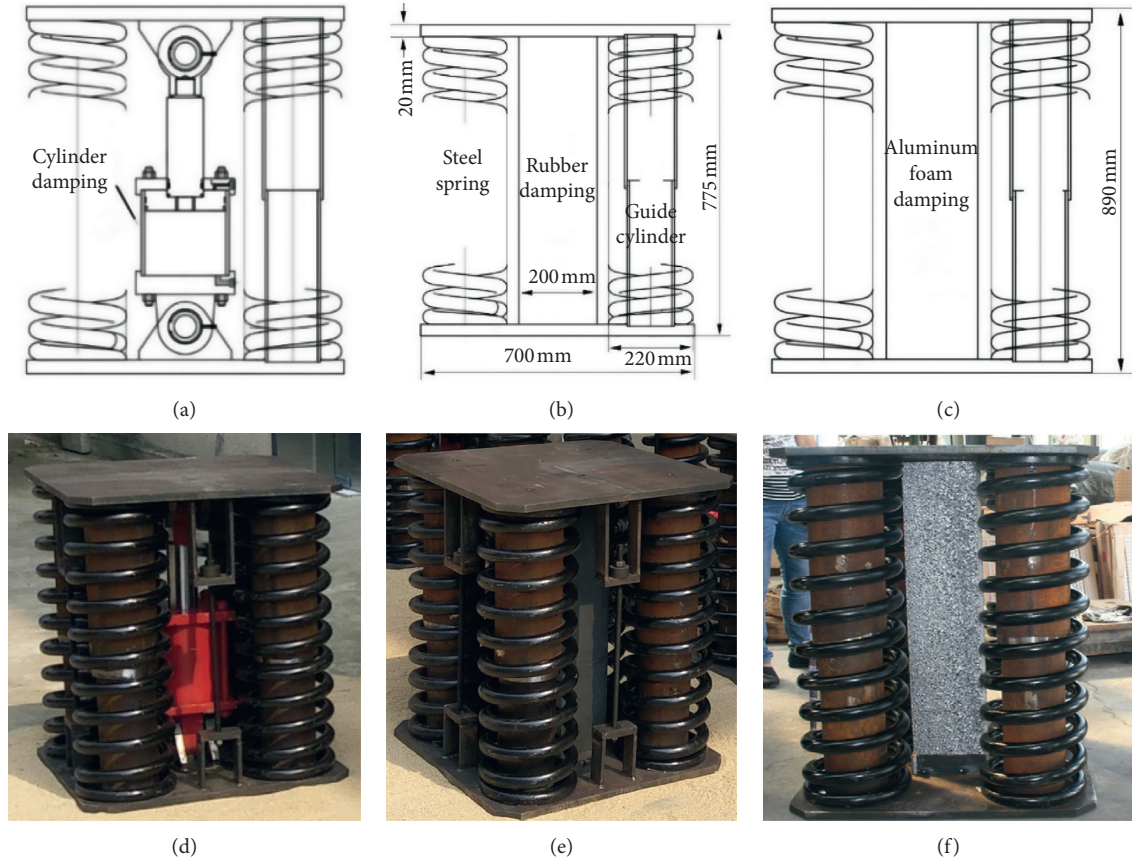


FIGURE 1: Schematic diagrams and physical diagrams of combined isolation devices. (a) Schematic diagram of TQGG. (b) Schematic diagram of TXJG. (c) Schematic diagram of TPMLG. (d) Physical diagram of TQGG. (e) Physical diagram of TXJG. (f) Physical diagram of TPMLG.

TABLE 2: Main parameters of steel spring.

Material	Wire diameter $D_1$ (mm)	Pitch diameter $D_2$ (mm)	Height $H$ (mm)	Bearing capacity $F$ (kN)	Allowable deformation $d$ (mm)	Stiffness $k$ (N/mm)
60Si2MnA	35	220	850	45.22	340	133

represent the damping of the actual structure. For a low-damping system, higher accuracy can be obtained by calculating damping ratios of the response peaks or troughs with few intervals. The formulas for calculating the parameters can be found in [16].

**2.3.1. Measured Acceleration Time-History Curves.** According to the test results of the drop hammer impact test, the typical measured time-history curves of acceleration

were selected for each isolation device, as shown in Figures 4–6.

It can be seen from Figures 4–6 that for the same type of combined isolation device, the measured acceleration time-history curves have different vibration amplitude. This is because the drop hammer height of each test and the initial impact speed of drop hammer on the isolation device is different. The counterweight of the isolation device does reciprocating movement in the vertical direction together



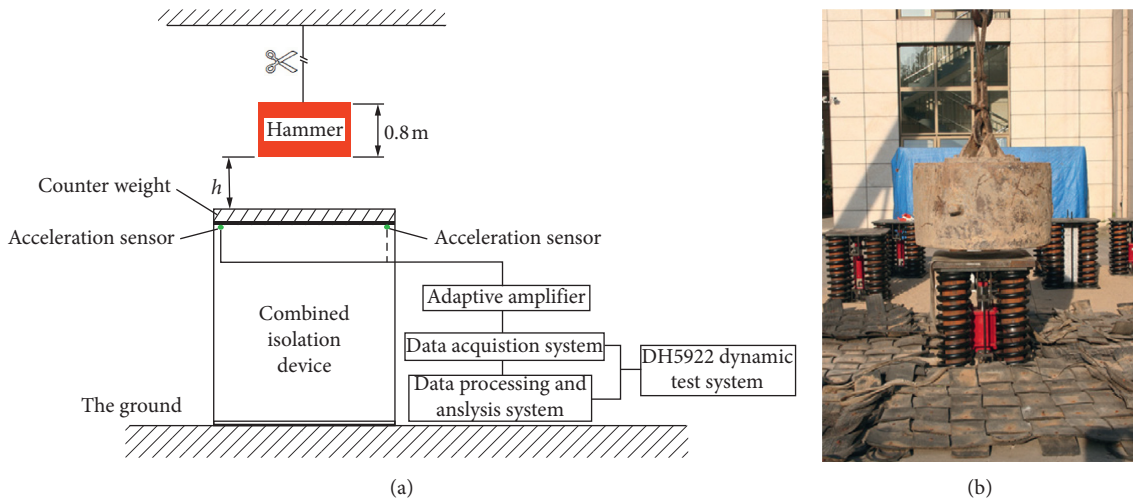


FIGURE 2: The diagram of experimental test. (a) Schematic diagram. (b) Actual test figure.

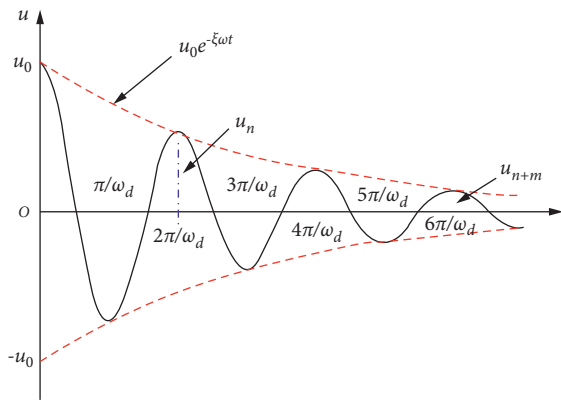


FIGURE 3: Time-history curve of free vibration for a typical low-damping system.

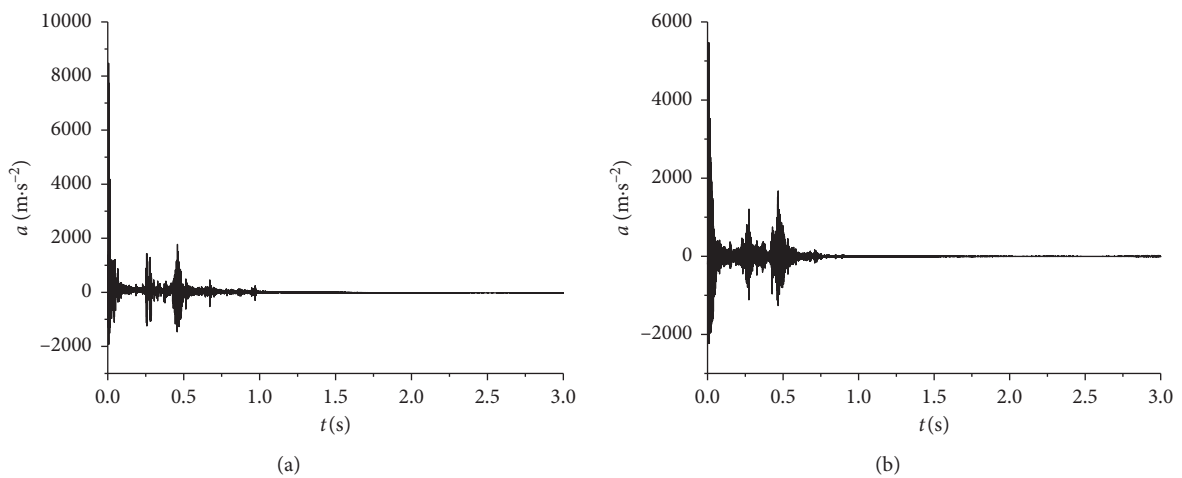


FIGURE 4: Measured acceleration time-history curves of spring-cylinder isolation device. (a) TQGG1. (b) TQGG2.

during the vibration process, so that the acceleration time-history curve vibrates up and down at the equilibrium position, and there are multiple peaks. With the damping

force, the vibration amplitude of the acceleration curve rapidly decays to zero. The vibration form of acceleration curve of the isolation device with different damping bodies is

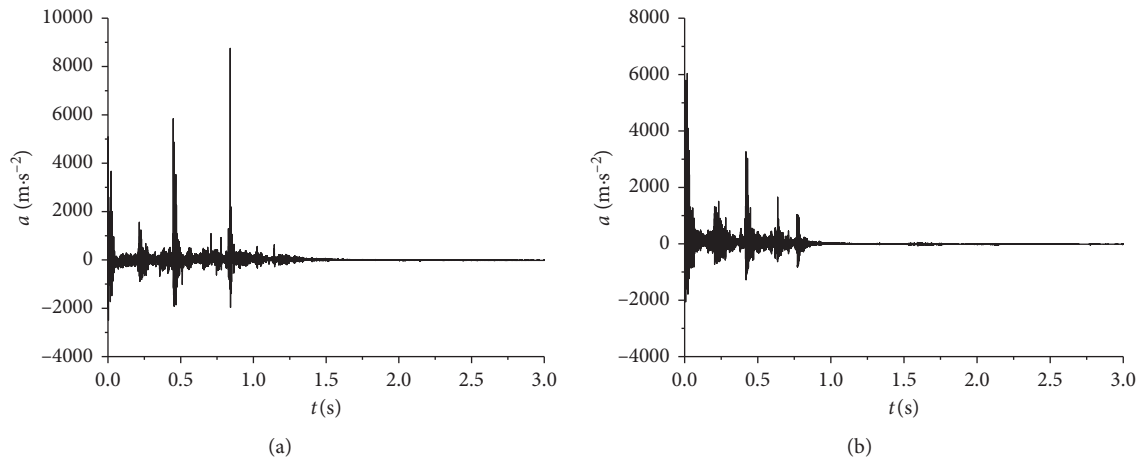


FIGURE 5: Measured acceleration time-history curves of spring-rubber isolation device. (a) TXJG1. (b) TXJG2.

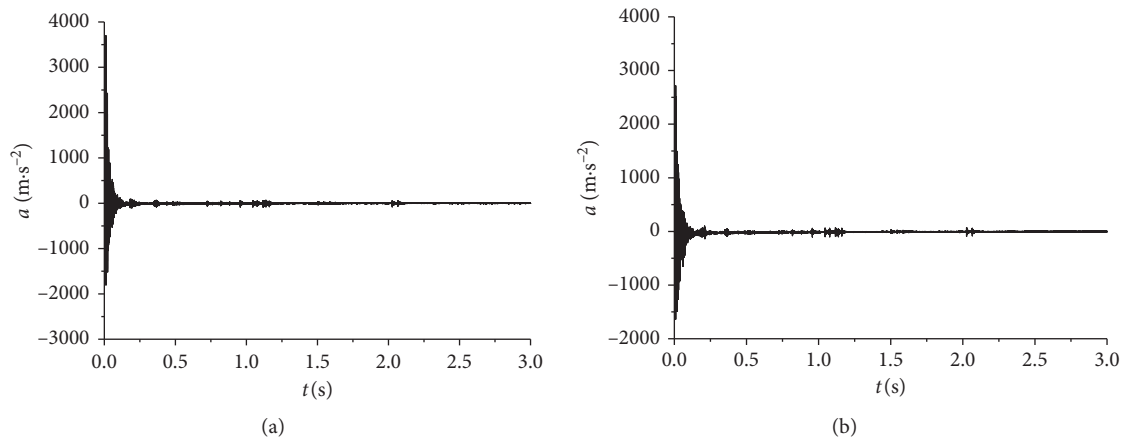


FIGURE 6: Measured acceleration time-history curves of spring-aluminum foam isolation device. (a) TPMLG1. (b) TPMLG2.

quite different. The vibration form of acceleration curve of the spring-cylinder isolation device and the spring-rubber isolation device is similar, which has many peaks, and the subsequent peaks even exceed the initial peaks. However, the acceleration curve of spring-aluminum foam isolation device shows a single peak value.

**2.3.2. Displacement Time-History Curves.** Based on the frequency domain integration method, the measured acceleration time-history curves of isolation device are integrated twice to obtain the corresponding displacement time-history curves, as shown in Figures 7–9.

It can be seen from Figures 7–9 that the displacement time-history curve of the counterweight of the isolation device oscillates up and down at the equilibrium position, the existence of the damping body in the isolation device causes the energy of the isolation system to be consumed gradually, and the peak value of the vibration displacement decreases rapidly with the increase of time. Within 3 s, the isolation system basically recovered to its original static state.

The 3~4 peaks in the displacement time-history curves of the free vibration stage of each isolation device are selected for analysis. The specific coordinates of the calculation area selected for the calculation of characteristic parameters of each isolation device are shown in Figures 7–9.

**2.4. Characteristic Parameters of Combined Isolation Devices.** According to the analysis in Section 2.3.2, the dynamic characteristic parameters of each combined isolation device can be obtained, and the average value of the dynamic characteristic parameters of the same type of isolation device is acquired, as shown in Table 3.

It can be seen from Table 3 that the frequency range of the three kinds of combined isolation devices is between 1.901 Hz and 3.106 Hz, and the damping ratio range is between 12.5% and 13.2%. The damping material not only has a good absorption performance, but also plays a supporting role in the isolation devices, so it changes the natural period or frequency of the isolation device.

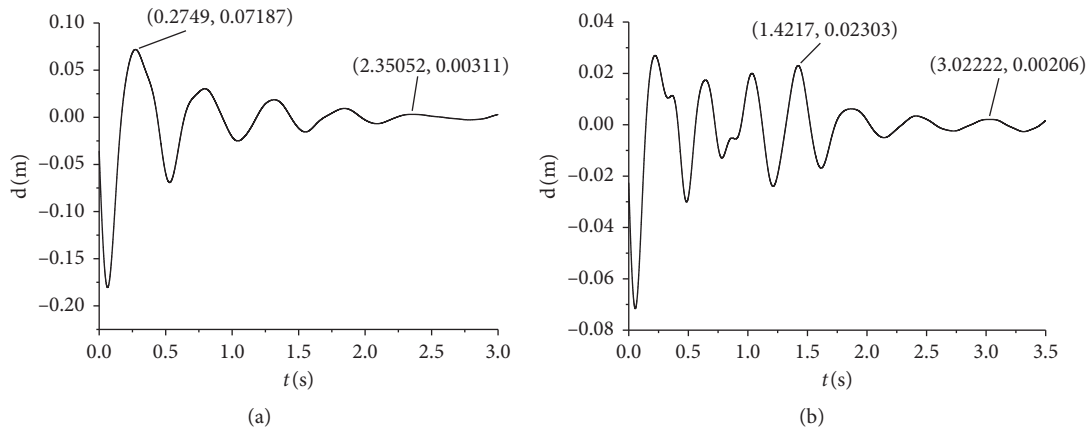


FIGURE 7: Displacement time-history curves of spring-cylinder isolation device. (a) TQGG1. (b) TQGG2.

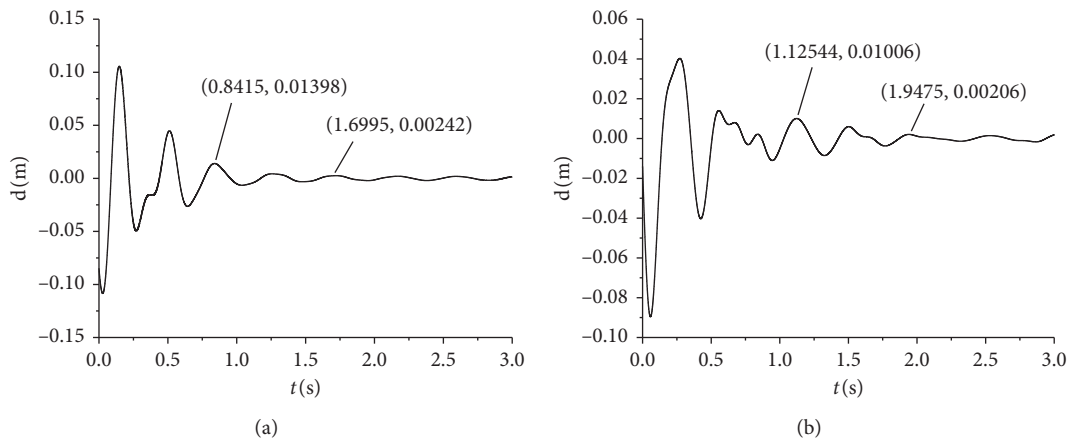


FIGURE 8: Displacement time-history curves of spring-rubber isolation device. (a) TXJG1. (b) TXJG2.

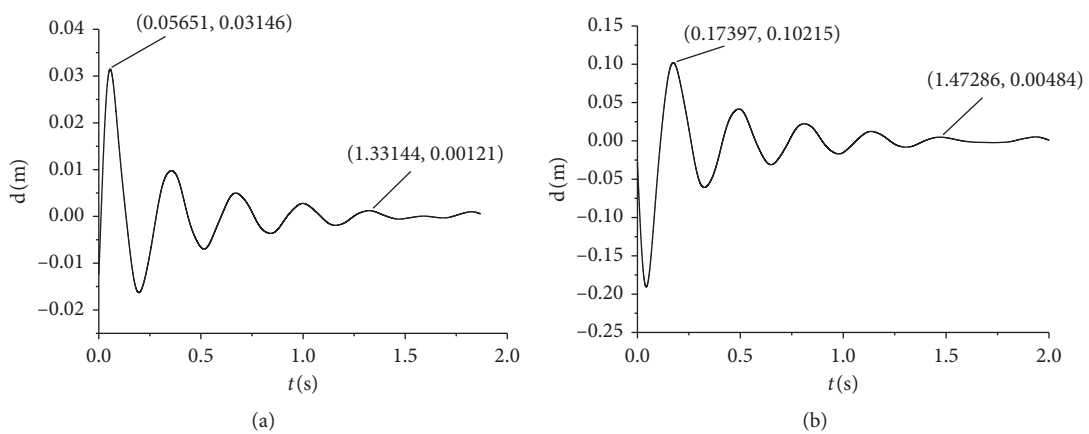


FIGURE 9: Displacement time-history curves of spring-aluminum foam isolation device. (a) TPMLG1. (b) TPMLG2.

TABLE 3: Dynamic performance parameters of combined isolation devices.

Abbreviation	Natural vibration period $T$ (s)	Frequency $f$ (Hz)	Damping ratio $\xi$ (%)
TQGG	0.526	1.901	12.6
TXJG	0.420	2.381	13.2
TPMLG	0.322	3.106	12.5

### 3. Calculation of Isolation Performance of Isolation System

**3.1. Excitation Load of Isolation System.** In this paper, the excitation load  $F(t)$  of the isolation system is a short-duration explosion load with exponential attenuation. The following formula gives the specific attenuation form of the explosion load [17]:

$$F(t) = 1.5 \times 10^5 \left[ 0.53 \left( \frac{0.006}{t + 0.006} \right)^{16.5} + 0.47 \left( \frac{0.006}{t + 0.006} \right)^{1.26} \right] \cdot \left( 1 - \frac{t}{0.029} \right). \quad (1)$$

When the duration of explosion load  $F(t)$  is much less than the natural vibration period of the isolation system, the response of the isolation system  $x(t)$  mainly depends on the impulse of the explosion load, and the shape of the time-history curve of the explosion load has little influence on the system response [18]. In order to obtain the analytical solution of the response of the isolation system subjected to blast load, the rectangular impulse load  $F(t)$  with equal impulse is constructed to replace the real blast load  $F(t)$ . If the peak value of rectangular pulse load is the same as the peak value of explosion load  $F_{\max}$ , then the duration time of rectangular pulse load is as follows:

$$t_1 = \frac{1}{F_{\max}} \int_0^{t_+} F(t) dt, \quad (2)$$

where  $F_{\max}$  and  $t_+$  are the peak value and positive over-pressure duration time of explosion load, respectively.

The equivalent rectangular pulse  $f(t)$  is expressed as

$$f(t) = \begin{cases} F_{\max}, & 0 \leq t \leq t_1, \\ 0, & t > t_1. \end{cases} \quad (3)$$

#### 3.2. Analytical Solution of Isolation Rate of Isolation System

**3.2.1. Analytical Solution of Motion Equation of Isolated System.** The shock and vibration isolation system in this paper belongs to a single-stage active isolation system. It is assumed that the mass of the isolation system is  $m$ , the blast load received by the isolation system is  $F(t)$ , the stiffness of the isolation system is  $k$ , the damping coefficient is  $c$ , and the response displacement of the isolation system along the vertical direction is  $x$ , as shown in Figure 10. Then the motion differential equation of the isolation system is as follows:

$$m\ddot{x} + c\dot{x} + kx = F(t). \quad (4)$$

By introducing the damping ratio ( $\xi = c/2m\omega_n$ ), the motion equation can be rewritten as

$$\ddot{x} + 2\xi\omega_n\dot{x} + \omega_n^2x = \frac{F(t)}{m}, \quad (5)$$

where  $\omega_n = \sqrt{k/m}$  is the undamped angular frequency of isolation system.

The Duhamel integral formula of the response of the isolation system with viscous damping under the general explosion load  $F(t)$  is as follows [16]:

$$x(t) = \frac{1}{m\omega_D} \int_0^t F(\tau) \sin \omega_D(t - \tau) \exp[-\xi\omega_n(t - \tau)] d\tau, \quad (6)$$

where  $\omega_D = \omega_n \sqrt{1 - \xi^2}$  and  $\omega_D$  is the damped angular frequency of the isolation system.

- (1) When  $0 \leq t \leq t_1$ , the equivalent rectangular pulse load  $f(t) = F_{\max} = \text{const}$ . The isolation system is in the forced vibration stage:

$$x(t) = \frac{F_{\max}}{m\omega_D} \int_0^t \sin \omega_D(t - \tau) \exp[-\xi\omega_n(t - \tau)] d\tau, \quad (7)$$

After second times of partial integration, the expression of response displacement  $x(t)$  of isolation system is obtained:

$$x(t) = \frac{F_{\max}}{k} \left[ 1 - \exp(-\xi\omega_n t) \left( \cos \omega_D t + \frac{\xi}{\sqrt{1 - \xi^2}} \sin \omega_D t \right) \right]. \quad (8)$$

Take the derivative of time to get the expression of response velocity of the isolation system as follows:

$$\dot{x}(t) = \frac{F_{\max}\omega_n}{k\sqrt{1 - \xi^2}} \sin \omega_D t \cdot \exp(-\xi\omega_n t). \quad (9)$$

- (2) When  $t > t_1$ , the equivalent rectangular pulse load  $f(t) = 0$ . At this time, the isolation system is in the stage of free vibration. The displacement  $x(t_1)$  and velocity  $\dot{x}(t_1)$  at the time  $t_1$  of forced vibration stage are taken as the initial conditions of damped free vibration. The displacement response is calculated as follows:

$$x(t) = \left[ x(t_1) \cos \omega_D(t - t_1) + \left( \frac{\dot{x}(t_1) + x(t_1)\xi\omega_n}{\omega_D} \right) \cdot \sin \omega_D(t - t_1) \right] \exp(-\xi\omega_n(t - t_1)), \quad (10)$$

where

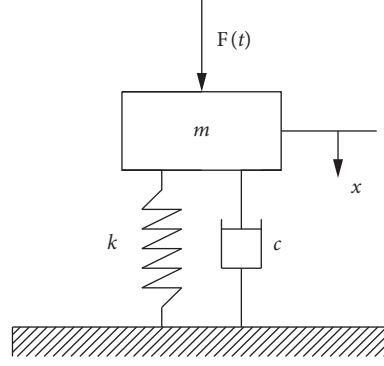


FIGURE 10: Mechanical model of combined isolation system.

$$x(t_1) = \frac{F_{\max}}{k} \left[ 1 - \exp(-\xi\omega_n t_1) \left( \cos \omega_D t_1 + \frac{\xi}{\sqrt{1-\xi^2}} \sin \omega_D t_1 \right) \right], \quad (11)$$

$$\dot{x}(t_1) = \frac{F_{\max} \omega_n}{k \sqrt{1-\xi^2}} \sin \omega_D t_1 \cdot \exp(-\xi\omega_n t_1). \quad (12)$$

The displacement  $x(t_1)$  and velocity  $\dot{x}(t_1)$  at time  $t_1$  are substituted into equation (10). The following results are obtained:

$$x(t) = \frac{F_{\max}}{k} (A - B e^{-\xi\omega_n t_1}) e^{-\xi\omega_n (t-t_1)}, \quad (13)$$

where

$$A = \cos \omega_D (t - t_1) + \frac{\xi}{\sqrt{1-\xi^2}} \sin \omega_D (t - t_1), \quad (14)$$

$$B = \cos \omega_D t + \frac{\xi}{\sqrt{1-\xi^2}} \sin \omega_D t.$$

Take the derivative of time to get the expression of response velocity of the isolation system as follows:

$$\dot{x}(t) = -\frac{F_{\max} \omega_n}{k \sqrt{1-\xi^2}} \left[ \sin \omega_D (t - t_1) - \sin \omega_D t \cdot e^{-\xi\omega_n t_1} \right] \cdot e^{-\xi\omega_n (t-t_1)}. \quad (15)$$

Equations (8) and (9) and equations (13)–(15) are the analytical solutions of response displacement  $x(t)$  and response velocity  $\dot{x}(t)$  of the differential motion equation of the isolated system during  $0 \leq t \leq t_1$  and  $t > t_1$ , respectively.

### 3.2.2. Calculation of Isolation Rate of Isolation System.

For a single-stage active isolation system, its input is the external excitation load  $F(t)$ , and its output is the disturbance force  $n(t)$  transmitted by the isolation system to the foundation. From the mechanical model of single-stage active isolation system in Figure 10, it can be seen that

$$n(t) = kx + c\dot{x}. \quad (16)$$

According to the definition of the transmission rate of the isolation system, the transmission rate of any isolation system is equal to the maximum value of the ratio of the system's output and input [19]. For the combined isolation system proposed in this paper, the transmission rate of the system is the ratio of the disturbance dynamic amplitude of the given foundation to the initial excitation load amplitude  $F_{\max}$ . Therefore, the time-history curves of the transmission rate  $T_q(t)$  can be defined as

$$T_q(t) = \frac{|n(t)|}{F_{\max}}, \quad (17)$$

where  $F_{\max}$  is the peak value of explosion load.

By substituting the analytical solutions of the response displacement  $x(t)$  and the response speed  $\dot{x}(t)$  into equation (16), it can be concluded that the disturbance force of the foundation is as follows:

$$n(t) = \begin{cases} F_{\max} (1 - C e^{-\xi\omega_n t}), & 0 \leq t \leq t_1, \\ F_{\max} (D - C e^{-\xi\omega_n t_1}) e^{-\xi\omega_n (t-t_1)}, & t > t_1, \end{cases} \quad (18)$$

where

$$C = \cos \omega_D t - \frac{\xi}{\sqrt{1-\xi^2}} \sin \omega_D t, \quad (19)$$

$$D = \cos \omega_D (t - t_1) - \frac{\xi}{\sqrt{1-\xi^2}} \sin \omega_D (t - t_1).$$

Combining formulas (17) and (18), we can obtain

$$T_q(t) = \begin{cases} |1 - C e^{-\xi\omega_n t}|, & 0 \leq t \leq t_1, \\ |(D - C e^{-\xi\omega_n t_1}) e^{-\xi\omega_n (t-t_1)}|, & t > t_1, \end{cases} \quad (20)$$

In the process of vibration, the time-history curves  $\eta(t)$  of isolation rate have the following relationship with  $T_q(t)$ :

$$\eta(t) = 1 - T_q(t). \quad (21)$$



TABLE 4: Primary performance parameters of combined isolation devices.

Abbreviation	Mass $m$ (kg)	Stiffness $k$ (N·mm <sup>-1</sup> )	Angular frequency $\omega_n$ (rad·s <sup>-1</sup> )	Damping ratio $\xi$ (%)	Duration time $t_1$ (ms)
TQGG	2700	617	15.117	12.6	2.44
TXJG	2700	942	18.679	13.2	2.44
TPMLG	2700	1596	24.313	12.5	2.44

TABLE 5: The transmissibility and isolation rate of the combined isolation devices.

Abbreviation	Transmissibility $T_q$ (%)	Vibration isolation rate $\eta$ (%)
TQGG	3.1	96.9
TXJG	3.9	96.1
TPMLG	7.3	92.7

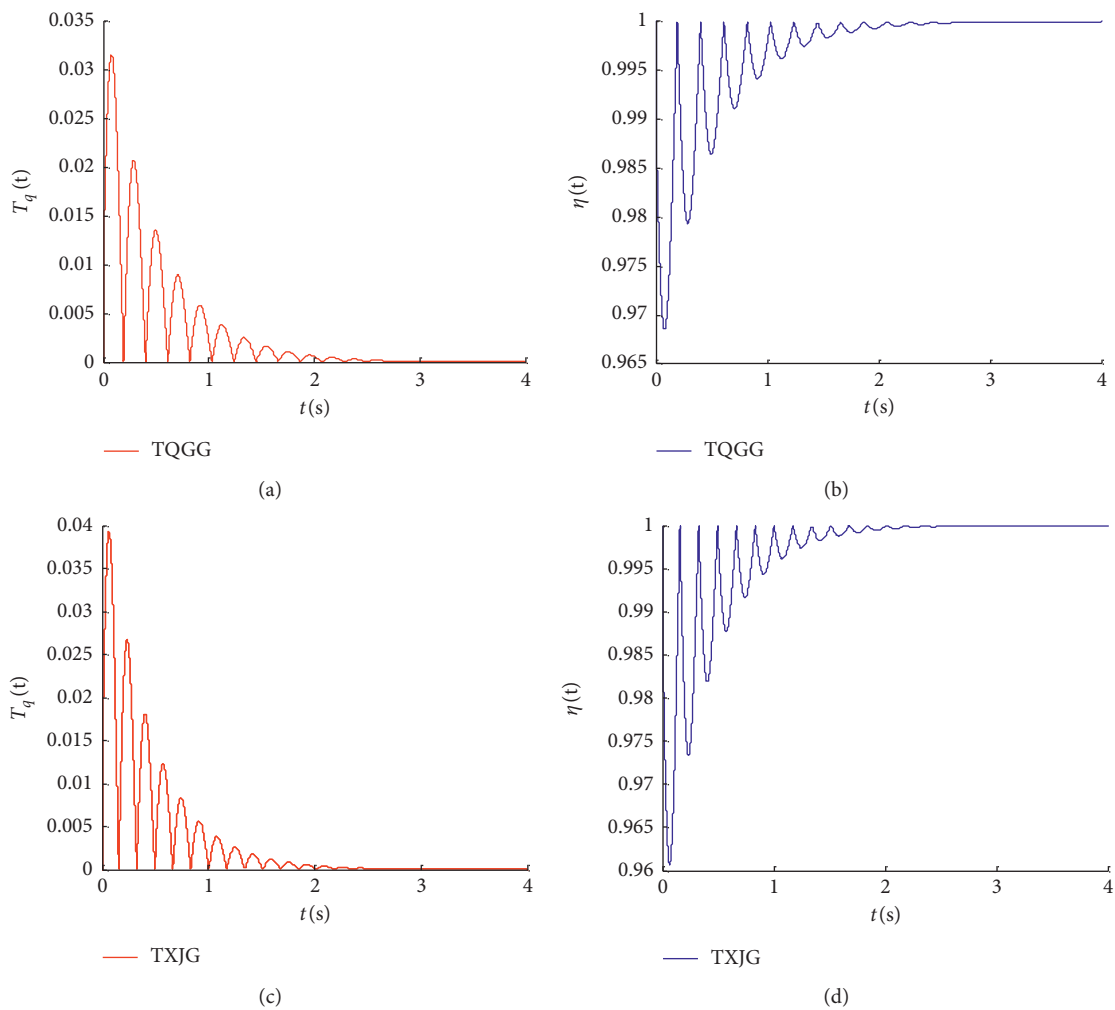


FIGURE 11: Continued.

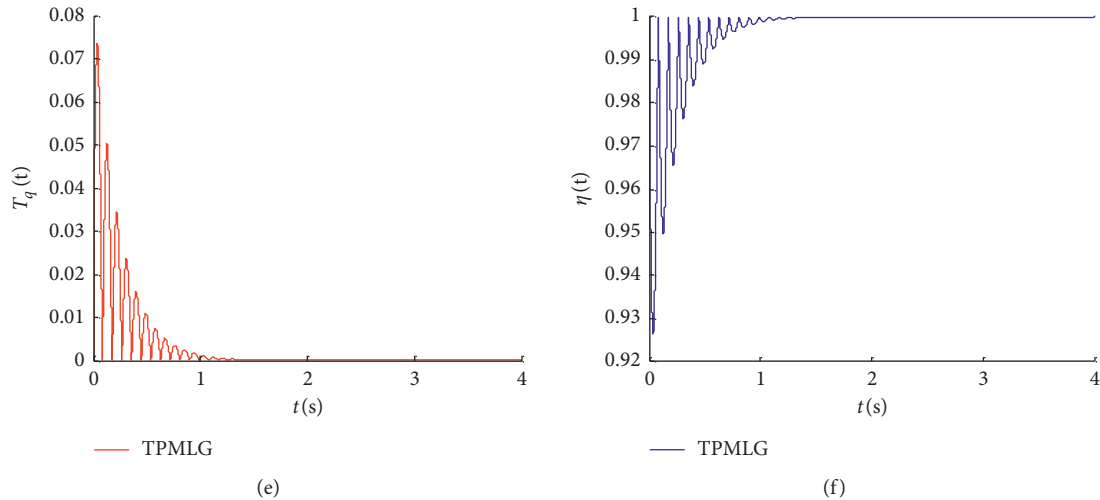


FIGURE 11: Transmissibility and vibration isolation rate time-history curves of combined devices. (a) Transmissibility curve of spring-cylinder isolation device. (b) Vibration isolation rate curve of spring-cylinder isolation device. (c) Transmissibility curve of spring-rubber isolation device. (d) Vibration isolation rate curve of spring-rubber isolation device. (e) Transmissibility curve of spring-aluminum foam isolation device. (f) Vibration isolation rate curve of spring-aluminum foam isolation device.

The isolation rate  $\eta$  and the transmission rate  $T_q$  of the isolation system are obtained by taking the maximum values of  $\eta(t)$  and  $T_q(t)$ , respectively.

### 3.3. Analysis of Isolation Rate of Combined Isolation Device.

In order to further compare and analyze the isolation effect of the isolation devices, the basic parameters of the combined isolation devices obtained from the tests have been used to calculate the transmissibility and vibration isolation rate using the isolation rate formula derived in this paper. The main performance parameters of the three kinds of isolation devices are shown in Table 4. It is worth mentioning that the stiffness  $k$  of the combined isolation device in Table 4 is calculated based on the natural vibration period obtained from the dynamic test and the mass (4191 kg) during the test, which is the dynamic stiffness of the isolation device. The mass of the combined isolation device under normal working condition is only 2,700 kg. Based on this mass, the angular frequency  $\omega_n$  of the isolation device is recalculated. After calculation, the transmissibility and isolation rate curves of three kinds of combined isolation devices under the same rectangular pulse load are shown in Figure 11.

As can be seen from Figure 11, the transmissibility and isolation rate curves of the isolation devices under the same explosion load are similar in shape, but the peak value and attenuation speed of each curve are different. The spring-cylinder isolation device is better than spring-rubber isolation device and spring-aluminum foam isolation device. The higher the damping ratio of the isolation device, the less the frequency of subsequent wave peaks of the transmission rate and isolation rate and the faster the attenuation, indicating that the more obvious the energy dissipation effect is, the better the isolation and absorption performance is.

The transmissibility and isolation rate of the three kinds of combined isolation devices are shown in Table 5.

In the strong shock and vibration environment caused by explosion, a good isolation device not only requires a high isolation efficiency, but also requires a good performance of the reuse of the isolation device, especially the damping material. Due to the inevitable plastic deformation in the response process, aluminum foam is not suitable as an ideal damping material. It can be seen from Table 5 that compared with aluminum foam damping body, rubber damping body and cylinder damping body have higher reliability in working state.

## 4. Parametric Analysis of Isolation Performance

For the isolation system subjected to explosion loads, when its bearing quality is certain, the isolation effect of the isolation device is affected by a variety of factors [20, 21]. In order to further analyze the influencing factors of the isolation performance, the isolation rate of the isolation device with different stiffness, damping ratio, and angular frequency is calculated.

**4.1. Effect of Stiffness.** In order to study the influence of the stiffness of the isolation device on the isolation rate under the rectangular pulse load, the variation law of the isolation rate with different stiffness is obtained. In this paper, the calculation formula of the isolation rate of the isolation system derived from Section 3.2 is used to obtain the isolation rate curves changing with the stiffness under three different damping ratios, as shown in Figure 12.

From Figure 12, it can be seen that the isolation rate decreases with the increase of stiffness. With the increase of damping ratio, the decrease trend of isolation rate decreases

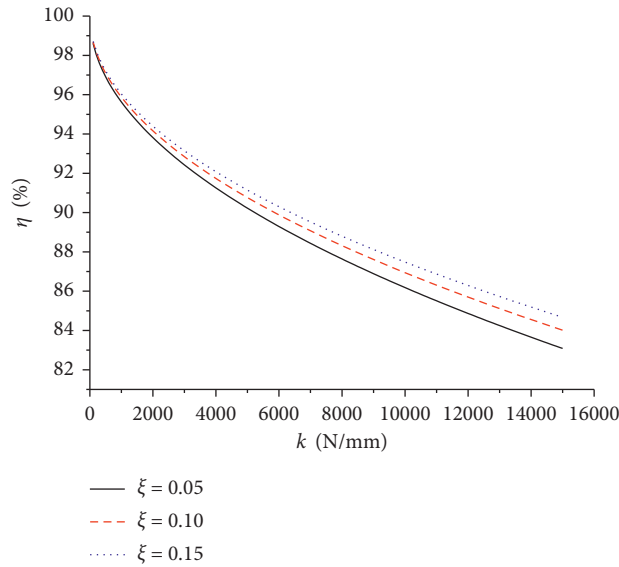


FIGURE 12: Vibration isolation rate curve of isolation device with changing stiffness.

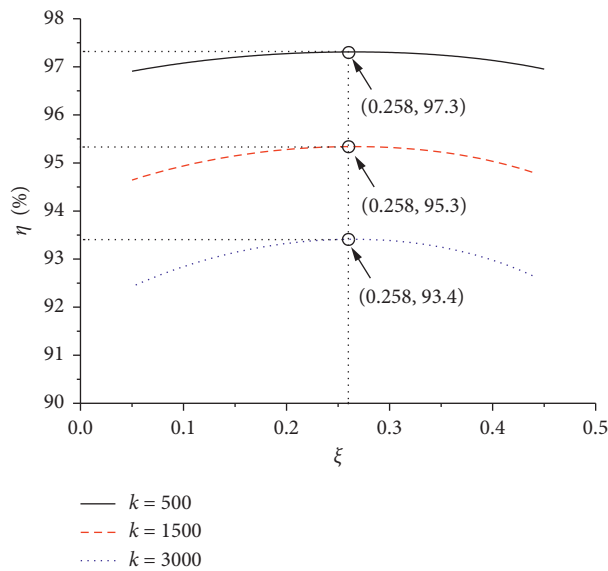


FIGURE 13: Vibration isolation rate curve of isolation device with damping ratio.

with the increase of stiffness. When the stiffness is small, the isolation rate of the isolation device with three damping ratios is basically the same.

**4.2. Effect of Damping Ratio.** In order to analyze the influence of damping ratio on isolation rate of isolation device, the change curves of isolation rate with damping ratio under three different stiffness conditions are calculated, as shown in Figure 13.

It can be seen from Figure 13 that the isolation rate of the isolation device increases first and then decreases with the increase of the damping ratio. Compared with the curvature of the three curves, the greater the stiffness is, the greater the

influence of the damping ratio on the isolation rate is. There is an optimal damping ratio in the isolation device, which is independent of stiffness. The optimal damping ratio is 25.8%, and isolation device has the highest isolation rate and the best isolation effect under this condition.

**4.3. Effect of Angular Frequency.** In order to analyze the influence of the angular frequency on the isolation rate of the isolation device, the variation curve of the isolation rate with angular frequency under three different damping ratios is obtained, as shown in Figure 14.

As can be seen from Figure 14, the isolation rate of the isolation device decreases approximately linearly with the

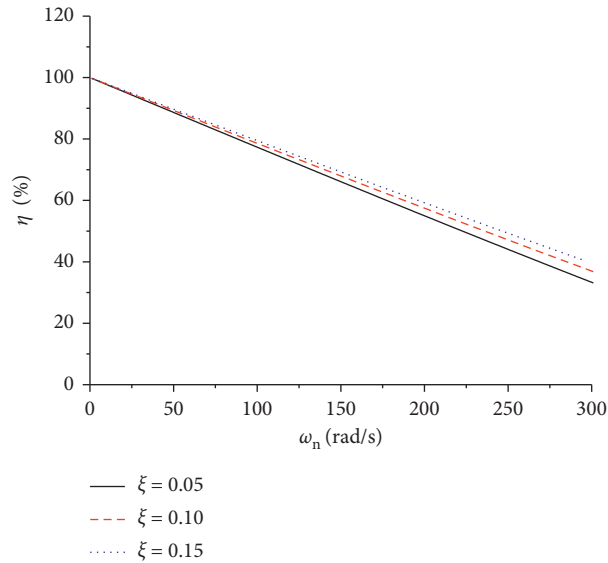


FIGURE 14: Vibration isolation rate curve of isolation device with angular frequency.

increase of natural vibration angular frequency. The slope of isolation rate is related to the damping ratio. The lower the damping ratio, the slower the decreasing trend of isolation with the increase of stiffness.

## 5. Conclusions

In this paper, three new kinds of combined isolation devices are designed and manufactured, and experimental and theoretical studies are carried out. Based on the Duhamel integral principle, the analytical expression of isolation rate of the isolation device is obtained, and the isolation performance of the combined isolation device and its influencing factors are analyzed. The main conclusions are as follows.

- (1) The damping ratio of spring-cylinder isolation device, spring-rubber isolation device, and spring-aluminum foam isolation device developed in this paper ranges from 0.125 to 0.132, and the vibration isolation rate is above 92%, which has good anti-explosion and impact isolation performance.
- (2) The three kinds of damping materials not only have absorption effect, but also play a supporting role in the isolation system. The damping effect of the cylinder damping body on the isolation device is the smallest, but the damping ratio is the largest. The supporting effect of the aluminum foam damping body is the largest, and its damping ratio is closer to the rubber damping body.
- (3) The isolation rate of the isolation device decreases with the increase of stiffness and angular frequency. With the increase of the damping ratio, the isolation ratio increases first and then decreases, and there is an optimal damping ratio, which is independent of the stiffness of the isolation device.

## Data Availability

The data used to support the findings of this study are included within the article.

## Conflicts of Interest

The authors declare that there are no conflicts of interest regarding the publication of this paper.

## Acknowledgments

This research was supported by the National Natural Science Foundation of China under Grant nos. 11872072, 11402304, and 51304219.

## References

- [1] G. Dong, Y. Zhang, Y. Luo, S. Xie, and X. Zhang, "Enhanced isolation performance of a high-static-low-dynamic stiffness isolator with geometric nonlinear damping," *Nonlinear Dynamics*, vol. 93, no. 4, pp. 2339–2356, 2018.
- [2] Z. Q. Lang, P. F. Guo, and I. Takewaki, "Output frequency response function based design of additional nonlinear viscous dampers for vibration control of multi-degree-of-freedom systems," *Journal of Sound and Vibration*, vol. 332, no. 19, pp. 4461–4481, 2013.
- [3] C. Ho, Y. Zhu, Z.-Q. Lang, S. A. Billings, M. Kohiyama, and S. Wakayama, "Nonlinear damping based semi-active building isolation system," *Journal of Sound and Vibration*, vol. 424, pp. 302–317, 2018.
- [4] M. Harris Cyril, E. Crede Charles, and J. P. Den Hartog, "Shock and vibration handbook (second edition)," *Journal of Applied Mechanics*, vol. 44, no. 2, pp. 364–389, 1977.
- [5] S. P. Shang, Z. W. Quan, and X. L. Cui, "The research of three-dimensional seismic isolation pier vibration isolation performance," *Earthquake Engineering and Engineering Dynamics*, vol. 38, no. 1, pp. 156–162, 2018.

- [6] X. Y. Li and S. D. Xue, "Experiment of 3-dimensional seismic isolation bearing combined with frictional sliding system and disc springs," *World Earthquake Engineering*, vol. 27, no. 3, pp. 1-7, 2012.
- [7] D. M. Zeng, *Experimental Study on Stiffness Characteristics of Rubber Isolation Bearing and Performance of Isolation Building*, Academy of Building Research, Beijing, China, 2007.
- [8] H. B. Xiang, Q. Fang, W. Wang, and Z. M. Gong, "Numerical simulation on shock isolation of blast-resistant structure with magnetorheological dampers," *Journal of Vibration and Shock*, vol. 26, no. 11, pp. 106-111, 2007.
- [9] D. J. Yan, D. G. Tang, and Q. H. Qian, "Isolation properties of double mass-spring system under blast shock and vibration," *Journal of Vibration Engineering*, vol. 14, no. 3, pp. 339-344, 2001.
- [10] Y. Xia, "Seismic performance analysis and isolation study of large liquid-storage tank," *Journal of Disaster Prevention and Mitigation Engineering*, vol. 45, no. 2, pp. 113-120, 2017.
- [11] Y. F. Du and X. H. Zeng, "Simulation of uninterrupted collapse isolated structure under blast load in basement," *Journal of Lanzhou University of Technology*, vol. 27, no. 3, pp. 1-7, 2019.
- [12] D. B. Li and Q. H. Lu, *Analysis of Experiments in Engineering Vibration*, Tsinghua University Press, Beijing, China, 2015.
- [13] J. Wang and X. Hu, *Application of MATLAB in Vibration Signal Processing*, China Water & Power Press, Beijing, China, 2006.
- [14] P. Y. Chen, *Study on Several Dynamic Signal Processing Techniques and Their Applications*, Nanjing University of Aeronautics and Astronautics, Nanjing, China, 2012.
- [15] P. X. Gao, "Effect and removal of trends on parameters identification in time domain," *Journal of Vibration, Measurement & Diagnosis*, vol. 14, no. 2, pp. 20-26, 1994.
- [16] R. W. Clough and J. Penzien, *Dynamics of Structures*, Higher Education Press, Beijing, China, 2006.
- [17] N. Q. Wang, *The Calculation Principle and Design of Protective Structure*, Engineering Institute of Corps of Engineers, Nanjing, China, 2002.
- [18] W. J. Ding, *Vibration and Damping Theory*, Tsinghua University Press, Beijing, China, 2014.
- [19] S. J. Zhu, J. J. Lou, and Q. W. He, *Vibration Theory and Vibration Isolation*, pp. 25-31, National Defense Industry Press, Beijing, China, 2008.
- [20] V. I. Babitsky and A. M. Veprik, "Universal bumpered vibration isolator for severe environment," *Journal of Sound and Vibration*, vol. 218, no. 2, pp. 269-292, 1998.
- [21] Z. Q. Lang, X. J. Jing, S. A. Billings, G. R. Tomlinson, and Z. K. Peng, "Theoretical study of the effects of nonlinear viscous damping on vibration isolation of sdof systems," *Journal of Sound and Vibration*, vol. 323, no. 1-2, pp. 352-365, 2009.



## Research Article

# Replacing Detonation by Compressed Balloon Approaches in Finite Element Models

Pierre Legrand,<sup>1,2</sup> S. Kerampran,<sup>2</sup> and M. Arrigoni <sup>2</sup>

<sup>1</sup>SIXENSE NECS, 192 Rue Houdan, 92330 Sceaux, France

<sup>2</sup>ENSTA-Bretagne, 2 Rue François Verny, 29200 Brest, France

Correspondence should be addressed to M. Arrigoni; [michel.arrigoni@ensta-bretagne.fr](mailto:michel.arrigoni@ensta-bretagne.fr)

Received 17 January 2020; Accepted 21 April 2020; Published 12 May 2020

Academic Editor: Piotr Sielicki

Copyright © 2020 Pierre Legrand et al. This is an open access article distributed under the Creative Commons Attribution License, which permits unrestricted use, distribution, and reproduction in any medium, provided the original work is properly cited.

The evaluation of blast effects from malicious or accidental detonation of an explosive device is really challenging especially on large buildings. Indeed, the time and space scales of the explosion together with the chemical reactions and fluid mechanics make the numerical model really difficult to achieve acceptable structural design. Nevertheless, finite element methods and especially Arbitrary Lagrangian Eulerian (ALE) have been extensively used in the past few decades with some simplifications. Among them, the replacement of the explosive event by a compressed balloon of detonation products has been proven useful in numerous different situations. Unfortunately, the ALE algorithm does not achieve a proper energy balance through the numerical integration of the discrete scheme; this important drawback is not compensated by the use of the classical compressed balloon approach. The paper focuses on increasing the radius of the equivalent ideal gas balloon in order to achieve better energy balance and thus better results at later stages of the blast wave propagation.

## 1. Introduction

The evaluation of blast effects from the malicious or accidental detonation of an explosive device on structures is a multiphysics issue involving widely different time and space scales. Indeed, the detonation process of high explosives implies chemical reactions propagating within the solid explosive for a few microseconds. This reaction will create detonation products, in other words high pressure and temperature gases which will first react with themselves to create secondary reactions called afterburning. These gases then will expand and also react with the surrounding air and create a blast wave propagating outwards in the air for a few milliseconds, a possible fireball, and high pressure and temperature gradients. An extensive description of the detonation process can be found in [1]. Finally structural components will be impacted by the blast wave and may collapse over a few seconds. All those phenomena come with different space scales from the cm of the explosive sources to the dozens of meters of the structure.

In practical use, when there is a need for shorter calculation times, cost reduction, and structural optimization, dealing with all phenomena is challenging, especially on a commonly available high performance computer (HPC). In order to speed up the calculation, a lot of effort has been made in the last 50 years to find suitable methods to evaluate the behavior of structures loaded by blast waves in a reasonable computational time. Among them, one of the most efficient methods consists in calculating the blast wave without taking the actual detonation process into consideration. In fact, for structural design, the pressure-time curve and specifically both overpressure and impulse transmitted to the structure are the most important parameters [2, 3]. In spite of neglecting the chemical detonation and so close-in effects (afterburning, fireball) the proposed method leads to proper time-history pressure curves and thus adequate structural design.

Several approaches can be used to evaluate the properties of a blast wave from a given explosive charge. Taylor [4], and several authors after him (see, for example, [5–7]), managed to obtain adequate analytical blast wave models for strong

explosions by making two main assumptions: (1) all explosive energy is concentrated in one central source point. (2) The blast overpressure should be much greater than the ambient pressure. They managed to establish a relation between the maximum pressure  $P_{\max}$  and the radial position of the shock  $R$  given by

$$P_{\max} = 0.155m e_i R^{-3} = 0.155e_i (Rm^{-1/3})^{-3}, \quad (1)$$

where  $e_i$  is the internal energy released per unit mass at one source point and  $m$  the total mass of the explosive. The factor  $Rm^{-1/3}$  is called the scaled distance and denoted  $Z$  hereafter. Unfortunately, neither of the assumptions of this model is fulfilled in the case of explosions implying conventional explosives. In fact, for the intensively studied TNT, both conditions are fulfilled in a fairly narrow scaled distance range around  $Z = 1 \text{ m}\cdot\text{kg}^{-1/3}$ . At larger scaled distances, the overpressure is no more than ten times the ambient pressure and, close to the charge, the scaled distance is less than ten times the explosive diameter and so the point source assumption is no longer appropriate. Alternatively, empirical or semiempirical approaches have been used to obtain reliable loading values [8–10]. The technical manual from the US Army, UFC-3-340-2 [8], is mainly used as the state of the art in structural design offices and constitutes the most widely used experimental database for both civilian and military infrastructure design since it offers the most complete open database of blast wave parameters. Those empirical solutions have the benefit of relying on experimental data but have several drawbacks. The first one is the lack of reliable data for scale distance smaller than  $0.5 \text{ m}\cdot\text{kg}^{-1/3}$ . Indeed, it is more than questionable to use these databases for close-in structures [11, 12]. This is mainly due to the chemical reactions between the detonation products and the surrounding air. Secondly, data are available only for the incident blast wave and possible reflections cannot be easily taken into account. This prevents any of these solutions from being applied in confined or urban space. Finally, only simple geometries for both the charge and the structure can be considered (spherical charge and plan wall).

Another widespread solution is the use of explicit numerical software. Nevertheless, in spite of all efforts made to enhance finite elements and finite volumes solvers, modeling different aspects of physics at different time scales remains a considerable challenge. In particular, a time step lower than the characteristic time of the detonation from a few orders of magnitude is required to obtain a proper model of the detonation process. Furthermore, an explicit numerical method makes calculation for each and every time step; thus, a small time step directly increases the overall computational time. Some hybrid solution using the UFC-3-340-2 data is added to numerical simulation in order to obtain a rapid loading for a given structure [13–15]. These methods are based on empirical data and suffer from the same problem as them, namely, they do not account for waves reflection and recombination in a confined or urban area and full simulation of the detonation process are needed.

According to the ideal detonation process, the reaction front propagates within the high explosive at a speed of about  $7000 \text{ m}\cdot\text{s}^{-1}$  for TNT [16, 17]. Just behind this reaction front, the Chapman-Jouguet [18] model predicts a pressure of  $P_{CJ} = 21 \text{ GPa}$ . The Chapman-Jouguet wave velocity is denoted as  $D_{CJ}$ . In fact, the time step will be about less than a microsecond which leads to calculation times above the acceptable range for a commonly available HPC. Instead of losing accuracy and trying to poorly represent the detonation process, it is possible to only model the relaxation of the detonation products. In numerical software, the detonation products can be initially modeled as a homogeneous volume of high pressure and temperature gas, referred to as a balloon.

For simplicity's sake, the chemical composition of the detonation products is most of the time considered as air and they are not allowed to react with either themselves or the surrounding air. The multiphysics detonation problem is reduced to a fluid mechanics problem, namely, the relaxation of high pressure and temperature gases. An equation of state needs to be chosen to describe the behavior of the relaxation of the gas mixture within the balloon. Several choices are available. The most used equation of state in commercial software is the John Wilkins Lee (JWL) equation of state (2):

$$P = A \left( 1 - \frac{\omega}{R_1 V} \right) e^{-R_1 V} + B \left( 1 - \frac{\omega}{R_2 V} \right) e^{-R_2 V} + \frac{\omega E}{V}. \quad (2)$$

The parameters of this equation are explosive dependent and have been extensively studied. The values given, for TNT at a density of  $1630 \text{ kg}\cdot\text{m}^{-3}$ , by Dobratz [16] and Souers [17] yield results in relatively good agreement with the UFC-3-340-2. Nevertheless, the JWL equation of state induces a large amount of computational effort by requiring high initial pressure state within the detonation products. These high pressure gradients lead towards small element sizes (less than 1 mm).

In fact, for current HPC, the number of finite elements should not be higher than 5 million, which represents a volume of  $10 \text{ cm}^3$  in the case of a mesh element size of 1 mm, and is clearly not enough to model a full-scale infrastructure. In spite of the non-representation of the detonation, the balloon filled with JWL gas is not suitable for a fast and accurate numerical model. As soon as the 1950s, Brode [19] proposed to simplify the model and consider the ideal gas law to model the evolution of the detonation products. The ideal gas equation of state has been used over the past couple of decades to represent the relaxation of the detonation products in numerical simulations of realistic events [20, 21] or laboratory scale experiments [22]. All these authors have used ideal gas with different values of pressure, density, and energy for representing the physical state of the detonation products.

In 2010s, Blanc [23] showed that the key parameters for monitoring the balloon-induced blast wave are density and specific energy of the explosive source. For Dobratz's TNT parameters, this yields  $\rho_b = \rho_{TNT} = 1630 \text{ kg}\cdot\text{m}^{-3}$  and  $e = e_{TNT} = 4.3 \text{ MJ}\cdot\text{kg}^{-1}$ . These parameters account for the

best accuracy for all relevant blast wave parameters (overpressure, impulse, and arrival time) with respect to the ideal detonation model. Other sets of parameters can be used to describe the relaxation of the high pressure gas inside the balloon thanks to the ideal gas equation of state (Chapman-Jouguet parameters: [24], isochoric compression [19], isothermic compression, etc.). The main approaches are presented in Table 1.

In this work, the approach of [23] is selected since it gives the better agreement with respect to the ideal detonation process, and relatively acceptable physical values for the density and pressure of the balloon gas in its initial state. As a consequence, the requirements for the element size are less constraining, but the resulting blast wave properties could be underestimated, especially in the near field. Another benefit of reducing the high pressure and energy gradient at the early stage of the relaxation is the mitigation of one unbalanced total energy, which is one of the remaining issues of the finite element model [25]. In fact, to deal with discontinuities in pressure, density, and energy, finite element software needs to add artificial viscosity [26] to smooth discontinuities in the pressure, energy, mass, and material speed in order to perform the derivation of the pressure function needed for finite element analysis. Also referred to as numerical damping, this will artificially reduce the total energy, especially at early stages of the blast wave propagation because of the large pressure gradients. Then it leads to higher errors made by commercial software.

This work addresses this issue from an end-user standpoint, by increasing the radius of the compressed balloon up to ten times the initial radius of the explosive. This main novelty is leading towards the following:

- (i) A better energy balance for finite element algorithm.
- (ii) A better accuracy with experimental data from the UFC-3-340-2, [8] at later stage of the blast wave propagation.
- (iii) A reduced computational time for engineering applications.

First, the numerical model is presented and the ideal gas equation of state for the detonation products is compared with the classical JWL equation of state. In a second part, the influence of the balloon radius is investigated and all models are evaluated with respect to experimental data found in the UFC-3-340-2. All numerical results are compared to the chosen reference (the UFC-3-340-2), an experimental database accepted by authorities for structural design. A mesh sensitivity analysis is performed to validate the results and finally the impact on the energy balance is evaluated.

## 2. The Compressed Balloon Model

Altair Hyperworks<sup>SR</sup> suite is used to build all numerical models and the explicit finite element code. Radioss<sup>SR</sup> is used for the simulations. The solver used is call legacy and it is a classical Arbitrary Lagrangian Eulerian (ALE) finite element/finite volume mixed solver. The conservation equations for mass and energy are solved at the center of each

TABLE 1: Compressed balloon possible sets of parameters.

	Chapman-Jouguet parameters	Isochoric compression	Density-energy approach
Pressure (GPa)	21	21	2.8
Internal energy (MJ·kg <sup>-1</sup> )	32	4.3	4.3
Density (kg·m <sup>-3</sup> )	1630	12209	1630

element and the momentum conservation equation is solved at each node. The first model, the most used, takes JWL equation of state as presented in the introduction together with the chosen parameters for TNT from [16]; it is hereafter referred to as the “JWL model.” All other gases are modeled by a hydrodynamic fluid material using a polynomial equation of state (3).

$$P = C_0 + C_1\mu + C_2\mu^2 + C_3\mu^3 + (C_4 + C_5\mu)e, \quad (3)$$

where  $e$  is the energy per unit volume,  $\mu$  is the dilation coefficient  $= \rho/\rho_0 - 1$ , and  $P$  is the pressure.

By choosing  $C_0 = C_1 = C_2 = C_3 = 0$  and  $C_4 = C_5 = 0.4$ , the hydrodynamic polynomial law describes an ideal diatomic gas with a specific heat ratio  $\gamma = 1.4$ . In order to model the ambient state of the air, the density and the energy per unit volume are, respectively, set to  $\rho_{air} = 1.225 \text{ kg}\cdot\text{m}^{-3}$  and  $e_{air} = 0.25 \text{ MJ}\cdot\text{m}^{-3}$  with respect to (3). As detailed in the introduction, for the compressed balloon approach, the density and the internal energy per unit volume of the balloon are set to the TNT values:  $e_{balloon} = 7000 \text{ MJ}\cdot\text{m}^{-3}$  and  $\rho_{balloon} = 1630 \text{ kg}\cdot\text{m}^{-3}$ . Parameter beta is defined by equation (4). It is the ratio of the balloon radius over the radius of the TNT equivalent spherical charge. This ratio will be varied between one and ten in this study:

$$\beta = \frac{R_{balloon}}{R_{TNT}}. \quad (4)$$

The total mass and energy of the explosive source should not be modified by the increase of the balloon radius. Thus, the density  $\rho_\beta$  and the specific energy  $E_\beta$  are reduced by the coefficient  $\beta^3$ :

$$\rho_\beta = \frac{E_{TNT}}{\beta^3}, \quad (5)$$

$$E_\beta = \frac{E_{TNT}}{\beta^3}. \quad (6)$$

Two types of mesh are studied, with equivalent element size. The first one is a Cartesian mesh, which is of a more convenient use in structural design offices since it is easier to create and better fits with most fluid-structure interfaces. The second one is a radial structured mesh. Even if it is harder to obtain, the radial mesh is more accurate [27] and more adapted to immersed fluid-structure interfaces. Both radial and Cartesian meshes used for the balloon model are presented in Figure 1.

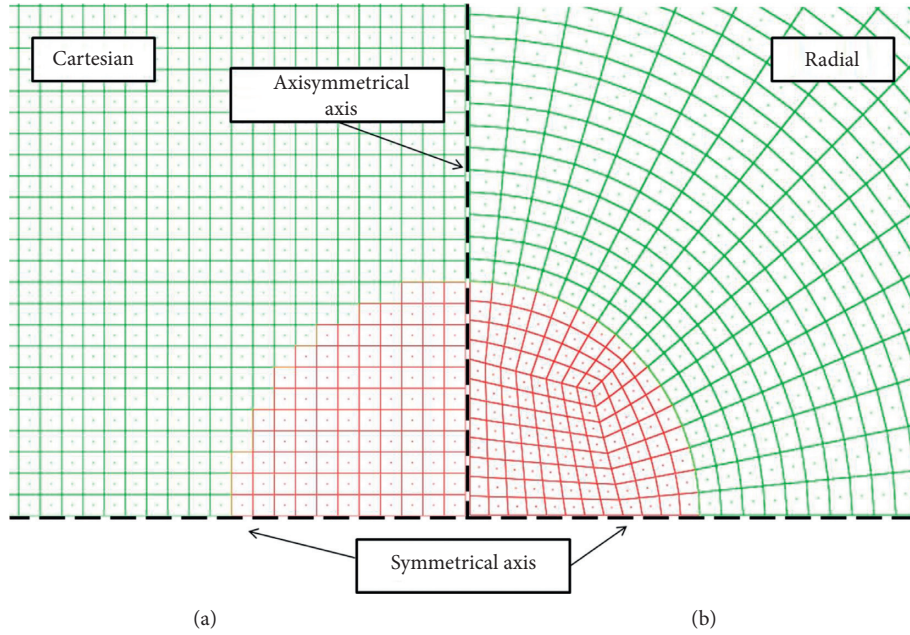


FIGURE 1: Cartesian (a) and radial (b) mesh structure for the numerical simulation.

The Cartesian mesh is straightforward; each element is a regular square and the mesh is not impacted by the increase in  $\beta$ . On the opposite, the radial mesh is in two parts: the first one is Cartesian from the center of the charge to two-thirds of the explosive radius and the rest is a radial mesh. This radial mesh is adapted for each beta in order to reduce the mesh distortion at the transition between the Cartesian and radial parts. This has no consequence on the blast wave propagation because the mesh size in the propagation direction is kept identical in all  $\beta$  models.

An axisymmetrical boundary condition is enforced on the vertical axis to ensure the spherical propagation of the blast wave. Likewise, a symmetry condition is applied on the horizontal axis in order to reduce the computational domain to one-fourth of the space.

The scaled mesh size is defined as the actual mesh over the mass of equivalent high explosive at the cubicle root:

$$dx_{scaled} = \frac{dx}{m^{1/3}}. \quad (7)$$

The results of pressure as a function of time are highly dependent on the scale mesh size [25]. In practical use,  $5 \text{ mm} \cdot \text{kg}^{-1/3}$  is among the smallest possible scaled mesh sizes for acceptable CPU time for civil engineering applications (around 5 million elements). It is then used in this section for the element size.

In order to evaluate the simplified approach of the  $\beta$  balloon, two parameters are considered, maximum overpressure and positive impulse. Indeed, both play an important part in the structural behavior of the loaded structure, one being usually more significant than the other depending on the natural frequencies of the structure. The overpressure is defined as the maximum of the pressure history and the positive impulse is the integration of the positive part of the pressure history curve defined more precisely by

$$I = \int_{t_1}^{t_2} P(T) dt, \quad (8)$$

with  $t_1$  and  $t_2$  arbitrarily chosen as follows in order to avoid numerical noise:  $t_1$  the time where  $P > 0.01P_{\max}$  and  $t_2$  the time where  $P < -0.01P_{\max}$ .

Furthermore, two relative difference ratios are defined with respect to the UFC-3-340-2 in

$$\delta_p = \frac{p_{\max}(\text{model}) - p_{\max}(\text{UFC})}{p_{\max}(\text{UFC})}, \quad (9)$$

$$\delta_I = \frac{I_{\max}(\text{model}) - I_{\max}(\text{UFC})}{I_{\max}(\text{UFC})}. \quad (10)$$

Figures 2 and 3 show, respectively, the evolution of  $\delta_I$  and  $\delta_p$  as functions of the scaled distance. Gauges have been placed in the numerical simulation to record the pressure history every 20 cm from the center of the charge and the relevant parameters have been extracted and compared with values given by the UFC-3-340-2. Furthermore, the finite volume method computed with the python module clawpack developed by Washington University [28] is also compared with the finite element calculation. All  $\delta_I$  curves show a high gradient for scaled distances lower than  $1 \text{ m} \cdot \text{kg}^{-1/3}$ , which could be explained by the difficulty to get experimental data so close to the explosive charge [29].

For scaled distances larger than  $1.5 \text{ m} \cdot \text{kg}^{-1/3}$ ,  $\delta_I$  curves tend to stabilize and exhibit a clear dependency on the mesh type (Cartesian or radial). As expected, the radial mesh gave better results and all  $\delta_I$  for radial meshes are smaller than those for Cartesian meshes. The same trend is seen on the  $\delta_p$  graphs but all differences between models are smaller.

On both pressure and impulse, finite volumes give better results. Unfortunately, the blast-structure interaction between Lagrangian finite element representing the structural



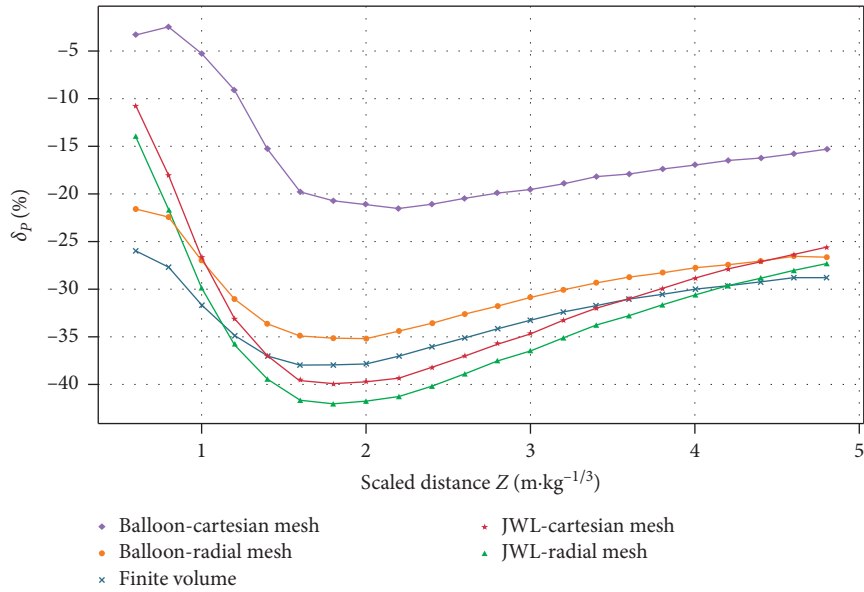


FIGURE 2: Relative difference with UFC-3-340-2 for impulse  $\delta_P$ , for all models as a function of scaled distance  $Z$ .

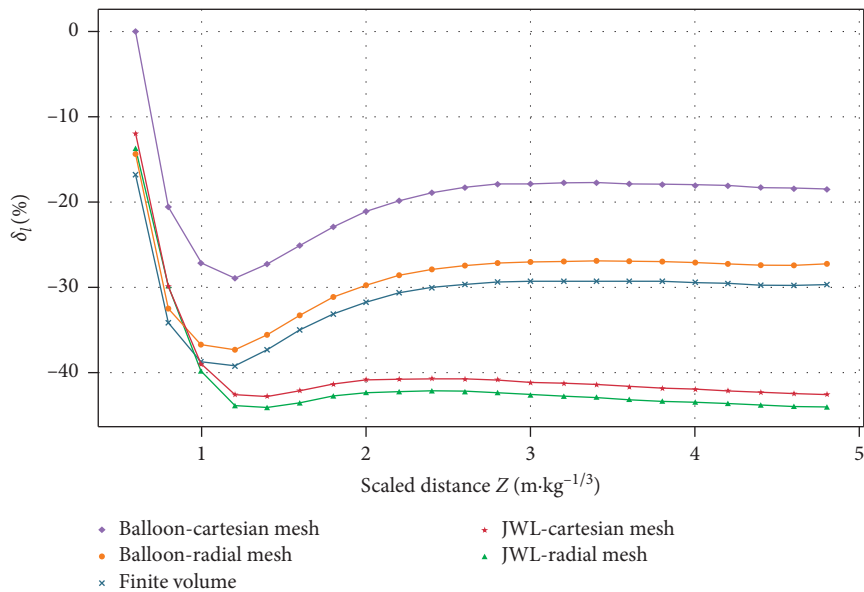


FIGURE 3: Relative differences with UFC-3-340-2 for overpressure, for all models as function of scaled distance.

part and finite volume representing the air domain remains challenging for all commercial software. Structural design is hardly possible with finite volume involved for the air model, especially if nonlinear material and displacement are taken into account.

### 3. Results

In order to evaluate the  $\beta$ -methods which could be used for civil engineering application, all data are extracted from the radial structured mesh at a scaled mesh size of  $5 \text{ mm} \cdot \text{kg}^{-1/3}$ . The Central Processing Unit (CPU) time of the computation of these models is reasonable for parametric studies

(30 min for 10 ms of blast wave propagation on 16 CPU) and the radial mesh is commonly used for 3D industrial applications.

First, Figures 2 and 3 will be extended to all beta values from one to ten and the relative discrepancies between the beta models and UFC-3-340-2 ( $\delta$  see equations (9) and (10)) will be studied, leading to a critical distance  $d(\beta)$  where the beta models become more accurate than the models using JWL equation of state for the description of the relaxation of detonation products, for a given mesh. In a second time, the mean values of  $\delta$  for all scaled distances are plotted for both mesh types to get a more global idea of the influence of  $\beta$  in the scaled distance range of interest.



**3.1. Influence of Balloon Radius.** Figure 4(a) shows that, close to the explosion center,  $\delta_p$  quickly increases with increasing values of  $\beta$ . This is to be expected due to the lack of the proper distribution of the pressure and density. In the case of an explosive charge, once the blast wave is created all the mass and energy are concentrated within a few centimeters behind the shock discontinuity. On the opposite, with balloon models, the mass and the energy of the gaseous products of detonation are spread uniformly in the entire balloon volume and it takes a few-balloon radius to concentrate it on the shock front. At larger scaled distances, all  $\delta_p$  are smaller than the  $\delta_p$  of the model with JWL model. On Figure 4(b) iso-values of relative error to UFC-3-340-2 are extrapolated for intermediate values of mesh size and beta.

From  $\beta=3$  to  $\beta=10$ , all  $\delta_p$  curves cross the  $\delta_p(\text{JWL})$  curve. This implies that there is a distance from which the beta model becomes more accurate for the predicted peak overpressure than the JWL one, for the considered mesh size. This scaled distance is hereafter denoted  $d$  and plotted in Figure 5.

For scaled distances greater than  $1.5 \text{ m}\cdot\text{kg}^{-1/3}$ , the beta balloon models presented in this study give an overpressure closer to the one given in the UFC-3-340-2. This means that if a concrete wall is far enough from the explosive center, the beta balloon model will give better results than the model using JWL equation of state for the relaxation of the detonation products. There are no points before  $\beta=3$  in Figure 5 because for  $\beta$ , 3 beta balloon models are better than JWL model even close to the explosive center.

Concerning the impulse on Figure 6, high positive  $\delta_I$  is observed in the vicinity of the high explosive, which means that the impulse is severely overestimated before about  $0.8 \text{ m}\cdot\text{kg}^{-1/3}$ . Furthermore, the impulse results are more complicated to analyze due to the numerical damping changes the blast wave shape. See Figure 7, where the pressure-time curves and impulse-time (computed as defined in 2) of  $\beta=5$  and JWL model are plotted for two scaled distances of  $1.4 \text{ m}\cdot\text{kg}^{-1/3}$  and  $2.6 \text{ m}\cdot\text{kg}^{-1/3}$ . Indeed, the rising time (defined as the time from ambient pressure to maximum pressure) is increased between both measurements at  $1.4$  and  $2.6 \text{ m}\cdot\text{kg}^{-1/3}$ . The model considering the JWL equation of state exhibits a larger increase than the  $\beta=5$  model. Thus the total area under the pressure-time curve (the impulse) is greater and closer to values given by the reference UFC-3-340-2 for the JWL equation of state. This accuracy is artificial because the shape of the profile is changed and so is the loading on the structure. In order to get a meaningful value of distance  $d_I$  for the structural behavior, the correlation between the increased rising time and the structural design should be studied. Considerations such as materials or natural frequencies are not taken into account in the present work and thus changes in the blast profile are not addressed by the authors in this study.

In some practical applications, especially for confined explosions, there is no particular distance of interest and the blast wave should be accurate in the entire air domain. For example, in a room full of equipment, the peak overpressure and the impulse should be as accurate as possible at every scaled distance of each standoff point. This is why the mean

of the relative differences  $\delta_i$  and  $\delta_p$  is studied in the next section.

**3.2. Average Discrepancies.** For a given mesh size of  $5 \text{ mm}\cdot\text{kg}^{-1/3}$ , Figures 8 and 9 show the average performance of all balloon models for, respectively, impulse and overpressure. The performance is defined as the average value of all relative differences  $\delta_p$  or  $\delta_I$  for all scaled distances from  $0.5$  to  $5 \text{ m}\cdot\text{kg}^{1/3}$ . The value  $\beta=0$  corresponds to the JWL equation of state model.

The behavior for both meshes is really different regarding the blast wave impulse; see Figure 8. Indeed, the radial mesh shows increase relative differences with respect to UFC-3-340-2 for increasing beta while the other, the Cartesian, shows decreasing relative differences with UFC-3-340-2.

On the opposite, both curves look similar for the overpressure; see Figure 9. Both show an extremum for values of  $\beta$  depending on the kind of mesh considered:  $\beta=2$  for the Cartesian mesh and  $\beta=5$  for the radial one. This results from the trade-off between poor accuracy at early stage of the simulation and accuracy of the big balloon at larger scaled distances. In conclusion for this section, there is an optimal  $\beta$  value for a given mesh (element size and mesh type). In the discussion, these results will be extended to other element sizes.

**3.3. Computational Time.** The main parameter ruling the calculation time is the time step. In Radioss<sup>R</sup>, as in most finite element software, a needed condition must be fulfilled in order to ensure numerical stability. This condition was established by Courant, Friedrich, and Levy (CFL) [30]. Unfortunately, the CFL condition is required to ensure the stability of the numerical scheme but it is not sufficient and it is possible that the time step should be decreased even further in order to allow the calculation to run until the end. According to Radioss<sup>R</sup> documentation, the stability condition is calculated for each element following the CFL following equation (11). Then the smaller time step  $\Delta t$  is used for the whole calculation.

$$\Delta t = k \frac{\Delta l}{c + v - w}, \quad (11)$$

with  $\Delta t$  being the time step,  $\Delta l$  the element size,  $v$  the material velocity,  $w$  the ALE grid velocity, and  $k$  the CFL coefficient 1.

$c$  is the speed of sound, calculated in (12).

$$c = \frac{\partial P}{\partial \rho}, \quad (12)$$

with  $\rho$  being the density and  $P$  the pressure.

At early stages of the blast wave propagation, results obtained with small  $\beta$  models, as well as with the model considering the JWL equation of state ( $\beta=0$ ), exhibit larger overpressures than large  $\beta$  models. This leads to smaller time steps. Figure 10 shows the specific example of two radial balloon models for  $\beta=1$  and  $\beta=10$ . Before few hundredths of milliseconds, the time step is smaller for  $\beta=1$ . However, at

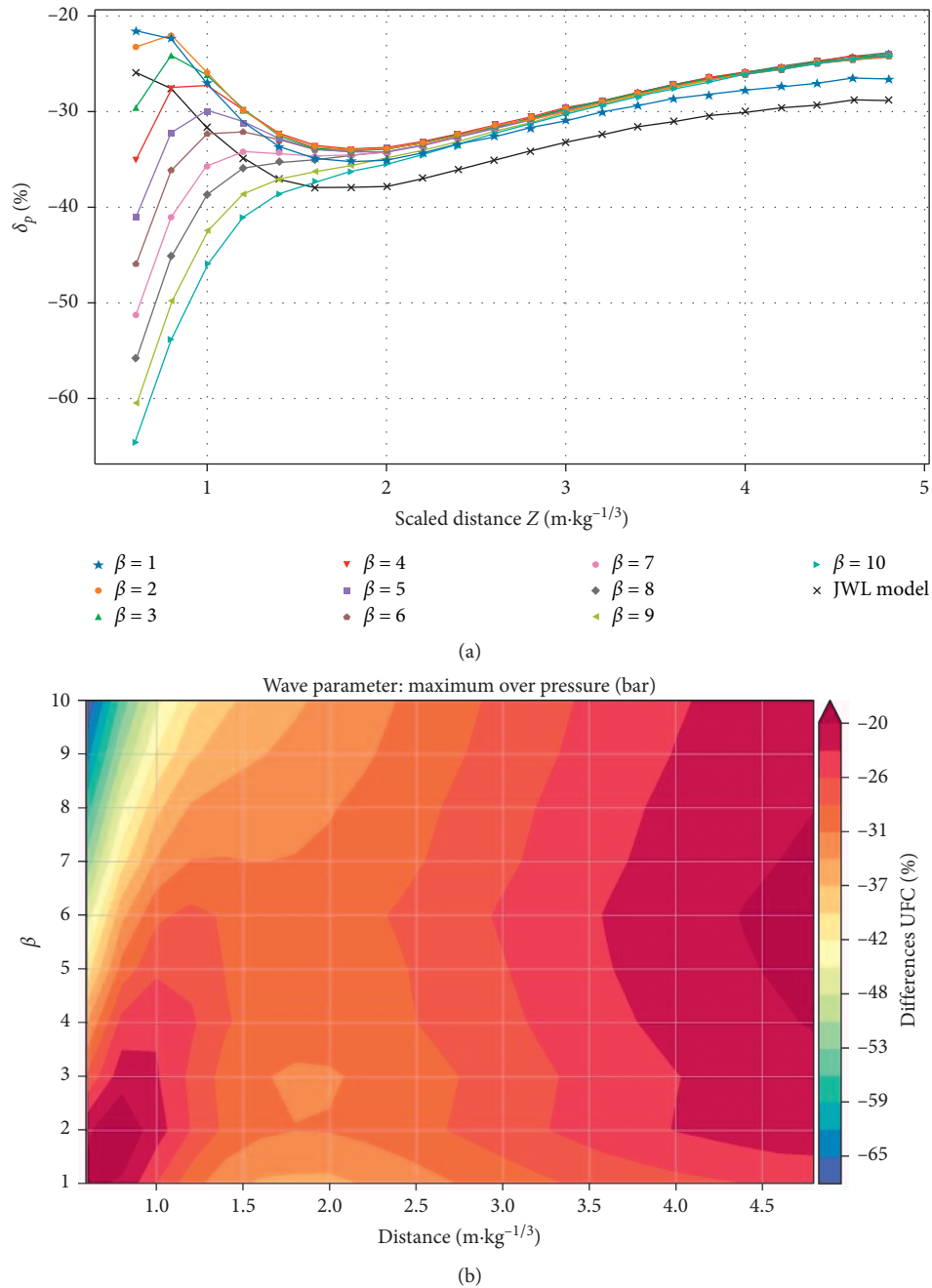


FIGURE 4: Pressure relative difference  $\delta_p$  with UFC-3-340-2 for all beta models as function of distance (a) or distance and  $\beta$  (b).

later stages of the blast wave propagation, the trend is reversed and the  $\beta=10$  model time step decreases due to higher maximum overpressures than for small  $\beta$  balloon at the same time. The dotted curves show the mean value of the time step that account for both parts of the calculation.

The later stage (after 4 ms) supersedes the early one and the mean time step (dotted line) is smaller for  $\beta=10$ ; thus the calculation lasts up to twice as long as the calculation with  $\beta=1$ . The  $k$ -parameter presented in equation (11) should be reduced to 0.1 to ensure numerical stability due to mesh distortion of the radial mesh. Nevertheless, large  $\beta$  balloon models decrease pressure gradients and thus allow

the use of greater  $k$  than for the model with JWL equation of state or small  $\beta$  balloon models. In Figure 11, the increase in  $k$  is taken into account for the calculation of the mean time step in the radial mesh. On the contrary, the Cartesian mesh exhibits no numerical stability issues preventing the calculation from running until the end.

The evolution of the mean time step and thus the CPU time is therefore different for both meshes. Indeed, broadly speaking, the increase in the CFL condition's parameter  $k$  presented previously benefits only the radial mesh. Then, the larger the balloon, the higher the time step and thus the lower the calculation time. On the opposite, this parameter is

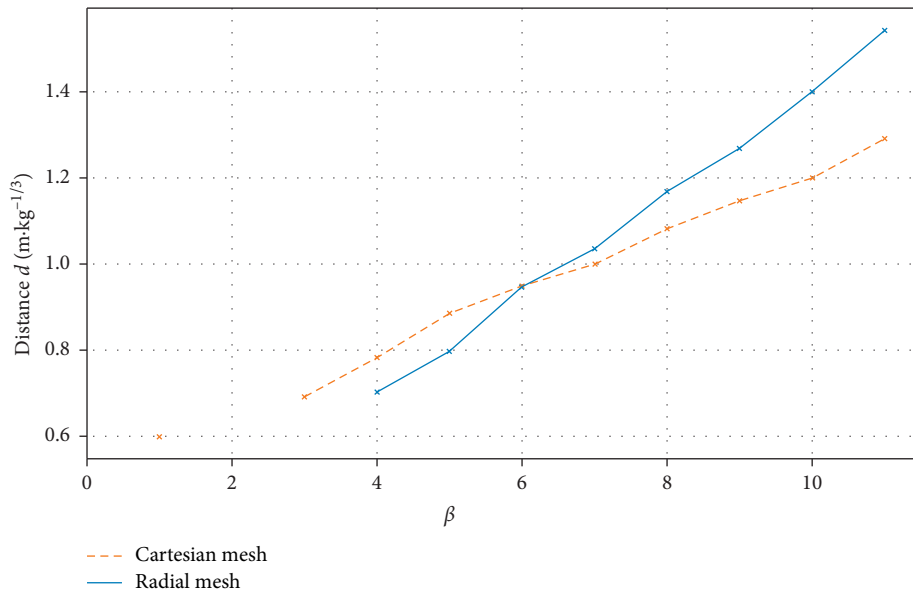


FIGURE 5: Scale distance  $d_p$  as function of  $\beta$ .

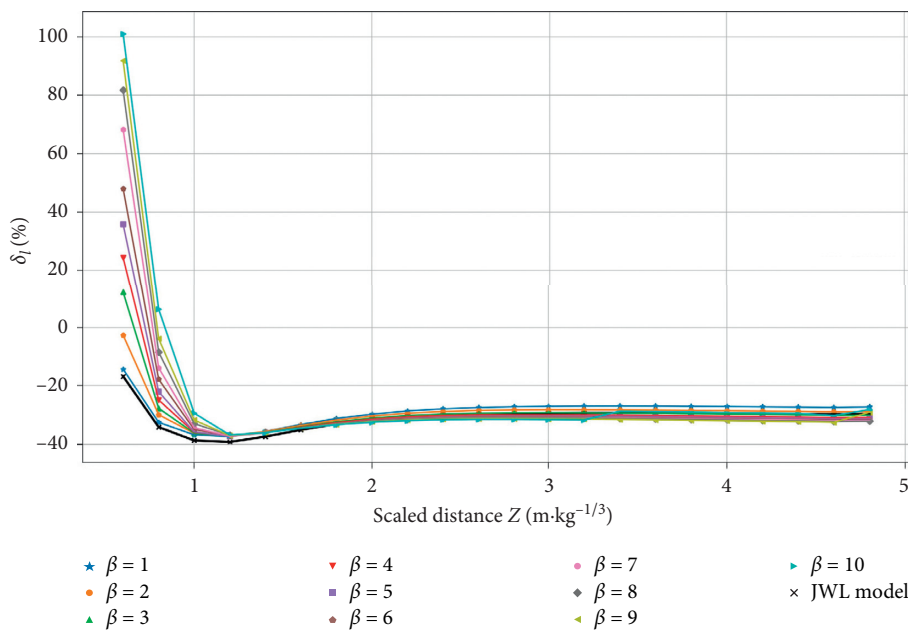


FIGURE 6: Impulse relative difference  $\delta_I$  with UFC-3-340-2 for all  $\beta$  models.

kept as high as possible ( $k = 0.9$ ) for the Cartesian mesh and thus the trend is reversed and the larger the balloon, the lower the time step. To conclude this part, the amplitude of variation of  $\delta_P$  and  $\delta_I$  is really large in the first few dozens of  $\text{cm}\cdot\text{kg}^{-1/3}$ . Nevertheless,  $\beta$  balloon models give better overpressure with respect to the UFC-3-340-2 after a scaled distance  $d$  between  $0.8$  and  $1.5 \text{ m}\cdot\text{kg}^{-1/3}$ . The average values of  $\delta_P$  and  $\delta_I$  give results within 10% for all beta values and cannot be used to evaluate the  $\beta$  model. The first goal of using these methods was to simplify, and thus fasten, the calculation. This is obtained by increasing the numerical stability for the radial mesh. Optimal values of  $\beta$  can be found based on the maximum overpressure. In this respect,

$\delta_P$  is the smallest between  $\beta = 5$  and  $\beta = 6$  for the Cartesian mesh and around  $\beta = 2$  for the radial mesh. This result is important from a practical point of view, when trying to fasten or increase the accuracy of calculation. Unfortunately, the scaled mesh size is the key parameter for calculation which deals with blast wave effects on large structures and the beta balloon solution has to be validated for a wider range of reduced mesh size.

#### 4. Discussion

4.1. Mesh Sensitivity Analysis. All blast wave results are highly dependent on the element size. All presented methods

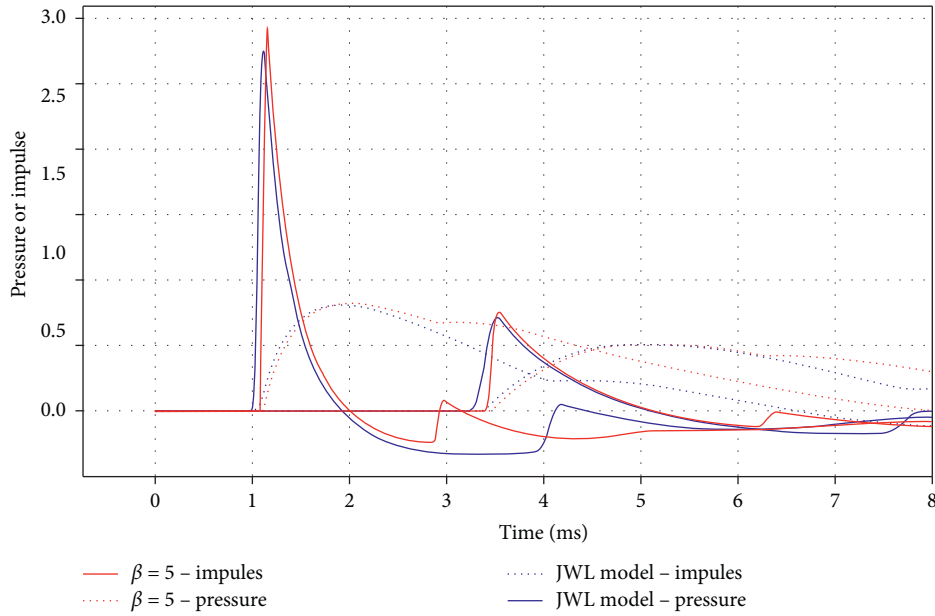


FIGURE 7: Temporal evolution of overpressure and impulse for both JWL and  $\beta = 5$  models at two scaled distances:  $1.4$  and  $2.6 \text{ m}\cdot\text{kg}^{-1/3}$ .

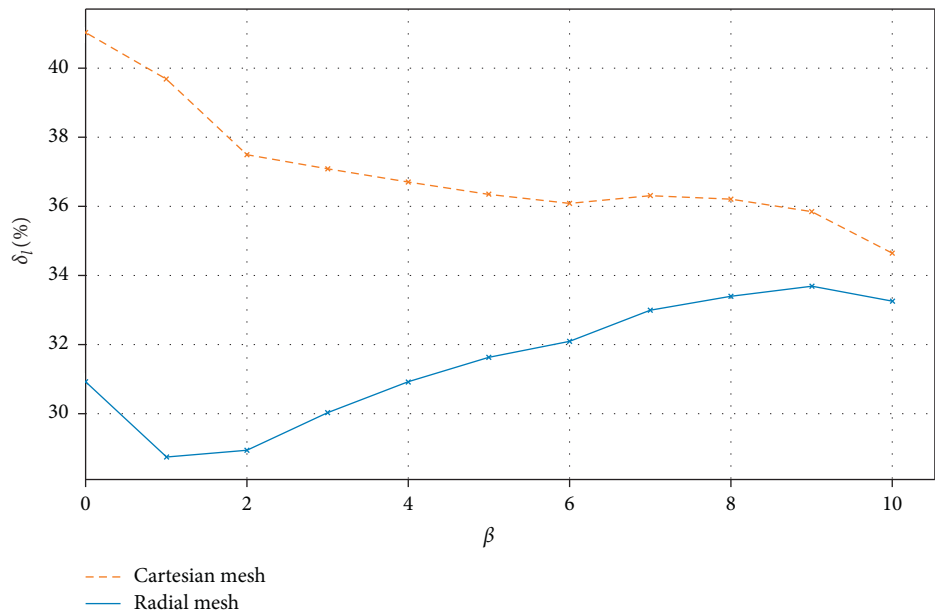


FIGURE 8: Impulse average error with UFC-3-340-2 as a function of balloon size  $\beta$ .

try to enable a larger mesh size for a given accuracy and/or a better accuracy for a given mesh size. A mesh sensitivity analysis is therefore required to evaluate the performances of the proposed beta balloon model with reduced element size from  $1 \text{ mm}\cdot\text{kg}^{-1/3}$  up to  $15 \text{ mm}\cdot\text{kg}^{-1/3}$ .

Firstly, the mean value of  $\delta_P$  is plotted, see Figure 12, for all the following scaled element sizes:  $1 \text{ mm}\cdot\text{kg}^{-1/3}$ ;  $2 \text{ mm}\cdot\text{kg}^{-1/3}$ ;  $5 \text{ mm}\cdot\text{kg}^{-1/3}$ ;  $10 \text{ mm}\cdot\text{kg}^{-1/3}$ ; and  $15 \text{ mm}\cdot\text{kg}^{-1/3}$ . In Figure 12(b), iso-values of relative error to UFC-3-340-2 are extrapolated for intermediate values of mesh size and beta.

On one side, for the smallest scaled mesh size, the numerical damping is limited and small  $\beta$  models are more

accurate by about 20%. On the other, for larger element sizes, the numerical damping is more important and the gain from large  $\beta$  is noticeable with an ideal size of  $\beta = 5$ . As an example, starting at point ( $\beta = 1$ ,  $dx = 7 \text{ mm}\cdot\text{kg}^{-1/3}$ ), the iso-value of the average relative difference with the UFC-3-340-2 shows an extremum in scaled mesh size of  $14 \text{ mm}\cdot\text{kg}^{-1/3}$ . As a rough estimate, twice the scaled mesh size means a twice longer time step and so a reduced computational time. On this model, the total elapsed time of the computation is reduced to 80% as fast without losing any average accuracy. The differences between  $1 \text{ m}\cdot\text{kg}^{-1/3}$  and  $15 \text{ m}\cdot\text{kg}^{-1/3}$  decrease from almost 30% for  $\beta = 1$  to less than 10% for  $\beta = 10$  which indicates that models with large values of  $\beta$  are less sensitive

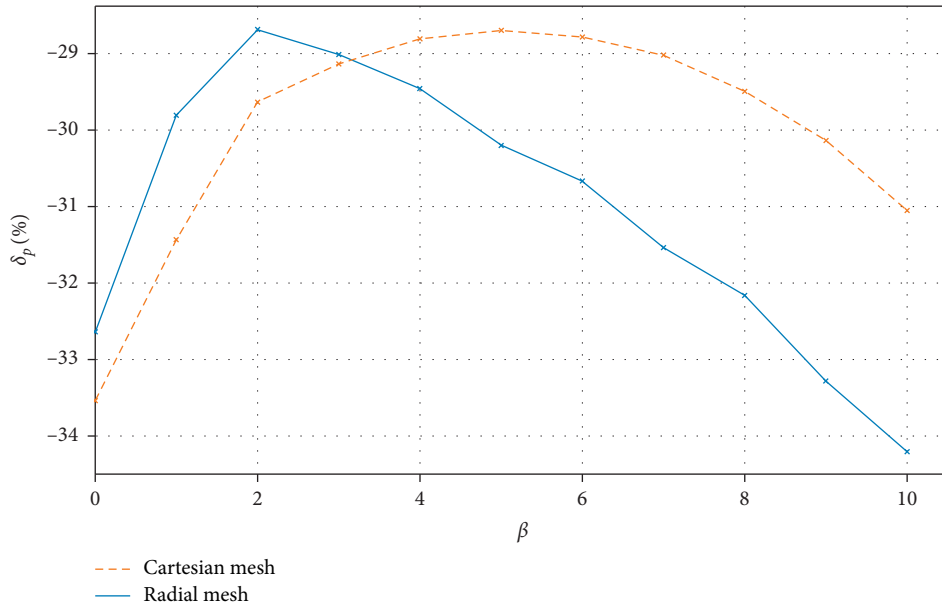


FIGURE 9: Pressure average error with UFC-3-340-2 as a function of balloon size  $\beta$ .

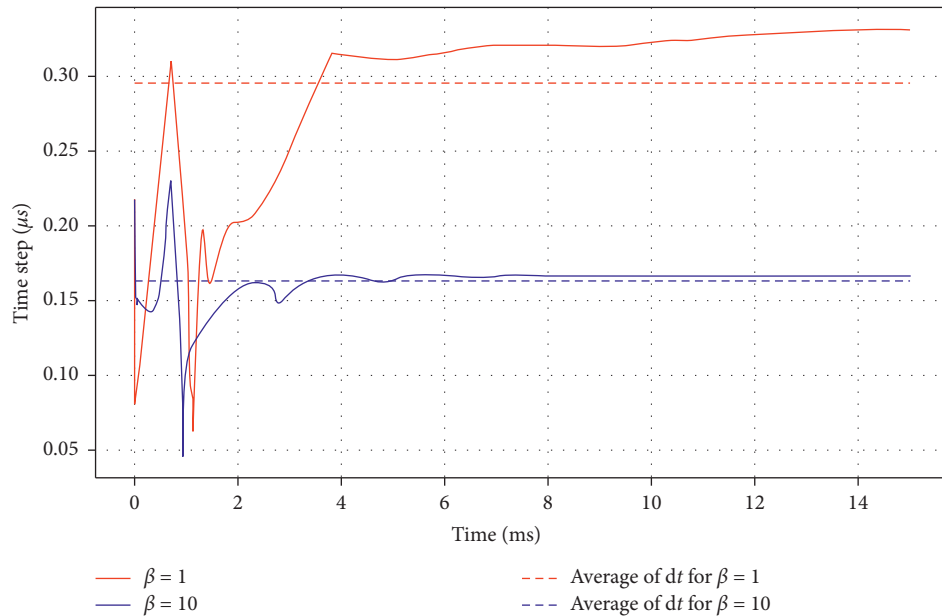


FIGURE 10: Time step temporal evolution for both  $\beta=1$  and  $\beta=10$  balloon models. Radial model.

to element size. In fact, on one side, at least 5 elements are required within the blast wavelength in order to represent properly the blast wave. On the other side, balloons with small values of  $\beta$  create the blast wave with smaller wavelength than balloons with large values of  $\beta$  due to increasing wave length with scaled distances [8, 9]. Thus, small  $\beta$  models require smaller elements to represent the blast profile than large  $\beta$  models and so they are more sensitive to element size.

Figure 13 shows the pressure as a function of time for all mesh sizes at a given scaled distance of  $3 \text{ m} \cdot \text{kg}^{-1/3}$ . The artificial viscosity is more visible for larger mesh sizes. As a

consequence, in spite of the larger mesh size, the impulse will increase and the relative difference with respect to UFC-3-340-2 will decrease. Yet, this is only due to numerical artifacts that should not lead to hasty conclusions.

Figure 14 is an extension of Figure 5 and shows the distance  $d$  where the balloon model becomes more accurate than the JWL model for the same scaled mesh size. All iso-values are computed using the linear extrapolation method. “Never better” means the distance is higher than  $3.7 \text{ m} \cdot \text{kg}^{-1/3}$ , and thus the JWL model is more accurate than every  $\beta$  model, or  $\delta_p(\text{JWL}) < \delta_p(\beta = [1, \dots, 10])$ . On the other side, “always better” means  $\delta_p(\beta = [1, \dots, 10]) < \delta_p(\text{JWL})$ .



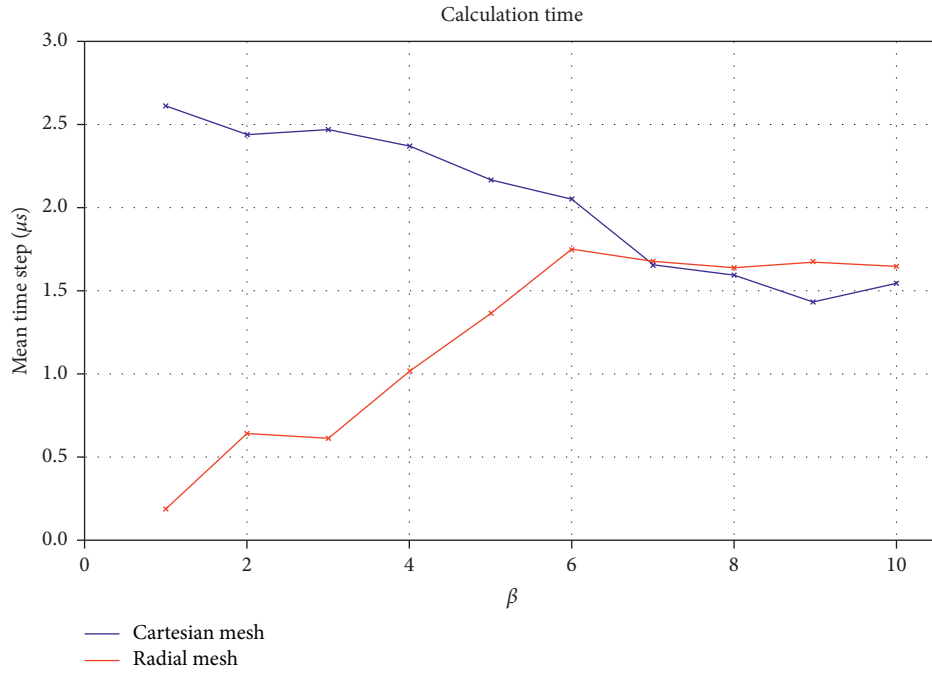
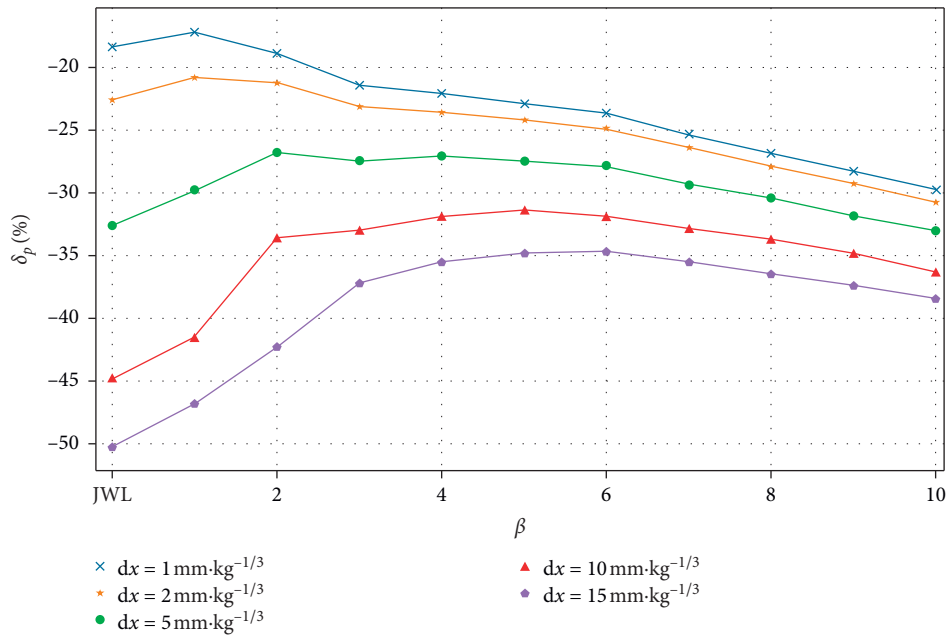


FIGURE 11: Evolution of the mean time step as a function of the balloon size for Cartesian and radial meshes.



(a)

FIGURE 12: Continued.

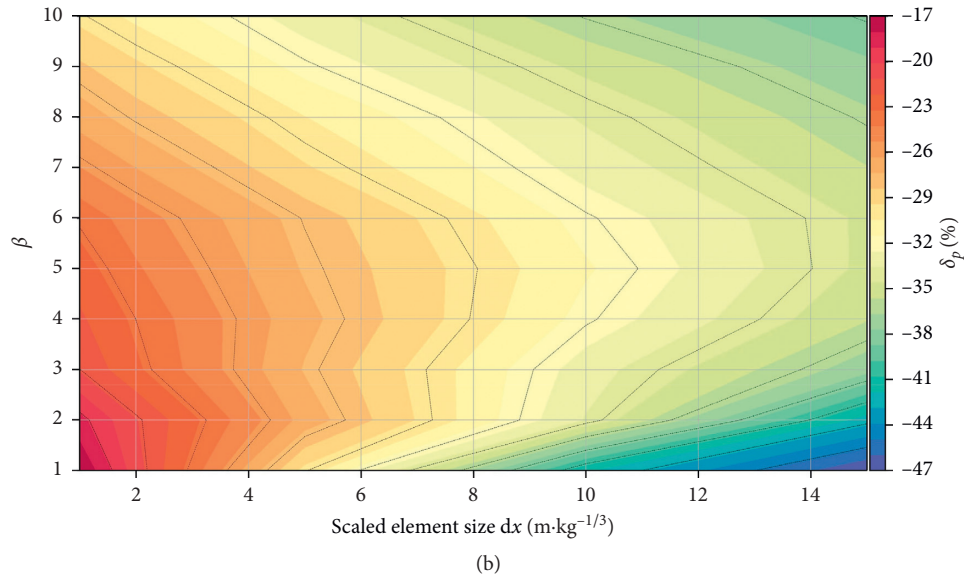


FIGURE 12: Relative peak of overpressure difference with UFC-3-340-2 for all beta parameter and all studied scaled mesh sizes.

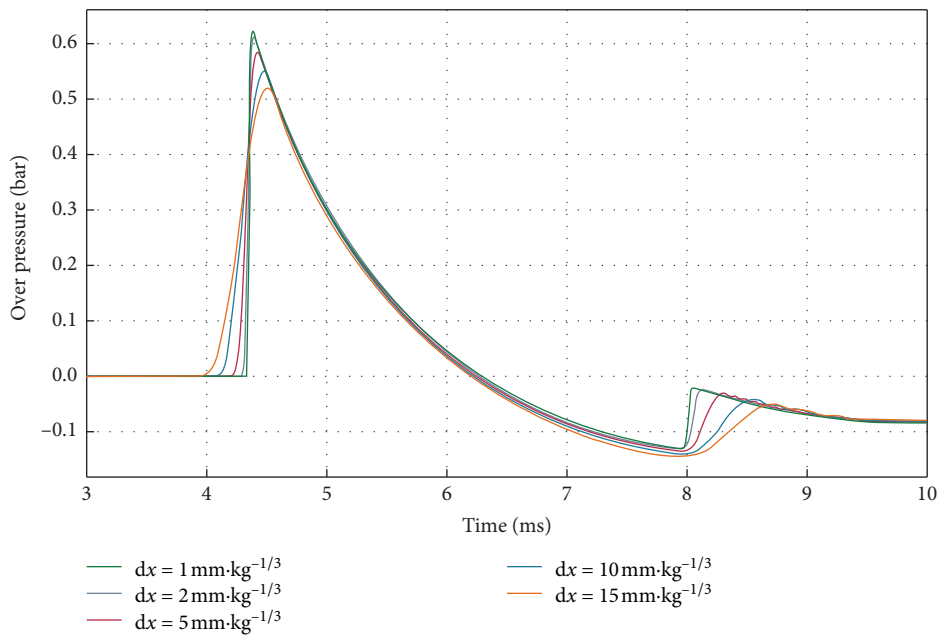


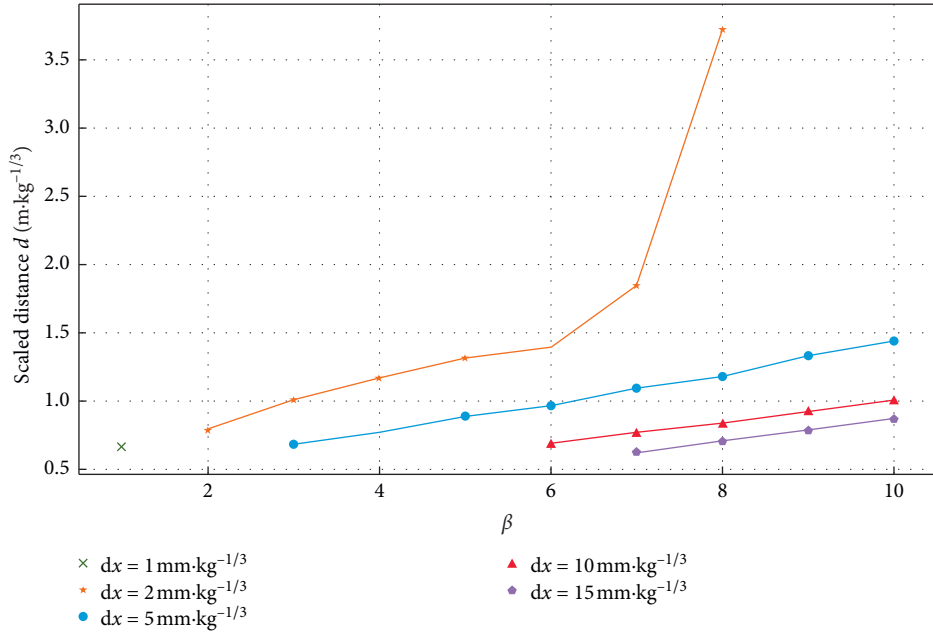
FIGURE 13: Overpressure at  $3 \text{ m}\cdot\text{kg}^{-1/3}$  for  $\beta = 3$ , obtained with various reduced mesh sizes.

The blue domain in Figure 14 shows the parameters leading to a more accurate overpressure estimation obtained by the balloon model with respect to the JWL one. For  $dx = 1 \text{ mm}\cdot\text{kg}^{-1/3}$ , only the  $\beta = 1$  balloon is more accurate than the JWL model so there is only one point on the curve in Figure 11. For all other mesh sizes, the distance  $d$  increases with the mesh size. Nevertheless, for mesh sizes larger than  $5 \text{ mm}\cdot\text{kg}^{-1/3}$ , distance  $d$  is less than  $1.5 \text{ m}\cdot\text{kg}^{-1/3}$ , which is a likely standoff scaled distance for the first target wall.

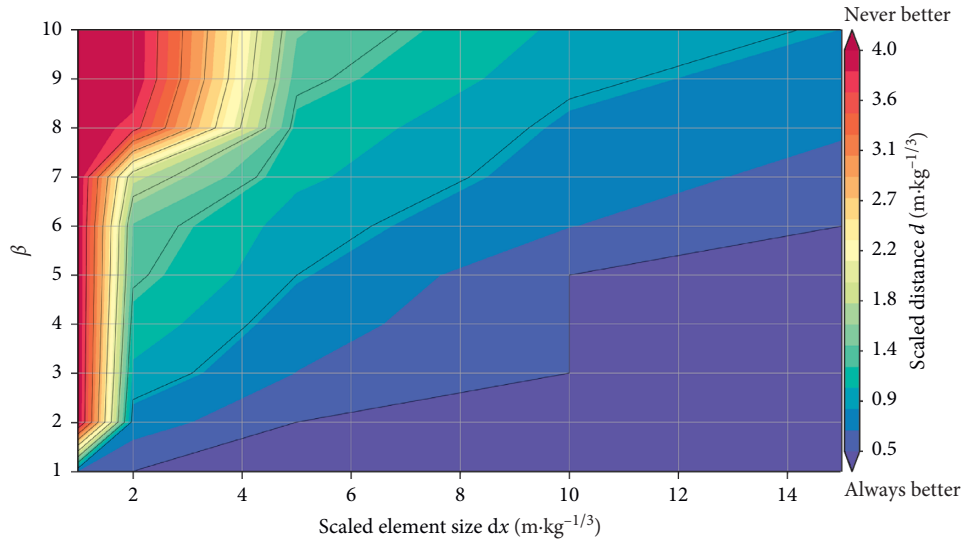
The beta balloon model performs better when the mesh is not good enough and so it takes over the large element size

or the mesh distortion to ensure better accuracy and shorter calculation times.

**4.2. Energy Balance.** The ALE algorithm used in all presented simulations is of interest because it allows a direct coupling between the fluid and the structure. The momentum equation is solved at mesh nodes so the material speed is also calculated at nodes, as it is with the Lagrangian algorithm. It is then easy to interface the fluid and the structure by just equating the material speed of the two parts in the direction normal to the interface. Unfortunately, the



(a)



(b)

 FIGURE 14: Scaled distance  $d$  as function of the beta parameter and the reduced mesh size  $dx$ .

counterpart of this is the non-conservation of the total energy in the fluid part that is related to the discrete integration of the conservation equations made by finite element method [31]. Figure 15 shows the total energy as a function of time for all  $\beta$  models together with the JWL model.

The initial energy is computed on the Cartesian mesh because the mesh is constant from a  $\beta$  value to another. Nevertheless, no relationship giving the specific (nor per unit volume) energy set in the absorbing condition (noted ABS) has been found, so the value is extracted from the  $\beta$  balloon models. In fact a single element model has been made with only one absorbing cell of  $1\text{ m} \times 1\text{ m}$ ; thus the total energy is easily extracted directly per unit volume.  $e_{ABS} = -0.25\text{ MJ}\cdot\text{m}^{-3}$ . In equations (13) and (14), all capital  $E$  stand for total energy and all small  $e$  stand for per unit volume.

$$E_{tot} = \sum_n E_n = E_{tnt} + e_{air}V_{air} + E_{abs}. \quad (13)$$

with  $E_{tnt} = 4.3\text{ MJ}$  the energy of 1 kg of TNT,  $e_{air} = 0.25\text{ MJ}\cdot\text{kg}^{-3}$  the energy of air per unit volume, and  $E_{ABS} = 0.589\text{ MJ}$  the energy of the absorbing elements.

Furthermore, energy values for the axisymmetric model are given per radian and only one half of the spatial domain is modeled. So, for  $\beta = 1$ ,

$$E_{axi} = \frac{E_{tot}}{2\pi} = 15.91\text{ MJ} \cdot \text{rad}^{-1}. \quad (14)$$

The difference in the initial energy balance should be really small. Indeed, one of the strong hypotheses of the  $\beta$  balloon is that the total energy of the high explosive is constant and spread on a larger volume. Furthermore, the

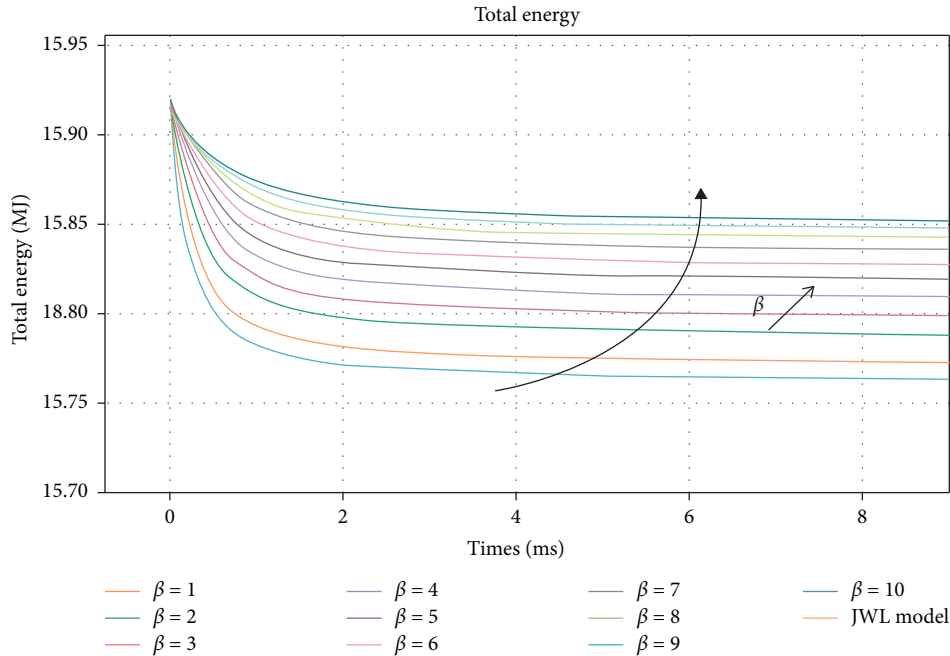


FIGURE 15: Total energy variation as a function of the time. Cartesian mesh.

total volume of numerical domain is also constant in all simulations. As a consequence, the total amount of air is reduced for larger beta model and thus also the initial total energy. This small variation in the amount of air within the simulation explains the small differences at  $t=0$  ms in Figure 15.

The energy loss due to the ALE algorithm in the first millisecond is more significant for small balloons and for the model considering the JWL equation of state. The loss is directly correlated to the actual energy, pressure, and density inside a specific element. As a consequence, the large  $\beta$  balloon spreads more energy and pressure gradients, the loss per element is less important, and thus those models present a better energy balance. The overpressure decay is also less important from 2 ms, which corresponds to a maximum overpressure of about 0.14 MPa. This explains the numerical damping reduction and the stabilization of the energy balance. The presented  $\beta$  balloon models manage to mitigate the numerical damping by spreading the initially high pressure and energy over a larger volume. By reducing the energy per unit volume within a single element, the gradient between two elements is also reduced and thus the energy loss proportional to this gradient is also reduced. The increase in energy balance leads to smaller  $\delta$  as presented in Section 3, especially at larger scaled distances.

## 5. Conclusion

Based on the initial work of Brode and the latest papers, a compressed balloon has been studied to replace the detonation process of high explosive in numerical simulations of blast waves impacting structures. The previous models did not account for the numerical damping acting in every finite element explicit scheme. The main goal of this paper was to

address this issue. To do so, the radius of the ideal gas balloon has been increased up to ten times the initial explosive radius. Two structured meshes were considered: Cartesian and radial. Increasing the size of the compressed balloon reduces all pressure and energy gradients at early stages of the blast wave propagation. The gradient reduction leads to a reduction of artificial viscosity and numerical damping and thus more accurate blast wave at large reduced distances. Indeed, there is a specific scaled distance where the lack of proper equation of state and volume of the detonation product is outweighed by the better conservation of the total energy. After about  $1 \text{ m} \cdot \text{kg}^{-1/3}$ , large compressed balloons start to be in better accordance with respect to the UFC-3-340-2. All blast wave numerical simulations are highly dependent on the mesh size, respecting the trend the smaller the size, the more accurate the result. The presented work enables a larger mesh size for the same accuracy and/or a better accuracy for the same mesh size if the  $\beta$  parameter is increased. To be more specific, it is possible to double the mesh size without losing any accuracy on the maximum overpressure. In practical use, an optimum  $\beta$  has been found to be around  $\beta = 5$  which could allow a reduction of computer time around 80% for equivalent accuracy with respect to the UFC-3-340-2. Furthermore, for an equivalent mesh size, the large beta models reduce the calculation time especially for radial meshes that face a challenge for achieving numerical stability. For radius greater than or equal to six times the initial (Brode) radius, the calculation time is six or seven times faster than the initial calculation with the JWL equation of state used for the relaxation of the detonation gases involved in the modeling of the high explosive charge. In addition, to provide faster computational times, the balloon model does not require any specific knowledge, set of parameters, on the explosive charge except its TNT equivalent.

This compressed balloon approach could be applied on finite volume algorithm which is, theoretically, conservative for the total energy and that does not need artificial viscosity. Some of those algorithms are under investigation but the finite volume-finite element coupling between, respectively, Eulerian and Lagrangian parts is challenging, specifically for industrial and commercial software. Another approach could be to increase the initial energy in order to achieve the wanted blast energy at the time the shock front is impacting the structure but it would lead to inaccurate results at other distances.

## Data Availability

Our article will be published on ResearchGate and Academia an HAL (<https://hal.archives-ouvertes.fr/>).

## Conflicts of Interest

The authors declare that there are no conflicts of interest regarding the publication of this study.

## Acknowledgments

The authors would like to thank the Radioss developing team, especially Daniel Chauveheid for the quality of the answers regarding issues encountered with the finite element software. The authors thank also the DGA (French Armament Procurement) for having co-funded the PhD work.

## References

- [1] W. Fickett and W. C. Davis, *Detonation: Theory and Experiment*, Courier Corporation, Berlin, Germany, 2000.
- [2] M. Aleyaasin, "A predictive model for damage assessment and deformation in blast walls resulted by hydrocarbon explosions," *Advances in Civil Engineering*, vol. 2019, Article ID 5129274, , 2019.
- [3] J. Yan, Y. Liu, and F. Huang, "Improved SDOF approach to incorporate the effects of axial loads on the dynamic responses of steel columns subjected to blast loads," *Advances in Civil Engineering*, vol. 2019, Article ID 7810542, , 2019.
- [4] G. I. Taylor, "The formation of a blast wave by a very intense explosion I. Theoretical discussion," *Proceedings of the Royal Society of London. Series A. Mathematical and Physical Sciences*, vol. 201, pp. 159–174, 1950.
- [5] A. Sakurai, "On the propagation and structure of the blast wave, I," *Journal of the Physical Society of Japan*, vol. 8, no. 5, pp. 662–669, 1953.
- [6] J. M. Dewey, "The air velocity in blast waves from TNT explosions," *Proceedings of the Royal Society of London A: Mathematical, Physical and Engineering Sciences*, vol. 279, pp. 366–385, 1964.
- [7] G. G. Bach and J. H. S. Lee, "An analytical solution for blast waves," *AIAA Journal*, vol. 8, no. 2, pp. 271–275, 1970.
- [8] National Institute of Building Science, "Unified Facilities Criteria (UFC): structures to resist the effects of accidental explosions," *Technical Reports UFC*, vol. 3402 pages, 2014.
- [9] G. F. Kinney and K. J. Graham, *Explosive Shocks in Air*, Springer Berlin Heidelberg, Berlin, Heidelberg, 1985.
- [10] C. N. Kingery and G. Bulmash, *Airblast Parameters from TNT Spherical Air Burst and Hemi-Spherical Surface Burst*, US Army Armament and Development Center, Ballistic Research Laboratory, Berlin, Heidelberg, 1984.
- [11] P. D. Smith and J. G. Hetherington, *Blast and Ballistic Loading of Structures*, Butterworth-Heinemann, Berlin, Heidelberg, 1994.
- [12] T. Rose and P. Smith, "An approach to the problem of blast wave clearing on finite structures using empirical procedures based on numerical simulations," in *Proceedings of the 16th International Symposium on Military Aspects of Blast and Shock*, Oxford, UK, 2000.
- [13] P. Sielicki and M. Stachowski, "Implementation of sapper-blast-module, a rapid prediction software for blast wave properties," *Central European Journal of Energetic Materials*, vol. 12, no. 3, pp. 473–486, 2015.
- [14] P. W. Sielicki, T. Łodygowski, H. Al-Rifaie, and W. Sumelka, "Designing of blast resistant lightweight elevation system-numerical study," *Procedia Engineering*, vol. 172, pp. 991–998, 2017.
- [15] A. Neuberger, S. Peles, and D. Rittel, "Scaling the response of circular plates subjected to large and close-range spherical explosions. part i: air-blast loading," *International Journal of Impact Engineering*, vol. 34, no. 5, pp. 859–873, 2007.
- [16] P. Crawford and B. Dobratz, *LNL Explosives Handbook: Properties of Chemical Explosives and Explosive Simulants*, Lawrence Livermore National Laboratory, Livermore, CA, USA, 1985.
- [17] P. C. Souers and J. W. Kury, "Comparison of cylinder data and code calculations for homogeneous explosives," *Propellants, Explosives, Pyrotechnics*, vol. 18, no. 4, pp. 175–183, 1993.
- [18] E. Jouguet, "Sur la propagation des réactions chimiques dans les gaz," *Journal de Mathématiques Pures et Appliquées*, vol. 7, p. 347, 1905.
- [19] H. L. Brode, "Blast wave from a spherical charge," *Physics of Fluids*, vol. 2, no. 2, p. 217, 1959.
- [20] M. Larcher and F. Casadei, "Explosions in complex geometries—a comparison of several approaches," *International Journal of Protective Structures*, vol. 1, no. 2, pp. 169–195, 2010.
- [21] C. Catlin, M. Ivings, M. S. Myatt, D. Ingram, D. Causon, and L. Qian, *Explosion Hazard Assessment: A Study of the Feasibility and Benefits of Extending Current HSE Methodology to Take Account of Blast Sheltering Technical Reports*, vol. 34, 2001.
- [22] S. Trelat, I. Sochet, B. Autrusson, K. Cheval, and O. Loiseau, "Impact of a shock wave on a structure on explosion at altitude," *Journal of Loss Prevention in the Process Industries*, vol. 20, no. 4–6, pp. 509–516, 2007.
- [23] L. Blanc, S. Santana Herrera, and J. L. Hanus, "Simulating the blast wave from detonation of a charge using a balloon of compressed air," *Shock Waves*, vol. 28, no. 4, pp. 641–652, 2018.
- [24] A. M. Benselama, M. J.-P. William-Louis, and F. Monnoyer, "A 1D-3D mixed method for the numerical simulation of blast waves in confined geometries," *Journal of Computational Physics*, vol. 228, no. 18, pp. 6796–6810, 2009.
- [25] Y. Han and H. Liu, "Finite element simulation of medium-range blast loading using LS-DYNA," *Shock and Vibration*, vol. 2015, pp. 1–9, 2015.
- [26] H. H. Goldstine and J. V. Neumann, "Blast wave calculation," *Communications on Pure and Applied Mathematics*, vol. 8, no. 2, pp. 327–353, 1955.
- [27] J. Tang, "Free-field blast parameter errors from Cartesian cell representations of bursting sphere-type charges," *Shock Waves*, vol. 18, no. 1, pp. 11–20, 2008.



- [28] R. J. LeVeque, *Finite Volume Methods for Hyperbolic Problems*, Cambridge University Press, Cambridge, UK, 2002.
- [29] V. Karlos, G. Solomos, and M. Larcher, “European commission, and joint research centre,” *Analysis of Blast Parameters in the Near-Field for Spherical Free-Air Explosions*, Publications Office, Luxembourg, 2016.
- [30] R. Courant, E. Isaacson, and M. Rees, “On the solution of nonlinear hyperbolic differential equations by finite differences,” *Communications on Pure and Applied Mathematics*, vol. 5, no. 3, pp. 243–255, 1952.
- [31] R. Loubere, “Contribution to Lagrangian and Arbitrary-Lagrangian-Eulerian numerical schemes,” 2013.